STAR-NET
Regional Network for Education
and Training in Nuclear Technology

SAPIENZA
UNIVERSITÀ DI ROMA

CONFERENCE PROCEEDINGS
Modern Trends In Physics

Baku, 01-03 May, 2019

ISSN 2522-4352

Proceedings indexed in the Web of Science Clarivate Analytics System

Dedicated to the 100th anniversary of the Baku State University

GENERAL INFORMATION

Host organization:

Baku State University (BSU), Baku, Azerbaijan

Co-organizers:

1. Ministry of Education of the Republic of Azerbaijan
2. Regional Network for Education and Training in Nuclear Technology (STAR-NET), Vienna, Austria
3. Joint Institute for Nuclear Research (JINR), Dubna, Russia
4. Sapienza University of Rome, Rome, Italy

Topics:

1. Nano, -opto electronics and Materials Science;
2. Theoretical, Mathematical and High Energy Physics;
3. Physical and Technical Foundations of the Alternative Energy Sources;
4. Biological and Medical Physics;
5. Condensed Matter Physics. International Conference

Sponsor:

Baku State University

Conference Site: http://www.mtphysics.org; http://www.mtphysics.az

Editors:

M.A. Ramazanov,	Baku State University, Baku, Azerbaijan
A.H. Kazim-zada,	Baku State University, Baku, Azerbaijan
H.M. Mamedov,	Baku State University, Baku, Azerbaijan
A.A. Slavnov,	V.A. Steklov Mathematical Institute of RAS; M.V.Lomonosov Moscow State University, Moscow, Russia
G. Dvali,	Max-Planck-Institute LMU, Munich, Germany; New-York University, USA
A.E. Lobanov,	Moscow State University, Moscow, Russia; Baku branch of MSU, Baku, Azerbaijan
V.Ch. Zhukovsky,	M.V.Lomonosov Moscow State University, Moscow, Russia
V.A. Huseynov,	Baku State University, Baku, Azerbaijan
V.G. Bagrov,	Tomsk State University, Tomsk, Russia
B.A. Arbuzov,	Skobeltsyn Institute of Nuclear Physics of MSU, Moscow, Russia
D.M. Gitman,	P.N.Lebedev Physical Institute, Moscow, Russia; Institute of Physics, University of Sao- Paulo, Brazil; Tomsk State University, Tomsk, Russia
V.I. Man'ko,	P.N.Lebedev Physical Institute, Moscow, Russia
Luca Di Palma,	Sapienza University of Rome, Rome, Italy
Angelo Chianese,	Sapienza University of Rome, Rome, Italy
A.V. Ruzaev,	Joint Institute for Nuclear Research, Dubna, Russia
A.S. Sorin,	Joint Institute for Nuclear Research , Dubna, Russia
E.M. Shpilevsky,	SSPA, Scientific and Practical Materials Research Centre of NAS of Belarus, Minsk, Belarus
V.E. Rochev,	National Research Centre Kurchatov Institute - Institute of High Energy Physics, Protvino, Moscow Region, Russia
I.V. Ivonin,	Tomsk State University, Tomsk, Russia
A.B. Arbuzov,	Joint Institute for Nuclear Research, Dubna, Russia
M.S. Dvornikov,	N.V. Pushkov IZMIRAN, Troitsk, Moscow Region; Tomsk State University, Tomsk, Russia
A.S. Bhatti,	COMSATS Institute of Information Technology, Islamabad, Pakistan
M.K. Suleymanov,	COMSATS Institute of Information Technology Islamabad, Pakistan
A.A. Khelashvili,	Institute of High Energy Physics of I. Javakhishvili Tbilisi State University, Tbilisi, Georgia
V.I. Berezhiani,	E. Andronikashvili Institute of Physics of I. Javakhishvili Tbilisi State University, Tbilisi, Georgia
T. Inagaki,	Hiroshima University, Hiroshima, Japan
A.N. Kosilov,	Regional Network for Education and Training in Nuclear Technology, Vienna, Austria

H. Ihara,	Kumamoto University, Kumamoto, Japan
S.G. Abdulvahabova,	Baku State University, Baku, Azerbaijan
N.M. Gojayev,	Baku State University, Baku, Azerbaijan
N.F. Gahramanov,	Baku State University, Baku, Azerbaijan
E.A. Masimov,	Baku State University, Baku, Azerbaijan
A.Sh. Abdinov,	Baku State University, Baku, Azerbaijan
V.M. Salmanov,	Baku State University, Baku, Azerbaijan
J.M. Gulizada,	Baku State University, Baku, Azerbaijan
M.N. Aliev,	Baku State University, Baku, Azerbaijan
R.J. Gasimova,	Baku State University, Baku, Azerbaijan
M.A. Jafarov,	Baku State University, Baku, Azerbaijan
F.H. Pashaev,	Baku State University, Baku, Azerbaijan
M.R. Rajabov,	Baku State University, Baku, Azerbaijan
M.B. Muradov,	Baku State University, Baku, Azerbaijan
F.V. Hajiyeva,	Baku State University, Baku, Azerbaijan
Sh.A. Mammadov,	Baku State University, Baku, Azerbaijan
Sh.S. Aghayev,	Baku State University, Baku, Azerbaijan
R.G. Jafarov,	Baku State University, Baku, Azerbaijan
K.I. Alisheva,	Baku State University, Baku, Azerbaijan
E.Sh. Alakbarov,	Baku State University, Baku, Azerbaijan
M.H. Maharramov,	Baku State University, Baku, Azerbaijan
I.V. Gorbunov,	Tomsk State University, Tomsk, Russia
G.A. Safarova,	Baku State University, Baku, Azerbaijan
Sh.A. Shamilova,	Baku State University, Baku, Azerbaijan
Sh.A.Humbatov,	Baku State University, Baku, Azerbaijan
H.A. Shirinova,	Baku State University, Baku, Azerbaijan
A.H. Karimova,	Baku State University, Baku, Azerbaijan

Publisher: © Baku University Publishing House, Baku, 2017
Contacts: Z.Khalilov str. 23, Az1148, Baku, Azerbaijan
Web: http://publish.bsu.edu.az/en Tel: +994 12 539 05 35

TABBLE OF CONTENTS

Mais Suleymanov

DESIGN AND DEVELOPMENT OF HEUSLER ALLOYS FOR MAGNETIC REFRIGERATION APPLICATIONS

Amdulla O. MEKHRABOV* and M. Vedat AKDENIZ
Novel Alloys Design and Development Laboratory (NOVALAB), Department of Metallurgical and Materials Engineering, Middle East Technical University, DumlupinarBlv. No: 1, 06800-Ankara, Turkey

Cooling systems are used in houses, cars, hospitals, defence systems and many other such areas. However, the gases (chlorofluorocarbons and hydrochlorofluorocarbons) present in today's refrigerant systems are harmful to the environment and cause global warming. Moreover, today's cooling technology is expensive and low-efficiency technology. Therefore, new and cost-effective with higher energy efficiencies cooling systems have begun to be developed to eliminate the use of these harmful gases. Among them, magnetic refrigeration has attracted increasing interest in the materials research communities because of its higher cooling efficiency and environmentally friendliness. Full Heusler alloys are magnetic ternary intermetallic compounds with the $L2_1$-type crystal structure. Typically, these alloys undergo a low temperature martensitic transformation (austenite↔martensite), a magnetic transformation (ferromagnetic↔paramagnetic) and relatively high temperature atomic ordering (order↔order and order↔disorder) transformations. After the discovery of the ferromagnetic shape memory (FSM) and giant magnetocaloric effects (GMCE) in Ni-Mn-Ga alloy, Ni-Mn based Heusler alloys have received considerable attention due to their unique magnetic and structural properties. In this present study compositional dependence of structural and magnetic properties of off-stoichiometric Ni-rich Ni-Mn-Ga Heusler alloys have been investigated, in order to determine an alloy composition where a coupled magneto-structural transformation occurs and to measure the MCE near this temperature. Structural and magnetic properties of Ni-Mn-Ga Heusler alloy system were investigated by means of X-ray diffraction (XRD), scanning electron microscopy (SEM) and vibrating sample magnetometer (VSM) measurements.

Key words: Ni-based Heusler Alloys, Magnetocaloric Effect, Magnetic Refrigeration, Relative Cooling Power
PACS: 61.66.-f, 61.82.Bg, 64.70.K, 75.20.En, 75.30.Sg, 81.30.Hd

1. Introduction

Nowadays, in developed countries and communities, energy consciousness are disscussed and taken up at the highest level. Recently, instead of research on the use of limited energy resources in the most efficient manner, researchers are focused on technologies which reduce energy consumption. Instead of conventional gas-cycle refrigeration technology which reduces the energy consumption and increases the efficiency, scientists and engineers have still been working on new cooling technology based on different material properties such as thermoelectric, thermoacoustic, sorption and magnetic cooling. From these technologies, magnetic refrigeration is a technology based on Magnetocaloric Effect (MCE) defined as response by changing the temperature of a solid material in applied magnetic field. Full Heusler alloys are magnetic ternary intermetallic compounds with the $L2_1$-type crystal structure. Typically, these alloys undergo a low temperature martensitic transformation (austenite↔martensite), a magnetic transformation (ferromagnetic↔paramagnetic) and relatively high temperature atomic ordering (order↔order and order↔disorder) transformations. After the discovery of the ferromagnetic shape memory (FSM) and giant magnetocaloric effects (GMCE) in Ni-Mn-Ga alloy, Ni-Mn based Heusler alloys have received considerable attention due to their unique magnetic and structural properties [1-9]. Ni-Mn based Heusler alloys which exhibit GMCE can be used as magnetic refrigerant materials in magnetic refrigerators. Magnetic refrigeration (MR) is an alternative cooling technology which offers high energy efficiency. A large MCE (the change in magnetic entropy, ΔS_M) of 5 $JKg^{-1}K^{-1}$ was reported for Ni-Mn-Ga alloys for the second order magnetic transition (ferromagnetic ↔paramagnetic) [5, 10]. However, the highest ΔS_M values of ~20 $JKg^{-1}K^{-1}$ were obtained at the coupled magnetic (ferromagnetic↔paramagnetic) and structural (martensite↔austenite) transition in Ni-Mn-Ga Heusler alloys [7, 10]. The coupled (magneto-structural) transition can be achieved through compositional tuning of the structural and magnetic transitions temperatures. Ferromagnetism plays a crucial role in magnetocaloric properties and long term aging (near 660 K) is necessary to increase the amount of ferromagnetic $L2_1$ phase in these alloys due to the lower $L2_1$↔B2 transition temperatures of these alloys. It was shown that, stoichiometric Ni_2MnGa alloy undergoes a relatively low temperature martensitic transformation (T_M) at around 202 K, a magnetic transition (T_C) near 376 K, order-order and order-disorder transitions at 1071 K and 1382 K, respectively [11,12]. Near stoichiometric Ni_2MnGa alloys have been investigated thoroughly in literature [13-25]. Upon cooling, a first order structural transformation occurs in Ni-Mn-Ga alloys from the cubic structure to a tetragonal [12] or orthorhombic [26, 27] structure. T_M of Ni-Mn-Ga alloys span over a wide range, from 160 K to 620 K [18, 29-31] and these temperatures are very sensitive to composition of alloy system. Tuning of T_M is possible by changing the Ni/Mn/Ga composition ratios and it was well established that T_M increases with increasing e/a (electron concentration) [3].

The goal of the present study is to investigate compositional dependence of structural and magnetic properties of off-stoichiometric Ni-rich Ni-Mn-Ga Heusler alloys, to determine an alloy composition where a coupled magneto-structural transformation occurs and to measure the MCE near this temperature. Structural and magnetic properties of Ni-Mn-Ga Heusler alloy system were investigated by means of X-ray diffraction (XRD), scanning electron microscopy (SEM) and vibrating sample magnetometer (VSM) measurements.

2. Experiment

Polycrystalline samples were prepared by conventional arc melting method in argon atmosphere. The method involves repeated melting of the elements in an argon atmosphere. All the alloys were prepared from high purity (%99.99) starting elements of Ni, Mn and Ga. The mixture of elemental components was placed on a copper-hearth inside the arc melting chamber. Prior to each melting, the chamber was evacuated to $5Ç10^{-5}$ mbar and backfilled with argon gas for four times. Melting was done under a protective Argon atmosphere and alloys were melted turned over and remelted four times to ensure homogeneity. After the melting process, the alloys were cut into ~1.5 mm slices by using a linear precision saw.

XRD measurements were conducted to determine the effects of composition and heat treatment on crystal structures and atomic ordering in the samples at RT. XRD was performed using a Rigaku diffractometer in which Cu-Kα radiation was utilized in the diffraction angle (2θ) range of 20-100°. Scanning electron microscopy (SEM) studies were performed using a JSM-6400 Electron Microscope (JEOL) equipped with NORAN System 6 X-ray Microanalysis System &Semafore Digitizer. Energy dispersive spectroscopic analyses (EDS) were employed to determine the general compositions of alloys. Optical microscopy is employed in the investigation of the microstructure of the samples. Magnetization measurements were conducted on ADE Magnetics Model EV9 Vibrating Sample Magnetometer (VSM) with an optional temperature controller. These measurements were performed as a function of temperature and magnetic field up to 22 kOe. Measurement of MCE is done by providing following steps: i) determination and characterization of the phase transitions that occur in the sample by M-T measurements. M-T measurements were performed on both cooling and heating in order to determine the order of these transitions; ii) performing isothermal M-H measurements in the vicinity of the phase transition temperatures. Prior to each isothermal measurement the sample was heated above T_C to achieve demagnetization; iii) calculation of ΔS_M values by employing the M-H data in Equation (3) given below.

3. Results and discussion

The compositions of the investigated Ni-Mn-Ga Heusler alloys determined by EDS analyses are given in Table 1 together with calculated e/a values and lattice parameters.

For Ni-Mn-Ga alloys e/a ratio have been calculated by using following equation,

$$e/a = \frac{10\times(Ni\ at.\%)+7\times(Mn\ at.\%)+3\times(Ga\ at.\%)}{100} \tag{1}$$

Number of 3d+4s electrons for Ni, Mn and Ga was taken as 10, 7 and 3 respectively. Calculated lattice parameters are consistent with the previously reported values [28, 31]. XRD measurements were performed to investigate the effect of composition on crystal structure of the Ni-rich Ni-Mn-Ga alloys. P. J. Webster et al. determined the crystal structure of the cubic parent phase of Ni_2MnGa alloy as the $L2_1$ structure [12]. XRD patterns of the as-cast $Ni_{49+x}Mn_{25-x}Ga_{26}$ (x=0, 5 and 7) alloysare given in Figure 1. All the fundamental peaks related to the A2 phase are present in the XRD pattern of the as-cast $Ni_{49}Mn_{25}Ga_{26}$ alloy. In the A2 phase, Ni, Mn and Ga atoms are randomly distributed over the body centered lattice sites of the $L2_1$ –type crystal structure. Because of the texturing in the polycrystalline Ni-Mn-Ga alloys the reflections related to the next nearest neighbor ordering and unique to the fully ordered $L2_1$ phase were not observed in many cases. Conventionally, although the observed reflections indicate the presence of A2 or B2 phases, the structure was treated as if it was the fully ordered $L2_1$ phase [32].

Table 1. Compositions, lattice constants (a, b and c) and e/a for investigated Ni-Mn-Ga alloys.

Nominal Composition	Ni (at.%)	Mn (at.%)	Ga (at.%)	a=b (E)	c (E)	e/a
$Ni_{49}Mn_{25}Ga_{26}$	48.91	25.13	25.96	5.82	-	7.43
$Ni_{54}Mn_{20}Ga_{26}$	54.15	20.06	25.79	7.65	6.62	7.59
$Ni_{56}Mn_{18}Ga_{26}$	55.77	18.20	26.03	7.65	6.62	7.63

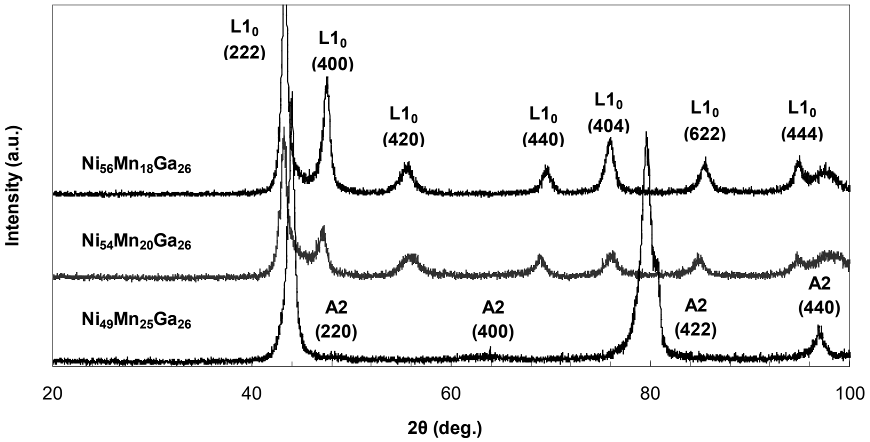

Figure 1. XRD pattern for the as-cast $Ni_{49+x}Mn_{25-x}Ga_{26}$ (x=0, 5 and 7) alloys measured at RT.

The XRD data shown in Figure 1 shows that as-cast $Ni_{49}Mn_{25}Ga_{26}$ alloy (e/a=7.43) has the cubic $L2_1$-type crystal structure, on the other hand, both the as-cast $Ni_{54}Mn_{20}Ga_{26}$ (e/a=7.59) and $Ni_{56}Mn_{18}Ga_{26}$ (e/a=7.63) alloys have martensitic $L1_0$-type crystal structure at RT. It is evident from Figure 1 that, the splitting between the (222) and (440) peaks is more pronounced and the intensity of (400) peak is higher in $Ni_{56}Mn_{18}Ga_{26}$ alloy compared to the $Ni_{54}Mn_{20}Ga_{26}$ alloy. This can be attributed due to the higher e/a value of $Ni_{56}Mn_{18}Ga_{26}$ alloy. Magnetic field and temperature dependence of magnetization are measured for the as-cast $Ni_{49+x}Mn_{25-x}Ga_{26}$ (x=0, 5 and 7) alloys with the intention of characterizing the magnetic behavior and phase transitions in these alloys. M-H curve at RT and temperature dependence of magnetization M-T curve for the as-cast $Ni_{54}Mn_{20}Ga_{26}$ alloy is given in Figure 2. It is evident from Figure 2(a) that as-cast $Ni_{54}Mn_{20}Ga_{26}$ alloy exhibit a strong ferromagnetic behavior, because large magnetization is obtained in this alloy on application of relatively small magnetic fields and in addition to that, magnetization saturates above a certain field.

It can be seen from Figure 2(b) that the magnetic transition in Ni-rich $Ni_{54}Mn_{20}Ga_{26}$ alloy have characteristics typical of a first order magneto-structural transition because of the following reasons. The magnetization of as-cast $Ni_{54}Mn_{20}Ga_{26}$ alloy drops significantly from high values to nearly zero. As shown in this Figure, $Ni_{54}Mn_{20}Ga_{26}$ alloy is ferromagnetic at RT and a significant decrease in magnetization near T_C is expected to occur in this alloy. Therefore, the decrease in magnetization at around 345 K for $Ni_{54}Mn_{20}Ga_{26}$ alloy can be attributed to the ferromagnetic↔paramagnetic transition. A marked hysteresis observed in cooling and heating data (Fig. 2(b)) indicates the occurrence of a first order transition near 345 K for the $Ni_{54}Mn_{20}Ga_{26}$ alloy. At RT, the $Ni_{54}Mn_{20}Ga_{26}$ alloy have tetragonal $L1_0$-type structure determined by XRD (Figure 1) and it is assumed that the low symmetry $L1_0$-type structure transforms to a high symmetry $L2_1$-type structure as a result of the first order martensitic transformation around 345 K for the $Ni_{54}Mn_{20}Ga_{26}$ alloy. The relatively high temperature $L2_1$-type structure could not be confirmed with XRD measurements because of the absence of a temperature control unit in the diffractometer employed in this investigation. Consequently, it can be assumed that magnetic and martensitic transformations merge and a ferromagnetic ($L1_0$) ↔ paramagnetic ($L2_1$) transformation occurs around 345 K in the $Ni_{54}Mn_{20}Ga_{26}$ alloys. Coupling of structural and magnetic phase transitions similar to the ones observed in this study were reported for various Ni-rich Heusler alloys [7].

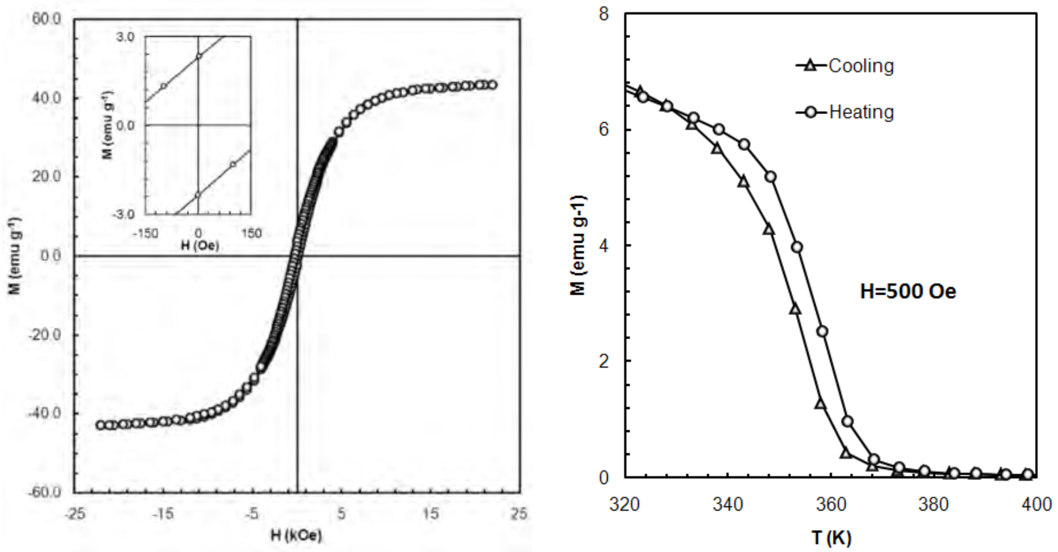

(a) **(b)**

Figure 2. (a)Hysteresis loop for the as-cast $Ni_{54}Mn_{20}Ga_{26}$ alloy measured at RT; inset shows the hysteresis in more detail; (b) Temperature dependence of magnetization for the as-cast $Ni_{54}Mn_{20}Ga_{26}$ alloy under a constant magnetic field of 500 Oe.

In order to calculate ΔS_M values around the coupled martensitic and magnetic transformations (magneto-structural transformation) the isothermal M-H measurements were performed. Experimentally determined M(H) isotherms can be used to calculate ΔS_M by employing following equation [33],

$$\Delta S_m(T,H) = S_M(H_1,T) - S_M(H_0,T) = -\int_{H_0}^{H_1} \left(\frac{\partial M}{\partial T}\right)_H dH \tag{2}$$

It is evident from Equation (2) that, ΔS_M is directly proportional to $(\partial M/\partial T)$. The greatest change in magnetization with respect to temperature is expected to occur at the magneto-structural transition, therefore, the ΔS_M values are calculated in the vicinity of this transition. For magnetization measurements made at discrete temperature intervals, ΔS_M can be calculated by numerical integration of equation (2), which can be given by

$$\Delta S_m(T,H) = \sum_i \frac{M_{i+1}(T_{i+1},H) - M_i(T_i,H)}{T_{i+1} - T_i}\Delta H \tag{3}$$

Where $M_{i+1}(T_{i+1}, H)$ and $M_i(T_i, H)$ represent the values of the magnetization in a magnetic field H at the temperatures T_{i+1} and T_i, respectively. Equation (3) can be used for calculations of ΔS_M from M-H isotherms when the sample undergoes a second order transformation since at the first order transformation it is infinite. Nevertheless, it is goes to infinity only in ideal first-order phase transitions and in real materials it has finite values. This allows one to use Equation (3) in this case.

Figure 3(a) show the isothermal M-H curves measured for the $Ni_{54}Mn_{20}Ga_{26}$ alloys. The M-H curves were acquired in 2K steps in applied fields up to 22 kOe. Samples were heated above T_C prior to each measurement in order to achieve demagnetization and a paramagnetic↔ferromagnetic transition is observed in Figure 3 for the as-cast $Ni_{54}Mn_{20}Ga_{26}$ alloys. At high temperatures M-H curves are linear and magnetization values are relatively small. Upon cooling there is a marked increase in magnetization values. Another point worth mentioning is that, there is a significant increase in the curvature of the M-H curves upon cooling. The isothermal M-H curve measured for the $Ni_{54}Mn_{20}Ga_{26}$ alloy were used to estimate the ΔS_M values as a function of temperature for this alloy.

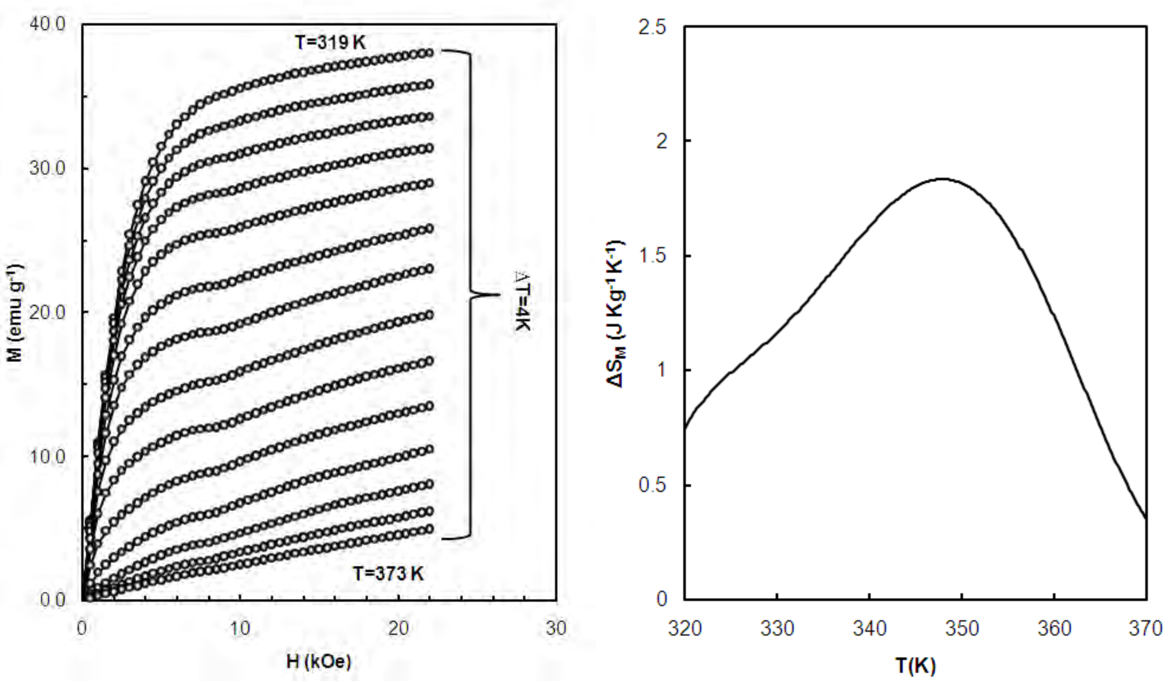

(a) **(b)**

Figure 3. (a)Magnetization of the as-cast $Ni_{54}Mn_{20}Ga_{26}$ alloy as a function of magnetic field measured in the temperature interval of 319 K<T<373 K, ΔT=4K for clarity; (b) Magnetic entropy change of the as-cast $Ni_{54}Mn_{20}Ga_{26}$ alloy as a function of temperature.

The ΔS_M dependencies on temperature were calculated by using Equation (3) in a magnetic field change of $\Delta H = 22$ kOe. ΔS_M is given as a function of temperature in the vicinity of the magneto-structural transition for the as-cast $Ni_{54}Mn_{20}Ga_{26}$ alloy in Figure 3(b). It is evident from Figure 3(b) that ΔS_M has its maximum near 345 K and this temperatures coincide with the magneto-structural transitions temperature for the $Ni_{54}Mn_{20}Ga_{26}$ alloy. The maximum values of $|\Delta S_M|$ is determined as 1.84 $JKg^{-1}K^{-1}$ for $Ni_{54}Mn_{20}Ga_{26}$ alloys. A.A. Cherechukin et al. reported that besides the saturation magnetization, $|\Delta S_M|$ is also correlated by the Mn content [7].

4. Conclusion

Compositional dependence of structural, magnetic and magnetocaloric properties of off-stoichiometric Ni-rich Ni-Mn-Ga full Heusler alloys have been investigated. It was shown that the partial substitution of Ni for Mn in $Ni_{54}Mn_{20}Ga_{26}$ alloy increases the e/a electron concentration and a ferromagnetic martensite alloy with a $L1_0$-type structure was observed in this alloy at RT. As-cast $Ni_{54}Mn_{20}Ga_{26}$ alloy exhibit a strong ferromagnetic behavior and saturation magnetization, M_{sat}, decreases with the substitution of Mn with Ni in these alloys. Magnetic measurement reveal that this alloy undergo a magneto-structural transition from ferromagnetic ($L1_0$) to paramagnetic ($L2_1$) near RT. XRD results indicate that at RT, the $Ni_{54}Mn_{20}Ga_{26}$ alloy have tetragonal $L1_0$-type ferromagnetic structure. Therefore it is assumed that the low symmetry $L1_0$-type ferromagnetic structure transforms to a high symmetry $L2_1$-type paramagnetic structure as a result of the first order martensitic transformation around 345 K for the $Ni_{54}Mn_{20}Ga_{26}$ alloy. The coupling of the magnetic and structural transformations observed in off-stoichiometric Ni-Mn-Ga alloys is important for the occurrence of MCE effect in these alloys. A maximum change in magnetic entropy, ΔS_M, of 1.84 $JKg^{-1}K^{-1}$ was determined at the vicinity of magneto-structural transition temperatures of $Ni_{54}Mn_{20}Ga_{26}$ alloys.

References

1. Moya X., Planes A., Krenke T., Acet M., Morin M., ZarestkyJ. L, Lograsso T.A., Phys. Rev. B. 74, 6(2006).
2. Vasil'ev A.N., Khovailo V.V., Dikshtein I.E., Shavrov V.G., Buchelnikov V.D., Matsumoto M., Suzuki S., Takagi T., Tani, J. Phys. Rev. B.59, 1113 (1999).
3. Chernenko V. A., Scr. Mater.40, 523 (1999).
4. Hu F., Sun J., App. Phys. Lett.76, 3460 (2000).
5. Marcos J., Manosa L., Casanova F., Batlle X., Labarta A., Martinez B., Phys. Rev. B. 66, 224413 (2002).
6. Albertini F., Cirafici S., FranceschiE. A., Napoletano M., Paouzi A., Pareti L., Solzi M., J. Magn. Magn. Mater.272-276, 2047 (2004).
7. CherechukinA. A., Matsumoto M., BuchelnikovV. D., Phys. Lett. A326, 146 (2004).
8. Jiang C., Muhammad Y., Deng L., Wu W., Xu H., Acta Mater. 52, 2779 (2004).
9. Zhou X., Li W., Kunkel H.P., Williams G., J.Magn. Magn. Mater.293, 854 (2005).
10. ParetiL., Solzi M., Albertini F., Paouzi A., Eur. Phys. J. B.32, 303 (2003).
11. OverholserR. W., Wuttig M., Neumann D.A., Scr. Mater.40, 1095 (1999).
12. WebsterP. J., ZiebeckK. R. A., TownS. L., PeakM. S., Philos. Mag.B49, 295 (1984).
13. HosodaH., Sugimoto T., Ohkubo K., MiuraS., MohriT., MiyazakiS.,Int. J. Appl. Electromagn. Mech.12, 9 (2000).
14. MullnerP., Chernenko V.A., Kostorz G., J. Appl. Phys.95, 1531 (2004).
15. Pirge G., Hyatt C.V., Altintas S., J. Mater. Proc. Tech.155-156, 1266 (2004).
16. HosodaH., Wakashima K., Sugimoto T., Miyazaki S., Mater. Trans.43, 852 (2002).
17. Chernenko V.A., Pons J., Segui C., Cesari E., Acta Mater.50, 53 (2002).
18. KokorinV.V., Wutting M., J. Magn. Magn. Mater.234, 25 (2001).
19. KiraT., Murata K., Shimada T., JeongS-J., Inoue S., KoterazawaK., InoueK., Mater. Sci. Forum 426–432, 2207 (2003).
20. HosodaH., Sugimoto T., Miyazaki S., Trans. Mater. Res. Soc. Japan.26273 (2001).
21. LiangY., Kato H., Taya M., Mori T., Scr. Mater.45, 569 (2001).
22. HeczkoO., Straka K., Ullako K., J. Phys. IV France.112, 9459 (2003).
23. ChernenkoV. A., L'vovV., PonsJ., Cesari E., J. Appl. Phys.93, 2394 (2003).
24. BesseghiniS., Pasquale M., Passaretti F., Sciacca A., Villa E., Scr. Mater.44, 2681 (2001).
25. Stipcich M., Manosa L., Planes A., Morin M., Zarestky J., Lograsso T., Stassis C., Phys. Rev. B 70, 054115 (2004).
26. SozinovA., LikhachevA. A., Lanska N., Ullakko K., Appl. Phys. Lett.80, 1746 (2002).
27. UllakkoK., Ezer Y., Sozinov A., Kimmel G., YakovenkoP., LindroosV.K., Scripta Mater. 44, 475 (2001).

28. WebsterP. J., ZiebeckK. R. A.in “Alloys and Compounds of d-Elements with Main Group Elements”, Springer-Verlag Berlin Heidelberg, 1988.
29. MartynovV. V., KokorinV. V., J. Phys. III.2, 739 (1992).
30. ManosaL., Comas A.G., Obrado E., PlanesA., Phys. Rev. B.55, 11068 (1997).
31. PonsJ., ChernenkoV. A., Santamarta R., Cesari E., Acta Mater.48, 3027 (2000).
32. ChernenkoV.A., Cesari E., Pons J., Segui C., J. Mat. Res.15, 1496 (2000).
33. Vansovskii S.V., Magnetism, Israel Program Sci. Translations, Jerusalem, 1974.

***Corresponding author**: amekh@metu.edu.tr

PHOTOVOLTAIC PROPERTIES OF In_2O_3-InSe-Pt SYSTEM

A.G.KYAZIM-ZADE[1], V. M.SALMANOV[1*], A.G.GUSEINOV[1], R.M.MAMEDOV[1],
A.A.SALMANOVA[2], N.D.DASHDAMIROVA[1]
[1]Baku State University, Z.Khalilov str., 23, Baku, Azerbaijan, Az1148
[2] Azerbaijan State University of Oil and Industry, Azadliq ave. 20, Baku, Azerbaijan, AZ1010

Based on a layered InSe crystal, In_2O_3-n-InSe-Pt diode structures were fabricated. The thickness of the transparent and conducting In_2O_3 layer was 650ç1200 A^0 and had the following physical parameters: ρ~ (0.2ç7) Ω·cm, μ = (4ç12) $cm^2/V{\cdot}s$, n~(1÷2,6)10^{20} cm^{-3}. The current-voltage characteristics, capacitance-voltage characteristics, and In_2O_3-n-InSe-Pt photosensitivity spectra were experimentally studied. It was shown that the coefficient of rectification of the studied samples reaches ~100 at U = 0.5 V, the photosensitivity spectra cover the range from 1 to 0.7 microns.

Keywords: InSe, diode structure, current-voltage, voltage-capacitance characteristics, photosensitivity spectra.
PACS: 72.40. +*w*, 72.80.Ey

1. Introduction

InSe layered semiconductors have recently become the subject of intense research. Along with nonlinear phenomena previously discovered in these substances at high levels of optical excitation, InSe crystals are currently very promising materials as photoconverters and ultrafast receivers [1, 2]. The ultrathin layers of indium monoselenide have unique properties that qualitatively distinguish it from the other two-dimensional crystals. In two-dimensional samples of indium monoselenide, the electron mobility is the highest (~ 7000 $cm^2/V{\cdot}s$). This material parameter is extremely important from the point of view of improving the speed of devices that can be created on its basis. Due to the peculiarities of chemical bonds, these crystals have a low concentration of surface electronic states and surface effects, such as adsorption, are less pronounced than in conventional isotropic crystals. In addition, InSe single crystals have a high elasticity at a thickness of d<100 μm, so that photoconverters based on them can be mounted on flexible substrates. According to scientists, indium monoselenide has wide prospects for further practical use, since its thin layers combined with graphene and some other functional two-dimensional crystals, have every chance to compete with silicon (Si) as the main material of modern electronics. Another interesting property of indium monoselenide is that, unlike dichalcogenides and silicon, this crystal is a so-called direct-gap semiconductor (E_g~1.30 eV), which makes them a promising material for creating solar energy converters.

This paper is devoted to the experimental study of some electrical and photoelectric properties of In_2O_3-InSe-Pt diode structures based on InSe thin films.

2. Experiment

The investigated n-InSe crystals were grown by the Bridgman method. Samples with thicknesses of 10 ç 80 μm and geometrical dimensions of 3x3 mm were made by splitting from large ingots. According to Hall measurements at 300 K, the mobility reaches a value of ~700 $cm^2/V{\cdot}sec$, a specific resistance of ρ ~ 80 ç 300 Ω·cm, the concentration of current carriers is n~$1{\cdot}10^{14}$ cm^{-3}. Transparent and conductive In_2O_3 layers were obtained by evaporating a mixture of In_2O_3 powder (90%) and indium (10%) using the method described in [3]. The use of a transparent In_2O_3 layer as an ohmic contact was stimulated by the fact that the refractive indices of InSe single crystals and the In_2O_3 layer are close. If we take into account that the coefficient of light absorption by InSe single crystals in a wide range of the spectrum is α~10^3 cm^{-1}, this allows efficient conversion of light when the structure is illuminated from the side of the transparent In_2O_3 layer, with a relatively small thickness of the base region. The evaporation of In_2O_3 was carried out under oxygen pressure of ~$8{\cdot}10^{-5}$ mm Hg. The deposition rate of the films was ~20 A^0/min. The thickness of the In_2O_3 layer was measured by an interference microscope and was 650 ç 1200 A^0. The In_2O_3 layers with the same thickness on the glass substrate had the following parameters: ρ~(0.2ç7) Ω·cm, μ=(4ç12) $cm^2/V{\cdot}s$, n~(1ç2.6)·10^{20} cm^{-3}. The transmission of such layers of In_2O_3 in the visible spectral region reached 80%. Thermal evaporation was applied to the back surface of the sample by a translucent Pt layer, which forms a Schottky barrier with n-InSe. A gold contact comb was applied on top of the platinum, which was connected to a chain using silver paste.

3. Results and discussion

The volt – ampere characteristic (CVC) of the structures studied is shown in Fig. 1. The direct branch of the CVC starting at 50 mV obeys the usual expression $I = I_0\, exp(qU/\beta kT)$, where the typical value of the saturation current is $I_0 \approx 9 \cdot 10^{-6}$ A/cm^2, and the ideality coefficient is $\beta \approx 2.88$, which agrees well with the data of [4]. The deviation from the indicated dependence at relatively high voltages seems to be due to the influence of the spreading resistance, which is $R_S \approx 110$ Ω. The rectification coefficient for some samples reaches ~100 at U = 0.5 V. The indicated value of I_0 corresponds to the height of the Schottky barrier ~0.6 eV. The relatively large value of β suggests that at 300 K, the contribution of the thermal current is not dominant and it is difficult to determine the height of the Schottky barrier from the temperature dependence of the parameter I_0. In the range of 300ç370 K and at voltages of U<0.5 V, the temperature dependence of the forward current can be represented as $I \approx exp(-\Delta E/kT)$, where the parameter $\Delta E \approx 0.32$ eV and agrees well with the depth of the donor levels in InSe. The reverse branches of the CVC in the double logarithmic scale are linear, with an inclination of ~0.7.

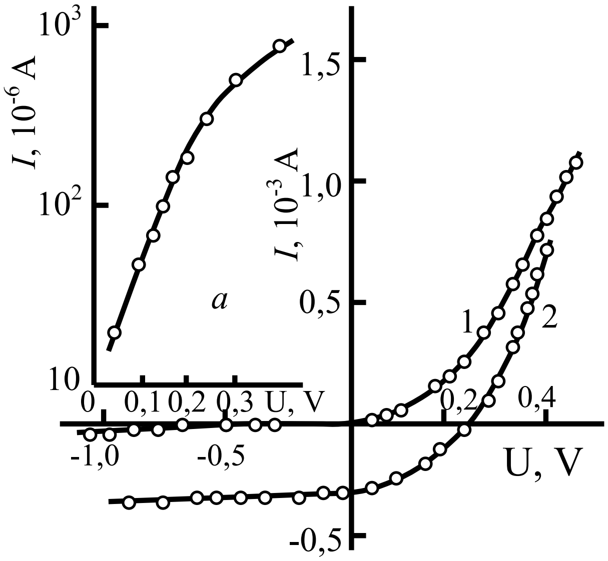

Fig.1. CVC of the contact In_2O_3-n-InSe-Pt in the dark (1) and under illumination (2): a - a direct branch of the CVC in a semi-log scale.

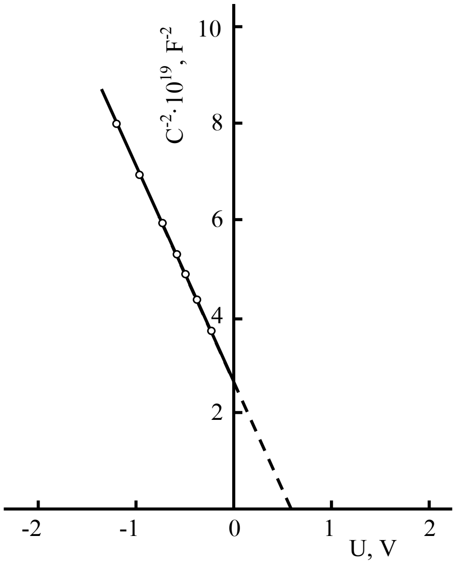

Fig.2. The volt is the farad dependence of the contact In_2O_3-n-InSe-Pt at 300K.

The capacitance-voltage characteristics of the structures studied at a frequency of 1 MHz are linear on the scale $C^{-2}=f(U)$ (Fig. 2). In this case, the diffusion potential gets the value $V_D \approx 0.52$ V. The thickness of the space charge layer, estimated from the value of the capacitance at zero voltage, is $W \approx 3.12$ μm. The photosensitivity spectrum when the structure is illuminated from the side of the In_2O_3 layer is shown in Fig.3. The measurements were carried out at a constant photon flux using a double monochromator with a holographic grating. A 250 watt halogen lamp was used as the light source. Adding to the experimental spectrum of the calculated, allows you to determine the main parameters of the structures used, namely, the diffusion length of minority carriers.

When calculating the photosensitivity spectrum, we took into account two contributions in the case of uniform illumination of a semiconductor with a thickness d in a direction parallel to the axis-c.

a) the current contribution of nonequilibrium carriers is described by the diffusion equation

$$D\frac{\partial^2 n}{\partial x^2}-\frac{n-n_0}{\tau}=-\alpha\Phi_0\,exp(-\alpha x) \tag{1}$$

where D is the diffusion coefficient of the generated photocarriers, Φ_0 is the photon density, n_0 and n are hole concentrations in the equilibrium and non-equilibrium states, respectively; τ – is the lifetime of nonequilibrium carriers.

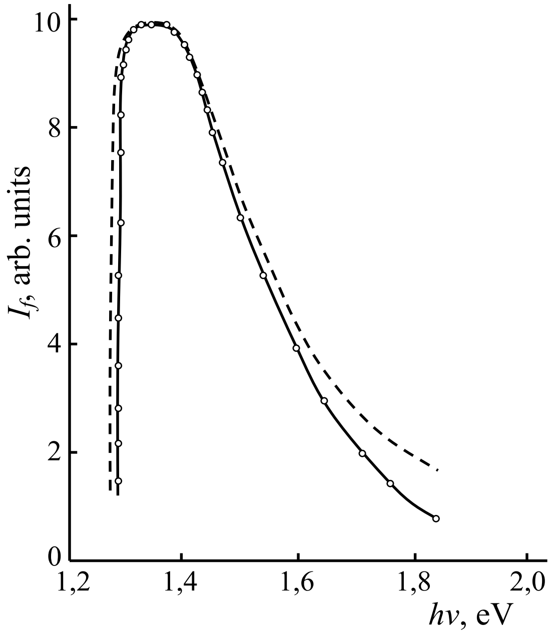

Fig.3. The spectral distribution of the photosensitivity of the contact In_2O_3-n-InSe-Pt when illuminated from the side of In_2O_3 (the solid curve). The solid curve is an experiment, the dotted one is a calculation.

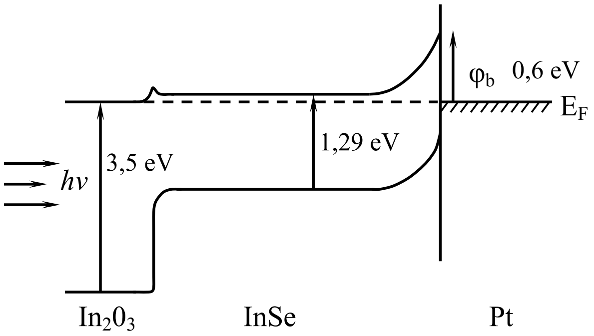

Fig.4. Energy diagram of the system In_2O_3-n-InSe-Pt.

Taking into account the boundary conditions:

$$n|_{x=d}=n_0 \quad \text{и} \quad \frac{dn}{dx}|_{x=0}=0\,.$$

We have the following solution [4]:

$$I_p=q\Phi_0\frac{\alpha^2L_p^2}{\alpha L_p^2-1}\left[\frac{1}{ch\frac{\alpha}{L_p}}-exp(-\alpha d)(1+\frac{1}{\alpha L_p}th\frac{d}{L_p})\right] \tag{2}$$

b) the contribution of the generated photocarriers in the depleted layer with thickness W:

$$I_W=q\Phi_0\,exp(-\alpha d)(1-exp(-\alpha W)) \tag{3}$$

Full photocurrent $I_\Phi=I_p+I_W$.

The calculated curve (Fig. 3, the dashed curve) is consistent with the experimental curve for the following parameters: W = 3 μm, d = 12 μm, L_p = 2 μm.

Energy diagram of the system In_2O_3-n-InSe-Pt presented in Fig.4. As can be seen from the figure, the band gap of In_2O_3 is 3.5 eV. The magnitude of the potential barrier determined from the IV characteristics of structures in the dark is ~ 0.61 eV.

Estimates conducted by us on the basis of theoretical and experimental data show that the light conversion factor, based on the In_2O_3-n-InSe-Pt system, reaches ~ 6%.

4. Conclusion

The electrical and photoelectric characteristics of the In_2O_3-n-InSe-Pt diode structure were studied experimentally and their main parameters were determined: rectification coefficient, volume charge layer thickness, diffusion length of minority charge carriers, photosensitivity region. From the energy diagram, the In_2O_3 band gap is determined, which turned out to be 3.5 eV. Estimates show that the light conversion ratio to In_2O_3-n-InSe-Pt reaches a value of ~ 6%.

References

1. Kyazim-zade A.G., Aqayeva A.A., Salmanov V.M., Moxtari A.H. Inorganic materials. 43, 12, 1-5, (2007).
2. Shuming Yang and David F. Kelley. J. Phys, Chem. B, 109, 12701 -12708, (2005).
3. Katerynchuk V.M., Kudrynskyi Z.R. Semiconductor Physics, Quantum Electronics & Optoelectronics. 15, 2, 214-217, (2012).
4. Evtodiev I.G., Caraman I.U., Davidescu D., Dafinei A., Nedeff V., Caraman M., Cuculescu E. Journal of optoelectronics and advanced materials. 11, 6, 797 – 812, (2009).

***Corresponding author**: *vagif_salmanov@ yahoo.com*

DEPENDENCE OF PHOTOCONDUCTIVITY ON THE ELECTRICAL FIELD IN n-InSe

R.F.BABAYEVA

Azerbaijan State University of Economics (UNEC), Istiqlaliyyat avenue, 6, Baku, Azerbaijan, AZ 1001

The main characteristics of photoconductivity in indium monoselenide crystals with different initial dark resistivity were experimentally investigated at temperatures of 77ç300 K and electric field strengths of $E \leq 2.5\cdot 10^3$ V/cm. In high-resistance crystals at temperatures below 200ç250 K, under the action of an electric voltage corresponding to a non-linear region of a static I – V characteristic, the effect of an electric field on the photoconductivity was detected. A model is proposed that qualitatively satisfactorily explains the experimental results obtained.

Keywords: single crystal, semiconductor, intrinsic photoconductivity
PACS: 72.40.+W; 64.70.K, 75.20.En,

1. Introduction

Indium monoselenide crystals (n-InSe) are one of the promising semiconductor materials for optoelectronics and solar energy [1-2]. The study of various aspects of the photoelectric properties of this semiconductor has considerable scientific and practical interest.

The present paper reports experimental results on the effect of an electric field on the photoconductivity of n-InSe crystals undoped and erbium doped.

2. Experiment

Samples scaled from various large single-crystal unalloyed (with a specific dark resistance at 77 K $\rho_0 \approx 10^3$ç10^7 $\Omega\cdot$cm) and doped with erbium (with $N_{Er} \approx 10^{-5}$ç10^{-1} at.%) ingots had the shape of a rectangular parallelepiped. Their thickness in the direction perpendicular to the (001) plane of the crystal [3] did not exceed ~ 350 μm, and the transverse dimensions along this plane were ~6.00x5.00 mm x mm. The current contacts located on the sample surfaces opposite in the (001) plane were created by soldering tin and indium, as well as applying silver paste. When measuring the beam of light falling on them and the current flowing through them were directed perpendicular to the natural layers - the (001) plane of the crystal.

The measurements were carried out in the region T≈77ç300 K, with illuminations of monochromatic light with different wavelengths (λ) and intensity (I_0), using an installation assembled on the basis of an MDR-12 type monochromator, with a special electronic-computer system. At the same time, the wavelength and intensity of light incident on the sample under study varied within λ=0.30ç2.00 μm and $I \approx 5\cdot 10^0$ç$5\cdot 10^2$ Lx, and the electric field intensity was $E \approx 1.0\cdot 10^1$ç$2.5\cdot 10^3$ V/cm. A further increase in the value of E was limited by the effect of bistable switching in the sample under study [4]. The spectrum and lux-ampere characteristic of photoconductivity were measured in all the studied samples by measuring stationary photoconductivity.

3. Results and discussion

It has been established that in the low-temperature region (T≤200ç220 K) at voltages (U), corresponding to the initial linear section of the static current - voltage characteristic ($U<U_{1-2}$ [5]) and low illuminances, the main characteristics of the photoconductivity of different samples of both groups (undoped and doped erbium) crystals are different.

In undoped crystals, with increasing initial (taking place at 77 K) values of specific dark resistance (ρ_0), the photoconductivity spectrum expands to a longer wavelength, and the magnitude and duration of the photoconductivity relaxation time increase significantly (Fig. 1, curve 1; Fig. 2 curves 1 and 2).

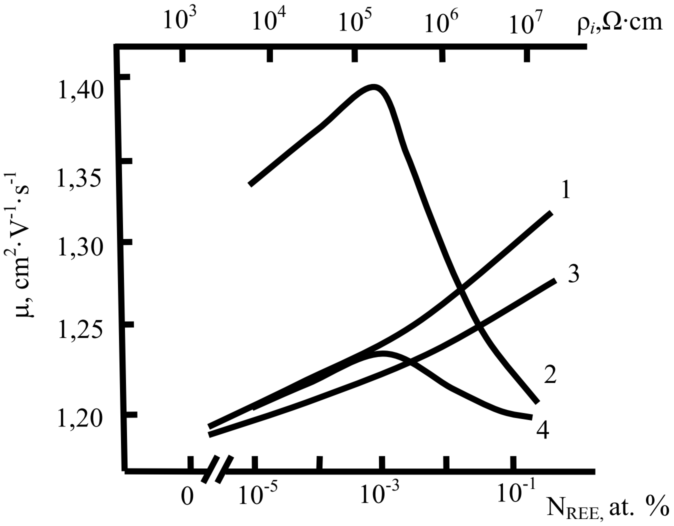

Fig. 1. Dependence of the long-wave boundary (λcr) of the photoconductivity spectrum on the initial resistivity value (ρ_0) in undoped (curves 1 and 3) and impurity content (N_{Er}) in erbium-doped (curves 2 and 4) n-InSe single crystals at different values electrical voltage.
T=77 K; λ = 0.95 μm; Φ=0.15 Φ_m; 1, 2 - $U<U_{1-2}$; 3, 4 - $U \geq U_{PLT}$.

In n-InSe<Er> crystals, the dependences of the main characteristics of photoconductivity on the N_{Er} value are non-monotonic (Fig. 1, curve 2 and Fig. 2, curves 3 and 4) and the maximum deviation relative to that occurring in the lowest-resistance undoped crystal is observed at $N_{Er} \approx 10^{-3}$ at.% (Fig. 1, curve 2 and Fig. 2, curve 3). The n-InSe<Er> crystals with $N_{Er} \approx 10^{-1}$ at.% in their photoelectric characteristics are close to undoped crystals with the lowest ρ_0. In addition, they manifest themselves as crystals with more stable and reproducible photovoltaic parameters and characteristics. With an increase in T and I_0, the features of photoconductivity found in high-resistance unalloyed and doped erbium with $N_{Er} \leq 10^{-2}$ at.% crystals gradually disappear.

In the region of low T and weak I_0, when the stresses create a noticeable injection, in both groups of crystals, the influence of the electric field on the photoconductivity characteristics is observed (Fig. 1, curves 3, 4 and Fig. 2, curves 5 and 6). Moreover, in undoped crystals, the dependence of photoconductivity on E increases with increasing ρ_0, and with increasing I_0 and T, weakening, disappears. In the latter case, the photoconductivity characteristics of all crystals, regardless of the ρ_0 value, coincide with the corresponding photoconductivity characteristics of undoped crystals with the lowest ρ_0.

The effect of the electric field on the photoconductivity in both groups of crystals becomes more noticeable at voltages greater than the voltage of the complete filling of traps (U_{PLT}) [5], in samples with more high-injecting current contacts. With increasing E in high-resistance undoped and doped erbium with $N_{Er} \leq 10^{-2}$ at.% crystals, the photoconductivity characteristics gradually approach the characteristics for crystals with the lowest ρ_0 or with $N_{Er} \approx 10^{-1}$ at.%, respectively.

In the studied crystals, the changes in the photoconductivity characteristics caused by the action of the injecting electric field are not memorizing. In contrast, the changes detected by doping are irreversible.

A static analysis of the experimental results shows that the observed dependences of the photoconductivity characteristics of indium monoselenide crystals on the electric field are not caused by any effects of a strong electric field, or only by the interaction of non-equilibrium charge carriers with different point centers [6, 7]. In this case, it is also necessary to take into account the spatial heterogeneity of the investigated crystals, i.e. the presence of chaotic random macroscopic defects in them. These defects, which have arisen as a result of weak (van der Waals) connections between neighboring natural crystal layers, in turn determine the presence of recombination and drift barriers in the free energy zones of the semiconductor. Therefore, in addition to the due to inter band generation, in such a semiconductor sample, photoconductivity due to tunneling through recombination barriers of nonequilibrium charge carriers can also occur.

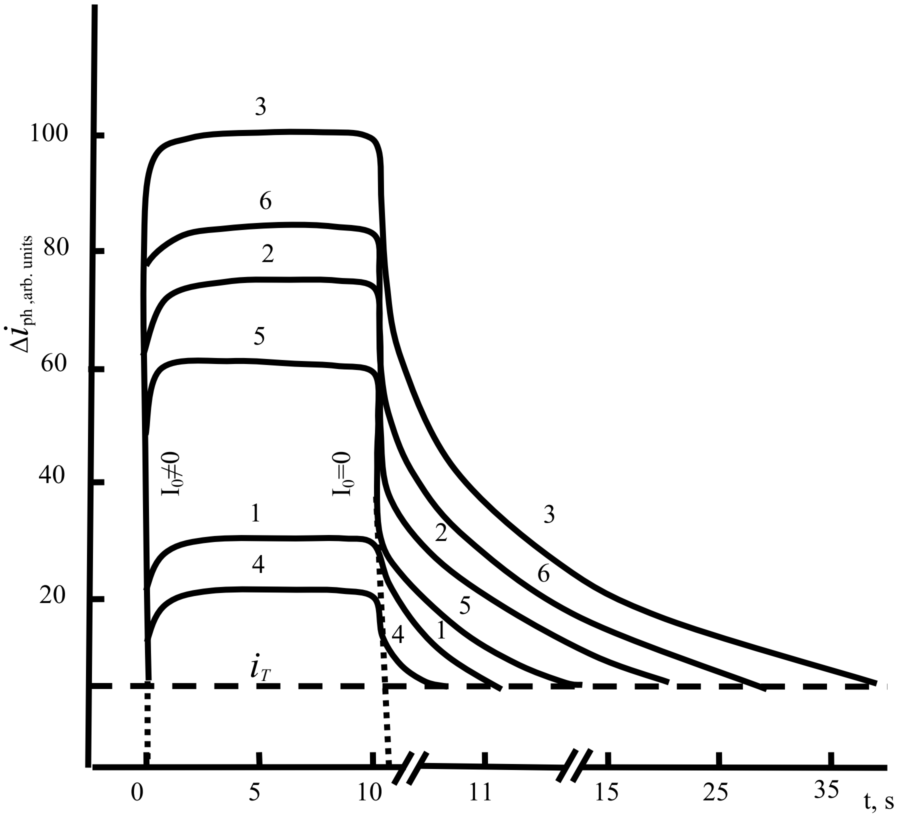

Fig.2. Kinetics of photoconductivity in undoped (curves 1, 2, and 5) and doped with erbium (curves 3, 4, and 6) with different initial values of resistivity (ρ_0) and impurity content (N_{Er}), respectively, n-InSe single crystals at different values of electrical voltage.

T=77 K; Φ=0.15 Φ_m;
ρ_0, $\Omega\cdot$cm: 1 - $3\cdot 10^3$; 2, 5 - $2\cdot 10^7$.
N_{Er}, at.%: 1, 2, 5 - 0; 3, 6 - 10^{-3}; 4 - 10^{-1}.
1, 2, 3, 4 - $U<U_{1-2}$; 5, 6 - $U \geq U_{PLT}$.

The latter causes the expansion of the photoconductivity spectrum towards longer wavelengths. Within the framework of such a two-barrier energy model, the sharp dependence of photoconductivity on the light intensity at low illuminances is explained by light straightening of the drift barriers [8]. At high electrical voltages, the excess charge of the injected carriers, gradually compensating for the volume charges of macroscopic defects, reduces their effect on the photoconductivity characteristics. In erbium-doped crystals, the ions of the introduced impurity, accumulating on macroscopic defects, increase their size. Therefore, with an increase in N_{Er}, first (at $N_{Er} \leq 10^{-3}$ at.%) the effect of macroscopic defects on photoconductivity increases, and then (at $N_{Er} > 10^{-3}$ at.%) due to overlapping of the space charge regions of neighboring macroscopic defects - decreases [9].

4. Conclusion

In conclusion, it can be noted that the influence of the electric field on the photoconductivity characteristics of indium monoselenide crystals is due to the partial compensation of the space charge of the chaotic macroscopic defects existing in them.

References

1. Tamalampudi S.R., Lu Y.Y., Kumar U.R., Sankar R., Liao C.D., Moorthy B.K., Cheng C.H., Chou F., Chen Y.T., Nano letters 14, 2800 (2014).
2. Milutinovic A., Lazarevic Z.Z., Jakovljevic M., Hadzic B., Petrovic M., Gilic M., Dobrowolski W.D., Romcevic N.Z., Journal of Physics and chemistry of solids 89, 120 (2016).

3. Abdinov A.Sh., Babayeva R.F., Semiconductors 52, 1662 (2018), ISSN 1063-7826.
4. Abdinov A.Sh., Babayeva R.F., News of the Baku University, series of physico-mathematical sciences 3, 139 (2009).
5. Lampert M, Mark P., Injection currents in solids, Moscow: World, 1973, 416 p.
6. Conuell E., Kinetic properties of semiconductors in strong electric fields, Moscow: World, 1970, 384 p.
7. Vorob'ev, L.E., Danilov, S.N., Zegrya, G.G., Firsov, D.A., Shalygin, V.A., Yassievich, I.I., Beregulin, N.V., Photoelectric effects in semiconductors and quantum-confined structures, Saint Petersburg: Science, 2001, 248 p.
8. Kazimzade A.G., Panaxov M.P., Tagirov V.I., Technical Physics Letters 6, 1040 (1980)
9. Shklovskii, B.I. and Efros, A.L., Electronic properties of doped semiconductors, Moscow: **Science**, 1979, 416 p.

Corresponding author: babaeva-rena@yandex.ru

INFLUENCE OF EXTERNAL AND INTRACRYSTALLINE FACTORS ON THE MOBILITY OF CHARGE MEDIA IN n-InSe SINGLE CRYSTALS

A.Sh. ABDINOV[1], R.F. BABAYEVA[2*]
[1]*Baku State University, Z. Khalilov str., 23, Baku, Azerbaijan, Az1148,*
[2]*Azerbaijan State University of Economics (UNEC), Istiqlaliyyat avenue, 6, Baku, Azerbaijan, AZ 1001*

Effect of temperature, electric field, light, doping, and the initial conductivity of the sample on the mobility of the main charge carriers was experimentally investigated in crystals of indium monoselenide. Based on a comparative analysis of the results obtained, their scientific discussion was conducted.

Keywords: main charge carriers, electrophysical parameters, injection, charge volume
PACS:72.80.-r; 72.20.-I; 64.70.K, 75.20.En,

1. Introduction

Due to the layered structure of the n-InSe single crystals [1], in addition to their characteristics for many other semiconductors [2], they also have a number of specific features reflected in the electrophysical properties and parameters [3-5]. The study of the influence of various factors - temperature, light, electric field, doping, initial conductivity on generation-recombination processes, and drift of free charge carriers is one of the powerful tools for identifying these features and clarifying their physical mechanism.

Based on this, in the present work, we carried out complex experimental studies of the dependence of the mobility of main charge carriers (electrons) on temperature, the effect of electrical voltage, initial conductivity (existing at 80 K), and doping in n-InSe single crystals.

2. Experiment

Samples necessary for experimental studies were cut from large, unalloyed and doped samples obtained by the method of slow cooling with various quantitative contents ($N_{REE} \leq 10^{-1}$ at.%) of gadolinium (Gd), holmium (Ho) of single-crystal ingots. The measurements were carried out in the temperature range $T \approx 80$ç300 K, at various values of the electric voltage (U). Monochromatic light, wavelength (λ) and intensity (I_0) were used to illuminate the samples under study, which, if necessary, gradually changed in the ranges $\lambda \approx 0.30$ç2.00 μm and $I_0 \approx 1\cdot10^1$ç$3\cdot10^2$ Lx, respectively. For this purpose, an MDR-12U type grating monochromator and various light attenuators were used.

3. Results and discussion

It was established that at $T<300$ K, the specific conductivity (σ) of different samples of both groups (undoped and doped) crystals noticeably differ. The initial conductivity (σ_0) of different non-alloyed samples is $1.8\cdot10^{-3}$ç$2\cdot10^{-8}$ $\Omega^{-1}\cdot$cm^{-1}, and doped - depending on the value of N_{REE} varies non-monotonously within $2.2\cdot10^{-3}$ ç$9\cdot10^{-8}$ $\Omega^{-1}\cdot$cm^{-1} and reaches its minimum value ($\sigma_0 \approx 9\cdot10^{-8}$ $\Omega^{-1}\cdot$cm^{-1}) at $N_{REE} \approx 10^{-3}$ at.%. In undoped crystals with the highest σ_0, as well as in doped REE with $N_{REE} \geq 10^{-2}$ at.%, as the temperature rises to 300 K, the σ values and the mobility of the main charge carriers (μ) do not change (amount $\sim3.0\cdot10^{-3}$ç$3.5\cdot10^{-3}$ $\Omega^{-1}\cdot$cm^{-1} and $\sim9.8\cdot10^2$ç$1.1\cdot10^3$ cm^2 V^{-1} s^{-1}, respectively).In undoped crystals with the lowest value of σ_0 and in doped REE impurities with $N_{REE}<10^{-2}$ at. % of σ and μ with increasing T to 300 K increase (Fig. 1) exponentially (σ, $\mu \sim \exp\left(-\frac{\Delta\varepsilon}{kT}\right)$, where k is the Boltzmann constant, $\Delta\varepsilon$ is the activation energy σ and μ), which is anomalous for spatial homogeneous crystalline semiconductors [6].

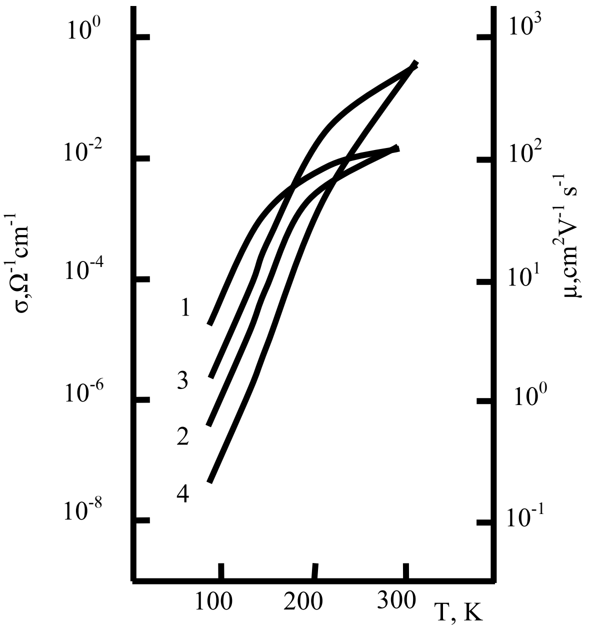

Fig. 1. Temperature dependence of conductivity (curves 1 and 2) and mobility of main charge carriers (curves 3 and 4) in undoped (curves 1 and 3) and doped with holmium impurities (curves 2 and 4) in n-InSe single crystals. σ_0, $\Omega^{-1}\cdot$cm^{-1}: 1, 3 - $9\cdot10^{-7}$; N_{REE}, at.%: 1, 3 - 0; 2, 4 - 10^{-3}; $U<U_{1-2}$

In the crystals under study at T<300 K, the dependences $\mu(\sigma_0)$, $\mu(N_{REE})$, $\mu(E)$ and $\mu(I_0)$ from the point of view of the theory of spatially homogeneous crystalline semiconductors [6] are also anomalous. In particular: in undoped crystals with increasing σ_0, the value of μ increases (Fig. 2, curve 1); in doped crystals, the $\mu(N_{REE})$ dependence is non-monotonic, while μ has its smallest and greatest value when $N_{REE}\approx10^{-3}$ at.% and $N_{REE}\approx10^{-1}$ at.%, respectively (Fig. 2, curve 2); the influence of the chemical nature of REE impurities on the magnitude and dependence of external factors μ is not observed; the dependence of μ on the electric voltage is observed at electric field strengths (E), significantly less than the critical intensity for heating free-carrier (E_{cr}) in the studied crystals [7].The course of dependences $\mu(\sigma_0)$ (Fig. 2, curve 3) and $\mu(N_{REE})$ (Fig. 2, curve 4) at the considered values of the electrical voltage is preserved, but the value $\Delta\mu_E\approx\mu_S-\mu_L$ (where μ_L and μ_S are the values of μ at voltages $U<U_{1-2}$ and $U>U_{2-n}$ [8], respectively,) at higher E changes its sign. When the sample is illuminated with its own light, the value of μ increases relative to its dark value and with increasing I_0 this difference monotonously increases.

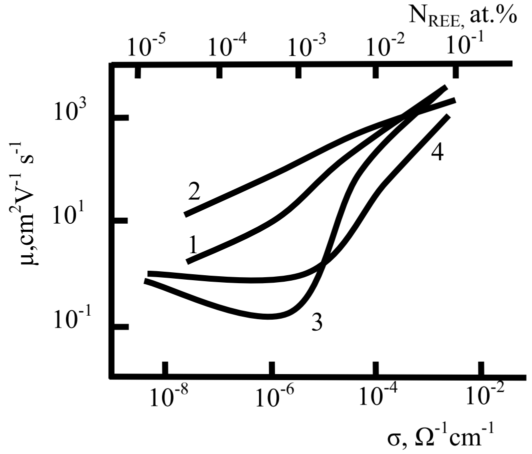

Fig. 2. Dependence of the mobility of the main charge carriers on the initial value of the specific conductivity in undoped (curves 1 and 2) and the quantitative impurity content (curve 3 and 4) in n-InSe single crystals doped with holmium at various electrical voltages T≈80 K. 1, 3 - $U<U_{1-2}$; 2, 4 - $U>U_{2-n}$

In all undoped and doped samples at T>300 K, as well as in undoped crystals with $\sigma_0>1.2.10^{-3}\ \Omega^{-1}\cdot\mathrm{cm}^{-1}$ and doped crystals with $N_{REE}>10^{-2}$ at.% the observed in the dependences $\mu(\sigma_0)$, $\mu(N_{REE})$, $\mu(E)$ and $\mu(I_0)$ anomalies disappear.

The experimental results obtained from a unified position are not explained in the framework of the notions of the interaction of carriers with phonons and (or) impurity centers in a spatially homogeneous crystal semiconductor [6, 7]. In this case, it is also necessary to take into account the presence of random drift barriers with different sizes in the free zones of the investigated semiconductor and their influence on the charge carrier drift processes. When the temperature rises, the effects of its own light and creating a noticeable injection of the electric field intensity, as well as when doping with REE impurities, the dimensions of these drift barriers change. In particular, with increasing T, exposure to its own light and (or) injecting electrical voltage due to partial compensation of the space charge of the drift barriers with a charge of thermally and photogenated, as well as injected carriers, the temperature and light respectively occur also electric rectification of drift barriers. The latter, in turn cause an anomalous increase in the mobility of charge carriers with increasing temperature, light intensity and intensity of the injecting electric field. In the case of doping, the situation is somewhat different. At the same time, the ions of the introduced impurity are added to the initial volume charges of the drift barriers to increase their dimensions. However, such an increase in the size of drift barriers nonmonotonously changes their effect on the magnitude and dependence on various factors μ. At first (up to $N_{REE}\approx10^{-3}$ at.%) with increasing size of the barriers their influence on the process of carrier drift increases and, accordingly, the value μ decreases with increasing N_{REE}. With further growth of N_{REE}, the space charge regions of neighboring drift barriers gradually overlap and, therefore, their effect on the carrier mobility decreases, and the value of μ increases and approaches that occurring in a spatially homogeneous crystalline semiconductor [9].

Regarding the nature of the drift barriers, it can be said that in the studied semiconductor, their presence is primarily due to the layer structure of the crystal structure.

4. Conclusion

In n-InSe single crystals at temperatures T<300 K, the magnitude of the mobility of the main charge carriers for different samples is significantly different and its dependence on the effects of temperature, voltage, doping, light have an anomalous character. These anomalies in undoped samples increase with decreasing initial conductivity, do not depend on the chemical nature of impurities in REE-doped samples, change nonmonotonically with increasing impurity content and are due to the presence of drift barriers created by crystallization structure of the investigated semiconductor.

References

1. Abrikosov N.Kh., Bankina V.F., Poretskaya L.V., Skudnova E.V., Chizhevskaya S.N., Semiconductor chalcogenides and alloys based on them, Moscow: Science, 1975, 220 p.
2. Peter Y.Yu., Manuel Cardona, Fundamentals of Semiconductors, Springer, 2010, 793 p.
3. AbdinovA.Sh., Babaeva R.F., Rzaev R.M., Inorganic materials 48, 781 (2012).
4. Mustafaeva S.N., Ismailov A.A., Asadov M.M., Low Temperatures Physics 36, 310 (2010).
5. DmitrievA.I., VishnjakV.V., Lashkarev G.V., Karbovskyi V.L., Kovaljuk Z.D., Bahtinov A.P., Physics of the Solid State 53, 622 (2011).
6. Smith P., Semiconductors, Moscow: World, 1982, 560 p.
7. Vorob'ev, L.E., Danilov, S.N., Ivchenko E. L., Levinstein M. E., Firsov D. A., Shalygin V. A., Kinetic and optical phenomena in strong electric fields in semiconductors and semiconductor structures. Saint Petersburg: Science, 2000, 160 p.
8. Lampert M, Mark P., Injection currents in solids, Moscow: World, 1973, 416 p.
9. Shklovskii, B.I. and Efros, A.L., Electronic properties of doped semiconductors, Moscow: Science, 1979. 416 p.

***Corresponding author**: babaeva-rena@yandex.ru

THERMAL CONDUCTIVITY IN $TlIn_{1-X}Yb_XSe_2$ SOLID SOLUTIONS

A.M.AHMEDOVA
Azerbaijan State University of Economics (UNEC), Baku, Istiglaliyat st., 6. Az 1001

The work is devoted to the study of thermal conductivity of solid solutions of the $TlInSe_2$-$TlYbSe_2$ system. The mechanisms of phonon scattering in them are determined. The diagram “Composition - thermal properties” of this system in the field of solubility is constructed.It is established that in solid solutions $TlIn_{1-x}Yb_xSe_2$, as the content of ytterbium in the compositions increases, the lattice thermal conductivity and the exponent in its temperature dependence decrease significantly.

It was found that in these solid solutions, at temperatures above Debye, phonon scattering simultaneously with three-phonon flip processes an active role is played by normal processes and scattering on point defects.

Keywords: thermal conductivity, solid solutions, phonon
PACS: 72.15.Cz; 65.40.−b; 74.25.Kc

1. Introduction

$TlInX_2$-(X - S,Se,Te) type triaxial semiconductor compounds can be controlled by high stability, stability of the characteristic semiconductor parameters and their composition change, and so on. they have different features. One of these objects is $TlIn_{1-x}Yb_xSe_2$ solid solutions present in the $TlInSe_2$-$TlYbSe_2$ limited solution zone. As shown in [1-2], $TlInSe_2$ is a triangle with tallium atoms +1 and indium atoms are +3. The ion radii of the triangular indium atoms are close to the radius of the triangular isotropic ions, and in this respect, the triangular indium ions in the $TlInSe_2$ combination are gradually replaced by triangular itterbium ions, and as a result $Tl^{+1}In^{+3}Se_2^{+2} \rightarrow Tl^{+1}In_{1-x}^{+3}Yb_x^{+3}Se_2^{-2}$ solid solutions are formed on the $TlInSe_2$-$TlYbSe_2$ system in the $TlInSe_2$ merger. [2] Studies show that the present system exists in the solution zone and covers 0ç11 mol% $TlInSe_2$ at room temperature. Solid solutions of all $TlIn_{1-x}Yb_xSe_2$crystallized into tetrachronic singanon as the initial $TlInSe_2$ compounds, and their melting temperature increases as the relative amount of itterbium in the composition increases.

Investigation of "electrical properties" shows that all solids are semiconductors with p-type conductivity, which have the character of memory converter.

Investigation of the "composition- heat properties" diagram allows for the identification of additional heat transfer and scattering mechanisms and other features that can not be observed in these materials in the initial components. In this regard, the investigation of thermal conductivity in solid solutions observed in $TlInSe_2$-$TlYbSe_2$is of great interest

2. Experimental part

Monocrystalline samples for the study were obtained by the Bricmen method and all of them have p-type permeability.

Thermal conductivity in the samples was measured by the stationary method [001] and [100] for the perpendicular and parallel oriented thermal flood plains in the direction of the arrows. The specimens are made of 4x5x10 mm^2 size paralelopiped. The heat contact between the heater and the refrigerator was made with a silver paste. Measurement accuracy of heat transfer coefficient + 6%.

3. Results and discussion

The temperature dependence of the total heat transfer coefficient (χ) for the investigated samples is shown in Figure 1. According to the Videman-Franse's law, the cost of electron collecting electron capture is $10^{-2} - 10^{-3} W/(m \cdot K)$ and we accept that the 1% of the total heat transfer coefficient is drawn, and the heat plays an important role in the heat transfer.

As can be seen in the graphs, there is strong anisotropic conductivity in all compositions.

For example, in the $TlInSe_2$ compound, the initial component was a temperature gradient of 100 K at a temperature parallel to the layers, while the cage heat transfer coefficient was $\chi^{\perp}_{100K} = 3{,}85W/(m \cdot K)$ perpendicular to $\chi^{//}_{100K} = 6{,}8W/(m \cdot K)$ layer. These amounts were $\chi^{//}_{200K} = 3{,}05W/(m \cdot K)$, $\chi^{\perp}_{200K} = 2{,}1W/(m \cdot K)$, $\chi^{//}_{300K} = 1{,}85W/(m \cdot K)$, and $\chi^{\perp}_{300K} = 1{,}42W/(m \cdot K)$ in the 200K and 300K temperatures respectively.

There is a certain displacement factor in the change of thermal conductivity due to the increase in the atomic weight of the composition when the atoms are transferred from solid components to the solid solutions formed on their basis in the crystal cage (figure 1). This is due to the fact that when localized triangular indium atoms are replaced by three-pointed itterbium atoms on the basis of $TlInSe_2$, local dot defects occur. This causes the localized change of defective density and elastic properties. This, in turn, leads to the emergence of additional scattering mechanisms, in contrast to the original components, in solid solutions of varying composition.

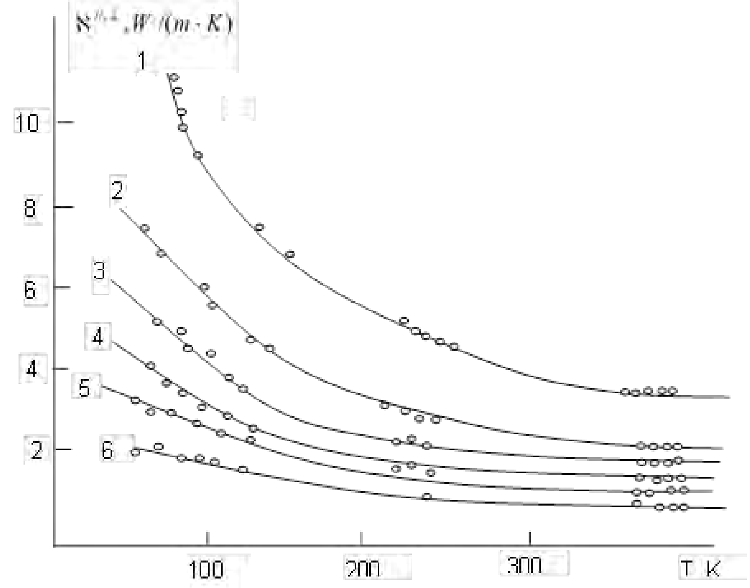

Figure 1.$TlIn_{1-x}Yb_xSe_2$ solid solutions, coefficient of thermal conductivity coefficients in layers $\chi^{//}$ and perpendicular to layers temperature dependencies in $\chi^{\perp}$ directions

Determination of the basic scattering mechanisms of phonons in $TlIn_{1-x}Yb_xSe_2$ solid solutionsthe experimental prices of the heat transfer coefficient were compared with the calculated values, taking into account the triangle transition processes (U-processes) and the scattering of the point defects by the Climax [5,7] at room temperature. According to [1] and [4-7], the $\frac{1}{\tau} = \frac{1}{\tau_N} + \frac{1}{\tau_U}$ (1) is reimbursed for the entire period of relaxation. Here $\frac{1}{\tau_N} = A\omega^4$ and $\frac{1}{\tau_U} = B\omega^4$ are τ-defects, and τij are relaxation periods in U-processes. If we take this expression of complete relaxation times in the generalized heat transfer equation for phonons with heat transfer, then $\chi_q = \frac{3}{(2n)^3} \int v_{qr}^2 \cos\theta\tau(\vec{q}) d^3 \dot{q}$ (2) for the coefficient of thermal conductivity. Here C_f - phonon temperature, $\tau(q)$-is the general relaxation period for phonons. (The 3-factor is included in the three branches of the dance spectrum).

In case of dot defects after the integration, take the heat transfer coefficient $\chi_{adm} = \frac{k_0}{2\pi^2 \bar{v}_0} \cdot \frac{\omega_0}{B} arctg\left(\frac{\omega_{\max}}{\omega_0}\right)$ (3). Here, $\omega_0^2 = \frac{B}{A}$ has didactic unit, ω_{max} is the maximum speed corresponding to the Debay model, υ_0 - the average sound speed. For the non-detecting state, the crystal heat conductivity coefficient is obtained from the condition A=0 $\omega_0 = \frac{k_0 \omega_{\max}}{2\pi^2 \bar{v}_0 B} \Rightarrow \frac{B}{\omega_{\max}} arctg\left(\frac{\omega_{\max}}{\omega_0}\right)$ (4) From the combination of (4) and (3), $\chi_{adm} = \chi_0 \frac{\omega_0}{\omega_{\max}} arctg\left(\frac{\omega_{\max}}{\omega_0}\right)$ (5) is taken.It follows from this that it is necessary to know ω_0/ω_{max}- to calculate χ_{adm}. Using the expression (4), we get $\frac{\omega_0^2}{\omega_{\max}^2} = \frac{B}{A\omega_{\max}^2} = \frac{k_0}{2\pi^2 \bar{\upsilon}_0 \chi_0 \omega_{\max} A}$ (6) from the following transformations.If χ_0 is known, then the ratio $\frac{\omega_0}{\omega_{\max}}$ can be calculated by knowing A. It is also difficult to calculate the quantity A if the local changes in elastic properties and density occur in the crystal. But if the change of elastic properties in the crystal is negligible and it is impossible to ignore it, then phonons are exposed to defects due to local variations of density, and in this case it is simpler to calculate the quantity A. Because our indium and substitute isterbium atoms that are substituted by $TlIn_{1-x}Yb_xSe_2$are triangular, we can take into account the change of elastic properties in such substitution and the defects in the solid solutions we observe are the result of local variations in density in the crystal due to the difference between the triangular indium and itterbium ion radius occurs.

For tetrachonal sinchology $\Omega_0 = a^2 C$.Solid solutions that can be described can be described as $TlIn_{1-x}Yb_xSe_2 \rightarrow Tl\left[InSe_2\right]_{1-x}\left[YbSe_2\right]_x \rightarrow \left[TlInSe_2\right]_{1-x}\left[TlYbSe_2\right]_x$ then we can write $\frac{\Delta M}{\overline{M}} = \frac{\overline{M}_{TlYbSe_2} - \overline{M}_{TlInSe_2}}{(1-x)\overline{M}_{TlInSe_2} - x \cdot \overline{M}_{TlYbSe_2}}; M = \sum_i x_i M_i$ (7). Here, $\overline{M}_{TlInSe_2} = 143{,}6$ and $\overline{M}_{TlYbSe_2} = 158{,}16$

For each intermediate composition, the average value of transverse and longitudinal ultraviolet waves for tetrahedral axes along the initial component $TlInSe_2$has been determined. The flow temperature is determined by the Lindeman method: $\theta_D = C_L T_{er}^{\frac{1}{2}} A^{-\frac{5}{6}} \rho^{\frac{1}{3}}$. Here, the T_m -crystalline melting temperature is stable for ρ- $q/sm^3$and its density, and C is stable for the crystalline structure.

Since the $TlIn_{1-x}Yb_xSe_2$solid solutions studied are based on the $TlInSe_2$ triangle combination, the values of the coil heat transfer coefficients in the corresponding crystallographic arrows (*a* and *c*) of the $TlInSe_2$ combination for the coefficient of thermal conductivity with no defects are calculated while calculating the ratio $\frac{\omega}{\omega_D}$ for these solutions.

No additional scattering occurs with respect to the initial $TlInSe_2$ combination for x=0.(A=0) (4) and the ratio of frequencies turns into infinity. $\frac{\omega_0}{\omega_D} = \infty$. Since $\frac{\omega}{\omega_D} < 1$ for the intermediates studied, (5) can be expressed as $\frac{\chi_L}{\chi_q} = \frac{\omega}{\omega_D} \sum_{n=0}^{\infty} (-1)^n \left[\left(\frac{\omega_D}{\omega_0}\right)^{2n+1} \Big/ (2n+1) \right]$ (9).As the calculations derived from this statement are well-suited to experimental results, the reality of the $Tl\left[InSe_2\right]_{1-x}\left[YbSe_2\right]_x$ radical substitution is reaffirmed.

The calculations show that the consideration of the effects of local density changes on the ceiling heat transfer in solid solids in the solid solids significantly improves the experimental results and theoretical calculations. However, the temperature resistance still remains in all the components. The reason for this is the effect of N-processes on heat transfer. It is known that the normal processes do not directly affect the phonon splashes. However, as a result of normal processes, the wave vectors of the phonons vary so they can subsequently participate in U processes, and consequently assess the effects of normal processes on heat resistance. In the solid solutions containing $TlIn_{1-x}Yb_xSe_2$, we have a real opportunity to observe these cases..

Figure 2 shows the temperature ratio of the thermal conductivity coefficients in the $TlIn_{1-x}Yb_xSe_2$ solids in the $\vec{a}$ and $\vec{c}$ arrows and figure 3 depicts the dependence of these quantities on the composition. As shown in this dependence, the anisotropic in heat transfer is the lowest at low temperatures and the initial $TlInSe_2$combination. But with the rise in temperature, as well as the relative amount of itterbioids in the composition, anisotropic activity decreases. At the same time, the anisotropic content decreases with the growth of atomic masses. At the same time, the reduction in the atomic mass of the components and the overall heat transfer coefficient of graphs are well adapted to the theory.

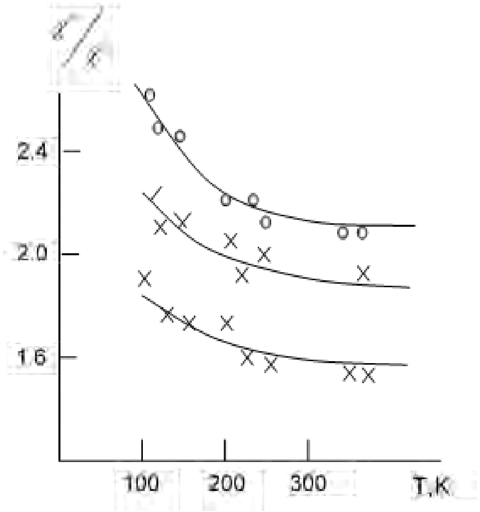

Figure 2. Temperature dependence of the thermal conductivity ratios of $\chi^{//}/\chi^{\perp}$ in parallel $\chi^{//}$ and perpendicular $\chi^{\perp}$ directions in solid solutions $TlIn_{1-x}Yb_xSe_2$

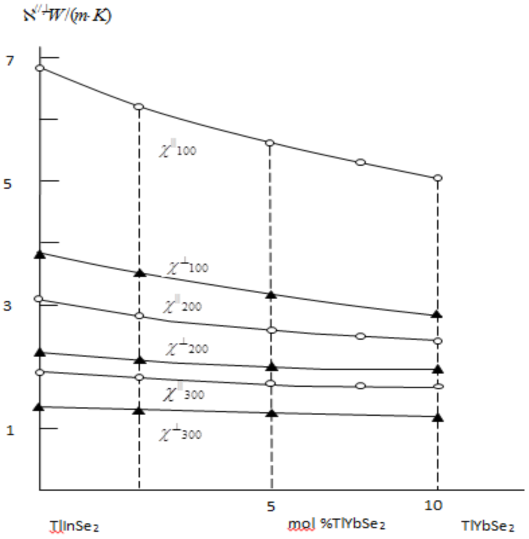

Figure 3.$TlIn_{1-x}Yb_xSe_2$ solids in parallel $\chi^{//}$ to the layers and in the perpendicular $\chi^{\perp}$ to the layers, the thermal conductivity ratios are dependent on the content of 100 K, 200K and 300K

4.Conclusion

It has been established that in $TlIn_{1-x}Yb_xSe_2$containing solids, as in the initial $TlInSe_2$combination, the heat is mainly carried by the heat dance of the crystal cage, the fundamental role in the phonon splashes in the initial components is triplicate transformation processes (U-processes) and in solid solutions with high temperatures U-processes as well as normal processes and scatterings play a key role in dipstick defects (local change in the density of indium atoms replacing the crystal cage).

References

1. Ahmadova A.M., Materials of the International Scientific Conference dedicated to the 90th anniversary of BSU 265 (2009).
2. Zarbaliyev M.M., Ahmadova A.M., Zarbaliyeva U.M., Baku University News, series of physics-mathematical sciences 1, 176 (2011) (in Russian).
3. Popov P.A., Fedorov P.P., Kuznetsov S.V., Konyushkin V.A., Osiko V.V., Basiev T.T., Physics reports 53, 353 (2008).
4. Sobolev B.P., Golubev A.M., Herrero P., Crystallography Reports 48, 141 (2003)
5. Kutasov V.A., Luk'yanova L.N., Konstantinov P.P., Semiconductors 34, 376 (2000).
6. Tagiev M.M., Agaev Z.F., AbdinovD.Sh., Inorganic materials 29, 998 (1993).
7. Popov P. A., Matovnikov A. V., Moiseev N. V. , Buchinskaya I. I., Karimov D. N., Sorokin N. I., Sulyanova E. A., Sobolev B. P., Krutov M. A., Crystallography Reports 60, 111 (2015).

***Corresponding author:** arzu.70@bk.ru

DISTINCTIVE FEATURES OF EMISSION SPECTRA OF CRUDE OILS OF THE ABSHERON PENINSULA

A.M. PASHAYEV[1], A.A. MUSAYEV[1], N.A. VELİYEV[2],B.G. TAGİYEV[1], Y.M. BAGHİROV[1], K.R. ALLAHVERDİYEV[1*], I.Z. SADİKHOV[1]

[1] *Azerbaijan National Aviation Academy, Mardakyan avenue 25, AZ1045, Baku/Bina, Azerbaijan*
[2]*State Oil Company of Azerbaijan Republic*

Laser induced fluorescence (LIF)KA-14 LIDAR (Light Identification Detection and Ranging), developed at the National Aviation Academy (NAA) of Azerbaijan have been used for detection of crude oil spills on the surface of Caspian sea as well as on the earth surface of Absheron peninsula[1]. KA-14 LIDAR used in present research work has been developed with the financial support of State Oil Company of Azerbaijan Republic (SOCAR) in a frame of Project “Control of the Environment by LIDAR During Oil-Gas Production” under Contract No1. Results of some measurements were published in [2]. It is well known, that oil spills may take place due to leakage of oil from differentOil-Gas-Production Departments (OGPD). It isknown - there are totally 12 OGPDs in Azerbaijan, including 8 SOCAR Departments belonging to AzNeft and 4 Joint Ventures.

Keywords: laser induced fluorescence, LIDAR, remote sensing, oil spills detection
PACS: 01.10Fv, 33.50.Dq, 42.62.Fi, 42.68.Wt, 42.68.Xy

1.Introduction

Technical characteristics of KA-14 LIDAR are as follows: •laser CRF 200-type QUANTEL, λ = 355 nm; •diameter of laser beam spot ∅ = 5.35 mm (after collimation- 40 mm); •frequency of excitation f = 20 Hz;•the pulse time duration τ = 7 ns;•the pulse power 60 mJ; •diameter of Newtonian-type telescope is 200 mm; •angle range of telescope measurements relative to horizon: from -20 to +20 degrees;•spectral range of measurements from 350 nm to 750 nm; •the number of spectral channels is 32;•maximum range of measurements not less than 250 m[1-3].

Crude oil consists of mixture of amines, salts (e.g. NaCl), hydrocarbons (e.g. aromatics, paraffins etc.), metals (e.g. Ni, Fe etc.), and S and S compounds (e.g. sulfides). Main important components of crude oil include:•carbon (83 - 87 %);•hydrogen (11 - 14 %);•oxygen (up to 3 %);•nitrogen (0.1 to 2 %);•sulfur (0.05 to 6 %) and as micronutrients – •metals (< 0.1 %; the most common metals are: •Fe;•Ni;•Cu and •V [4,5].Crude oil is usually considered as a solution of hard resin and paraffin substances in hydrocarbon liquid.

Detection of oil spills on water surface is a very important for the environment protection of coastal sea basins as well as navigable rivers and lakes. The analysis of crude oil using fluorescence techniques has become popular due to the high fluorescence nature of the constituent components of crude oil. Main advantage of fluorescence detection (in general) is obtaining not expensive and high sensitivity information about object studied. Oils irradiated by UV (ultraviolet) laser light will emit fluorescence light at longer wavelength. It is naturally to expect that oil taken from different OGPDs will emit different light. By the other word clear difference in emitted signal will clarify a source of oil (by the other words- which OGPDs it belongs).

2. Experiment

According to literature the fluorescence range of crude oil is from ~ 260 nm up to ~ 700 nm and is most significant in the spectral range of 270÷400 nm [4-6]. Considering LIDAR as an active remote sensing system it gets clear how useful and important to detect oil spills on water and earth surfaces.

Methodology used in present work includes KA-14 LIDAR.This LIDAR system consists of three units: •the laser;•the detection system; •the acquisition unit. The laser radiation at 355 nm is emitted by an Nd:YAG laser (third harmonic at 355 nm of CRF-200 Laser, QUANTEL, France)[1-3]. The returned radiation is collected on the entire visible spectral range (380÷ 750 nm). The detection unit includes a telescope with 200 mm aperture and focal distance 635 mm, Optical Multichannel Analyser (OMA), Grating Spectrometer (OCEANOPTICS, model MAYA 2000 Pro) with Charge Coupled Device (CCD) camera)) a polychromator with two concave diffraction gratings and an optical detector which combines an image intensifier and a linear CCD camera. KA-14 LIDARcan be used for measurements in water basins and vegetation.General view of KA-14 LIDAR developed at NAA is shown in Fig. 1 a,b.Three units mentioned above for KA-14 LIDAR are clearly seen in **Fig**. **1a**,**b**.

In addition to LIDAR measurements, we also performed the measurements of density and sulfur content of crude oils studied. Some results of these measurements have been presented in Ref. [2]. These analyses have been conducted at Marmara Research Center (MRC) of Turkish Scientific and Technological Research Council (TUBITAK), Gebze/Kocaeli, Turkey during business trip of prof. K. Allahverdiyev to MRC [2].

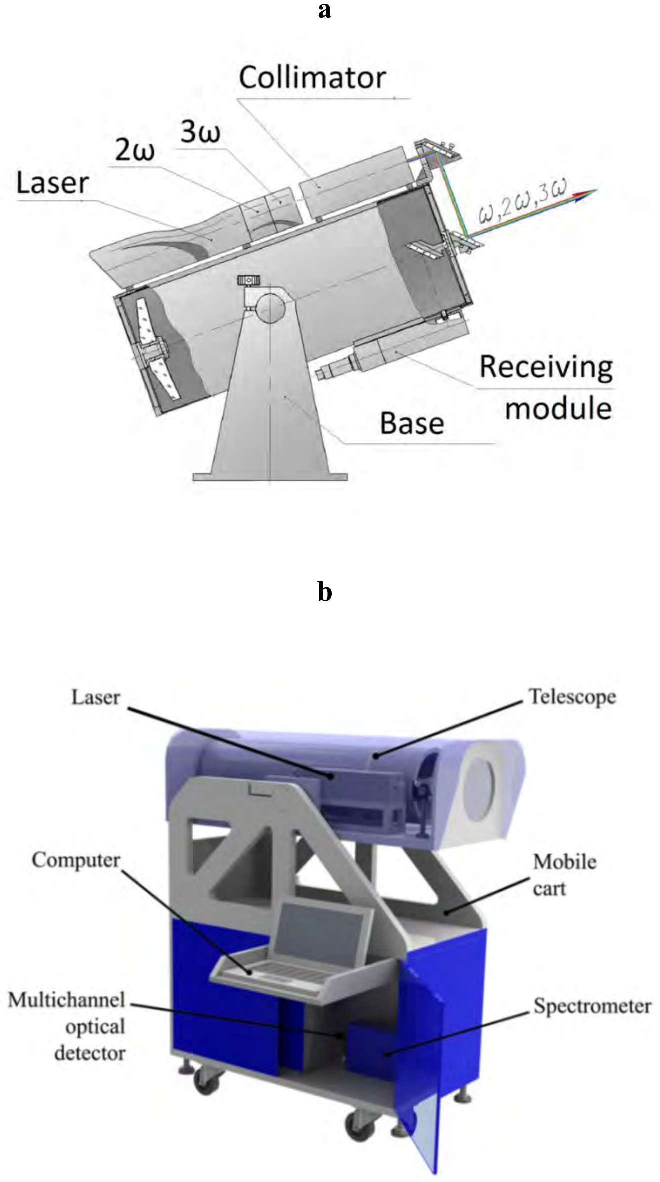

Fig. 1 (a,**b)**.General view of KA-14 LIDAR developed at NAA.

3. Results and discussion

Measurements of fluorescence spectra of crude oils were performed in sequence described below[2]:•first, background measurement have been done with close output of laser system (laser was in operation); • second, the measurement of fluorescence spectra of crude oil was performed; •third (final), background spectrum was substracted from the fluorescence spectrum of crude oil and recorded. Signal accumulation time in all measurements was ≈ 120 second [2].

The spectra shown below were selected as a typical from seven measurements for crude oil taken from given oil wells of OGPD and JV (**Fig**.**2** and **Fig**. **3**).

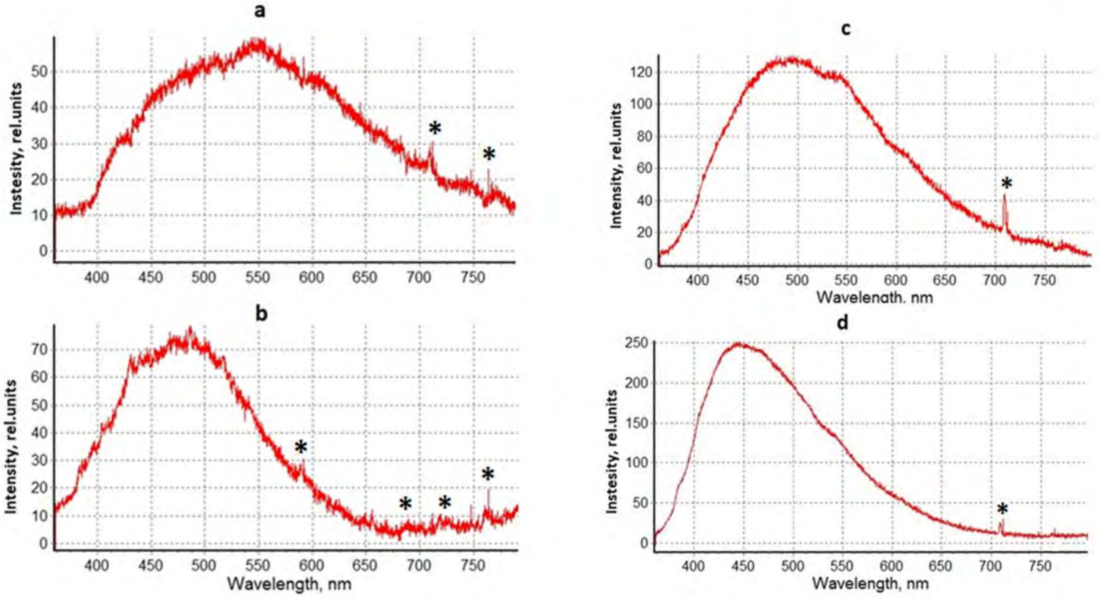

Fig. **2**.Room temperature fluorescence spectra of crude oils as measured by KA-14 LIDAR developed at NAA and excited by 355 nm CRF 200 laser line (∗- **noise**). **Pirallahy** (**Absheron OGPD**) (**a**); **NeftDashlaryOGPD** (**b**); **Gala** (**Taghiyev OGPD**) (**c**); **Surakhany Oil** (**Surakhany JV**) (**d**) [2].

It is seen (**Fig**. **2a**) that oils taken from **Absheron OGPD** is characterized with one broad emission band in the spectral range of 350÷750 *nm* with maximum at ≈ 550 *nm*. The peculiarities include weak "shoulders" (or weak peaks) in the wavelength range of fluorescence spectra at ≈ 435 *nm*, ≈ 510 *nm*, ≈ 610 nm and ≈ 740 *nm*.

Fluorescence spectra of crude oils from **NeftDashlary**is also characterized with broad band in the spectral range of 350÷650 *nm* (**Fig**. **2b**). Please, note that the band observed is considerably narrower than for spectrum shown in **Fig**. **2a**. In addition, weak "shoulders" are seen at ≈ 390 *nm*, ≈ 410 *nm*, ≈ 450 *nm* and ≈ 540 *nm*(see **Fig**.**2b**).

Oils taken from **Gala** (**Taghiyev OGPD**) is also characterized with a broad band in the spectral range of 350÷750 *nm*. In addition, weak "shoulders" are also revealed in the short-, and long- ranges of fluorescence spectrum at ≈ 380 *nm*, ≈ 540 *nm* and ≈ 610 *nm*(spectrum **c**in**Fig**. **2**).

Characteristic emission of crude oil taken from **SurakhanyOil**(**Surakhany JV**) is presented in **Fig**. **2d**). Fluorescence is characterized with one emission band in the spectral range of 350÷700 *nm* (it is typical for oils taken from different oil wells). Furthermore, weak "shoulders" are also clearly seen in the short- and long-wavelength range of emission spectra at ≈ 380 *nm* and ≈ 540 *nm*, respectively (spectrum**d** in **Fig**. **2**).

Systematic measurements allowed clarify distinctive features between the fluorescence spectra of different oil spills taken from different OGPD. Distinctive features of registered spectra included: •the spectral positions of fluorescence maxima; •the forms and the fine structures of spectra. Analysis allowed with a high degree of availability to determine from which OGPD (including OGPD “NeftjanijeKamni”) leakage took place on the surface of the Caspian sea and on the earth of the Absheron peninsula.

4. Conclusion

Results obtained seems to be useful for creation of a Data Bank of the fluorescence spectra of crude oils extracted on the earth of the Absheron peninsula of Azerbaijan as well as from adjacent water areas of the Caspian sea.This work is in progress with aim of creating the Data Bank of fluorescence spectra of oil spills taken from OGPD of SOCAR and JV of Absheron peninsula of Azerbaijan.

The authors are thankful to the State Oil Company of Azerbaijan Republic for support.

References

1. A.M. Pashayev, K.R. Allahverdiyev, B.G. Tagiyev, I.A. Sadikhov, Proc. of SPIE, 10226, 102260W-1 (2017).
2. A.M. Pashayev, B.G. Taghiyev, N.A. Veliyev, Y.M. Baghirov, A.A. Musayev, K.R. Allahverdiyev, I.Z. Sadikhov, Azərbaijan Oil Industry, 7-8, 67 (2018).
3. A.M. Pashayev, B.H. Taghiyev, K.R. Allahverdiyev, I.Z. Sadikhov, Book of Abstracts, International Conference Devoted to 10th Anniversary of Institute of Physics Problem of Baku State University, Baku, December 16-25, pp. 22 – 24, (2015).
4. A.A. Petrov, “Petroleum Hydrocarbons”, Springer-Verlag, Berlin, Heidelberg, New York, London, Paris, Tokio, p. 174, (1984).
5. F.I. Samedova, “Oil of Azerbaijan”, Baku: The science, p. 420, (2011).
6. P.A. Pantoja, J. Lopez-Gejo, G.A.C. Le Roux, F.N. Quinta and C.A.O. Naschimento, Energy Fuels, 25, 3598 (2011).

***Corresponding author:** kerim_allahverdi1@hotmail.com

THE ROLE OF EXCITONS IN THE FORMATION OF A PHOTOCURRENT IN A $TlGaSe_2$ SINGLE CRYSTAL

S.Z.DZHAFAROVA

Azerbaijan State University of Economics (UNEC), Istiglaliyat st., 6, Baku, Azerbaijan, Az1001

The paper presents data on the exciton states in the process of photocurrent formation in $TlGaSe_2$.An inverse correlation (maximum absorption - minimum photocurrent) between the exciton absorption lines and extremes of the photocurrent was established based on a detailed analysis of the photocurrent spectra and $TlGaSe_2$ crystal absorption in a wide energy range (2.0ç2.5 eV) and temperatures (1.8ç300 K).These are interpreted on the basis of non-photoactive absorption near the surface.

Studies of the temperature dependence of the photocurrent showed that it is non-monotonic with discontinuous features. The non-monotonic temperature dependence of the photocurrent is explained by the presence of recombination levels (r- and s-centers) in the gap with active interaction with sticking levels. It was also established that the observed abrupt changes in the photocurrent at 105, 117 and 210 K are associated with phase transformations in $TlGaSe_2$.

Keywords: $TlGaSe_2$, single crystal, absorption, photocurrent, exciton, defects.
PACS: 71.35.-y; 73.50.Pz.

1. Introduction

The principal theoretical and practical interest is the question of the participation of excitons in photoelectric processes [1-3]. Excitons as electrically neutral formations do not transfer charge. However, their interaction with other quasiparticles, electric fields, crystal defects and impurity centers can lead to the appearance of free carriers. The discovery of the optical spectrum of an exciton showed that the question of the contribution of excitons to the photocurrent should be solved using spectral methods and low temperatures [4, 5].

With the development of semiconductor technology, active experimental studies of the photoelectric properties of promising semiconductor compounds have begun and the creation on this basis of prerequisites for expanding the possibilities of their practical application [6-8].

Continuously growing interest and needs of modern semiconductor technology are not satisfied with known materials and require the creation of new materials. The search for new semiconductor materials is one of the main problems of today's solid state physics. Creating new materials opens up new perspectives and allows you to solve new technical problems. The interest in photovoltaic cells comes from environmental considerations, which makes them the most promisingamong renewable energy sources.

$TlGaSe_2$ is known to be primarily known for its physicochemical properties. The ability of these layered crystals to cleave on plates with specular faces, which is a consequence of the sharp asymmetry of chemical bonding, makes them promising materials for photoelectric converters.

This paper summarizes our studies on the detection and determination of the role of excitons in photoconductivity in a $TlGaSe_2$ single crystal, including their behavior during phase transformations [9].

2. Experiment

The experiments were carried out on single-crystal samples grown by the Bridgman-Stockbarger method. $TlGaSe_2$, as it is known, crystallizes in a monoclinic structure with a space group of C_s^4, has a layered structure and high photosensitivity, p-type conductivity and resistivity 10^7-10^8Om·m at 300 K. Ohmic contacts were created by applying In-Ga paste; and also by spraying In or Al in high vacuum with preliminary surface cleaning by ion bombardment and heating.

3. Results and discussion

Figure 1 shows the spectral distributions of the photocurrent (curves *a*, *c*) and the absorption coefficient (curve *c*) of a $TlGaSe_2$ single crystal at room temperature (curve *a*) and 77 K (curves *b*, *c*). As can be seen from the figure, at a temperature of 300 K, a broad maximum is observed in the spectral distribution of the photocurrent, with a sharp drop in the photocurrent in the long-wavelength part and a decrease in the photocurrent in the short-wavelength, due to surface recombination of current carriers.

The coincidence of the energy position of the sharp drop in the long-wavelength part of the photoconductivity spectrum and the fundamental absorption edge, as well as their low-temperature behavior, indicate the excitonic nature of photoconductivity. A decrease in temperature to 77 K leads to a high-energy shift of the long-wave edge of the photoresponse and the appearance of four sharp structures (Fig. 1, curve *c*): near the edge E_{A1}=2.127 eV and E_{A2}=2.212 eV and in depth of own absorption E_{B1}=2.355 eV and E_{B2}=2.387 eV. Studies of the absorption spectra at 77 K revealed two peaks with energies E_A=2.164 eV and E_B=2.372 eV (curve *c*). A comparison of the photoresponse spectra and absorption at 77 K shows that the maxima of the absorption peaks correspond to minima in the photoresponse spectra of the two structures, which is possible due to non-photoactive absorption near the surface in the region of the maxima of the exciton absorption peaks. Another possible explanation is the presence of a potential barrier in the near-contact region, leading to concentration of the applied field in the barrier and the “splitting” of the exciton peaks is unlikely, since the applied voltages did not exceed 10 V at a distance between contacts of ~ 1 mm.

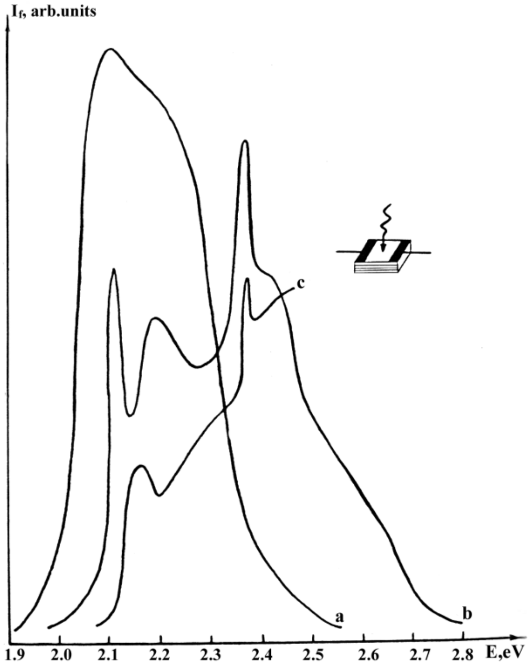

Fig.1. Photocurrent spectra (curves *a,b*) of the absorption coefficient (curve *c*) of a single crystal at 300 (curve a) and 77K (curves *b, c*)

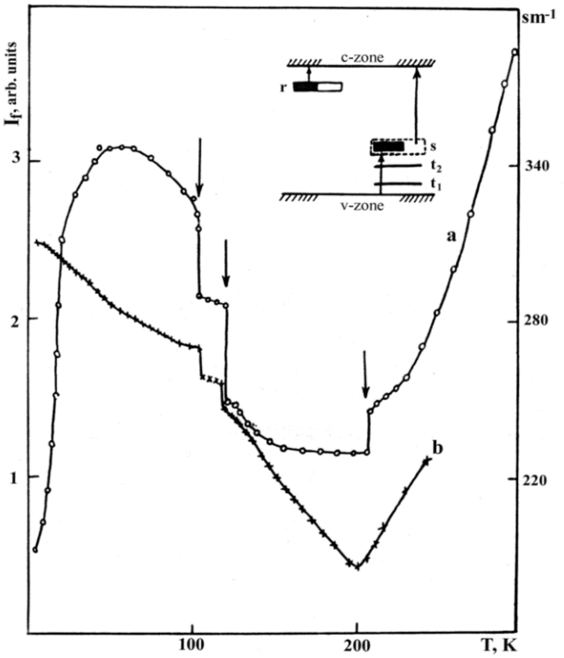

Fig.2. Temperature dependence of own photoconductivity (curve *a*) and absorption coefficient (curve *b*) at the point of maximum E_{A1}

It is interesting to note that with a decrease in temperature in the short-wave part of the photocurrent (at 77 K, curve *c*), there is some increase in the photocurrent due to a possible increase in the mobility and lifetime of excitons with decreasing temperature, which allows them to leave the defective surface layer (where they die, mostly non-photoactively) deep into the crystal and cause a photocurrent as a result of interaction with the centers. Naturally, the photocurrent output in the exciton line in the depth of its own absorption will also increase.

Figure 2 shows the temperature dependence of intrinsic photoconductivity (curve *a*) and absorption coefficient (curve *b*) at the point of maximum E_A of a $TlGaSe_2$ single crystal in the temperature range 1.8-300 K. As follows from the figure, the variation in intrinsic photoconductivity and absorption coefficient with temperature is nonmonotonic with hopping features at 105; 117 and 210 K, associated with phase transformations in a $TlGaSe_2$ single crystal.

As is known, in many photoconductors, in particular in compounds $A^{II}B^{VI}$ [10], the non-monotonic temperature dependence of the photocurrent is usually explained by the presence of a number of adhesion levels in the band gap and recombination for the main carriers. Therefore, the non-monotonic dependence of the photocurrent on temperature — the growth of the photocurrent with increasing temperature in the range 1.8–50 K and above 210 K can be explained by the participation in the processes of photoconductivity of recombination centers (r and s-centers) and adhesion (t-centers) with their active interaction .

In this case, at low temperatures, the growth of the photocurrent is due to thermal activation of electrons from shallow sticking levels (t-centers). Due to the fact that the depth of t-centers is less than r-centers, the temperature quenching of photoconductivity in this temperature range is insignificant. With increasing temperature, the contribution of photocurrent quenching by r-centers increases, making activation of the photocurrent by t_1-centers less effective. As a result, in the temperature range 50ç70 K, the photocurrent remains almost constant. A further increase in temperature causes an intense temperature quenching of the photocurrent, and in the temperature range of 70ç100 K, the photocurrent decreases with increasing temperature. But at the same time, the t_1-centers are still not fully ionized and the dependence I_f (T) is distorted. At temperatures above 120 K, shallow t_1- centers are completely ionized, and the temperature dependence of the photocurrent is controlled by r centers and deeper t_2- centers. At temperatures above 120 K, the activation of holes from the t_2 center overcomes the quenching by r-centers and the photocurrent increases with increasing temperature. The energy diagram of the hole states in the $TlGaSe_2$ band gap is shown in the upper left part of Fig. 2.

The conducted studies show the great potential of low-temperature photoelectric exciton spectroscopy in diagnosing and controlling the near-surface and bulk properties of a semiconductor crystal.

References

1. Jailaubekov A.E., Willard A.P., Tritsch J.R., Chan W.L. and other, Nature Materials 12, 66 (2013).
2. Subha N., Mahalakshmi M., Myilsamy M., Lakshmana N. and other , International Journal of Hydrogen Energy 43, 3905 (2018).
3. Etzold F., Howard I. A., Mauer R. and other, Journal of the American Chemical Society 133, 9469 (2011).
4. Qross E.F., Kaplyanskiy A.A., Technical Physics 25, 9, 1661 (1955).
5. Qross E.F., Kaplyanskiy A.A., Novikov B.V., Technical Physics 26, 3, 913 (1956).
6. Atabaev I.G., Matchanov N.A., Khazhiev M.U., Saidov D.V., Physics of the Solid State 47, 11, 2025 (2005).
7. Dneprovskiy V.S., Sorosov educational magazine 6, 8, 88 (2000).
8. Batyrev A.S., Bisengaliev R.A., Novikov B.V., Tagirov M.O., Semiconductors 47, 9, 1153 (2013).
9. Abutalybov G.I., Razbirin B.S., Neimanzade I.K., Salaev E.Yu., Starukhin G.V., Soviet Physics Semiconductors 80, 9, 1699 (1986).
10. Lashkarev V.B., Lyubchenko A.V., Sheykman M.K., Nonequilibrium processes in photoconductors, Kiyev, 264 p. (1981).

***Corresponding author**: exiton_1992@mail.ru

AB-INITIO CALCULATIONS OF ELECTRONIC STRUCTURE OF CdFeTe AND ITS OPTICAL PROPERTIES

[1]M.A.MEHRABOVA*, [2,3]H.S.ORUJOV, [2]H.R.NURIYEV, [4]N.H.HASANOV,
[3]A.A.ABDULLAYEVA, [2]Z.I.SULEYMANOV
[1]Institute of Radiation Problems of ANAS, B.Vahabzade str.9, Baku, Azerbaijan, Az1143
[2]Institute of Physics of ANAS named after academician G.M.Abdullayev, H.Javid ave. 131, Baku, Azerbaijan, AZ1143
[3]Azerbaijan Technical University, H.Javid ave. 25, Baku, Azerbaijan, AZ107
[4]Baku State University, Z.Khalilov str., 23, Baku, Azerbaijan, Az1148

First principle calculations based on density functional theory by the pseudopotential method, by use of Local Spin Density Approximation in AtomistixToolKit program carried out to define band gap, density of states, total energy, magnetic moments, number of electrons, Fermi levels of $Cd_{1-x}Fe_xTe$. $Cd_{1-x}Fe_xTe$ epitaxial films on glass substrate were obtained. Absorption and transmission spectra were investigated. It was defined, that with an increase in Fe concentration there is an increase in the band gap.

Keywords: Semimagnetic semiconductor, ab-initio, electronic structure, magnetic moments, absorption spectra, transmission spectra
PACS:71.20.-b, 71.15.-m

1. Introduction

Semimagnetic semiconductors (SMS) are the unique materials for electronic devices. These materials are obtained by the substitution of some classical semiconductors, by magnetic elements and transition metals, such as Co, Ni, Mn, Fe [1] in the semiconductor compound. The doped CdTe by Mn or Fe atoms have a wide range of applications in spintronics [2] such as infra-red detectors, solar cells, visible and infra-red lasers and etc. [3,4].

The best known wide gap semimagnetic semiconductors $Cd_{1-x}Fe_xTe$ is one of the less studied SMSs, and the solubility of Fe atoms is about 2-15% which are far below the solubility in the Mn based SMS.

In this paper ab initio calculations have been performed to study electronic band structure of $Cd_{1-x}Fe_xTe$ SMS and optical properties as absorption and transmission spectra. We investigated the role and effect of doping material (Fe) on investigated properties, and compare them with literature data.

Ab initio calculations of electron structure and magnetic properties of $Cd_{1-x}Fe_xTe$ were carried out in work [5]. Unlike these one we carried out first principle calculations based on density functional theory (DFT) by the pseudopotential method, by use of Local Spin Density Approximation (LSDA) in the AtomistixToolKit(ATK) program. It were defined band gap, density of states (DOS), total energy, magnetic moments, number of electrons, Fermi levels for $Cd_{1-x}Fe_xTe$.

2. Electronic structure of supercell Cd3Fe1Te4

Ab initio calculationswere performed in ATK program within the spin-polarized DFT and LSDA+U on the DZDP basis. We have used Hubbard-U potential U_{Fe}=2.42eV for *3d* states of Fe atoms [6] and spin polarized *Tight Tier* 1 basis set with *FHI* (Z=8) *pseudopotential.*

Firstly it was calculated electron band structure of supercell Cd4Te4 and was defined band gap E_g=1.53eV (fig.1) [7].Then supercellCd3Fe1Te4 was constructed on the base of supercell Cd4Te4 and crystal structure was optimized (fig.2.).

It is known, that the nature of band gap in the Fe based SMS differ from that of Mn based SMS. Because the substitutional Fe^{2+} possesses both spin and orbital momentum and contains one more electron than the Mn^{2+} so the Fe^{2+} $3d^6$ level is located above the Mn^{2+} $3d^5$ state in the semiconductor band structure. It was calculated electron band structure, DOS of $Cd_{1-x}Fe_xTe$ (x=0.25) (fig.3) and defined that the band gap increases linearly with an increase in the Fe concentration, but there occurs an insignificant decrease in the lattice parameter.

Partial density of states (PDOS) were studied for analysis of the character of electron band structure formation (fig 4). PDOS analysis shows that upper levels of valence band located in the range of [-5; 0] eV, mainly comes from *p*-states of Te atoms, *s*-states of Cd atoms and *s*-states of Fe atoms with some contribution of *d*-states of Fe atoms. Lower levels of conductivity band located in the range of [0; 5] eV, mainly comes from *d*-states of Te atoms, *p*-states of Fe atoms and *p*-states of Cd atoms with some contribution of *d*-states Fe atoms.

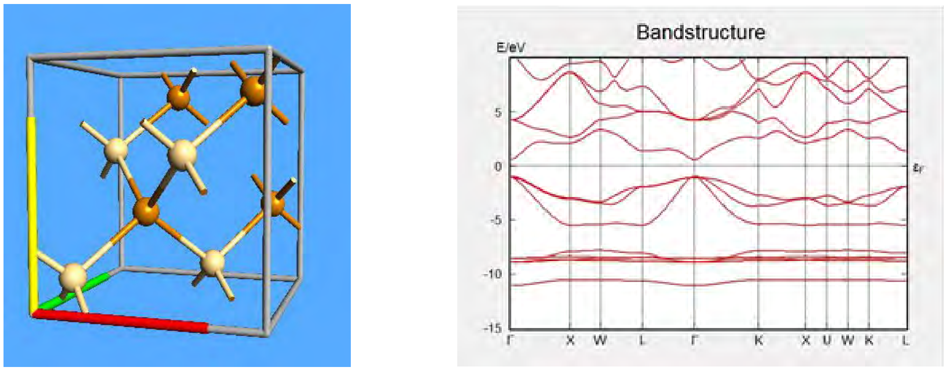

a) b)

Fig.1. Supercell Cd4Te4 a) crystal structure b) electron band structure

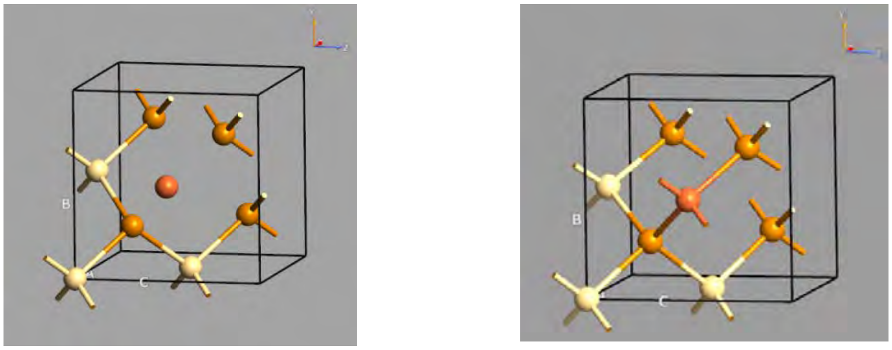

a) b)

Fig.2. Crystal structure of $Cd_{1-x}Fe_xTe$ (x=0.25) a) before optimization, b) after optimization

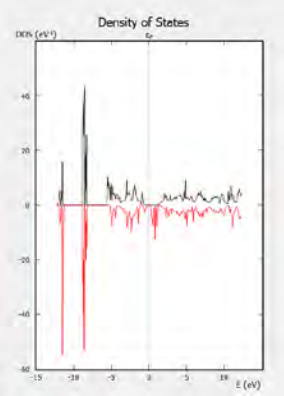

Fig.3. DOS of $Cd_{1-x}Fe_xTe$ (x=0.25)

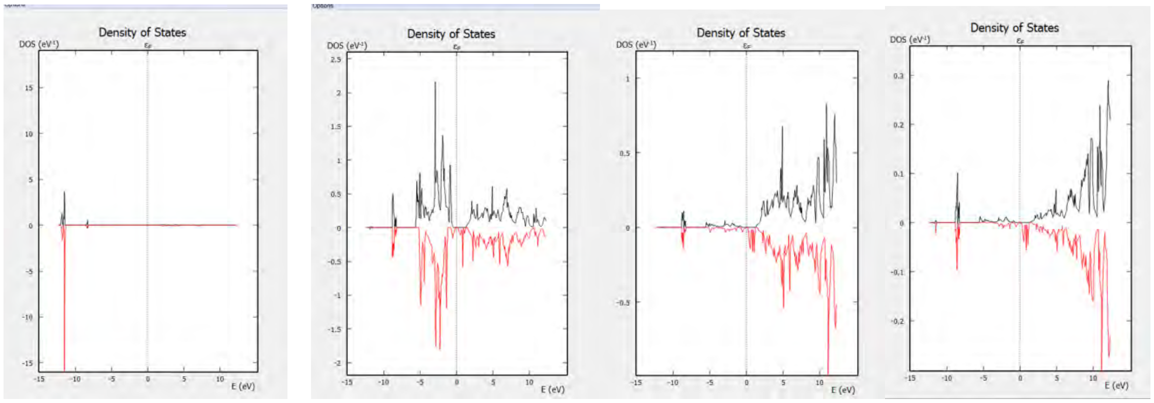

Te-*s*-states Te *p*-states Te-*d*-states Te *f*-states

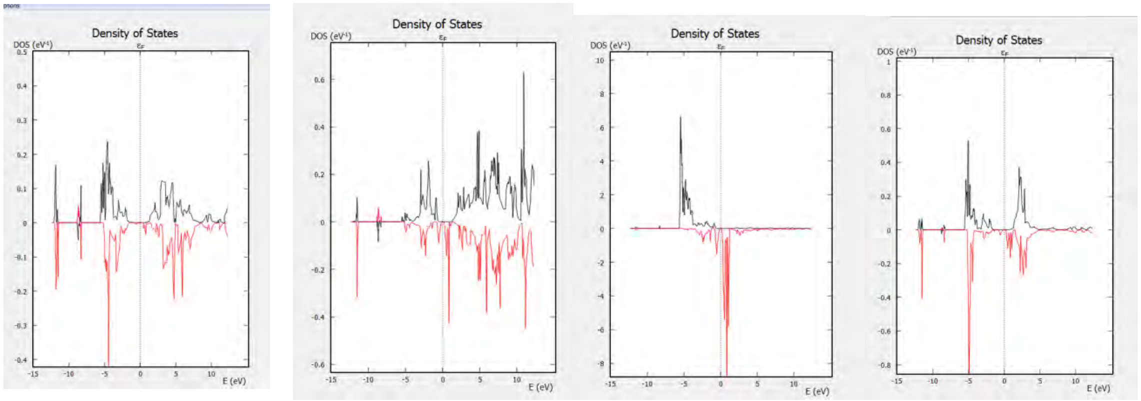

Fe-*s*-states Fe-*p*-states Fe-*d*-states Cd-*s*-states

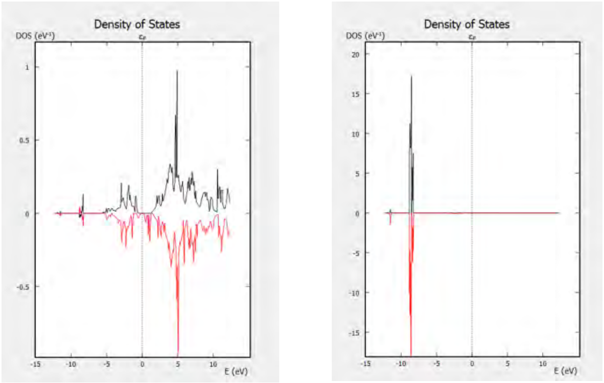

Cd-*p*-states Cd-*d*-states

Fig.4. Partial density of states of $Cd_{1-x}Fe_xTe$

The presence of Fe atoms leads to formation of magnit momentum and total magnetic moment $\mu=5\mu_B$, where μ_B is the Bohr magneton. Calculated total energy was E_t=-6308.427eV.

3. Optical spectra of $Cd_{1-x}Fe_xTe$

$Cd_{1-x}Fe_xTe$ (x=0.03, 0.08, 0.25) epitaxial films were obtained on glass substrates in a vacuum of 10^{-4}Pa by Molecular Beams Condensation method. It is defined the optimal conditions for creation of epitaxial films with perfect structure and clean, smooth surface. The substrate temperature was 673K, source temperature was 1100K and film thickness was d=0.5µm. Dark spots, observed on the film surface, were removed after use of source of compensating Se vapors in the growth process. The crystal structure and surface morphology were controlled by X-ray diffraction method on Bruker D8 Advance XRD and SEM method on Carl Zeiss Sigma VP respectively.

Absorption and transmission spectra of $Cd_{1-x}Fe_xTe$ (x=0.03, 0.08, 0.25) epitaxial films on glass substrates were investigated. The spectra have been measured on UV-Visible SPECORD 210 PLUS spectrophotometer in the wavelength region λ=190-1100 nm(fig.6). It is established that the films absorb the light to the wavelength λ=825nm, afterwards there occurs a sharp decrease in the absorption coefficient.

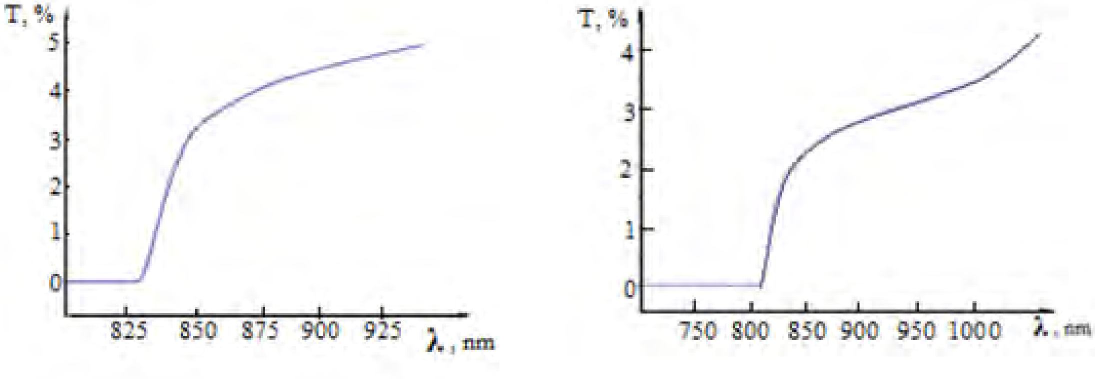

a) b)

Fig.6. Transmission spectra of $Cd_{1-x}Fe_xTe$ a) x=0.03, b) x=0.08

The band gap of $Cd_{1-x}Fe_xTe$ epitaxial films was determined. It was defined, that with an increase in Fe concentration in the $Cd_{1-x}Fe_xTe$, there is an increase in the band gap. Results correspond to our theoretical calculations as well as to literature data.

4. Conclusion

Ab initio calculations based on Density Functional Theory by the pseudopotential method, by use of Local Spin Density Approximation. Experimental investigations of absorption and transmission spectra of $Cd_{1-x}Fe_xTe$ epitaxial films showed, that with an increase in Fe concentration there is an increase in the band gap.

References

1. SharmaV.K., Xalxo R., Varma G.D. Structural and magnetic studies of Mn-doped ZnO. Cryst. Res. Technol. 42, 1, 34-38 (2007)
2. Sato K., Bergqvist L., Kudrnovskg J., Dederichs P. H., et al. First-principles theory of dilute magnetic semiconductors, Rev. Modern Phys. 82,1633–1690 (2010)
3. Furdyna J.K. Diluted magnetic semiconductors. J. Appl. Phys. 64, R29 (1988)
4. Kossut J., Beer A.C., Furdyna K. Diluted Magnetic Semiconductors, Semiconductors and Semimetals, Academic, New York (1988)
5. Ait Raiss A., Sbai Y., Bahmad L., Benyoussef A. Magnetic and magneto-optical properties of doped and co-doped CdTe with (Mn, Fe): Ab-initio study. Journal of Magnetism and Magnetic Materials. 385, 295–301 (2015)
6. Kaczkowski J., Jezierski A. DFT+U Calculations of Transition Metal Doped AIN. Acta Physica Polonica, 116, 5, 924-926 (2009)
7. Mehrabova M.A. Electron structure, defect formation energy of chalcogenides $A^{II-IV}B^{VI}$ and effect of ionizing irradiation on their physical properties. Doctoral dissertation. 387 (2018)

***Corresponding author**: m.mehrabova@science.az
mehrabova@mail.ru

VAPOR-PHASE SYNTHESIS OF COPPER-BASED NANOSTRUCTURES

D.JISHIASHVILI[1,2*], A.CHIRAKADZE[1], Z.SHIOLASHVILI[1], N.MAKHATADZE[1], A.JISHIASHVILI[1], V.GOBRONIDZE[1]

[1]*Georgian Technical University.V.ChavchanidzeInstitute of Cybernetics. 5, Z. Andjaparidze St., 0186, Tbilisi, Georgia*
[2]*Tbilisi State University. E.Andronikashvili Institute of Physics. 6, M. Tamarashvili St, 0177, Tbilisi, Georgia*

The vapor-phase synthesis of Cu-based nanomaterials using inorganic volatile Cu precursors is a key for controlling the composition, morphology and structure of copper containing nanomaterials. In this paper, we have shown that annealing of a solid Cu or CuO sources in the ambient of ammonium chloride and hydrazine decomposition products leads to the formation of volatile CuCl species. The mass transfer from source to the substrate, which was located in the "cold" zone of the reactor, was accomplished by these CuCl species. After condensation on Si substrate heated up to 400°C, they were interacting with hydrazine and ammonium chloride decomposition products forming, the agglomerated Cu microcrystals in case of Cu source. Different nanomaterials were synthesized when CuO was used as a source. These nanomaterials included Cu-based nanocrystals, nanowires and elongated microbubbles. Further investigations are planned to determine the composition and structure of these nanomaterials.

Keywords: CuO, cuprous chloride,pyrolytic synthesis
PACS: 61.46.+w; 68.37.Hk

1. Introduction

The rising interest to copper-based nanomaterials is caused not only by their unique properties but also by the flexibility and the cost-effectiveness of their growth technologies [1-3]. The copper oxides (CuO, Cu_2O) and chlorides (CuCl, $CuCl_2$) are the most studied and the most prospective copper compounds, which already found applications in different devices [4-6]. The electrochemically deposited copper films are inherent parts of microelectronic circuits since 1997, when IBM demonstrated the excellent performance of electrochemically deposited copper interconnect layer [7, 8]. However, the modern trends in micro-and nanotechnology clearly reveal that the vapor-phase growth is the most promising technology for producing copper-based nanomaterials [9]. CuCl and different metal-organic compounds form the majority of precursors, which are used to accomplish the vapor-phase synthesis of copper-based nanomaterials [10-12].The formation of volatile Cu molecules on the surface of nanostructured solid copper compounds and their subsequent evaporation may cause the copper depletion of a compound. This can serve as a flexible mean for the precise control of copper content in the compound. We encountered the problem of Cu content regulation when synthesizing NiCu nanoparticles for the magnetic hyperthermia of cancer cells. The Cu content should be kept at ~25 at.%, otherwise, the Curie temperature will exceed the dangerous value of 43°C or it will be below 41°C, which is insufficient for killing the cancer cells. In case of an excess Cu content, the controlled evaporation of Cu from NiCu alloy and subsequent homogenization may produce nanoparticles with the desired composition.

The purpose of this work was to present the preliminary results of our study on the formation of different nano- and microstructures by condensing the volatile precursors that were synthesized on the surface of a solid Cu source after its annealing in gaseous ambient containing ammonium chloride and hydrazine. In addition, a small illustrative data are also presented on the growth of nanostructures formed after annealing of CuO source in the same gaseous ambient.

2. Experimental.

1 mg of analytical grade copper foil or CuO powder sources, together with 0.01 mg of ammonium chloride were placed in 2 cm height alundum crucible. It was then covered with polished Si substrate and placed on the bottom of the vertical quartz reactor. The reactor was evacuated down to 2×10^{-5}Torr and filled with a gaseous mixture of hydrazine+3 mol. % H_2O up to its saturated vapor pressure of 10 Torr. The sources were annealed in the range of 450-750°C by means of an external resistive furnace. As is known, at 338 °C NH_4Cl decomposes

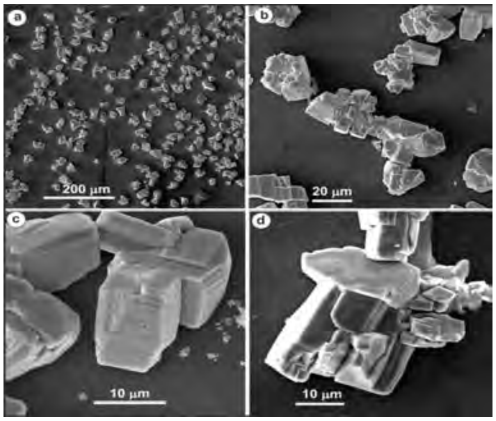

Fig.1. SEM image of Cu microcrystals grown at 400°C onto the Si substrate (a); SEM images of agglomerated Cu microcrystals (b-d).

to gaseous NH_3 and HCl, which are mixed with moistened hydrazine vapor forming the reactive ambient. The details of the technology are presented elsewhere [13].

Scanning Electron Microscopy (SEM-VEGA 3, LMU) and Energy Dispersive Spectroscopy (EDS-Oxford Systems) were used to analyze the morphology and composition of nanomaterials. The structure of synthesized materials was studied by X-ray diffraction (XRD) method using Shimadzu XRD-6000 diffractometer.

3. Results and discussion

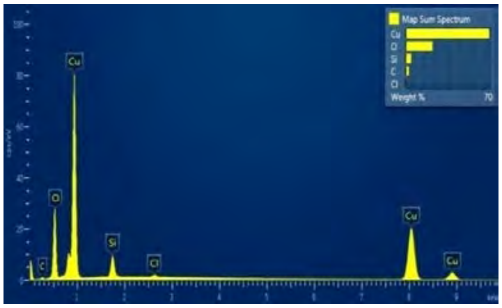

Fig.2. EDS spectrum of Cu microcrystals

Fig. 1 presents SEM images of microstructures formed at the Si substrate after annealing of Cu source in the mixture of ammonium chloride and hydrazine at 560°C. The temperature of Si substrate, which was located at 2cm above the source, was 400°C. The agglomerated particles have sizes exceeding tens of micrometers and they are scattered all over the Si substrate. The crystals with different morphologies were observed and most of them coincided with that of Cu microcrystals considered in [14]. The surfaces of particles are faceted, indicating that they have the crystalline structure. One can see clear step-terrace structures in Fig. 1c and d, which are formed during the homoepitaxial growth from the vapor phase.

Fig. 2 shows the EDS spectrum of one of the microstructures presented in Fig.1. It consists mainly of copper with a small amount of oxygen and even smaller concentration of carbon and Cl. The peak of Si comes from the substrate. The oxygen and carbon appear after the exposure of samples to atmosphere.

The microcrystals synthesized at identical process parameters, were scratched off of the Si substrate, mixed and analyzed by XRD method. The XRD pattern of microcrystals is shown in Fig.3. Three peaks at 2θ values of 43.6, 50.8, and 74.5 deg were observed. These peaks can be assigned to (111), (200), and (220) planes of face centered cubic copper (JCPDS, copper file No. 04–0836). These results may serve as a direct evidence for the formation of pure copper micro-sized crystals on the Si substrate surface after annealing of Cu source in the ammonium chloride and hydrazine vapor.

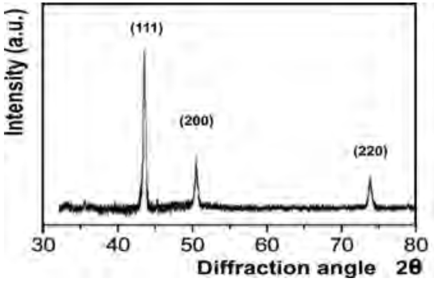

Fig.3. XRD spectrum of the copper microstructure.

Fig. 4 presents the distribution of areas of Cu crystallites that are shown in Fig. 1 a. As can be seen, most of Cu crystals have areas within 200-400 □m^2 and their total area covers 11% of the Si surface. The rough estimation of deposited Cu mass yielded ~1 mg/cm^2 assuming the average thickness of crystallites to be 10 □m. This value corresponds to the formation of a solid copper film with a thickness of 1.1 □m and the deposition rate of 0.37 □m/h (~ 6 nm/min). The obtained deposition rate value is quite compatible with the best results described in the literature for the vapor-phase grown Cu films [9]. The presence of chlorine in the EDS spectrum proves that the only volatile Cu precursors, which accomplish the mass transfer from Cu source to Si substrate, are copper halides. CuCl may be formed onto the Cu source surface due to the following spontaneous exothermic reaction (T=670°C):

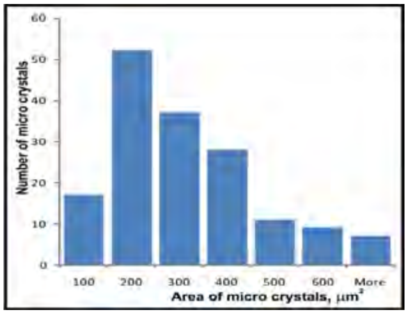

Fig.4.Histogram depicting the distribution of areas of Cu crystallites that are shown in Fig. 1 a.

$$HCl(g)+Cu(s)+NH(g)= CuCl(g)+0.5N_2(g)+H_2(g)\Delta G=-244kJ/mol \quad (1)$$

NH radicals, together with NH_2, NH_3 and H_2, appear in the reactor due to pyrolytic decomposition of hydrazine [15, 16]. CuCl has a high vapor pressure, which is close to tens of Torr at 670°C [17]. After adsorption onto the Si substrate heated up to 670°C CuCl may be reduced to Cu by molecular hydrogen or by NH and NH_2 radicals:

$$CuCl + NH = Cu + HCl + 0.5N_2\Delta G=-360 \text{ kj/mol} \quad (2)$$

$$(2CuCl + 0.5NH_2 = Cu + HCl + 1/4N_2\Delta G=-109 \text{ kj/mol} \quad (3)$$

Regarding the $CuCl_2$ it should be noted that this compound may be formed on the Cu surface by reacting withHCl and oxygen, which may appear in the reactor as a residual gas:

$$2HCl+Cu+0.5O_2=CuCl_2+H_2\Delta G=-63 \text{ kj/mol} \quad (4)$$

$CuCl_2$ may be produced also by reactions involving Cu, HCl and NH_2, which originates from the pyrolytically decomposed hydrazine:

$$2HCl + Cu + NH_2 = CuCl_2 + 0.5N_2 + 2\ H_2\Delta G =-88 \text{ kj/mol} \quad (5)$$

The reactions (1) - (5) provide a high concentration of volatile Cu precursors, which enable the synthesis of Cu crystallites with a sufficiently high growth rate.

In the second set of experiments, CuO was used as a source material instead of Cu. It was annealed at 580°C and 620°C in the same ambient gases as the Cu source i.e. the mixture of NH_4Cl and N_2H_4+3 mol.% H_2O. As is known, CuO is a stable compound with a high melting and boiling points (1201°C and 2000°C respectively). These temperatures are quite high in comparison with the temperature used in our experiments for the annealing of CuO source. It means that the appearance of any Cu containing substances on the surface of Si substrate can serve as evidence for the formation of volatile Cu compounds at the surface of the source and their subsequent condensation onto the Si substrate. Fig. 5 a, b shows the nanostructures synthesized onto the Si substrate heated at 470 and 430°C (the corresponding CuO source temperatures were 620 and 580°C). In contrast to Cu source, the annealing of CuO source caused the formation of a variety of nanostructures on the Si substrate (Fig. 5 a-d). At lower growth temperature the microtubes were formed on the substrate and the surface between these tubes was covered with nanoparticles having diameters from tens to hundreds of nanometers (Fig. 5 a, c). Besides nanoparticles, the formation of one-dimensional nanowires is also observed in Fig. 5 c.

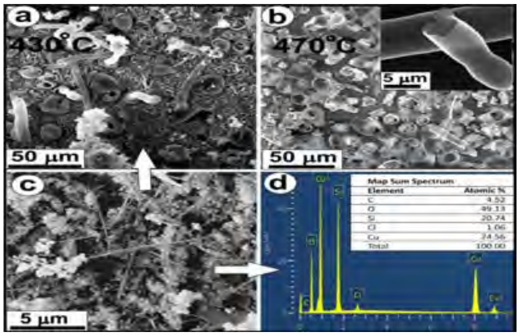

Map Sum Spectrum	
Element	Atomic %
C	4.52
O	49.13
Si	20.74
Cl	1.06
Cu	24.56
Total	100.00

Fig.5. Nanostructures annealed at 430° C (a) and 470°C (b, c) and EDS spectrum of nanomaterials grown at 430 °C (d).

Only microtubes were formed at elevated temperatures as it is shown in Fig. 5 b. The inset depicts the enlarged view of a part of a broken microtube. The thickness of its wall was estimated to be less than 100 nm. The area between microtubes is clear from nanomaterials as compared to nanostructures grown at lower temperature (Fig. 1 a).

Fig. 5 d shows the EDS spectrum of nanostructures depicted in Fig. 5 c. In contrast to the material, grown from Cu source, the nanostructures synthesized from CuO source are containing a higher amount of oxygen and chlorine. The formation of such a large variety of nanostructures is attributed to the synthesis of different precursors and to the complicated chemical reactions that take place during the condensation of volatile precursors. The detailed analysis of nanomaterial composition and structure, together with chemical reactions that lead to the formation of a nanostructure with a specific morphology, needs appropriate experiments, which are currently performed by our scientific group.

4. Conclusions

The novelty of this work is in the application of the gaseous mixture of ammonium chlorie and moistened hydrazine for producing Cu-based nano- and microstructures. In this work we have demonstrated that the gaseous medium formed after pyrolytic decomposition of NH_4Cl and moistened hydrazine (3 mol.% H_2O) may serve for the production of volatile Cu molecules at the surface of Cu and CuO. The novelty of the technology is in the formation of Cu precursors directly in the reaction chamber with their further application for the synthesis of Cu-based nanomaterials. The FCC copper particles were condensed on the Si substrate after annealing of Cu source at 560°C in the above-mentioned mixture of gases.

Analyzing the reaction precursors and the composition of produced materials we suggest that CuCl is the main precursor, which is synthesized at the surfaces of Cu and CuO sources. CuCl reaches the surface of Si substrate, located above the source, and after interacting with H_2 reduces to a pure Cu. Copper may appear also after interaction of CuCl with NH and NH_2radicals formed after pyrolytic decomposition of hydrazine**.**

When CuO source was annealed at 430 and 470°C in the same gaseous medium, the condensed nanomaterials were also containing copper and increased oxygen and chlorine concentrationin comparison with that produced from Cu source. As a result, different nanomaterials were produced including nanoparticles, nanowires and microtubes with wall thicknesses less than 100 nm. Further investigations are needed to understand in details the processes which lead to the formation of such nanomaterials.

Acknowledgment

This work has been supported by a joint STCU (#7089) and Shota Rustaveli GNSF (#2017–20) grunts.

References

[1] Tamilvanan A., Balamurugan K., Ponappa K., Kumar B.M. International Journal of Nanoscience 13(2), 1430001-(22 pages), (2014).
[2] Copper Metal for Semiconductor Interconnects. In: Noble and Precious Metals. Properties, Nanoscale Effects and Applications. Editor: M. Seehra. Intechopen. 2018, 430 p.
[3] Bhanushali S., Ghosh P., Ganesh A., Cheng W. 1D Copper Nanostructures: Progress, Challenges and Opportunities. Small 11, 1232 (2015).
[4] Zhang Q., Zhang K., Xu D., Yang G., Huang H. Progress in Materials Science, 60(1), 208-337, (2014).
[5] Zoolfakar A.S., Rani R.A., etc all. Journal of Materials Chemistry, C 2, 5247 (2014).
[6] Zamfirescu C., Dincer I., Naterer G.F. International Journal of Hydrogen Energy, 35, 4839 (2010).
[7] Andricacos P.C., Uzoh C., Dukovic J.O., Horkans J., Deligianni H. IBM Journal of Research and Development, 48(5), 567 (1998).
[8] Baklanov M.R., Adelmann Ch., Zhao L., De Gendt S. ECS Journal of Solid State Science and Technology 4(1), Y1-Y4, (2015).
[9] Gordon P.G., Kurek A., Barry S.T. ECS Journal of Solid State Science and Technology 4(1), N3188 (2015).
[10] Chemistry of Electronic Materials. Collection Editor: Andrew R. Connexions, Rice University, Houston, Texas, 2012, 359p.
[11] ClaessenR. Design of Volatile Non Halogenated Precursors for the Chemical Vapor Deposition (CVD) of Copper: Understanding Key Molecular Properties in a CVD Process Feasibility Study. Books on Demand, 2002, 212 p.
[12] Park K-H., Marshall W.J. Journal of American Chemical Society 127, 9330.(2005).
[13] Jishiashvili D., Shiolashvili Z., Chirakadze A., Makhatadze N., GobronidzeV., Jishiashvili A. Nano Studies 17, 67-72, (2018).
[14] Yasnikov I.S., Pavlova A.P. Letters on Materials 4(1), 41 (2014).
[15] de Medeiros J.E., Valenza G.P. Brazilian Journal of Chemical Engineering 15(2), 121 (1998).
[16] Pakdehi Sh.G., Salimi M. Researches and Applications in Mechanical Engineering 3, 21 (2014).
[17] Shelton R.A.J. Transactions of the Faraday Society57, 2113-2118, (1961).

***Corresponding author**: d_jishiashvili@gtu.ge

STUDIES OF THE COMPARATIVELYLOW-TEMPERATURE SYNTHESIS AND PRELIMINARY TOXIC CHARACTERISTICS OF SILVER DOPED LANTHANUM MANGANITE NANOPARTICLES USING CONVENTIONALAND MICROWAVE HEATING

A.CHIRAKADZE[1], D.JISHIASHVILI[1,3], N.MITAGVARIA[2], I.LAZRISHVILI[2], Z.SHIOLASHVILI[1], A.JISHIASHVILI[1], N.MAKHATADZE[1], Z.BUACHIDZE[1], N.KHUSKIVADE[1*]

[1]Georgian Technical University,Kostava St 77, Building 4, 0160, Tbilisi, Georgia
[2]Beritashvili Experimental Biomedicine Center,St, 0160, Tbilisi, Georgia
[3]Tbilisi state University. E.Andronikashvili Institute of Physics. 6, M. Tamarashvili St, 0177, Tbilisi, Georgia

The research is dedicated to microwave and conventional methods of solution combustion synthesis of the relatively new nanomaterial proposed for magnetic hyperthermia of cancer cells and preliminary assessment of the toxicity of developed materials based on the behavioral methods and techniques at the levels far below of commonly registered by means of usualy and widely applied assays for humans. Farther research is needed to optimize the methods of synthesis of silver doped lanthanum manganites with required characteristics.

Keywords: magnetic hyperthermia, microwave synthesis, nanoparticles
PACS:87.19.xj; 61.46.+w; 75.75.−c

1.Introduction

As is known, lanthanum manganites attracted a lot of attention due totheir interesting physical properties like colossal magnetoresistance, ferroelectricity, superconductivity, charge ordering spin transport, thermo-power, high catalytic capacity and the variation in the properties caused by doping with different metals. After the pioneering research performed in 1993 [1] on heating ferromagnetic nano-fluids under the external electromagnetic field, these materials become a subject of an active research as a prospective agents for magnetic hyperthermia of biological tissues. Magnetic hyperthermia (MHT) is a promising method, which can significantly increase the efficiency of chemotherapy and radiotherapy when used as adjuvant mean and can reduce the required amount of drugs and doses of radiation by several times.The location of heating can be effectively controlled by a magnetic field, which allows it to be concentrated and retained at the site of the tumor. Parameters of the nanofluids and alternating magnetic field should be carefully selected to provide optimal heating velocity, controlled heating temperature T (41-43°C) and dose of thermal exposure. In case when T exceeds 43°C it can damage the healthy tissues. If T is close to 39°C the corresponding hyperthermal process, on the contrary, can stimulate the rapid multiplication of cancer cells. That is why, providing a self-regulated process of heating is highly important. The optimal way to perform this is the development of magnetic heating agents with controlled Curie temperature (T_c) near to 41-42°C, avoiding surgical intervention and invading of special thermometers. Another important problem of MHT is the achievement of uniform heating of the cancer tumor, which depends on how homogeneously the nanoparticles are distributed in the tissue. Magnetic nanoparticles for hyperthermia should be non-toxic or low toxic; ensure an uniform strictly localized distribution in the tumor and prevent thrombogenesis; have appropriate dimensions for effective penetration into cells; provide effective heating in an alternating magnetic field with the amplitude and frequency limited by the medical restrictions; allow to facilitate the “self-regulated” heating and control of T_c in the required temperature range At the same time, volume production of the materials requires higher capacity and lower costs of the production process. Several groups of compounds can be proposed to be the object of the detailed research. However, the above requirements “narrow” the possible choice and reduce it to a small group of compounds, among which two materials have been intensively synthesized and studied in the Tbilisi State University and Beritashvili Experimental Biomedicine Center: Ni-Cu and $La_xAg_{1-x}MnO_3$. Nano-alloys with T_c = 41-45^{0}C have been actively synthesized and tested as material for self-regulating magnetic hyperthermia during last decades. Recently, the nanostructured $La_xAg_{1-x}MnO_3$ has attracted great attention for magnetic hyperthermia applications as a nanomaterial with very specific properties and a therapeutic heating agent with precisely regulated and controlled T_c. However, there are no available data on their toxicity under the conditions of relatively low exposure.The scope of the research is focused on the conventional and microwave-enhanced synthesis of $La_{0.8}Ag_{0.15}MnO_3$nanomaterials applicable for magnetic hyperthermia; improving of dispersity, uniformity, magnetic characteristics of the nanoparticles and reducing the synthesis time; as well as preliminary estimating the level of toxicity of developed materials for mammals. A novel bapproach to the development and application of widely differing methods of testing toxicity of MNPs was used because a special attention should be paid to the methodologies of toxicity testing with regard to animal right activists around the world who are increasingly opposing the use of animals. The approach is aimed to provide a reliable assessment of the toxic impacts far below the commonly registered by means of usually and widely applied assays for humans.

2. Experimental

Comparatively low temperature solution combustion method described in [2] was utilized to prepare the nanopowders.We used the stoichiometric compositions with slightly (for 5-10%) increased amount of glycine as fuel. The prepared solution was heated under continuous mixing to 80-85°C (conventional heating) or to 65 °C (microwave heating [3-4]) of precursors.Theobtained gel was put through a water-pipe previously heated to 300-320°C. After boiling the process product was annealed in air atmosphere at 790-810°C for 5-6 hours (conventional heating) or 670-690 °C for 4 hours (microwave heating).

Experiments on toxicity assessment [5-9] were conducted on laboratory rats of both sexes. Prior to the injection of the test substances and the initiation of hyper-thermal exposure, experiments were conducted on control animals to reveal the initial state of learning and memory processes, the fear and anxiety levels. Rodents are learning to move on optimum trajectory by a trial and error method. Changes in the number of errors (entry into the deadlock compartments of the maze) and the time of maze passage were used for evaluation of the process of learning. To be adapted to experimental conditions, all groups of animals prior to the beginning of experiments for a few days were placed in a nest-box.At the beginning of the experiment an animal was placed on the start-platform and it had to find out the correct way to the nest-box. Every subsequent movement on the platform brought the animal to a novel situation and it was a stimulus for a new movement ahead. Reaching the target-box by the animal was delivering from non-ethological conditions and was regarded as an essential reward and served as a motivation for forward moving through the maze [5-9].Anxiety reduction in the plus-maze was indicated by an increase in the ratio of times spent in the light and darkened arms. The total number of entries into both arms sometimes was used as the measure of general activity. The results of testing of toxicity of the developed nanofluids were compared with the impact of widely used nanomaterials for magnetic hyperthermia [3, 10].

Scanning Electron Microscopy (SEM-VEGA 3, LMU) and Energy Dispersive Spectroscopy (EDS) were used to analyze the morphology and composition of nanomaterials. The structure of synthesized materials was studied by X-ray diffraction (XRD) method using Shimadzu XRD-6000 diffractometer. Magnetic characterization of obtained materials was executed using vibration scanning magnetometer (VSM EZ9). Standard electric oven LY-612 was used for conventional heating, while MX BAOHENG WBF Y201 microwave reactor based unit was used for microwave heating of precursors' gel.

To assess the learning and memory processes, a standard multi-branch maze was used, while assessment of the levels of anxiety and fear were carried out using the elevated plus-maze and methodology of testing in the so-called "open field" [9].

3. Results and discussion

Scanning Electron Microscopy (SEM), Energy Dispersive X-Ray Spectroscopy and Vibrating-Sample Magnetometry (VSM) of $La_xAg_{1-x}MnO_3$nanomaterials synthesized by means of conventional and microwave) heating, EDS spectra and magnetic hysteresis curves of nanomaterials formed under conditions of conventional microwave heating and annealin of $La_{0.9}Ag_{0.1}MnO_3$, $La_{0.85}Ag_{0.15}$MnO3 and $La_{0.8}Ag_{0.2}MnO_3$ samples were developed and used for characterization of the morphology, magnetic properties and structure of the obtained nanoparticles. The average concentration (in at. %) of main constituent chemical elements in tested samples is given in Table 1.

The average concentration (in at.%) of main constituent chemical elements in tested samples is given in Table 1.

Table 1. The average concentration (in at.%) of main constituent chemical elements in tested samples.

Sample	La	Ag	Mn	O
Microwave heating and annealing	16,05	3.06	20.05	60.15
Conventionalheating and annealing	16.30	2.55	22.45	61.85

Fig.1 represents the utilized unit for combined exposing of test animals to the whole body hyperthermia and injection of developed nano-fluids based on saline solutions located in the laboratory of the cerebral blood circulation and metabolism department of the Beritashvili Center of Experimental Biomedicine. The results of toxicity assessment of the developed nanomaterials were compared with the analogue characteristics of the widely used iron based nanomaterials and nanocomposites for magnetic hyperthermia.

Fig. 1. The utilized unit for combined exposing of test animals to the whole body hyperthermia and injection of developed nano-fluids.

Testing of the learning and memory processes in rats and assessment of the toxicity of developed materials can be facilitated through various maze and “open field” techniques of behavioral responses and learning and memory processes in animals were used to assess the toxicity of the developed nanoparticles in comparison with ferric oxide nanoparticles [10]. The typical dependence of the maze passage time on the days of the continuous experimental study for intact, saline and Hyperthermia + nano-fluid treated cases was used for preliminary toxicity assessment. The obtained data are given in Figures 2-4 for the silver doped lanthanum manganite, NiCu and Fe_2O_3 nanoparticles respectively.

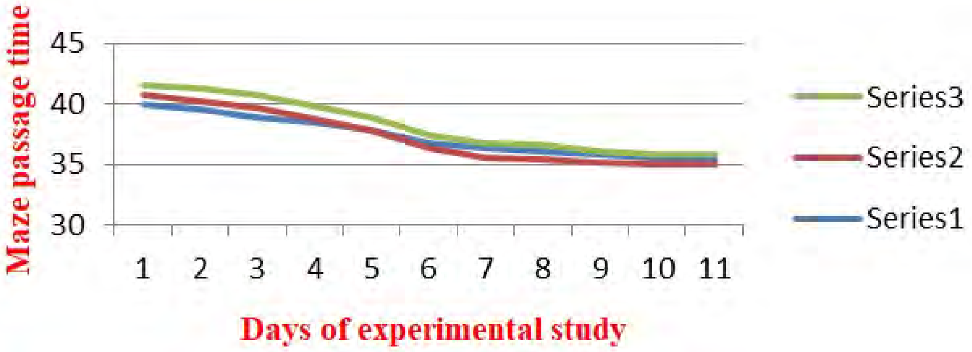

Fig, 2. Dependence of the maze passage time on the days of the toxicity testing experiment: S1-intact; S2- saline solution injections; S3-silver doped lanthanum manganite nanoparticles

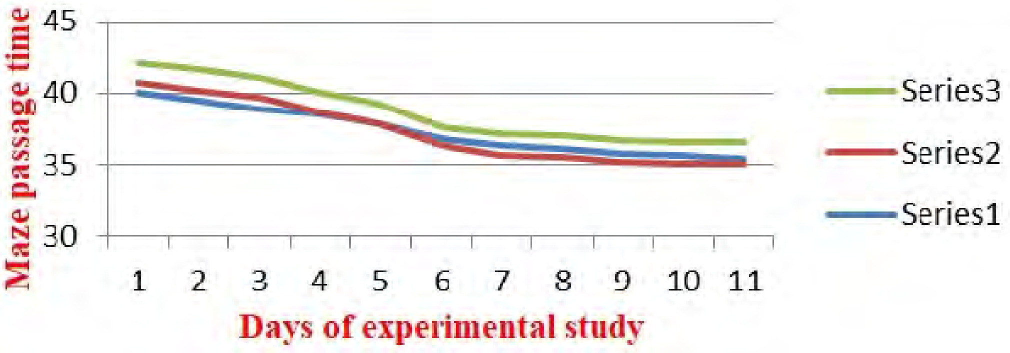

Fig. 3. Dependence of the maze passage time on the days of the toxicity testing experiment: S1-intact; S2- saline solution injections; S3- NiCu nanoparticles

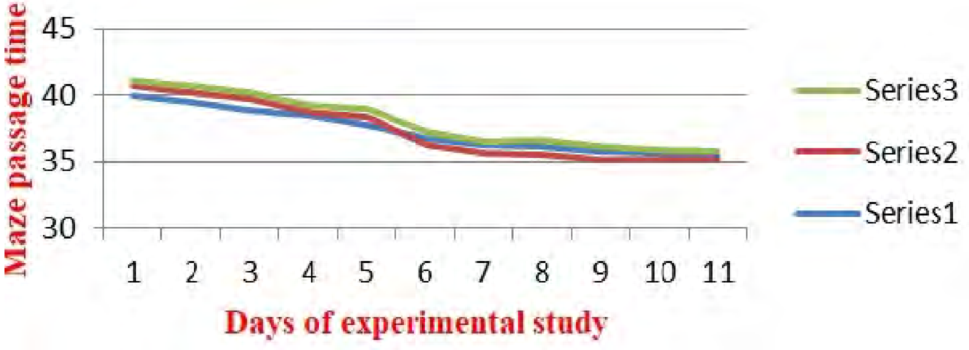

Fig. 4. Dependence of the maze passage time on the days of the toxicity testing experiment: S1-intact; S2- saline solution injections; S3- Fe_2O_3

Testing of the developed samples also showed that microwave assisted processes provide improved morphology and reduced temperature and duration of synthesis and annealing, which can yield in increased energy effectiveness and capacity of production. Preliminary toxicity assessment of the developed nanomaterials showed their comparative safety regarding the widely used nanoparticles for magnetic hyperthermia.

4. Conclusions

The obtained preliminary data given above show that toxicity of both silver doped lanthanum manganite and Ni-Cu nano-fluids is close to the toxicity of the widely used nano-fluids containing Fe_2O_3 nanoparticles. Moreover, after about 10 days the treated animals completely restore their learning and memory skills. A favorable nanomaterial for magnetic hyperthermia of cancer cells is the product of the microwave enhanced synthesis of the silver doped lanthanum manganite, characterized with high mono-cristallinity, sufficient magnetic properties, improved homogeneity and mono-dispersive fractions, and compositions very close to stoichiometric. The temperature an duration of microwave enhanced synthesis and annealing is significantly lower compared to the characteristic temperatures and durations under the conditions of conventional heating. The most important finding is that microwave treatment enhances the silver doping process and promotes the production capacity, as well as energy saving during the production cycle. This nanomaterial is characterized by sufficient magnetic properties, improved homogeneity and mono-dispersity, and compositions very close to stoichiometric. The typical temperature and duration of microwave enhanced synthesis and annealing is significantly lower as compared to the characteristic temperatures and durations used in conventional heating method. According to the data of preliminary assessment, toxicity of all developed Ag doped lanthanum manganite nanoparticles does not exceed the toxicity of the widely used nanoparticles for magnetic hyperthermia. On the other hand, additional studies are needed to assess the favorable material for magnetic hyperthermia of cancer cells taking into account the mass producing capacity, treatment effectiveness and toxicity of the developed materials.

Acknowledgement

This research has been funded in the frame of a joint STCU (#7089) and SRNSF (STCU-2017- 20) grant project.

References

[1]. Jordan A., Wust P., Fahling H., John W., Hinz A., Felix R.. International Journal of Hyperthermia, 9, 1, 51–68 (1993).
[2]. Nagabhushana B.M., Sreekanth B., Chakradhar R. P., Ramesh K. P, Shivakumara C., Chandrappa G.T. Mater. Res. Bull., 41, 9, 1735–1746 (2006).
[3]. Chirakadze A., Jishiashvili D., Buachidze Z., Gorgadze K., Shiolashvili Z.,Jishiashvili A., Mitagvaria N., Lazrishvili I. Journal of Low Dimensional Systems, 2,1, 8-22 (2018).
[4]. Kervalishvili P. D., Chirakadze A., Buachidze Z. , Jishiashvili D., Bjalava T., Kervalishvili G.,
Toscano W., Gvakharia V., Sergeenko G. Nuclear Radiation Sensors and NanosensorySystems.Edited by Paata J.Kervalishvili (PhysicsDepartment of Georgia Technical University,Tbili, Georgia) and Panos H. Yannakopoulos (Department of Electronic Computer Systems, Engineering, Piraeus University of AppliedSciences). Selected paper from the Advanced Research Workshop which was held in Tbilisi, March 6-9 2014.Springer, 22-86(2013).
[5]. Mitagvaria N., Lazrishvili I., Devdarian iM., Davlianidze L., Nebieridze M., Saginadze N., Kvachakidze I., Gumberidze L., Sikharulidze N.. Journal of Biological Physics and Chemistry, 15,187-193 (2015).
[6]. Carobrez A. P., Bertoglio L J. Biobehav. Rev. 29, 1193–1205 (2005).
[7]. Crusio W. E., Sluyter F., Gerlai R. T. Ethogram of the mouse. In: Crusio W.E., Sluyter F., Gerlai R.T.,Pietropaolo S. Cambridge, United Kingdom: Cambridge University Press. 17–22, ISBN 978-1-107-03481-5 (2013).
[8]. Hogg S. A. Pharmacol. Biochem.Behav. 54: 21–30. doi: 10.1016/0091-3057(95)02126-4, (1996).
[9]. Sturman O., Germain P..L., Bohacek J. Stress: 1–10. doi:10.1080/10253890.2018.1438405. PMID 29451062 (2018).
[10]. Wang Y., Ding L., Yao C., Li C., Xing, Y. Huang, Gu T., Wu M. Science China materials, 60,2, 93-108, Springer (2017).

[*] **Corresponding author:** nanakhuskivadze53@gmail.com

MAGNETOTHERMOELECTRIC PROPERTIES OF THERMAL ELEMENTS ON THE BASIS OF CRYSTALS OF SOLID SOLUTIONS BISMUTH-ANTIMONY AND BISMUTH TELLURIDE-ANTIMONY TELLURIDE

B.SH.BARKHALOV[*,1], M.M.TAGIYEV[2,1], G.D.ABDINOVA[1]

[1] *Institute of Physics of Azerbaijan National Academy of Sciences, Huseyn Cavid avenue,131, Baku, Azerbaijan, Az1148*

[2] *Azerbaijan State Economic University, Istiglaliyyat str., 6, Baku, Azerbaijan, Az1001*

This paper presents the results of a study of temperature gradients arising on thermoelements manufactured on the basis of n-type Bi-Sb solid solutions (with 15 at.% Sb) and 69% Sb_2Te_3+27% Bi_2Te_3+4% Sb_2Se_3 in the temperature range from 130 K to 300 K and magnetic field induction from B = 0 to B = 1.0 T. Crystals of solid solution 69% Sb_2Te_3+27% Bi_2Te_3+4% Sb_2Se_3 were grown by the Bridgman method and at 300 K had a thermoelectric figure of merit Z =$3.2x10^{-3}K^{-1}$. It is shown that the changes observed in the values of Z and ΔT on thermoelements under the action of a magnetic field are mainly due to the change in the thermoelectric parameters of n-branches made of Bi-Sb crystals. It is shown that the main thermo- and magneto-thermoelectric parameters of energy converters developed on the basis of the extruded materials are close to the parameters of coolers manufactured on the basis of single-crystal materials.It was found that thermoelements and converters based on the developed material are distinguished by high reliability of parameters and are suitable for operation as part of electronic devices.

Keywords: thermoelement, electronic coolers, magnetic field, temperature gradient, thermoelectric figure of merit
PACS: 84.60.-h; 72.15.Jf; 85.80.Fi

1. Introduction

Bi-Sb solid solutions (especially with 6.5-9 at.% Sb) with n-type conductivity are promising materials for creating electronic coolers at a temperature level below 200 K [1-6]. Therefore, a sufficient amount of works has been devoted to the study of their thermoelectric properties in a wide range of temperatures and magnetic induction. However, the question of creating cooling elements on the basis of n-type bismuth-antimony crystals and studying their thermoelectric parameters at low temperatures depending on the magnetic field induction remains little studied.

2. Experiment

This paper presents the results of the study of temperature differences arising on thermoelements created on the basis of n-type Bi-Sb solid solutions (with 3 at.% Sb) and 69% Sb_2Te_3 + 27% Bi_2Te_3 + Sb_2Se_3 (hereinafter Bi-Te-Se) p-type in the temperature range from 130 K to 300 K and magnetic field induction from B = 0 to 1.1 T. Crystals of Bi-Te-Se solid solutions of p-type were grown by the Bridgman method and at 300 K had a thermoelectric figure of merit Z=$3.2x10^{-3}K^{-1}$.

The branches of the investigated thermoelements had the shape of rectangular parallelepipeds with a height of about 14 mm. The optimal ratio of the sizes of the branches was selected according to the expression:

$$\frac{(l_n / S_n)}{(l_p / S_p)} = \sqrt{\frac{\sigma_n \chi_n}{\sigma_p \chi_p}},$$

where $l_n, S_n, \sigma_n, \chi_n$ and $l_p, S_p, \sigma_p, \chi_p$ are length, cross section, electrical conductivity and thermal conductivity of *n*- and *p*-branches, respectively. In measurements, the magnetic field induction vector was directed along the bisector axis of Bi-Sb crystals, and the electric current along the trigonal axis of Bi-Sb crystals and along the layers in Bi-Te-Se crystals. The measurements were carried out in a vacuum of ~10^{-3} Torr. The temperature of the cold and hot junctions was determined using copper-constantan thermocouples.

3. Results and discussion

On the Fig.1 dependence of the thermoelectric figure of merit for $Bi_{97}Sb_3$ alloy on the magnetic field induction B at different temperatures is presented.

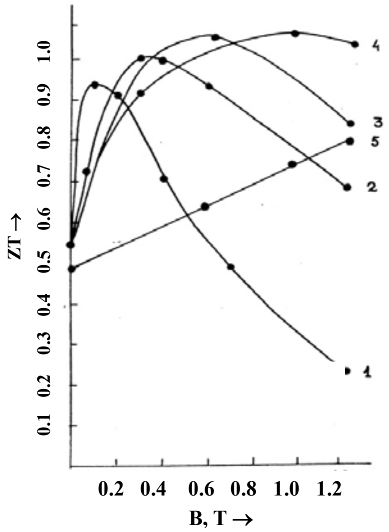

Figure 1. Dependence of the thermoelectric figure of merit for $Bi_{97}Sb_3$ alloy on the magnetic field induction B at different temperatures: 130 K (1), 160 K (2), 180 K (3), 200 K (4), 300 K (5).

Fig. 2 shows the dependence of the maximum temperature difference $\Delta T_{\max}$ on the thermoelement at different temperatures from the magnetic field induction B.

In Fig. 3 the dependence of the relative change in temperature difference on a thermoelement at different temperatures from the magnetic field induction B is presented. Here $\Delta(\Delta T) = \Delta T - \Delta T_0$, where ΔT and ΔT_0 are temperature gradients on coolers at a certain value of B and at B=0 respectively.

From the data in Fig. 2 and 3 it follows that the magnetic field significantly (up to 35%) increases the temperature gradient on the thermoelement. At the same time, the optimal value of the magnetic field induction, corresponding to the maximum increase in ΔT with decreasing of the temperature reduces and is 0.2 T at 130 K.

The temperature gradient arising on the cooling element is determined by its thermoelectric figure of merit Z, which in turn depends on the basic parameters of the thermoelement branches as follows:

$$Z = \frac{\alpha^2 \sigma}{\chi},$$

where α, σ, χ are the coefficients of thermo-e.m.f., specific electrical conductivity and thermal conductivity of the branches respectively.

When a thermoelement is placed in a magnetic field, the contribution to the total current of fast carriers in the n-branch of Bi-Sb single crystals increases.Therefore, the average energy of the current carriers increases, which leads to a significant increase in the thermo-e.m.f. coefficient of this branch. In addition, in the magnetic field an electron component of the thermal conductivity of the Bi-Sb branch is somewhat reduced. Therefore, in a magnetic field despite a slight decrease in the electrical conductivity coefficient (due to magnetoresistance), there is a significant increase in the thermoelectric figure of merit of the n-branch of Bi-Sb (for example, at 180 K from $3.0\text{x}10^{-3}K^{-1}$ at B= 0 T to $5.5\text{x}10^{-3}K^{-1}$ at B = 0.6 T [2, 3]), and therefore thermoelement as a whole. As a result, in a magnetic field the temperature difference on the thermoelement grows. Experiments have shown that the magnetic field does not significantly affect the thermoelectric parameters of the p-branch from Bi-Te-Se, i.e. the change in the ΔT in the thermoelement under the action of the magnetic field is almost entirely due to the change in the parameters of the n-branch of the Bi-Sb crystals.

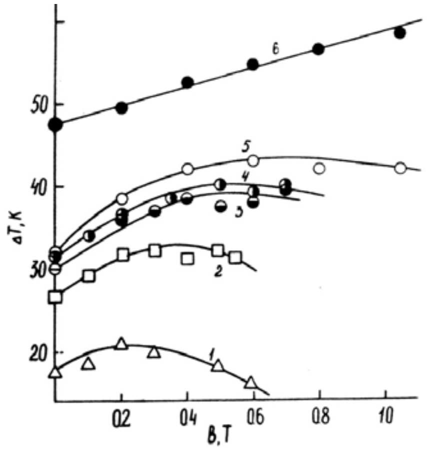

Figure 2. Dependence of the maximum temperature difference $\Delta T_{\max}$ on the thermoelement from the magnetic field induction B at different temperatures, T: 130 K (1), 150 K (2), 170 K (3), 180 K (4), 200 K (5), 300 K (6).

.

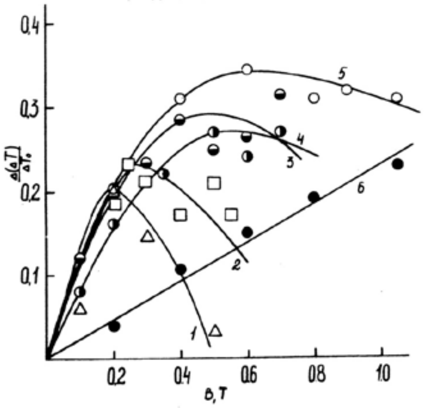

Figure 3. Dependence of the relative change in temperature difference on the thermoelement $\frac{\Delta(\Delta T)}{\Delta T_0}$ for the magnetic field induction B at the temperatures of 130 K (1), 150 K (2), 170 K (3), 180 K (4), 200 K (5), 300 K (6).

4. Conclusion

The results of a study of temperature gradients arising on thermoelements manufactured on the basis of n-type Bi-Sb solid solutions (with 15 at.% Sb) and 69% Sb_2Te_3+27% Bi_2Te_3+4% Sb_2Se_3 in the temperature range from 130 K to 300 K and magnetic field induction from B = 0 to B = 1.0 T. Crystals of solid solution grown by the Bridgman method at 300K had a thermoelectric figure of merit $Z=3.2\mathrm{x}10^{-3}K^{-1}$. It is shown that the changes observed in the values of Z and ΔT on thermoelements under the action of a magnetic field are mainly due to the change in the thermoelectric parameters of n-branches made of Bi-Sb crystals. It was found that thermoelements and converters based on the developed material are distinguished by high reliability of parameters and are suitable for operation as part of electronic devices.

References

1. Ivanov G.A., Kulikov V.A., etc all, Fizika i Tech. Poluprovodnikov, 6, 926 (1972).
2. Zemskov V.E., Gusakov V.P., Belaya A.D., Roslov S.A., Izvestiya AN SSSR, Metalli 3, 198 (1975).
3. Zemskov V.S., Borodin P.G., Belaya A.D., Roslov S.A., Dep.VINITI, No. 83-78, Moscow (1978).
4. Yim W.M., Amith A., Solid-State Electronics 15, 1141-1145 (1972).
5. Shakhtakhtinskiy M.G., Tomtiyev D.S., Kuliyev A.A., Izv. AN Azerbaijan SSR. Ser. Phys.-tech. and Math. Sciences 4, 27 (1968).
6. Osipov Ye.V. Solid-state cryogenics, Kiyev,"Naukova Dumka"(1977).

***Corresponding author**: bbarhal@mail.ru

DIELECTRIC PROPERTIES OF CdMnTe(Se) SEMIMAGNETIC SEMICONDUCTORS

[1]M.A.MEHRABOVA[*], [2]H.R.NURIYEV,[3]N.H.HASANOV, [1]T.I.KERIMOVA, [4]A.I.KAZIMOVA, [5]N.A.SAFAROV, [2]A.M.NAZAROV
[1]*Institute of Radiation Problems of ANAS, B.Vahabzade str.9, Baku, Azerbaijan, Az1143*
[2]*Institute of Physics of ANAS named after academician G.M.Abdullayev, H.Javidave. 131, Baku, Azerbaijan,Az1143*
[3]*Baku StateUniversity, Z.Khalilov str., 23, Baku, Azerbaijan, Az1148*
[4]*Ganja State University,Shah Ismayil Khataiave 187, Ganja, Azerbaijan, Az2000*
[5]*Khazar University, 11 Mahsati Ganjavi rd, Baku Azerbaijan, Az1096*

It was investigated temperature dependences of dielectric permittivity and conductivity of CdMnTe(Se) semimagnetic semiconductors at measurement frequencies of 25 Hz-1 MHz and temperatures of 294-550 K. It was found that with increasing of temperature, an increase in capacitance *c,* dielectric permittivity ε and conductivityσ is observed, the slope of the curves remains constant. It have been defined that in the all dependences the higher the frequency of the measuring field, the later begins the growth of *c,* ε and σ. The parameters remain almost unchanged up to temperature of ≈480ç500 K over the entire studied frequency range. A maximum are observed at a temperature of 500ç550 K. The conductivity at temperature of 500 K at low frequencies is 2.5x10^{-6} S/cm.

Keywords: Semimagnetic semiconductor, crystal structure, dielectric permittivity, conductivity, measurement frequency, temperature dependence
PACS:07.50.-e, 72.40.+w

1. Introduction

Semimagnetic semiconductors (SMS) are a group of materials that attract a great deal of attention because of their unique properties which promise many potential applications [l,2]. SMS differ from ordinary semiconductors because a fraction of their metallic ions are replaced by some species of magnetic ions. Mn^{2+} ions has a relatively large magnetic moment (S = 5/2) due to the $4s^0$ $3d^5$ electronic configuration in its outer shells. In these materials, the large sp-d exchange interaction between magnetic ions and electrons in valence band can lead to a number of unusual electronic, optical and magneto-optical properties including the ability to magnetically tune the band gap [1,2]. These properties make SMSs promising candidates for fabricating magneto-optical devices such as magnetic field sensors, isolators, magneto-optical switches [3] and solar cells, γ- and x-ray detectors and etc.

Thin film formation of these materials have been carried out employing different techniques, includes thermal evaporation, molecular beam epitaxy, hot wall epitaxy, low-pressure metal-organic chemical vapor deposition and chemical bath deposition. Exact knowledge of the dielectric permittivity, refractive index, absorption coefficient and optical band gap of CdMnTe(Se) thin films is indispensable for the design and analysis of various optical and magnetooptical devices. There are a few reports that analyze the static dielectric permittivity.

In this paper we have investigated temperature dependences of dielectric permittivity and conductivity of CdMnTe(Se) semimagnetic semiconductors at frequencies of 25Hz-1MHz, at temperatures of 294-550K.

2. Methods

CdMnTe(Se) SMS were synthesized and crystal structure has been studied by X-ray diffraction method on the BRUKER D8 ADVANCE XRD (fig.1) [4,5].

Dielectric permittivity ε was carried out on a digital E7-20 immittance meter at measurement frequencies of 25 Hz-1 MHz in a temperature range of T = 294 - 550K. The amplitude of the measuring field did not exceed 1V cm^{-1}. The sizes of sample were 0.2 x 0.4 x 0.6 mm.

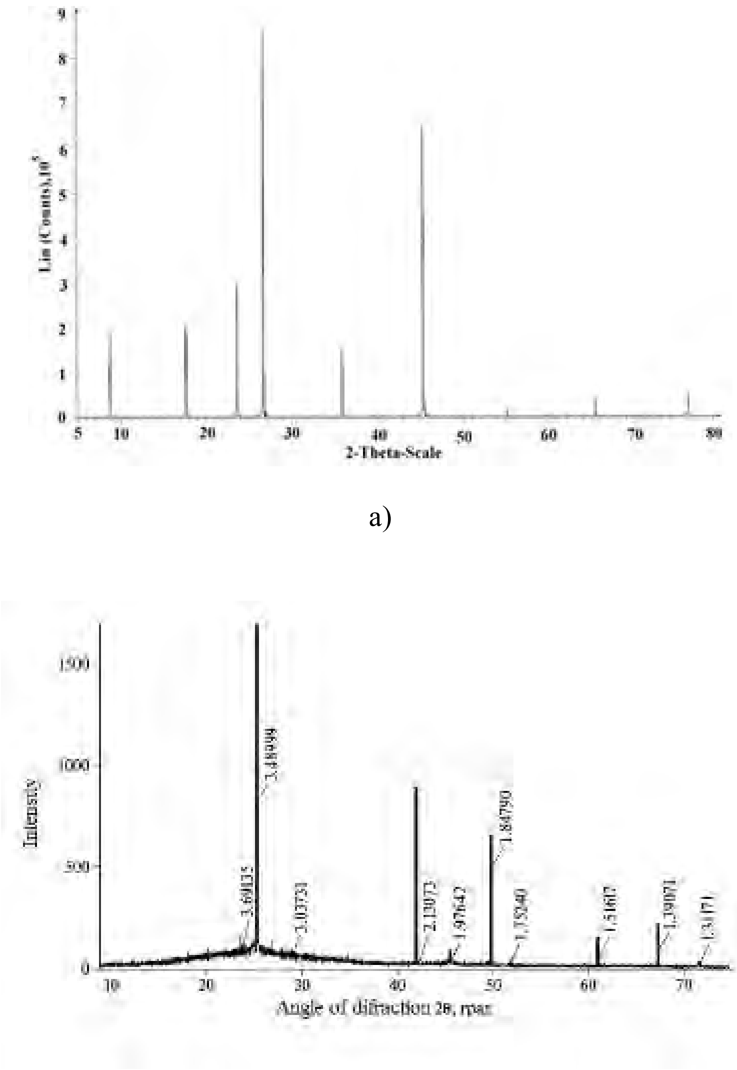

a)

b)

Fig.1. XRD spectra a) $Cd_{1-x}Mn_xTe$ (x=0.1), b) $Cd_{1-x}Mn_xSe$ (x=0.3)

3. Experimental and discussions

In our previous works we have investigated dielectric properties of $Cd_{1-x}Fe_xTe$ and effect of γ-irradiation on these properties [6.7]. In this paper, we have investigated dielectric properties of $Cd_{1-x}Mn_xTe$ (x=0.1). To measure the dielectric permittivity of the samples there were made capacitors by applying silver paste.

Dielectric permittivity and capacitance measurements performed within the frequency range of 25ç10^6Hz at alternating current.

The temperature dependences of capacitance of $Cd_{1-x}Mn_xTe$ (x=0.1) were investigated and the temperature dependences of dielectric permittivity and conductivity were defined (fig.2, fig.3). Fig.2 shows the temperature dependences of capacitance c at different measurement frequencies and fig. 3 shows the temperature dependences of dielectric permittivity ε at alternating current at different measurement frequencies. With increasing of temperature, an increase in ε is observed and sharp growth shifts to the higher measurement frequencies. The higher the measurement frequency, the later the growth of ε begins. It can be seen from the figure that at low temperatures the dielectric permittivity of the samples at different measurement frequencies is about 200.

The temperature dependences of conductivity *σ(T)* of $Cd_{1-x}Mn_xTe$ (x=0.1) defined on the base of measurements of dielectric permittivity. The boundaries of the temperature range for each frequency were determined (fid.4). Fig. 4 shows the temperature dependences of conductivity σ at different measurement frequencies.

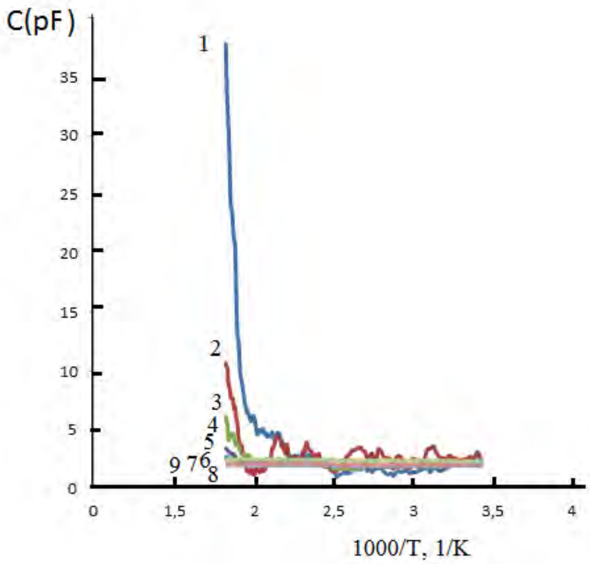

Fig.2. Temperature dependence of capacitance of $Cd_{1-x}Mn_xTe$ (x=0.1) at measurement frequencies 1)25Hz, 2)100Hz, 3)200Hz, 4)500Hz, 5)1kHz, 6) 10kHz, 7)100kHz, 8)500kHz, 9)1MHz

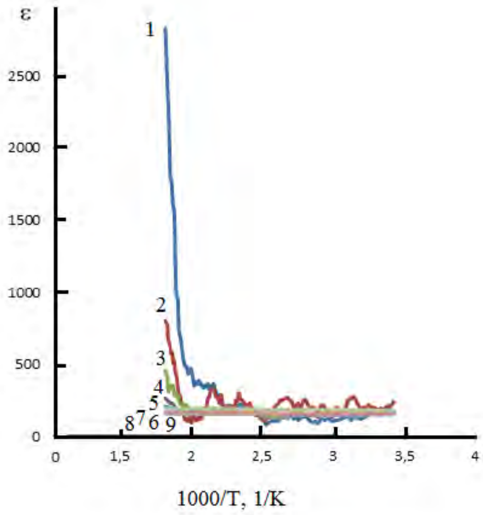

Fig.3. Temperature dependence of dielectric permittivity of $Cd_{1-x}Mn_xTe$ (x=0.1) at measurement frequencies 1)25Hz, 2)100Hz, 3)200Hz, 4)500Hz, 5)1kHz, 6) 10kHz, 7)100kHz, 8)500kHz, 9)1MHz

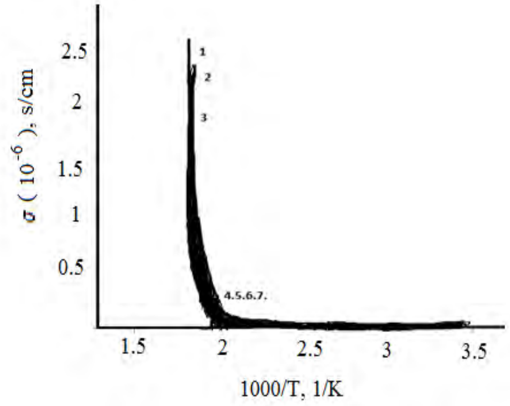

Fig.4. Temperature dependence of conductivity of $Cd_{1-x}Mn_xTe$ (x=0.1) at measurement frequencies 1)25Hz, 2)100Hz, 3)200Hz, 4)500Hz, 5)1kHz, 6) 10kHz, 7)100kHz

4. Conclusion

It was found that with increasing of temperature, an increase in *c, ε* and *σ* are observed, the slope of a curves remains constant. It have been defined that in the all dependences the higher the measurement frequency, the later begins the growth of *c, ε* and *σ*. The parameters remain almost unchanged up to temperature of ≈480ç500K over the entire studied frequency range. A maximum are observed at a temperature of 500ç550K. The conductivity at temperature of 500K at low frequencies is $2.5x10^{-6}$ S/cm. With an increase in measurement frequency, the features on the curves of *ε(T)* and *σ(T)* shift to lower temperatures.

References

1. Twardowski A., Dietl T., Demianiuk M. The study of the s-d type exchange interaction in $Zn_{1-x}Mn_xSe$ mixed crystals. Solid State Commun,48,10, 845-848(1983)
2. Furdyna J. K. Diluted magnetic semiconductors. Journal of Applied Physics, 64, R29 (1988)
3. Hwang Y.H, Um Y H, Furdyna J.K. Temperature dependence of the band-edge photoluminescence of $Zn_{1-x}Mn_xSe$ films. Semiconductor Science and Technology.19, 5, 565 (2004)
4. Nuriyev I.R. Mehrabova M. A., Hasanov N.H. Structure and Surface Morphology of $Cd_{1-x}Mn_xSe$ Epitaxial Films. Journal of Surface Investigation: X-ray, Synchrotron and Neutron Techniques. 12, 3, 504–506 (2018)
5. Мехрабова М.А., Нуриев И.Р., Керимова Т.И., Касымов Р.Д. Абдуллаева А.А. The structure of $Cd_{1-x}Mn$ (Fe) $_x$Se epitaxial films and effect of gamma irradiation on their optical properties. Azerbaijan Journal of Physics, 3, 130-132 (2018)
6. Мехрабова М.А., Керимова Т.И., Нуриев И.Р., Оруджев Г.С., Абдуллаева А.А. Dielectric properties of $Cd_{1-x}Fe_xTe$ epitaxial films. AzTU, 326-328 (2018)
7. Mehrabova M.A., Hasanov N.H., Huseynov N.I., Kazimova A.I., Asadov F.G. Effect of gamma irradiation on dielectric properties of $Cd_{1-x}Fe_xTe$ semimagnetic semiconductors. Journal of Radiation Reserches, 5, 2, 51-54 (2018)

***Corresponding author**: m.mehrabova@science.az
mehrabova@mail.ru

SUPERSTRUCTURE FORMATION IN $TlIn_{1-x}Sn_xS_2$ EPITAXIAL FILMS

E.SH. ALEKPEROV
Baku State University, AZ1148, Z.Khalilov str.23, Baku, Azerbaijan

By electron – diffraction examination method there have been investigated the phase transformations of $TlIn_{1-x}Sn_xS_2$films 30 nm in thickness obtained by method of thermal evaporation in vacuum. The use of given method allows the even, defect-free samples on KJ substrate to be produced. It is established that the interaction of ternary compound atoms with Sn interstitial atoms as an impurity results in the formation of substitutional solid solutions with superstructure within $0.02 \le x \le 0.09$ composition with controllable physical properties. There has been revealed the existence of phase transitions from one modification into another and superstructures with tetragonal syngony having triple parameters in relation to the initial phase.

Keywords: crystallization; thin films; electron diffraction; doping; epitaxial.
PACS: 544.344; 538.97; 539.216.2; 539.23

1. Introduction

For creating new devices the new semiconducting materials with controlled physical properties and high mobility of charge carries are needed. Semiconducting materials of $A^{III}B^{III}C_2^{VI}$ group ternary compounds used as photosensors and detectors of optical radiation are described in particular papers[1-3]. In most compounds of above-mentioned group the certain part of cation sites is racaut. Depending on the impurity content of IV group in periodic table added to $TlInS_2$ semiconductor it is possible to achieve a rather high concentration of free charge carries. Above mentioned ternary compound have five structural modifications [4-6]. $TlInS_2$ compounds are typical ones of $A^{III}B^{III}C_2^{VI}$ partial valence semiconducting compound having special structure of crystal lattice. Thin epitaxial films can be obtained by molecular beam epitaxy, Gas-phase chemical deposition from organometallic compounds,hybrid gas-phase epitaxy and etc. [7]. We deal with the kinetics of $TlIn_{1-x}Sn_xS_2$ ($x = 0.02 \div 0.09$) amorphous film crystallization [8]. In given paper there has been investigated the influence of Sn impurity on the formation of $TlInS_2$ epitaxial films with tetragonal.

2. Experiment

Epitaxial films under investigation have been obtained on VUP-5 installation by thermal evaporation method in vacuum $3\times10^{-2}\,Pa$ on NaCl, KCl, KJ celluloid and single crystal substrates at T 230-323 K controlled by copper-constantan thermocouple. The samples on KJ substrates are distinguished by high quality and turn out to be the most suitable for further investigations. Obtained films are kept in carbon capsule 2-3 nm in thickness to avoid oxidation and evaporation by thermal treatment. The distribution of condensate composition in coordinates on the condensation plane has been determined by the familiar formula in crystallography [4]:

$$q = \frac{Q}{4\pi h^2}\frac{1}{(1+\alpha)^{\frac{3}{2}}}$$

Here g is the number of substance per unit of substrate surface plane, Q is the number of evaporated substance, h is the distance from evaporation source to any point on the condensate plane, coefficient $\alpha = x/h$ where x is the distance of the point being immediately under the evaporator to any point on substrate plane. Film thickness obtained by vacuum evaporation is calculated from the formula:

$$H = \frac{q}{\rho}$$

Where, ρ is the density of substance. Besides film thickness is controlled by spectrometer Specor-250, and the composition is controlled by spectrometer “Shimadzu AA-6300”. Amorphous, polycrystalline and single crystal films under consideration have been obtained on above – mentioned substrates. The possibilities of existing phase transitions from one modification into another and forming superstructures proportional to one or another phase have been investigated by the method of high energy electron diffraction.

3. Results and discussion

$TlIn_{1-x}Sn_xS_2$ thin films under investigation ($x=0.02 \div 0.09$) produced on the substrates at T~215K are in amorphous state and have a uniform fine-grained structure of 3.5-4.0 nm grains in size. On electron diffraction pattern of $TlIn_{1-x}Sn_xS_2$ amorphous film two diffuse maxima with values $S=4\pi sinsin\,\theta/\lambda$ (where $\lambda$is the electron wavelength, θ is the Bragg angle) equal to 27.34; 38.26 nm^{-1} have been recorded (Fig.1). To keep amorphous films in vacuum 10^{-2} Pa at room temperature for 3 months causes the drop in crystallization temperature by ~20K.

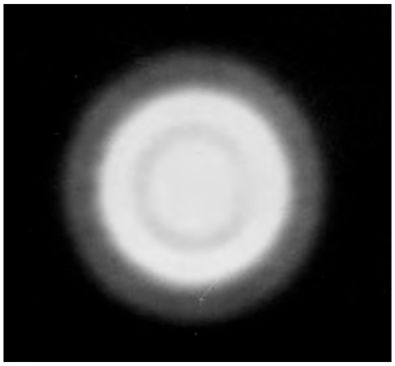

Figure.1. Electron diffraction pattern of $TlIn_{1-x}Sn_xS_2$amorphous film.

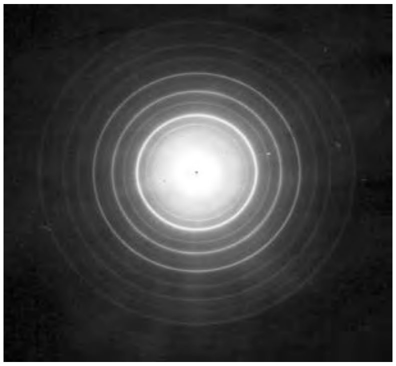

Figure.2. Electron diffraction pattern of $TlIn_{1-x}Sn_xS_2$polycrystalline film.

Thermal treatment of amorphous films of 30 nm in thickness at T~338 K for 20 minutes with the subsequent cooling down to room temperature in vacuum at the rate 5 K/min results in the formation of $TlIn_{0.93}Sn_{0.07}S_2$ crystalline solid solution with the parameters of tetragonal syngony unit cells increased up to 5%(Fig.2). While continuing the film thermal treatment including disoriented small crystals at T=488K for 30 minutes we observe the phase transition with the formation of perfect texture film. By substance deposition on KJ single crystal substrate heated up to 468 K the film epitaxial growth is noted. After thermal treatment of the obtained epitaxial films on KJ substrates at T=508 K for 10 minutes with the subsequent cooling down to room temperature with rate 21 K/min there have been occurred the formation of $TlIn_{0.93}Sn_{0.07}S_2$ super structural phase films with lattice periods being triple in relation to initial phase: $a=3a_0=2.197$ nm ; $c=3c_0=7.618$ nm. Measured electron diffraction patterns at an angle $\varphi=35 \div 55^{\circ}$ allows the above – mentioned parameter of "c" period crystal lattice to be calculated (Fig.3).

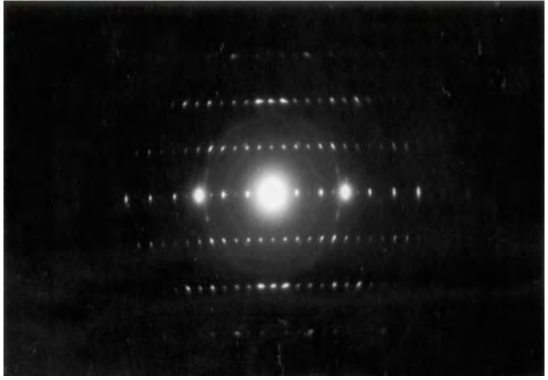

Figure.3. Electron diffraction pattern of single crystal of $TlIn_{1-x}Sn_xS_2$, $\varphi=45^{\circ}$ substrate and film

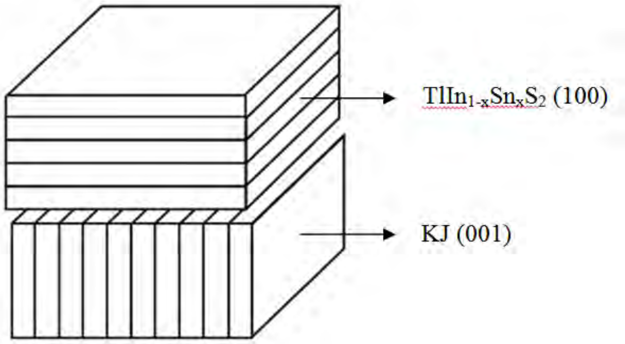

Figure.4. The layout of the planes of the substrate and film.

By the law of reflex extinction the electron diffraction patterns derived from $TlIn_{1-x}Sn_xS_2$ super structural single crystal films are indexed in tetragonal syngony with space group I4/mcm.Temperature rise of the substrate up to 490 K and decrease of condensate deposition rate down to the minimum leads to the increase of epitaxial film structure perfection. The unit cell of super structural phase have been aligned with 3 cells of KJ substrate. Discrepancies between aligned grids of substrate-film lattices are ~3.5%. Orientational ratios at epitaxial growth of films under investigation can be expressed as follows: (100) $TlIn_{1-x}Sn_xS_2$// (001) KJ as it is shown in fig.4.

4. Conclusion

We note that the possible deviations of $TInS_2$ composition from stoichiometry, the significant impurity concentration, the tendency to oxidation and all kinds of lattice structure violations as well as the polytypeness are due to the difficulties to interpret results. The analysis of obtained data shows that the interaction of ternary compound with Sn impurity atoms brings about the formation of substitutional solid solutions and the development of $TlIn_{1-x}Sn_xS_2$ film superstructures with triple lattice periods in relation to the initial phase [9]. Solid solutions can be formed by both direct exchange atoms in places and their movement through vacant sites of crystal lattice with close packing. There has been observed film ageing influenced on thermodynamic stability, i.e. temperature of thermal treatment decreases. Based on the ideas presented in [10] we assume that Sn atoms are arranged in crystal lattice sites.

References

1. Pashayev A.M., Djafarov T.D. Physical foundations of nanoelectronics, Baku, pp.87 (2014).
2. Kavetskyy T.S., Shpotyuk O.I., Boyko V.T., J. Phys. and Chem. Of solids, 68, pp.712 (2007).
3. Filachev A.M., Taubkin I.I., Trishenkov M.A., Solid state photoelectronics, pp.363 (2012).
4. Isaacs T.I., Z. Krustallogr.,. B., 141, № 1–2, 104 (1975).
5. Henkel W., Hochheimer H.D., Carlone C. et al., Phys. Rev. B., 26, 6, 3211, (1982).
6. Najafov A.I., Alekperov O.E., Guseinov H.H. Inorganic Materials, 41, 2, 138 (2005).
7. Vasiliev V.I., Qaqis Q.S., Kuchinski V.I., Danilchenko V.Q., Semiconductors, 49, 984 (2015).
8. AlekperovE.Sh., Inorganic Materials, 54, 8, 767, (2018).
9. Avilov A.S., Thesis of doc.of phys.-math.-science: 01.04.18. Moscow , pp.274 (1999).
10. Abdullayev Y.B., Djafarov T.D., Atomic diffusion in semiconducting structures. M. Atomizdat, pp.280 (1980).

***Corresponding author**: aeldar@bsu.edu.az
alekperoveldar@mail.ru

EFFECT OF TEXTURING REGIMES ON THE EFFICIENCY OF p-Si/*textured*-Si/$ZnS_{1-x}Se_x$ HETEROJUNCTIONS SOLAR CELLS

H.M.MAMMADOV*, M.A.JAFAROV, E.F.NASIROV, E.A.CHANMAMMADOVA, G.H.MAMEDOVA
Baku State University, Z.Khalilov str., 23, Baku, Azerbaijan, Az1148

In this paper the p-Si/*textured*-Si/$ZnS_{1-x}Se_x$heterojunctionswere fabricated by electrochemical deposition of $ZnS1_{-x}Se_x$ (x = 0; 0.1 and 0.2) films onto the crystalline p-Si/SK and p-Si/SH substrates (SK and SH are textured silicon etched in KOH+C_3H_8O and HF+HNO_3, respectively). Photoelectrical properties of heterojunctions were investigated depending on the etching duration, solution temperature and concentration of solids in solutions (KOH and HF (1-5 wt%); C_3H_8O and HNO_3 (3-10 vol%).It has been established that the efficiency of the p-Si/*textured*-Si/$ZnS_{1-x}Se_x$solar cells depends on the etching regime. The optimal concentration of solids(KOH-3wt% +C_3H_8O- 6 vol%; HF-5wt% + HNO_3-8 vol%), solution temperature (80^0C) and etching duration (40 min) were determined for maximum efficiency of solar cells: for p-Si/SK4/ZnS–*FF*=0.58; η=9.36%; for p-Si/SH4/ZnS-*FF*=0.5; η=7.1%; for p-Si/SK4/$ZnS_{0.9}Se_{0.1}$–*FF*=0.6; η=10.6% and for p-Si/SH4/$ZnS_{0.9}Se_{0.1}$/-*FF*=0.56; η=9.1%.

Keywords: heterojunctions, texturing, solar cells
PACS: 84.60.Jt; 73.50.Pz; 79.60.Jv

2. Introduction

Cost distribution of c-Si solar cells is clearly dominated by material costs, especially by the costs of the silicon wafer. But besides low-cost technologies (chemical deposition methods), cell efficiency is the main lever to reduce costs even more. In order to reduce the light loss via reflection, the texturing of front surfaces on crystalline silicon solar cells is mostly performed for the improvement of the cell efficiency, by means of its antireflection properties and light trapping [1-6]. Since, application of wide-gap semiconductors of CdS, ZnS, ZnSe and its solid solutions as an optical window in silicon-based hetero junctions, to some extent, allows minimizing the free charge losses due to surface recombination. Application of the ternary and even quaternary solutions of above-mentioned semiconductors has succeeded in reducing the lattice mismatch, but it has not been possible to achieve sufficient value of efficiency due to the large value of silicon refractive index [7-9]. The use of textured silicon allows solving problems with surface reflections related to the refractive index of silicon. There are many reports of p-Si/textured-Si/ZnS heterojunction solar cells [10-12]. But textured silicon-based heterojunction solar cells with n- $ZnS_{1-x}Se_x$ have seldom been reported.

Based on the above, this paper aims to improve the p-Si/$ZnS_{1-x}Se_x$ solar cell conversion efficiency by developing improved surface texture.

2. Experiment

Monocrystalline wafers of p-Si (100) with thicknesses 800 μm and resistivity (0.8-1) Ω·cm were used as absorber. Before texturization, the Si wafers were cleaned by acetone, ethanol, and deionized water and dried by N_2 gas. The texturing of wafers was carried out in two types of solutions: KOH (1-5 wt%) + C_3H_8O (3-10 vol%) + H_2O (100 ml) and HF (1-5 wt%) + HNO_3 (3-10%) + H_2O (100 ml). The samples with dimension of 2 Ç 2 cm^2 were separated from one wafersof p-Si, and each sample was etched in differentsolutions, temperature and etching time (Table 1). After texturing, the p-Si wafers were cleaned by ethanol, deionized water and dried by N_2 gas. Samples with 1Ç1 cm^2 dimension were separated from each textured Si wafers and used as substrate (as a cathode) for electrochemical deposition of $ZnS_{1-x}Se_x$ films. Electrochemical deposition of the $ZnS_{1-x}Se_x$ (x=0; 0.1; 0.2) films onto the textured p-Si substrates was carried out at temperature of 80°C. The electrodeposition bath system is composed of $ZnSO_4$ as source of cation, SeO_2 and $Na_2S_2O_3$ as source of anions, H_2SO_4 as pH control, K_2SO_4 as inert electrolyte and distilled water. Cyclic voltammetry was used to monitor the electrochemical reactions in solutions of $ZnSO_4$, SeO_2 and $Na_2S_2O_3$, then in their combined solution of the same concentration and pH. The cyclic voltammograms was scanned in the potential range 1.2 V to –1.2 V versus graphite (or Ag/AgCl) electrodes. Depending on the deposition time, $ZnS_{1-x}Se_x$films with thickness up to

520÷530nm with different morphology were deposited from a solution.Pure aluminium (Al) was used as the back electrode contact. The front contact was made by Al, and indium (In) materials in a grid form.

Table 1

Samples	KOH concentration, wt%	C_3H_8O concentration, vol%	Solution temperature, ^{0}C	Texturing time, min
SK1	1	3	80	20
SK2	1	3	80	30
SK3	2	6	80	30
SK4	3	6	80	40
SK5	3	10	90	50
SK6	5	10	80	60
	HF concentration, wt%	HNO_3concentration, vol%	Solution temperature, ^{0}C	Texturing time, min
SH1	1	3	80	20
SH2	2	3	80	30
SH3	3	6	80	30
SH4	5	8	80	40
SH5	6	9	90	50
SH6	5	10	80	60

3. Results and discussion

It is established that the etching in HF + HNO3 (SH samples in Table 1) and KOH+ C_3H_8O (SK samples in Table 1) solutions results to formation of oval shaped pitsand pyramids on the silicon surface, respectively, which morphology and size depends on the solution temperature, concentration of contents and etching time (different etching regimes are shown in Table 1). SEM pictures show that the pits and pyramids began to appear after 20-30 min etching time (samples SH1, SH2, SH3, SK1, SK2 and SK3). The surface these samples were uneven. It is established that the required distribution of pits and pyramids can be get by controlling the solution concentration. After the etching for 40 min the surface of silicon (sample SH4 and SK4)was covered with oval shaped pits and pyramids distributed relatively evenly and Si wafers was flat,which is very important for improving the stability of solar cells (Fig. 1a and 1b). There was no change in the surface morphology of Si wafers at future increase of solutions concentration, etching time and temperature (samples SK5, SK6, SH5 and SH6).

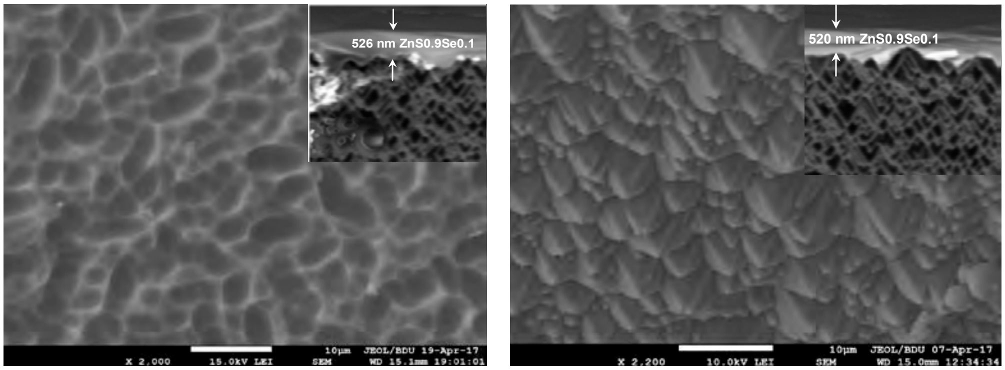

a) b)

Figure 1. SEM pictures of textured SH4 (a) and SK4 wafers (b).

Fig.1a and b shows also the cross section SEM pictures of textured p-Si/$ZnS_{1-x}Se_x$ junctions. As seen the $ZnS_{1-x}Se_x$ films are uniformly deposited on the p-Si substrate. Chemical composition analysis of $ZnS_{1-x}Se_x$films was done by EDS technique. Fig.2 show EDS spectra of $ZnS1_{-x}Se_x$ (x=0.1) films.

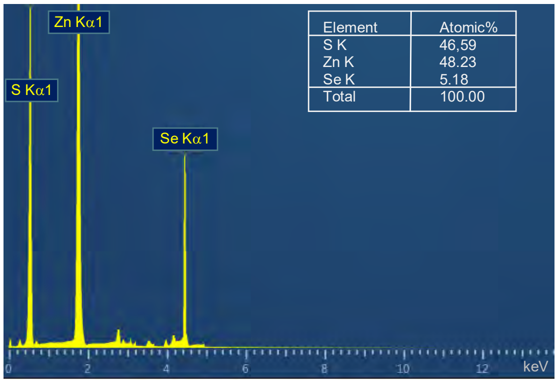

Fig. 2. EDS spectra of $ZnS_{1-x}Se_x$ (x=0.1) films

Table 2

Samples	U_{oc} (mV)	I_{sc} (mA/cm^2)	FF	η (%)
as-cut p-Si/ZnS	315	22	0.4	2.8
p-Si/SK1/ZnS	489	28.62	0.44	6.2
p-Si/SK4/ZnS	502	32.2	0.58	9.36
p-Si/SK4/$ZnS_{0.9}Se_{0.1}$	510	34.5	0.6	10.6
p-Si/SK4/$ZnS_{0.8}Se_{0.2}$	490	30	0.42	6.23
p-Si/SH1/ZnS	470	25.16	0.44	5.26
p-Si/SH4/ZnS	480	29.5	0.5	7.1
p-Si/SH4/$ZnS_{0.9}Se_{0.1}$	500	32.38	0.56	9.1

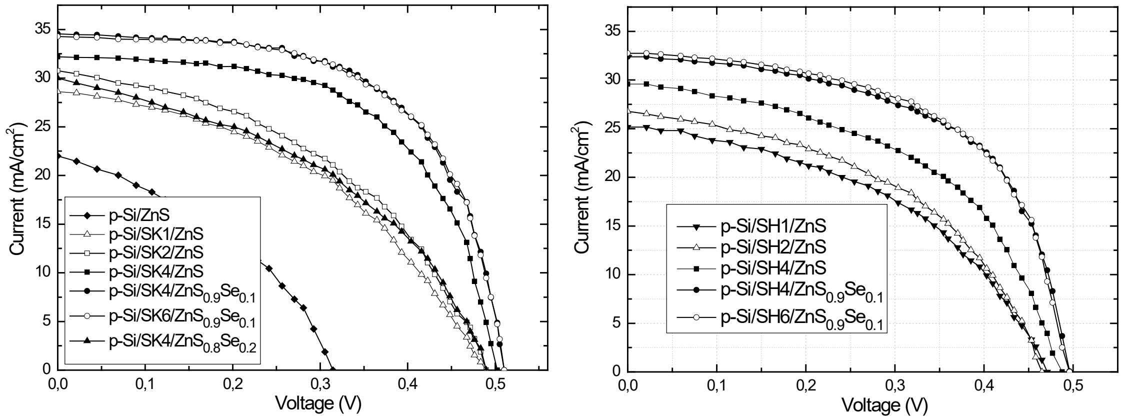

a) b)

Fig. 3.Photovoltaic output characteristics for p-Si/textured-Si/$ZnS_{1-x}Se_x$Solar cells.

All investigated heterojunctions solar cells based on textured silicon under standard test conditions demonstrated photovoltaic performances under AM1.5 illumination (W=100 mW/cm^2), which sign of open circuit photo-voltage (U_{oc}) does not change in all region of photosensitivity. However, the maximum values of U_{oc} and J_{sc} non-monotonically dependent on the texturization regimes (Table 2). Light J-V characteristics of the p-Si/textured-Si/$ZnS_{1-x}Se_x$ measured under AM 1.5 standards, depending on the texturization regimes are shown in Fig. 3. As seen the highest value of efficiency show the cells textured in KOH+C_3H_8O solution (SK4 samples), which can be explain by the flatness of the pyramids. A slight addition of selenium (x=0.1) leads to sharp increase in efficiency and further increase in selenium concentration (x=0.2) led to decrease in efficiency, which can be explain by the lattice matching between $ZnS_{1-x}Se_x$ and Si. As seen from Fig. 3a and 3b, texturization in high concentration of solutions does not change the efficiency (samples SH5, SK5, SH6 and SH6).

We investigated the spectral distribution of photocurrent depending on the texturization regime (Fig. 4). However, long-wavelength peak of spectrum is due to the direct interband transitions in Si.

There occurs a reconstruction of the photosensitivity spectrum after texturization, i.e. the spectrum broadens. As the solution concentration increased, photosensitivity in short wavelength region sharply increased. It is clear that this is due to the morphology of the selenium surface, i.e. degree of light absorption, which is determined by the morphology of texturized silicon.

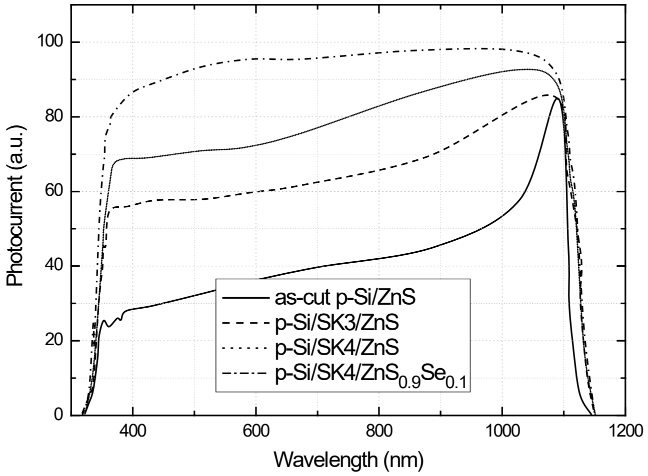

Fig. 3.Spectral distributions of photocurrent in p-Si/SK/$ZnS_{1-x}Se_x$solar cells.

4. Conclusion

p-Si/*textured*-Si/$ZnS_{1-x}Se_x$ heterojunctions were fabricated by electrochemical deposition Efficiency of heterojunctions can be regulate by etching duration, solution temperature and concentration of solids in solutions of KOH and HF (1-5 wt%); C_3H_8O and HNO_3 (3-10 vol%). Solar cells of p-Si/SK4/$ZnS_{0.9}Se_{0.1}$ show best efficiency (10.6%) after the etching in solution of KOH-3wt% +C_3H_8O - 6 vol%.

References

5. Edited by Prof. Leonid A. Kosyachenko, Solar Cells - Silicon Wafer-Based Technologies, InTech, 2011, 364 p.
6. FıratEs, GğlsenBaytemir, Mustafa Kulakci, RaşitTuran, Solar Energy Materials & Solar Cells 160, 269 (2017).
7. Wisam J. Aziz, AsmietRamizy, K. Ibrahim, Khalid Omar, Z. Hassan, Journal of Optoelectronics And Advanced Materials 11, 1632 (2009).
8. Altinoluk SH, Ciftpinar HE, Demircioglu O, Es F, Baytemir G, Akar O, et al., Energy Procedia 92, 291 (2016).
9. Basu P.K., Khanna A., Hameiri Z., Renewable Energy 78, 590 (2015).
10. Zhao J, Wang A, Green MA., Applied Physics Letters 73, 1991 (1998).
11. Mamedov H., Mammadov V., Mammadova V., AhmedovaKh. , Tagiyev E., Agazade L., Journal Of Optoelectronics and Advanced Materials 20, 468 (2018).
12. Abdinov A., Mamedov H., Amirova S., Thin Solid Films 511-512, 140 (2006)
13. Mamedov H., Konya Z., Muradov M., Kukovecz A., Kordas K., Hashim D., Mamedov V., J. Solar Energy Engineering 136, 044503 (2014).

14. Kaifu Q., Depeng Q., Lun C., Shenghao L., Weiliang W., Zongcun L., Hui Sh., Materials Letters 198, 23 (2017).
15. Kaifu Q., Qi X., Depeng Q., Lun C., Weiliang W., Wenjie L., Zhirong Y., Bin A., Zongcun L., Hui Sh., Solar Energy 165, 35 (2018).
16. Liang-Wen J., Yu-Jen H., I-Tseng T., Teen-Hang M., Chien-Hung L., Jenn-Kai T., Tien-Chuan W. and Yue-Sian W., Nanoscale Research Letters 8, 470 (2013)

*__Corresponding author__: mhhuseyng@bsu.edu.az
mhhuseyng@gmail.com

FLUCTUATION OF THE MAGNETIC MOMENT OF MAGNETITE PARTICLES DEPENDING ON THE SIZE OF PARTICLES.

M.A.RAMAZANOV*[1], H.A.SHIRINOVA[1]
Baku State University,23Z.Khalilov Street, Baku, Azerbaijan, Az-1148 mamed_r50@mail.ru

In the present work were investigated the structure and magnetic properties of the magnetite nanoparticles with a different size range. The average size of Fe_3O_4 nanoparticles was studied by SEM. Differences in the structure were investigated by IR and XRD spectroscopies.XRD analysis showed that with the changing of the size of nanoparticles lattice parameters of the material also change. On the other hand, the magnetic properties of the nanoparticles at room temperature were investigated. Relatively small particles show the superparamagnetic effect at room temperature. Besides, the value of saturation magnetization is the same (69emu/g) for both samples. It is one of the most important properties of stable superparamagnetic materials.

Keywords: Nanocomposite materials magnetization, Fe_3O_4 nanoparticles, Neel relaxation time.
PACS: 75.90.+w, 75.75.+a, 75.70.Cn

1. Introduction

The Fe_3O_4 nanoparticles are one of the more interesting semi-metallic nanoparticles due to theirsuperparamagneticpropertie, chemical stability, very big surface area, low toxity and high bio-compatibility [1, 2]. The researches show that magnetic properties of the nanoparticles are directly depending on their size, purity, and homogeneity. [3-5]. So the main magnetic properties of magnetic nanoparticles such as Ms, Mr, and Hc can be controlled depending on size and the domain structure. When the size of the particle is smaller, energetically favorable for the particle to form a single domain state than the multi-domain state [6]. According to some references the d <70 nm limitation given for the transition from a multi-domain to single-domain [5, 7-9]. Single-domain magnetic nanoparticles exhibit superparamagnetic properties. The size of the particles for superparamagnetic behaviour is less than 30 nm [10-11]. The effect of thermal-fluctuations on their magnetic properties increases with decreasing particle size [12-13]. Influence of the external magnetic field stops, the spin of the particle randomly turn due to the thermal fluctuation. Relaxation time is the main parameter of the magnetic particles. It is clear that when the temperature increases the thermal fluctuation occurs faster and relaxation time decreases.

In the present work, was investigated the size dependence magnetic properties of magnetic iron oxide nanoparticles in room temperature. For this purpose were analyzed two samples of the magnetite nanoparticles with different size.

2. Experiment

2.1 Materials

$Fe_3O_4\cong9$-Magnetite nanoparticles were obtained by co-precipitation in an alkaline medium. The average nanoparticle size is 5–17 nm [6].

$Fe_3O_4\cong28$ samples were obtained from the skyspringnanomaterials company. F 3320DX Iron Oxide Nanopowder / Nanoparticles (Fe_3O_4, 98+%, 20-30 nm)

2.2 Research Methods

2.2.1. IR Study

IR spectra of the samples were recorded on a spectrometer FT-IR Varian-3600 Excalibur Series, allowing recording the spectra in the range of 4000–400 cm−1.

2.2.2 XRD

X-ray diffraction analysis was performed on Rigaku Mini Flex 600 XRD diffractometer at ambient temperature. In all the cases, Cu Kα radiation from a Cu X-ray tube (run at 15 mA and 30 kV) was used. The samples were scanned in the range of angles 2θ of 20°–70°.

2.2.3 Measurements of the magnetic moment as function of the magnetic field m(H)

Magnetization curves acquired at 300K (room temperature) by a Quantum Design SQUID magnetometer in the field range ± 50 kOe. The magnetization is reported per gram of measured sample.

For the m(H) measurements of the magnetic moment as a function of magnetic field, the sample was first thermally stabilized to the measurement temperature in absence of magnetic field. Then, the field was ramped with a sweep rate of to reach 9 Tesla, then back to Tesla, and finally to ±9 Tesla again to acquire the complete m(H) loop. For performing the measurements, we have taken out from the original batches only a 3-mm-diameter disk for each sample. In particular, we have decided to take the samples in a position corresponding to the half of the radius (Figure 1b). A deeper study of the behavior of the sample properties as a function of position on the batch could be interesting to study the homogeneity of entire large sample.

3. Results and discussion

The main properties of Fe_3O_4nanoparticles are given in Table1.

Table1. Research objects

sample	**$Fe_3O_4\cong28$**	**$Fe_3O_4\cong9$**
Appearance	dark brown nanopowder	dark brown nanopowder
APS:	20 - 30 nm	5- 15nm
SSA:	40-60 m^2 /g	-
Morphology:	spherical	spherical
True density:	4.8-5.1 g/cm^3	-

The TEM and SEM images of $Fe_3O_4\cong28$ nanoparticles are shown in figures1 (a) and (b), respectively. Figure 2 demonstrates SEM image of the $Fe_3O_4\cong9$ nanoparticles.

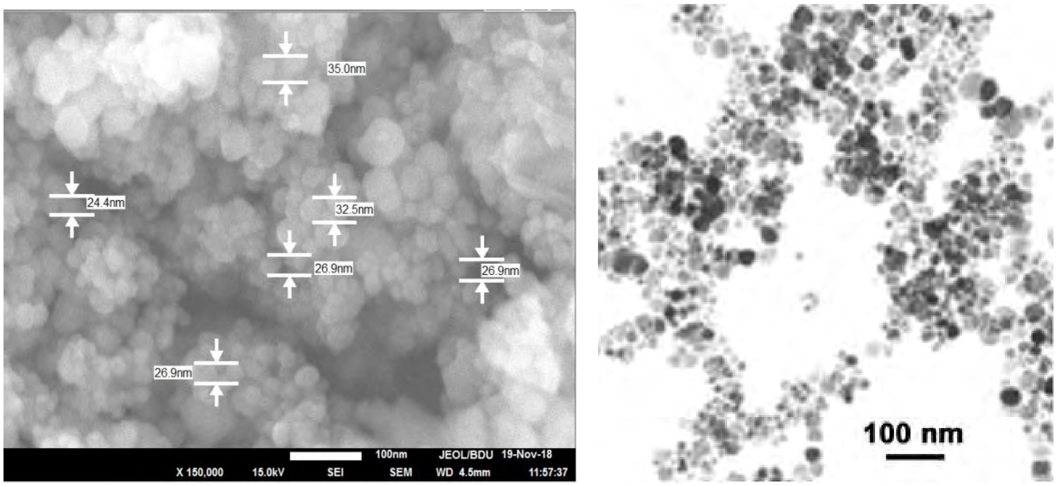

a) b)

Figure1. SEM and TEM images of $Fe_3O_4\cong28$ nanoparticles
a)SEM images of $Fe_3O_4\cong28$ nanoparticle; b) TEM images of $Fe_3O_4\cong28$ nanoparticles

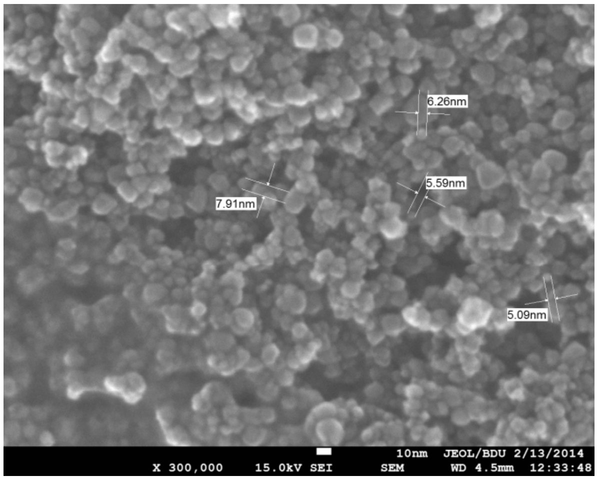

Figure2. SEM images of $Fe_3O_4 \cong 9$ nanoparticles

SEM images show that both types of nanoparticles are in the spherical shape and have homogenous size distribution. The randomly selected 100 particles size observed from SEM images was used to determine statistical parameters of the particle size distribution.

Figure 3 shows the lognormal distribution of two different Fe_3O_4 nanoparticles by size.

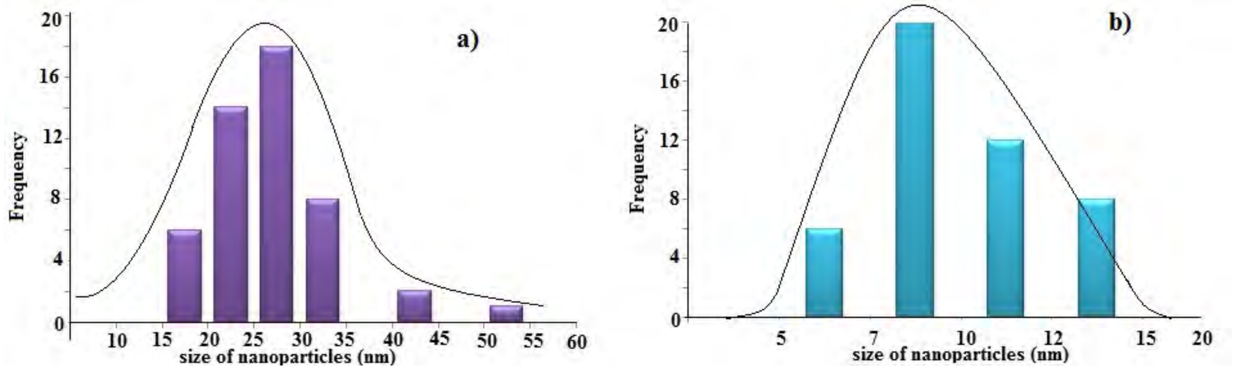

Figure3. Particle size histogram bu SEM investigation
a)$Fe_3O_4 \cong 28$ b) $Fe_3O_4 \cong 9$

The values of the lognormal distribution parameters of the Fe3O4 nanoparticles are reported in Tables 2: the average size of the particle, standard deviation, the maximum and minimum size of particles. As can be seen from the table, by the average size both nanoparticles are in the range of stable single domain particle [13-14].

Table2. The log-normal values of the parameters (distribution interval, average value (d), standard deviation (σ))of Fe_3O_4 particles size distribution

samples	d_{min}-d_{max} (nm)	$\bar{d}$ (nm)	σ
$Fe_3O_4 \cong 28$	15,1-60,6	~28,65	8.82
$Fe_3O_4 \cong 9$	5,09-16,8	~9.08	2.98

Figure 4 shows X-ray diffractograms of both types of Fe_3O_4 nanoparticles. Both nanoparticles were found to belong to cubic space group No227, Fd-3m. According to [222], [311], [511], [440] hkl indices $Fe_3O_4 \cong 9$ nanoparticles correspond to the DB card number 00-101-1032. But $Fe_3O_4 \cong 28$ sample correspond to the DB card number 00-900-2320 and characterized by the [222], [311], [400],[422], [511], [440] Miller indices. The preponderance of the amorphous phase for $Fe_3O_4 \cong 9$ sample indicated that the crystalline behavior of magnetite nanoparticles was suppressed due to the presence of PEG [15]. Scherrer formula is used to calculate the average size of crystallites. The most relevant and high intense peak of the diffractogram- [311]-was selected for calculation. The calculated crystallite sizes of nanoparticle samples were 108Å and 233Å, for $Fe_3O_4\cong9$ and $Fe_3O_4\cong28$ nanoparticle samples, respectively. This sizes very well correlated with SEM results.

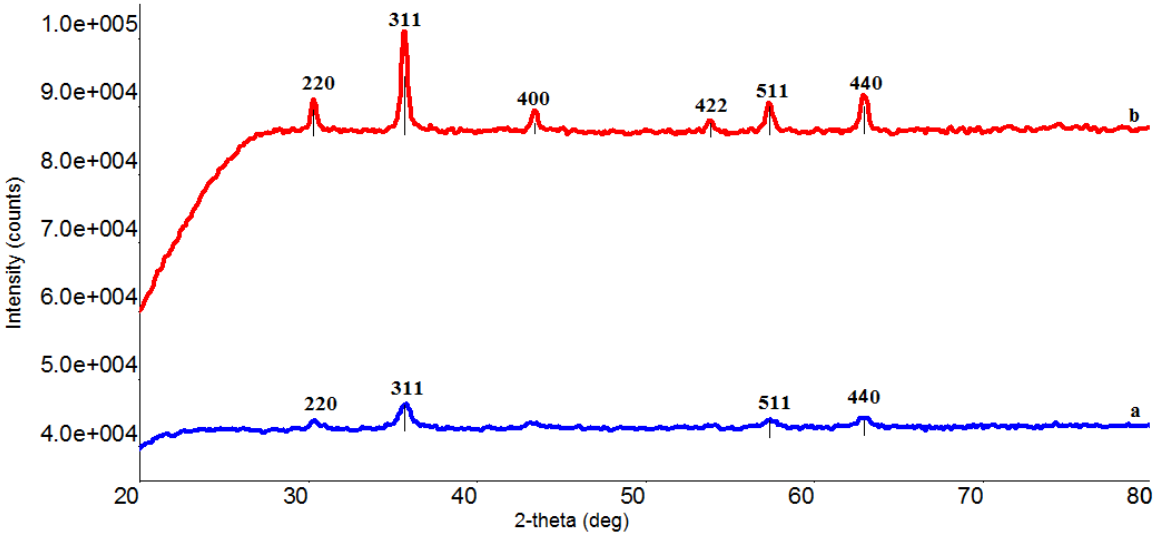

Figure4. XRD images of nanoparticles a)$Fe_3O_4\cong9$ b) $Fe_3O_4\cong28$

It was also found from XRD analysis that with the decreasing size of the particle the lattice parameter increases (Table 3). It is known that in Fe_3O_4 crystal oxygen anions form an fcc closed packing and iron (cations) locates at the interstitial tetrahedral and octahedral sites. The electron can hop between Fe^{2+} and Fe^{3+} ions in the octahedral sites at room temperature imparting half metallic property to magnetite. The magnetic moment of the unit cell comes only from Fe^{2+} ions with a magnetic moment of $4\mu_B$ [3]. The observed increase in unit cell volume with reduction in particle size of Fe_3O_4 particles, perhaps implies an increase in Fe^{2+} content in the sample, since ionic radius of Fe^{2+} is larger than that of Fe^{3+}. So the increase in magnetization with decrease in size could be justified.

Table 3. XRD parameters of nanoparticles

Samples	Size(ang.)	Unit cell parameter (ang.)	Unit cell volume (ang^3.)
$Fe_3O_4\cong28$	233	8,27	566,4
$Fe_3O_4\cong9$	108	8,35	581,3

FTIR spectroscopy of two different size Fe_3O_4 nanoparticles were measured between 400 and 4000 cm^{-1} region(Figure5). FTIR spectroscopy analysis showed peaks at 3428, 1624, 1084, 634, 580, 442cm^{-1} for $Fe_3O_4\cong9$ sample.The bands at 3428, 1624 cm^{-1} areassociated with stretching frequency of the O-H bond. The bands at 1084cm^{-1} is related with vibration of the C-O band. This is due to the PEG surfactant used to stabilization of the nanoparticles[15]. The band 634, 580, 442 cm^{-1} correspond to Fe--O bond(Figure 5-a).

The bond observed 634, 584, 448 cm^{-1} in the IR spectrum of $Fe_3O_4\cong28$ nanoparticles are related with Fe-O-Fe bond[16](Figure-5-b).

The two samples present similar features compatible with iron oxide (magnetite) nanoparticles (Figure6). Differences are evident in the low field range (right panel) where the largest $Fe_3O_4\cong28$ clearly show a hysteretic behavior (open cycle) with coercive field of 71 Oe and remanence of c.a. 10 emu/g. This result is due to the "large" size of the nanoparticles which are expected to be in the "blocked" regime at room temperature. On the contrary, the smallest nanoparticles (Fe$_3$O$_4$≅9) are superparamagnetic at this temperature as they show negligible coercivity and remanence. The saturation magnetization, Ms, is very similar for both samples (69emu/g). Even though this should be the "ideal" expectation, in practice, a decrease of the saturation value is commonly observed when the size is strongly reduced. The negligible hysteresis for Fe$_3$O$_4$@9 nanoparticles are related with relaxation of magnetic dipoles in nanoparticles.The main magnetic parameters of samples demonstrated in Table 4.

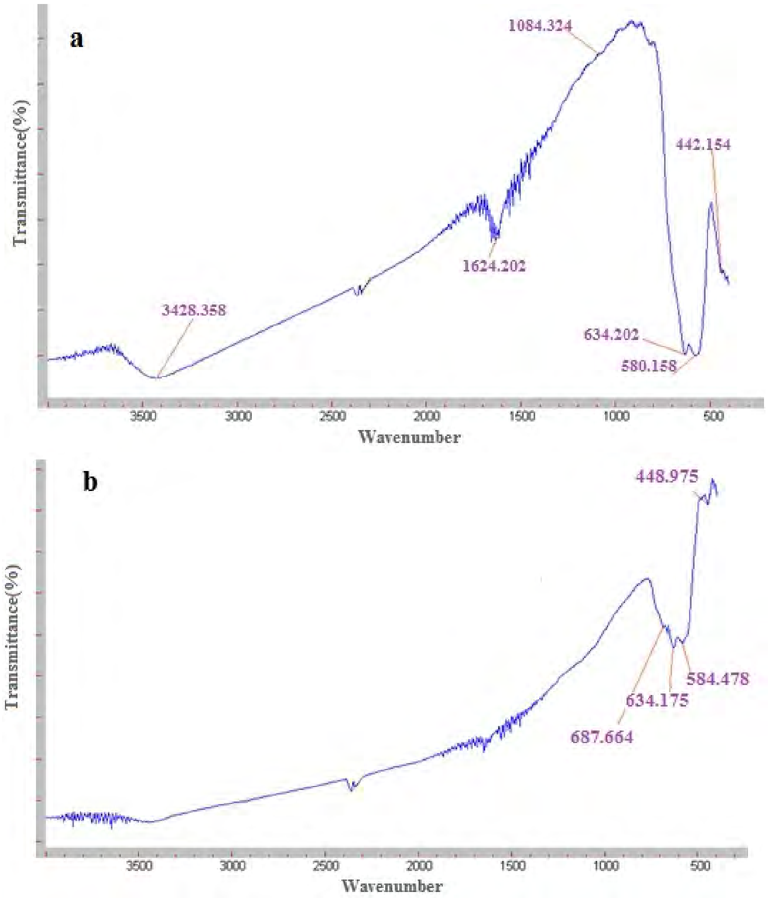

Figure5. FTIR spectra of Fe$_3$O$_4$ nanoparticles: a)Fe$_3$O$_4$≅9 b) Fe$_3$O$_4$≅28

Table 4.Magnetic characterization of both samples

Fe$_3$O$_4$NPs	**Ms** (emu/g)	**Mr**(emu/g)	**Hc(Oe)**
Fe$_3$O$_4$≅9nm	69.2	1.28	-
Fe$_3$O$_4$≅28nm	69	10.03	70.98

Ms = saturation magnetization (taken as M≅50 KOe) value); Mr = remanent magnetization; Hc = coercive field

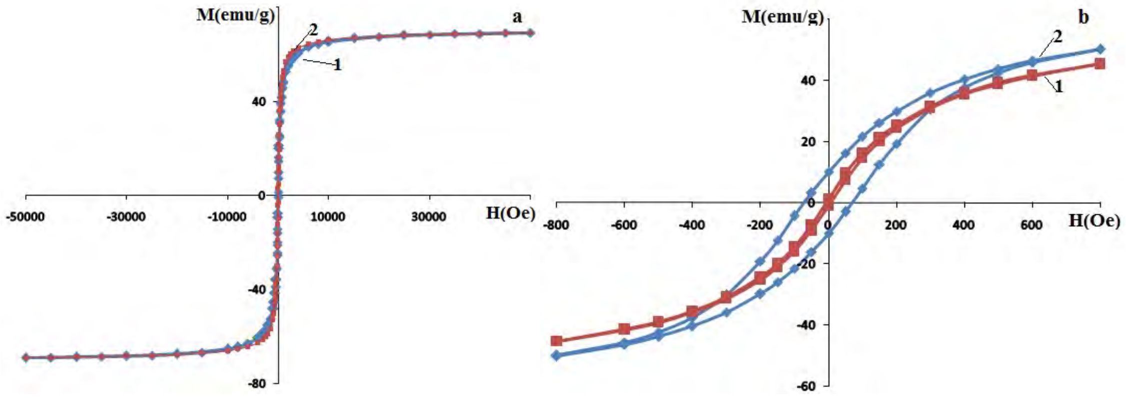

Fig6. M(H)curves of Fe_3O_4 nanoparticles with different size: 1-Fe_3O_4 ≅9nm; 2- Fe_3O_4 ≅28nm
a) M(H) Magnetization versus magnetic field
b) M(H) Magnetization versus magnetic field near zero field

The dependence of the differential susceptibility of nanoparticles on the intensity of the external magnetic field was studied using the M(H) curve[18].Figure 7 demonstrates field dependencies of differential susceptibility of the bothFe_3O_4 nanoparticles. From the graph in Fig. 7, we obtain that the magnetization reversal of the sample has a hysteretic behavior in the ±1000Oe field range.

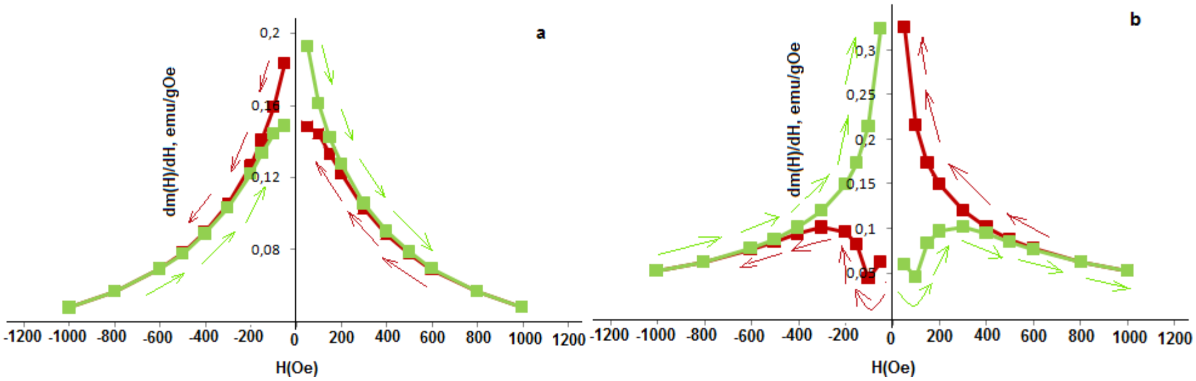

Fig7. Field dependences of differential susceptibility of Fe_3O_4 nanoparticles. The arrows designated the direction of the field sweep. a) Fe_3O_4≅9 b) Fe_3O_4≅28

It has been discovered that for both nanoparticles the values of the magnetic susceptibility in the direction of increasing(green arrows) and decreasing (red arrows) the magnetic field strength differs from each other. Both when the field is increased and the field is decreased, there are local maxima in the dependence dm(H)/dH for each sample, and its magnitude is smaller when the absolute value of the magnetic field increases. For the decreasing absolute value of the field, the amplification of the susceptibility maximum is related to the hysteresis of the magnetization in large fields and is obviously a consequence of this hysteresis[23].

For the Fe_3O_4≅28nm nanoparticles absolute maximum value of differential susceptibility for the ascending magnetic field is five time higher than the maximum value observed for descending field. Furthermore, the character of differential magnetic susceptibilities graphics for the ascending and descending magnetic field is different.

For Fe_3O_4≅9nm nanoparticles, absolute maximum value of differential susceptibility for the ascending magnetic field is 1.5 time higher than the maximum value observed for descending field. Also, the character of differential magnetic susceptibilities graphics for the ascending and descending magnetic field is same.

The dependence of the relaxation times of the magnetic moment of the nanoparticles on their size was also calculated.

The relaxation time (τ) measures the stability of the particle momentNeel relaxation time of the magnetization vector of the isolated magnetic particles[19]:

$$\tau = \tau_0 \exp\left(\frac{\Delta E}{k_B T}\right) \quad (1)$$

Here τ_0-is the pre-exponential time constant, often used as $\tau 0=10^{-9}$ s for magnetite [22]. ΔE-is energy required to rotate the magnetization vector. This energy called activation energy barrier.Buenerjiaktivasiyabaryeriadlanır. This energy described by the following formula:

$$\Delta E = KV \quad (2)$$

Here K is magnetization anisotropy;V is geometrical volume of magnetic nanoparticles.

$$V = \frac{\pi}{6}(D)^3 \quad (3)$$

Let to put expressions (2) and (3) in (1):

$$\tau = \tau_0 \exp\left(\frac{\pi K}{6 k_B T} D^3\right) \quad (4)$$

It is clear that relaxation time of magnetic momentum depends on size of particles. If the average size of nanoparticles are$28,65\times10^{-9}$m and $9,08\times10^{-9}$m,the effective anisotropy constant K=13kJ/m^3, and τ_0 is 10^{-9} sec, we can easily calculate relaxation time for samples.At T=298 K for nanoparticles with the size 9,08 nm relaxation time was 10^{-8} sec.

If the time window of the measurement (τ_m) is longer than the time needed for the particle's magnetic moment to flip ($\tau_m/\tau>1$), the particle is said to be in a superparamagnetic state [21]. the characteristic time of magnetic measurement is τ_{ex} =100sec. It is seems from calculations that for nanoparticles with average size 9.08nm,$\tau_m>\tau_0$.But fornanoparticles with average size 28,65nm it was found that $\tau_m<\tau_0$. In this case, the particle behaves as an ordinary single-domain particle.

Thus, an increase in the number of magnetic particles in a magnetic cluster leads to increasing interaction between them, and formation additional magnetization which in turn leads to increasing Neel relaxation time [22].

4. Conclusion

In this work were investigated the structure and magnetic properties of the magnetite nanoparticles with the spherical shape and two different sizes. The particles size observed from SEM images was used to determine statistical parameters of the particle size distribution. The average size of the particles was 9nm and 28nm, respectively. VMM investigation shows that the saturation magnetization, Ms, is very similar for both samples (~69emu/g). The smallest nanoparticles ($Fe_3O_4 \cong 9$) are superparamagnetic at this temperature as they show negligible coercivity and remanence. The dependence of the relaxation times of the magnetic moment of the nanoparticles on their size was also calculated. An increase in the number of magnetic particles in a magnetic cluster leads to increasing interaction between them, and formation additional magnetization, which in turn leads to increasing Neel relaxation time.

Reference

1. Y.S.Lim., C.W.Lai., S.B.A. Hamid., et.al., J. Materials Research Innovations 18, S6-457(2014).
2. LiyunFeng.,MinhuaCao.,XiaoyuMa.,et.al., J. Hazardous Materials217–218, 439(2012).
3. DeepaThapa., V.R.Palkar., et.al.,Materials Letters58, 2692,(2004).
4. Ashwani Kumar Singh., O. N. Srivastava., Kedar Singh., Nanoscale Research Letters**12**, 298 (2017)
5. Qing Li., Christina W. Kartikowati., Shinji Horie., et.al., Scientific Reports**7**, 9894 (2017).
6. M. A. Ramazanov., A. M. Maharramov., R. A. Ali-zada., *et.al.,*J.Theoretical and Applied Physics 12,7(2018)
7. Butler R.F., Banerjee S.K., J. Geophysical research 80,4050(1975)
8. http://www.irm.umn.edu/hg2m/hg2m_d/hg2m_d.html
9. Sergei P Gubin., YuryKoksharov., Gb Khomutov., *et.al* Russian Chemical Reviews74, 539, (2005)
10. VahakMarghussian.,Nano-Glass Ceramics. Processing, Properties and Applications. William Andrew 2015, p292Benyettou F., Milosevic I., Olsen JC., et.al., J. Bioanalysis&Biomedicine S5(2012)
11. Petrof.Y.I.,.Physics of Small Particles, Science, Moscow 1982,p328.

12. Frolov G.I., Bachina O.I., ZavyalovaMM.,Ravochkin S.I.,J.Technical Physics 53(8),1059 (2008).
13. Victoria Reichel., AndrbsKovbcs., Monika Kumari., et.al., J.Scientific Reports7,45484 (2017)
14. ChiranjibNayek., Kaustuv Manna., GourabBhattacharjee., et.al. J. Magnetochemistry3, 19,(2017).
15. T. Saranya,, K. Parasuraman., M. Anbarasu., *et.al.*J.Nano Vision 5(4-6), 149, (2015).
16. E. F. Chagas., A. S. Ponce., R. J. Prado.,et.al, J. Applied Physics 116(3), 033901 (2014).
17. G. V. Stepanov., D. Y. Borin., Y. L. Raikher., et.al, J. Phys.: Condens. Matter 20, 204121 (2008).
18. William T. Coffeya., Yuri P. Kalmykov, J.Applied Physics 112, 121301 (2012).
19. Rudolf Hergt., Silvio Dutz., Matthias Zeisberger.,J.Nanotechnology 21(1):015706(2010).
20. M. Osaci., C. Abrudean., A. Berdie., J.ACTA PHYSICA POLONICA A 112,1203(2007)
21. Xiangyu Zhao., Qingsong Liu.,Science China Earth Science 53(7), 1071(2010)
22. Andrii V. Bodnaruk., Alexander Brunhuber., Viktor M. Kalita., et.al., J. Applied Physics **123**, 115118-1 (2018).

***Corresponding author:**mamed_r50@mail.ru

INFLUENCE OF ELECTROTHERMOPOLARIZATION CONDITIONS ON STRENGTHAND ELECTRET PROPERTIES OF PP+ZrO_2 NANOCOMPOSITIONS.

[a]M. A. RAMAZANOV*, [b]H.S.IBRAHIMOVA,[a]F.V.HAJIYEVA
[a]Baku State University,23 Z.Khalilov Street, Baku, Azerbaijan, Az-1148
[b]Institute of Physics. Azerbaijan National Academy of Sciences, pr. H.Javid 33 Baku,AZ-1143

This paper deals with the investigation results of electret state mechanical and electric strength before and after electrothermal treatment. There have been presented AFM images of PP+ZrO_2 nanocomposition after and before electrothermal polarization (ETP). It is established that electrothermal polarization has a profound effect on electret and strength properties of nanocomposition and it is due to the accumulation charge at the phase interface between nanocompositecomponents.

Keywords: Nanocomposite materials, polypropylene, nanoparticles, electrothermal polarization
PACS:61.46.w;82.35.Np;71.38.k

1. Introduction

Nowadays nanocomposites owing to their impressed physical and chemical properties are of advantage in most various spheres of production of electron and impulse technology,electronics, medicine and etc. [1-3]. By using in different devices of polymer nanocomposite elements, they undergo the effect of different external factors including the effect of external electric field [4-5]. It is known that most dielectrics have electret properties after applying the external constant electric field [6]. It is revealed that electrothermalpolarization changes charge state of nanocomposition and it can change their strength properties and electret states. This paper deals with the investigation results of influence of electrothermal polarization on strength properties and electret states of nanocompositions on the base of polypropylene and zirconium dioxide.

2. Experiment

As a polymer matrix, the isotactic polypropylene in size from 0,5-1,0 mkm particle is used as a filler the zirconium dioxide(ZrO_2) nanoparticles in size 21 nm particle, stabilized by 3% ittrium oxide (Y_2O_3). Production of PP+ZrO_2-based nanocomposites has been carried out by injecting ZrO_2 nanoparticles into polymer solution [7].

Compositions have been obtained by method of hot pressing at melting temperature of polymer matrix under the pressure 15 MPa for 10 min with subsequent quick cooling with the rate 2000deg/ min . Polymer compositions undergo the electrothermal polarization at Tp=353K for 1 hour under the effect of electric field , then they are cooled down to room temperature [8].

3. Results and discussion

In fig.1 (a, b,c) have been given dependences of electret charge surface density σ on the storage time r of PP+ZrO_2nanocompositions at ZrO_2 different contents in polypropylene . From the figure it is seen that by increasing nanoparticle content in PP the electret charge surface density and storage time measured by increasing ZrO_2 volume content.

It is shown that the electret charge surface density and storage time depends on polarization conditions. Given magnitudes (σ and τ) gain their maximum values at $E_{tr}=10\cdot10^6$ V/m .From figure it is seen that by increasing polarization intensity up to the given value the electret properties have been improved, but after $E_{tr}>10\cdot10^6$ V/m the volume charge concentrations are increases. At bigger nanocomposite contents the conductive chains of Zrmolecules preventing polarization processes have been formed. In brings about the deterioration of nanocomposition electret properties.

In fig.2. there have been presented dependences of electric and mechanical strengths of PP+3%ZrO_2nanocomposition not undergone and undergone electrothermal polarization (ETP) effect on the treatment durability in electric field at $T_p=393K$ for t_p equal to1 hour.

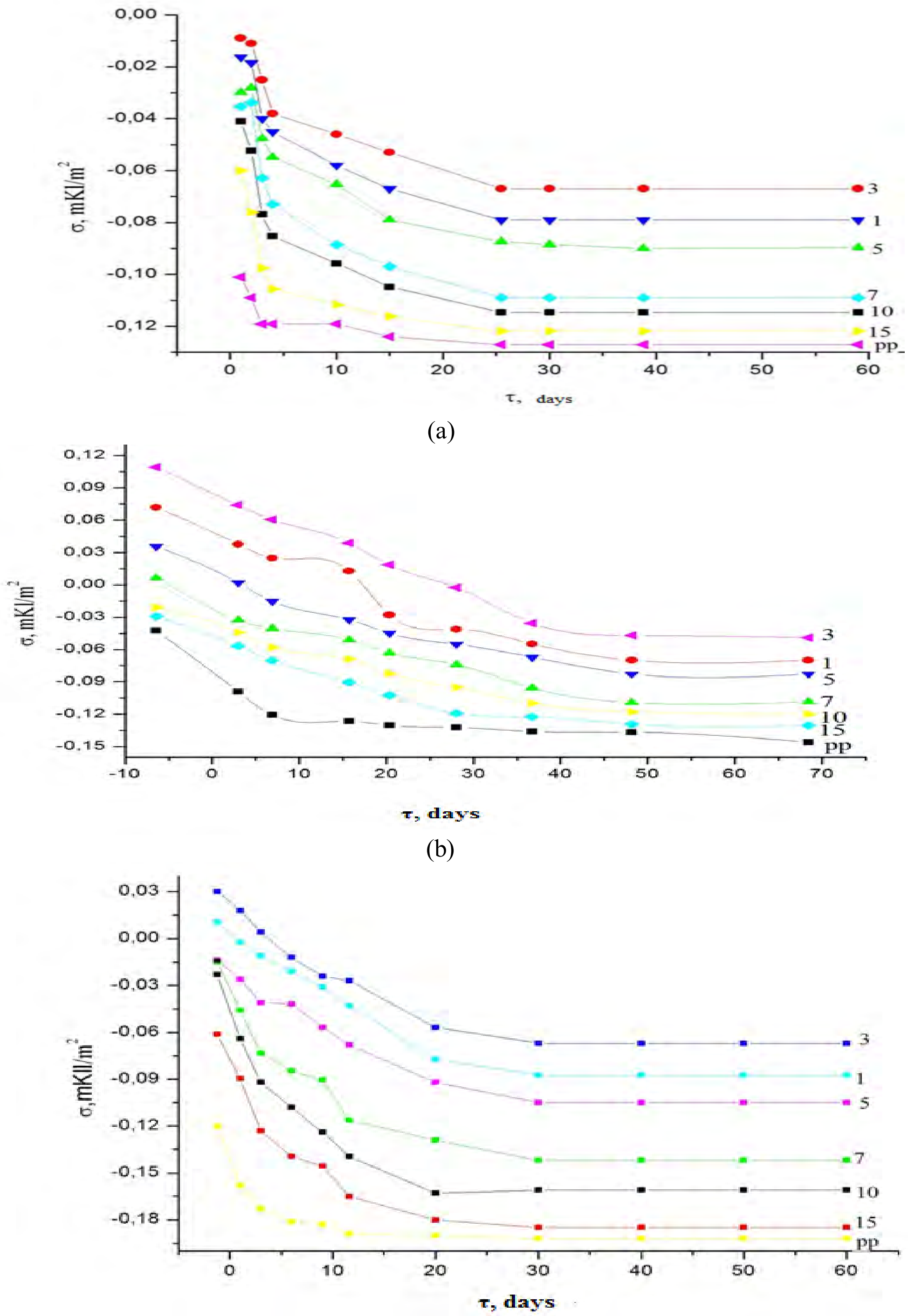

(a)

(b)

(c)

Fig.1. Change of charge surface density for PP+ZrO_2nanocompositions in size d≤21 nm nanoparticles undergone electrothermal treatment in different percentages: a)$E_{tr}=5\cdot10^6$ V/m, b) $E_{tr}=10\cdot10^6$ V/m, c) $E_{tr}=15\cdot10^6$ V/m for 1 hour 1- PP+3%ZrO_2, 2- PP+1%ZrO_2 , 3- PP+5%ZrO_2 , 4- PP+7%ZrO_2 , 5- PP+10%ZrO_2 6- PP+15%ZrO_2 7-PP

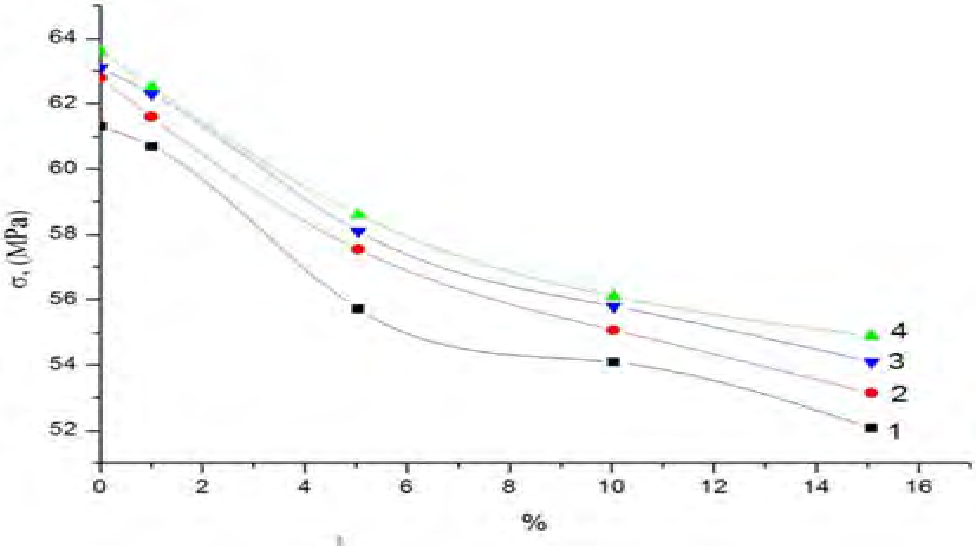

(a)

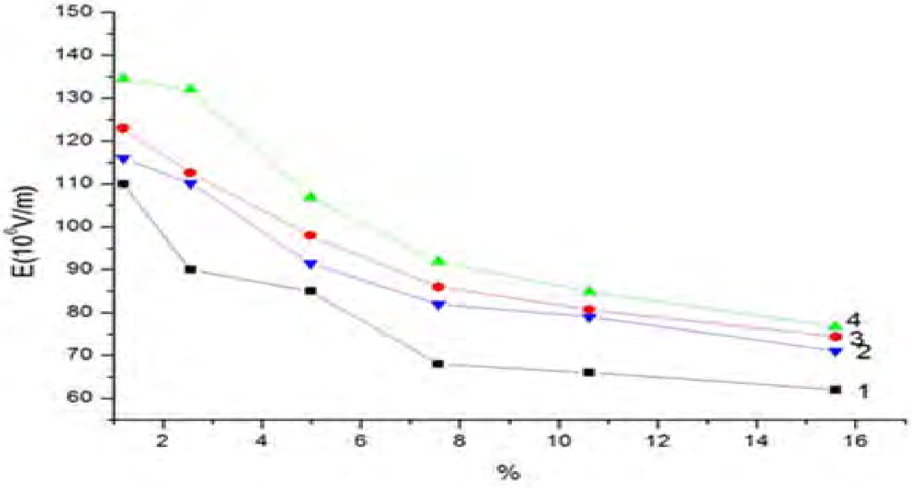

(b)

Fig.2. Mechanical (a) and electric (b) strength for PP+3%ZrO_2nanocomposities in size d≤21 nm nanoparticles not undergone and undergone the electrothermal treatment for 1 hour.
1-$E_{tr}=0$, 2- $E_{tr}=5\cdot 10^{6}$V/m, 3- $E_{tr}=15\cdot 10^{6}$V/m, 4- $E_{tr}=10\bullet 10^{6}$V /m

As it is seen from fig.2 after electrothermal polarization for PP+3%ZrO_2nanocomposition there has been observed the increase of electric and mechanical strength up to certain values, then decreases. We think that this fact is related to the migration polarization which leads to the interphase interaction growth. Increase of interphase interactions causes the growth of nanocomposite strength. In fig.3 there have been given shown AFM images of PP+3%ZrO_2nanocomposition before (a) and after (b) the electrothermal polarization. From fig.3it is seen that after electrothermalpolarization the morphology of nanocomposition changes strongly, i.e. ordering of surface structural elements is taken place.

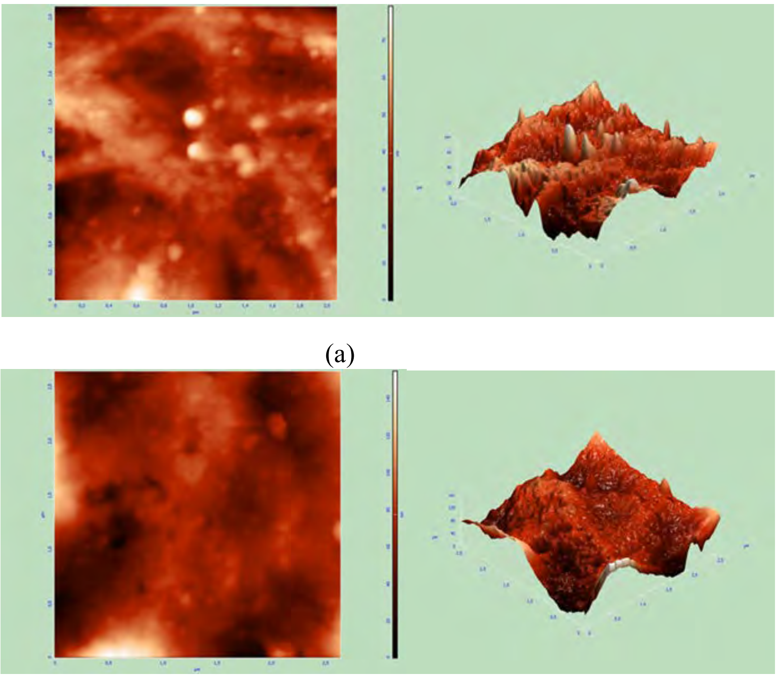

(a)

(b)

Fig.3. AFM images of nanocompositions before (a) and after (b) ETP in alternating electric field.

4. Conclusion

Thus from above mentioned experimental results one can conclude that electrothermal polarization has a strong influence on electret and strength properties of nanocomposition which is due to the charge accumulation at the phase interface between nanocomposite components.

Reference

1. RamazanovM.A, Quseynova A.S.,Mehdiyeva S.I, Abasov S.AMaterial for Electret material Republic of Azerbaijan Patent 2007,0059(2007)

2 M.A. Ramazanov, Z.G. PanahovaPiezocomposite sensor for registration artery pulse wave
Instruments and Experimental Techniques, 40, 708 (1997).

3. Ramazanov M.A., Huseynova A.S.Optoelectronics and advanced materials-Rapid Communications 7, 789 (2013).
4. RamazanovM. A., IbrahimovaKh. S., and AbasovS. A. Surface Engineering and Applied Electrochemistry, 48, 380 (2012).
5. RamazanovM.A., HadiyevaA.A., AlekperovV.A. Journal of OvonicResearch 10, 101(2014)
6. Sessler G.M, Electrets Ed., Heidelberg, New York: Springer Verlag, 1980, 453p.
7. RamazanovM.A. ,HajievaF.V., MaharramovA.M., HasanovaU.A. J. Ferroelectrics, 507, 1 (2017)
8. AbasovS.A., RamazanovM.A., IbrahimovaH.S., MustafayevZ.E.. Physics and chemistry of material treatment 5,87(2003)

***Corresponding author:** mamed_r50@mail.ru

TEMPERATURE DEPENDENCED CONDUCTIVITY OF PtSi/n-Si SCHOTTKY DIODES WITH SELF-ASSEMBLED PATCHES

I.M.AFANDIYEVA[1*], Sh. ALTINDAL[2]

[1]*Baku State University, Z.Khalilov str., 23, Baku, Azerbaijan, Az1148*
[2]*Physics Department, Faculty of Sciences, Gazi University, Ankara, Turkey*

Electrical conductivity of PtSi/n-Si Scottky diodes with the contact area of 8Ç10^{-6} cm^2 have been investigated by using impedance spectroscopy method (ISM) in the wide temperature range of 79-360 K and voltage range of ±2V, using of a small *ac* signal (20 mV) at 500 kHz, respectively. The values of activation energy E_a are obtained from the slope of the $\ln(\sigma) - \frac{q}{2kT}$ plots decreased from 0.39eV to 0.1eV with increasing of the temperature from 79 K to 360 K. This fact indicates that in this temperature range hopping conductivity with variable hopping length over localized states is observed. According to Mott equations, the length of jump (R=26,6-18,2 E) over localized states and the density of localized states near the Fermi level have been calculated. Obtained result attributed to the presence of self assembled patches in PtSi/nSi diodes.

***Keywords*:** PtSi/n-Si Schottky diodes; Self-assembled patches; Hopping conductivity.
PACS: 84.60.Jt; 73.50.Pz; 79.60.Jv

1. Introduction

The development of science and technology requires the creation of new devices with a small dimension, fabricated by simple technology. On the other hand, the decrease in the area of contact leads to an increase of the role of the non-uniform charge distribution over the area. In this case, the natural fluctuations of the semiconductor, which caused with the discrete character of the space-charge distribution, always occur [1]. Schottky diodes (SDs) on the basis of metal-semiconductor (M/S) contact in comparison with p-n junctions, as ease of the fabrication and wide choice of contact materials has many advantages [1,2]. Knowledge of the influence of temperature on electrical characteristics of the silicide/Si contact structure is important for creating of new devices, for understanding the formation of barriers. The reason for choosing this structure is threefold: first, the contact of PtSi/Si characterized by the big barrier height. Second, crystal lattice of n-Si (111) contains hexsagonal voids [3]. Third, interface of Schottky diodes with contact siliside/Si formed below the initial surface of the silicon. In the present paper the influence of temperature and applied voltage of the electrical conductivity of PtSi /n-Si SDs with a very low area of 8x10^{-6} cm^2 have been investigated by using impedance spectroscopy method (ISM) in the temperature range of 79-360 K, voltage range of ±2V and a small *ac* signal (20 mV) at 500 kHz, respectively.

2. Experimental procedure

The PtSi /n-Si SDs with an area of 8x10^{-6} cm^2 were fabricated by the use of a magnetron sputtering method. As the semiconductor substrate n-type (P doped) Si with 5.08 cm diameter, (111) surface orientation, 0,7 Ω cm resistivity and 3,5 µm thickness was used. The silicon plates were annealed in the chamber of the system at a vacuum of 6x10^{-5} Torr and 573 K during 300 seconds and then the platinum film was deposited. Argon gas was used to create the plasma. For the fabrication of the platinum silicide (PtSi), the substrate (Pt /n-Si) was annealed for 10 minutes in a 6x10^{-5} Torr vacuum and 773 K temperature. To produce a homogenous silicide film (PtSi) the silicon substrate was annealed in a special ampule outside the chamber for 30 minutes. The process passed in this condition: at the temperature 783 K in an atmosphere of gases N_2 and H_2. In addition, the fabricating structure (PtSi/n-Si) was washed in aqua regia to remove unreacted platinum. To prevents the penetration of Al through a silicide film between PtSi and Al was located an amorphous layer of TiW alloy as diffusion barrier [3,4,5].

For the investigation of conductance have been used C–V and G/x–V measurements which performed at the temperature in the range 79- 360K and applied *dc* voltage in the range of ±2V by using a HP 4192A LF impedance analyzer and small sinusoidal test signal of 20 mVp _ p from the external pulse generator. All measurements were carried out with the help of a microcomputer through an IEEE-488 ac/dc converter card.

3. Results and discussion

In the present paper, the temperature dependence of *ac* electrical conductivity σ_{ac} of PtSi /n-Si SDs for various temperature in the range 79-360K and applied voltage in the range of ±2V has been calculated by the following equation [6,7,8]:

$$\sigma_{ac} == \frac{Gd_i}{A} \qquad (1)$$

where d_i is the thickness of the dielectric gap, A is the rectifier contact area of the structure in cm^{-2} (Fig.1A). The thickness of the dielectric gap has been obtained using the maximal capacitance of the metal-semiconductor structure in the strong accumulation region ($C_i = \varepsilon_i\, \varepsilon_o A/d_i$).

The change in the dependence of conductance on temperature is associated with a change in the concentration of defects. It is known, that hopping mechanism is the main transport mechanism in disordered systems with localized states. In this case, the value of activation energy (E_a) can be obtained from the Arrhenius plot as given the following relation [6-12]:

$$\sigma = \sigma_0 \exp\left(-\frac{qE_a}{2kT}\right) \qquad (2)$$

Fig.1B shows the $ln\sigma\ vs\ q/2kT$ plot for the PtSi/n-Si SD for various forward bias voltages. As can be seen in this figure, on the dependence at the dc voltage as 0.2V, 0.6V, 0.8V, 1.0V and 1.2V there are three temperature areas: (79-160)K, (160-250)K and (250-350)K. Only, when dc voltage is 0,4V exponential dependence persists in the temperature region (120-350)K. Such behavior of the Arrhenius plot was confirmed that the conduction at high and low temperature is considerably different due to the different hopping mechanisms and restructure and reordering charges at surface states under temperature and voltage effects. Values of E_a determined from the slope of $ln\sigma - q/2kT$ plots of the PtSi/n-Si structure for various dc voltages at 500 kHz are changed from 0.39eV to 0.1 eV. Obtained values of activation energy revealed, that activation energy decreased with decreasing of the temperature. At the temperature in the range (200-250)K (for the 0,6-1,2V dc voltage) and 79-120K for (0,4V dc voltage) the conductivity not depended on temperature, practically. In these temperature ranges nonactivation hopping conductivity is observed. This fact indicates that in this temperature range hopping conductivity with variable hopping length over localized states is observed.

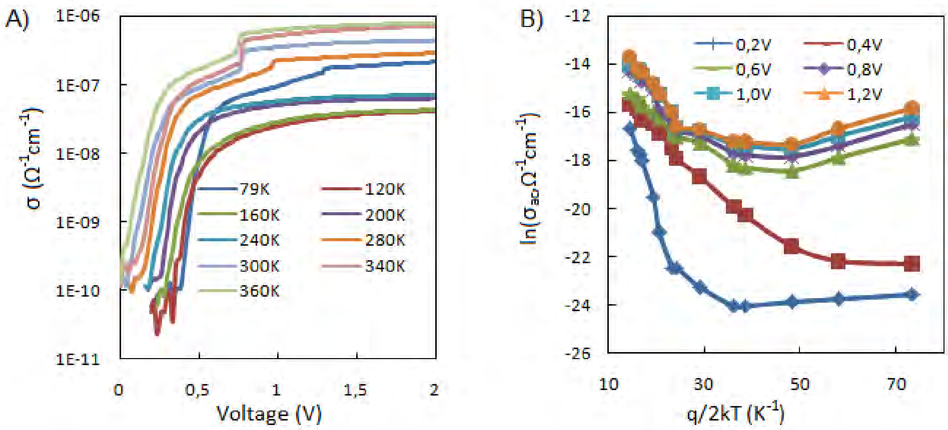

Fig.1. (A) The dependence of conductance *vs* applied voltage for PtSi/n-Si SD at various temperatures; (B) The temperature dependence of $\ln\ \sigma_{ac} - q/2kT$ for PtSi/n-Si SD at various applied *dc* voltage.

According to Mott equation, the relation of σ and T can be expressed as [5]

$$\sigma(T) = \frac{\sigma_0}{T^{\frac{1}{2}}} \exp\left[-\left(\frac{T_0}{T}\right)^{\frac{1}{4}}\right] \tag{3}$$

As seen in Fig.2, Mott plot has a good straight line in almost the whole temperature range. Thus, the Mott plot on the basis of Eq. (3) and Fiq.3, the characteristic temperature T_0 has been calculated for 0.4 V *dc* voltage (T_0= 2,5x10^7 K) and for 0,8V *dc* voltage (To=1,1x10^7K), respectively.

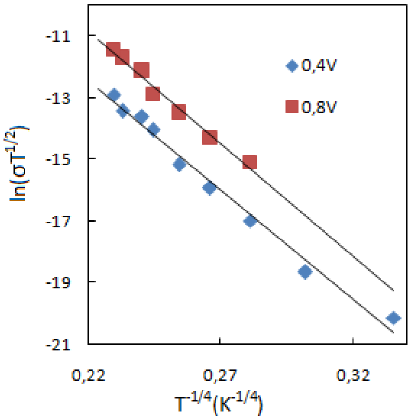

Fig.2. The temperature dependences of the conductivity of the PtSi/n-Si structure in Mott's coordinates for 0.4 V *dc* voltage obtained at 500 kHz.

Within the framework of the considered model, the length of jump (R) over localized states for a given temperature T has been calculated from the expression [6-9]

$$R(T) = \frac{3}{8} a \left(\frac{T_0}{T}\right)^{1/4} \tag{4}$$

In Eq. 4, a is the radius of the localization. We accepted the value of a=3 E for Si [8]. On the basis of obtained results, the length of jump (R) over localized states decreased from 26,6 to 18,6 E with the increasing of the temperature from 79 to 350K

The density of localized states near the Fermi level was determined for 0.4 V *dc* voltage by using the formula [6-12]

$$N_F = \frac{16}{T_0 k a^3} \tag{5}$$

where k is the Boltzmann constant. Obtained results for N_F are 2.7x10^{20} eV^{-1} cm^{-3}(0,4V) and 6.26E+20 (0,8V) well correlate with results for structure of erbium doped hydrogenated amorphous silicon films [9]. On the basis of results has been revealed, that at the changing of temperature from 79 to 350K dc voltage +-2V, ac voltage 500kHz, 20mV in PtSI/nSi Schottki diodes there is a hopping mechanism of conduction near the Fermi level with absorption or emission of a phonon. Conductivity activation energy corresponds to the jump energy in the area 0,39-0,1eV. It is known, that the existence of localized states in the forbidden band is due to the presence of structural defects in crystals. The crystal structures Si(111) contains deformed hexagonal voids (A=14,22 E ^{2}) [3]. It should be taken into account that the surface of the silicon substrate is a corrugated hexagonal layer that is parallel to the plane (111) and characterized by numerous interfaces and a huge inner surface. This suggests that in the process of contact formation of contact, the diffusion of platinum atoms into voids Si(111) has occurred. In result irregular formation of self-assembled local patches has occurred, due to the diffusion of platinum atoms into voids Si(111) [3].Obtained length of jump (R) over localized states 26,6 and 18,6 E is in a good agreement with the radius of self-assembled patches (R =78 E).

4. Conclusions

The *ac* conductivity (σ_{ac}) was calculated from the measured experimental C and G values in the temperature range (79-350)K. On the basis of temperature dependence of conductivity has been revealed, in this temperature range hopping conductivity with variable hopping length over localized states is observed. The values of activation energy E_a are obtained from the slope of the $\ln(\sigma) - \frac{q}{2kT}$ plots for different dc voltages. The value of E_a decreased from 0.39 eV to 0.1 eV with decreasing of the temperature from 79 K to 360 K. According to Mott equations, the length of jump (R=26ç18 E) over localized states and the density of localized states (N_F = 2.7x10^{20} eV^{-1} cm^{-3}ç6.26E+20 eV^{-1} cm^{-3}) near the Fermi level have been calculated. Obtained result has been attributed to the formation of local pathes (R_p~78 E) and irregular formation of a lot of self-assembled quantum wells, due to the existence of hexagonal voids of Si (111).

References

1. V.I. Strikha, Theoretical Bases of Metal-Semiconductor Contact Work, Naukova Dumka, Kiev, (1974) (in Russian).
2. S.M. Sze, Physics of Semiconductor Devices, 2nd ed., Wiley, New York, 1981.
3. I. M. Afandiyeva, Ş. Altındal, L. K. Abdullayeva, and A. İ. Bayramova, Journal of Semiconductors, 39, 5,p. 054002-1- 7(2018)
4. I.M. Afandiyeva, SH.G. Askerov, L.K. Abdullayeva, SH.S. Aslanov, Solid-State Electronics, 51, 1096 (2007).
5. Kwak Joon Seop, Kang, Ki Man, Park Min Joo, Pyo. Myoungho, Science of Advanced Materials, 6,10, 2249 (2014).
6. Mott N.F., Conduction in non-crystalline materials". Phil. Mag. 19: 835 (1969).
7. Mustafaeva S.N. Asadov, S.M, Kerimova, E.M, , Semiconductors, 52, 2, 156-159 (2018).
8. Kon.kov O.I, Terukov E.I.,. Granitsina L.S, Semiconductors, 36, 11,1332-1336 (2002)
9. S.P. Zimin, D.S. Zimin, Yu.V. Ryabkin, A.N. Bragin. Phys. Status Solidi A, 182, 221 (2000)
10. Zankat, Alpa; Boricha, Hetal; Shrimali, V. G., Journal of alloys and compounds, 788, 623-631 (2019)
11. Abdel-Khalek, H.; Abd-El Salam, Mohamed; El-Mahalawy, Ahmed M., Journal of electronıc materıals, 48, 6, 736-3752 (2019).
12. Duan, Xiu-Zhi; He, Zhi-Hao; Yang, Yang; et.al. Physıcal revıew B, 99, 9, 094204 (2019).

***Corresponding author**: afandiyeva@mail.ru
I_afandiyeva@yahoo.com

MOLECULAR DYNAMICS OF NANOSCALE PHENOMENA: COMPUTER DESIGN FOR NEW DRUGS AND MATERIALS

MIRZOAZIZ KHUSENOV[1,*], DILSHOD NEMATOV[1], AMONDULLO BURHONZODA[1],
KHOLMIRZO KHOLMURODOV[2,3,*], ALEKSANDR DOROSHKEVYCH[2],
NELLY DOROSHKEVYCH[2], TATYANA ZELENYAK[3], SUBRATA MAJUMDER[4]

[1]*Tajik Technical University named after M.S. Osimi, 724000, Dushanbe, Republic of Tajikistan*
[2]*Joint Institute for Nuclear Research,141980, Dubna, Moscow Region, Russian Federation*
[3]*Dubna State University, 141980, Dubna, Moscow Region, Russian Federation*
[4]*National Institute of Technology, N.I.T., Patna: 800 005, India*

In this work a complex study of the DNA immobilization and conformation processes on the zirconium dioxide (ZrO_2) surface. The DNA+ZrO_2 nanoparticles and nanosized films were investigated with the MD modeling, experimental spectral and integral methods, including nuclear physics. Using the MD hybrid classical and quantum chemistry potentials, for the DNA solvated with water the DNA+ZrO_2 surface interactions were simulated We have generated series MD models, thereby simulating a different scenario of the DNA with possible charge modifications. The DNA charge modification were introduced in the DNA central region via its two phosphorus atoms, P_a and P_b, and for several set of MD models for the relaxed DNA structures we have estimated the positional changes of the distance $D[DNA(P_a,P_b) - ZrO_2(O)]$ between the phosphorus atoms (P_a,P_b) and selected oxygen atoms of the ZrO_2 surface. The work is aimed to the development of functional hetero-junctions such as a biological molecule - wide-gap dielectric. These hetero-junctions are intended for using in the field of molecular electronics, in particular, for the creation of biochips, memory arrays and computer architectures of the future.

Key words: Immobilization of DNA molecules on the surface of dielectrics, molecular electronics, nanotechnologies, modular-dynamic modeling, DNA conformation in the electric field, genotoxic effects
PACS: 02.70.Ns; 62.23.−c; 87.15.−v

1.Introduction

Molecular simulation studies are performed within the research activities of Molecular Dynamics (MD) modeling groups of the Neutron Optics sector in the Department of Neutron Investigations of Condensed Matter, Frank Laboratory of Neutron Physics (FLNP), Joint Institute for Nuclear Research (JINR), Dubna, Russian Federation and Faculty of Energetic, Tajik Technical University named after M.S. Osimi, Dushanbe, Republic of Tajikistan, thereby outlining the international research collaborations closely performed with Japanese (Keio University, Waseda University, RIKEN, etc.) and Indian groups (National Institute of Technology, NIT.-Patna). The examples have to cover a general issue on “Computer Design for New Drugs and Materials”, which demonstrate the efficient use of computer MD in both classical (conventional) and quantum chemical methods implementations. Some aspects of our recent studies include computer modelling of non-equilibrium chemo-electronic conversion of water adsorption on the surface of yttria-stabilized zirconia. The tasks of the work include the simulation of radiation induced conformations of a DNA chain on a zirconia dioxide (ZrO_2) surface by MD (molecular dynamics) method. Interdisciplinary research in the field of nanotechnology has a breakthrough potential and the main hopes of nanoscale technologies are associated with new effects at the intersection of the physics of chemistry and biology. The combination of biomolecules with solid nanoparticles generates a new class of materials, primarily for new electronic sensory and optical systems, the prospects for the development of molecular electronics, the creation of biochips, memory arrays and computer architectures of the future become real. DNA molecules have good electrical conductivity, are able to store and transmit by copying terabytes of information self-reproducing and moving in the electric field, therefore, are extremely interesting as a functional element of bio-electronic devices. The purpose of this work is to obtain biologically modified structures by immobilizing of DNA molecules on the surface of biocompatible crystals, an experimental and theoretical study of the fundamental mechanisms of physical-chemical interaction and dynamics of the DNA molecule on interfaces with a solid bases under the influence of external electric fields and radiation fluxes [1-14].

2. Methodical part

For a triple system DNA + water + ZrO_2 surface, all the interatomic interactions are described with standard molecular mechanics potentials, as a sum of two-, three-, and four atom terms. All-atom interactions include harmonic bonds, angles, improper torsions, and dihedral angles The long-range interactions include Lennard-Jones van der Waals potentials and electrostatic potentials between atom-based partial charges:

$$U(\boldsymbol{r}) = U_b + U_\theta + U_\varphi + U_\omega + U_{LJ} + U_{el} + U_{HB} + \ldots$$

Here valence length potential, $U_b = \frac{1}{2}\sum_b K_b\,(r - b_0)^2$, the valence angle potential, $U_\theta = \frac{1}{2}\sum_\theta K_\theta\,(\theta - \theta_0)^2$, the torsion dihedral potential, $U_\varphi = \frac{1}{2}\sum_\varphi K_\varphi\,[\cos(n\varphi - \delta) + 1]$, the Van-der-Waals interaction and hydrogen bonding potentials are Lennard-Jones (LJ; 12-6) or (12-10) types, $U_{LJ} = \sum_{i,j}\left[\frac{A}{r_{ij}^{12}} - \frac{B}{r_{ij}^{6}}\right]$ and $U_{HB} = \sum_{i,j}\left[\frac{A'}{r_{ij}^{12}} - \frac{B'}{r_{ij}^{10}}\right]$, the electrostatics potential, $U_{el} = \sum_{i,j}\frac{q_i q_j}{\varepsilon r_{ij}}$, represents long-range interactions in the system. For the DNA solvated with water, based on the experimental data, *ab initio* and semiempirical electronic structure calculations, a number of self-consistent and well-tested sets of parameters are published and available (see, for example, all-atom sets in CHARMm22; Brooks et al., 1983). For ZrO_2 surface we have used Buckingham interaction potential,

$$U(r) = A\exp\left(-\frac{r}{\rho}\right) - \frac{C}{r^6}$$

with the interaction parameters A, C and ρ.

In Figs.1(a,b) the initial position of a DNA chain on ZrO_2 (zirconia dioxide) surface and the whole system solvated with water are shown, respectively. The DNA chain was located at a well-separated distance from the zirconia dioxide. After appropriate preparation of the DNA+ZrO_2 surface a water box was introduced. The MD trajectory calculations performed for multiple DNA+water+ZrO_2 models were next used to simulate the effect of the radiation introduced on a DNA side chain with consequent conformation changes [9-14].

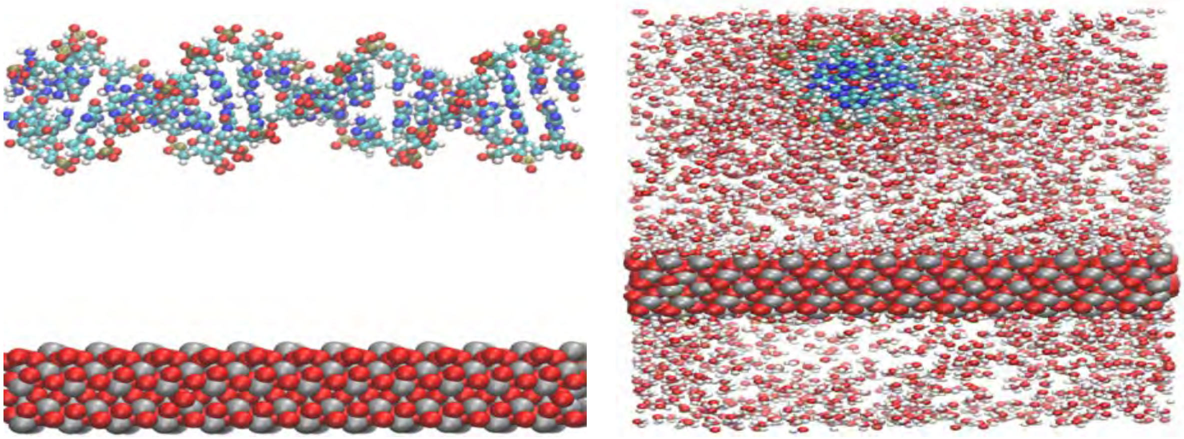
(a) **(b)**

Figs.1(a,b). The initial position of DNA chain on ZrO_2 (zirconia dioxide) surface.

3. Results and discussion

For the DNA molecule solvated with water and interacting with the ZrO_2 surface we have consider different model structures, thereby simulating different scenario of the DNA possible charge modification. From two opposite DNA directions we have arbitrarily chosen two P (phosphorus) atoms as possible damage sites. The

DNA charge modification we have introduced in its central region through two set of MD models (set A: models 1-3 and B: models 4-6) for both phosphorus atoms P_a and P_b.

In Figs. 2-3 the MD simulation results are shown for the D[DNA(P_a,P_b) - ZrO_2(O)] dynamics for the models 1-3 (Q(P_a)=+1,1659|e|, Q(P_a)=0 and Q(P_a)=-1,1659|e|, native DNA and two damaged versions, respectively) and models 4-6 (Q(P_b)=+1,1659|e|, Q(P_b)=0 and Q(P_b)=-1,1659|e|), native DNA and two damaged versions, respectively).

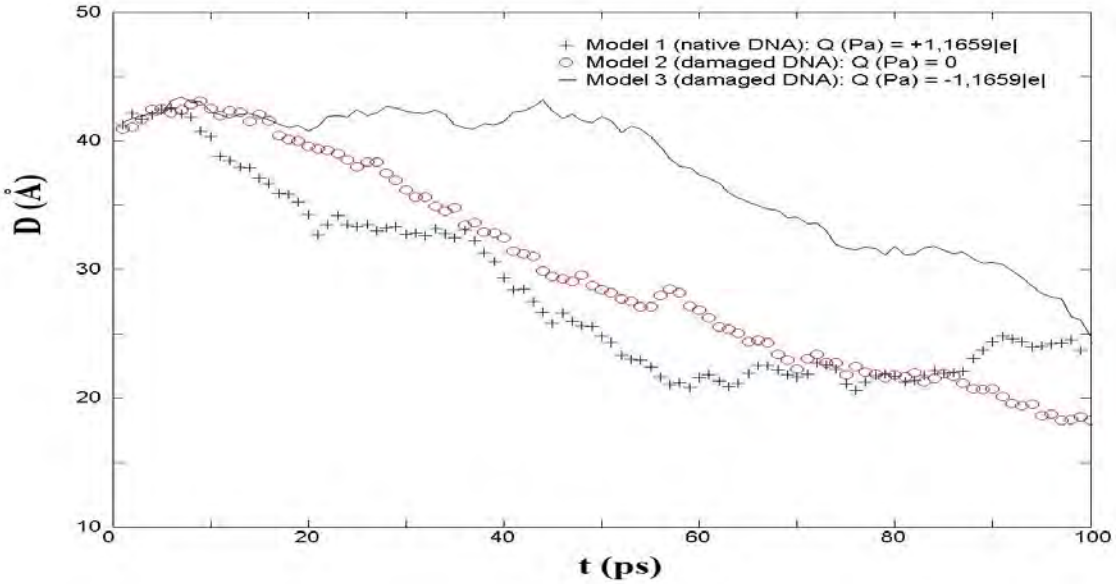

Fig. 2. The distance D[DNA(P_a) - ZrO_2(O)] between phosphorus (P_a) and selected oxygen (O) atoms of the zirconium dioxide surface for the MD models 1-2-3.

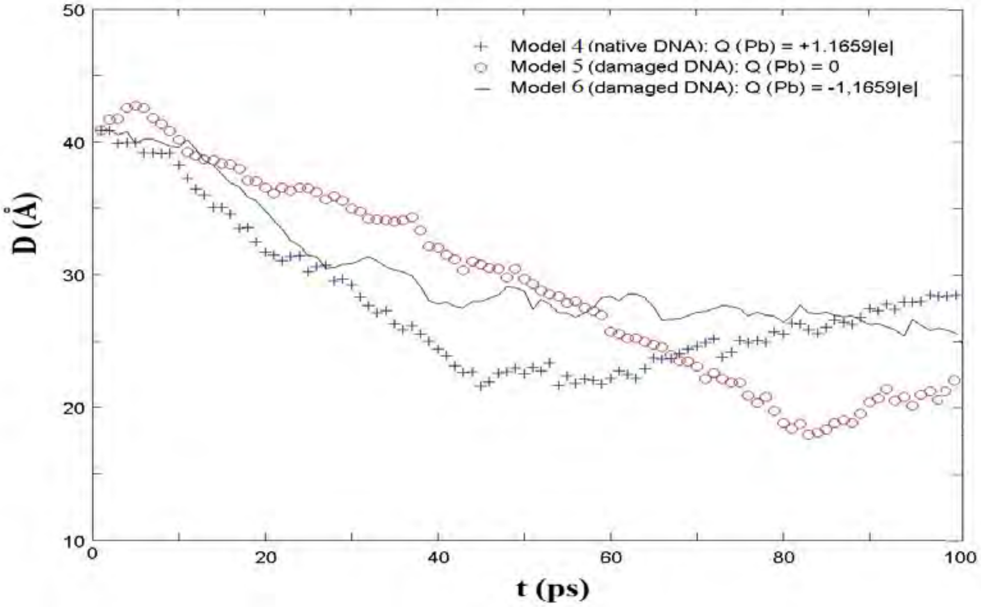

Fig. 3. The distance D[DNA(P_b) - ZrO_2(O)] between phosphorus (P_b) and selected oxygen (O) atoms of the zirconium dioxide surface for the MD models 4-5-6.

The distance distribution D[DNA(P_a,P_b) - ZrO_2(O)] between the phosphorus (P_a,P_b) and selected oxygen (O) atoms of the zirconium dioxide surface are compared for the native DNA (Q(P_a,P_b)=+1,1659|e|) and two damaged versions (Q(P_a,P_b)=0 and Q(P_a,P_b)=-1,1659|e|). The charge state of the phosphorus (P_a,P_b) atoms mimics the effect of external radiation (UV or other) induced on the site of DNA, such that the value of Q(P_a,P_b) spontaneously vary in the interval [+1,1659;-1,1659]|e|. From the distance diagrams in Figs. 2-3 we can see both different D[DNA(P_a,P_b) - ZrO_2(O)] time dependent behavior and different DNA-surface close contact on a final state. So far, starting from the same relaxed state (but with different Q(P_a,P_b)) the DNA molecule while interacting with ZrO_2 surface will undergo a different conformational shape, thereby approaching the surface.

It is worth noting that the above choice of phosphates in the DNA charge modification introduced by Figs. 4-5, were due to the DNA - ZrO_2 surface interactions as in paper (J. Phys. Chem. B, 2015, 119 (11030-11040)), where the author have studied via molecular dynamics simulations several DNA phosphate and surface silanol groups, hydrophobic bonding between DNA base and silica hydrophobic region. Also they have find two major binding mechanisms to be attractive interactions between DNA phosphate and surface silanol groups, hydrophobic bonding between DNA base and silica hydrophobic region.

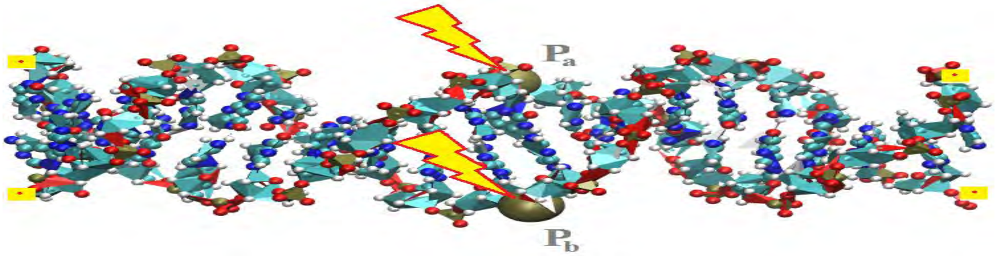

Fig. 4. The position of two P (phosphorus) atoms (P_a and P_b; grey color) of the DNA molecule are shown as possibly DNA damaged sites.

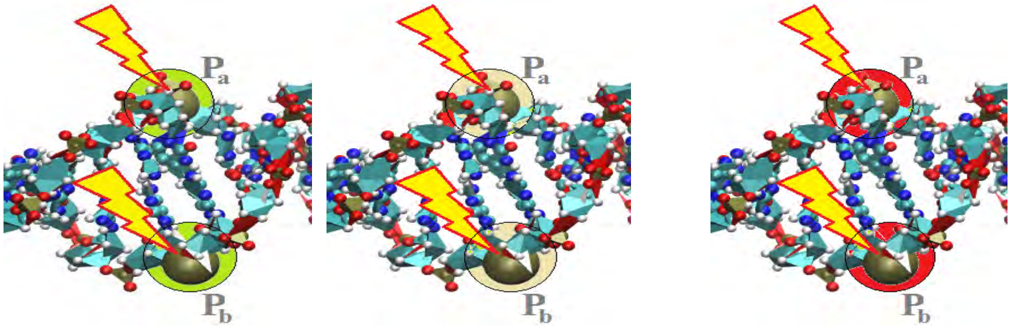

Model 1 (native DNA) **Q (P)=+1,1659|e|**

Model 2 (damaged DNA) **Q (P)=0**

Model 3 (damaged DNA) **Q (P)=-1,1659|e|**

Fig. 5. The charge modification on two P (phosphorus) atoms of the DNA damaged sites.

Next, the DNA conformational behavior have built through a graphical 3-D representation analysis. We have used MD trajectory calculations for the DNA chain to investigate the DNA interaction and immobilization processes on the ZrO_2 surface. In Figs. 6 the DNA orientation dynamics on ZrO_2 are presented for the models 1-2-3 (model 1: Q(P_a)=+1,1659|e|, model 2: Q(P_a)=0, and model 3: Q(P_a)=-1,1659|e|; native DNA and two damaged versions, respectively). The MD simulation results in Figs. 6 demonstrate the DNA/ZrO_2 dynamical changes and distance distributions D[DNA(P_a) - ZrO_2(O)] between the phosphorus (P_a) and selected oxygen (O) atoms of the zirconium dioxide surface. The Figs. 6 compare the MD results for the native DNA (model 1: Q(P_a)=+1,1659|e|) and two damaged versions (models 2: Q(P_a)=0 and 3: Q(P_c)=-1,1659|e|). In Figs. 7 the DNA orientation dynamics on ZrO_2 are presented for the models 4-5-6 (model 4: Q(P_b)=+1,1659|e|, model 5: Q(P_b)=0, and model 6: Q(P_b)=-1,1659|e|, native DNA and two damaged versions, respectively). The MD simulation results in Figs. 7 demonstrate the DNA/ZrO_2 dynamical changes and distance distributions D[DNA(P_b) - ZrO_2(O)] between the phosphorus (P_b) and selected oxygen (O) atoms of the zirconium dioxide surface. The Figs. 7 compare the MD results for the native DNA (model 4: Q(P_b)=+1,1659|e|) and two damaged versions (models 5: Q(P_b)=0 and 6: Q(P_b)=-1,1659|e|).

D[DNA(P_a)-ZrO_2(O)]-----XY~f(T)-----Models 1-2-3

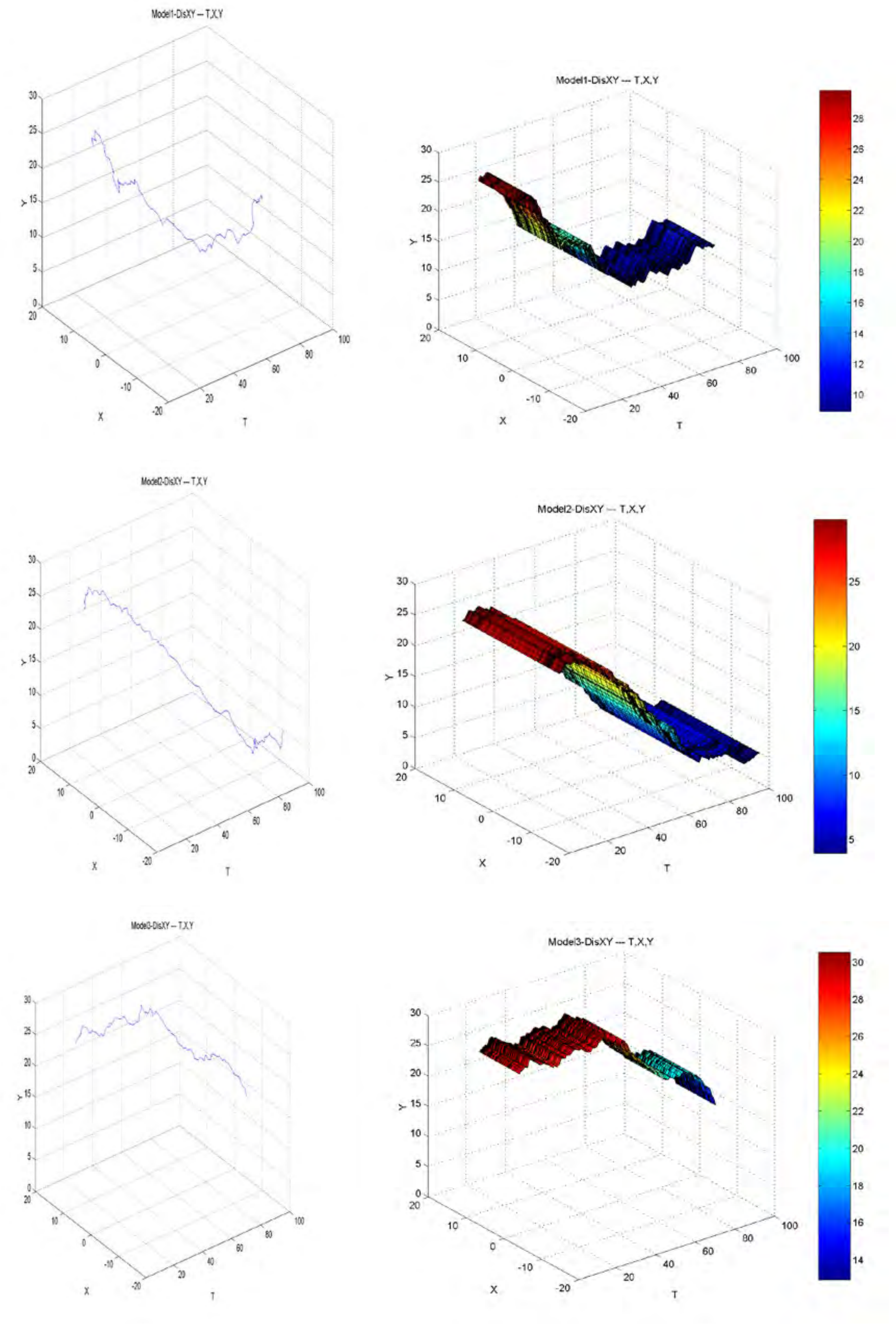

Figs. 6. The distance D[DNA(P_a) - ZrO_2(O)] between phosphorus (P_a) and selected oxygen (O) atoms of the zirconium dioxide surface for the MD models 1-2-3.

D[DNA(P_b)-ZrO_2(O)]-----XY~f(T)-----Models 4-5-6

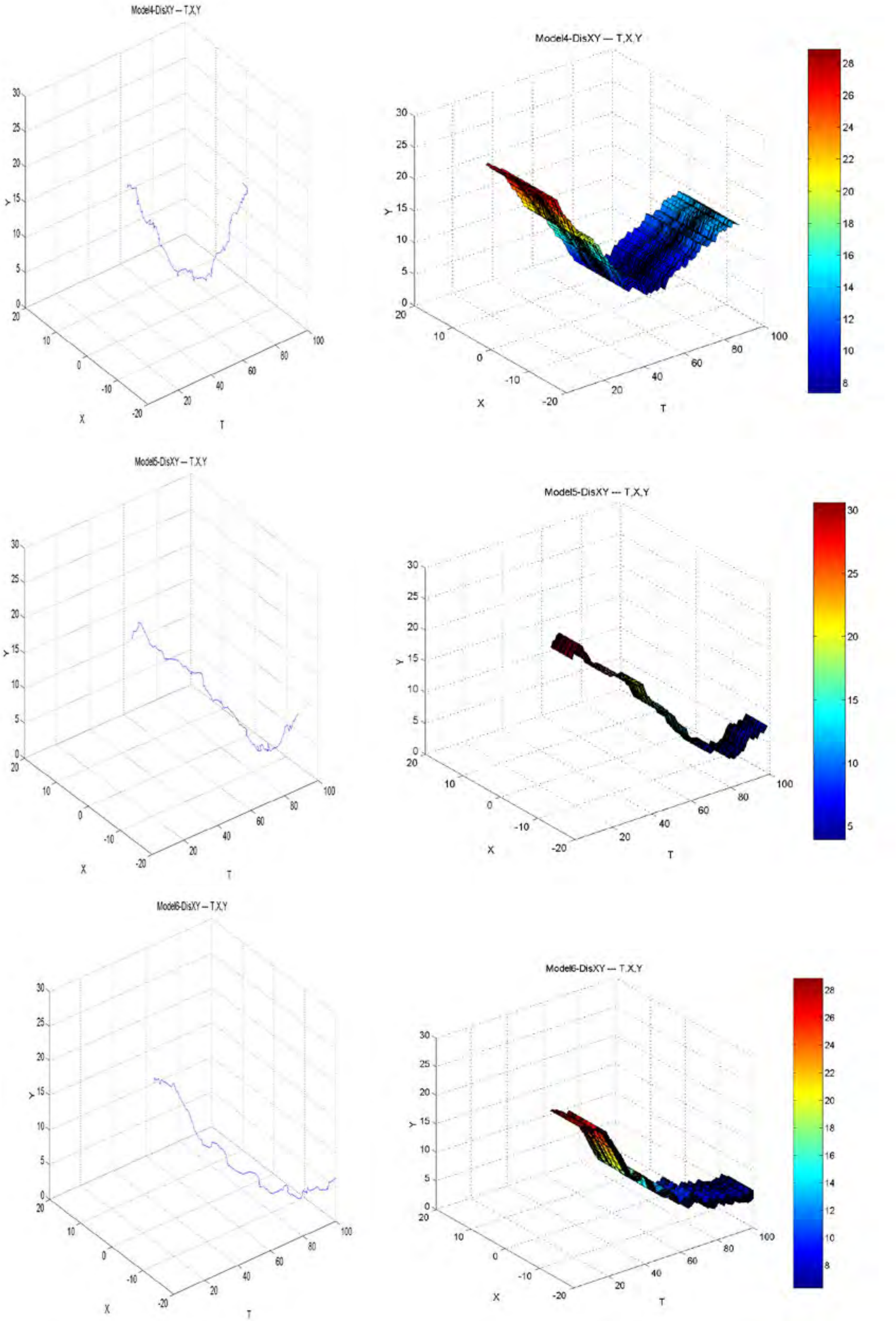

Figs. 7. The distance D[DNA(P_b)-ZrO_2(O)] between phosphorus (P_b) and selected oxygen (O) atoms of the zirconium dioxide surface for the MD models 4-5-6.

The MD simulation results in Figs. 6-7 for the distance D[DNA(P_a,P_b) - ZrO_2(O)] diagrams demonstrate the interaction and conformation processes for the DNA/ZrO_2 system. For time dependent behavior D[DNA(P_a,P_b) - ZrO_2(O)] we have seen a different DNA-surface conformational changes. It is important that, starting from the same relaxed state (but with different Q(P_a) and Q(P_b)) the DNA molecule while interacting with ZrO_2 surface will undergo a different conformational shape, thereby approaching the surface.

4. Conclusions

For a triple system DNA + water + ZrO 2 surface we built several set of MD models as setA (Model 1 (native DNA): Q(P_a) = +1,1659|e|; Model 2 (damaged DNA): Q(P_a) = 0; Model 3 (damaged DNA): Q(P_a) = -1,1659|e|) and setB (Model 4 (native DNA): Q(P_b) = +1,1659|e|; Model 5 (damaged DNA): Q(P_b) = 0; Model 6 (damaged DNA): Q(P_b) = -1,1659|e|), where e is electron charge, thereby simulating different scenario of the DNA possible charge modification.

From two opposite DNA directions we have arbitrarily chosen two P (phosphorus) atoms as possible damage sites. The MD results compare the DNA conformational behavior at the initial and final states and the DNA orientation dynamics on ZrO_2 were presented for the native DNA (Q(P_a,P_b) = +1,1659|e|) and two damaged versions (Q(P_a,P_b)=0 and Q(P_a,P_b)=-1,1659|e|), respectively. So far, starting from the same relaxed state (but with different Q(P_a,P_b)) the DNA molecule while interacting with ZrO_2 surface will undergo a different conformational shape, thereby approaching the surface. We have relate the DNA molecular orientations due to the immobilization process or similar to the B-Z-transition happening on the zirconium dioxide (ZrO_2) surface. The DNA conformations arise when the relative orientation of individual parts of the molecule changes as a result of the rotation of atoms or groups of atoms around simple bonds, bending of bonds, etc. For example, the DNA B-Z-transition can be stimulated by an increase in the content of ions in solution (say, zirconium dioxide ZrO_2 surface) or by certain proteins that stabilize the Z-form of DNA. When a molecule transitions from B- to Z-form, the double helix of DNA unfolds, and then turns in the other direction, turning from right-wound into left-wound [1-14]. In conclusion, for today the DNA+ZrO_2 system emerges itself as a breakthrough potential material for developing new nano-bio-electronics tools as well as the interdisciplinary research target in the field of nanotechnology. Wherein, the questions of the DNA interaction and immobilization with the mentioned oxide material as ZrO_2 have not been studied yet. A novel data obtained above for the DNA conformational behavior through a graphical 3-D representation analysis provide the DNA/ZrO_2 interaction and immobilization processes on the atomic/molecular level. The zirconium dioxide (ZrO_2) has seen to be a promising material as DNA or RNA molecules absorber due to a good biocompatibility and a high dielectric constant (ε=25). For today the combination of bio-molecules with solid nano-particles generates a new class of materials, primarily for new electronic sensory and optical systems. The prospects cover the development of molecular electronics, the creation of biochips, memory arrays and future computer architectures as well. In this respect, the DNA and RNA molecules have good electrical conductivity, capable to store and transmit by copying terabytes of information with self-reproducing and moving in the electric field, therefore, are extremely interesting as a functional element of bio-electronic devices [15-16].

Acknowledgments

This work is performed within the framework of a collaborative research program under Indo-Russian Joint Research-2016 (DST-RFBR), grant No. 17-52-45062 “Studies of the molecular orientation and radiation damage of DNA adsorbed on Zirconia”. This work in part is supported by the IGSF (International Fund for Humanitarian Cooperation), based in JINR, Dubna, ISTC (International Innovative Nanotechnology Center) of the CIS. This work in part is supported by JINR=ASRT (ARE) grant "Molecular Modeling Analysis of the Effect of Nano-Metal Oxides on Biological Molecules".

References

1. Subrata Majumder, I. Mishra, U. Subudhi, and Shikha Varma. "Enhanced biocompatibility for plasmid DNA on patterned TiO2 surfaces". Appl. Phys. Lett., (2013), 103, 063103.
2. H.B.Gray, J.R.Winkler, "Electron transfer in proteins", Annu. Rev. Biochem, (1996), v. 65, pp.537-561.
3. J. Deisenhofer, J.R.Norris, (eds.), "The Photosynthetic Reaction Center", Academic Press, N.Y., (1993), II, p.500.
4. Q.Gu, C.Cheng, R.Conela, et al., Nanotechnology, (2006), v. 17, R 14.
5. Bernard R. Brooks Robert E. Bruccoleri Barry D. Olafson David J. States S. Swaminathan Martin Karplus, "CHARMM: A program for macromolecular energy, minimization, and dynamics calculations". Journal of Computational Chemistry (1983) https://doi.org/10.1002/jcc.540040211
6. David A. Case, Thomas E. Cheatham, Tom Darden, Holger Gohlke, Ray Luo, Kenneth M. Merz, Alexey Onufriev, Carlos Simmerling, Bing Wang, and Robert J. Woods. "The Amber Biomolecular simulation programs". Journal of Computational Chemistry, 26(16), p.1668-1688, 2005.
7. Smith W., Forester T. R. DL_POLY_2.0: "A general-purpose parallel molecular dynamics simulation package". J. Mol. Graph. 14, 136-141 (1996).
8. Smith W., Forester T.R. and Todorov I.T., "THE DL POLY 2 USER MANUAL", STFC Daresbury Laboratory Daresbury, Warrington WA4 4AD Cheshire, UK, Version 2.19, April (2008).
9. Kholmirzo Kholmurodov (Ed.), "Molecular Simulation Studies in Material and Biological Sciences. International Workshop", Nova Science Publishers Ltd., 2007, 196p., ISBN: 1-59454-607-x
10. Kholmirzo Kholmurodov (Ed.), "Molecular Simulation in Material and Biological Research", Nova Science Publishers Ltd., 2009, 155p., ISBN: 978-1-60741-553-4.
11. Kholmirzo Kholmurodov (Ed.), "Molecular Dynamics of Nanobistructures", Nova Science Publishers Ltd., 2011, 210p., ISBN: 978-1-61324-320-6.
12. Kholmirzo Kholmurodov (Ed.), "Models in Bioscience and Materials Research: Molecular Dynamics and Related Techniques", Nova Science Publishers Ltd., 2013, 219p., ISBN: 978-1-62808-052-0.
13. Kholmirzo Kholmurodov (Ed.), "Computational Materials and Biological Sceinces", Nova Science Publishers Ltd., 2015, 208p., ISBN: 978-1-63482-541-2
14. Kholmirzo T. Kholmurodov (Ed). «Computer Design for New Drugs and Materials. Molecular Dynamics of Nanoscale Phenomena», (Leading Scientist, Frank Laboratory of Neutron Physics, Joint Institute of Nuclear Research, Dubna, Moscow Region, Russia), ISBN: 978-1-53612-082-0, Nova Science Publishers, New York (2017), 231 p.
15. Arivazhagan Rajendran, Masayuki Endo, Kumi Hidaka, and Hiroshi Sugiyama. Direct and Real-Time Observation of Rotary Movement of a DNA Nanomechanical Device // Journal of American Chemical Society. 2013. V. 135 (3). P. 1117–1123.
16. Chengde Mao, Weiqiong Sun, Zhiyong Shen & Nadrian C. Seeman. A nanomechanical device based on the B–Z transition of DNA // Nature. 14 January 1999. V. 397. P. 144–146.

[*] **Corresponding authors e-mails:** mirzo85@inbox.ru,
mirzo@jinr.ru

ROLE OF OXYGEN AND HIDROGEN BONDS IN PHOTOLUMINESCENCE OF POROUS SILICON

F. A. RUSTAMOV, *N. H. DARVISHOV, V. E. BAGIEV, M. Z. MAMEDOV, G. M. EYVAZOVA, E. Y. BOBROVA, H. O. QAFAROVA.
Semiconductor Physics Division, Institute for Physical Problems, Baku State University, Baku AZ 1148, Azerbaijan

The effect of posttreatment in HNO_3 on the photoluminescence properties and surface chemical bonds of stain etched porous silicon were investigated. It was shown that, such posttreatment results in reversible quenching of photoluminescence. It is found that the photoluminescence quenching associated with significant desorption of hydrogen from the surface of porous silicon under the HNO_3 action, and its subsequent recovery associated with surface oxidation in air. This recovery of luminescence is correlated with the appearance of absorption on the oxygen bonds at 1180 cm^{-1} and 1045 cm^{-1}.

Keywords: porous silicon, photoluminescence, oxygen bonds, absorption
PACS: 78.55.Mb.71.24+q

1. Introduction

The porous silicon (PS) obtained by electrochemical or stain etching method exhibits visible photoluminescence (PL). This is explained by quantum size effect of bandgap expansion of crystallites with decreasing the size of nanoparticles in PS [1, 2]. After etching, a significant number of unsaturated dangling bonds is formed on the silicon surface. These dangling bonds, being non-radiative recombination centers, suppress the PL. In as-prepared PS some part of dangling bonds is saturated by hydrogen bonds and as a results porous silicon exhibits visible PL. However, hydrogen bonds saturating dangling bonds are unstable, and upon exposure at ambient conditions the more stable oxygen bonds [3, 4] gradually replace them. Upon exposure at ambient conditions the PL intensity decreases slightly during the first hours after PS formation, nevertheless the PL peak position is stable enough. Study of FTIR spectra shows that the oxygen bonds are already exist in the as-prepared samples of stain etched PS, what is associated with the presence of HNO_3 in the etching solution [5]. Such behavior suggests the complex nature of the PS surface oxidation. On the one hand, PS surface oxidation process leads to the replacement of unstable Si-H_n bonds by more stable Si-O bonds. These oxygen bonds saturate the centers of nonradiative recombination, which in PS are Si- dangling bonds. On the other hand, nanocrystallites oxidation process may reduce their size and, consequently, to expand the bandgap due to the quantum confinement effect, which appears as a shift of the PL peak to high energy region [6]. Finally, according to study of Delarua at al [7, 8] the process of surface oxidation in high porous PS leads to the appearance of the localized radiative recombination levels in bandgap of nanocrystallites. These levels suppress the radiative recombination via band-to-band transition in silicon nanocrystallites. Despite the reduction in the size of the particles and accordingly the expansion of bandgap of high porous PS, obtained by conventional methods, the observed maximum in the PL spectrum does not exceed ~2.1 eV in the PS [9-11].

2. Methodical part

The effect of room temperature posttreatment in HNO_3 on the photoluminescence properties of stain etched porous silicon was investigated in the given report. Analysis of obtained data was performed by means of FTIR spectroscopy to clarify the roles of the various oxygen bonds.

The porous silicon samples were prepared by stain etching on the monocrystalline p-type wafers with 10 Om·cm resistivity and (111) orientation. PS formation is performed in a HF:HNO_3:CH_3COOH solution in volume proportion 1200:1:1200, i.e. at oxidant insufficiency [12]. After etching, the samples were washed in bidistilled water, then in isopropanol and were dried by N_2 jet. Some of the samples immediately after preparation of PS layers posttreated at room temperature in concentrated HNO_3.

3. Results and discussion

Fig.1 shows the changes in the PL peak intensity of the samples untreated and posttreated in HNO_3 for 10 min, with exposure time in ambient conditions. From this figure one can see, that PL of untreated samples is degraded with time, and PL peak intensity decreases ~1,3 times for 3 months. But in the samples posttreated in HNO_3 the peak intensity of PL spectrum initially is minimal and then increased tenfold with time. In this case, first the intensity is growing very quickly and then its growth is slowing down. After ~ 3 month, the intensities of the untreated and posttreated samples differ only in 1.25 times.

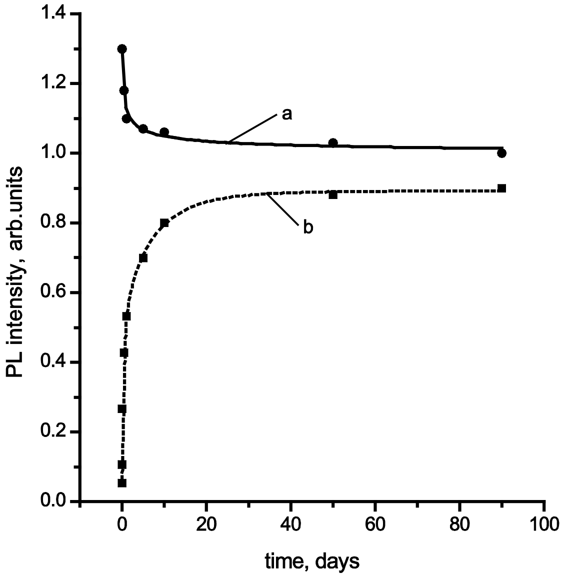

Fig.1. PL peak intensity of stain etched PS without (a) and with (b) posttreatment in HNO_3 for 10 min upon exposure to air.

Fig.2 and 3 show the FTIR spectra of the samples, untreated and posttreated in concentrated HNO_3 at room temperature. In as-prepared untreated PS samples, immediately after preparation, can be seen (Fig.2) absorption bands at 2100-2150 cm^{-1}, corresponding to stretching mode of SiH_n; the band at 902 cm^{-1} corresponding to scissor mode of SiH_2; the band of 1108 cm^{-1} corresponding to Si-O-Si (asymmetric stretching of interstitial oxygen in Si) and absorption peaks at 882 cm^{-1} and 2245 cm^{-1} corresponding to O_3-SiH bending and stretching mode [5, 13-15]. Over time when exposed to air, the absorption intensity is reduced on the SiH_n bonds with simultaneous significant increase in absorption peak at 1180 cm^{-1} and 1045 cm^{-1}, corresponding to Si-O-Si stretching modes (LO and TO modes).

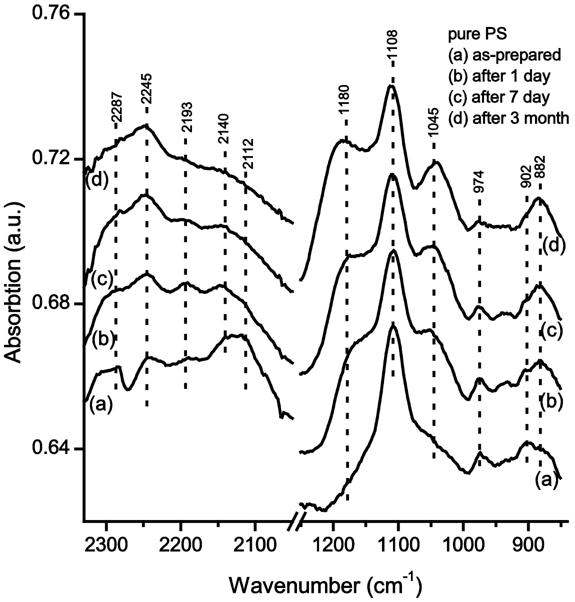

Fig.2. FTIR spectra of stain etched PS upon exposure to air.

In the samples, posttreated in concentrated HNO_3 at room temperature immediately after preparation, can be seen (Fig.3) the absorption peaks at 1108 cm^{-1} and 886 cm^{-1} corresponding to Si-O-Si and O_3-SiH bonds, respectively. The vibrations, corresponding to stretching modes of SiH_n (2100-2150 cm^{-1}) are almost absent. Upon exposure of these samples under ambient conditions, over time there is a significant increase in absorption at 1180 cm^{-1} and 1036 cm^{-1} corresponding to Si-O-Si stretching bonds. Upon exposure to air of both types of samples, the absorption bands at 1108 cm^{-1} corresponding to Si-O-Si bond and at 882 cm^{-1} corresponding to O_3-SiH bond remain unchanged.

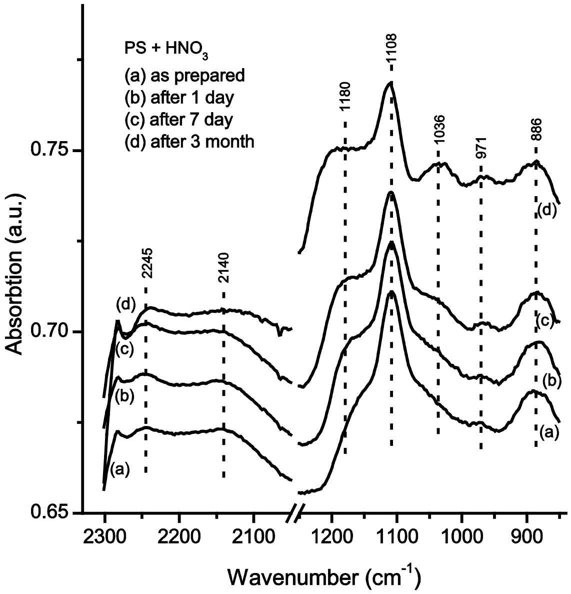

Fig.3. FTIR spectra of posttreated for 10 min in HNO_3 stain etched PS upon exposure to air.

From Fig.2 is seen that in as-prepared PS sample immediately after preparation, the absorption peaks are observed on the bonds SiH_n (2100-2150 cm^{-1}), Si-O-Si (1108 cm^{-1}) and O_3-SiH (882 cm^{-1} and 2245 cm^{-1}).This means, that such bonds on the surface of stain etched porous silicon is already formed during the PS formation process. Such saturation of Si- dangling bonds by SiH_n bonds is the cause of the high PL efficiency in as-prepared PS samples. However, over time the hydrogen desorption occurs (Fig.2, b, c, d) and the intensity of SiH_n vibrations decreases at an almost constant level of signal from the Si-O-Si vibrations (1108 cm^{-1}) and O_3-SiH vibrations (882 cm^{-1}). Simultaneously with the hydrogen desorption there is a significant increase in the absorption on another Si-O-Si bonds (1180 cm^{-1} and 1045 cm^{-1}). That is, more stable oxygen bonds gradually replace unstable hydrogen bonds. But, apparently, compensation of unsaturated bonds on the PS surface is partially defective, which results in some degradation in PL properties and some decrease in luminescence intensity (Fig.1). At the same time, a PL peak almost no shifts during the atmospheric oxidation process. Therefore, it can be assumed that these Si-O-Si bonds (1180 cm^{-1} and 1045 cm^{-1}) leads only to saturation of dangling bonds on the PS surface, blocking the non-radiative recombination channels and do not affect the radiative recombination levels in the bandgap of the PS nanocrystallites. Stability of PL peak position correlates only with invariably level of absorption signals on Si-O-Si vibrations at 1108 cm^{-1} and O_3-SiH vibrations at 882 cm^{-1} (Fig.2). Thus, perhaps it is these oxygen bonds give rise to local levels within the bandgap, responsible for radiative recombination in the PS, according to theoretical studies of Delarua at al [7, 8]. Meanwhile, the role of these bonds in compensation of dangling bonds on the surface of the PS is not clear from these spectra. To confirm the assumptions the IR spectra of HNO_3 posttreated samples were investigated.

Fig.3 shows IR absorption spectra of PS samples, posttreated in HNO_3 at room temperature. As in the case of untreated samples, immediately after drying the samples are seen absorption bands corresponding to vibrations on the Si-O-Si bonds at 1108 cm^{-1}, but the absorption on the SiH_n bonds is almost absent. As can seen, posttreatment of PS in HNO_3 at room temperature, leads to significant hydrogen desorption without changing the degree of surface oxidation. The absorption intensity on SiH_n bonds (2100-2150 cm^{-1}) in comparison with the absorption intensity on Si-O-Si bonds are much smaller in posttreated samples than in untreated. These data correlate with the data of PL spectra, presented at the Fig.1. Hydrogen desorption from the PS surface leads to the PL quenching, despite the presence of oxygen bonds Si-O-Si (1108 cm^{-1}) and O_3-SiH (882 cm^{-1}). So, these oxygen bonds can not saturate the dangling Si- bonds, which are the nonradiative recombination centers. The role of these oxygen bonds are revealed in further atmospheric oxidation of PS surface. As can be seen from Fig.2 and 3, with increasing air exposure time for PS samples of both types, there is a further oxidation of the surface and appear absorption bands associated with Si-O-Si vibrations (1180 cm^{-1} and 1045 cm^{-1}) at a fixed position and level of signals from Si-O-Si vibration at 1108 cm^{-1} and O_3-SiH vibration at 882 cm^{-1}.

4. Conclusion

These data suggest a different role of various oxygen bonds in the mechanism of photoluminescence. On the basis of a joint analysis of the FTIR and PL spectra of the stain etched PS samples, untreated and posttreated in HNO_3, it can be concluded that the Si-O-Si bonds at 1108 cm^{-1} or O_3-SiH bonds at 882 cm^{-1} give rise to localized levels in the bandgap of PS nanocrystallites and provide the stability of the PL peak position. On the other hand, the Si-O-Si bonds at 1180 cm^{-1} and 1045 cm^{-1} is responsible for saturation of dangling bonds that are the centers of nonradiative recombination.

Acknowledgments

This work was supported by Baku State University 50+50 grant project.

References

1. L.T. Chanham, Appl. Phys. Lett. 57 (1990) 1046.
2. V. Lehmann, U. Gosele, Appl. Phys. Lett. 58 (1991) 856.
3. E. Kayahan, Appl. Surf. Sci. 257(9) (2011) 4311.
4. E. Galeazzo, A. Beltran, F. J. Ramirez-Fernandez, Brazilian Journal of Physics, 27/ A, 4, (1997) 170.
5. Y.Q. Jia, L.Z. Zhang, J.S. Fu, B.R. Zhang, J.C. Mao, J. Appl. Phys. 74 (12) (1993) 7615.
6. F.A. Rustamov, N.H. Darvishov, M.Z. Mamedov, E.Y. Bobrova, H.O. Qafarova, J. Lumin., 131 (2011) 2078.
7. M.V. Wolkin, J.Jorne, P.M. Fauchet, G. Allan, C. Delerue, Phys. Rev. Lett. 82, 1 (1999) 197.
8. C. Delerue, G. Allan, M. Lannoo, Phys. Rev. B 48, 15 (1993) 11024-.
9. Md. N. Islam, S. Kumar, J. Appl. Phys. 93, 3 (2003) 1753.
10. A. Ramirez-Porras, S.Z. Weisz, Surf. Sci. 515, 2-3 (2002) 18.
11. F.A. Rustamov, N.H. Darvishov, V.E. Bagiev, M.Z.Mamedov, E.Y. Bobrova, H.O. Qafarova, J. Lumin., 154 (2014) 2024.
12. F.A. Rustamov, N.H. Darvishov, M.Z. Mamedov, E.Y. Bobrova, H.O. Qafarova, Azerb. J. Physics. 18, 3 (2012) 44.
13. L.T. Chanham, Properties of porous silicon. EMIS Data Review Series No. 18, London, 1997.
14. Y. Vbzsonyi, E. Szilbgyi, P. Petrik, Z. Horvath, T. Lohner, M. Fried, G Jalsovszky, Thin Solid Films. 388 (2001) 295.
15. V.P. Tolstoy, I.V. Chernyshova, V.A. Skryshevsky, Handbook of infrared spectroscopy of ultrathin films, John Wiley & Sons, Inc., Hoboken, New Jersey, 2003.

[*] **Corresponding author**: n_darvishov@bsu.edu.az
n_darvishov@mail.ru

ESTABLISHMENT OF THE INITIAL MELTED ZONE AT THE START OF THE ALLOY WHEN THE DISTRIBUTION COEFFICIENT EXCEEDS THE UNIT

N.F.GAHRAMANOV, E.S.GARAYEV, A.I.HASHIMOVA
Baku State University, Z.Khalilov str., 23, Baku, Azerbaijan, Az1148

When the distribution coefficient is more than unit creation the first melt zone in the beginning of the initial alloy of binary solid solutions is discussed. At first the concentration of the second component in the beginning melted zone is determined. As the final alloy is made in two different stages of crystallization (zone melting and Bridjman method) to find the content distribution we solve the continuity equation at two different initial conditions and then them “Sew together”. The content distribution showers that such an alloy can successfully be used as a feeding alloy to grow single crystals of binary solid solution by puling from a melt. In apply to $Ge-Si$ system such single crystals are useful to make varyzone structures [4-6,7].

Keywords: binary solution, monocrystal, alloy, nutrient, component, distribution.
PACS: 81.10.Aj; 81.10.–h; 81.10.Fq

1.Introduction

In the previous study [2,3], we used a zone-melting method to change the distribution of the composition across the binary solid alloy obtained by the directed crystallization and showed that, when the distribution coefficient is k >1, the more favorable option is to create the first melted zone at the end of the alloy. But in some cases when k >1, it is also possible to get a successful result by creating the initial melted zone at the first step of the alloy by the directed crystallization process. In this study, we will investigate the case as well.

2. Experiment

The scheme of use of the initial alloy is shown in Figure 1. Here the initial melting zone is made at the start point of the alloy. In this case, the change of concentration of the second component along the initial alloy is expressed as follows [1]:

$$C_S(t) = kC_0\left(1-\frac{vt}{L}\right)^{k-1} \tag{1}$$

Here C_0 the average concentration of the second component at the initial alloy, L its length, v crystallization velocity.

It is required to know the concentration of the second component in the initial melted zone to determine the redistribution of the composition in the scraped melt. For this purpose, it is necessary to find the mass of the second component at the start ℓ length of the alloy (initial alloy) obtained from the directed crystallization and divide it into the volume ℓS of the zone (S the cross-sectional area of the alloy):

$$C_z(0) = \frac{\int_0^{t'} C_S(t) S\upsilon dt}{\ell S} = \frac{\upsilon}{\ell}\int_0^{t'} kC_0\left(1-\frac{\upsilon t}{L}\right)^{k-1} dt = \frac{k\upsilon C_0}{\ell}\int_0^{t'}\left(1-\frac{\upsilon t}{L}\right)^{k-1} dt \tag{2}$$

Here $t' = \frac{\ell}{\upsilon}$.

Let's take a new substitute to solve the integral in (2):

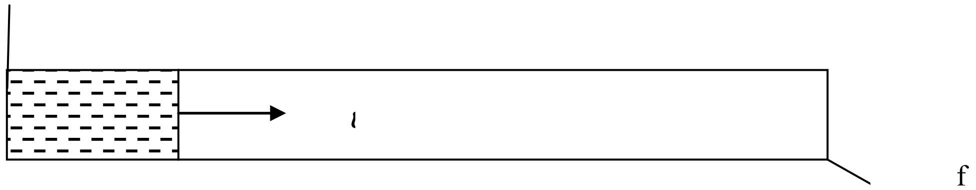

Fig.1. In k >1 case, the scheme of creation of the melted initial zone at the start of the

$$1-\frac{\upsilon t}{L}=y, \quad t=\frac{L}{\upsilon}(1-y), \quad dt=-\frac{L}{\upsilon}dy \tag{3}$$

It is clear from here that, y = 1 when t = 0 and $y=1-\frac{\ell}{L}$ when $t=t'=\frac{\ell}{\upsilon}$

Taking into consideration the new substitude in (2):

$$\begin{gathered}C_z(0)=\frac{kC_0\upsilon}{\ell}\int_1^{1-\frac{\ell}{L}}y^{k-1}\left(-\frac{L}{\upsilon}\right)dy=-\frac{kC_0L}{\ell}\int_1^{1-\frac{\ell}{L}}y^{k-1}dy= \\ =-\frac{kC_0L}{\ell}\cdot\frac{1}{k}y^k\Big|_1^{1-\frac{\ell}{L}}=-\frac{L}{\ell}C_0\left[\left(1-\frac{\ell}{L}\right)^k-1\right]=C_0\frac{L}{\ell}\left[1-\left(1-\frac{\ell}{L}\right)^k\right]\end{gathered} \tag{4}$$

To get the second component's change law, we must solve the continuity equation for the new mode.
The continuity equation for melting zone [1]:

$$\mathrm{C_m}(\mathrm{t})+\frac{\mathrm{kv}}{\ell}\mathrm{C}_m(\mathrm{t})=\frac{\upsilon}{\ell}\mathrm{C_S}(\mathrm{t}), \tag{5}$$

Its solution in general case:

$$C_\mathrm{m}(t)=\exp\left(-\frac{k\upsilon}{\ell}t\right)\left\{\frac{\upsilon}{\ell}kC_0\int\left(1-\frac{\upsilon t}{L}\right)^{k-1}\exp\left(\frac{k\upsilon}{\ell}t\right)dt+A\right\} \tag{6}$$

Here $C_S(t)$ the current exchange magnitudes of the concentration of the second component along the initial alloy. But in the equation we must consider that, the change law along the initial alloy must be expressed as in the form (1), in melt the start concentration of the second component (the concentration at the first melted zone) should be taken equal to (4).

In (6) instead of $C_S(t)$, let's put its (1) form and find the solution of the continuity equation:

$$C_\mathrm{m}(t)=\exp\left(-\frac{k\upsilon}{\ell}t\right)\left\{\frac{\upsilon}{\ell}kC_0\int\left(1-\frac{\upsilon t}{L}\right)^{k-1}\exp\left(\frac{k\upsilon}{\ell}t\right)dt+A\right\} \tag{7}$$

Here A is the integration constant and its magnitude must be found according to the starting condition.
Let's take a new integration variable to solve the integral in (7):

$$\frac{k\upsilon t}{\ell}=x, \quad t=\frac{\ell x}{k\upsilon}, \quad dt=\frac{\ell dx}{k\upsilon} \tag{8}$$

If we consider the new integration variable, (7) will become as follows:

$$\begin{gathered}C_\mathrm{m}(t)=\exp\left(-\frac{k\upsilon}{\ell}t\right)\left\{\frac{\upsilon}{\ell}kC_0\int\left(1-\frac{\ell}{kL}x\right)^{k-1}\exp\ x\frac{\ell}{k\upsilon}dx+A\right\}= \\ =\exp\left(-\frac{k\upsilon}{\ell}t\right)\left\{C_0\int\left(1-\frac{\ell}{kL}x\right)^{k-1}\exp\ xdx+A\right\}\end{gathered} \tag{9}$$

To solve the integral in (9) k-magnitude should be known. Here is the simplest solution that has practical meaning k = 2**.** For this case, let's calculate the integral in (9) separately. We will denote it by the letter J.

$$\begin{gathered}J=\int\left(1-\frac{\ell}{kL}x\right)^{2-1}\exp xdx=\int\exp xdx-\frac{\ell}{kL}\int x\exp xdx=\exp x-\frac{\ell}{kL}x\exp x+ \\ +\frac{\ell}{kL}\int\exp xdx=\exp x-\frac{\ell}{kL}x\exp x+\frac{\ell}{kL}\exp x=-\frac{\ell}{kL}\exp x+\left(1+\frac{\ell}{kL}\right)\exp x\end{gathered} \tag{10}$$

Let's put (10) back in (9) and consider that $k=2$:

$$\begin{aligned} C_{\mathrm{m}}(t) &= \exp\left(-\frac{k\upsilon}{\ell}t\right)\left\{C_0\left[-\frac{\ell}{kL}x+\left(1+\frac{\ell}{kL}\right)\right]\exp x + A\right\} = \\ &= \exp\left(-\frac{2\upsilon}{\ell}t\right)\left\{C_0\left[1-\frac{\ell}{kL}\cdot\frac{k\upsilon}{\ell}t+\left(1+\frac{\ell}{kL}\right)\right]\exp\left(\frac{k\upsilon}{\ell}t\right)+A\right\} = \\ &= C_0\left(1+\frac{\ell}{2L}-\frac{\upsilon}{L}t\right)+A\exp\left(-\frac{2\upsilon}{\ell}t\right) \end{aligned} \tag{11}$$

The constant A is found from the start condition. Remember that, the concentration of the second component at the melted zone is determined with (4). If $t = 0$ in (11), $C_{\text{я}}(0)$ is found as follows:

$$C_{\mathrm{m}}(0) = C_0\left(1+\frac{\ell}{2L}\right)+A \tag{12}$$

Getting from (2) and (4) that:

$$C_0\left(1+\frac{\ell}{2L}\right)+A = C_0\frac{L}{\ell}\left[1-\left(1-\frac{\ell}{L}\right)^2\right]$$

Let's find A from here:

$$\begin{aligned} A &= -C_0\left(1+\frac{\ell}{2L}\right)+C_0\frac{L}{\ell}\left[1-1+2\frac{\ell}{L}-\frac{\ell^2}{L^2}\right] = \\ &= C_0\left[-1-\frac{\ell}{2L}+2-\frac{\ell}{L}\right] = C_0\left(1-\frac{3}{2}\cdot\frac{\ell}{L}\right) \end{aligned} \tag{13}$$

Let's put (13) back in (11):

$$C_{\mathrm{m}}(t) = C_0\left\{\left(1+\frac{\ell}{2L}-\frac{\upsilon}{L}t\right)+\left(1-\frac{3}{2}\cdot\frac{\ell}{L}\right)\exp\left(-\frac{2\upsilon}{\ell}t\right)\right\} \quad 0\le t\le\frac{L-\ell}{\upsilon} \tag{14}$$

This addiction will remain in its power until the front of the melt zone reaches the other end of the alloy. So, we find the change law of the second component on the solid phase along the first length part $(L-\ell)$ of the alloy as follows:

$$\begin{aligned} C_x(t) &= kC_{\mathrm{m}}(t) = 2C_0\left\{\left(1+\frac{\ell}{2L}-\frac{\upsilon}{L}t\right)+\left(1-\frac{3}{2}\cdot\frac{\ell}{L}\right)\exp\left(-2\frac{\upsilon}{\ell}t\right)\right\} = \\ &= C_0\left\{\left(2+\frac{\ell}{L}-2\frac{\upsilon}{L}t\right)+\left(2-3\frac{\ell}{L}\right)\exp\left(-2\frac{\upsilon}{\ell}t\right)\right\} \quad 0\le t\le\frac{L-\ell}{\upsilon}=t_1 \end{aligned} \tag{15}$$

The crystallization mode is changed starting from the moment the front of the melt zone reaches the end of the alloy. In the last section, in which the length is equal to ℓ, the process takes place by the directed crystallization. In this part the solution of the continuity equation is as follows [1]:

$$C_{\mathrm{m}}(t) = A_1'\left(\frac{L}{\upsilon}-t\right)^{k-1}, \quad t\ge t_1 \tag{16}$$

We have denoted the integration constant A_1' for differentiating. Because the initial condition is different, the magnitude of the integral constant will differ from the previous one. We find the magnitude of A_1' in (12) and (14) at the moment $t = t_1$ by "building" one another.

We can find C_{m} from (16), when $t = t_1 = \dfrac{L-\ell}{\upsilon}$:

$$C_{\mathrm{m}}(t_1) = A_1'\left(\frac{L}{\upsilon}-t_1\right) \tag{17}$$

Here, we have considered that k = 2. $C_{\text{я}}$ is found at the moment $t = t_1$ from (14):

$$C_{\mathrm{m}}(t_1) = C_0\left\{\left(1+\frac{\ell}{2L}-\frac{\upsilon}{L}\cdot t_1\right)+\left(1-\frac{3}{2}\cdot\frac{\ell}{L}\right)\exp\left(-\frac{2\upsilon}{\ell}t_1\right)\right\} \tag{18}$$

Let's equalize the right sides of (17) and (18):

$$A_1'\left(\frac{L}{\upsilon}-t_1\right)=C_0\left\{\left(1+\frac{\ell}{2L}-\frac{\upsilon}{L}t_1\right)+\left(1-\frac{3}{2}\cdot\frac{\ell}{L}\right)\exp\left(-2\frac{\upsilon}{\ell}t_1\right)\right\}$$

Then we must put the magnitude of t_1 back in here, and make some simplifications:

$$A_1'\left(\frac{L}{\upsilon}-\frac{L-\ell}{\upsilon}\right)=C_0\left\{\left(1+\frac{\ell}{2L}-\frac{\upsilon}{L}\frac{L-\ell}{\upsilon}\right)+\left(1-\frac{3}{2}\cdot\frac{\ell}{L}\right)\exp\left(-2\frac{\upsilon}{\ell}\cdot\frac{L-\ell}{\upsilon}\right)\right\}$$

$$A_1'\cdot\frac{\ell}{\upsilon}=C_0\left\{\frac{3}{2}\cdot\frac{\ell}{L}+\left(1-\frac{3}{2}\cdot\frac{\ell}{L}\right)\exp\left(-2\frac{L-\ell}{\ell}\right)\right\}$$

We can find A_1' as so:

$$A_1'=C_0\frac{\upsilon}{\ell}\left\{\frac{3}{2}\cdot\frac{\ell}{L}+\left(1-\frac{3}{2}\cdot\frac{\ell}{L}\right)\exp\left(-2\frac{L-\ell}{\ell}\right)\right\} \qquad (19)$$

Let's put the magnitude of A_1' back in (16):

$$C_m(t)=C_0\frac{\upsilon}{\ell}\left\{\frac{3\ell}{2L}+\left(1-\frac{3\ell}{2L}\right)\exp\left(-2\frac{L-\ell}{\ell}\right)\right\}\left(\frac{L}{\upsilon}-t\right),\quad \frac{L-\ell}{\upsilon}\le t\le\frac{L}{\upsilon} \qquad (20)$$

We can get a new distribution along the alloy at last *l* lenght so:

$$C_x(t)=kC_m(t)=2C_0\frac{\upsilon}{L}\left\{\frac{3\ell}{2L}+\left(1-\frac{3\ell}{2L}\right)\exp\left(-\frac{2(L-\ell)}{\ell}\right)\right\}\left(\frac{L}{\upsilon}-t\right),\quad \frac{L-\ell}{\upsilon}\le t\le\frac{L}{\upsilon}\ . \qquad (21)$$

3. Results and discussion

If we combine (15) and (21), along the whole alloy after melting zone the change law of the concentration of the second component can be expressed in a compact manner as follows:

$$\frac{C_x(t)}{C_0}=\begin{cases}\left(2+\frac{\ell}{L}-2\frac{\upsilon}{L}t\right)+\left(2-3\frac{\ell}{L}\right)exp\left(-2\frac{\upsilon}{\ell}t\right), & 0\le t\le\frac{L-\ell}{\upsilon}\\ \frac{\upsilon}{\ell}\left[\frac{3\ell}{L}+\left(2-\frac{3\ell}{L}\right)exp\left(-\frac{2(L-\ell)}{\ell}\right)\right]\left(\frac{L}{\upsilon}-t\right), & \frac{L-\ell}{\upsilon}\le t\le\frac{L}{\upsilon}\end{cases} \qquad (22)$$

The change law of $\frac{C_x(t)}{C_0}$ ratio that is expressed by (22) is shown in the figure 2 and table 1.

It can be seen from the picture that, it is possible to use this kind of alloy successfully to produce binary solid for growing monocrystals for varizoned structures, it is also necessary to use the end of the alloy as the beginning of the feeder. In addition, this kind of alloy can be used, even when a special distribution of the additive is required throughout the monocrystal. Even both two points can be taken as the starting of the feeder.

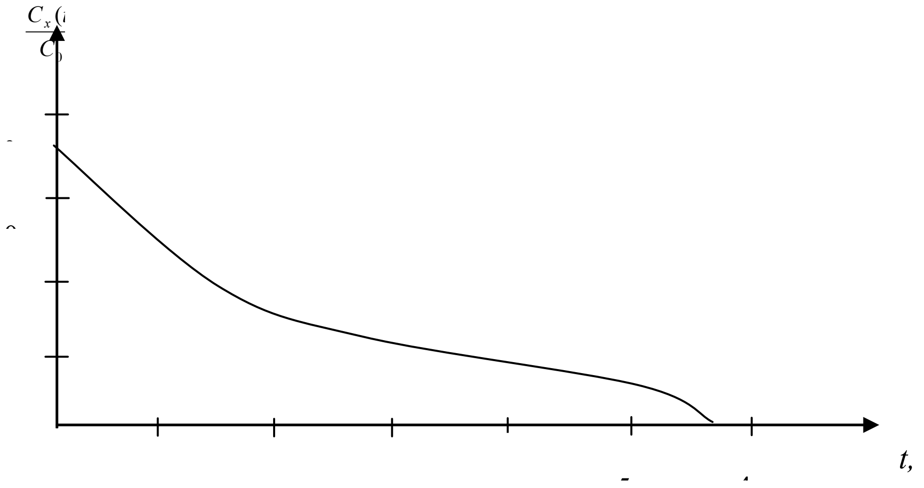

Fig. 2. The change law of $\frac{C_x(t)}{C_0}$ ratio throughout the alloy that is expressed by

The change law of $\frac{C_x(t)}{C_0}$ ratio throughout the alloy that is expressed by (22)

Table 1

t, hour	$\frac{C_x(t)}{C_0}$	t, hour	$\frac{C_x(t)}{C_0}$
0	3,8	35,0	0,70
2,5	2,62	37,5	0,60
5,0	2,13	40,0	0,50
7,5	1,88	42,5	0,40
10,0	1,73	45,0	0,30
12,5	1,61	45,5	0,027
15,0	1,50	46,0	0,024
17,5	1,40	46,5	0,021
20,0	1,30	47,0	0,018
22,5	1,20	47,5	0,015
25,0	1,10	48,0	0,012
27,5	1,00	48,5	0,009
30,0	0,90	49,0	0,006
32,5	0,80	49,5	0,003

It is clear from the distribution curve which is given at the picture 2 that, it is suitable to use this method for material cleaning. It can be extremely effective for increasing the degree of purity of the material in the same direction by remelt zone method. This time, if, it is required to use the middle part of the alloy is opportune. Because within the substance in which $k < 1$ and uncontrolled additives can be gathered at the end of the alloy.

4. Conclusion

The research shows that, it will be successful to create the initial melted zone at the start of the alloy when k >1. The general principle of the proposed method for obtaining maximum mono-crystals of binary solids with strong segregation by application of the alloy, the second component was determined by investigating solutions of the substance flood continuous equation within different starting and boundary conditions. It is possible to solve the continuous equation for k >1 while obtaining this alloy, and by using the component distribution throughout the alloy, by getting the melted zone at the beginning of the alloy, it can be possible to eliminate extreme cooling on the crystallization front and obtain the perfect monocrystals of solid solutions.

References

1. Takhirov V.I., Takhirov Yu.V., Gahramanov N.F., Semiconductor Physics, SSU, Sumgait, 320, (2006).
2. Takhirov V.I., Salamova A.I., Jafarov T.G., Gahramanov N.F., J. Scientific News, 12, 4, 3, (2012).
3. Takhirov V.I., Gasanov Z.Yu., Takhirov Yu.V., Gahramanov N.F., ANAS “Reports”, 65, 3, 590, (2009).
4. Takhirov V.I., Aghamaliev Z.A., Sadikhova S.R., Guliyev A.F., Gahramanov N.F., Semiconductors, 46, 3, 304, (2012).
5. Takhirov V.I., Semiconductor solid solutions Ge-Si, Baku, Science, 208, (1983).
6. Huchishvili E.V., Kekelidze N.G., Kekua M.G., Golikhova O.A., Semiconductors, 15, 5, 970, (1981).
7. Karimov M.K., Abbasov Sh.M., Aghaverdieva K.T. et ol, Problems of Power Engineering, 2, 60, (2003).

[*] **Corresponding authors e-mails:** hasimovaaynur@gmail.com

SYNTHESIS AND STRUCTURE OF HYBRID POLYMER NANOCOMPOSITES BASED ON PP +CdS/ZnS.

F.V.HAJIYEVA
Baku State University, Z.Khalilov str. 23, Baku, AzerbaijanAZ 1148

In this paper in first time was synthesized and characterized of hybrid polymer nanocomposites based on PP+CdS/ZnS. It was found that for nanocomposites based on PP+ZnS the band gap is 3.65 eV, for PP+CdS-2.8 eV and for PP+CdS/ZnS nanocomposite it is 4.25 eV. SEM images of polymer nanocomposites show that ZnS and CdS nanoparticles are equally uniformly distributed inside the polymeric polymer matrix of polypropylene. Photoluminescent analysis of nanocomposites has shown that for such hybrid nanocomposites, the spectral sensitive spectral region is expanded.

Keywords: polypropylene, cadmium sulfide, zinc sulfide, nanoparticles, hybrid nanocomposite
PACS: 72.80.Tm, 75.75.-c, 61.46.+w, 61.46.-w, 78.67.-n

1. Introduction

It is known that the optical properties of nanoscale semiconductor crystals depend not only on their composition, structure and size, but also on the state of the interface of their phases or surface. Thus, defects on the surface of nanoparticles, such as impurities of extraneous atoms or point defects in the structure, can play the role of potential wells or barriers for holes and electrons. As a rule, this leads to a change in the band structure and optical properties of NPS of semiconductors and with a decrease in the size of these nanoparticles, these changes become even more sensitive to defects. Usually, the process of passivation, in which surface atoms bind to atoms of another substance, is used to eliminate and prevent such phenomena. It is important that the band gap of the second junction should be greater than the previous one. In other words, particles of one compound are covered with a layer of another compound, which is called a "core-shell" (core in a shell) with nanoscale particles. It is established that coating nanoparticles of one semiconductor with a layer of another semiconductor significantly improves the optical properties of nanoparticles, bringing them closer to the properties of isolated nanoclusters. This effect is especially pronounced when studying the photoluminescent properties of nanoscale systems[1,2].

In this article, for the first time new hybrid polymer nanocomposites based on PP+CdS/ZnS were synthesized, the structure and optical properties of these composites were studied.

2. Experimental section

2.1. Materials

All chemicals were used as received without purification: polypropylene(PP grade Moplen HF500N, homopolymer); density 0,92g/cm3 at 25 °C, Mw=250000, Mn =67000, Melt Mass-Flow Rate- MFR = 11,5g /10 min (2300 C, 2,16 kg), melting T=162°C), cadmium chloride ($CdCl_2\times5H_2O$, Sigma Aldrich C3141), sodium sulfide (Na_2Sx9H_2O, PLC 141687), CTAB (cetyltrimethylammonium bromide$C_{19}H_{42}BrN$, AB 117004, 98% chemically pure),zinc chloride ($ZnCl_2$, PLC 141779 - for analysis, anhydrous), toluene (PLC 141745).

2.2. Preparation of CdS, ZnS NPs and PP+CdS/ZnS based nanocomposites.

CdS and ZnS NPs were prepared by chemical cooprecipitation method [1,2].Nanoparticles were synthesized in presence of cationic surface active substance CTAB as follows: 0,05 M $CdCl_2$ solution was mixed together with 0,5% CTAB solution in a magnetic stirrerduring 10 minutes. Further solution of 0,05 M sodium sulfide (Na_2S) was added to the primary solution and was intensely stirred at ambient temperature during two hours. In order to remove non-interacting ions Cd^{2+} and S^{2-} and get purified CdS NPs, the mixture several timesdistilled with deionized water and ultracentrifuged during 10 minutes. Purified CdS NPs transferred into the petri dish and put it to dry during 24 hours. ZnS nanoparticles was prepared by same method.As precursors to synthesis ZnS nanoparticles have been taken 0,05 M $ZnCl_2$ and 0,05 M Na_2S solutions.

For synthesis of PP+CdS/ZnS nanocomposites, 0.1 g PP powder dissolved in toluene solution. CdS and ZnS NPs in different weight contents (3%,5%,10%) were added into PP solution and mixed on a magnetic stirrer for 4 hours almost at 80^0C. Then the homogeneous mixture was transferred to the petri dish and put it to dry during a day. For completely removing the solvent from the volume of the polymer nanocomposites dried in vacuum oven during 1 hour. Thin nanocomposite films were obtained by hot pressing method at the melting temperature of PP (170^0C) at a pressure of 10 MPa. The cooling of the nanocomposite films after hot pressing was carried out in water at a cooling rate of 200 deg/min.

2.3. Characterization

The morphology images of the nanocomposite samples were taken by the use of scanning electron microscopy (SEM, Jeol JSM-7600 F). Scanning was performed in SEI mode at an accelerating voltage of 15 kV and a working distance of 4.5 mm. Energy dispersive micro-X-ray analysis was performed using the device X-Max 50 (Oxford Instruments). The UV-vis spectra have been recorded on Spectrophotometer Specord 250 Plus at 200-700 nm and ambient temperature. Photoluminescent properties of nanocomposite films were examined using a spectrofluorimeter Varian Cary Eclipse at wavelength range 200-900 nm.

3. Results and discussion.

Figure 1 shows the absorption spectra and the optical absorption edge for polymer nanocomposites based on PP+ZnS, PP+CdS, and PP+CdS/ZnS. From the UV absorption spectra, the band gap was calculated by extrapolation and it was found that for nanocomposites based on PP+ZnS the band gap is 3.65 eV, for PP + CdS- 2.8 eV and for nanocompositePP+CdS/ZnS- 4.25 eV[1-5].

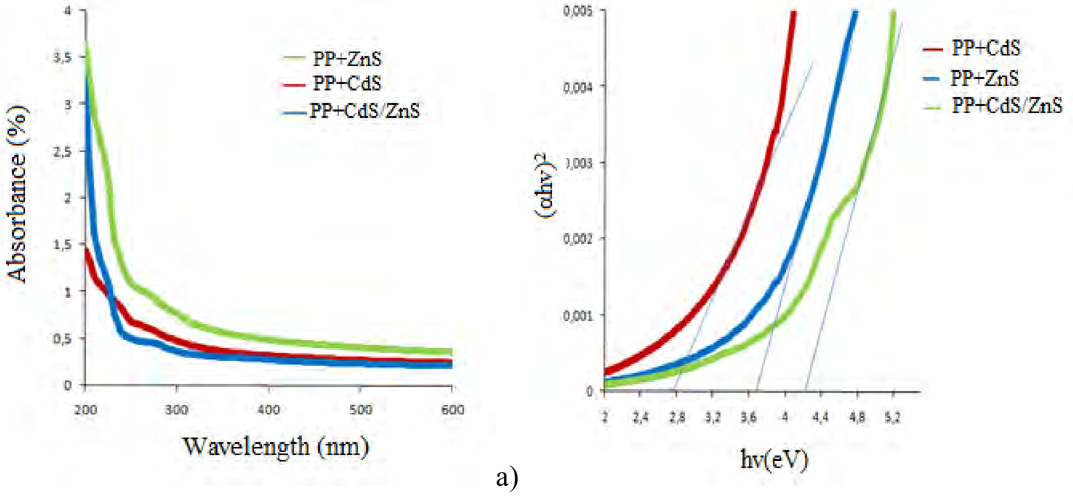

a) b)

Fig.1. Absorption spectra (a) and optical absorption edge (b) for nanocomposites based on PP+CdS, PP+ ZnS and PP+CdS/ZnS.

In Figure 2 shows the absorption spectra (a) and the optical absorption edge (b) for polymer nanocomposites based on PP+CdS/ZnS, depending on the concentration of ZnS and CdS nanoparticles. It is established that the band gap for hybrid nanocomposites based on PP+CdS/ZnS decreases with increasing content of ZnS and CdS nanoparticles (Table 1)[1-5].

All spectra are characterized by the absorption band in the UV and visible wavelength ranges and the absorption band in the 270-300 nm wavelength range belongs to CdS nanoparticles. However, the maximum and edge of the band vary, depending on the CdS concentration in the PP polymer matrix for a PP+10%

CdS/ZnS nanocomposite, the absorption band maximum shifts to the long-wavelength part of the spectrum. The appearance of a low-intensity absorption edge in the region of 400 nm (ZnS absorption) with an increase in the concentration of nanoparticles in a polymer, for sampleswith CdS/ZnS nanoparticles indicates that the nanoparticles are coated with a thin layer of ZnS.

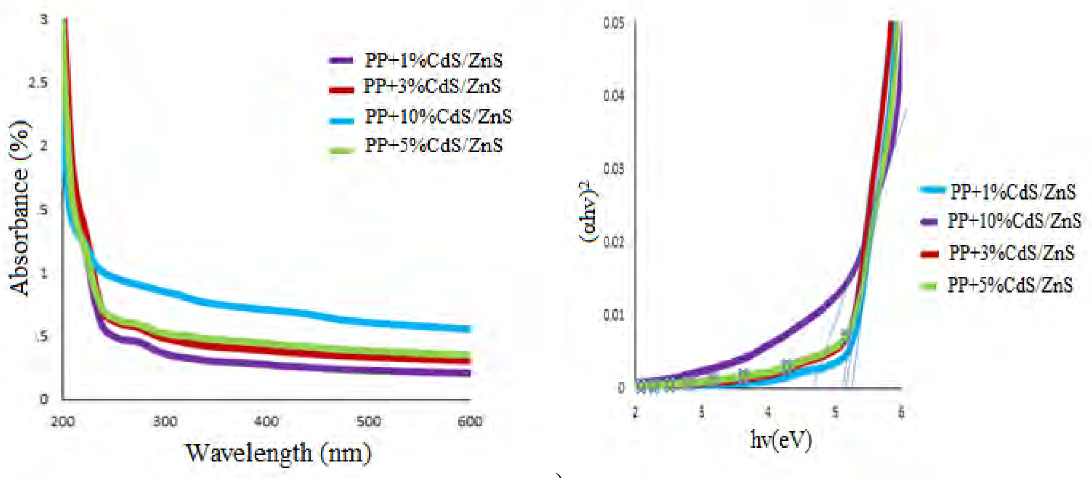

a) b)

Fig.2. Absorption spectra (a) and optical absorption edge (b) for nanocomposites based on PP+CdS/ZnS.

Table 1. The value of the band gap for nanocomposites based on PP+CdS/ZnS depending on the concentration of CdS and ZnS nanoparticles.

Samples of nanocomposites	Band gap (eV)
PP+CdS	2,8
PP+ZnS	3,65
PP+1%CdS/ZnS	5,2
PP+3%CdS/ZnS	5,1
PP+5%CdS/ZnS	5,1
PP+10%CdS/ZnS	4,6

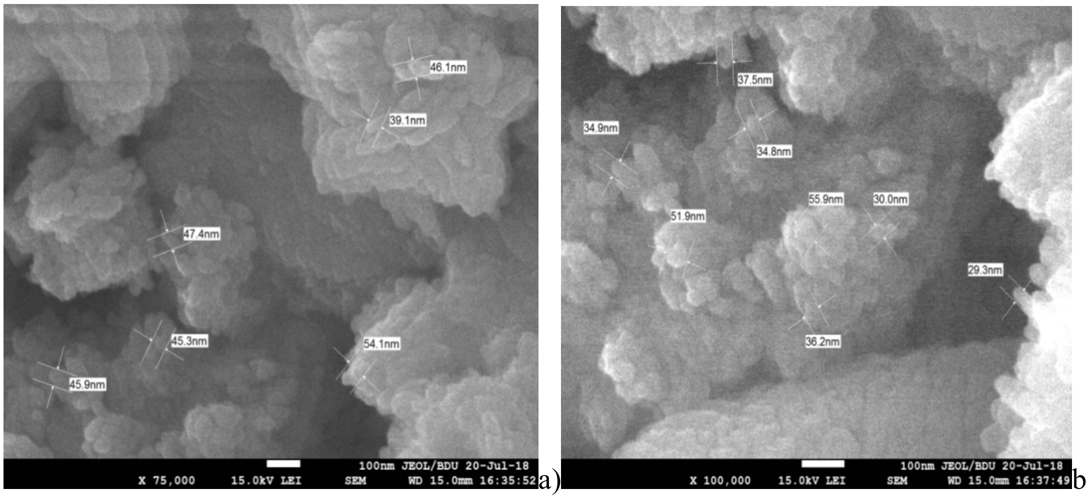

a) b)

Fig.3 SEM images of nanocomposites based on PP+CdS/ZnS depending on the concentration of ZnS and CdS nanoparticles: a) PP+3%CdS/ZnS; b) PP+5%CdS/ZnS.

Figure 3 shows SEM images of hybrid nanocomposites based on PP + CdS/ZnS, depending on the concentration of ZnS and CdS nanoparticles. SEM images show that ZnS and CdS nanoparticles are equally uniformly distributed within the polymer matrix. It has been established that with an increase in the concentration of nanoparticles, the average size of nanoparticles of both zinc sulfide and cadmium sulfide increases. The average size for a nanocomposite based on PP+3%CdS/ZnS is 40-54 nm, for PP+5%CdS /ZnS-29-56 nm.

Figures 4 and 5showthe element mapping and the EDS spectrum of hybrid nanocomposites and have been seen that the nanocomposite consists of pure CdS and ZnS nanoparticles and the polymer matrix of polypropylene. The element of platinum appeared as a result of the deposition of nanocomposites with a layer of platinum with a thickness of 10 nm to eliminate excess charge from the surface of the polymer nanocompositeduring SEM analysis. The Al element on the map appeared as a result of the use of an aluminum substrate during experiment.

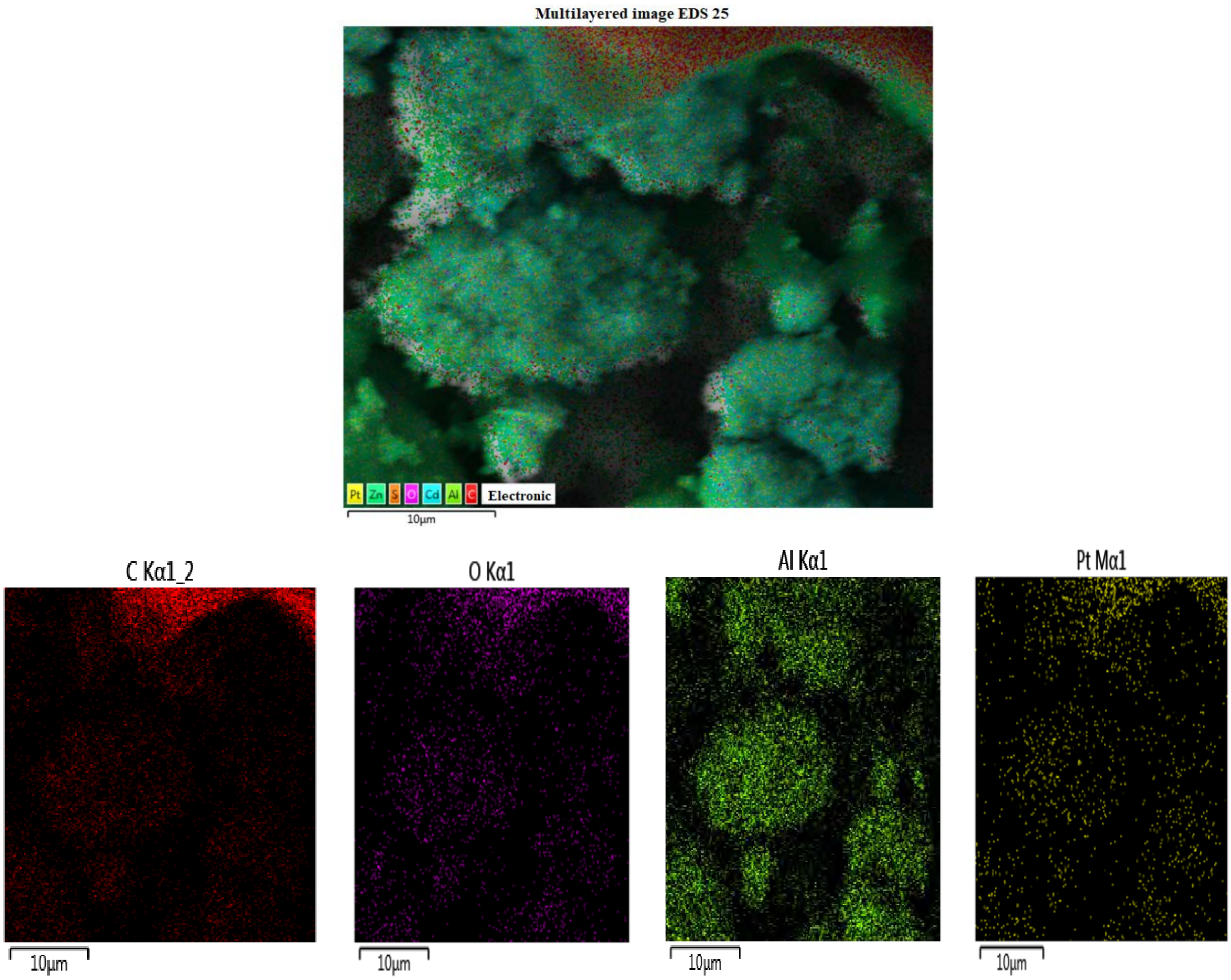

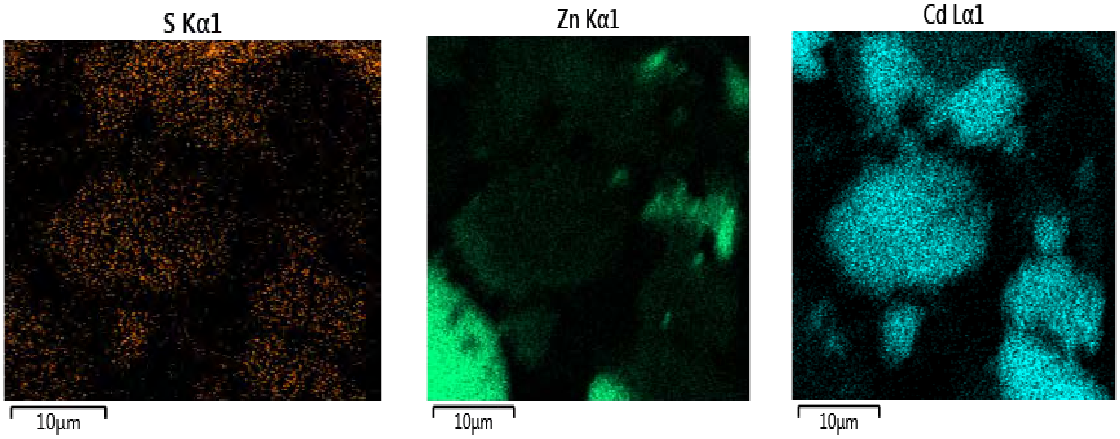

Figure 4.Mapping of a hybrid nanocomposite based on PP+CdS/ZnS by elements.

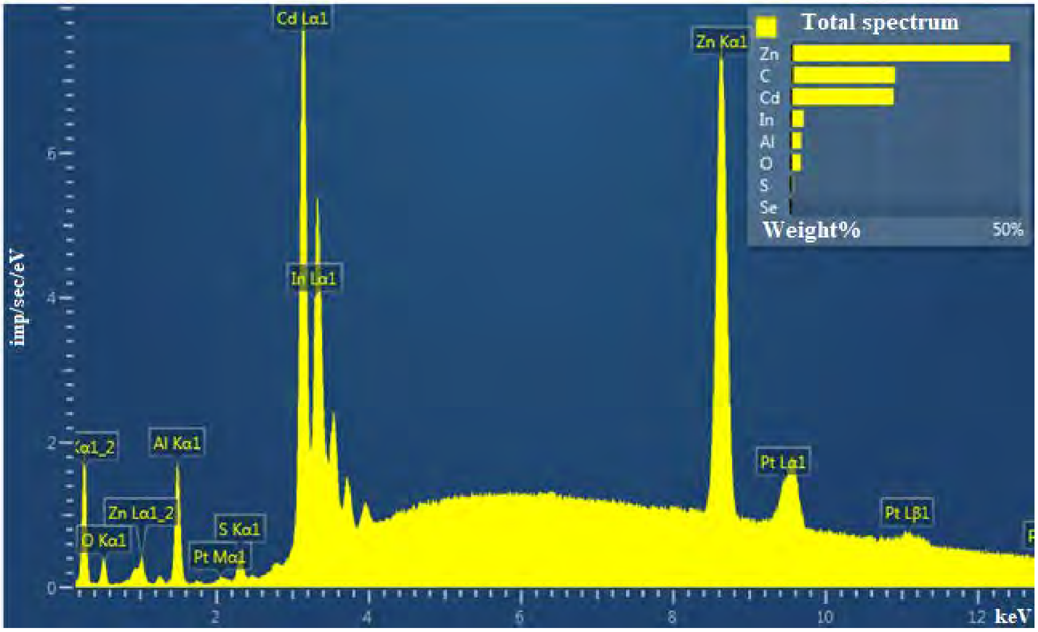

Fig.5. EDS spectrum of a hybrid nanocomposite based on PP+CdS/ZnS.

Figure 6 shows the photoluminescence spectra of nanocomposite on the base PP+CdS and hybrid nanocomposites based on PP+ CdS/ZnS, obtained by excitation with light with a wavelength of 475 nm.

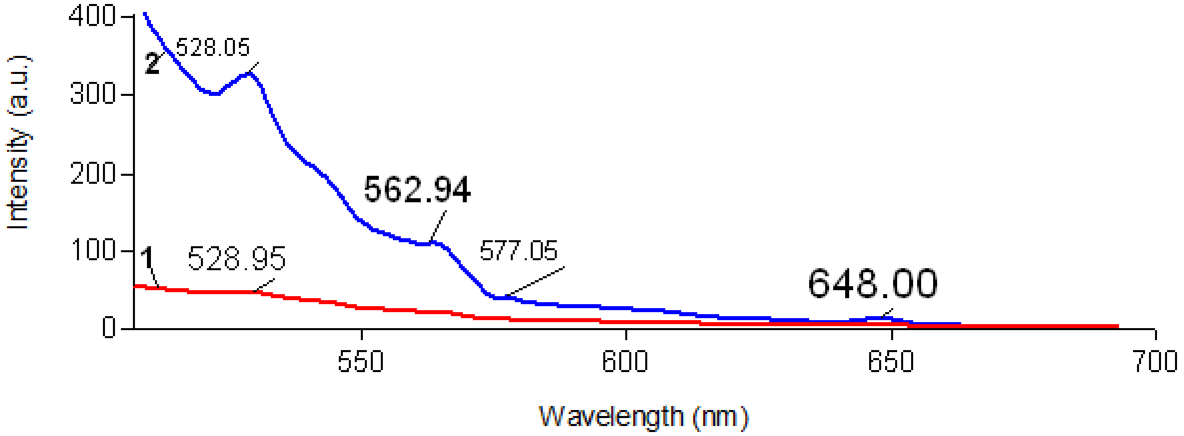

Fig.6. The photoluminescence spectrum of nanocomposites based on PP+CdS (1) and PP+CdS/ZnS (2) (χ_{exc} =475 nm).

In the PL spectra of nanocomposites based on PP+CdS/ZnS, two isolated bands are observed: with a maximum at 512 nm and 530 nm when excited in the 375 nm region; and with a maximum at 650 nm when excited by light with a wavelength of 475 nm. In the luminescence spectra of a sample with CdS nanoparticles, a band with a maximum at 650 nm is not observed. It can be assumed that the appearance of a band with a maximum at 650 nm is due to the coating of CdS nanoparticles with a ZnS shell[6-17].

4. Conclusion.

In this paper in first time was synthesized and characterized of hybrid polymer nanocomposites based on PP+CdS/ZnS. It was found that for nanocomposites based on PP+ZnSthe band gap is 3.65 eV, for PP+ CdS-2.8 eV and for PP+CdS/ZnS nanocomposite is 4.25 eV. SEM images of polymer nanocomposites show that ZnS and CdS nanoparticles are equally uniformly distributed inside the polymeric polymer matrix of polypropylene. Photoluminescent analysis of nanocomposites has shown that for such hybrid nanocomposites, the spectral sensitive spectral region is expanded.

References

1. M.A.Ramazanov, F.V.Hajiyeva, Y.A.Babayev, G.V.Valadova, S.G.Nuriyeva, H.A.Shirinova Journal of Elastomers & Plasticshttps://doi.org/10.1177/0095244319827989
2. M.A.Ramazanov, F.V.Hajiyeva, A.M.Maharramov, H.A.Shirinova, Y.A.Babayev, G.V.Valadova Proceedings of International Conference of Young Scientists Problems of Physics and Astronomy, 30(2018)
3. A.M.Maharramov, M.A.Ramazanov, A.B.Ahmadova, F.V.Hajiyeva,U.A.Hasanova Digest Journal of Nanomaterials and Biostructures, 11(3), 781(2016)
4. Pattabi M and Saraswathi AB, Nano Composite Inter, 17, 103(2010).
5. Wu X.C, Bittner A.M and Kern K. J PhysChem B 109,230(2005).
6. Fang D.F., Zhang Z.M., Wang Z.P. and Ding Z.J. Physics Procedia, 32,92(2012)
7. AnujaDatta, Subhendu K. Panda and SubhadraChaudhuri,J. Phys. Chem. C, 111, 17260(2007)
8. Hitanshu Kumar, Manoj Kumar, P.B.Barman, Ragini Raj Singh Appl. Phys. A, 2014, Published on-line.

9. Limin Qi, Jiming Ma, Humin Cheng, Zhenguo Zhao Colloids and Surfaces A Physicochemical and Engineering Aspects, 111,195(1996)
10. NidaQutub, Bilal MasoodPirzada, Khalid Umar, OwaisMehraj, M. Muneer, SuhailSabirPhysicaE, 74 (2015)
11. Le Wang, Zhipeng Li, Shouqing Ni, Quanqin Zhao, Hongwei Wei Nano-Micro Lett. 3 (1), 6(2011)
12. Shih-Yuan Lu,Mei-Ling Wu and Hsin-Lung Chen, Appl. Phys., 93()9, 2003
13. Novruzova A.A, Ramazanov M.A, Chianese A, et al. ChemEngTrans, 60, 61(2017)
14. Magerramov A.M, Ramazanov M.A, and Hajiyeva F.V J OptoelectronAdv Mater Rapid Commun, 2(11), 743(2008)
15. Magerramov A.M, Ramazanov M.A, and Hajiyeva F.V. J OptoelectronAdv Mater Rapid Commun 3(12): 432,2009
16. Magerramov A.M, Ramazanov M.A, and Hajiyeva F.V J Surf Eng. Appl Electrochemistry 46(5), 120 (2011)
17. Magerramov AM, Ramazanov MA, Gadzhieva FV, et al. J Surf Eng. Appl Electrochemistry 47, 428(2011)

*Corresponding author: flora_1985@mail.ru

ELECTROCHEMICAL OBTAİNİNG OF SELENIUM-CONTAINING RHENIUM CLUSTERS

SALAKHOVA E.A.,[1] TAGIYEV D.B.,[1] RAMAZANOV M.A.,[2] AGHAMALIYEV Z.A.,[2]
IBRAHIMOVA K.F.,[1] KALANTAROVA P.E.[1]
[1] Institute of Catalysis and Inorganic Chemistry, NAS of Azerbaijan, 113 H.Javid ave, AZ1143, Baku, Azerbaijan
[2] Baku State University, Academic Zahid Khalilov Street - 23; AZ1148.

Electrochemical obtaining of nano-coatings in the system Re-Cu-Se on platinum electrode during voltammetric cycling was studied. The research was carried out using sulphate solution containing selenium dioxide, potassium perrenate and copper chloride. According to the researches of voltammetric dependences during co-electrodeposition of potassium perrenate ions (VII), selenium (IV) and copper (II) from sulphate electrolytes on Pt electrode the conditions of potentiostatic deposition of thin films in the system Re-Cu-Se were established. To study the morphology of films on platinum and copper substrates the surface of an electrode was investigated using scanning electron microscope. It was determined that agglomerates consisting of spheric particles with average size of ~20-25 nm are observed on the surface of an electrode.

Keywords: nanotechnology, nano films, electrochemical method, chalcogen, rhenium clusters
PACS: 61.46.−w, 61.46.Bc, 73.63.−b

1. Introduction

Thanks to many unique physical and chemical properties of nanoparticles and nanostructures the creation of functional nanomaterials on their basis is of great interest. Magnetic and semi-conductor nanomaterials have been recently given special attention, and interest in them is steadily increasing. This is connected with a huge practical value of these classes of materials for the development of information technologies. Superparamagnetic materials based on nanocrystal transition metals are used in devices with a memory of extra-high-density [1-3]. Semiconductor nanomaterials exhibit unique optical properties and are prospective materials for active elements of lasers, with tunable wavelength, elements of non-linear optics and devices of nano electronics. Therefore, their application in the development of creation technologies of new materials requires systematic studies directed to expansion, improvement and search of new methods of their synthesis, in particular, electrochemical method. In this connection optimization of electrochemical methods of synthesis of such type of compounds as ecologically more safe, the study of an electrochemical activity of synthesis products becomes more relevant. Rhenium and its alloys have wide application areas. Rhenium chalcogenide (S, Se and Te) films are widely used in various areas of electronics. Thus, obtaining of semi-conducting triple rhenium alloys is of great interest. From this point demand for electrochemical obtaining of nano films grows. Electrochemical obtaining of high photo effective semi-conducting thin and nanofilms in visible region of solar spectrum and study of their properties is a topical problem. In our previous works we studied electrochemical obtaining process of thin films of rhenium chalcogenide alloys [4-9].

The aim of research work is the electrochemical obtaining of thin films of rhenium chalcogenide alloys.

2. Experiment

Platinum plate with surface of 4 cm^2 was used to determine chemical and phase compositions, but platinum cathode with surface of 0,15 cm^2 and as an anode platinum plate were used to determine microstructure of Re-Cu-Se alloys.

IVIUMSTAT electrochemical analyzer – potentiostate was used to study electrochemical obtaining process of Re-Cu-Se thin films. Silver/silver chloride electrode was used as a reference electrode. Temperature is regulated with accuracy of $\pm$ 0,1^{0}C using U-10 thermostat.Then rhenium is separated from selenium and copper by extracting with isoamyl alcohol. When both Se and Re are separated, it is determined at SPECORD 50 PLUS using spectrophotometric method. Determination of copper in Re-Cu-Se system is conducted at AA 280 FS FAST Sequential Atomic Absorption Spectrometer Varian. X-ray analysis of Re-Se-Cu alloys thin films was conducted at“Bruker” Germany powdery “D2 Phaser” diffractometer in CuK$_{\alpha}$ – radiation. For study morphology of films on platinum and copper substrates and the surface of the electrode was examined on a JEOL JSM7600F scanning electron microscope at various magnifications, and EDAX analysis with mapping of distribution of main components using an Oxford X-MAX 50 detector. The sample was scanned in the subordinate electron mode at accelerating voltage ~15 keV.

3. Results and discussion

To study co-electrolytic process of rhenium seenium and copper the deposition process of these metals from separate electrolyte must be studied. For this purpose we studied electrolytic deposition of rhenium, selenium and copper from sulphate solutions. After electrodeposition the samples were washed with distilled water, and open-air annealed for 10 minutes at temperature 410 ºC. The phase composition of the received films was determined by RPhA on diffractometer.

Thus, electrodeposition from electrolytes containing ions of rhenium (VII), copper (II) and selenium (IV) on the background of 2 mol/l sulphuric acid in chosen conditions of electrolysis and annealing permits to obtain the thin coatings Re-Cu-Se. On the basis of data described in the present article the preliminary model of the mechanism of electrodeposition of thin coatings Re-Cu-Se was suggested. Here, we can note three basic research electrochemical stages:

The first stage–absorption and reduction of the selenium particles on a surface of the platinum electrode. The second stage – adsorption between Cu^{2+}ions with adsorbed compounds of selenium with intermediate degree of oxidation. The third stage - the formation of the alloy Re-Cu-Se. Ions of Cu^{2+} and Se^{4+}reacting with rhenium ions forms the thin films of Re-Cu-Se.

To study the morphology of films on platinum and copper substrates the surface of an electrode was investigated using scanning electron microscope. According to a number of experiments done correspondingly at amplifications of 160000 (a) and 200000 (b) times, it was established that agglomerates of different geometrical forms consisting of spherical particles with a typical average size of ~20-25 nm observed on an electrode (Fig.1.).

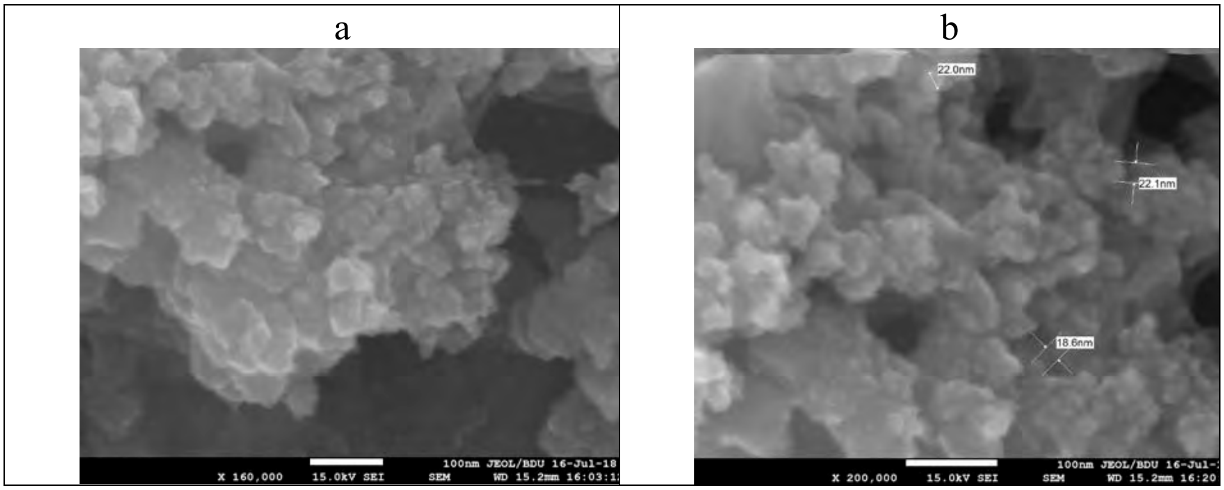

Fig.1. SEM images of thin Re-Cu-Se nano-coatings on the surface of a platinum electrode at magnifications of 160000 (a), 200000 (b)

The images at a less amplification show an equal distribution of agglomerates on the surface of platinum substrate. This fact is also confirmed by the cards of distribution of elements. As the studies of these cards showed elemental composition of observed agglomerates is presented by the main components of an alloy and allows concluding that obtained clusters are elements of the system Re-Cu-Se, as it was expected during the process (Fig.2.).

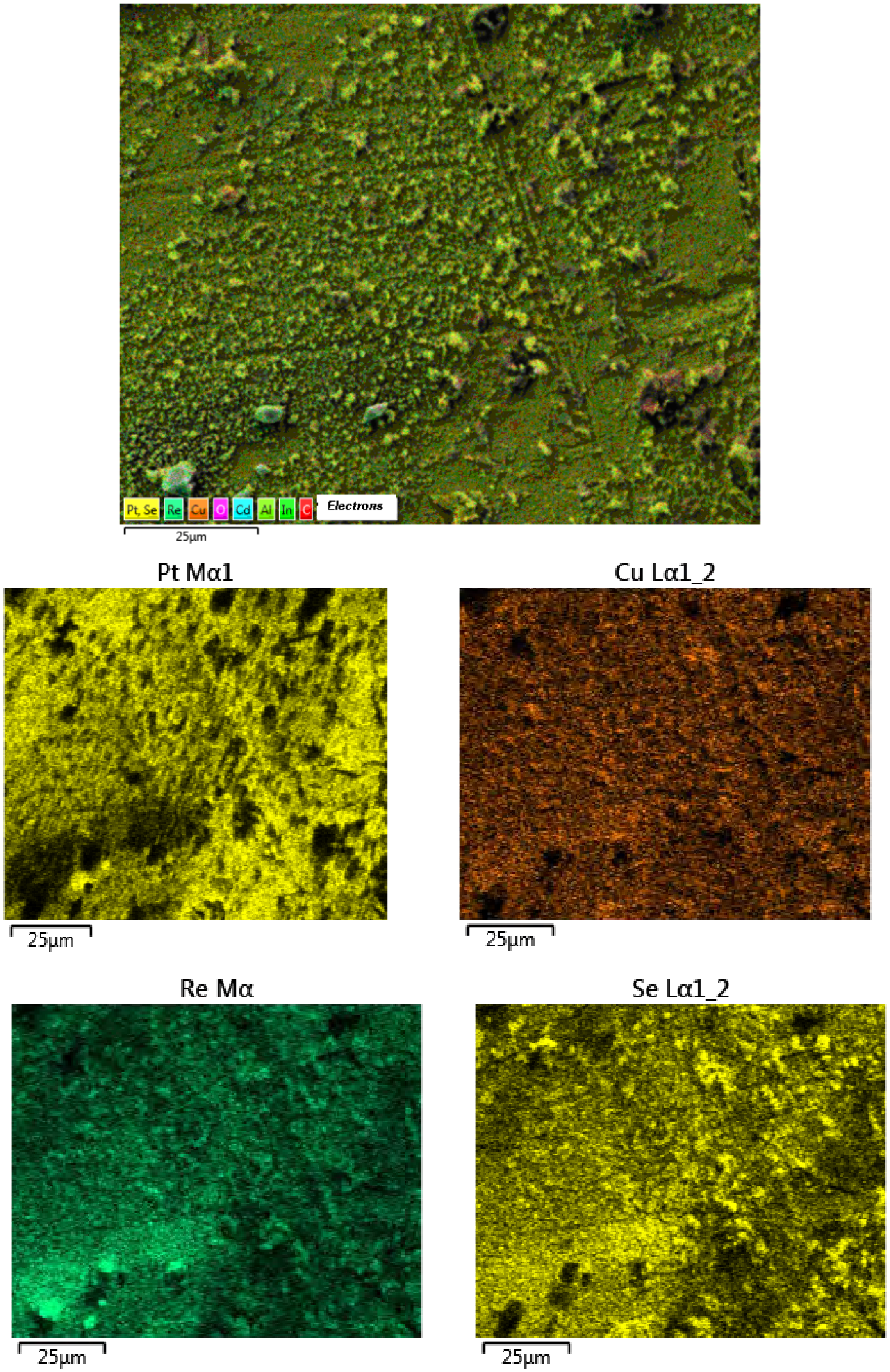

Fig.2. Multilayer image and distribution maps of the main component thin Re-Cu-Se nano-coatings on the surface of the platinum electrode

Spectrum of X-ray radiation indicates the presence of these components of the system, as well as allows conducting a qualitative analysis of samples. As the diagram shows the distribution on weight percent the content of components of the system is presented for Re-12%, Cu-5%, Se-10%. The specific peaks of hydrogen and oxygen in the spectrum is explained by residual effects during obtaining process (Fig.3.).

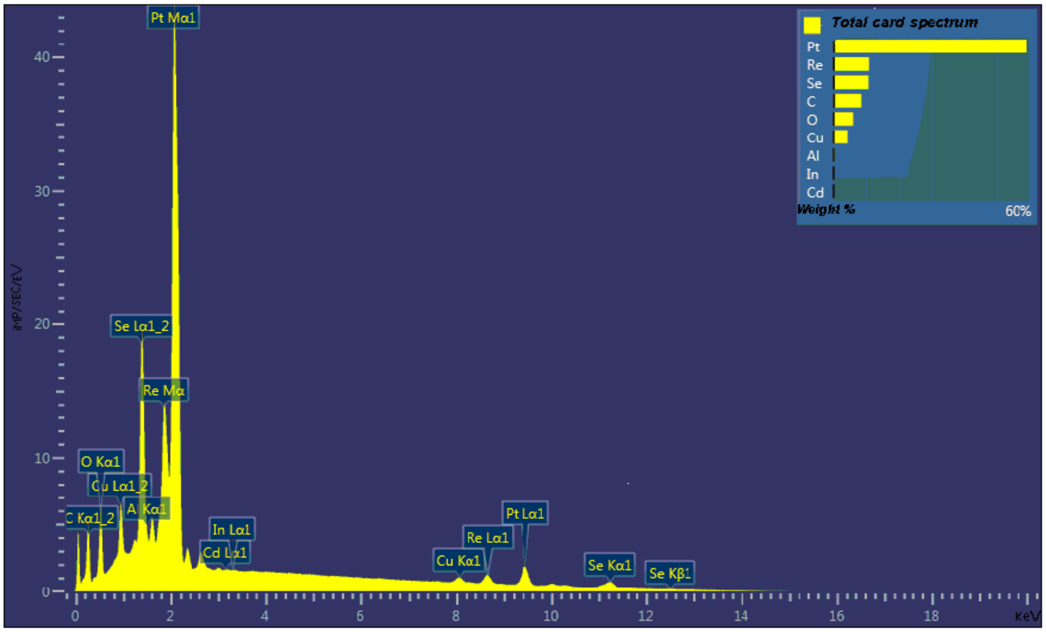

Fig.3. Spectrum of the characteristic x-ray study of the main components of Re-Cu-Se nano-coatings on the surface of the platinum electrode

4. Conclusion

To study the morphology of films on platinum and copper substrates the surface of an electrode was investigated using scanning electron microscope. It was determined that agglomerates consisting of spheric particles with average size of ~20-25 nm have been observed on the surface of an electrode.

References

1. Adriyevskiy R.A., Ragulya A.V. Nanostructural Materials. Publishing Centre "Academy", Moscow,(2005), 117
2. Alymov M.I., Zelenskiy V.A, MIFI, Moscow, (2005), 52
3. Galochkin V.A, Introduction in nanotechnology and nanoelectronic. Workbook, GOBUVPO PGUTI, Samara, Russia 367, (2013)
4. Enyashin Andrey, Popov Iqor. Phys. State Solidi B, 246, № 1, 114-118, (2009).
5. Thomas G.Gray, Christina M.Rudzinski, Emily E.Meyer, and Daniel G.Nocera.Excited-State J.Phys.Chem.A.108 (16), 3238-3243 ,(2004).
6. Naor A., Eliaz N. et al. J. electrochem. Soc.157(7), D422-D427. (2010).
7. Salakhova E.A., The Journal "Inorganic Materials", 39, 142-146, (2003).
8. Salakhova E.A., Aliyev A.M., Journal of Advanced in Materials and Physics Chemistry, China ,2(4) 253-255, (2012).
9. Salakhova E.A., Tagiyev D.B., Kalantarova P.E., Ibrahimova K.F., Journal MSCE, India, 3, 82-87,(2015).

[*] **Corresponding authors e-mails:** elza_salahova@mail.ru

SYNTHESIS OF MWCNTs FROM MIXTURE OF XYLENE BY A-CVD METHOD

S.A.MAMMADOVA[1*], N.M.LYADOV[2], A.O.ISRAFILOV[3], S.H.ABDULLAYEVA[1,3], A.B.HUSEYNOV[3]
[1]G. M. Abdullayev Institute of Physics, ANAS, 131 H. Javidave., Baku, Azerbaijan,
[2]Zavoisky Physical-Technical Institute, FRC Kazan Scientific Center of RAS, 420029 Kazan, Russia
[3]Research & Development Center for High Technologies (RDCHT), MTCHT, 2 Inshaatchilarave., Baku, Azerbaijan

This research material deals with the synthesis of multi-walled carbon nanotubes (MWCNTs) by aerosol-assisted chemical vapor deposition (A-CVD) method.The effect of rarely used and less studied carbon source-mixture of the xylene (ortho- (o-), meta- (m-) and para- (p-))isomers on the quality, purity and cost of synthesized MWCNTs have been analyzed. Thus, the selected carbon source is more affordable and cheaper than orto-, meta- and para-xylene isomers separately. Separation of the xylene mixture, costly process and therefore have an impact on the price of the synthesized product. The surface morphology, shape and diameter distribution of the MWCNTs was analyzed using Scanning Electron Microscope.The purity,quality,structure, phase identification of the carbon nanotubes determined by Raman spectroscopy and XRD analysis.

Keywords: Aerosol-Assisted Chemical Vapor Deposition (A-CVD), Multi Walled Carbon Nanotube (MWCNT), SEM analysis, Raman spectroscopy
PACS:81.15.Gh; 8110-h

3. Introduction

A carbon nanotube (CNT) is a tubular structure made of carbon atoms, having diameter of nanometer order but length in micrometers.Due to extraordinary properties:stronger than steel, electrical conductivity higher than copper, thermal conductivity higher than diamond CNT has remained an exciting material in different fields of technology.There are different methods for CNTs synthesis.In comparison with arc-discharge and laser-ablation methods,CVD is more simple and economic technique for synthesize pure and large amount of CNTs at low temperature and ambient pressure.Moreover, CVD method makes it possible to use as raw material a large assortment of hydrocarbons in any state (solid, liquid or gas),allows CNT growth in a variety of forms, such as powder, films, aligned or entangled, straight or coiled nanotubes. The selected by us carbon source (mixture of xylene)is more affordable and cheaper than ortho, meta and para xylene isomers separately. Separation of the xylene mixture, costly process and therefore have an impact on the price of the synthesized product.

4. Experiment

a.Synthesis of MWCNTs

MWCNTs were synthesized by an Aerosol Assisted Chemical Vapor Deposition Method (A-CVD) on the experimental laboratory setup-Scientific Instruments Dresden GMBH, SCIDRE, Germany. The scheme of the A-CVD technique was show in the Figure 1.The aerosol CVD set-up equipped with carrier gas supply units (Inlet 1-3), ultrasonic aerosol generator (2), high temperature reactor-quartz tube(4) covered with moving tubular electric furnace(length = 0.35 m, heating up to 1200^0C) (3) and the vacuum system (leak test of the setup).The synthesis of MWCNTs was carried out in a horizontal laminar reactor (a cylindrical tube of the quartz glass with size: length = 1m, internal diameter = 33mm)[1].

For uniform deposition of carbon nanotubes, during the synthesis, the tubular electric furnace was automatically moved along the length of the reactor at a fixed rate of 10 mm/min, which allows the catalytic thermolysis of the hydrocarbon mixture and the synthesis of carbon nanotubes along the entire length of the tube.

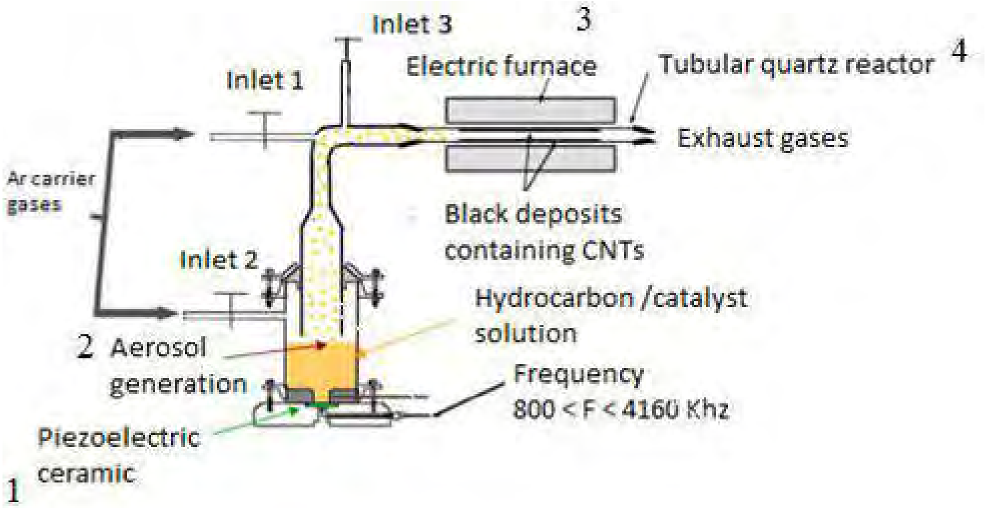

Figure 1. Scheme of Experimental setup of A-CVD technique

A mixture of ortho, meta and para Xylenes (o+m+p) was used as a carbon source and ferrocene (Fc) as a catalyst precursor. All reagents used in this work were of an analytical grade. The solution of mixture of xylene and ferrocene (20mg/ml) filled in chemical glass with a capacity of 200 ml and placed in the ultrasonic bath of the aerosol generator of the CVD equipment. Argon gas was used as carrier gas for transportation the formed aerosol to the quartz reactor. Hydrogen gas was used as a reductive gas during synthesis process.The synthesis of the carbon nanotubes was conducted at the optimum temperature of 900 ^{0}C, based on the experimental data of our group previous studies [2]. The tubular furnace moved through the reactor during synthesis process at a speed of 10mm/ min,hydrocarbon decomposed at 900°C over ther quarz glass tube inside reactor. The synthesis process was performed at atmosphere pressure with the duration of 85 minutes.After synthesis process, the aerosol generator and H_2 gas flow were switched off and purification of synthesized MWCNTs from polyaromatic and tarry impurity compounds was carried out with the displacement of the electric furnace in the opposite direction under the flow of argon gas (Ar inlet, 500ml /min), at a rate of 30mm/min for 40 minutes.Upon completing the experiments, the reactor was allowed to cool overnight in an argon stream. At the end of the purification process MWCNTs carefully scarped from quartz tube.The obtained MWCNTs are light, dark black material in a powder form.

2.2 Characterization

Scanning Electron Microscopy was used to study structure and surface morphology of the synthesized MWCNTs. Electron microscopy investigations were made using a SEM EVO 50 xvp (Carl Zeiss, Germany) microscope.All SEM images were obtained using secondary electrons (SE1 detector).The typical magnification used for the SEM was between 10.00 KX to 40.00KX and is denoted in the bottom of each image at 20kV electron beam. The Raman spectra was recorded on a Nanofinder 30 Confocal Laser (Tokio Instruments) microspectrometer. The experiments were carried out with an excitation wavelength of 532 nm laserfocused on the sample by means of a 50x objective with the 10 mW beam intensity, 600G/mm grating and 20 s exposure time.The XRD was taken in produced MWCNTs powdered samples using D2 Phase XRD, Bruker, Germany. XRD was taken at room temperature with 2θ degree ranges from 05^0 – 80^0, CuK$_{.}$ (λ=1,5406E).

5. Results and discussion

Fig.1 displays SEM images of the synthesized MWCNTs. As shown from the picture, the carbon nanotubes have tubular structure. From the pictures, it is obvious that pure and ideal multi-wall carbon nanotubes (MWNTs) are formed during the synthesis process using affordable carbon source.

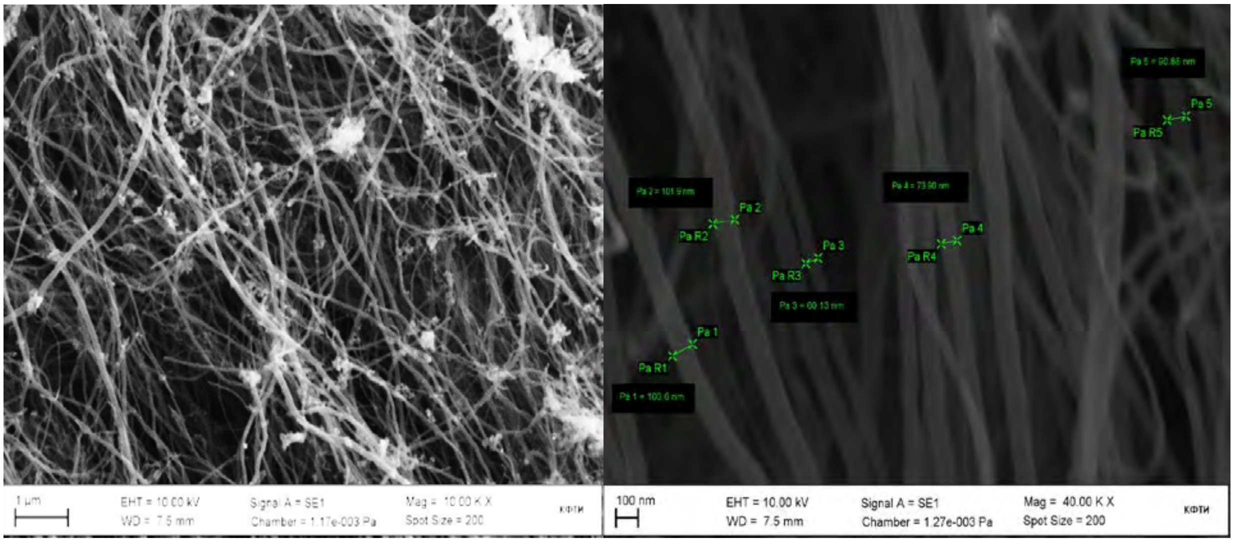

a) b)

Fig 1. SEM images of the MWCNTs synthesized by A-CVD method in different magnifications (a-Mag=10.00KX) ; (b-Mag=40.00KX)

The Fig.1 b shows the diameter distribution of the synthesized MWCNTs. The diameter of the CNTs ranges from 60-103nm. SEM analysis results proves that using mixture of Xylene without dividing them individual isomers, it is possible to synthesize high quality carbon nanotubes.

The Raman analysis was taken in order to verify the quality of the MWCNTs powder. Having a various allotropes of carbon, one can easily distinguish, in a quick experiment, the presence of multi walled carbon nanotubes and defects. The so-calledG-line is a characteristic feature of the graphitic layers and corresponds to the tangential vibration of carbonatoms. Another characteristic mode is a typical sign of defective graphitic structures (D-line). A comparison ofthe intensity ratios of these two peaks gives a measure of the quality of the bulk samples.

Fig. 2. Raman spectrum of the synthesized multi walled carbon nanotubes

Figure 2 shows the Raman spectra in the large-frequency region (-400-2000)cm^{-1} for the synthesized MWCNTs.The two main typical graphite bands are present in the Raman spectrum of MWCNTs bundles: the band at 1580 cm^{-1} (G band) assigned to the in-plane vibration of the C–C bond (G band) and 1342 cm^{-1} (D band) typical for defective graphite-like materials.The ratio of these peaks, in the range of G/D = 55/20, indicates that the carbon nanotubes exhibit a low defects on structure, which determine the high quality of the synthesized CNTs from the mixture of xylene.

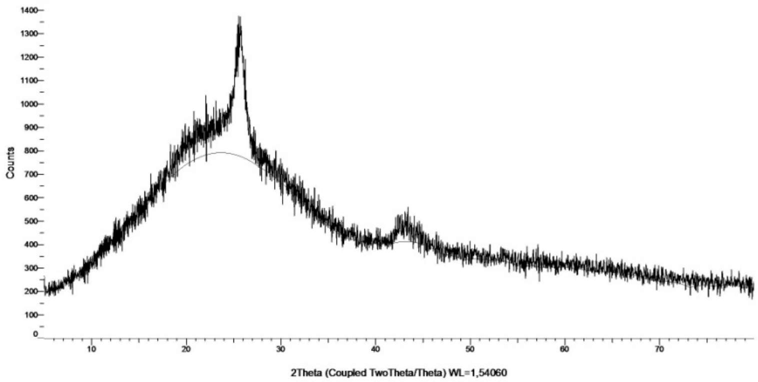

Figure 3. XRD peaks of the synthesized MWCNTs

The XRD results obtained for the synthesized MWCNTs were compared with Joint Committee on Powder Diffraction Standards (JCPDS) database and it showed that there are only two main peak point values achieved by XRD for the MWCNTs, which are 25.70 and 42.5, shown in Figure 3.This peak value shows the presence of carbon in the product and also the structure of the sample was identified as hexagonal with reference to JCPDS database.The XRD results confirm the obtained results by SEM and Raman spectroscopy analysis. It was possible to synthesize high purity, high quality, tubular structure large scale MWCNTs using affordable and cheap xylene mixture.

4. Conclusion

This paper is about the synthesis of MWCNTs byAerosol assisted chemical vapour deposition method using injection of carbon source mixture during synthesis process and characterization of the MWCNTs by different methods.SEM analysis results proved that tubular structure, nanosized MWCNTs were synthesized and Raman analysis verify high quality and purity of CNTs. The XRD analysis gave the structure of produced MWCNTs as hexagonal and nature as crystalline.These results indicate that it is possible to synthesize high quality, pure CNTs using mixture of Xylene which is cheaper that individual isomers of xylene and this directly affect the cost of synthesized MWCNTs.

References

1. S. H.Abdullayeva, S.A.Mammadova, M.B.Huseynova, A.B.Huseynov, et al. Azerbaijan Journal of Physics, 22, 31 (2017)
2. S. Abdullayeva, N. Musayeva, C. Frigeri, A. Huseynov et al. Journal of Advances in Physics. 11, 3229 (2015)

***Corresponding author**: s amiras416@gmail.com
samiramammadova@physics.science.az

INFLUENCE OF FULLERENES ON THRESHOLD VOLTAGE, DIELECTRIC AND CONDUCTIVITY PROPERTIES OF SMECTIC A LIQUID CRYSTAL 10NF

*T.D.IBRAGIMOV, A.R.IMAMALIYEV, G.F.GANIZADE
lnstitute of Physics of Azerbaijan National Academy of Sciences, H.Javid av.13I, Baku, Azerbaijan, AZ1143,

Influence of fullerenes on threshold voltage, dielectric and conductivity properties of smectic A liquid crystal is investigated. It is shown that the transverse component of the real part of dielectric permittivity increases at the additive of fullerenes while the longitudinal component decreases. At this case, a maximum of dielectric absorption shifts to the high-frequency region. Conductivity increases at low frequencies and decreases at the high ones. Experimental results are explained on the base of the Maier-Meier theory for anisotropic liquids and also participation of fullerenes in ionic conductivity of liquid crystal.

Keywords: *liquid crystal, fullerenes, dielectric permittivity, threshold voltage*
PACS: 64.70.mj; 64.70.pv; 78.15.e; 82.70.d.

1.Introduction

An additive of nanoparticles into liquid crystals (LC) can lead to essential changes their properties as they are distributed between LC molecules at low concentration. Fullerenes have the spherical form and the specified dimension about 1 nm. Currently, there is a small number of works devoted to liquid crystalline colloids based on pristine fullerenes. Particularly, influence of bias voltage on the liquid crystalline colloid based on pristine fullerenes is investigated in work [1]. Results of influence of laser radiation on electro-optic properties of similar colloids are presented in the work [2]. Changes of dielectric parameters of nematic LC study in works [3].

The aim of present work is the study of action of fullerenes C_{60} on the threshold voltage, dielectric and conductivity properties of the smectic A liquid crystal.

2. Experiment

We used smectic A liquid crystal 4- nitrophenyl -4'- decyloxybenzoic acid (10NF) as a matrix. The fullerenes C_{60} (U.S. Research Nanomaterials, In.) were added into the liquid crystal with 0.5 wt.% and were shaken in a vortex mixer for 1 hour at temperature 75°C, followed by sonication with dispergator Ultrasonic Cleaner NATO CD-4800 (China) for 4 hours.

The cell had a sandwich structure and consisted of two plane-parallel glass plates whose inner surfaces were coated with thin transparent and conductive indium-tin-oxide (ITO) layer. Planar orientation of molecules was attained by coating the inner substrate surfaces with rubbed polyimide layers. The cell thickness was fixed with calibrated 20 μm polymer spacers for measurements. Homeotropic orientation of molecules has been reached by mechanical shift of one substrate concerning another at frequency of 50 Hz for several minutes in the filled cell. Both the colloid and the pure LC were injected into the empty cell by capillary action at the isotropic state. The stuffed cell was kept in the special heater with temperature regulator GL-100 (China). The copper-constantan thermocouple was used for temperature control. An accuracy of temperature determination was 0.1°C.

Dielectric and conductivity measurements were carried out by the Precision LCR Meter 1920 (IET Labs. Inc., USA) in the frequency range of 20 Hz – 1 MHz. In this case, applied voltage was 1 V for both LC molecular orientations. A set-up for measurements of electro-optic parameters was assembled on the base of the Carl Zeiss polarization microscope. The electric impulses of the special form applied to the cell from the functional generator (model G6-28, Russia). A light passing through the cell fell on the photo diode and was registered by digital storage oscilloscope (model 6022BE, Hantek). The threshold voltage was defined using unipolar triangular impulses in the quasi-static regime. Besides, the value of the threshold voltage was supervised under the polarization microscope. The measurements were carried out at temperature 58°C.

3. Results and discussion

According to [4], particles do not disturb the director field of a LC if the anchoring parameter $\zeta = WR/K$ is much smaller than 1, where W is the anchoring energy of LC molecules with particle surfaces; 2R is particle size; K is the LC elastic constant. The values of anchoring energy are within 10^{-4} -10^{-6} J/m^2, the elastic constant of LC has an order of 10^{-12} N, and the fullerenes have sizes of 1 nm. Elementary calculations show that the anchoring parameter has an order between 10^{-1}-10^{-3}. It is much less than 1. Thus, the overall disturbance of the director field by fullerenes do not appears still less at similar concentration. Hence, the obtained colloids can be considered as a homogeneous media and they should behave as pure LCs but with the modified parameters.

Observation under polarization microscope has shown that the clearing temperature decreases from 76.8□Cto 75.2□C Spherical particles of fullerenes infiltrate between LC molecules reducing interaction in between. At this case, there is disordering of LC directions and, accordingly, reduction of order parameter *S*. As a result, temperature of transition from isotropic to smectic phase decreases according to expression [5]:

$$T_c = (1-f_o)\, T_p$$

where f_o is volume concentration of particles, T_p and T_c are clearing temperatures of pure LC and the colloid, correspondingly.

The frequency dependences of real ε' and imaginary ε" parts of dielectric permittivity of both the pure LC and the corresponding colloid at homeotropic and planar configurations and temperature 58^{0}C are presented in Fig.1 and Fig.2, correspondingly.

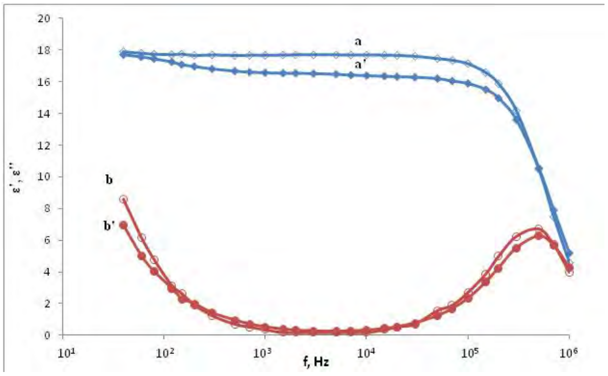

Fig.1. Frequency dependence of real ε' and imaginary ε" components of dielectric permittivity at homeotropic configuration (58^{0}C): (a) ε' of the pure LC, (a') ε' of the colloid, (b) ε" of the pure LC, (b') ε" of the colloid.

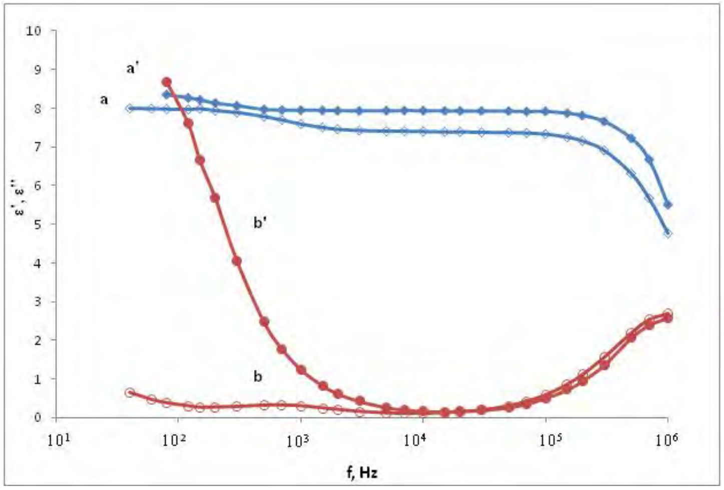

Fig.2. Frequency dependence of real ε' and imaginary ε" components of dielectric permittivity at planar configuration (58^{0}C): (a) ε' of the pure LC, (a') ε' of the colloid, (b) ε" of the pure LC, (b') ε" of the colloid.

As can see, the value of ε'_{II} of the colloid is less than for the pure LC while $\varepsilon'_{\perp}$ of the colloid is more than for the pure LC at all frequencies. These values marginally change up to 10^5 Hz then they drastically decrease. The value of ε'_{II} is equal to 17.71 for the pure LC while it corresponds to 16.42 for the colloid at 10 kHz. The value of $\varepsilon'_{\perp}$ equals to 7.39 for the pure LC while it corresponds to 7.93 for the colloid at the same frequency. A presence of fullerenes decreases the value ε''_{II} and increases $\varepsilon''_{\perp}$. At this case, a maximum of dielectric absorption shifts to the high-frequency region from 400 kHz to 500 kHz.

It is known that the relaxation time of LC molecules which is characterised by flip-flop motion of molecules around the short molecular axis defined as follows:

$$\tau = \frac{1}{2\pi f}$$

where f is the frequency of applied electric field. The additive of fullerenes decreases the relaxation time from $4.0\cdot10^{-7}$ s. to $3.2\cdot10^{-7}$ s. at 58°C.

It should be pointed out the dielectric anisotropy of the pure LC equals to 10.32 at the middle frequences while this value makes 8.49 for the colloid. In other words, the additive of particles reduces dielectric anisotropy.

The experimental facts can be explained by the Maier-Meier theory for anisotropic liquids according to which expressions for both components of dielectric permittivity are defined as follows [6]:

$$\varepsilon'_{//} = 1 + \frac{NHF}{\varepsilon_0}\left\{\gamma_{av} + \frac{2}{3}S\Delta\gamma + F\frac{p_e^{\,2}}{3k_BT}\left[1 - \frac{1}{2}\left(1 - 3\cos^2\beta\right)S\right]\right\}$$

$$\varepsilon'_{\perp} = 1 + \frac{NHF}{\varepsilon_0}\left\{\gamma_{av} - \frac{1}{3}S\Delta\gamma + F\frac{p_e^{\,2}}{3k_BT}\left[1 + \left(1 - 3\cos^2\beta\right)S\right]\right\}$$

Dielectric anisotropy is the difference of these quantities:

$$\Delta\varepsilon' = \frac{NHF}{\varepsilon_0}\left[\Delta\gamma - F\frac{p_e^{\,2}}{2k_BT}\left(1 - 3\cos^2\beta\right)\right]S$$

where F is reaction field factor, H is the cavity form factor, $\gamma_{av} = (\gamma_{II} + 2\gamma_{\perp})/3$ is the average value of polarizability of LC molecules, $\Delta\gamma = \gamma_{II} - \gamma_{\perp}$ is the anisotropy of polarizability, N is the number of LC molecules per unit volume, S is the order parameter, β is an angle between the point molecular dipole p_e and the axis of maximum molecular polarizability, ε_0 is dielectric permittivity of vacuum, k_B is Boltzmann constant, T is Kelvin temperature. Since the concentration of the colloid is very small, the number of embedded particles per unit volume is also small. That is, the number of LC molecules per unit volume N slightly decreases. A different matter the order parameter S which is defined as follows [7]:

Frequency dependences of specific conductance of the pure LC and the colloid are resulted in Fig.3.

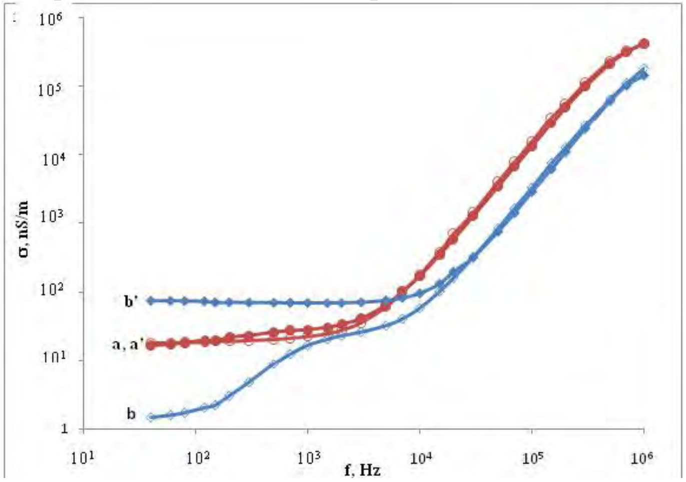

Fig.3. Frequency dependence of specific conductance components at temperature 58°C: (a) σ_{II} *of* the pure LC, (a') σ_{II} of the colloid, (b) $\sigma_{\perp}$ of the pure LC, (b') $\sigma_{\perp}$ of the colloid.

Here, the longitudinal component of specific conductance practically remains invariant at additive of fullerenes. It is equal to $1.67\cdot10^{-8}$ S/m at 40 Hz and slightly increases up to 5 kHz then it drastically rises achieving $4.19\cdot10^{-3}$S/m at frequency of 1 MHz. The transverse component of specific conductance is more for the colloid than the pure LC at low frequencies up to 20 kHz then it has the same value. In particular, the transverse component of specific conductance of the colloid is equal to $7.55\cdot10^{-8}$ S/m while it corresponds to $1.46\cdot10^{-9}$ S/m for the pure LC at the frequency 40 Hz. They have the same value at high frequencies and achieve $1.44\cdot10^{-9}$ S/m at 1 MHz. Obviously, an increase in the transverse component of conductivity at the additive of fullerenes is connected with the involvement of fullerene particles in the conductivity process since it is easier for them to move between the smectic layers which have the dimensions about 2 nm. At this case, the longitudinal component become less than transverse component□□We also can note that fullerenes□are not able to move in time with ions because of time lag at high frequencies. For this reason, the specific conductance of the colloid has just the same value as the pure LC.

It is known that the specific conductance may be presented as:

$$\sigma = 2\pi f\varepsilon_0\,\varepsilon''$$

It is obvious that the change of conductivity is correlated with the change of the imaginary part of dielectric permittivity and the frequency. Therefore, the specific conductance increases at increasing of indicated parameters. In connection with a difference of frequency ranges of a dispersion ε'_{II} and $\varepsilon'_{□}$, maxima ε''_{II} and $\varepsilon''_{□}$ are observed at various frequencies and, accordingly, $□_{II}$ and $□_{□}$ start to increase at the same frequencies. The additive of fullerenes shifts dispersion of dielectric permittivity to the high frequency region. Hereat, the same shift occurs with dispersion of specific conductance.

Additionally, the threshold voltage of planar-homeotropic transition decreases from 35V to 28V at the additive of fullerenes. According to [7], it is defined as follows:

$$U = \sqrt{\frac{Wd}{2\varepsilon_0|\Delta\varepsilon|\cdot l}}$$

here ℓ is length of molecule, *W* is sum of elastic energy and the energy connected with formation of disclinations and dispositions; $\Delta\varepsilon$ is anisotropy of dielectric permittivity, *d* is the layer thickness. Essential reduction of threshold voltage cannot be connected with a decrease in dielectric anisotropy. Apparently, it is caused by occurrence of new defects with which the growth of planar areas begins. Thus, the magnitude of W decreases, that is reflected in value of the threshold voltage.

4. Conclusion

The colloid based on the smectic liquid crystal and fullerenes with concentration of 0.5wt.% can be considered as a homogeneous medium. Spherical nanoparticles of fullerenes are located between LC molecules reducing their interaction and decreasing the order parameter. As a result, the transverse component of real part of dielectric permittivity increases while the longitudinal component reduces. Moreover, the relaxation time characterizing flip-flop motion of LC molecules around the short molecular axis decreases. The involvement of fullerene particles in the conductivity process leads to an increase of specific conductance at low frequencies. Occurrence of fullerenes in the LC increases number of defects. Hence, the threshold voltage of planar-homeotropic transition decreases.

References

1. San S. E., Okutan M., Aoysal O.K., Yerli Y., Chin. Phys. Lett., 25, 212-215 (2008).
2. San S.E., Koysal O., Okutan M., Journal of Non-Crystalline Solids, 351, 2798-2801 (2009).
3. Okutan M., San S.E., Basaran E.,Yakuphanoglu F., Physics Letters A, 339, 461-465 (2005).
4. Liquid Crystals beyond Displays. Chemistry, Physics, and Applications, Edited by Li Q. New Jersey, Hoboken: John Wiley and Sons, Inc. 2012, 573 p.
5. Gorkunov M.V., Osipov M.A., Soft Matter, 7, 4348–4356 (2011).
6. Blinov L., Structure and properties of liquid crystals, New York: Springer, 2011, 439 p.
7. Blinov L.M., Chiginov V.G., Electrooptic effects in liquid crystal materials. Springer Verlag, 1994, 488 p.

***Corresponding author**: tdibragimov@mail.ru

ELECTRICAL AND HEAT PROPERTIES OF BULK NANOSTRUCTURED SAMPLES OF $Bi_{85}Sb_{15}$ SOLID SOLUTION

M.M.TAGIYEV[1,2*], G.D. ABDINOVA[2]
[1]*Azerbaijan State Economic University, Baku, Istiglaliyyat str., 6, Baku, Azerbaijan, Az1001*
[2]*Institute of Physics of the National Academy of Sciences of Azerbaijan, H. Javid ave., 131, Baku, Azerbaijan, Az1148*

Extruded bulk nanostructured samples of the $Bi_{85}Sb_{15}$ solid solution were obtained by hot extrusion. It was found that their electrical parameters and lattice thermal conductivity substantially depend on the grain size and post-extrusion annealing. The data obtained are explained by the dependence of the electron concentration, the degree of texture, re-crystallization, and disorientation of particles in the sample on particle sizes, as well as phonon scattering at grain boundaries.

Keywords: extrusion, solid solution, electrical conductivity, thermal conductivity, particles
PACS: 72.15.Jf; 72.20.-i; 73.63.-b

1.Introduction

Bi-Sb solid solutions are highly efficient materials for creating low-temperature thermoelectric and magnetothermoelectric converters for practical use in thermoelectric generators at optimal charge carrier compositions and concentrations [1-7]. In recent years, the possibility of increasing the thermoelectric efficiency of materials through the use of size effects, both classical and quantum, has been intensively investigated [8, 9]. The manufacture of small-sized samples containing quantum wells [10] or quantum dots [11] is associated with the use of expensive equipment. In this sense, an interesting approach is based on the use of bulk nanostructured materials [12,13]. This technology is based on the use of ball mills to create a powder with particles of about 10 nm in size from the initial synthesized material and its subsequent hot pressing to obtain bulk nanostructured samples [14,15]. This approach is much more economical. These materials are also of interest from the point of view of studying the effect of the scattering of electrons and phonons at the boundaries on the transport properties of semiconductor samples.

2. Experiment

In order to study the influence of particle sizes on the transport of electric charge and heat in semiconductor materials. In this work bulk samples of $Bi_{85}Sb_{15}$ solid solution consisting of particles with average sizes of $2\cdot10^5$, 400, 32 и 20 nm were obtained and their electrical conductivity σ, thermo-e.m.f. α, Hall coefficient R_H and thermal conductivity χ have been investigated. The electrical parameters were studied in the temperature range of ~ 77-300 K and the thermal conductivity in the temperature range of ~ 90-300 K. Bulk nanostructured samples of solid solution were obtained using a ball mill (Mill activator) of brand AGO-2. The initial synthesized material of the solid solution $Bi_{85}Sb_{15}$ was used. The particle size in the powder was changed by changing the time of crushing the source material in the mill. The average particle size in the powder was determined in an XRD D8 ADVANCE X-ray unit, Bruker, Germany using the Sherrer formula [16].

Briquettes with a diameter of ~ 30 mm, convenient for extrusion were pressed from powders of the $Bi_{85}Sb_{15}$ solid solution. Pressing was carried out at room temperature and a pressure of ~ 3.5 T/cm^2. Extrusion was carried out on a hydraulic press with a diameter of 30 mm to a diameter of 6 mm using special tooling [17]. The extrusion temperature and pressure were ~ 475 K and 4.8 T/cm^2, respectively.

Samples for measurement were cut from extruded ponds using the electric-spark cutting method. The samples had the shape of a parallelepiped with dimensions of 0.2x0.4x1.5 cm. After cutting the samples from ponds, their surface was treated by electrochemical etching in a KOH + $C_4H_4O_6$ + H_2O solution. Electrical parameters and thermal conductivity were measured by the method described in [18] along the length of the sample (rod). Samples non-annealed after extrusion and samples previously annealed at ~ 503 K for 2 hours under vacuum were examined.

3. Results and discussion

The measurement results are presented in Figure 1 and Table 1. It can be seen that with decreasing powder sizes on the basis of which extruded samples were obtained, an increase in electrical conductivity σ and a decrease in the absolute values of the coefficients of thermo-e.m.f. α and Hall R_H is observed, i.e. the dependences of these parameters of the samples on the sizes of the powders are satisfactorily correlated. It is assumed that with decreasing crystallite size the density of the boundaries increases, which leads to an increase in the concentration of electrons in the samples. As a result, the values of σ increase, and α and R_H fall.

Unlike the sample with particle sizes of $2\cdot10^5$ nm, the electrical conductivity of nanostructured samples with particle sizes of 400, 32 and 20 nm decreases with increasing temperature, the absolute value of the thermo-e.m.f. coefficient increases, which corresponds to the metallic conductivity. This is evidenced by the temperature dependence of the concentration and mobility of current carriers.

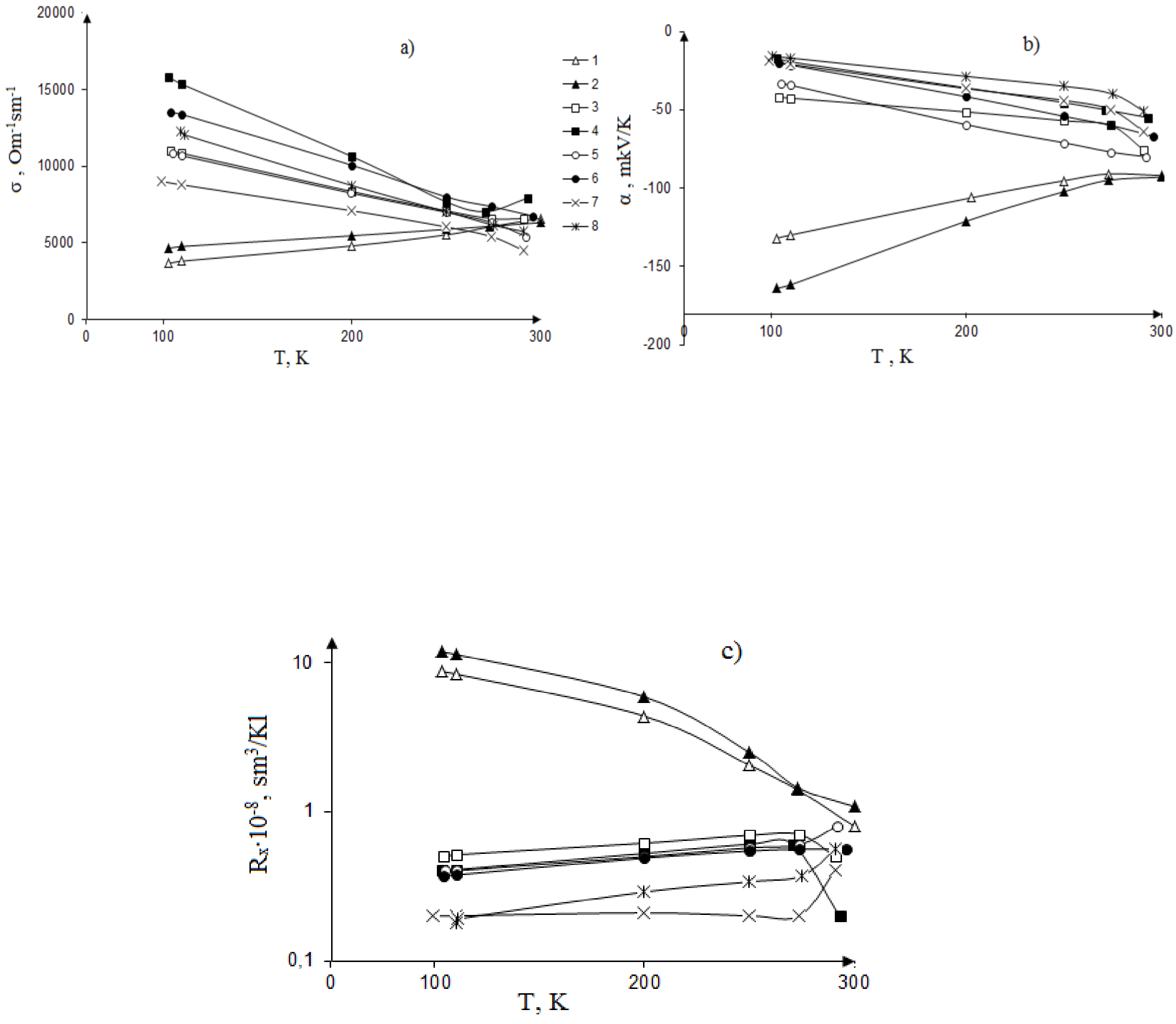

Fig.1. Temperature dependencies of conductivity (σ), thermo-e.m.f. (α) and the Hall coefficient (R_H) of extruded $Bi_{85}Sb_{15}$ samples with different grain sizes. Curves 1, 3, 5, 7 relate to samples that have not passed, and curves 2, 4, 6, 8 to the samples that have passed the post-extrusion annealing

Table 1

Dependencies of electrical conductivity σ ($Ohm^{-1}\cdot cm^{-1}$), thermo-e.m.f. α (μV/K) and Hall R_H (cm^3/C) coefficients, concentration n (cm^{-3}) and mobility ($cm^2/V\cdot s$) of extruded samples of $Bi_{85}Sb_{15}$ solid solution on the grains size

Particle size in powder, nm	At 300 K									
	Non-annealed samples					Annealed samples				
	σ, Ohm^{-1} cm^{-1}	α, μV/K	R_H, cm^3/C	μ, $cm^2/V\cdot$	n, cm^{-3}	σ, Ohm^{-1} cm^{-1}	α, μV/K	R_H, cm^3/C	μ, $cm^2/V\cdot s$	n, cm^{-3}
$2\cdot10^5$	6603	-92	1,45	9574	$4,3\cdot10^{18}$	6315	-93	3,3	20840	$1,9\cdot10^{18}$
400	6582	-76	0,34	2248	$18,4\cdot10^{18}$	7911	-55	1,13	9051	$5,5\cdot10^{18}$
32	5424	-80	1,58	8873	$4,0\cdot10^{18}$	6751	-67	1,73	9117	$3,6\cdot10^{18}$
20	4500	-64	1,45	7233	$4,3\cdot10^{18}$	5738	-51	1,49	7428	$4,2\cdot10^{18}$
At 77 K										
$2\cdot10^5$	3659	-132	8,7	31833	$0.7\cdot10^{18}$	4644	-164	11,8	54799	$0,5\cdot10^{18}$
400	10970	-42	1,71	18288	$3,6\cdot10^{18}$	15822	-17	0,76	12936	$8,2\cdot10^{18}$
32	10849	-33	0,79	8532	$8\cdot10^{18}$	13502	-20	1,39	15109	$4,5\cdot10^{18}$
20	9001	-19	1,09	9689	$5,7\cdot10^{18}$	12296	-16	0,6	5806	$10,4\cdot10^{18}$

From the data in the table also follows that the heat treatment of extruded samples greatly changes their electrical parameters. These changes are particularly strongly observed in the case of a sample on the basis of powder with 400 nm particle size. Such a change is associated with the general instability of particles of small size, mainly due to the phenomenon of re-crystallization and enlargement of particles.

To estimate the effect of boundary scattering on the lattice part of the thermal conductivity, the lattice thermal conductivity (χ_l) was calculated [19]. Figure 2 shows the dependence of the lattice thermal conductivity of samples on grain sizes at a temperature of ~ 90 K.

It can be seen that with a decrease in the grain size due to phonon scattering at the grain boundaries, the lattice part of the thermal conductivity decreases. In samples with grain sizes of ~ 20 nm, the lattice thermal conductivity is much smaller than in samples with grain sizes of $2\cdot10^5$ nm.

During extrusion, due to plastic deformation in samples of the $Bi_{85}Sb_{15}$ solid solution based on powders of various particle sizes, simultaneously occurs the formation of texture and structural defects [20].

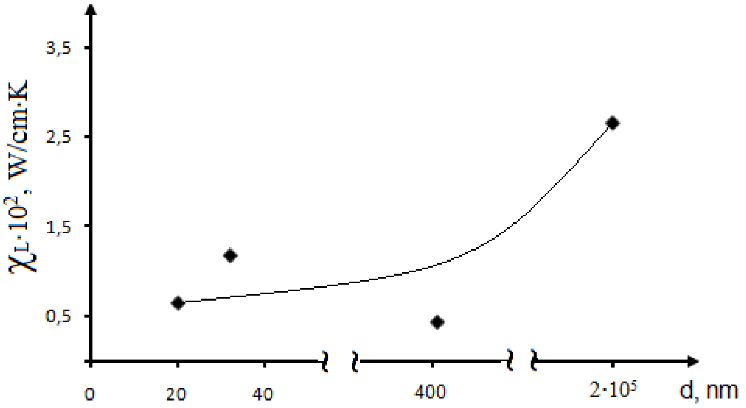

Fig.2. Dependence of the lattice part of the thermal conductivity of annealed $Bi_{85}Sb_{15}$ samples on grain sizes at ~90 K.

During heat treatment of textured samples re-crystallization occurs in them, the particles are misoriented due to thermal energy (i.e., a change in the degree of texture), and the concentration of thermodynamically non-equilibrium point defects decreases.

The degree of texture during extrusion, re-crystallization and disorientation of particles also depend on the size of the particles in the sample.

The dependencies of σ, α, R_H of nanostructured extruded $Bi_{85}Sb_{15}$ samples on the size of the initial powder and heat treatment are due to the change in the contribution of the listed factors to these electrical parameters.

4. Conclusion

Thus, extruded bulk nanostructured samples of the $Bi_{85}Sb_{15}$ solid solution were obtained. It was found that their electrical parameters and lattice thermal conductivity substantially depend on the grain size and post-extrusion annealing. The data obtained are explained by the dependence of the electron concentration, the degree of texture, re-crystallization and disorientation of the particles in the sample on the particle size, as well as phonon scattering at the grain boundaries.

References

1. Zemskov V.S., Belaya A.D., Borodin P.G. , Izv. AN USSR. Neorgan. Materials 18, 7, 1154 (1982) (in Russian).
2. Banaga M.G., Sokolov O.B., Dudkin L.D., Izv. AN USSR. Neorgan. Materials. 22, 4, 619 (1986) (in Russian).
3. Markov O.I., Advances in Applied Physics 2, 5, 447 (2014).
4. Stepanov N.P., Grabov V.M., FTP 36, 9, 1045 (2002).
5. Tagiyev M.M., Agaev Z.F., Abdinov D.Sh., Neorgan. Materials 30, 3, 375 (1994) (in Russian).
6. Tagiyev M.M., Samedov F.S., Agaev Z.F., Prikladnaya Fizika 2, 123 (1999) (in Russian).
7. Tagiyev M.M., Russian Physics Journal 60, 10, 1795 (2018).
8. Dresselhaus M.S., Chen G., Tang M.Y., Yang R., Lee H., Wang D., Ren Zh., J.P. Fleurial, Gogna P. Adv. Mater. 19, 1043 (2007).
9. Harman, T.C., Taylor, P.J., Walsh, M.P., La Forge B.E., Science 297, 2229 (2002)
10. Venkatasubramanian R., Silvota E., Colpitts T., Quinn O., Nature 413, 597, (2001).
11. Harman T.C., Taylor P.J., Spears D.L., Walsh M.P. J.Electron Mater/297 L 1-4 (2000)
12. Poudel B., Hao Q. Ma T., Lan Y. Minnich A., Yu B., Yan X., Wang D., Muto A., Vashaee D., Chen X., Liu J., Dresselhaus MS, Chen G., Ren Zh. Science 320, 634 (2008).
13. Bulat L.P., Osvenckiy V.B., Pivovarov G.I., Snarskiy A.A., Tatyanin E.V., A.A.O. Tay. Proc. VI Eur. Conf. On Thermoelectrics P.12-1 (2008).
14. Bulat L.P., Drabkin I.A., Karatayev V.V., Osvensky V.B., Pshenay-Severin D.A. FTT, 52, 9,1712 (2010) (in Russian).
15. Gusev, A.I., Nanomaterials, Nanostructures, Nanotechnologies, Fizmatlit, (2005). ISBN 978-5-9221-05828.
16. A.K. Singh (ed.), Advanced X-ray Techniques in Research and Industries. Ios pr inc 2005. ISBN1586035371.
17. Tagiyev M.M., Agaev Z.F., Abdinov D.Sh. Neorgan.materialy, V.30. No. 3, 375 (1994) (in Russian).
18. Okhotin A.S., Pushkarsky A.S., Borovikova R.P., Smirnov V.A. Methods for measuring the characteristics of thermoelectric materials and converters. M.: Science, (1974) 168 p. (in Russian).
19. Oskotsky V.S., Smirnov I.A. Defects in crystals. M.: Science, (1972).160 p. (in Russian).
20. Gorelik S.S., Dashevsky M.I. Materials science of semiconductors and dielectrics. M. Metallurgy. (1988). 574 p. (in Russian).

***Corresponding author**: mail_tagiyev@mail.ru

TEMPERATURE DEPENDENCE OF RAMAN SPECTRUM OF $CdGa_2Se_4$

TAIRA KERIMOVA, IRADA MAMEDOVA*, LATIF KENGERLINSKI,
NADIR ABDULLAEV, ZAFAR KADIROGLU, NAZIM MAMEDOV
Institute of Physics NAS Azerbaijan, ave. G.Javid, 131, AZ1143, Baku, Azerbaijan

The results of the temperature dependence of the Raman spectrum of $CdGa_2Se_4$ in the temperature range of 8 ç 300 K are presented. It is found that the half-width of the A^1 symmetry line connected with Se-breathing mode at 138, 9 cm^{-1} varies with temperature from 3,09 cm^{-1} to 5,3 cm^{-1}. It is established that the broadening of this line is connected with weak anharmonicity due to three-phonon decay.

Key words: Phonon spectrum, half-width of raman spectral line, three-phonon processes, acoustic phonons, anharmonicity, $CdGa_2Se_4$
PACS: 63.20.Ry; 63.20.Kr; 78.30.−j

1. Introduction

Knowing the phonon spectra, their dependence on temperature, pressure and other external factors are important for explaining the mechanisms of heat capacity, thermal expansion, thermal conductivity, sound absorption, etc. Joint theoretical and experimental studies of phonon spectra, lattice dynamics provide information about the phonon frequencies at the point Γ(000) of Brillouin zone (BZ) and interatomic bond constants, phonon-phonon, phonon-electron interactions, etc.

In harmonic approximation, the frequency of vibrations in a solid state does not depend on the interatomic distances. However, change in the frequency of optical phonons with temperature and pressure are observed experimentally. These effects are called anharmonic.

It is known that, the dependence of the frequency of an optical phonon and its line half-width on temperature is caused by two effects - thermal expansion of the lattice and scattering of phonons on phonons and lattice defects. Therefore, by studying of the temperature dependence of the frequencies of optical phonons, one can obtain information on the anharmonicity of interatomic interactions in a solid state. For this purpose, the Raman spectra of $CdGa_2Se_4$ were investigated in the temperature range of 8 ç 300 K.

2. Experiment

The measurements of the Raman spectra in the given temperature range were carried out on a set-up assembled on the basis of a DFS-24 spectrometer. The YAG: Nd infrared spectrometer (λ = -1.064 μm) was used as the excitation source. A photomultiplier tube FEU-79, operating in the photon counting regime, was used as a radiation detector. The temperature of the samples was controlled by a Constantan thermocouple. Single crystals were obtained by the gas transport reactions method. Crystalline iodine was used as a transporter. The grown crystals were subjected to x-ray analysis. The lattice parameters were determined a = 5,574E, c = 10,756E, c / a = 1,873. These results agree with the data of [1].

3.Results and discussion

In the Raman spectra of $CdGa_2Se_4$, with the temperature rises from 8K to 300K, no significant changes occur. The absence of a soft mode in the investigating temperature range confirms the conclusions [2] on the absence of structural phase transitions.

On the other hand, the width of the Raman lines in $CdGa_2Se_4$ increases with temperature from 8 K up to 300 K. Table 1 shows the widths of the intensive Raman line connected with Se- breathing mode at 138,9 cm^{-1}.

Tab.1 Temperature dependence of the half-width values of the Raman line at 138,9 cm^{-1} in the temperature range 8 ç 300 K

T, K	8	20	70	208	300
Half-width of line, (cm^{-1}) ω = 138,9 cm^{-1}	3,09	3,31	3,5	4,72	5,3

In the general case, the phonon damping coefficient γ consists of two components $\gamma = \gamma_a + \gamma_d$, where γ_a- damping, caused by phonon scattering on lattice defects [3]. γ_d is the damping due to phonon anharmonicity.

The temperature dependence of the line widths can be described quantitatively in the framework of a simple anharmonic model, which includes only three-phonon processes, when a phonon with frequency ω_0 undergoes decay into two phonons with frequency $\omega = \omega_0 / 2$ with opposite wave vectors. In this case, the temperature dependence of the line width in the Raman spectra is described by the following expression [4].

$$\Gamma(T) = \Gamma(0)\left[1 + 2\left(e^{\frac{\hbar\omega_{\phi}}{2kT}} - 1\right)^{-1}\right] \qquad (1)$$

where Γ (0) is the line width at 0 K. This model describes well the three-phonon silicon processes [4], GeS [5]. However, the attempt to describe the change of the Raman line with temperature in the framework of three-phonon processes in $CdGa_2Se_4$ was not successful. Fig. 1 presents the temperature dependence of the half-width of the phonon line of Γ_1 symmetry (138,9 cm^{-1}). The dashed curve is calculated by the expression (1).

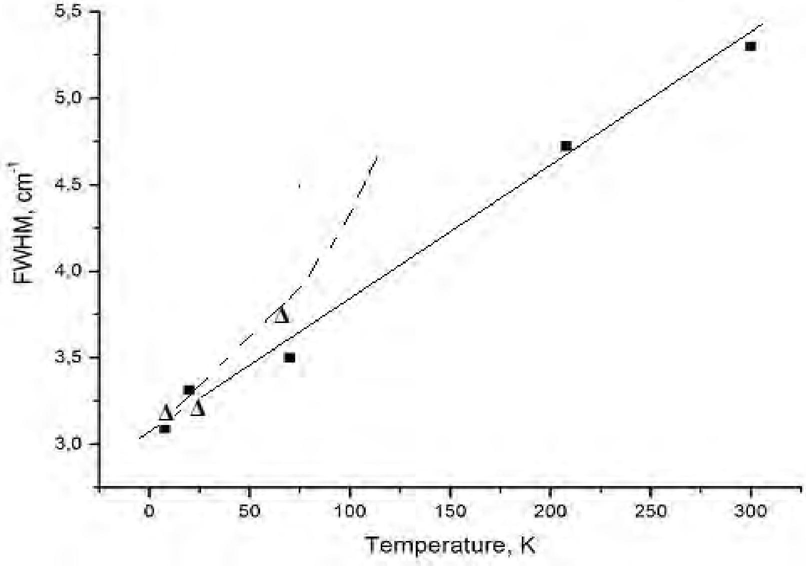

Fig. 1 Temperature dependence of half width of Raman line at 138,9 cm^{-1} (dashed line with triangles is derived from Eq. (1), full square- experiment)

It can be seen that the experimental points, with the exception of lower temperatures, do not fit the calculated curve and suggests that the temperature dependence of the change in the Raman line width of $CdGa_2Se_4$ cannot be described in terms of three-phonon processes. These results indicate a weak anharmonicity in the range of 8–300 K, i.e. the probability of three-phonon processes is small. A weak asymmetry of the Raman line at 138,9 cm^{-1} is observed, which also indicates a weak anharmonicity. In favor of such conclusion one can also lead the following: In $CdGa_2Se_4$, the half-width of the Raman line in 138,9 cm^{-1} in the temperature range 8ç300 K changes approximately 1,5-1,8 times, whereas in GeS [5], when the temperature changes from 80 to 300 K, the width of the Raman line at 242 cm^{-1} changes three times. In $ZnGa_2Se_4$ and $MnGa_2Se_4$ [6], the Raman lines at 143 cm^{-1} and 135 cm^{-1}, respectively, changes four times in the temperature range 4-300K.

In compounds with an ordered vacancy, the broadening process is explained by two factors: the anharmonic potential affecting the Se-vacancy breathing mode, due to the presence of an ordered vacancies in defect-chalcopyrite structures and a high density of 2TA (X) modes in zinc-blende compounds [7]. Therefore, in our case, in $CdGa_2Se_4$, the line broadening can be explained by the anharmonic phonon decay at 138,9 cm^{-1} into two acoustic phonons at ~ 70 cm^{-1} at the edge of the Brillouin zone. First principle calculations of the phonon density in $CdGa_2Se_4$ of throughout Brillouin zone revealed a high density of acoustic branches at X, P points of the zone [8]. Authors [9], also discussing the temperature broadening of the raman line at 138 cm^{-1} in $CdGa_2Se_4$ and 145 cm^{-1} in $ZnGa_2Se_4$ at temperatures 300 K and 570 K, concluded that the broadening is due to anh armonism of the oscillators.

4. Conclusion

In conclusion, it can be noted that a joint analysis of the literature data led to the conclusion that with a temperature from 8 K to 300 K, the broadening in the Raman A^1 symmetry line at 138,9 cm^{-1} $CdGa_2Se_4$ is due to a weak anharmonism, connected with the three-phonon decay and natural defects in crystal lattice.

Acknowledgment

The work was done with the financial support of the Foundation for the Development of Science under the President of the Republic of Azerbaijan (Grant No. EIF-BGM-3-BRFTF-2 + / 2017-15 / 02/1).

References

1. Hahn H., Frank G., Klinger W., Storger A.D., Storger G., Z. Anorg. Allg. Chem. 279, 241(1955)
2. Mamedov R.R., Aliev M.M., Kerimov I.G., Nani R.Kh., Phys.Stat.Sol.(a) 9, K149 (1972)
3. Vodopyanov L.I., Vinogradov E.A., Kopitov V.V., Mityagin Yu.A., Physics of the Solid State 16, 1419 (1974)
4. Hart T.R., Aggarval R.L, Benjamin Lax, Phys.Rev.B1, 2, 638 (1970)
5. Qolubev L.V., Vodopyanov Y.K., Proceedings of MPTI, 11, 53 (1979)
6. Alonso-Guitierrez P. and Sanjuan M. L., J. of Physics: Conference series 92, 012150 (2007)
7. Alonso- Guitierrez P. and Sanjuan M. L. Physical Review B 76, 165203 (2007)
8. Dzhakhangirli Z.A., Kerimova T.G., Abdullaev N.A., Mamedova I.A., Mamedov N.T., physics and techniques of semiconductors (Semiconductors) 51, N.5, 585 (2017)
9. Radautsan S.I., Tiginyanu I.M., Ursaki V.V., Fomin V.M., and Pokatilov E.P., Phys.stat.sol.(b) 162, K63 (1990)

[*] **Corresponding authors:** irada_mamedova@yahoo.com

THE STRUCTURAL FEATURES OF P(VDF-TeFE)/Si COMPOSITES MODIFIED BY GAMMA-RAYS

[2]I.M. NURUYEV, [1]A.M. MAHARRAMOV, [1]R.N. MEHDIYEVA, [1]M.A. NURIYEV
[1]1The institute of Radiation Problems of ANAS, AZ1143, B.Vahabzadeh 9, Baku, Azerbaijan
[2]Center for Strategic Scientific Research of ANAS,AZ1001, Baku, Istiglaliyyat st., 30

On the basis of comparative analysis of the IR spectra of Initial and gamma irradiated composites obtained on the basis of copolymers of polyvinylidene fluoride tetrafluoroethylene (P(VDF-TeFE)) and Si nanoparticles, we investigated the causes of changes in their structure.

Based on the analysis of IR spectra obtained before and after the gamma radiation of P(VDF-TeFE)/nano-Si composites, shown that the crystallization rate of the system is increasing as a result of the interaction of the active centers formed on the matrix with the surface of Si nanoparticles on the interphase boundary. The optical properties of P(VDF-TeFE)/nano-Si composites based on the P(VDF-TeFE) polymer is varied depending on the amount of filler and the dose of radiation, and this change provides the observed changes in the electrophysical properties of the composites.

Keywords: P(VDF-TeFE)/Si composites, gamma-rays, polyvinylidene fluoride tetrafluoroethylene, nanocomposites, Silicon filler, IR-spectra
PACS: 61.80Ed; 72.80Tm; 61.46+w;

1.Introduction

In modern time, the development of electronics and electrotechnics requires the creation of thin layers or composite materials that have electroactive properties. The study of changes in the structure after the change of technological parameters, composition, and the effect of gamma radiation is one of the actual problems of material science [1, 2]. Comparative analysis of IR-spectra of polymers and nano-dimensional filler-based composites allowing the discovery of relationships and hybrid communications, their structure, the difference between amorphous and crystalline phases, and inter-phase interaction between components. The typical frequencies of inter-component vibrations in the IR spectrum of the composites also depend largely on the chemical composition of the sample and the properties of the polymer matrix [3-6].

The study of polyvinylidene fluoride polytetrafluoroethylene copolymer P(VDF-TeFE) and composites based on them by IR spectroscopy allows for very interesting results in this approach. This copolymer has electroactive (piezo, - pyroelectric and electret) properties. According to his analysis of the IR spectrum given in his scientific literature, the dance of some groups of polymer chains is general for polymers both β and γ phases and the vibrations of other groups are associated with the amorphous phase of the polymer [3,7]. The classification of IR absorption strips characterizing by α, β and γ phases has been widely described in scientific literature [3,7,8]. In addition, depending on the preparation conditions, the same film may have one or more different crystalline structures. In general, peaks 489, 614, 766, 795, 855 cm^{-1} for α - phase and the peaks of 470, 510, 600, 745, 840, 1180, 1235 cm^{-1} are characteristic for β phase, but peaks 431, 512, 776, 812, 833, 1234 cm^{-1} for γ- phase are typically in PVDF and its copolymers. [9-12].

On the basis of comparative analysis of the IR spectra of Initial and gamma irradiated composites obtained on the basis of copolymers of polyvinylidene fluoride tetrafluoroethylene (P(VDF-TeFE)) and Si nanoparticles, we investigated the causes of changes in their structure.

2.Methodical part

For the sampling, firstly, 5% solution is prepared of P(VDF-TeFE) powder in acetone (C3H6O). For this purpose, the polymer and the acetone at a certain weight ratio in a closed container, mixed with intervals in the magnetic mixer until the solution is taken. For this purpose, obtained polymer and acetone at a specific weight ratio in a closed container, mix with intervals as long as the solution is taken in the magnetic mixer. In the 5% solution of P(VDF-TeFE), the soluble polymer is added to the nano-Si powder for a long time and mixed with the help of magnetic mixer. Finally, mixing the mix with vibro shaker at intervals of 1 hour and maintaining a 24 hour hermetically sealed condition for large-scale agglomerates collapse. The top, bottom, and relatively transparent part of the prepared solution, which stored within the day is filtered into Petri dishes and the solvent is dried until completely evaporated. In order to form more stable structure from the obtained composite layer, samples are prepared by thermal pressing at T=190ç200 ºC and P=10 MPa pressure. The quantity of filler in the composite is calculated based on the weight difference of the initial polymer and the composite. For the obtained by adding 2%vol nano-Si composites quantity of filler was~1.0% volume.

The IR spectra of P(VDF-TeFE) and its basis P(VDF-TeFE)/nano-Si samples were plotted at the range of 400-4000 cm^{-1} in the wave number (phase frequency) with the help of the Varian 640-IR FT spectrophotometry. Modification of composite samples was at room temperature (T=20°C) with gamma radiation was performed on the MPX-γ-25M device with ^{60}Co isotope.

3.Results and discussion

Now let's analyze IR spectroscopic spectra of samples of P(VDF-TeFE) and P(VDF-TeFE)/nano-Si composites taken by thermal pression. For this purpose, let's first analyze the IR spectrum of the P(VDF-TeFE) copolymer (Fig. 1). In the spectra, 440-600, 800-900, 1000-1450 cm^{-1} absorption strips characteristic of P(VDF-TeFE) are observed. There are three maximum wavelengths 509, 840, and 1279 cm^{-1} belonging to the β phase of the polymer in the IR spectrum. The peak around the 509 cm-1 wavelengths corresponds to δCF$_2$ vibrations (deformational vibrations of CF$_2$ groups) and the peak around the 840 cm^{-1} wavelengths corresponds to rCF$_2$+νsCC vibrations. There are a lot of peaks characterizing specific vibrations CF, CF$_2$, and in the range 1000-1400 cm^{-1} in the spectrum of the P(VDF-TeFE) sample. There are strong maxima for the vibrations of CF$_2$ connections at the band 1120-1280 cm^{-1}.

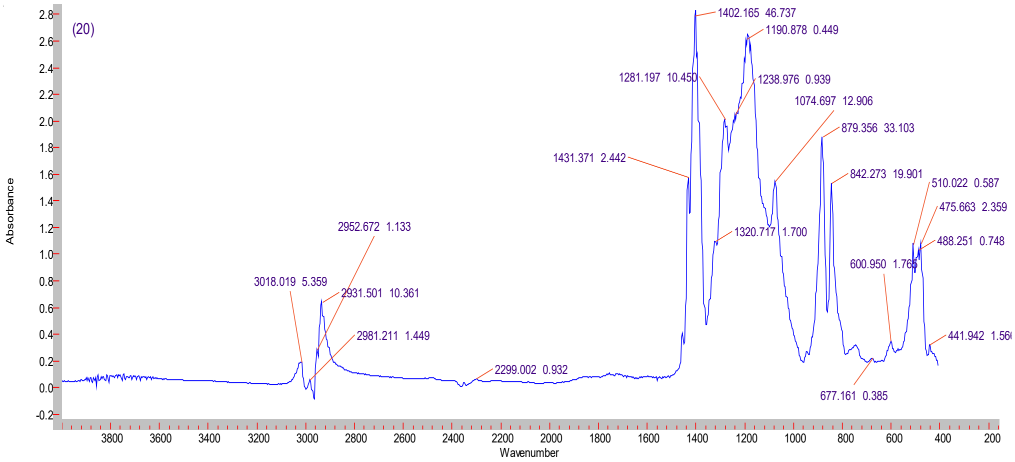

Fig.1. The IR spectrum of thecopolymer of P(VDF-TeFE)

It is known that, the crystalline β-phase of the P(VDF-TrFE) polymer is characterized by a conformational-sensitive absorbing mainly strip ~840 cm^{-1}. It is known that the crystalline β-phase of the P(VDF-TeFE) polymer is characterized by a conformational-sensitive absorbing mainly strip ~840 cm^{-1} and comparison of its intensity with the intensity of non-sensitive conformational ~880 cm^{-1} absorption strip allows estimating the amount of crystalline phase in the structure. [9,12-16].

Now, analyze the IR spectrum of the P(VDF-TeFE)/1% nano-Si composite (Fig. 2a). Comparing the IR spectrum of P(VDF-TeFE)/1% nano-Si composites to the IR spectrum of P(VDF-TeFE), we see that the intensity of the peak of 841 cm^{-1} has increased. Besides, the spectra also have new absorption strips 487, 1020, 1080, 1134, 1204 and 1280 cm^{-1}, which only can be explained by the presence of the filler. We hope that Si nanoparticles in the P(VDF-TeFE)/nano-Si composites participate as crystal centers in the matrix, which increases the intensity of the maxima crystallization phase in the spectrum [18]. On the other hand, the active interaction between the polar groups in the matrix and the highly effective surface of the nano-silica results in the emergence of new stripes in the IR spectrum.

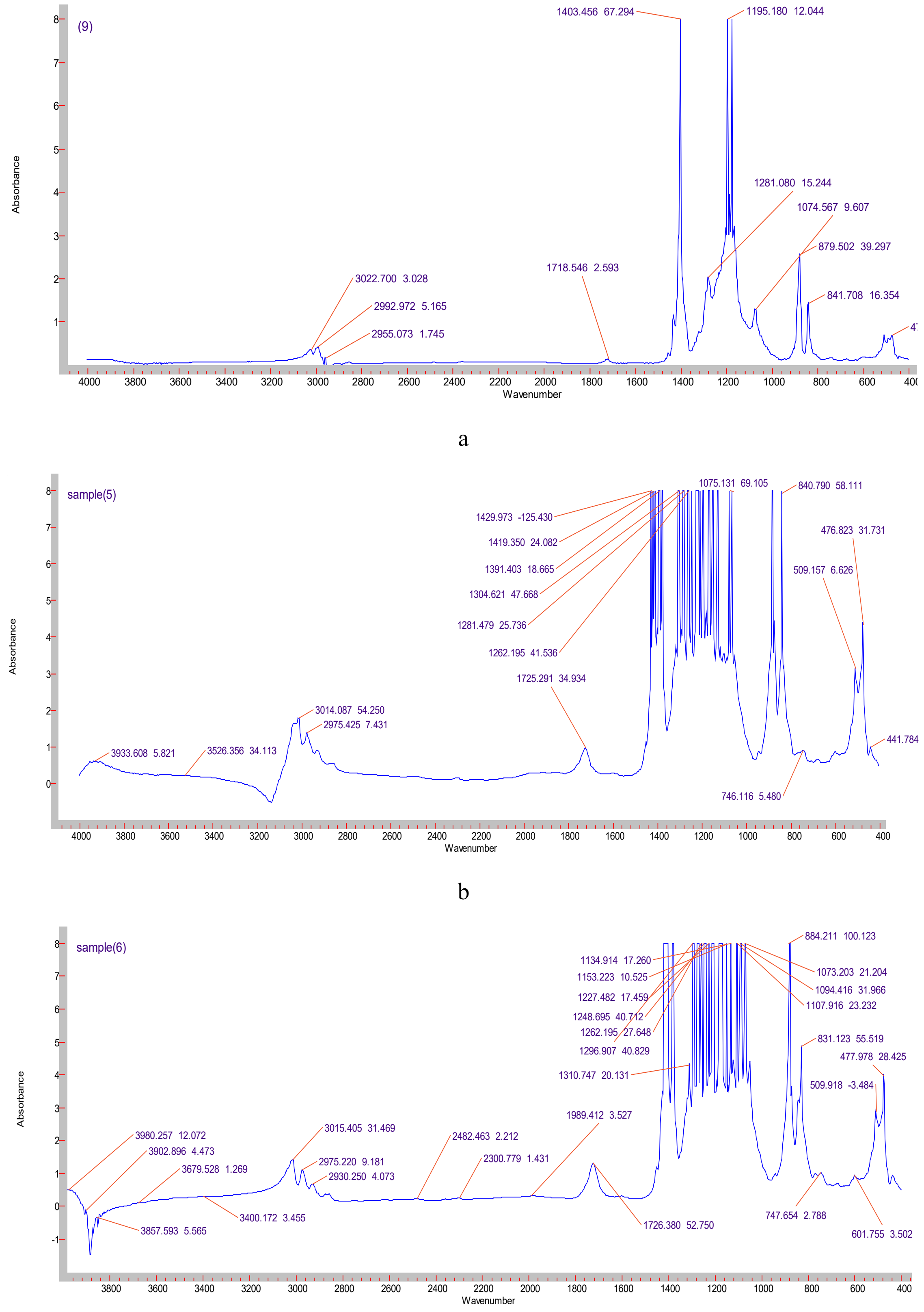

a

b

c

Fig. 2. IR spectra of initial (a) and P(VDF-TeFE)/1% nano-Si composites (b and c) modified with gamma rays: b- D = 300 kQy; c- D = 500 kQy;

As we know from the literature, the new 487, 951, 1020, 1080, 1134, 1204 and 1280 cm^{-1} frequency absorption strips observed in the IR spectrum of composites characterize vibrations and interaction effect of relations Si-H and Si-O-Si [17,19]. 761, 1069 and 1086 cm^{-1} absorbing strips in the spectrum of the composite indicate the presence of Si-O-C (1069 and 1086 cm^{-1}) and Si-C (761 cm^{-1}) connections [20].

The effects of ionizing radiation on these materials are very important from the control point of view of their properties. The effect of ionizing radiation on polymers observed by a number of processes such as crosslinking, destruction, and oxidation, depending on the power of the absorbed dose. In composites depending on the amount and type of filler, these processes are delayed or intensified. On the other hand, ionizing radiation is often used for the modification of materials ie, for managing properties of interest [1,2,8,10]. Therefore, the effect of gamma radiation on the composites we have investigated is very important from the point of view of relevance and the results of these studies have been summarized below. Structural changes occurring from the effects of gamma radiation in composites were carried out according to the results of comparative analysis of IR spectra before and after radiation (Fig.2). The results of the analysis are presented in Table 1.

Table 1

Changing of intensity for Si-C (761±5 cm^{-1}), Si-O-Si (1075±10 cm^{-1}) and Si-O-C (1069 and 1086 cm^{-1}) and C=O (1710-1740 cm^{-1}) bonds in IR spectrum of initial and irradiated P(VDF-TeFE)/1.0% nano-Si samples

D, kQy			0	100	300	500
№	K, cm^{-1}	Φ, volume %	I	I	I	I
1	761	~1,0	0,739	1,68	2,82	3,47
2	1075±10	~1,0	9,61	37,39	69,1	21,2
3	1710-1740	~1,0	2,6	14,83	34,9	52,7

We used the results of the change in the location and intensity of C=O carbonyl groups corresponding to the range 1710-1740 cm^{-1} in IR spectra of initial and irradiated composite samples to evaluate the structural changes in the P(VDF-TeFE)/nano-Si composite.

The table shows that, in the IR spectrum the samples P(VDF-TeFE)/1,0% nano-Si have the double C=C connections and C=O carbonyl groups due to breaks at the end of the polymer chain after irradiation. The emergence of these groups shows itself in increasing the intensity of the absorption strip in the spectrum between the ranges of 1720-1740 cm^{-1}. As expected, the intensity of maximal vibrations of C=O carbonyl groups increased when the increases of radiation dose rate. The kinetics of increment is high around the 1725 cm^{-1} wavelength (the maximum intensity) depending on the absorbed dose rate. We assume that this is due to the lower concentrations of concentrates and polymer destruction, and fast formation of C=O carbonyl groups due to oxidation.

During the gamma radiation of polymer, electron greed of fluorine in the chain of the polymer causes to break the C-F connections, decrease in the number of CF$_2$ groups and transforming some of them into the $\dot{C}F$ radical. The recombination of these radicals in the matrix results in the formation of inter-chain structure. The inter-chain connections increase the rigidity of the polymer matrix due to the increased Si-O-C (1069 and 1086 cm^{-1}) and Si-C (761 cm^{-1}) connections as well as Si-O-Si (1075±10 cm^{-1}) bonds resulting in an increase in the crystal phase in the interaction of the active centers in the matrix-nanoparticle interphase boundary. In the IR spectrum of the P(VDF-TeFE)/nano-Si system, an increase in the intensity of the 509 cm^{-1} and 840 cm^{-1} absorption strips characterizing crystalline β-phase on the matrix is evidence for that [9,19]. There is observed a decrease in the intensities of both Si-O-Si and Si-O-C (1069 and 1086 cm^{-1}) bonds passing through the peak at 300 kGy dose by the increase of dose for P(VDF-TeFE)/1,0% nano-Si samples. When the dose increase to 500 kQy, there are decreasing of Si-O-C bands (1069 and 1086 cm^{-1}), relative increasing of Si-C (761 cm^{-1}) bonds and an increasing in the corresponding intensities.

4. Conclusions

Thus, by summarizing all these statements, we can conclude that, based on the analysis of IR spectra obtained before and after the gamma radiation of P(VDF-TeFE)/nano-Si composites, we can say that the crystallization rate of the system is increasing as a result of the interaction of the active centers formed on the matrix with the surface of Si nanoparticles on the interphase boundary. The optical properties of P(VDF-TeFE)/nano-Si composites based on the P(VDF-TeFE) polymer is varied depending on the amount of filler and the dose of radiation, and this change provides the observed changes in the electrophysical properties of the composites.

References

1. Vannikov A.V., Matveev V.K., Sichkar V.P., Tyutnev A.P., Radiation Effects in Polymers.Electricproperties, Moskow, Science,1982, 272p.
2. Tyutnev A.P., Saenko V.S., Pozhidayev E.D., Kostyukov N.S.,The dielectric properties of polymers in the fields of ionizing radiation.,Moskow, Science, 2005, 453 p.
3. KochervinskiiV.V., PavlovA.S., KozlovaN.V., ShmakovaN.A., Vysokomolekulyarnye Soedineniya. Ser. A, 56, 509, (2014)
4. Sitnikova V.E., Spectroscopic study of the structure of polymer dispersion systems, dissertation abstract for the PhD of chemical sciences, 23, (2015)
5. Gregorio Jr. R. and Borges D. S., Polymer, 49, 4009, (2008)
6. Z.Li, B.Hou, Y.Xu, D.Wu, Y.Sun, W.Hu, F.Deng, J. Solid State Chem., 178, 1395, (2005)
7. Janakiraman S., Surendran A., Ghosh S., Anandhan S., Venimadhav A., Solid State Ionics, 292, 130,(2016)
8. Maharramov A.M., Proceedings of the Academy of Sciences of Azerbaijan, series. Phys.-Mat. and tech. Sciences, 19, 171, (2000)
9. Kochervinsky V.V., Uspeximii,65, 936, (1996)
10. Magerramov A.M., Nuruev I.M., VI Russian Conference "Actual Problems of High Energy Chemistry", 236, (2015)
11. Brzhezinskaya M.M., Morilova V.M., Baitinger E.M., Evsyukov S.E., Pesin L.A., Polymer Degradation and Stability, 99 (2), 176, (2014)
12. Sencadas V., Costa C.M., Moreira V., Monteiro J., Mendiratta S.K., Mano J.F., e-Polymers – № 002, 1, (2005)
13. Magerramov A.M., Sherman M.Ya., Lesnykh O.D., Korchagin A.G., Turyshev B.I., Vysoko molekulyarnye Soedineniya, 40A, 982, (1998)
14. Ghosh S. K., Alam M. M. and Mandal D., RSC Adv., 4, 41886, (2014)
15. Kim J.W., Cho W.J., Ha C.S. Morphology, Journal of Polymer Science Part B: Polymer Physics,40, 19, (2002)
16. Prest Jr W. and Luca D., J. Appl. Phys., 49, 5042, (1978)
17. Murashkevich A. N., Lavitskaya A. S., Barannikova T. I., Zharskii I. M., Journal of Applied Spectroscopy, 75, 730, (2008)
18. XiaomeiCai, Tingping Lei, DaohengSund, Liwei Linde, RSC Adv., 7, 15382, (2017)
19. Smith A.,Prikladnaya IK spektroscopiya. Translation from English. Moskow, Mir,(1982), 328p.
20. Efimova A.I., Infrokrasnaya spectroskopiya nanostructurirovannikh polyprovodnykov I dyelektrykov, Faculty of Physics, Moscow, (2014), 41p.

[*] **Corresponding author: nuruyev_ibrahim@mail.ru**

THE DESTRUCTION OF TRANSPARENT DIELECTRICS UNDER THE ACTION OF LASER RADIATION

V.M. SALMANOV[1*], A.G.GUSEINOV[1], A.A.SALMANOVA[2], R.M.MAMEDOV[1]
[1]*BakuStateUniversity, Z.Khalilov str., 23, Baku, Azerbaijan, Az1148*
[2]*Azerbaijan State University of Oil and Industry, Azadliqave. 20, Baku, Azerbaijan, AZ1010*

Was experimentally investigated the destruction of transparent dielectrics under the action of laser radiation. Ruby and neodymium lasers operating in single-pulse and peak-generation modes were used as the radiation source. It is shown that under the action of high-power laser radiation in transparent dielectrics visible damage occurs. The effect of the wavelength, duration and energy of a light pulse on the nature of the damage has been studied. It is established that optical damage in the studied dielectrics is caused by optical inhomogeneities, which are opaque inclusions, in sizes from microns and above.

Keywords:polymethylmethacrylate laser radiation, destruction, optical inhomogeneities.
PACS: 72.40. +w, 72.80.Ey

1.Introduction

From numerous publications on various scientific and technological applications of lasers, it is known that laser radiation has a super-strong electromagnetic field much higher than the intra-atomic electric fields E_a ($E_a \sim 10^9$B/cm). If you focus a laser beam that transfers energy E in time τ (pulse duration) to a spot with area S, then the generated energy flux density will be determined by the formula

$$q = \frac{E}{s\tau}.$$

It can be seen that it can be increased by increasing the beam energy and (or) reducing the duration of the laser pulse. From a technical point of view, it seems quite affordable to receive energy in the beam of ~ 10^3 J for times less than picosecond (10^{-12}s), although lasers with energies of several megajoules (~ 10^6J) and femtosecond durations (10^{-15}s) and even attoseconds (10^{-18}s) The reduction of the focal spot area is limited by diffraction - its minimum area is approximately equal to the square of the laser wavelength λ (for visible light it is ~ 10^{-8} cm^2). So, with the help of a laser, the beam of which focuses on a spot of such an area, it is possible to obtain energy flux densities of more than 10^{28} W / cm^2 (E ~ 100kJ, S = 10^{-8} cm^2, τ ~ 10^{-15}s). At such high intensities, various non-linear effects of interaction of radiation with matter begin to play a significant role, and the usual mechanisms for the absorption and scattering of light acquire a specific color due to the large specific energy release (~ 10^{10} J / cm^3).

At present, these phenomena attract much attention of researchers, and they consider both the specifics of the interaction of intense electromagnetic radiation with matter and applied questions in connection with the development of new technological operations, improvements in laser technology and the creation of protection against optical damage to equipment. In this connection, the question of the behavior of a solid medium under the influence of a powerful laser beam inevitably arises. Already in the lasers themselves, the active elements, the mirrors of the optical resonator, are exposed to laser radiation; in optical systems, the presence of lenses, light filters, etc. cannot be ignored.

It should be noted that since lasers were invented almost 60 years ago, researchers tried to create more intense pulses. However, by the mid-1980s, the road was complete. For short pulses it was almost impossible to increase the intensity of light without destroying the reinforcing material.

French scientist Gerard Moore and Canadian scientist Donna Strickland paved the way for the shortest and most intense laser pulses. A new method created by them, almost revolutionized laser technology. This allowed the radiation of very intense, short pulses of light, using a complex method to avoid the risk of destruction of the reinforcing material, instead of amplifying the light pulse directly, it first stretches in time, reducing its peak power, then the pulse is amplified, and when it is compressed, more light is collected in the same place - the light pulse becomes extremely intense. It was for this discovery that Gerard Moore and Donna Strickland, together with the American scientist Arthur Ashkin, who invented the “optical tweezers”, received the Nobel Prize in Physics for 2019 [1].

Experiments have shown that the effect of high-power laser radiation on a solid target in a very large number of cases does not remain without a trace for materials, leading to more or less significant damage. Therefore, an independent study of the destruction of solids under the action of intense laser radiation and, in particular, the question of the destruction of transparent materials is of great scientific and practical interest.

This paper is devoted to the experimental study of the optical damage of transparent materials under the action of laser radiation.

2. Experiment

Transparent dielectrics, polymethylmethacrylate(PMMA), polystyrol and plexiglass were chosen as objects for the study. The samples were parallelepipeds with polished edges and sizes varying in length from 0.1 to 25 cm and a cross-sectional area from 1 to 25 cm^2. Studies were carried out on neodymium ($\lambda = 1.06$ μm) and ruby ($\lambda = 0.69$ μm) lasers [2]. The use of both types of lasers was due to the desire to find out the effect of polarization and the wavelength of radiation on the nature of the damage. However, since it turned out that the qualitative nature of the destruction does not depend on the material of the working rod of the laser, the bulk of the experiments were later performed by a neodymium laser operating as in the peak generation mode (the duration of the light pulse $\Delta t = 5\cdot10^{-4}$s, $W = 1.2\cdot10^2$W/cm^2) in the mono-impulse mode ($\Delta t = 3\cdot10^{-9}$ sec, $W = 1.2\cdot10^7$ W/cm^2). The laser radiation was usually focused inside the sample, sometimes the focus was brought to the surface or outside the material. Some experiments were carried out in a parallel light beam. The nature of the damage was examined under a microscope, and the magnitude of the area of destruction was measured using a horizontal comparator.

3. Results and discussion

When exposed to samples of polymethylmethacrylate by laser radiation in them when energy flows in a pulse exceeding certain critical values, visible damage occurs [3]. First of all, it is necessary to note a significant difference in the nature of the damage during normal and giant impulses. An ordinary pulse in PMMA forms flat cracks located approximately at an angle of 45^0 to the axis of the laser beam and randomly distributed relative to the rotation of the plane of the crack around this axis (Fig. 1a). At energies of the beam, substantially large threshold, the number of cracks is large - several dozen, and they are separated from each other by areas of intact material up to several millimeters long and more. The destruction in PMMA caused by the focusing of a giant pulse has characteristic features. The area of destruction has the form of a strongly elongated cone consisting of very small (0.1-0.5 mm) cracks, the density of which gradually increases as it approaches the focus. In the area of focus, the number of cracks is usually so large that they form an area of continuous destruction (Fig. 1, b).

ab

Fig.1. Destruction by ordinary (a) and giant (b) impulses polymethyl methacrylate.

It should be noted that the results obtained by us are in satisfactory agreement with the results of the works of J. Moore and D. Strickland [1]. As shown by the authors of [1], short pulses of a femtosecond (10^{-15} s) laser cause less damage to the material than a million times more pulses of a nanosecond (10^{-9} s) laser.

As the experimental results showed, the features of the structure and mutual arrangement of the foci of destruction are to a certain extent determined by the kinetics of the propagation of the front of the area of destruction and the evolution of the development of a separate center of destruction. To obtain information on the kinetics of fracture development, we studied the effect of the intensity of the feeding beam on the magnitude and temporal nature of the light pulse transmitted through the sample [4].Figure 2,a shows a typical transmittance curve in PMMA for a typical pulse. As can be seen from the figure, in a very wide region of the intensity of the incident light, the light transmission remains almost unchanged.

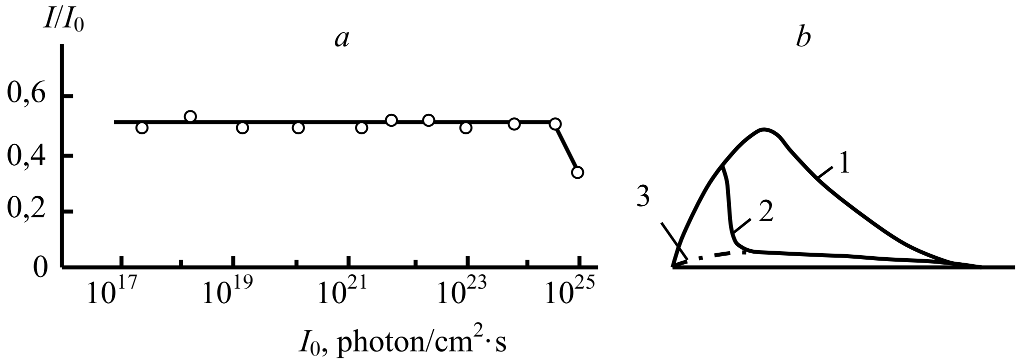

Fig. 2. a- Dependence of the relative transmittance of light on the intensity of the incident light; b - Oscillograms illustrating the kinetics of destruction: 1-momentum of transmitted light at energies below critical; 2 is the same with energy, more critical; 3- the same with repeated exposure.

With some intensity critical for a given substance, it drops sharply, and this moment coincides with the avalanche-like destruction of the substance. Figure 2, b shows oscillograms reduced to the same size, from which it can be seen that the destruction causes an almost complete shielding of the light beam and has time to develop during the pulse. Naturally, with a repeated light pulse (even of a very low intensity), the intensity of the transmitted beam corresponds to the transmission of the destroyed material (curve 3 in Fig. 2, b). This further indicates that the intensity decrease in the oscillogram of Fig. 2, b due to the development of destruction.

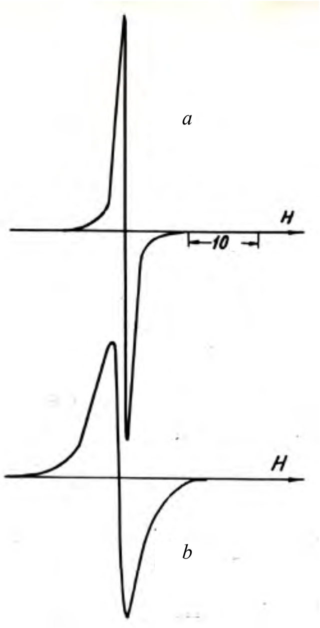

Fig.3. EPR spectra of PMMA laser irradiated.

When examining the original samples under a microscope in transmitted light, many inclusions in the size from microns and above were detected in them. Direct experiments have shown that on these inclusions there are pockets of optical damage to the material. The formation of the area of destruction occurs during the action of the light pulse. If the light beam is focused, the first foci of destruction appear in the area of focus; then their number grows in the opposite direction of the beam.

Along with the study of the nature, kinetics and statistics of the destruction of polymers under the action of a laser beam, we also investigated a number of secondary phenomena accompanying destruction. From this point of view, the effect of the appearance of paramagnetic centers in PMMC is of particular interest [5]. It was found that after exceeding a certain threshold value of the energy density, a distinct electron paramagnetic resonance (EPR) appeared. The EPR spectra recorded at both nitrogen and room temperature are singlet lines (Fig. 3). The lines are characterized by “g” factors close to 2.002 and have a small width.

For EPR signals in PMMC, the Curie law is well satisfied; magnetic susceptibility $\chi > 0$ and depends on temperature $\chi = \frac{c}{T}$ (T is the absolute temperature, c is a constant, depending on the type of substance). According to our estimates, the concentration of paramagnetic centers reaches 3 Ç 10^{15} cm^{-3}. The observed paramagnetic centers are very stable. So, for example, in PMMA, a noticeable decrease in the intensity of the EPR signal is not detected during long-term storage of samples at room temperature (about 500 hours), or when heated in oil to 200-230^{0}C for several minutes. At the same time, the fragmentation of samples in air or in liquid nitrogen leads to a significant decrease in the EPR signal, and the dissolution in dichloroethane leads to the complete disappearance of paramagnetic centers.

No difference was found in the magnitude and shape of the EPR signal when the samples were irradiated with light from ruby and neodymium lasers operating in the normal mode. The effect of ordinary and giant pulses (neodymium laser) was also identical. It is very significant that the appearance of paramagnetic centers takes place only when visible cracks form in the irradiated samples. Quantitative measurements made it possible to establish that the threshold in crack formation always, in our experiments, coincided with the threshold for the appearance of EPR. Turning to the question of the nature of the observed paramagnetic centers, it can be assumed that they are the products of a peculiar decomposition of polymers under the action of high-power laser radiation and high local temperatures developing in cracks. As such products one can imagine, for example, carbonation products or molecular ions.

4. Conclusion

It was found that when laser radiation acts on transparent dielectrics, when energy flows in a pulse exceeding certain critical values, visible damage occurs. Direct experiments have shown that the formation of a fracture region takes place during the action of a light pulse and the centers of destruction occur on micro-inhomogeneities, which have a lot of quantity in the starting material. The emergence of paramagnetic centers in PMMA exposed to laser radiation has been detected. It is assumed that the observed paramagnetic centers are products of a peculiar decomposition of polymers under the action of high-power laser radiation and high local temperatures developing in cracks. As such products one can imagine, for example, carbonation products or molecular ions.

References

1. Veiko V.P.Power optics M .: Fizmatlit, 312, (2008).
2. HuseynovA.G., SalmanovV.M., MamedovR.M., SalmanovaA.A., AhmedovaF.M.Optics and spectroscopy, 126,5, 538-543, (2019).
3. Claude R. Phipps, Leonid Zhigilei, PavelPolynkin et al.Introduction Journal of the Optical Society of America.35, 10, LIM1-LIM2, (2018).
4. AfoninV.I. Proceedings of the Chelyabinsk Scientific Center, 18, 21-26, (2003).
5. GriqoryantsA.G., BoqdanovaM.A. Electronic scientific and technical publication "Science and Education", FS77-30569, 1-15, (2012).

***Corresponding author**: vagif_salmanov@ yahoo.com

Fe/Pd BIMETALLIC NANOPARTICLES IN WATER REMEDIATION AND NITRATES TREATMENT

G.G.VALIYEVA*[1], LUCA DI PALMA[2], S.R.HAJIYEVA[1], M.A.RAMAZANOV[1], F.V.HAJIYEVA[1]
[1] *Baku State University, Z.Khalilov str., 23, Baku, Azerbaijan, Az1148*
[2] *Sapienza Universita` di Roma, Via Eudossiana 18, Rome, Italy, 00184*

In this paper bimetallic nanoparticles Fe/Pd were synthesized in the presence of surface-active substance medium by borohydride reduction method under deoxygenated conditions. Bimetallic nanoparticles characterization was performed by XRD, SEM techniques. The stable, well-dispersed bimetallic nanoparticle solution was produced by using sodium oleate stabilizer. SEM pictures have shown that the particle size for iron nanoparticles is 40-80 nm, but for Fe/Pd bimetallic nanoparticles - 20-30 nm.

The main goal of this research was the investigation of Fe/Pd bimetallic nanoparticles effectiveness in the catalytic removal of nitrate in water. The Fe/Pd bimetallic nanoparticles were synthesized in different weight ratio to fix the optimal percentage of Pd for nitrate reduction. Also the best concentration of Fe/Pd for nitrates removal was investigated. During 15 minute of tests nitrates concentration was analyzed in ion chromatography.

Keywords: bimetallic nanoparticles, sodium oleate, stabilization, iron, palladium
PACS: 12.20.Fv, 75.75. −c, 89.60.-k

1. Introduction

Iron nanoparticles have many applications in environment and have been used in water and soil treatment to decrease the concentration of pollutants. Zero-valent iron nanoparticles have unique physical and chemical characteristics different from bulk material. Coating of nZVI by other metals (Ni, Pd, Pt, Ag, Cu and Au is a new method for nitrates remediation. The second metal increases the reaction rate of reduction.

In this review reported the stabilization of bimetallic particles in aqueous media in the presence of surfactants as stabilizers. Iron nanoparticles usually can be obtained without use of dispersing agents. But dispersing agents can be added to prevent aggregation and agglomeration and to establish steric barriers between iron nanoparticles. Stabilized bimetallic nanoparticles containing Fe by Pd were synthesized in the presence of surface-active substance-sodium oleate and characterized by different methods (XRD, SEM).

Groundwater contamination by nitrates has become a big ecology problem due to their solubility and migration over ecology systems. The main source of nitrate contamination of groundwater has been the excessive use of nitrogenous fertilizers in agriculture. Some limits in drinking water were found for human health safety, the Maximum Contaminant Level (MCL) fixed for 45 mg NO3-/L by USEPA [10].

High concentration of nitrates can lead serious health problems (methemoglobinemia, cancer, hypertension, central nervous system, diabetes, birth defects, spontaneous abortions) and changes to the immune system.

With regard to removing nitrate from groundwater, chemical reduction of nitrate has garnered much attention, because it treat nitrate faster than biological and is more cost-effective than many physicochemical methods [11]. Nitrate removal methods such as the ion exchange, electrodialysis, reverse osmosis, biological denitrification have shown high effectiveness, but they cannot be applied in largescale water treatment plants [9].

However, a lot of studies about reducing nitrates from wastewater with bimetallic nanoparticles have been systematically reported. In this study, was used Pd as a catalyst of nZVI, cause of its fast reaction rate.

2. Experiment

Bimetallic nanoparticles were synthesized in a three necks flask with according to a widely known method. To avoid the agglomerating, several dispersing agents, as sodium oleate (SO), carboxymethylcellulose sodium salt (CMC), cetyltrimethylammonium bromide (CTABr), polyethylene glycol (PEG) were used during synthesis. It was found that in the presence of sodium oleate (PLC 113655) stabilizer, bimetallic nanoparticles were more effective stabilized against oxidation and agglomeration compared to other stabilizers.

Bimetallic nanoparticles were prepared by mixing 0.1M iron (III) chloride hexahydrate (PLC 141358) solution with 0.5% solution of sodium oleate with mixing on a magnetic stirrer at 500 rpm. After 15 min, different amount of Pd was added for testing which loading is better (0.1%, 0.3% and 0.5%). Then 100 ml of 0.3 M sodium borohydride solution was added into the above solution dropwise and well stirred. After synthesis bimetallic nanoparticles were washed 3 times with absolute ethanol and then used for nitrates removal. The morphology of particles was characterized by SEM (JEOL JSM-7600 F) with 15.0 kV operating voltages. The pH value was measured using a pH meter (PHS-25 C pH).

Nitrates stock solution was prepared by dissolving 0.17 g of $NaNO_3$ (LC24650) in 400 ml of distilled water. The batch experiments were performed with Fe/Pd bimetallic nanoparticles in different weight ratio (0.05g/L, 0.1 g/L, 0.2 g/L, 0.3 g/L, 0.4 g/L). Samples were analyzed each 1, 3, 5, 10 and 15 min for investigation the reaction rate. The concentrations of nitrate and nitrite were measured by ion chromatography (Dionex ICS - 5000).

3. Results and discussion

XRD Analysis. X-ray diffraction analysis of bimetallic nanoparticles was performed on Rigaku Mini Flex 600 XRD diffractometer. In all the cases was used Cu Kα radiation from a Cu X-ray tube (run at 15 mA and 30 kV) and scan area was 20~80°. When the standard deviation is higher (~4.82), the phase may not be detectable by XRD. This limitation of XRD has amorphous structure, which exhibits only short-range ordering. XRD of FePd bimetallic nanoparticles determined amorphous phase.

SEM Analysis. The morphologies of bimetallic Fe/Pd nanoparticles have been described by scanning electron microscopy (SEM, JEOL JSM-7600 F). Scanning was carried out in SEI mode with an accelerating voltage of 15 kV and a working distance of 4.5 mm.

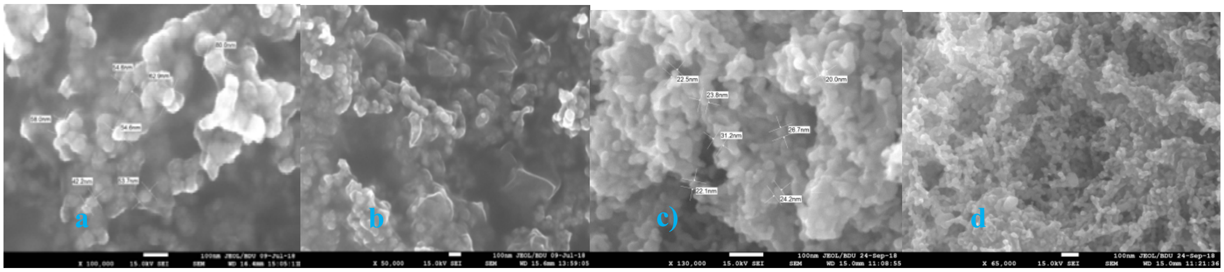

Fig. 1. SEM images of nZVI nanoparticles (a-b) and 0.5% Pd loading Fe/Pd bimetallic nanoparticles(c-d)

Figure 1 a-b shows the SEM images of synthesized nZVI nanoparticles without additional of the palladium. It is obvious from images that the iron nanoparticles are in the form of nanospheres, which have diameters of 40-80 nm. Figure 1 c-d were the SEM image of nano Fe/Pd particles. The particles were well dispersed and the specific surface area of particles increased due to the joining of nickel (20-30 nm).

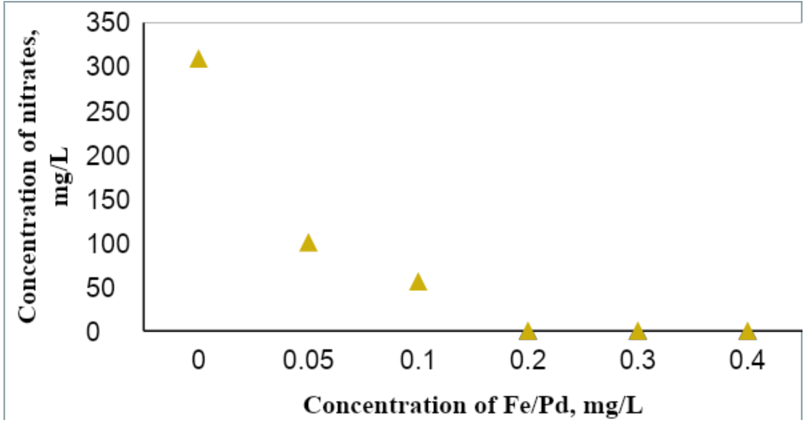

Fig. 2. Effect of different concentrations of Fe/Pd bimetallic nanoparticles (0.05, 0.1, 0.2, 0.3 and 0.4 g/L) on nitrate reduction with initial concentration of NO3 = 306.74 mg/L

As presented in Figure 2, the effect of Fe/Pd dosages on nitrate degradation was investigated. Five different concentrations of nanoparticles were tested to determine the optimal concentration of Fe/Pd required for nitrates remediation. Figure 2 shows that the nitrate removal efficiency increased with the increasing of Fe/Pd dosage. The five Fe/Pd concentrations investigated were 0.05 g/L, 0.1 g/L, 0.2 g/L, 0.3 g/L, 0.4 g/L. Optimal concentration of Fe/Pd nanoparticles for treatment nitrates pollutant water with initial concentration 306.74 mg/L was investigated. Figure 2 shows, that when was used 0.4 g/L of Fe/Pd bimetallic nanoparticles, the concentration of nitrate was 23.2 mg/L after 15 min of treatment. It is mean the 92.4% treatment of nitrates.

In the previously study the effect of nZVI on nitrates removal was also investigated [1]. Despite small doses of nitrates, it was not completely removed even after 150 minutes.

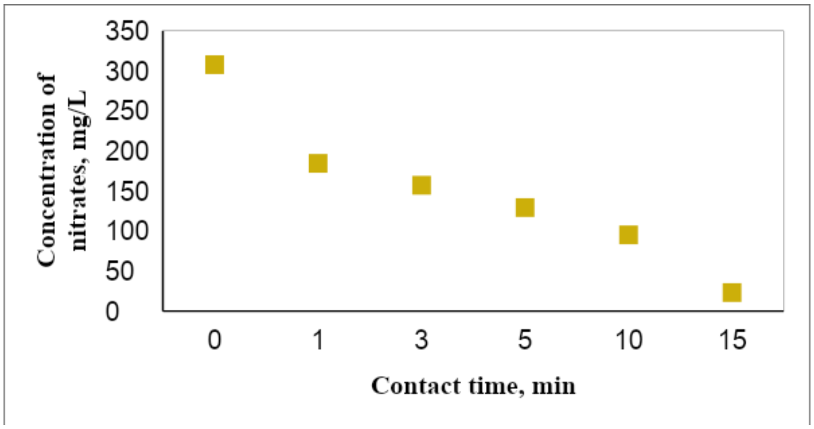

Fig. 3. Concentration of nitrates in the aqueous solution during treatment with 0.4 g/L Fe/Pd (initial NO3- concentration is 307.65 mg/L)

The optimum dosage of Fe/Pd was 0.4 g/L for the 309.37 mg/L nitrate degradation. Figure 3 shows the reduction rate in the first 15 minutes of treatment. According to these results, the removal was achieved after 15 minutes.

Different studies have shown that pH is a very important parameter for nitrates remediation process. They investigated that the rate of nitrates reduction was inversely related to pH of solution.

In this study was shown the rapidly increasing of solution pH to 8~9 in all reactions. Figure 4 shows the pH changes by time for the optimal concentration of Fe/Pd bimetallic nanoparticles (0.4 g/L). The solution pH increased from 5.2 to higher than 8 in the first 5 min of reaction. The final pH after 15 min reaction was around 8.9.

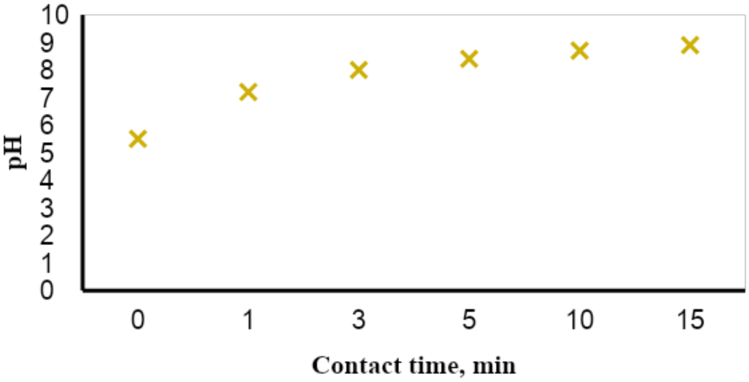

Fig. 4. Evolution of pH during treatment with Fe/Pd (concentration is 0.4 g/L) nanoparticles

4. Conclusion

Fe/Pd bimetallic nanoparticles were synthesized and used in different concentration for reduction of nitrates in water. More, than 90% of nitrates were reduced within 15 min. The results indicated that nanoscale bimetallic Fe/Pd could effectively reduce nitrate. The main reduction products are dissolved ammonium, ammonia and nitrogen gas. Despite the large amount of nitrates (more, than 300 ppm), results showed that the total (99%) removal was observed after 15 minutes and the optimal concentration of Fe/Pd was 0.4 g/L. In previously study also was shown the effect of uncoated nZVI, when nitrates were not complete removed even after 150 minutes (initial nitrates concentration was 57.25 ppm). Fe/Pd particles in nitrates remediation showed very high nitrate reduction rate, good properties of air stability compared with nZVI, which is important for nitrates removal.

References

1. Muradova G.G., Gadjieva S.R., Di Palma L., Vilardi G., Chemical Engineering Transactions 47, 205 (2016)
2. Di Palma L., Gueye M.T., Petrucci E., Journal of Hazardous Materials, 281, 70 (2015)
3. Westerhoff P., James J., Water Resources Research, 37, 1818 (2003)
4. Xia S.Q., Zhong F.H., Zhang Y.H., Li H.X., Yang X., Journal of Environmental Sciences, 22, 257 (2010)
5. Mahdieh R., Fatemeh Y., Behnam R., Hamid R., Journal of Applied Biotechnology Reports, 3, 353 (2016)
6. Kang H., Xiu Z., Chen J., Cao W., Guo Y., Li T. and Jin Z., Environmental Technology, 33, 2185 (2012)
7. Liu Y., Majetich S.A., Tilton R.D., Environmental Science & Technology, 39, 1338 (2005)
8. Zin M.T., Borja J., Hinode H., International Journal of Chemical, Nuclear, Materials and Metallurgical Engineering, 7, 12, 687 (2013)
9. Sparis D., Mystrioti C., Xenidis A., Papassiopi N., Desalination and Water Treatment, 51, 2926 (2013)
10. Fewtrell L., Environmental Health Perspectives, 112, 14, 1371 (2004)
11. Choi J., Won C. and Chung, Chemosphere, 86(8), 860 (2012)

***Corresponding author**: gunay111@hotmail.com

MODIFIED ZONE MELTING METHOD: MODELLING OF COMPONENTS CONCENTRATION DISTRIBUTION IN Ge-Si SINGLE CRYSTALS

Z.A. AGHAMALIYEV[1], G.KH. AZHDAROV[2]
[1]*Baku State UniversityAZ 1148, Baku, Z.Khaslilov str., 23*
[2]*Institute of Physics of Azerbaijan NAS AZ-1143, H.Javidave., 131*

The conception of modified zone melting method for growing of single crystals of semiconductor solid solutions is given. The task of component concentration distribution in Ge-Si crystals grown up by this method with use of germanium seed is solved in Pfann approximation. The axial concentration profiles of components in crystals grown at different values of operation parameters (melting zone length and composition of initial macro-homogeneous ingots Ge-Si) are calculated taking into consideration the complicated dependence of silicon segregation coefficient on melting zone composition. The possibility of control of component concentration distribution along Ge-Si crystals in wide range by way of change of melting zone length is shown.The analysis of obtained results determines the optimal technological operation parameters for growing Ge-Si crystal solid solutions with given homogeneous composition or gradient concentration profile of components on single crystal length.

Keywords: Growth models, solid solutions, single crystal growth, germanium silicon alloys.
PACS:81.00.,81.10.-h, 81.10.Aj

1. Introduction

The preparing of the material with given component concentration distribution in matrix and support of its monocrystallinity is the main problem of bulk crystal growth process of semiconductor solid solutions from the melt. Ge-Si system the composite components of which are the basis materials of modern micro- and optoelectronic industry takes the dominant place in wide range of semiconductor solid solutions.Si and Ge totally solving in each other in any ratios in both liquid and solid states, form the continuous series of exchange solid solutions [1].

The theoretical tasks on axial component distribution in Si-Ge crystals grown by modified zone recrystallization method using germanium seed are solved in present paper. The aim is the possibility determination of the modified method (and optimal technological operational parameters)for growth ofGe-Si single crystals with the given axial component concentration distribution. The analogous tasks on modeling the component concentration profiles in Ge-Si crystals grown from the melt by both conservative and non-conservative methods were solved earlier in works [2-9], the results of which showed the well agreement with experimental data.

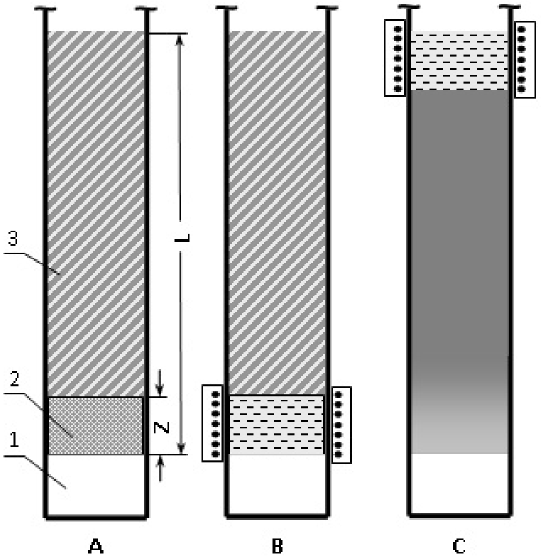

Figure 1. Schematic growth diagram of Ge –Si solid solution crystals by modified zone melting method with use of Ge seed.

2. The conception and theoretical basis

The schematic diagram of crystal growth of Ge-Si solid solutions by modified zone melting method is presented in fig.1. The monocrystalline seed (1) from Ge (fig.1A) is put into crucible of cylindric form. The previously prepared rods of corresponding diameter from germanium (2) and Ge-Si macro-homogeneous solid solution with the given composition (3) are put under the seed. The rod melting (2) from Ge situated directly under the seed (fig.1B) is carried out in vacuum conditions. The temperature on the melt boundaries with the seed and ingot is equal to germanium melting point in restarting moment of recrystallization. The crystal growth takes place on the seed from the moment of switching on of crucible movement mechanism relatively heater and continues up to total ingot recrystallization (3). The melting zone length is kept constant and equal to Z up to the moment of formation of final melting zone. Here the initial melting zone consists of the pure germanium unlike traditional method of zone melting [1,9]. This circumstance solves the seed problem [3]that is necessary for growth of Ge-Si solid solutions single crystals of different composition.

The task of component concentration distribution along Si-Ge crystal growth by modified zone melting method is solved in approximation of totally mixed melt (Pfann approximation)under following standard conditions [10]: the diffusion rate of Si and Ge atoms in the melt provides its homogeneity along whole volume; the component diffusion in solid phase is negligible one; the equilibrium between liquid and solid phases is on the crystallization front; the crystallization front is plane one; the segregation coefficients of melt components change with its composition in correspondence with diagram of equilibrium phase state of Si-Ge system; the composition of Ge-Si initial ingot is macro-homogeneous one; thermal expansion or compression of material at phase transitions is negligible one.

Let's introduce the following designations: V_m^0 and V_m are volumes of melting zone in initial and current moments; V_c is melt volume crystallizing in time unit; V_i is Ge-Si initial rod volume melting in time unit; C_m^0 is second component of atomic (Si) fraction in melting zone in initial moment; C_c , C_i , C_m are Si atomic fractions of in the growing crystal, initial polycrystalline rod and melt correspondingly; C is Si total atomic fraction in the melt; $K = C_c/C_m$ is Si equilibrium segregation coefficient; L is total length of initial rods from Ge and Ge-Si; ℓ is length of material recrystallized part in *t* moment; Z is melting zone length.

In frameworks of introduced designations we have the following:

$$C_m = \frac{C}{V_m};\ \frac{dC_m}{dt} = \frac{\dot{C}V_m - \dot{V}_m C}{V_m^2} \qquad и\, V_m = V_m^0 - (V_c - V_i)t \tag{1}$$

As in the case of traditional zone melting method [1,9] we consider by the statement of the problem that V_c doesn't depend on time,the values of Z and V_i parameters stay constant up to the moment of final melting zone formation. In this case the following equations take place in the region of L-Z length (fig.1):

$$V_m = V_m^0 ;\quad C_m^0 = 0;\quad V_i = V_c\, и\, \dot{C} = V_i C_i - V_c C_m K \tag{2}$$

From equations (1) and (2) after series of transformation we have:

$$\int_0^{C_m} \frac{dC_m}{C_i - C_m K} = \frac{V_c t}{V_m^0} = \frac{l}{Z} \tag{3}$$

Taking into consideration the equality $K = C_c/C_m$ equation (3) defines the component part composition on growing crystal length in the region from ℓ=0 up to ℓ = L-Z.

The following relations take place in final region from formation moment of finite melting zone having length Z:

$$V_i = 0,\quad V_m = \mathrm{V}_\mathrm{m}^0 - \mathrm{V}_\mathrm{c} t\ ,\quad \dot{V}_m = -V_c\ , \dot{C} = -V_c\, C_m K \tag{4}$$

Taking under consideration (4) from equation (1) after series of transformations and integration:

$$\int_{C_{mf}^0}^{C_m} \frac{dC_m}{C_{mf}^0 - C_m k} = \ln\frac{V_m^0}{V_m^0 - V_c t} \tag{5}$$

Here C_{mf}^0 is start concentration of Si atomic fraction in the melt in the moment of final melting zone formation. Designating the length and crystallized part of melt final part ($V_c t/V_m^0$) in t moment by l^* and γ symbols correspondingly let's write the equation (5) in the following form:

$$\gamma \equiv \frac{l^*}{Z} = 1 - \exp\left[- \int_{C_m}^{C_{mf}^0} \frac{dC_m}{C_m K - C_m} \right] \tag{6}$$

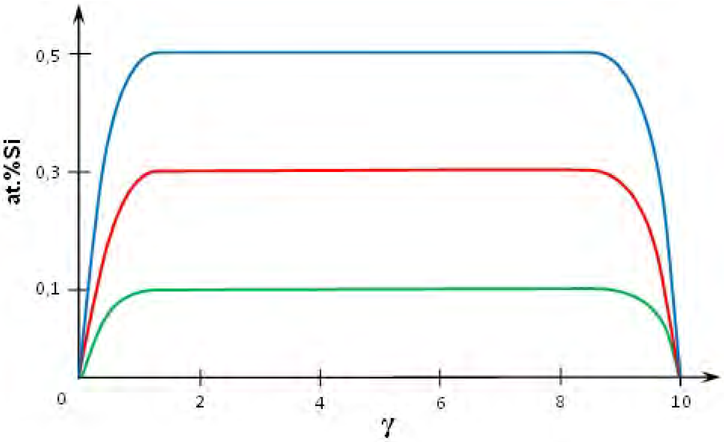

Figure 2The calculative concentration Si profiles along Ge-Si single crystals grown by modified zone melting method. The melting zone length Z=0,1L. The composition of initial macro-homogeneous ingots C_i are 1 –0.1, 2 –0.3 , 3 – 0.5.

The determination of l/Z and γ as C_m function (also as $C_c = K\,C_m$) along whole material length treated by zone crystallization requires to solve equations (3) and (6). The Si segregation coefficient (*K*) including in both these equations enough difficultly depends on C_m [4]. In paper [9] it is shown that the empirical curves temperatures of $T_l(C_m)$ liquids and $T_s(C_m)$ solidus ofGe-Si system diagram state in whole C_m change interval from 0 up to 1 are well enough described by following polynomials of fifth degree. Moreover, the dependence of K on C_m constructed on the base of these polynomials, is well described by following formula [9]:

$$K(C_m) = a + \frac{b}{c + C_m} \tag{7}$$

where $a = 0.32597$, $b = 0.7645323$ and $c = 0.1200377$. The absolute error in K value at definition its from formula (7) doesn't exceed 0,0057. Note that according (7) K value changes in interval from ~6.69 at $C_m \to 0$ up to ~1.00 at $C_m \to 1$. The equation (7) gives allows us to obtainthe corresponding value K in any given interval of C_m change. Introducing C_m values gradually in the required interval and determiningK values conjugated with them, the integrals in equations (3) and (6) we solve by numerical method.

3. Modelling of component concentration profiles in crystals

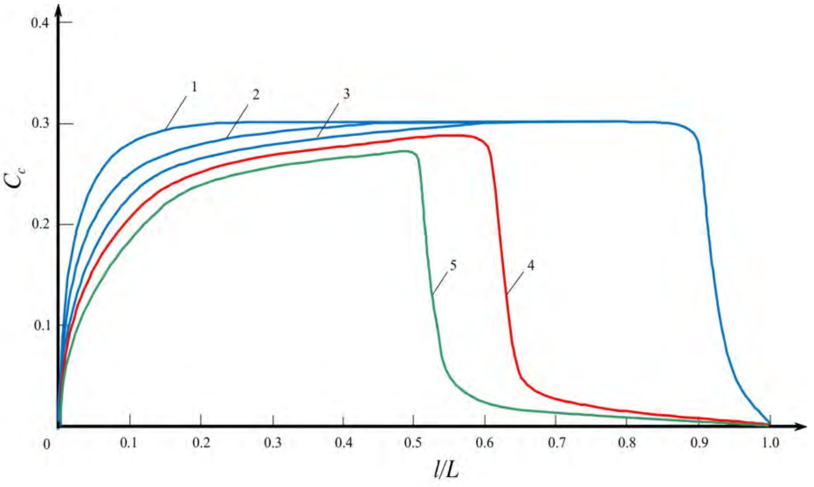

Figure 3 The calculative concentration Si profiles along Ge-Si single crystals grown by modified zone melting method at different values of melting zone length Z. Curves 1,2,3,4 are at values Z= 0.1, 0.2, 0.3, 0.4, 0.5L correspondingly.

The character curves of silicon concentration distribution along Ge-Si crystals for different Z values calculated from equations (3) and (6) with taking into consideration $C_c = C_m K$ are presented in fig.2.

As it is seen, Si increases on length from zero up to C_i corresponding value of initial macro-homogeneous ingot Ge-Si in beginning part of all crystals. Further, C_c value stays constant with crystal growth upto final zone formation having length Z=0.1L. In this part of ingot Si concentration begins to strongly decrease with ℓ increasing and goes to zero at ℓ=L.

The beginning part extent with increasing silicon concentration depends on initial ingot composition, K value and velocity of its change with melting zone composition. Note that rapid growth of Si concentration in beginning part of all ingots which causes the big output of single crystals of solid solutions with homogeneous composition.

The character curves of Si concentration distribution along two Ge-Si crystal groups at different values of z technological parameter calculated using (3) and (6) equations and relation $C_c = C_m K$ .are shown in fig 3. As it is seen, Z operation parameter essentially influences on component redistribution in both Ge-Si crystal groups. Moreover, the lengths and compositions of both homogeneous and heterogeneous crystal parts are determined by melting zone values Z and initial macro-homogeneous feeding rods of Ge-Si solid solutions.

4. Conclusion

Summarizing the above mentioned, one can conclude the following states. The math modeling results of axial component distribution in Ge-Si crystals shows the use availability of the modified zone melting methodfor growth of wide series of semiconductor solid solutions and give the possibility to make the evaluation of the optimal technological parameters for single crystal obtaining with the given axial concentration profile of components.

References

1. SchilzJ., RomanenkoV.N.. Bulk growth of Silicon-Germanium Solid Solutions,J. Materials in Electronics,V.6 (1995) 265-279.
2. CampbellT.A., SchweizerM., DoldP.et al.. Float zone growth and characterization of $Ge_{1-x}Si_x$ (x<10 at%)single crystals, J. Crystal Growth, 226 (2001) 231-237.
3. AbrosimovN.V., RossolenkoS.N., Thieme W. et al..Czochralski growth of Si- and Ge-rich SiGe single crystals, J. Crystal Growth, 174 (1997) 182-186.
4. AzhdarovG.Kh.,KucukomerogluT., VarilciA. et al.. Distribution of components in Ge-Si bulk single crystals grown under continuous feeding of the melt with the second component (Si), J. Crystal Growth, 226 (2001) 437-442.
5. AzhdarovG.Kh., KyazimzadeR.Z., Growth of homogeneous single crystals of Ge-Si solid solutions by the modified Bridgman method, Crystallography Reports, 50 (2005) S149-S153.
6. AzhdarovP.G., AgaevN.A.. Component distribution in Ge-Si crystals grown from the melt, Inorganic Materials, 35 (1999) №8, pp. 763-765.
7. Zakhrabekova Z.M.. Growth and electrical properties of Ge-Si crystals complex-doped by copper, aluminum and antimony, LAP LAMBERT AcademicPublishing, Germany (2013) 139.
8. Kazimova V.K.. Growth and electrical properties of Ge-Si crystals complex-doped by copper, indium and antimony, LAP LAMBERT AcademicPublishing, Germany (2013) 144.
9. Kostylev I., WoodacreJ.K., Lee Y.P.et al., Melt zone growth of Ge-rich Ge1-xSix bulk crystals, J. Crystal Growth, 377 (2013)147-157.
10. Qlazov V.M., Zemskov V.S. Physical and chemical fundamentals of semiconductor doping. M.: Nauka, (1967) 371.
11. OlesinskiR.W., AbbaschianG.J., Bulletin of Alloy Phase Diagrams, 5 (1984) 180.

*Corresponding author: a-zohrab@hotmail.com

THE ROLE OF PROGNOSIS AND ITS ESTIMATION IN THE MANAGEMENT OF CONSTRUCTION FIELD DEVELOPMENT

N.A.RAMAZANLI*
Baku State University, Z.Khalilov str., 23, Baku, Azerbaijan, Az1148

In the article the role of prognosis and planning in the management process of construction sector is investigated. The author has paid particular attentionto the application of the prognosismethod in the construction and achievements, the classification of business objectivesas a socio-economic system, the integrated assessment of socialhousing construction and so on.

The prognosis is investigated as a systematic approachto study thechanges in the environment of construction enterprises. Such an approach makes it possible to determine the probable state of environment as well as variation options and goals appropriateto those options . From this point of view, in this paper the prognosis is studied as task of management, the use of the resources and capabilities of the enterprisein agrement with theexternal environment is analyzed.

Key words: construction field, prognosis, management system, resources, goals.

1.Introduction

The construction site has a number of features that those must be taken into account in the planning and forecast calculations. One of the main features of the field stated is that production of products in this field is achieved due to labor, material and financial resources during long time. Significant resources are deducted from the current circulation and deposited into the area mentioned and the object is considered to be dead capital without being fully exploited. For this reason carrying out multi option calculations for this site is very important.

2. Forecasting factors.

The construction complex provides for the reprocessing of major production funds. Construction plays an important role in solving of social and economic problems. The construction sector serves for the technical progress in the national economy, rationalization of the country's productive forces, the rise in growth tempo, and improvement of area and territorial proportions in public production. From this point of view, a development of the construction sector should act as an special object of prognosis.

Construction is one of the most important tools for the development of all material production areas and non-production sphere, and the solution of housing problems. The building complex consists of two sectors that are interconnected - construction and industry sectors manufacturing construction materials, devices and details .

Scientific support of the complex consists of a network of scientific, project-search, design-technological organizations. In this context, prediction and planning of the construction industry are an important component of ensuring the competitiveness of the site. We are planning to predict and forecast the construction of the construction complex, make predictions about construction volumes, requires [1,2,3].

It should be noted, however, that the use of time as a competitive factor is beneficial to the consumer, so the consumer is ready to pay for a higher amount of meansfor that profit. In such a context, the effectiveness of the accuracyof the results is reflected in the effectiveness of the predictability of the results. More importantly, it should be emphasized that accurate forecasting of the development of construction enterprises depends on the choice of predictive method, its effectiveness affects its functional integrity and decreases the time and cost of prediction [4,5,6].

3. Results and discussion

The following key factors affect the selection of the prediction method:
- complexity of solved practical problems;
- dynamic featuresprediction object and market environment;

- information base (type and features of received information), imaginations about the type of prediction object;
- various life cycles of the preparation, implementation and operation of the product, as well as the construction enterprise itself;
- the stage of the waiting period and the ratio of its commodity product to predicted life cycles, its processing and implementation cycles;
- probable type of management: traditional, situational, systematic, etc.;
- requirements for the final results of forecasting.

The mentioned factors should be considered systematically.In such an aspect, the object of prediction is considered to be an integral part of the enterprise's internal and external environment. The pointis that changes in theenvironment will have a more impact on the continuous activity of enterprises in the context of market relations. It should be noted, however, that the forecasting is also aimed at studyingsystematic changes in the environment of construction companies. Such an approach makes it possible for the proposed environment to exist, the possible variation of options and the identification of goals that are appropriate to those options. From this point of view , the task of predictive management directs the resources and capabilities of the enterprise to the external environment so that it can gain the potential to besucceed. All of this requires the transformation of the potential required for future success based on internal and external environment analysis, and its transformation into its success factor. The company's development experience shows that the existing potential needs to be tested for the future, and as it becomes possible, its transformation to the potential for success. The fulfillment of these requirements implies that enterprises should be regarded as complex socio-economic systems,not just orientation to active market policies, but also to a complex socio-economic system, as well as balanced and interrelated relations with external environment, realization of their interests, to be achieved. Thus, enterprises that seek to grow, profit, and strengthen their positions in the market should predict their behavior and the opportunities for development in current and future periods in dynamic conditions.

4. Conclusion

Any development is related to the problem of re-forming, during which the consumption value of the product rises, production costs and exploitation of the facility are reduced. That is, the company's internal potential must be effectively transformed into market priority. In order to achieve this goal, enterprise management should be oriented to the market, and marketing should have a wide range of functions.

References

1. Mammadov M.A., Aliyev A.M., Abbasova A. A., Ibrahimov S.Sh.. Analysis of development trends of industrial and fuel power complex.Baku, Elm,- 380p.(2012).
2. G.A.Azizova. Investment and innovation policy of the state, Baku: "Economic University" Publishing House - (p. 212), p. 20. (2012).
3. Didkovskaya O.V. The system of value engineering as a basis for managing the cost of construction / Rationing and salary payment in construction. No. 1 p. 19-25.(2013).
4. Johansen, S., Determination of Cointegration Rank in the Presence of a Linear Trend, Oxford Bulletin of Economics and Statistics, 54, 383-397, (1992).
5. Hamilton P. Time Series Analyses, Princeton University Press, (2001).
6. Johnston, J., Econometric Methods, 3rd edn, McGraw-Hill International, London, (1984)

***Corresponding author:**nramazanli@yandex.ru

ELECTRIC DOUBLE LAYER INRAPIDLY CHANGING HELIUM PLASMA COLUMN

T.KH. HUSEYNOV, K.M. DASHDAMIROV, G.I. GARIBOV,
V.H. SAFAROV, E.A. RASULOV, SH.A. ALLAHVERDIYEV
BakuStateUniversity, Z.Khalilov str., 23, Baku, Azerbaijan, Az1148

Electric double layer in rapidly variablehelium plasma column was investigated. Measurements showed that the electron concentration at variable values of discharge current at different points of the discharge in the measured range of modulation depth of the electron concentration at low frequencies is equal to the modulation depth of the discharge current.

Keywords:gas discharge, electric double layer, movable cylindrical probe, electric field modulation effect, electron focusing effect
PACS: 52.20.-j, 52.25.Gj

1. Introduction

The appearance of an electrical double layer (DL) before narrowing the discharge tube and the potential jump associated with it can lead to gas rarefaction in the double layer region with the passage of the DL, the charged particles are accelerated and during collisions a part of the acquired momentum is transferred to neutral gas atoms and molecules. This leads to the displacement of gas from the DL region. At sufficiently high discharge current densities, a decrease in the gas density becomes significant, which impairs the conditions for the formation of new ions. The jump of potential in the DL increases, the active plasma resistance increases and a higher inter-electrode voltage is required to maintain the discharge. Reaching the ionization limit may cause either a complete current failure or a step-down. Failure or the step-down of current leads to a decrease of gas rarefaction in the narrowing, which again leads to the appearance or increase of the current. The work [1] shows that the formation of thin layers is associated with emergence of complex dynamic processes in collisionless space plasma during geomagnetic disturbances and near the reconnection domains. The article provides an overview of models describing thin current structures in the magnetospheric tail of the Earth. These models are based on the concept of quasi-adiabatic dynamics of ions in the relatively weak magnetic field of the neutral layer of neutral tail of the magnetosphere, where ions can demagnetize. It is shown that the ion distribution function can be represented as a function of particle motion integrals - the total energy and the quasi-adiabatic invariant. Various modifications of the initial equilibrium are considered, including the consideration of magnetized electron currents, contribution of oxygen ions, asymmetry of plasma sources and the effects associated with the “non-Maxwellian” form of the particle distribution function. Elsewhere[4, 7]it is shown how the present theory of fluctuations in a plasma, with the nonlinear fluctuations taken into account, leads to the determination of cross-sections of bremsstrahlung, which take into account all collective effects that are important for this process.The work [2] investigates positive gas discharge column in helium at greater depths of discharge current modulation excluding stepwise ionization, and shows that the modulation effect of the electric field, as well as the variation of the electron energy distribution function (EEDF) over the period occur at frequencies below the inverse value of ambipolar diffusion, while the process of current increase and decrease is repeated periodically and current oscillations occur. In [6] it was shown that the condition for the self-maintenance of a gas discharge plasma is derived from its ionization balance expressed in the Townsend form and may be used as a definition of a gas discharge plasma in its simplest form.

2. Experiment

In this regard, we have assembled an experimental installation, in which the discharge was generated in a cylindrical glass chamber of 55 mm in diameter and 700 mm in length. The anode was placed in a movable narrow glass tube with inner diameter of 18 mm. In the anode section, the discharge narrowed and an electric double layer of space charges was formed at the site of the narrowing.A movable cylindrical probe oriented across the tube allowed carrying out radial measurements in the area of the column narrowing. Moving the anode together with the narrow section of the tube along the discharge chamber, it is possible to move the DL relative to the probe or spectrograph slit, and axial distributions of electrical and optical parameters of the plasma can be measured. The measurements were carried out in spectroscopically pure helium within the pressure range of 0.1 ç 0.5 Torr and discharge currents of 20 ç 500 mA in the absence of strata oscillations. Based on the measured distributions and concentrations, the numbers of excitations and ionizations in the DL area were calculated. The calculation of the EEDF was made from the kinetic equation for the measured potential profile.

The EEDF was measured by the second derivative method; the flowchart of the installation is shown in Fig.1.

In the narrowing section, a transition region is formed, consisting of electrical double layer with an electron space charge on the cathode side and positive ions space charge on the anode side. According to the Poisson's equation, the potential distribution changes in this region, the field increases sharply, electrons acquire additional energy, resulting in strong increase of ionization in the boundary region in the narrow section of the tube. A complementary energy appears on the EEDF, which corresponds to the group of electrons accelerated in the DL. As it moves along the steeply increasing branch of the distribution, the complementary energy shifts toward high energies. The value of the secondary maximum decreases and disappears rapidly as a result of elastic and inelastic collisions of electrons with atoms.

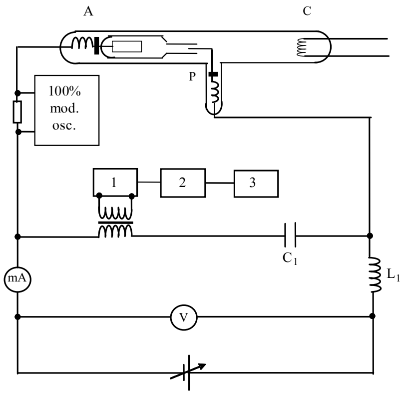

Fig. 1. Flowchart of installation for obtaining the second derivative of the probe current:
1– narrow-band amplifier, 2 – phase-lock detector, 3 – recorder.

In the narrowing section, the electron concentration increases sharply, then drops almost to the level of concentration in the wide section of the tube and, in some cases experiencing some such dramatic changes and reaches a constant value. This concentration behaviour is associated with the electron focusing effect, since the DL in the mouth of the narrow section has the shape of a spherical segment; hence, the accelerated electrons are focused towards the narrow section. The radial distribution of the concentration at the start of the tube's narrow section is substantially narrower than in more remote areas of the DL.

3. Results and discussion

Using the measured energy distributions of electrons, we calculated the numbers of excitations of different level groups with the principal quantum numbers 3 and 4. The cross sections from [5] were used for 3^3P_1(5) and 3^1P_1(6) levels.

Fig. 2 shows the distribution of the relative intensities of the lines λ = 388.9 nm (3) and λ = 501.6 nm (4), respectively. In the general distributions, a change in the excitation regime of the triplet and singlet levels can be seen. Some discrepancy in the calculations and measurements data can be explained by the neglect of the radial distributions of parameters and, hence, the difference in the parameter distribution on the axis and integrals over the cross section. Similar changes in population relationships are observed also for other singlets and triplets.

In [3] it was developed a method for a similar calculation of the distribution function (DF) in electric fields of a given configuration for the case, where the field and plasma concentration are non-uniform along the direction of current flow. The problem is solved for the case of small fields, when the energy balance is determined by quasi-elastic collisions. All collisions are subdivided into quasi-elastic and essentially inelastic, in which energy is lost, far surpassing the characteristic energy scale of DF decay by $\Delta\varepsilon$, and for the latter it is assumed that excitation of only one level with energy $\varepsilon_1$is taken into account. This scenario is often implemented in inert gases and is equally valid for the conditions of the experiments described above.

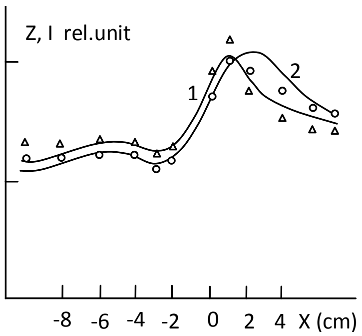

Fig. 2. Measurement of the relative intensity of spectral lines (1 - λ = 388.9 nm, 2 - λ = 501.6 nm) in the electric double layer (*He*).

In order to enhance the effect of electron acceleration in the double layer, experiments to determine the rates of stepwise excitation reactions were carried out in a tube with a narrow diameter of 18 mm. The variable component of the current with a modulation depth of = 20% at a modulation frequency ν = 63 Hz was superimposed on the constant component of the discharge current with the help of a sound generator.

Fig. 3 shows the dependence of the modulation depth of the intensity line λ = 667.8 nm on the strength of discharge current on the axis at a distance of 11 mm from the narrowing towards the cathode. This curve can be understood as follows.

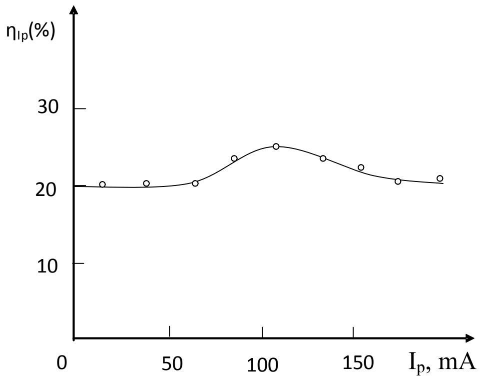

Fig. 3. Dependence of the modulation depth of the line intensity λ = 667.8 nm on the discharge current strength. P = 0.3 Torr, ν = 63 Hz, L = 11 mm, η_{Ip} = 20%.

For small values of the discharge current, the role of stepwise excitation in the population of the 3^1D_2level is small due to the small population of the metastable levels. With increasing current, the populations of metastable levels increase and, the depth of line intensity modulation increases due to the modulation of metastable levels - an additional source of population of the considered level. At high currents, due to saturation of the populations of metastable levels with respect to current, the depth of line intensity modulation decreases. Therefore, the speed of the stepwise excitation reaction was determined at the discharge current value I_p= 100 mA, P = 0.3 Torr. Measurements of the electron concentration at different values of the discharge current in various discharge points showed that in the measured range at low frequencies, the modulation depth of the electron concentration is equal to the modulation depth of the discharge current. Therefore, η_{Ip} instead of η_n was used, which greatly helps the measurement process.

Fig. 4 presents the dependence of $\eta_I - \eta_{Ip}$ on η_{Ip} at $P = 0.3$ Torr, $I_p = 100$ mA.

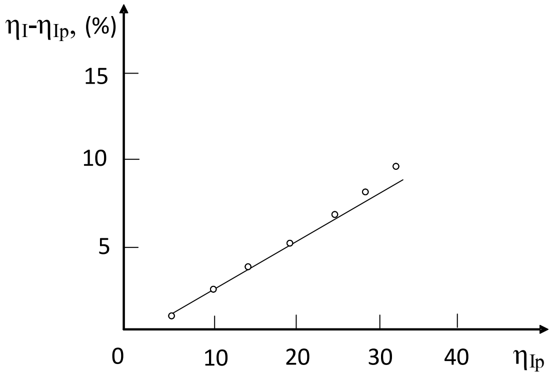

Fig.4. Dependence of $\eta_I - \eta_{Ip}$ on the modulation depth of the discharge current. $P = 0.3$ Torr, $I_p = 100$ mA, $\nu = 63$ Hz, $L = 11$ mm and $\lambda = 667.8$ nm.

4. Conclusion

Electric double layer in rapidly variable helium plasma column was investigated and measurements showed that the electron concentration at values of discharge current at different points of the discharge in the measured range of modulation depth of the electron concentration at low frequencies is equal to the modulation depth of the discharge current.The N_{m0} value is measured from the spectral line absorption $\lambda = 388.8$ nmin rapidly variable helium plasma, and $\alpha_{0m} = 3.5 \cdot 10^{-11}$ cm^3s^{-1} is calculated from the measured EEDF using direct excitation cross sections [5].

References

1. L.M. Zelenyi, Kh.V. Malova et al., Plasma Physics, 2, 137 (2011).
2. T. Kh. Guseinov, Izv. Vyssh. Uchebn. Zaved., Fiz. 60, 70 (2017).
3. L.D.Tsendin, Plasma Physics., II., Plasma Physics, 8, 169 (1982).
4. V.N. Tsytovich, Phys. Usp., 38, 87–108 (1995)
5. A.A. Mityureva, N.P. Pepkin, V.V. Smirnov, Optics and Spectroscopy, 66, 790 (1989).
6. B.M. Smirnov, Phys. Usp., 52 559–571 (2009).
7. Y.S. Akishev, A.A. Balakirev, V.B. Karalnik, Izv. Vyssh. Uchebn. Zaved. Fiz. 8, 70 (2017)

***Corresponding author**: htarlan@mail.ru

ISSUES OF ECONOMIC PROBLEMS' SOLVING OF RENEWABLE ENERGY SOURCES ACQUISITION

A.M.MAHARRAMOV[1], R.SH.SHAFAGATOV[2]*

[1]Baku State University, AkademikZahidXelilov Street 23, Baku, Azerbaijan, Az1148

[2] Academy of Public Administration under the President of Azerbaijan Republic, Lermontov Street 74, Baku, Azerbaijan, Az1001

Hereby in this article the issues on renewable energy sources acquisition were researched by the means of economic aspects. Development of the use of alternative energy sources within many world countries were studied and as a result optimal model was created. But to ensure the functionality of this theoretic model some real-life economic issues must be solved in convenient way. The main goal of this article is to discover the possibilities to achieve the realistic positive solution of those problems. At the end of current article as a conclusion there are given common renewable energy economic problem solution suggestions.

Keywords: alternative energy, renewable energy, problem solution, decision making, sustainable development, energy entrepreneurship, state support.

PACS:89.20.Bb, 89.30.Cc, 89.65.Gh

Continuous development of the world economy necessitates increasing demand for annual energy carriers where more and efficient use of renewable energy sources can substitutethem. In this regard, the acquisition of alternative and renewable energy sources is of great importance in terms of environmental, social and energy security impacts, but in many cases it faces various obstacles. This slows down the process of expanding the use of renewable energy sources, and sometimes ceases. Observations show that these obstacles can be related to political, legal, governance, socio-psychological, bureaucratic and economic factors. In industrially developing countries, where there is a great deal of exploitation of renewable energy sources, the biggest barrier in the slowdown is the difficulty to find a positive solution for economic problems. This is due to the fact that the alternative energy sector isa high investment requiredfield and, on the other hand, the long term maturity of investment. Although we are currently living in a period of extensive use of technological advances, but the acquisition of alternative energy sources is still in the high-risk business environment [1]. This is one of the most negative factors that prevents potential investors in the economic environment. For a state acquisition of alternative energy sources seems to be an additional burden on the budget as well as a sphere requiring the solution of issues such as personnel training, institutional reform and deepening of cross-sector coordination, and in most cases remain outside the priority interests of the state budget policy makers. Looking at all of this, municipalities have a clear advantage in the development of this sphere, but local self-governing bodies do not hurry to develop renewable energy sources. As an elective body, municipalities, who are afraid of long-term and financially viable projects, are practically always trying to direct their financial resources to the solution of local social problems. Thus, an unsuccessful closed socio-economic period has come.

Looking at the energy map of the world, it is possible to see that the most state interventions in the solution of economic problems of the development of this sphere occur in the countries with the most developed alternative energy sources utilization. This is sometimes due to the unique maximalist capabilities of natural environmental possibilities, sometimes due to the serious political will of the state in the field of sustainable development, and sometimes the extreme social-industrial energy needs. Al-Maktum solar energy park, created by the local authorities of the United Arab Emirates, seeking to benefit from unique climate opportunities for renewable energy, is expected to be the world's largest mega-project in the world, with a capacity of 1 gigawatt in 2020 and five gigawatts in 2050 [2]. By planning to be spent for construction about 14.2 billion UAE dirham (3.86 billion US dollars), it is being implemented by Dubai Electricity and Water Authority. In the UK, as a result of the continuous political and economic support of the government, the amount of electricity generated from wind parks is higher than that achieved by coal. And, most of the time, it provides energy purchases of all households in the country from wind installations [3]. Since 2017, Germany fullfils more than 85% of its energy needs through solar panels. Iceland fullfils its energy needs entirely from alternative energy sources. Although even China,being the world's largest industrial waste producer, is paying great attention to the acquisition of alternative energy sources due to its social and industrial needs. At present, 5 of the world's largest solar energy parks are in China. China is also the world's leading wind turbine manufacturer [4].

Figure1.

A state by improving the investment climate, by subsidizing the renewable energy sphere, by expanding its use of incentives or discounts shaping can build and manage the investment attractiveness of the renewable energy sector. The vast administrative, resource, and political capabilities of the state can play a key role in the initial formation and expansion of renewable energy sources. For the creation and support of entrepreneurship subjects for the production of alternative energy production facilities, the government can create favorable economic environment by providing concessional loans, applying tax privileges, canceling or reducing inspections, and providing direct assistance in designing and installation works. A systematic approach can ensure that the local economic environment is adapted to the dynamic change environment by pursuing a flexible customs policy. Formation and continuous improvement of the legal framework minimizes the litigation with entrepreneurship entities, thereby increasing the attractiveness of this field. Continuous institutional reforms lead to the progressive management of the renewable energy sector and the removal of bureaucratic obstacles. This minimizes the risks of the creation and expansion of the corruption-monopoly schemes. Such situation leads to a reduction in economic risks that, in turn, contributes to the financing of the field by banks. The state by playing an exceptional role in the initial formation of the alternative energy economy in the country is later gradually becomes a regulator-controller, giving its place to independent industry subjects over time. The interference of the state becomes minimized, with only minimal involvement of the state in order to maintain a competitive environment. Thus, the flagship of the renewable energy sphere is driven from the state side to private sector, leading to a complete economic cycle.

This model, which is put forward by us, is an actual document for the development of renewable energy sources in the territory of the Republic of Azerbaijan [5]. As can be seen from the foregoing, the completeness of the model is realized at three important stages. These are:

- Formation;
- Transition;
- Improvement stages.

The economic problems faced at each stage are different by means of essense and characteristics, and their solution requires the use of variable approaches. At the stage of formation, the state takes the economic burden and plays a natural monopoly role. In the transitional period, the most economically viable environment is created for entrepreneurship subjects that are active or operate on the renewable energy sphere, and investment attractiveness is ensured. At the improvement stage dynamic reforms are being carried out to ensure further sustainable development, and minimize the potential risks.

For the solution of economic problems in all three phases of the mentioned model, it is possible to offer the following suggestions:

- Given the geographical location of each region, considering the potential of various renewable energy sources, as well as the needs of the area's population and the level of economic development, priority should be given to localized methods rather than centralized methods for solving problems. It will increase the efficiency and reduce time loss and eliminate the possibility of various bureaucratic obstacles;

- Establish specialized funds to accelerate the rapid eradication of financial problems that may arise in the process of acquisition of renewable energy sources, especially in the transition period. For example, the State Fund for Renewable Energy;

- The role of the state during the transition period should not be limited to being a creatorof the private economic environment, the state must act as a trustworthy buyer, and should play the role of consumer or distributor of the energy obtained from various alternative energy sources by direct and timely payments on the basis of established tariffs that will ensure the competitiveness and competitiveness of entrepreneurship entities.This will significantly increase the activity of newly created private sector entities in the energy market and will enable them to succeed in the most risky early business period;

- During the initial formation, in the realm of the rule of absolute advantage of the state, it must play an active role in the process of establishing economic confidence, to ensure the full security of the inviolability of property, and to reassure the renewable energy sector by maintaining the principles of transparency, modernity and sustainability. Implementation of ASAN standards which have successfully tested in the territory of the Republic of Azerbaijan in the renewable energy sector can play an exceptional role in achieving the goal.

In our view, the aforementioned suggestions can lead to the solution of financial problems facing the alternative energy sector, as well as a flexible solution to various economic threats that can not be forecasted and neithertaken into account.

References:

1. Amil M. Maharramov, Rustam Sh. Shafagatov - Analysis of typical economic risks in the development of alternative energy sources,Modern Trends In Physics International Conference proceedings (2017)
2. Courtney Weatherby, Brian Eyler, Richard Burchill – Trends Report-UAE Energy Diplomacy (2018)
3. WindEurope, Wind in power 2017, Annual combined onshore and offshore wind energy statistics (2018)
4. Zifa Liu , Wenhua Zhang , Changhong Zhao and Jiahai Yuan, The Economics of Wind Power in China and Policy Implications, energies (2015)
5. RustamSh. Shafagatov, PhD Dissertation - Directions for improving the use of alternative and renewable energy sources in the Absheron economic region (2015)

***Corresponding author**: rustemshefagatov@gmail.com

ADJUSTMENT OF CONSUMPTION ELECTRIC ENERGY INCONDITIONS OF TRANSITION PERIOD

A.M. MAHARRAMOV [1], E.A. GARIBLI[2], G.Sh. MEHDIYEVA[3], R.SH.SHAFAGATOV[4]*
[1)]Baku State University,Z. Khalilov, 23, Baku, Azerbaijan, AZ1148
[2)] Azerbaijan State Economic University, Istiqlaliyyat 6, Baku, Azerbaijan, AZ1100
[3)]State Committee on Property Issues of Azerbaijan Republic, Baku, Azerbaijan, AZ1025
[4)]Academy of Public Administration under the President of Azerbaijan Republic, Lermontov Street 74, Baku, Azerbaijan, Az1001

Within the framework of the game theory, models for mathematical substantiation of the scientific and economic approaches to these topical issues describing the profitability of the use of energy sources in the housing and business complex and in the production sectors are being built. Some perspectives of the use of these models in the regulation of tariffs for the above types of communal-housing and industrial services in the conditions of monopoly for these services (the 'product') are given. The strategies of the consumer and producer are studied in detail for adjusting the tariff with the amount of consumed 'products'. The tariff issues are analyzed taking into account the interests of the consumer and the manufacturer of these products. Discussions are held on the results of the study and ways of prospective studies on these topics are given and the geography of the application of research results to price adjustments and consumed 'products' under conditions of a transition period and inflation is indicated.

***Keywords**:* Application of economics, tariffs of electrical energy, strategy of balanced tariffs, game theory
PACS: 88.05.Lg, 89.20.Bb, 89.65.Gh

Development of the economy in the field of electricity consumption in housing complex and production sectors is one of the most urgent tasks now in the countries of the post-Soviet period and in developing countries. In this context, issues related to the mentality of a specific region in the areas located in the far-away countries of developed capitalism, such as the West European countries, for example, Great Britain, Germany, France, Italy, etc., as well as the United States of America, Japan and some countries of Oceania, like Singapore, for example,play important role.

It is assumed that the tariff of the first kilowatt ($1kw$) of electrical energy is p_e conventional units (cu). If the lower and upper limits of the consumed electricity i -th family or industry (in the future sub i -th family or industry adopt the concept of "*consumer*"), denote through the parameters a_i and, accordingly, so the consumer's electricity costs can be expressed through the functions $e_i(x) = p_e x$ and $a_i \le x \le b_i$.

In this case, the consuming function of the electric consumer takes the following form: It is assumed that the complex consuming function of the consumer of electrical energy has the following form

$$\sum_{i=1}^{n} e_i(x_i) = \sum_{i=1}^{n} p_e x_i,\ a_i \le x_i \le b_i,$$

For certain consumption limits: $a_i \le x_i \le b_i$. To study the choice of tariffs $1kw$, it is assumed that the lower and upper limits of electricity tariffs are equal to $P_e^{\min}$ and $P_e^{\max}$. To construct an algorithm for calculating the function of the complex consumption of electricity consumption, the following notation is introduced:, $x = (x_1,...,x_n)$, $a = (a_1,...,a_n)$, $b = (b_1,...,b_n)$,. Then the complex consumption function of consumption of electric energy can be rewritten in the following form:

$$f(x, p_e) = \sum_{i=1}^{n} p_e x_i = p_e \sum_{i=1}^{n} x_i$$

with certain limits $a \le x \le b$ of consumption.

A completely logical and mutually beneficial option, in the conditions of the transition period of the economy, is the relationship between the producer and the consumer about the application of a uniform approach for the establishment of "*balanced tariffs*" by the Tariff Council and the "*water spills*" from the side of "*lean (economical) consumption*" by the consumer of these products. Functions of the financial loss of the manufacturer can be formulated as $f_{\Pr oducer}(x, p_e) = -f(x, p_e)$, and the consumer in the following form: $f_{Consumer}(x, p_e) = f(x, p_e)$. It should be noted that the problem considered by us is studied in terms of the 'loss function'. This same problem can be investigated in terms of 'function on profit'.

We will result research of the above-stated problem with definition of strategy of the consumer and manufacturer for averting from loss (losses). An arbitrary consumer (x) strategy belongs to a multitude, i.e. $[a, b]$. In terms of $1kv$ electricity tariffs $P_e^{\min}$, we can write the following set $(p_e) \in [P_e^{\min}, P_e^{\max}]$, which in turn leads to the fulfillment of the relationship

$$f_{Consumer}(x, p_e) + f_{\Pr oducer}(x, p_e) = 0.$$

Introducing the notation $E = [a, b]$ and $F = [P_e^{\min}, P_e^{\max}]$, we have that in the above relations, the vector of (x) consumed electricity belonging to the sets E is called "*customer strategies*", and the vector (p_e) determining the tariff for $1kv$ electric energy included in the above-stated sets F is "*producer strategies*". Obviously, the domain of definition of functions $f_{Consumer}$ and $f_{\Pr oducer}$, referred to as "the functions of financial losses of the consumer and the producer", respectively - is a set $E \times F$ whose values $R = (-\infty, +\infty)$ belong. Then, from the newly introduced function

$$G(x, p_e) = (f_{Consumer}(x, p_e),\ f_{\Pr oducer}(x, p_e)),$$

it follows that the values of this function belong R^2, i.e. $G(x, p_e) \in R^2$.

In the case of determining the strategies of the consumer and producer independent of each other, the game between them in a normal or strategic form is determined by means of a mapping $G(x, p_e)$ from a set $E \times F$ with a value in R^2 called the "*mapping of the bipoles*". To study consumer loss $f_{Consumer}$, if the consumer knows the manufacturer's strategy $(\tilde{p}_e)$ for choosing the tariff *cu* $\tilde{p}_e$ for the unit electric energy $1kw$, then the consumer should choose such a strategy $(\tilde{x}) \in E$ (i.e. those $\tilde{x}$ from the strategy area $a_i \le \tilde{x} \le b_i$), so that $f_{Consumer}(x, \tilde{p}_e)$ its loss function takes a minimum value. In other words, the consumer chooses his strategy from the following sets:

$$S_{Consumer}(\tilde{p}_e) = \{(\bar{x}) \in E : f_{Consumer}(\bar{x}, \tilde{p}_e) = \inf_{(x) \in E} f_{\Pr oducer}(x, \tilde{p}_e)\}.$$

The linear function of the financial loss of the consumer

$$f_{Consumer}(x, \tilde{p}_e) = \sum_{i=1}^{n} (\tilde{p}_e x_i)$$

takes its minimum value for an arbitrary $(\tilde{p}_e) \in F$, at a value $\bar{x} = a$, i.e. When the consumer reduces the consumption of electrical energy to a minimum. In this case, the only strategy that satisfies the consumer is the '*strategy of minimum consumer boundaries*'. Such a rule for making a decision is called the 'canonical rule of decision-making'. It should be noted that the compromise strategy $(a, P_e^{\max})$ leads to the so-called "*non-cooperative equilibrium*" of the canonical decision rule.

Since satisfying the following relations

$$f_{Consumer}(x, p_e) < f_{Consumer}(a, P_e^{\max})$$

and

$$f_{\Pr oduser}(x, p_e) < f_{\Pr oducer}(b, P_e^{\max}),$$

the strategists $(x, p_e) \in E \times F$ do not exist, it $(a, P_e^{\max})$ will be *Pareto-optimal*, which, as already noted above, does not meet the interests of both the consumer and the producer. It is obvious that the strategy $(a, P_e^{\min})$, which corresponds to the minimum consumption of electric energy and the minimum tariff, is the only strategy that satisfies the following condition:

$$f_{Consumer}(a, P_e^{\min}) = \inf_{\substack{(x)\in E \\ (p_e)\in F}} f_{Consumer}(x, p_e)$$

and it (this strategy) is more ideally acceptable in a mutually beneficial case. This case is calculated on the interest of the consumer on the part of the manufacturer and the so-called Tariff Council.

Also, obviously, the strategy $(b, P_e^{\max})$, with the maximum consumption of electricity and with the maximum value of the tariff, is the only strategy that satisfies the following condition:

$$f_{\Pr oducer}(b, P_e^{\max}) = \inf_{\substack{(x)\in E \\ (p_e)\in F}} f_{\Pr oducer}(x, p_e)\}$$

which is more profitable only for the manufacturer, i.e. this means increasing the producer's income at the expense of the consumer. In this case, the producer is enriched, and the consumer is depleted.

In this case, the *virtual minimum of the game* is determined by the following vector:, $f_{\Pr oducer}(b, P_e^{\max}))$.

It is also obvious that, in exceptional cases, there is a strategy (x, p_e) that satisfies the following conditions

$$f_{Consumer}(a, P_e^{\min}) = f_{Consumer}(x, p_e)$$

and

$$f_{\Pr oducer}(b, P_e^{\max}) = f_{\Pr oducer}(x, p_e)$$

that could be ideally acceptable for mutual benefit to both parties, both the consumer and the producer.

From the definition of the virtual minimum of the game [1], we obtain that for an arbitrary choice of the aggregate of consumption, and the electricity tariff (x, p_e), the following inequalities are satisfied:

$$f_{Consumer}(a, P_e^{\min}) \le f_{Consumer}(x, p_e) ,$$

$$f_{\Pr oducer}(b, P_e^{\max}) \le f_{\Pr oducer}(x, p_e) .$$

The questions of economic regulation of expenses for consumed electric power have been studied in detail and are presented on very specific recipes for solving regional economic problems on the economic consumption of priority household and industrial financial waste.

References:

1. Krushevsky A.V. Game theory. "Vishcha school", Kiev, 1977, 215 p.,;
2. Oben J.-P. Non-linear analysis and its economic applications. M .: The world, 1988, 264 p.;

***Corresponding author**: rustemshefagatov@gmail.com

SPATIAL STRUCTURE OF ACTH- (7-10)-PGP MOLECULES

L.N.AGAEVA*, A.A.ABDINOVA[2], S.R.AKHMEDOVA[3], N.F.AKHMEDOV[1]
[1]Baku State University, [2]Azerbaijan State Pedagogical University, [3] Azerbaijan Technical University,,Z.Khalilov str.,23,Baku, Azerbaijan,Az1148

The spatial structure of ACTH-(7-10)-PGP molecule has been investigated using theoretical conformational analysis method. The amino acid sequence of the N-terminal tetrapeptide fragment of Phe-Arg-Trp-Gly-Pro-Gly-Pro molecule conforms to the fragment 7-10 of ACTH hormone. It was shown that the spatial structure of heptapeptide molecule can be presented by 8 low-energy forms of the main chain. The optimal conformations of this molecule, the values of dihedral angles of the backbone and side chains of the amino acid residues, the energies of intra- and inter-residual interactions were determined.

Key words: ACTH-(7-10), theoretical conformational analysis, spatial structure, conformation
PACS: 36.20.Ey; 87.15.Aa; 87.15.He

1. Introduction

As peptides, which in their nootropic and neuroprotective activity would not be inferior to Semax, various fragments of ACTH: ACTH-(7-10)-PGP, ACTH-(4-10)-PGP, ACTH-(6-10)-PGP, ACTH-(5-7)-PGP were tested. These peptides not only exhibited nootropic and anxiolytic activity, but also increased the viability of cultured glial cells obtained from the cortex of the cerebral hemispheres of rats with ischemic brain damage. When studying the effect of ACTH- (4-10) -PGP on the size of the necrotic focus in rats, it turned out that this peptide, like Semax, reduces the size of necrosis during the development of ischemic stroke in rats by approximately 50%. All these drugs are planned to be used as medicines. With different routes of administration, a different set of hydrolysis products is formed from the initial peptides, and it is known that the resulting shorter peptides often have their own biological activity [1].This paper is devoted to the calculation of the spatial structure of the ACTH- (7-10) -PGP molecule (Phe7-Arg8-Trp9-Gly10-Pro11-Gly12-Pro13) and is a continuation of our previous research [2-5].

2. Method

To study of this peptide molecule, a method of theoretical conformational analysis, allowing to calculate the three-dimensional structure of biomolecules based on the known amino acid sequence, was used. The calculation was performed within the framework of a mechanical model of molecules, taking into account non-valent, electrostatic, torsion interactions and hydrogen bond energy. Non-valent interactions were assessed by Lennard-Jones potential. Electrostatic interactions were calculated in a monopole approximation according to the Coulomb's law using partial charges on atoms. The conformational possibilities of the molecule were studied under the conditions of the water environment, in connection with which the value of the dielectric constant was assumed to be 10. The energy of hydrogen bonds was estimated using the Morse potential. The calculation of the dihedral angles of rotation was carried out according to the standard nomenclature IUPAC-IUB [6].

3. Results and discussion

The spatial structure of the ACTH- (7-10) -PGP molecule was studied in fragments. At the first stage, the conformational possibilities of the N-terminal tetra peptide fragment Phe7-Arg8-Trp9-Gly10 and the C-terminal tripeptide fragment Pro11-Gly12-Pro13 were studied. Then three-dimensional structure of the His6-Phe7-Arg8-Trp9 fragment was calculated based on the low energy conformations of N-acetyl-L-histidine methyl amide, N-acetyl-L-phenylalanine methyl amide, N-acetyl-L-arginine methyl amide and N-acetyl-L-tryptophan methyl amide. Some of the over examined 200 structural variants of the tetra peptide molecule were sterically forbidden, the relative energy of the others was distributed from 0 to 20 kcal / mol.

The results of the calculation of the molecule ACTH- (7-10) show that energy differentiation takes place according to conformations and forms of the main chain. Eight forms of the main chain of eight shapes of fff, ffe, eef, efe, eee, fef, eff, fee fall into the energy interval of 0–3 kcal / mol. In these conformations, the contribution of non-valent interactions varies in the energy interval (-17.6) - (-15.0) kcal / mol, the contribution of electrostatic interactions varies in the energy interval 2.7 -4.3 kcal / mol, the contribution of torsion interactions varies in the energy interval 1.5 - 3.3 kcal / mol.

Table 1.

Relative energy (U_{rel}) and total energy (U_{total}) and energy contributions of nonvalent (U_{nonval}), electrostatic (U_{el}), torsional (U_{tors}) interactions of optimal conformations of the molecule ACTH-(7-10)-PGP

№	Shapes	Conformation	Energy				
			U_{nonval}	U_{el}	$U_{tors.}$	U_{total}	$U_{rel.}$
1	feffff	$R_2B_{3322}R_{33}RBPR$	-23.1	1.0	3.2	-18.9	0
2	efeeff	$B_1R_{3122}B_{23}BRRR$	-23.1	0.7	3.6	-18.8	0.1
3	feeeff	$R_2B_{2122}B_{13}BBPR$	-21.0	0.4	3.5	-17.1	1.8
4	ffeeff	$R_2R_{3322}B_{11}BBPR$	-20.3	0.5	3.1	-16.8	2.1
5	eeeeff	$B_2B_{2122}B_{11}BBPR$	-20.7	0.4	4.1	-16.3	2.6
6	ffffee	$R_2R_{3322}R_{21}RBPR$	-19.3	0.5	2.8	-16.0	2.9
7	efffff	$B_1R_{3122}R_{33}RBPR$	-21.4	0.4	5.4	-15.5	3.3
8	eeffef	$B_2B_{2322}R_{11}RRPR$	-17.3	0.1	5.5	-11.6	7.3

Table 2.

Energy of inside and between residual interactions in the conformations of the molecule ACTH-(7-10)-PGP $R_2B_{3322}R_{33}RBPR$ (U_{rel}=0 kcal/mol, first line), $B_1R_{3122}B_{23}BRRR$ (U_{rel}=0,1 kcal/mol, second line), $R_2B_{2122}B_{13}BBPR$ (U_{rel}=1.8 kcal/mol, third line), $R_2R_{3322}B_{11}BBPR$ (U_{rel}=2.1 kcal/mol, fourth line)

Phe7	Arg8	Trp9	Gly10	Pro11	Gly12	Pro13	
-0.4	-4.9	-3.3	0	-0.1	0	0	Phe7
-0.1	-5.0	-2.9	-0.7	-0.2	0	0	
-0.5	-4.7	-3.1	0	0	0	0	
-0.4	-4.6	-1.3	-0.3	-0.2	0	0	
	0.1	-1.2	-0.3	-2.7	-0.2	-0.4	Arg8
	0.3	-1.7	-0.2	0	0	-0.2	
	0.1	-2.1	-0.2	0	0	-0.2	
	0	-2.6	-0.2	0	0	-0.2	
		-0.6	-0.2	-1.6	-0.1	-0.8	Trp9
		-0.4	-2.5	-3.2	-0.4	-1.4	
		-0.8	-1.2	-2.6	-0.2	-0.6	
		-1.0	-1.3	-2.3	-0.3	-0.7	
			1.4	-2.6	-0.7	-2.5	Gly10
			1.2	-0.4	-0.8	-1.7	
			1.2	-0.7	-0.7	-2.8	
			1.2	-0.7	-0.7	-2.7	
				0.3	1.0	-1.4	Pro11
				0.3	-0.6	-1.2	
				0.3	1.1	-1.4	
				0.3	1.1	-1.4	
					1.3	-4.1	Gly12
					1.3	-3.3	
					1.3	-4.2	
					1.3	-4.2	
						1.5	Pro13
						1.4	
						1.5	
						1.5	

The global conformation of the ACTH- molecule (7-10) is $B_1R_{31}B_{23}B$ This conformation is simultaneously beneficial in non-valence and electrostatic interactions. In this structure, effective interactions of Phe7 with

Arg8, Phe7 with Trp9, Trp9 with Gly10, Arg8 with Gly10 occur, which contribute the total energy of -13.9 kcal/mol. As can be seen from the amino acid sequence the molecule ACTH- (7-10) consist of polyatomic amino acid residues Phe, Arg, Trp and in the low-energy conformations of all eight forms the effective stabilizing interactions appear between them. The theoretical conformational analysis of the Pro11-Gly12-Pro13 tripeptide fragment showed that the relative energy of the possible 16 forms of the main chain varies from 0 to 5.1 kcal / mol. To calculate the spatial structure of the heptapeptide molecule ACTH- (7-10) -PGP, the initial variants from eight forms of the main chain of the tetra peptide fragment Phe7-Arg8-Trp9-Gly10 and from sixteen forms of the main chain of the tripeptide fragment Pro11-Gly12-Pro13 were formed . The calculation of the heptapeptide molecule ACTH- (7-10) -PGP has shown that there is a strong energy differentiation between the shapes, the main chain forms and the conformations. Some folded conformations were not sterically possible. The relative energy of sterically possible conformations varies in the energy range of 0–15 kcal / mol. The combinations of the lowest-energy conformations according to the forms of the main chain Phe7-Arg8-Trp9-Gly10 and Pro11-Gly12-Pro13 were chosen from these conformations. These conformations, the contributions of non-valent, electrostatic and torsion energy, their total and relative energy are listed in Table 1. The relative energy of these conformations varies in the energy range of 0-7.3 kcal / mol. The relative energy of the conformations of the shape family presented in table 8, is less than 4.0 kcal / mol (Table 1). The contribution of non-valent interactions to the total energy of these conformations varies in the energy range (-23.1) - (-17.3) kcal / mol, electrostatic interactions in the range of 0.1–1.0 kcal / mol, torsion interactions in the range of 2.8– 5.5 kcal / mol (Table 1).

Table 2 shows the energy inside and inter-residual interactions in the best four conformations of each structural type, and the numerical values of the geometric parameters of these conformations are shown in Table 3. Figure 1 shows the spatial arrangement of amino acids in these conformations. The global conformation of the molecule ACTH- (7-10) -PGP is $B_2B_{3322}R_{22}$RBPR. It is beneficial for non-valence interactions, the contribution of which is -23.1 kcal / mol. In this conformation, efficient interactions arise between Phe7 with Arg8 and Trp9, the contribution of which is (-8.2) kcal / mol, the contribution of interactions of Arg8 with the remaining residues is (-4.9) kcal / mol, Trp9- (-3.3) kcal / mol, Glu10- (-5.8) kcal / mol (Table 2). In addition to the Arg8 residue, all residues form spiral-like structures. A hydrogen bond is formed between the C = O atoms of Gly10 and N-H of the last peptide group. The conformation $B_1B_{3122}B_{23}$BRRR has a half-turn of the backbone. There are effective interactions between Phe7 with the remaining residues and Trp9 with the remaining residues, which contribute, respectively, the contribution (-8.9) kcal / mol and (-7.9) kcal / mol to the total energy (Table 2) in this structure.

Table 3.

Geometric parameters (in degrees) of low energy conformations of the molecule ACTH-(7-10)-PGP

Residue	Conformation			
	$R_2B_{3322}R_{33}$RBPR	$B_1R_{3122}B_{23}$BRRR	$R_2B_{2122}B_{13}$BBPR	$R_2R_{3322}B_{11}$BBPR
Phe7	-96 -48 176 -169 84	-105 145 179 178 88	-96 -45 179 -169 85	-95 -46 177 -171 84
Arg8	-99 120 -176 -58 -62 -176 -179	-111 -66 -174 -71 81 171 -175	-101 113 179 -58 -63 -172 -178	-97 -52 177 -58 -63 -174 -178
Trp9	-101 -58 176 -58 91	-158 151 -179 178 73	-158 151 179 49 -86	-147 149 -178 53 -86
Gly10	-68 -64 179	-84 122 -176	-89 121 179	-89 123 179
Pro11	-60 120 179	-60 -52 -179	-60 115 -179	-60 115 -179
Gly12	132 -79 167	-84 -79 -177	127 -76 168	128 -76 169
Pro13	-60 -51 179	-60 -55 179	-60 -51 179	-60 -51 179
U_{rel}	0	0.1	1.8	2.1

Comment: The values of dihedral angles in the table are in the following order φ, ψ, w, χ_1, χ_2...

All low-energy structures of the ACTH- (7-10) -PGP molecule form the semi-coiled forms of the backbone. In the six of the eight low-energy forms of C-terminal tripeptide fragment Pro-Gly-Pro forms the ff shape of the peptide skeleton. In the low-energy conformation with a relative energy of 2.9 kcal / mol of the ffffee shape, the

N-terminal pentapeptide forms a spiral structure, and the C-terminal tripeptide fragment has unfolded form of the backbone departs from it (Table 1).

The $B_2B_{2322}R_{11}$RRPR conformation of the eeffef shape has a rather high energy (7.3 kcal / mol) dramatically different from other low-energy conformations. It is not beneficial for non-valence and torsion interactions (Table 1).

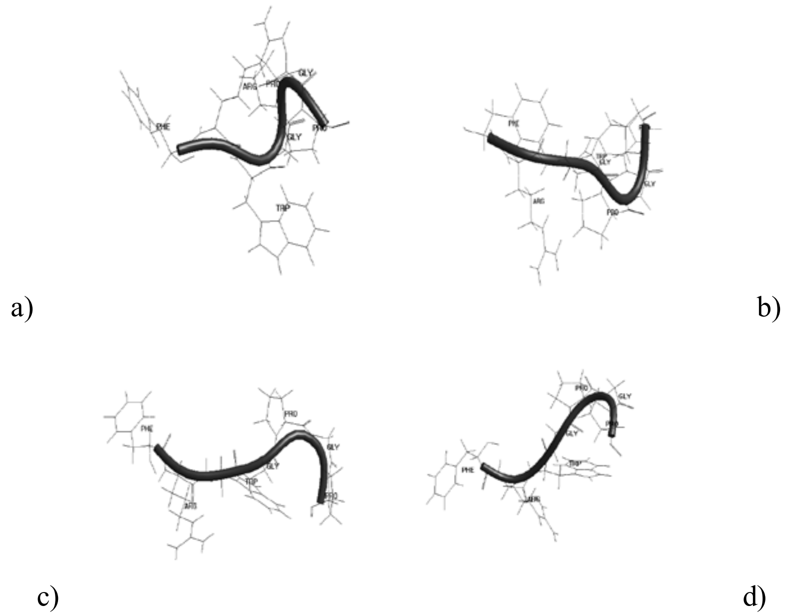

a) b)

c) d)

Figure 1. Atomic model of spatial structure of the ACTH- (7-10)-PGP molecule a), b), c) and d), corresponded to the structures with the relative energies 0 ;0.1 ; 1.8 and 2.1 kcal/mol,respectively.

4. Conclusion

The side chains of Phe7, Arg8 and Trp9 aminoacid residues have sufficient conformational freedom in the low-energy structures of the molecule under study and it can be assumed that they can participate in interaction with the receptors and other residues.

Thus, the theoretical conformational analysis of the heptapeptide molecule ACTH- (7-10)-PGP led to such structural organization, which does not exclude the realization by this molecule of a whole range of functions requiring strictly specific interactions with various receptors.

References

1. Shevchenko K.V., Dulov S., Andreeva L.A., Nagaev I.Yu., Shevchenko V.P., Radilov A.S., Myasoedov N.F. Journal of Bioorganic Chemistry, (In Russian). 42, 171 (2016).
2. Akhmedov N.A., Tagiyev Z.H., Hasanov E.M., Akverdieva G.A. J.Molecular Structure 646, 75 (2003).
3. Akhmedov N.A., Ismailova L.I., Agayeva L.N., Gocayev N.M. Current Topics in Peptid and Protein Research, 87, 11 (2010).
4. Gadjieva Sh.N., Akhmedov N.A., Masimov E.A., Godjaev N.M. Biophysics, , (In Russian), 58, 587 (2013).
5. Hasanov E.M., Akhmedov N.A . International Journal of Innovative Science and Research Technology 3, 72 (2018).
6. IUPAC-IUB, Quantify, Units and Symbols in Physical Chemistry, 39 (1988).

[*] **Corresponding author:** leylanamig@mail.ru

MOLECULAR MECHANICS AND DYNAMICS STUDY OF HYPOTENSIVE PEPTIDE NOVOKININ

G.A.AGAEVA* [1], U.T.AGAEVA[1], N.M.GODJAEV[1,2]
1- Baku State University, Z.Khalilov str., 23, Baku, Azerbaijan, Az1148
2- Baku Engineering University, Baku -Sumqait Road,16 km, Azerbaijan, Az0101

The conformational properties of the hypotensive peptide novokinin have been studied by molecular mechanics and molecular dynamics methods in vacuum and in environment with water molecules. Calculations have shown that spatial structure of novokinin can be describe as the few compact folded structures in both environments. It was established that the spatial structure of this hexapeptide molecule has tendency to keep a folded quasi-cyclic conformation, stabilized by hydrogen bonds. It was determined the values of dihedral angles of all possible conformations and their intermolecular interactions energies.

Key words: hexapeptide, novokinin, conformation, molecular mechanics method, molecular dynamics simulation.
PACS: 36.20.Ey; 87.15.Aa; 87.15.He

1. Introduction

Novokinin (Arg-Pro-Leu-Lys-Pro-Trp) is a potent vasorelaxing and hypotensive peptide designed based on the structure of ovokinin 2-7, a bioactive peptide derived from ovalbumin [1-4]. It has attracted much attention due to its variety of pharmacological and biological characteristics. Novokinin, having affinity for the AT2 receptor, shows the antihypertensive, vasorelaxing and antiopiod activities. Novokinin also inhibited the KCl- and $CaCl_2$-induced vasocontraction. The experimental results show that relaxed effect of novokinin on porcine coronary arteries might relate to the function of nitric oxide (NO), cyclic guanosine monophosphate (cGMP) and the synthesis of prostaglandin, but not involve adrenergic β-receptor [5]. The wide range of physiological activity of novokinin has been attributed to the lack of specificity of this hexapeptide for a particular receptor type. Hence there is considerable interest in novokinin as potential target for drug design. A molecular conformation is largely determined by its environment, so the aim of this present work is the study the differences in the conformations of the hexapeptide in a vacuum and in aqueous environments using a molecular dynamics method. The major aim of the present article is the investigation of conformational dynamics for novokinin, with the purpose of getting insight into basic structural requirements for determination of mechanism of interaction of peptide with receptor. The conformational behavior of novokinin and conformational dynamics of its side chains at the present article have been investigated by molecular mechanics and molecular dynamics methods, which allow to determine a whole sets of energetically preferred conformers of novokinin molecule.

2. Methods

Molecular mechanics (MM) study of novokinin conformation involves multi-staged extensive computations of even-increasing fragments, with a set stable forms of each preceding step used as a starting set in the next step. Only those conformations are retained whose energies are smaller than some cut-off values [6]. But it can be varied to make sure that higher energy states can justifiably be neglected. The sequential method was used, combining all low-energy conformations of constitutive residues. The conformational potential energy of a molecule is given as the sum of the independent contributions of nonbonded, electrostatic, torsional interactions and hydrogen bonds energies. The conventions used for torsion angles are those of IUPAC-IUB Commission [7]. Molecular dynamics (MD) simulations with ever improving force fields and longer time scales have been providing molecular level details of such systems. MD involves the calculation of solutions to Newton's equations of motions. Often an MD trajectory will become trapped in a local minimum and will not be able to step over high energy conformational barriers. Runs were performed for 300 ps at 300K. These calculation were carried out with software package: HyperChem. 8.01 [8]. MD simulations were performed for peptides in vacuum as well as in water solution using modeling package [9]. The force field parameters were those of the all atom version of AMBER by Cornell et al [10,11].

3. Results and discussion

Molecular mechanics study of novokinin has shown that its spatial structure may be described by set of low-energy conformations with identical structure of the N-terminal tetra peptide. Only two low-energy conformations of the novokinin are fall in the 0-5 kcal/mole relative energy interval. It is shown that two preferred conformations have very similar backbone form and values of the relative energy. Both conformations contain some turn at the sequence, but the one of them has β-turn structure at the N-terminal tetra peptide Arg^1-Pro^2-Leu^3-Lys ^{4} segment. These β-turns are confirmed by distance between C$^\alpha$ atoms of the i and i+3 residues (< 7 E). The lowest energy structures of novokinin exhibit the most favorable dispersion contacts and therefore may be expected to become the most preferred in medium, when electrostatic interactions do not play a significant role. The lowest energy structure of novokinin is stabilized by network of hydrogen bonds. This analysis has shown that novokinin can form one global, i.e. the lowest-energy structure, which is consist one β-turn of N-terminal part, formed follow hydrogen bonds: CO(Pro^2)…NH(Arg^1), COO(Trp^6)…NH$_2$ (Arg^1), COO(Trp^6)…NH$_3$ (Lys^4). Corresponding values of dihedral angles of two lowest energy conformations of novokinin are presented in Table 1.

Table 1.

The values (in degrees) of φ,ψ, ω, χ dihedral angles of two novokinin lowest energy conformations.

Residue	Conformation	Backbone angles			Side chain angles				
		φ	ψ	ω	χ_1	χ_2	χ_3	χ_4	χ_5
Arg	I	-65	145	185	185	175	180	180	-
	II	-65	145	185	185	175	180	180	-
Pro	I	-60	-53	187	-	-	-	-	-
	II	-60	-55	186	-	-	-	-	-
Leu	I	-95	145	181	59	186	180	180	-
	II	-96	172	179	64	183	178	180	-
Lys	I	-140	80	179	-59	-56	180	180	180
	II	-106	149	176	67	-61	180	180	180
Pro	I	-60	-35	181	-	-	-	-	-
	II	-60	115	182	-	-	-	-	-
Trp	I	-130	-42	184	55	93	-	-	-
	II	-85	152	180	58	93	-	-	-

MD simulation, using the two starting lowest energy structures of novokinin were shown the significant differences in the conformations of the molecule in a vacuum and in an aqueous environment. Structural reorganization of the global conformation of novokinin at the molecular dynamic simulation in vacuum and in water solution are shown in Figure 1. The MD simulations revealed the possible deviation by ±10° from the optimal values of φ,ψ, ω, χ dihedral angles in vacuum as compared to ±20° in water. The low energy changes of $\chi1$ for Trp 6 from 184 to 66° are possible. The deviations by ±20° from minimal values are possible for $\chi1$ angle of Lys4 residue. The mobility of the backbone and side chain of the Leu3 is more restricted as compared to preceding residues of molecule in vacuum as well as in water. In contrast to water simulations, where the φ angle for Lys4 may be changed by retained, generally the bond stretching frequency of water, the trajectory has to be recorded at an interval no larger than 4 femtoseconds. In lowest energy structure is kept only one hydrogen bond after simulation in water solution. Figure 1(b) shows the preferable structure of the novokinin as a result of the molecular simulation in aqueous environment. MD simulations show that the backbone of molecule can adopt a limited number forms while the side chains of the residues may populate different rotamers.

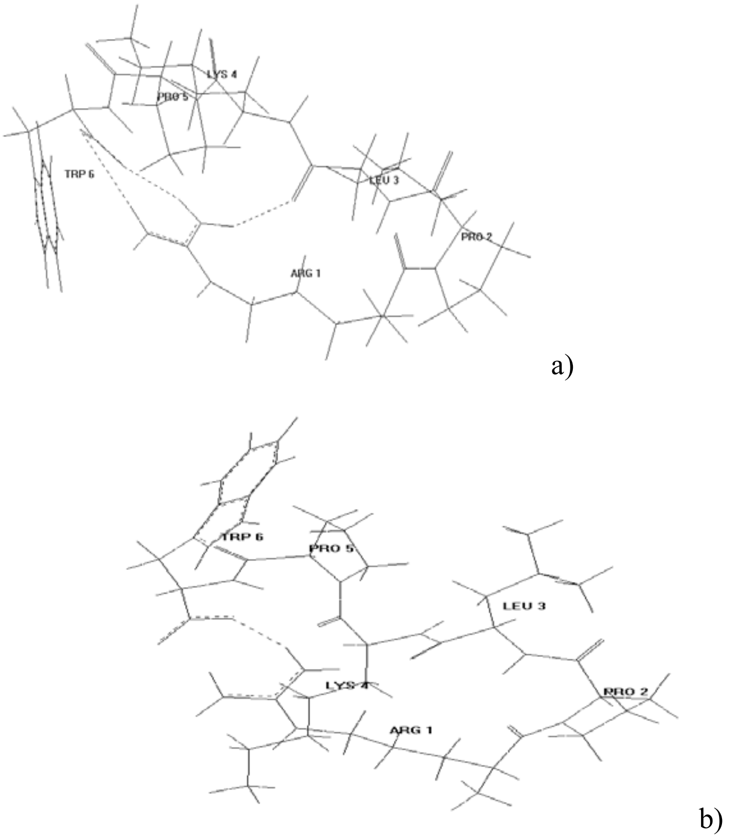

Figure 1. Conformational reorganization of the novokinin molecule at the molecular dynamic simulation in vacuum (a) and in water (b). Hydrogen bond is shown dashed line.

The conformational properties of Lys 4 residue in the lowest energy conformation of novokinin are investigated as the energy dependency of $\chi 1$ side angle of the rotation. The Lys4 fluctuates by ±20° from its optimal value as shown in Figure2.

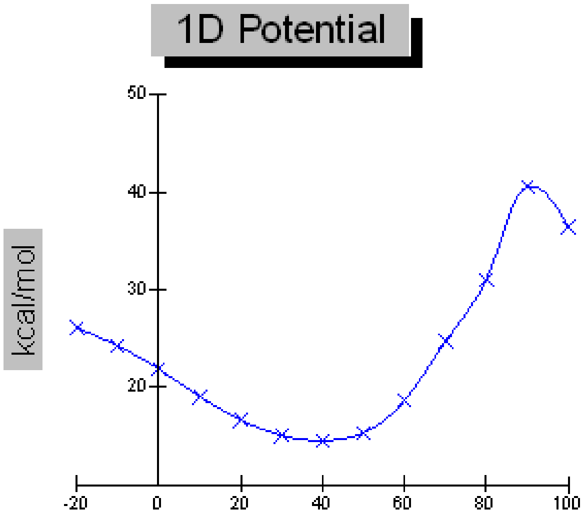

Figure 2. The 1D potential (energy) surface for Lys 4 residue in the lowest energy conformations of novokinin.

So, the flexibility of backbone of residues in the 4th and 6th positions is limited by 10° as compared to the preceding part of molecule. This fact can be explained due to the important role of these residues in the formation of β-turn. Each angle varied about a single value, close to one of the set of possible angles calculated from molecular mechanics energy minimization.

4. Conclusions

We have carried out detailed analysis of the flexibility of the novokinin molecule by employing the molecular mechanics and dynamics methods. The obtained results and discussion lead to the following conclusions: (I). molecular mechanics method and molecular dynamics simulations in vacuum as well as in aqueous solution confirm the small flexibility of the sequence of novokinin ; (II). the β-turn conformation on Arg1-Lys4 segment of peptide was more stabilized with the predominant hydrogen bonds CO(Pro^2)…NH(Arg^1), COO(Trp^6)…NH_2 (Arg^1), COO(Trp^6)…NH_3 (Lys^4) ; (III) the molecular dynamics simulation for novokinin indicated that relatively high stability of the low-energy conformations resulted not only from dispersion interactions between residues but also from hydrogen bonds networks ; (IV) the β- turn conformation at the N-terminal part were more stabilized in vacuum than in polar medium. The calculated stable structures of novokinin may be used as the basis for the design of further selective new analogs.

References

1. Yoshikawa M, Ohinata K, Yamada Y, Current pharmaceutical design 19(17), 3009 (2013).
2. Ohinata K., Fujiwata Y., Shingo F., Masaru I., Masatsugu H., Yoshikawa M., Peptides,30(6), 1105 (2009).
3. Yamada Y, Yamauchi D, Usui H, Zhao H, Yokoo M, Ohinata K, Iwai M, Horiuchi M, Yoshikawa M. Peptides.29(3), 412 (2008).
4. Yamada Y, Yamauchi D, Yokoo M, Ohinata K, Usui H, Yoshikawa M., Biosci Biotechnol Biochem. 72(1), 257 (2008).
5. Xu P.H., Wang T., Li L., Zhang B., Wu C.X., Yao Y.L., Zhang Z., Protein and peptide letter 22(12),1083 (2015).
6. Agaeva G.A., Agaeva U.T.,Godjaev N.M, Biophysics (Russian) 60,365,(2015).
7. IUPAC-IUB Quantity. Units and Symbols in Physical Chemistry 39, Blackwell Scientific Publications, Oxford (1988).
8. Chemo 3D Pro, “Molecular Modeling and Analysis,” Cambridge Soft Corporation, 875 Massachusetts, 02139 U.S.A (2005).
9. Mc Common J.A. Harvey S.C. in: Dynamics of Proteins and Nucleic Acids (Cambridge Univ. Press, New York) (1987).
10. Cornell W.D., Cieplak P., Bayly C.I., Gould I.R., Merz K.M., et al. J. Am. Chem. Soc. 117, 5179 (1995).
11. Allinger N.L., Yuh V.,QCPE-395, Indiana University (2000).

***Corresponding author**: gulshen@mail.ru

THEORETICAL STUDY OF THYMOMIMETIC PEPTIDE H-LYS-GLU-OH (VILON) AND ITS COMPLEX WITH THE RECEPTOR

G.A. AKVERDIEVA*, S.D. DEMUKHAMEDOVA, N.M. GODJAYEV
Institute for Physical Problems, Baku State University, Z.Khalilov str., 23, Baku, Azerbaijan, Az1148

The present study of thymomimetic peptide H-Lys-Glu-OH (vilon) has been performed using computer modeling and molecular docking methods. The conformational profiles of this dipeptide were investigated within molecular mechanics framework. The calculation results showed that two types of conformation, folded and extended, are realized for this molecule. The electronic characteristics of these structures were analysed by quantum chemical calculations. The obtained results indicate that the folded structure is more stable in electronic parameters. The optimal structures of vilon were docking onto the T-cell Receptor. It was shown that folded structure of vilon complements well a cleft on the surface of the specific receptor.

Keywords: thymomimetic peptide H-Lys-Glu-OH(vilon), molecular mechanics, quantum chemistry, molecular docking
PACS: 36.20.Ey; 87.15.Aa; 87.15.He; 87.15.Kg

2. Introduction

The peptide H-Lys-Glu-OH (vilon) is a structural element of many thymic hormones. This dipeptide was constructed on the basis of a statistical analysis of the amino acid composition of the preparation Thymalin [1]. The data obtained from the experimental studies of the biological action of vilon allow to recommend this peptide as a hero-protector drug. The obtained results show safety of vilon administration and allow to use this preparation for geroprotection and prophylaxis of age pathology. The use of vilon in geriatrics is appropriate for the correction of age-related disorders of angiogenesis and immunogenesis, as well as modulating cell proliferation and inhibition carcinogenesis [2-6].

2. Methods

The present study of thymomimetic peptide vilon has been performed using computer modeling and molecular docking methods. The conformational behavior of this dipeptide has been investigated by molecular mechanics. The conformational energy calculations were made with an IBM computer using version of ECEPP (Empirical Conformational Energy Program for Peptides) [7,8]. The proqram was developed from the matrix method principle of Hermans and Ferro [9]. The investigations were carried out within molecular mechanics framework as described in [10]. The quantum-chemical calculations of this molecule were conducted by method CNDO, parameterized for calculating of the electronic structures of biopolymers using the demonstration version of software package HyperChem [11]. The molecular docking of this ligand and its receptor was performed by AutoDock Vina [12] software. T-cell Receptor 3D structure was retrieved from the protein data bank at http: //www.rcsb.org (pdb for 4MNH). The crystallographic waters were removed from the original .pdb file using AutoDock Tools v.1.5.6 [12]. The coordinates of vilon were taken from our calculation results. PyMol [13] and PLIP [14] were used to visualize and analyse the ligand-receptor 3D interactions.

3. Results and discussion

The massiveness of the side chains of the composed amino-acid residues as well as the presence of four charged groups (N- and C-terminal oppositely charged groups of atoms and wholenumberious charge on the side chains of lysine and glutamic acid) are important factors, which form the stabilizating forces: dispersion interactions of side chains of amino-acid residues and electrostatic interactions between the charged groups. Therefore the energy of dipeptide is very sensitive to the positions of the side chains of the amino-acid residues. The conformational profiles calculation indicated that this molecule has such structural organization which not exclude the realization of folded and extended type of conformation. The observed differentiation in energy of the calculated conformations is mainly determined as by the electrostatic interactions and dispersion contacts. The energy and geometrical parameters for the favorable conformations of dipeptide are obtained. The folded ($E_{rel.}$=0.0 kcal/mol) and extended ($E_{rel.}$=0.6 kcal/mol) optimal conformations of both shapes of the investigated dipeptide are illustrated in Fig.1. The geometry parameters of these structures are given in Table 1. Note that in the folded conformations of this dipeptide the side chains of lysine and glutamic acid residues are coplanar and thus interact more efficiently. Such spatial arrangement of the side chains makes the molecule compact and also ensures the proximity between the atoms of the side chains and the atoms of the amino or carboxyl groups at the terminals of the molecule. It was established that in the optimal folded structure the distances from H atom of N-terminal amino group to O atoms of carboxyl group of side chain of Glu and to O atoms of C-terminal carboxyl group are 7.0 E and 4.7 E, respectively; the distances from N atom of amino group of side chain of Lys to O atoms of carboxyl group of the side chain of Glu and to O atoms of C-terminal carboxyl group are 3.0 E and 7.8 E, respectively. It was established that in the extended structure the distances from H atom of N-terminal amino group to O atoms of carboxyl group of side chain of Glu and to O atoms of C-terminal carboxyl group are 7.1 E and 6.0 E, respectively; the distances from N atom of amino group of the side chain of Lys to O atoms of carboxyl group of side chain of Glu and to O atoms of C-terminal carboxyl group are 11.7 E and 5.4 E, respectively. The above data demonstrates that the distances from the atoms of positive charged amino group of side chain of Lys to atoms of negative charged carboxyl group of side chain of Glu in the optimal folded structure of this dipeptide molecule are shorter than those in the optimal extended structure and, thus, favours efficient interactions.

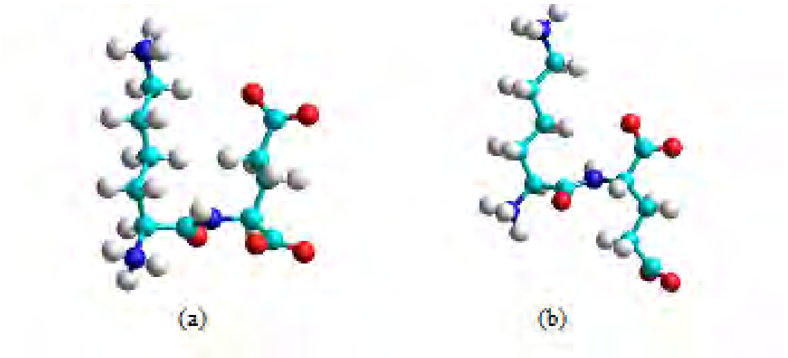

Fig. 1. The optimal folded (a) and extended (b) structures of vilon

Table1. The geometry parameters (in degrees) of the optimal folded and extended structures of vilon

Conformation	Angles	
	Lys	Glu
Folded	φ= -88, ψ= -74 ω= -169, χ_1=177 χ_2=166, χ_3=178 χ_4=170, χ_5= -179	φ= -132, ψ= - 21 χ_1= 59, χ_2= 180 χ_3= 92
Extended	φ= 173, ψ= 146 ω= 180, χ_1=176 χ_2= 180, χ_3= 177 χ_4= -179, χ_3= 180	φ= -130, ψ= 57 χ_1= -60, χ_2= 180 χ_3= 90

In the optimal folded structure of the investigated molecule three hydrogen bonds are formed: between the hydrogen atoms of amino group of side chain of lysine and oxygen atom of the carboxyl group of side chain of Glu (d=2.22 Å, E= -0.73 kcal/mol), between the hydrogen related by the peptide bond with the nitrogen atom of the main chain of Glu and two oxygen atoms of the C-terminal group (d=2.38 Å, E= -0.48 kcal/mol and d=2.38 Å, E= -0.48 kcal/mol). In the optimal extended structure of this peptide two hydrogen bonds are formed only between the terminal amine cation and the oxygen related by the peptide bond with the carbon of the main chain of lysine (d=2.86 E, E= -0.12 kcal/mol and d=2.31 E, E= -0.57 kcal/mol).

The optimal conformations of this dipeptide were refined by quantum chemistry. On the basis of values of the effective charges on atoms, of the analysis of the distribution electrostatic potential, of the energy parameters characterizing the electronic structure the electronic-conformational properties of the molecule under study were studied. The calculation revealed the differences in the electronic structure between two optimal characteristic conformations of vilon peptide. The contours of the electrostatic potential for these structures are illustrated in Fig.2 and Fig.3. The parameters of electronic structure of this dipeptide are listed in Table 2. As seen from this table the total, binding isolated atomic energies and heat of formation of the mentioned conformations are not different. However, their electronic energies differ appreciably: E_{el} = -681607 and -666709 kcal/mol for folded and extended structures, respectively; and so do the nuclear interaction energies: E_{nucl} = 542901 and 528020 kcal/mol for folded and extended structures, respectively. The folding of the peptide chain of this dipeptide molecule led to increase of energy gap by1.71 eV. The conformational differences cause the electron redistribution, and consequently, affect on the electron population, the orbital energies and, as result, the effective charges on the atoms. These parameters proved to differ noticeably for the two structures. There are changes in the charges of the atoms of the side chains of the both amino acid residues at folding. The result can be explained if we take into account the atomic distances; the atoms of the side chains of two residues in the folded structure are closer with one another and also with the backbone atoms than in the extended structure. There are differences in the charges of N and H atoms of amino group of the side chain of lysine, of C and O atoms of the carboxyl group of the side chain of glutamic acid residue. The changes take place also in the charges of C and O atoms of the terminal carboxyl group, also in the charges of N and H atoms of the terminal amino group.

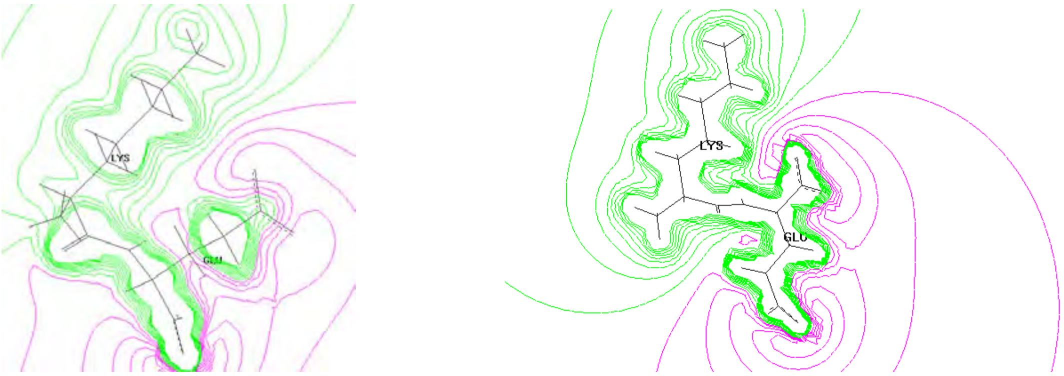

(a) (b)

Fig. 2. The 2D contours of the electrostatic potential in the optimal folded (a) and extended (b) structures of vilon

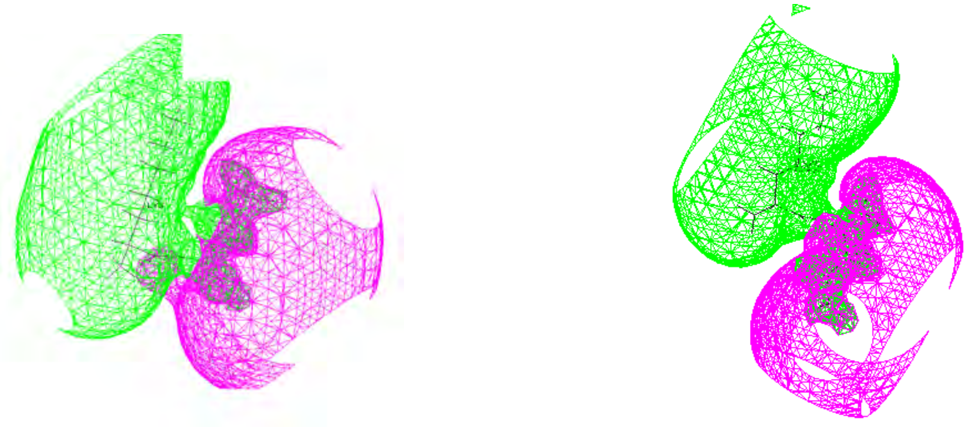

(a) (b)

Fig. 3. The 3D contours of the electrostatic potential in the optimal folded (a) and extended (b) structures of vilon

Table 2

The electronic parameters of the optimal folded and extended structures of vilon

Electronic parameters of the molecule	Folded structure	Extended structure
Total energy, kcal/mol	-138706	-138689
Binding energy, kcal/mol	-10148	-10131
Isolated atomic energy, kcal/mol	-128558	-128558
Electronic energy,kcal/mol	-681607	-666709
Core-Core interaction energy, kcal/mol	542901	528020
Heat of formation, kcal/mol	-6537	-6520
Dipole moment, debyes (D)	45	57
HOMO (eV)	-5.76	-4.84
LUMO (eV)	0.02	-0.77
Energy gap (eV)	5.78	4.07

The atomic charge changes are reflected on the occupancy ratios of the atomic orbitals. The analysis of the population coefficients allowed us to investigate the changes in the distribution of electron density It was shown that there are the electron density redistributes at folding of peptide chain. Moreover, only p_x, p_y, orbitals of the O atom of main chain, of CE atom of side chain of Lys and p_x, p_y, p_z orbitals of N, CA, O atoms of main chain, of OE1 atom of side chain of Glu are involved in this process of electron density overflow. As a result of folding of the peptide chain the redistribution of charges affects the decrease in dipole moment. As seen from the Table 2 the dipole moment of the folded structure is 12 Db lower than that of the extended structure owing to the approach of the charged terminal groups of the molecule. The obtained results indicate that the folded structure is more stable in electronic parameters.

The docking of vilon molecule onto the T-cell receptor 4MNH were assessed. There are the parameters of nine poses of vilon in the minimized structure of the vilon-TCR 4MNH complex are represented.

Table 3

Comparison of the binding energy of vilon and TCR 4MNH

Mode	Affinity (kcal/mol)	Distances from best mode	
		Rmsd l.b.	Rmsd u.b.
1	-6.1	0.000	0.000
2	-5.9	2.561	5.447
3	-5.8	2.632	4.901
4	-5.7	1.495	1.879
5	-5.6	2.626	5.185
6	-5.6	1.517	2.952
7	-5.5	2.243	4.042
8	-5.4	2.818	5.754
9	-5.3	2.084	3.012

The calculated binding energy and rmsd one can conclude that folded structure of vilon complements well a cleft on the surface of the T-cell receptor 4MNH, shown to be the attachment site (Fig. 4). Distinquishly, the extended structure of vilon is cannot enter the substrate binding cavity due to steric restrictions. It could bind very weakly on the receptor surface apart from the active center.

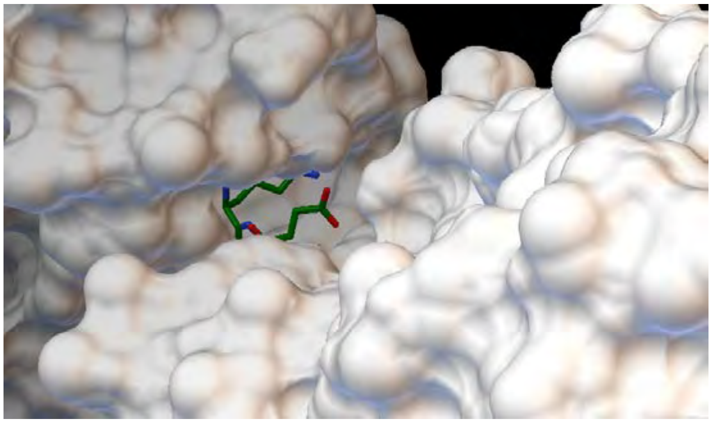

Fig.4. The best pose of vilon in the minimized structure of vilon-TCR 4MNH complex

4. Conclusion

The represented results showed that although two types of conformation, folded and extended, are realized for vilon molecule, but the folded structure is more stable in the electronic parameters. It was shown that the folded structure of vilon complements well a cleft on the surface of the specific receptor.

The received results provide an improved description of the structure-functional relationship and ligand-receptor interaction for vilon. The proposed complex can be used for the construction of pharmacophore model of the ligand-receptor interaction to search for new thymomimetics.

References

8. Khavinson V.Kh., Anisimov V.N., Dokl.Biol.Sci., 261 (2000).
9. Khavinson V.Kh., Neuroendocrinol. Lett, Special Issue,144 (2000).
10. Khavinson V.Kh., Morozov V.G., Neuroendocrinol. Lett. 24, 233 (2003).
11. Tan C.Y., Zhang X., Jiang Y.F., Zhang D.M.,Chinese Pharmacological Bulletin, 2, 233 (2007).
12. Khavinson V.Kh., Kuznik B.I., Ryzhak G.A., Advances in Gerontology, 4, 346 (2014).
13. Khavinson V., Micans P., Maryanovich A. Peptides in the Epigenetic Control of Ageing: Discoveries and Prospects ,Great Britain: Profound Health Ltd. (Publ.), 2017, 116 p.
14. Godjayev N.M., Maksumov I.S., Ismailova L.I. Program of semiempirical calculations of conformations of molecular complexes, J.Struct.Chem., (in Russian), 4, 147 (1983).
15. Akverdieva G, Godjayev N., J.Modern Technology & Engineering, 2, 140 (2017).
16. Hermans J. and Ferro D., Biopolymers, 10, 1121 (1971).
17. Godjayev N.M., Akyuz S., Akverdieva G.A., J.Mol. Structure, 403, 95 (1997).
18. Allinger N.L.,Yuh Y., QCPE 395, Quantum chemistry program exchange, Indiana Univ., Indiana, 1982, http://ww.hyper.com
19. Trott O., Olson A. J., Journal of Computational Chemistry, 31, 455 (2010).
20. DeLano W.L. The PyMOL molecular graphics system, 2010, http://www.pymol.org
21. Salentin S., Schreiber, Haupt V.J., Adasme M.F., Schroeder M., Nucleic Acids Research, 1, 1 (2016).

***Corresponding author**: hagverdigulnara@gmail.com

STUDYİNG OF STRUCTURAL CHARACTERISTICS IN WATER-POLYETHYLENE GLYCOL-LiOH, NAOH, KOH SYSTEMS BY VISCOSIMETRY AND PYCNOMETRY METHODS

B.G. PASHAYEV*

Baku State University, Z. Khalilov str., 23, Baku, Azerbaijan, Az1148

In process, dynamic viscosity and density of water-PEG, water-PEG-LiOH, water-PEG-NaOH and water-PEG-KOH systems are measured at 293,15-323,15 K temperature and at 0-0.001 molar portion concentration interval of PEG. Fractions with molecular mass of PEG 1500 and 6000 have been analyzed, and concentration of alkalis (LiOH, NaOH, KOH) is taken 0.01 molar portion at water-PEG-LiOH, water-PEG-NaOH, water-PEG-KOH systems. Activation parameters of viscous flow at given temperature and concentration interval and partial molar volume of PEG in solution are calculated by using experimental results and dependency of these parameters from concentration of PEG is investigated as well. It is defined that PEG effects structure of both water and water-LiOH, water-NaOH and water-KOH systems, however, presence of LiOH, NaOH, KOH decrease this structuring effect in certain amount.

Keywords: polyethylene glycol, LiOH, NaOH, KOH, activation parameters of viscous flow, partial molar volume, structure of water.
PACS: 61.20.Ne, 66.20.+d, 82.60.Lf, 61.25.Hq.

1. Introduction

It is clear that structure and thermodynamic state of water change while solving different substances in water. This has impact on all of occurring biological processes. That's way learning effects of biologically substantial substances to water structure is essential. Polyethylene glycol (PEG) is one of such materials. As PEG does not contain toxic characteristics, it is widely used in pharmacology and food industry. PEG molecule ($HO-[-CH_2-CH_2-O-]_n-H$) contains both hydrophobic (CH_2) and hydrophilic (OH) groups [1]. (OH) group of PEG, $-O-$ and $-H$ atoms can form hydrogen bond with water molecule, CH_2 groups form hydrophobic effect. It is expected that presence of hydrophobic effect at PEG can strengthen formation of hydrogen bond between hydrophilic group of PEG and water molecules. Thus, as a result of interaction between molecules of PEG and water, structure of water have to change in water-PEG system at small concentration of PEG. Metal ion generated as a result of dissociation of substances when alkali or salt is added to the water-PEG system interacts with PEG molecule. Investigation of rheological characteristics of water-PEG-alkali (salt) systems is necessary in order to study such interactions.

In process, structural characteristics of water-PEG, water-PEG-LiOH, water-PEG-NaOH and water-PEG-KOH systems are investigated with the help of viscometery and pycnometery methods at 293,15-323,15 K temperature and at 0-0.001 molar portion concentration interval of PEG. Fractions of polyethylene glycol (PEG) with molecular mass $M_{PEG}=1500$ and $M_{PEG}=6000$ are analyzed and concentration of alkalis (LiOH, NaOH, KOH) is taken 0.01 molar fraction at water-PEG-LiOH, water-PEG-NaOH, and water-PEG-KOH systems. Viscosity and density of analyzed solutions are measured at given temperature and concentration interval and according to experimental values, activation Gibbs energy of viscous flow ($\Delta G_\eta^{\neq}$), activation enthalpy of viscous flow ($\Delta H_\eta^{\neq}$), activation entropy of viscous flow ($\Delta S_\eta^{\neq}$), partial molar volume ($\widetilde{V}$) of PEG in solution are calculated and dependency on concentration of PEG are investigated properly.

2. Experiment

Object and methods of investigation. PEG with 1500 and 6000 molecular mass, LiOH, NaOH, and KOH are taken as a investigation object. Chemically raw materials are used. Distilled water is utilized for preparing solutions. In work viscosity is is measured with viscometer and density is measured with pycnometer.

According to Eyring theory [1, 2] of viscous flow of fluids, activation Gibbs energy of viscous flow ($\Delta G_\eta^{\neq}$) is defined with equation below:

$$\Delta G_\eta^{\neq} = RT \ln \frac{\eta}{\eta_0} \tag{1}$$

According to Eyring theory [1, 2]:

$$\eta_0 = \frac{N_A h \rho}{M} \tag{2}$$

Here, *R*- Universal gas constant, N_A- Avogadro number, *h*- Plank constant. *M*- molar mass of solution and determined by formula below [1]:

$$M = \sum_{i=1}^{N} x_i M_i \tag{3}$$

x_i and M_i are the molar fraction and molar mass of component *i*. Dynamic viscosity of fluid and density are determined in experiment at *T* absolute temperature. Formula is substituted in formula known from thermodynamics [1]

$$\Delta G_\eta^{\neq} = \Delta H_\eta^{\neq} - T\Delta S_\eta^{\neq} \tag{4}$$

and dividing all components into *T* gives us equation below:

$$R \ln \frac{\eta}{\eta_0} = \frac{\Delta H_\eta^{\neq}}{T} - \Delta S_\eta^{\neq} \tag{5}$$

(5) equation shows that activation enthalpy ($\Delta H_\eta^{\neq}$) of viscous flow equals to:

$$\Delta H_\eta^{\neq} = R \frac{\partial \ln(\eta/\eta_0)}{\partial (1/T)} \tag{6}$$

After determining $\Delta G_\eta^{\neq}$ from equation (1) and $\Delta H_\eta^{\neq}$ from equation (6), activation of viscous flow ($\Delta S_\eta^{\neq}$) is calculated by (4) formula.

Partial molar volume of PEG ($\widetilde{V}$) in solution

$$\widetilde{V} = V_m + (1-x)\left(\frac{\partial V_m}{\partial x}\right)_{p,T} \tag{7}$$

is defined by following formula [1]. Here, V_m- molar volume of solution and $V_m = \frac{M}{\rho} = \frac{\sum x_i M_i}{\rho}$ calculated with following equation [1].

3. Results and discussion

Activation Gibbs energy ($\Delta G_\eta^{\neq}$) of viscous flow of water-PEG, water-PEG-LiOH, water-PEG-NaOH, and water-PEG-KOH systems at 293,15 K temperature and activation enthalpy ($\Delta H_\eta^{\neq}$) of viscous flow dependences on PEG concentration (x) are shown in Table 1 and Table 2 and activation entropy ($\Delta S_\eta^{\neq}$) of viscous flow dependences on PEG concentration (x) are demonstrated in Fig. 1 and Fig. 2.

It is shown from the Table 1, Table 2 and Fig. 1, Fig. 2, activation parameters of viscous flow ($\Delta G_\eta^{\neq}$, $\Delta H_\eta^{\neq}$, $\Delta S_\eta^{\neq}$) increase as the concentration increases at given temperature for investigated systems. It is obvious that $\Delta G_\eta^{\neq}$ is the energy used for activation 1 *mole* molecule, $\Delta H_\eta^{\neq}$ and $\Delta S_\eta^{\neq}$ characterize changes in solution in terms of energy and characterized the change in solution in terms of structure. Thus, as concentration increases with rise of $\Delta G_\eta^{\neq}$ leads to more energy requirement to pass potential barrier, increase of $\Delta H_\eta^{\neq}$ leads to possess more stable structure, rise of $\Delta S_{\eta}^{\neq}$ leads to pass more modified structure [3-8]. According to activation parameters ($\Delta G_{\eta}^{\neq}$, $\Delta H_{\eta}^{\neq}$, $\Delta S_{\eta}^{\neq}$) of viscous flow dependency on concentration, it can be stated that researched systems pass more modified structure as concentration of PEG increases at given temperature.

Table 1 Activation Gibbs energy of viscous flow of water-PEG, water-PEG-LiOH, water-PEG-NaOH, water-PEG-KOH systems dependence on PEG concentration (*J/mol*). ($T = 293.15K$, $x_{LiOH} = 0.01$, $x_{NaOH} = 0.01$, $x_{KOH} = 0.01$).

x	$M_{PEG} = 1500$			
	Water-PEG	**Water-PEG-LiOH**	**Water-PEG-NaOH**	**Water-PEG-KOH**
0	9292	9598	9549	9457
0.0001	9463	9758	9700	9618
0.0002	9682	9937	9881	9803
0.0004	10023	10294	10242	10171
0.0006	10405	10761	10511	10754
0.0008	10735	11129	10984	10921
0.001	11149	11382	11339	11073
x	$M_{PEG} = 6000$			
	Water - PEG	**Water-PEG-LiOH**	**Water-PEG-NaOH**	**Water-PEG-KOH**
0	9292	9598	9549	9457
0.0001	10525	10777	10730	10663
0.0002	11656	11977	11534	11579
0.0004	13417	13303	13576	13529
0.0006	14938	15116	14779	15043
0.0008	16154	16326	16297	16562
0.001	17261	17834	17499	17055

Table 2 Activation enthalpy of viscous flow of water-PEG, water-PEG-LiOH, water-PEG-NaOH, water-PEG-KOH systems dependence on PEG concentration (*J/mol*). ($T = 293.15K$, $x_{LiOH} = 0.01$, $x_{NaOH} = 0.01$, $x_{KOH} = 0.01$).

x	$M_{PEG} = 1500$			
	Water-PEG	**Water-PEG-LiOH**	**Water-PEG-NaOH**	**Water-PEG-KOH**
0	17397	17619	17417	16753
0.0001	17633	17896	17680	16960
0.0002	17908	18150	17951	17188
0.0004	18407	18708	18500	17981
0.0006	18870	19145	18767	18621
0.0008	19390	19543	19392	18940
0.001	19869	20010	19866	19264
x	$M_{PEG} = 6000$			
	Water -PEG	**Water-PEG-LiOH**	**Water-PEG-NaOH**	**Water-PEG-KOH**
0	17397	17619	17417	16753
0.0001	18818	19062	18898	18370
0.0002	20093	20296	19788	19557
0.0004	22091	21849	22086	21705
0.0006	23880	23999	23600	23519
0.0008	25262	25387	25271	25166
0.001	26685	27222	26699	26051

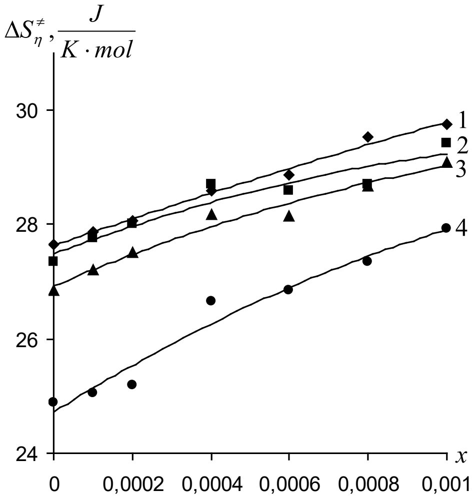

Fig. 1. Activation entropy of viscous flow of Water-PEG (1), Water -PEG-LiOH (2), Water -PEG-NaOH (3), Water -PEG-KOH (4) systems dependence on concentration of PEG($M_{PEG} = 1500$)

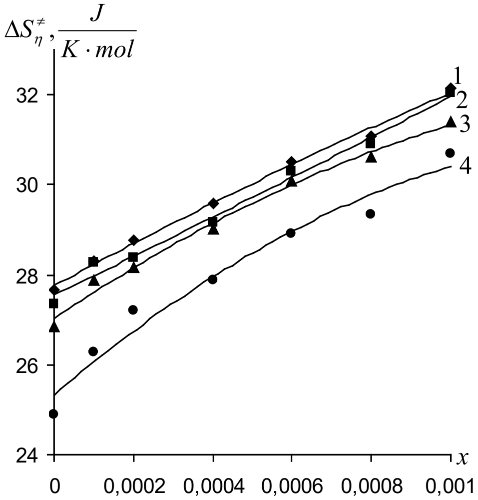

Fig. 2. Activation entropy of viscous flow of Water PEG (1), Water -PEG-LiOH (2), Water -PEG-NaOH (3), Water -PEG-KOH (4) systems dependence on concentration of PEG($M_{PEG} = 1500$)

($T = 293.15K$, $x_{LiOH} = 0.01$, $x_{NaOH} = 0.01$, $x_{KOH} = 0.01$).

Fig. 1 and Fig. 2 illustrates that when equal concentration of LiOH, NaOH, and KOH is added to PEG system at given temperature and concentration, value of $\Delta S_\eta^{\neq}$ decreases in proper sequence. This shows that when LiOH, NaOH, KOH is added to the water-PEG system, modification of structure by PEG is getting weaker accordingly. This means that LiOH, NaOH, KOH have and destructive influence on PEG system and this effect increases in given sequence. In order to explain this result, hydration process which is generated by electrostatic interaction between ions and water molecules will be taken as a base. It should be noted that Na^+ in comparison with Li^+ ion, and in comparison with Na^+ ion, K^+ possesses less hydration [1, 9], it seems, NaOH in comparison with LiOH, KOH in comparison with NaOH have more destructive effect at given temperature and concentration.

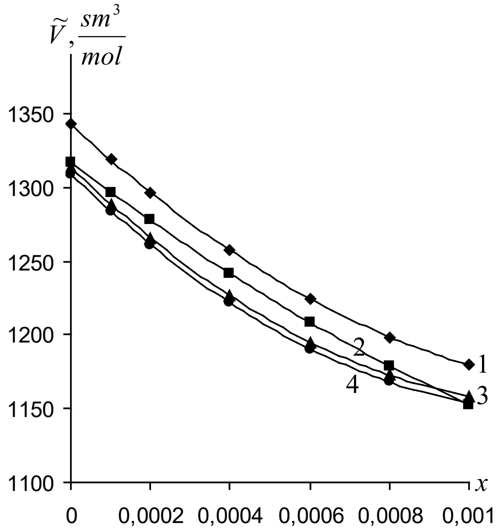

Fig. 3. PEG partial molar volume dependence on concentration of PEG at water-PEG (1), water-PEG-LiOH (2),Water-PEG-NaOH (3), and water-PEG-KOH (4) systems ($M_{PEQ} = 1500$).

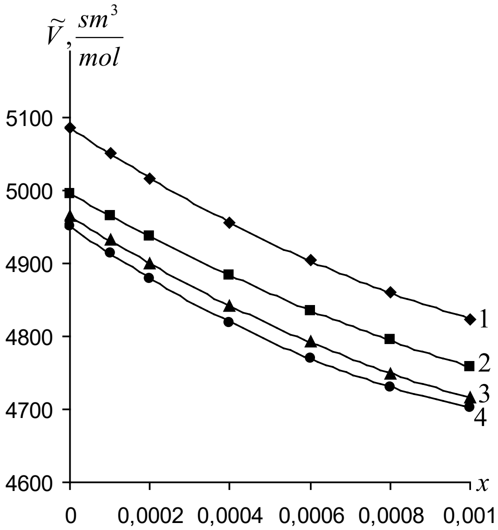

Fig. 4. PEG partial molar volume dependence on concentration of PEG at water-PEG (1), water-PEG-LiOH (2), water-PEG-NaOH (3), and water-PEG-KOH (4) systems ($M_{PEQ} = 6000$).

($T = 293.15K$, $x_{LiOH} = 0.01$, $x_{NaOH} = 0.01$, $x_{KOH} = 0.01$).

Dependency of molar volume ($\widetilde{V}$) on concentration (x) of PEG is shown in Fig. 3 and Fig. 4 at Water-PEG, water-PEG-LiOH, water-PEG-NaOH and water-PEG-KOH systems at 293,15 *K*.

It is obvious from figure 3 and Fig. 4, partial molar volume of PEG ($\widetilde{V}$) in solution is inversely proportional with concentration of PEG. It is clear that partial molar volume of component i equals to change in volume while adding 1 mole adequate component to the system [1, 10]. It can be stated that volume fraction of big sized associates in space is smaller than volume fraction of separate parts in total and vice versa. According to binary water structure [1, 11], water consists of different sized clusters which are connected with hydrogen bond and free water molecules between these clusters. According to dependency of partial molar volume on concentration, it can be assumed that PEG molecules first bond with free water molecules by hydrogen bond. As concentration increases, partial molar volume of PEG in solution increases in final. This shows that solution passes more modified structure as concentration increases.

4. Conclusion

Thus, according to both activation entropy of viscous flow and dependency of partial molar volume of PEG in solution on concentration, it can be stated that PEG have and structuring effect on both water and water-LiOH, water-NaOH, water-KOH systems, however, presence of LiOH, NaOH, KOH accordingly weakens structuring effect of PEG. This is related to the destructive effect of LiOH, NaOH, KOH accordingly to water structure.

References

1. Masimov E.A., Hasanov H.Sh., Pashayev B.G. Liquid viscosity. Baku, "Publishing House Laman", 2016, 285 p.
2. Glesston S., Leidler K., Eyring G. The theory of absolute velocities. M.: Publishing house inostr. Lit., 1948, 600 p.
3. Masimov E.A., Hasanov H.Sh., Pashayev B.G. Journal of Physical Chemistry (in Russian), vol. 87, №6, 948 (2013).
4. Masimov E.A., Pashayev B.G., Hasanov H.Sh., Musayeva S.I. Journal of Physical Chemistry (in Russian), vol. 87, 12 (2105).
5. Masimov E.A., Pashayev B.G., Hasanov H.Sh., Hasanov N.H. Journal of Physical Chemistry (in Russian), vol.89, 7, 1244 (2015).
6. Masimov E.A., Pashayev B.G., Hasanov H.Sh. Journal of Physical Chemistry (in Russian), vol.91, 4, 667 (2017).
7. Dakar G.M., Korableva E.Y. Journal of Physical Chemistry (in Russian), vol.72, 4, 662 (1998).
8. Dakar G.M. Journal of Physical Chemistry (in Russian), vol.75,4, 656 (2001).
9. Samoylov O.Y. M., Docl.AN SSSR, 9 (in Russion), 76 (1957).
10. Atkins P., De Paula J. Physical chemistry. Oxford University Press. 2006. 1067 p.
11. Nemethy G. Istituto superiore di sanita -V.le Regina Elena, 299-Roma. Vol. VI fascicule special 1, 492 (1970).

***Corresponding author**: p.g.bakhtiyar@gmail.com

COMPARATIVE STUDY OF CONFORMATIONAL BEHAVIOUR OF ANGIOTENSIN CONVERTING ENZIME INHIBITORY TRIPEPTIDES

N.M.GODJAEV[1,2], G.A.AGAEVA* [1], U.T.AGAEVA[1]
1- Baku State University, Z.Khalilov str., 23, Baku, Azerbaijan, Az1148
2- Baku Engineering University, Baku -Sumqait Road,16 km, Azerbaijan, Az0101

The conformational properties of two angiotensin converting enzyme (ACE) inhibitory tripeptides LKP and IQW have been investigated by energy calculation methods. It is shown that the spatial structure of these tripeptides can be described by set of low-energy conformations. The obtained results have shown that the stable conformers of LKP tripeptide have tendency adopt a beta-strand structure, but the stable conformers of IQW tripeptide prefer to form a fully folded quasi-cyclic structure. Calculations produced the values of all dihedral angles of the backbone and side chains of the optimal conformations as well as intra- and inter-residue interactions energies.

Keywords: tripeptide, angiotensin converting enzyme (ACE) , conformation, molecular mechanics method
PACS: 36.20.Ey; 87.15.Aa; 87.15.He

1. Introduction

Antihypertensive peptides with angiotensin converting enzyme (ACE) inhibitory properties are of research interest due to the high prevalence of hypertension. Hypertension is a major risk factor for developing cardiovascular diseases [1,2]. Angiotensin-converting enzyme plays a critical role in blood pressure control systems as it converts angiotensin I into angiotensin II, leading to the development of hypertension. A number of pharmacological drugs have been used in the management of hypertension and many of these drugs require lifelong adherence to therapy. Some functional foods are derived from natural sources and generally considered safe and hence these have become potential alternatives to synthetic pharmacological drugs.

In work [3] is shown that two angiotensin converting enzyme (ACE) inhibitory tripeptides,Ile-Gln-Trp (IQW) and Leu-Lys-Pro (LKP), were previously characterized from egg white protein ovotransferrin. ACE is a key enzyme of the renin-angiotensin system (RAS) which generates angiotensin II from its precursor and increases blood pressure (BP) in the body. This study tested the blood pressure lowering potential of orally administered IQW and LKP in spontaneously hypertensive rats. IQW and LKP treatment decreased mean blood pressure (MAP). The change in BP was accompanied by the preservation of nitric oxide dependent vasorelaxation and lowering of plasma Angiotensin II levels. Furthermore IQW, but not LKP, also reduced intercellular adhesion molecule-1 (ICAM-1) expression and nitrotyrosine levels in arteries, suggesting additional protective effects against inflammation and oxidative/nitrosative stress. These results demonstrate antihypertensive effects of IQW and LKP in vivo and a reduction of circulating Angiotensin II levels, with additional anti-inflammatory and antioxidant effects mediated by IQW [3].

In present work was studied the spatial structure of IQW and LKP tripeptide molecules by molecular mechanics method with atom-atom potentials. For determination a mechanism of action these tripeptides and to compare their conformational properties is required the knowledge of the conformational specificity and flexibility of backbone and side chains of molecules allowing a rational design of functional groups acting selectively at their receptor level.

2. Methods

This investigation were carried out using molecular mechanics method and above potentials with energy and geometry parameters as described in Refs.[4]. The conformational energy is considered the sum of independent contributions of nonbonded E_{nb}, electrostatics E_{els}, torsional interactions E_{tor} and hydrogen bonding E_{hb} energies. The first term is described by the Lennard-Jones potential with the parameters proposed by Scott and Scheraga [5]. The electrostatic energy is calculated in a monopole approximation, with atom centered charges obtained by Momany et al [6]. The dielectric constant is assumed to equal ten. Torsional potentials and barriers to rotation about bonds N-C$^{\alpha}$ (φ), C$^{\alpha}$-C′ (ψ), C′-N (ω), and about side chain bonds C$^{\alpha}$-C$^{\beta}$ (χ) were as proposed by Scheraga [7]. The hydrogen bond energy calculated from the Morse potential are supposed to be weakened with maximum energy of 1.5 kcal/mol. Bonding lengths and angles are those given Corey and Pouling. The proline ring is assumed to be planar with a structure given by Ponnuswamy et al [7]. Computations were carried out on the computer using universal programs complex [8]. This program calculates the conformational energy of a peptide as a sum of nonbonded, hydrogen-bonded and electrostatic energies for pairwise atomic interactions and torsional potential energies for rotation about bonds. Bond lengths and bond angles are fixed at standard values [9], and only dihedral angles are allowed to vary. The conformational state of each amino acid residue is conveniently described by backbone φ, ψ,ω and side chain χ_n dihedral angles. All backbone forms of a dipeptide can be classified into two types, referred to as shapes: folded and extend. For a tripeptide, all possible backbone forms can be found in besides β-strand and γ-turn structures. The dihedral angle values corresponding to the lowest energy states of monopeptides were used as starting conformations. The conventions used for torsion angles are those of IUPAC-IUB Commission [9].

3.Results and discussion

The spatial structure of two tripeptides Leu-Lys-Pro and Ile-Gln-Trp have been investigated basing on the low-energy conformations of monopeptides. Therefore our investigation of conformational possibilities of these tripeptides is started with conformational analysis of their initial variants. The starting conformations of the tripeptides LKP and IQW were obtained by combining the low-energy structures of constitutive residues. In LKP tripeptide the second residue Lys has large side chain structure and therefore its side chain is relatively flexible, but C-terminal residue Pro has not a free side chain. These structure variants exhibit 300 conformers for a tripeptide LKP belonging to two types of interactions, due existing of the Pro residue. After energy minimization had been performed a rather limited number of conformations lay in the ΔE energy interval. After minimization of the 300 initial conformers, 20 optimal LKP conformers thus obtained were subjected to the rotation operation performed on the all dihedral angles. For investigation of IQW tripeptide spatial structure were selected 360 conformers. The values of dihedral angles of the side chains were taken to be 60, 180, and -60^{0} for Ile, Gln and Trp residues. The angle χ_2 of side chain of both Gln and Trp residues were taken to be equal to 90 and -90^{0}. But after minimization of the initial conformers for IQW tripeptide were found 40 optimal conformers.

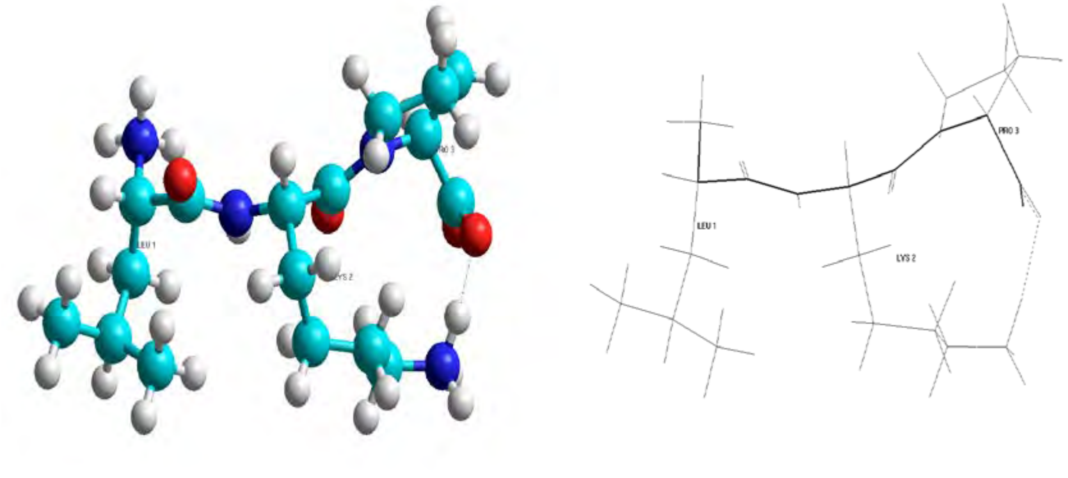

a) b)

Figure 1. The molecular models of preferred calculated conformation of the Leu-Lys-Pro tripeptide: a) in balls and cylinders and b) in sticks. Hydrogen bond is shown dashed line, peptide backbone is shown thick line.

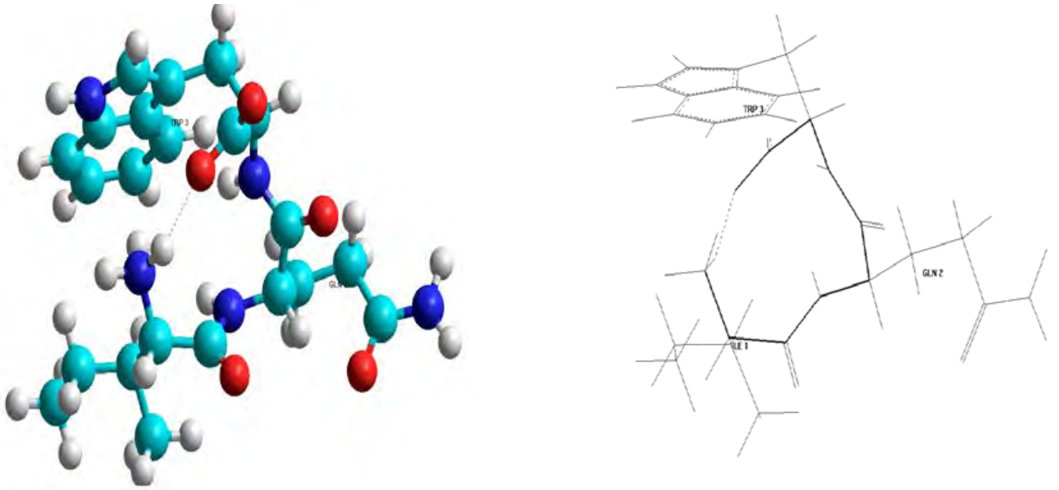

a) b)

Figure 2. The molecular model of preferred calculated conformation of the Ile-Gln-Trp tripeptide: a) in balls and cylinders and b) in sticks. Hydrogen bond is shown dashed line, peptide backbone is shown thick line.

The most stable conformers of two tripeptides LKP and IQW is shown in Figure 1 and Figure2, respectively. The spatial models of these molecules were built in HyperChem 8.01 [10].The energy minimization of the obtained set of the structural variations for these tripeptides, revealed a remarkable energy differentiation among the optimal conformations. The effective interactions of the opposite charged atom groups of side chain of Lys residue and C-terminal backbone oxygen atom was possible in these conformations due to the formation of H-bonds between distant residues. The preferred conformations of two tripeptides LKP and IQW are compared. Calculations have shown that in global conformation of LKP the Lys side chain formed the hydrogen bond with oxygen atom of C-terminal carboxyl group. Bur a most stable conformation of IQW has an H-bond between C-terminal carboxyl oxygen atom and N-terminal amid group. These contacts have the electrostatic nature. In Figure 3 are presented the conformational flexibilities of the second residue in the lowest energy conformations of two tripeptides LKP and IQW as the energy dependency of the $\chi1$side corner of the rotation.

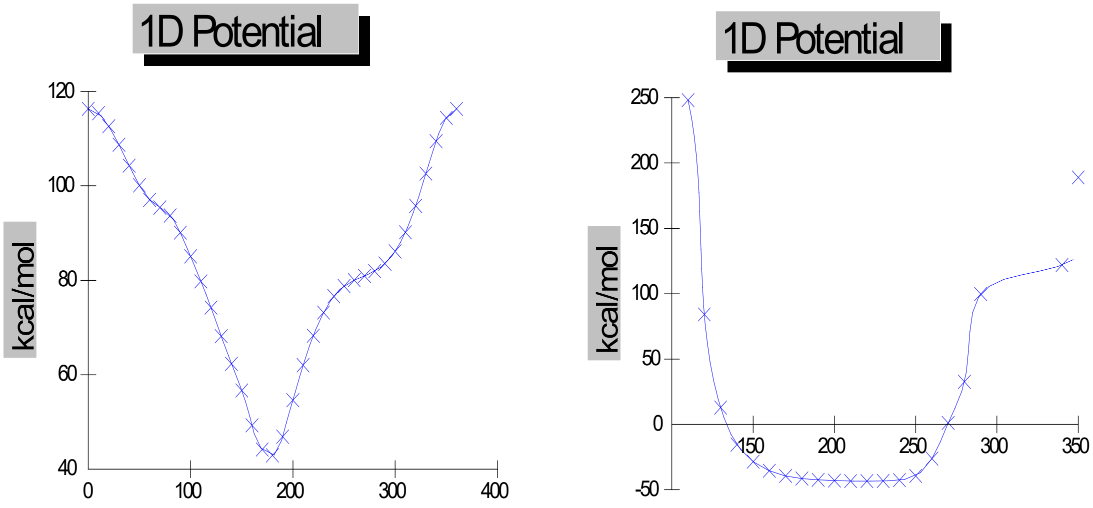

a) b)

Figure 3. Conformational properties of the second residues in the lowest energy conformations of two tripeptides LKP and IQW. (a) the 1D potential (energy) surface for Lys residue in LKP; (b) the 1D potential (energy) surface for Gln in IQW.

The values of dihedral angles of lowest-energy conformaions of LKP and IQW tripeptides are presented in Table 1 and Table 2 accordingly. Structural characteristics of the obtained stable tripeptide conformers were carefully analyzed. This investigation demonstrated a definite difference in the conformational behavior and stability of LKP and IQW tripeptides.

Table 1. The values of the dihedral angles of low-energy structures of LKP molecule:
I - (E_{rel}= 0.0 kcal/mole), II - (E_{rel}=1.1 kcal/mole), III -(E_{rel}=1.7 kcal/mole), IV - (E_{rel}= 2.2 kcal/mole), V - (E_{rel}=2.9 kcal/mole)

Amino acid	Conformation	Backbone angles			Side chain angles				
		φ	ψ	ω	χ_1	χ_2	χ_3	χ_4	χ_5
Leu	I	-60	146	177	181	70	179	176	-
	II	-159	84	179	171	60	179	176	-
	III	-152	86	178	174	165	190	181	-
	IV	-74	147	178	57	74	179	169	-
	V	-154	112	177	185	70	191	180	-
Lys	I	-121	92	164	187	-63	189	179	176
	II	-123	90	162	188	-65	192	179	177
	III	-148	149	165	68	90	195	167	180
	IV	-144	146	167	67	91	195	169	170
	V	-145	144	165	67	90	193	165	180
Pro	I	-60	83	-	-	-	-	-	-
	II	-60	88	-	-	-	-	-	-
	III	-60	99	-	-	-	-	-	-
	IV	-60	101	-	-	-	-	-	-
	V	-60	98	-	-	-	-	-	-

Table 2. The values of the dihedral angles of low-energy structures of IQW molecule: I - (E_{rel}= 0.0 kcal/mole), II - (E_{rel}=0.2 kcal/mole), III - (E_{rel}=0.2 kcal/mole), IV - (E_{rel}= 0.4 kcal/mole), V - (E_{rel}=0.8 kkal/mole)

Amino acid	Conformation	Backbone angles			Side chain angles			
		φ	ψ	ω	χ_1	χ_2	χ_3	χ_4
Ile	I	-39.7	-64.7	160.6	-62.8	186.5	181.9	190.1
	II	-38.9	-63.9	156.9	-61.6	186.6	186.0	189.5
	II	-39.0	-64.0	157.0	-61.6	186.7	185.1	189.5
	IV	-38.9	-63.7	162.8	-61.8	186.9	182.0	190.1
	V	-36.6	-63.2	164.5	-61.3	186.4	181.4	190.5
Gln	I	-84.8	-39.5	-191.3	180.3	-62.8	-95.6	-
	II	-89.2	-38.3	-188.2	-61.9	-68.7	93.5	-
	II	-89.2	-38.4	-187.9	-62.0	-68.8	93.4	-
	IV	-85.5	-37.5	-189.7	-60.5	180.3	87.4	-
	V	-82.9	-38.9	-192.6	182.6	177.0	-87.3	-
Trp	I	-74.8	-39.6	180	62.3	90.9	-	-
	II	-75.7	-39.7	180	61.2	91.5	-	-
	II	-75.7	-39.8	180	61.2	91.6	-	-
	IV	-74.8	-40.0	180	62.4	91.3	-	-
	V	-74.3	-39.0	180	62.8	91.0	-	-

4. Conclusions

Our calculations of the spatial structures of two biologically active tripeptides demonstrated that investigated tripeptide molecules have a limited set of the stable structures that are characterized by different backbone form. The obtained results have shown that the stable conformers of LKP tripeptide have tendency adopt a beta-strand structure, but the stable conformers of IQW tripeptide prefer to form a fully folded quasi-cyclic structure. The determination of difference in conformational preference of LKP and IQW tripeptides expects the different mechanism of the action of these molecules.

The conformational analysis helped reveal a number of special features of spatial arrangement of these drug-based tripeptides, which may be useful as a base for a directed search and synthesis of their more effective structural analogs.

References

1. Kivimdki M. ,Steptoe A., Nat. Rev. Cardiol. 15, 215 (2018).
2. Bernstein K.E., Khan Z., Giani J.F., Cao D.Y. ,Bernstein E.A., Shen X.Z., Nat. Rev. Nephrol. 14, 325 (2018).
3. Majumder K., Chakrabarti S., Morton J.S.,Panahi S., Kaufman S.,Davidge S.T., Wu J., Journal of Functional Foods, 50 (2015).
4. Agaeva G.A.,Agaeva U.T.,Godjaev N.M., Biophysics (in Russian) 60, 365 (2015).
5. Scott R.A. ,Scheraga H.A., J.Chem.Phys., 45, 2091 (1966).
6. Momany F.A., McGuire R., Burgess A.W., Scheraga H.A., J.Phys.Chem., 79, 2361 (1975).
7. Ponnuswamy P.K., McGuire R.F., Scheraga H.A., Int.J.Pept.Protein Res.,5 ,73 (1973).
8. Godjaev.N.M., Maksumov I.S., Ismailova L.I., J.Chem.Struc.(in Russian), 24, 147 (1983).
9. IUPAC-IUB Quantity. Units and Symbols in Physical Chemistry 39, Blackwell Scientific Publications, Oxford (1988).
10. Chem 3D Pro, “Molecular Modeling and Analysis,” Cambridge Soft Corporation, 875 Massachusetts, 02139 U.S.A (2005).

***Corresponding author**: gulshen@mail.ru

INTERACTION OF PROTEIN AND STARCH MOLECULES WITH NANOPARTICLES

I.S.AHMADOV, M.A.RAMAZANOV
Baku State University, Z.Khalilov str., 23, Baku, Azerbaijan, Az1148

The interaction of nanoparticles with biological molecules is the basis of their biological reactivity. During this interaction, are formed nanoparticle – bimolecular complexes with new properties. Into the biological environment the surface of nanoparticles gets coated with various biomolecules, forming so called corona. In this studies was determinate the possibility formation of corona on the surface of nanoparticles by the starch and protein molecules. The results of experiments show that forming corona depends on the concentrations of biomolecules and types of nanoparticles. In these experiments with starch and egg albumin, a decrease in fluorescence intensity was observed. The degree of decreasing depends on the starch concentration. In high concentrations it may be due to thickness of starch corona. But in case of protein (egg albumin) the decrease in fluorescence intensity depends on the types and surface characteristics of nanoparticles.

Keywords: nanoparticle, biological molecules, protein, starch
PACS: 01.50.Pa; 81.20.–n; 87.15.Kg

1. Introduction

As soon as nanoparticles (NPs) get into biological systems, for example, into a cell, their interaction with biological molecules occurs. These interactions lead to a change in the properties of the NPs themselves as well as biological molecules. The interaction of NPs with biological molecules is the basis of their biological reactivity. During this interaction, are formed nanoparticle – bimolecular complexes with new properties. Into the biological environment the surface of NPs gets coated with various biomolecules, forming so called corona. This corona may be formed from proteins, lipids or carbohydrates [1]. It is very important to characterize affinities, rates and stoichiometry of biomolecules binding to the NPs surface in order to understand nanomaterial interaction with cells and its functional processes. The corona from biomolecules at surface of nanoparticle can define its interaction with cell membrane, the action of nanoparticles inside the cell, its metabolism and its effect on intracellular processes, receptors, allow enter and transport nanoparticles into cells, degradation and removal from cell, binding of medicine and luminescent molecules and even genes. On the other hand, conformational changes occur in biological molecules adsorbed on the surface of the nanoparticles to form a corona, and their biological activity increases. The clarification of the nature of the interaction of nanoparticles with biological molecules allows the creation of highly controlled bio nanoparticle complex.

Geometrical structure, the surface electrical charges and dimensions of nanoparticles, plays an important role in their stability and interaction with biological molecules. There are paradigm assumes that the formation of nanoparticle -protein corona depends upon the surface charge, coating, shape, roughness, and reactivity of nanoparticles, on the pH, ionic strength, and temperature of solvent and the amphiphilicity, charge, pKa, chemical composition, and folding dynamics of proteins. It has been established that the adsorption of proteins to the surface of nanoparticles depends on their size and the blood plasma protein adsorbed to the surface of nanoparticles at 80 nm was 23% and 34%, respectively, by the adsorption to the surface of 171 nm and 240 nm of nanoparticles [2-5]. The surface charges of nanoparticles play a special role in their interaction with proteins. The adsorption of proteins to the surface of the nanoparticles increases with the increase the surface charges. Isoelectric point on positively charged nanoparticles adsorbs proteins at pI<5.5. For example, surfactant adsorbents with negatively charged nanoparticles albumin at pI > 5.5 [6]. The adsorption of plasma proteins has increased as the surfactant density increases the surface charge of negatively charged nanoparticles [2]. Surface charges denature the adsorbed proteins. It has been established that, if the surface of the nanoparticles is positive or negative, the adsorbed proteins are denatured, but when the neutral is normal, the protein structure does not change. İn the dependence on the specificity of proteins and type of nanoparticles the lifetime of protein-nanoparticle complexes typically ranges from 100 s to many hours [8-9].

The protein corona at surface of nanoparticles may be monolayer or multilayer. The first layer of protein that formed corona is found to be tightly absorbed to nanoparticle surface and formed hard corona, but weakly bound second monolayer formed soft corona. In the first layer proteins interacts directly with surface of nanoparticles, but the proteins of second monolayer interacts each other[7]. There are evidences that at protein-fullerene interaction the driving force is π-stacking and during increasing the number of hydroxyl groups resulted in a decreased binding affinity and wherein variations in protein structure and dynamics upon nanoparticle binding no observed [10]. During the formation of protein coronas on the NP surface, conformational changes can occur and the function of the adsorbed protein changes. It was shown that conformational changes in the structure of bovine serum albumin (BSA) occur on the surface of gold NPs, and this change depends on the dose [11], whereas during adsorption on the surface of C60 carbon NP was not registered significant conformational changes [12]. Conformational changes also occur on the surface of titanium dioxide (TiO2) and in this case polymerization of tubulin, which is an important cytoskeleton protein, decreases [13]. Thus, the study of the characteristics and analysis of biological molecules associated with NP surface allows us to understand the true nature of NP-mediated biological effects.

It turns out that the size, shape and surface characteristics NPs play important roles in the adsorption of biomolecules, as well as modify the structure of adsorbed biological molecules. Understanding the dynamics of the interaction of biomolecules with nanoparticles can provide useful information about cytotoxic, inflammatory potential and other key properties of these new materials.

2. Experiment

Protein. In experiments, the chicken egg cell was used as a protein molecule (albumin). By the spectrophotometric methods was found to contain 15.82 g / 100 g or 54% albumin in the egg white. 10 g of fresh egg white have been extracted and various nanoparticles were added and denaturation in the water bath. The denaturized albumin was analyzed by fluorescence and FTIR spectrometer after crystallization.

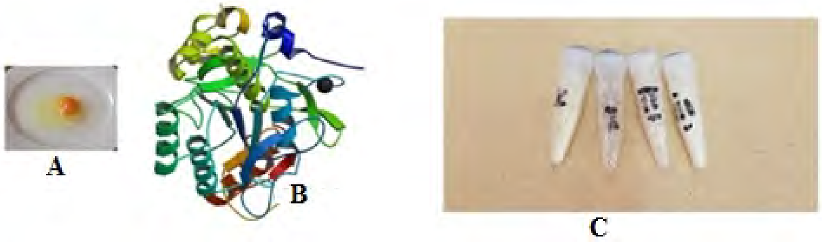

Figure 1.Egg white (A), albumin molecules (B) and crystals of albumin-NPs complex

Starch. Starch was purchased from "The science world" store. Starch is composed of amylase and amylopectin polysaccharides and monomer is alpha glucose. 1%, 5% and 10% solution of starches were prepared and added to Fe_3O_4 nanoparticles in 1mg / ml, was crystallized in water bath. Then these crystals were analyzed by UV-vis, fluorescence and FTIR spectrometry.

Nanoparticles. Nano powders of Fe_3O_4 (20-30 nm), ZnO (10-30 nm) and CuO (40nm) nanoparticles was purchased from Sky Spring Nanomaterials, Inc. company

FTIR analysis. For characterization of NPs -protein and NPs-starch complexes was used FT-IR spectrometer (Varian 3600). FTIR spectrometers can recording spectra with of 4 cm−1 spectral resolution and a time resolution of 40 ms. This transmission measurements rely on the absorption of IR radiation as it passes through the sample mixture of dry crystals in potassium bromide (KBr) matrix is pressed into thin pellets.

Fluormetric analysis. Examples of starch-nanoparticles and protein-nanoparticle complexes was analyzed in the Fluorescence Spectrophotometer (Varian, Cary Eclipse).Fluorescence spectra was get on the excitation of samples with light 335 nm wavelength.

3. Results and discussion

The interaction of starch molecules with the surface of the nanoparticles. To study the interaction of starch molecules with the surface of the nanoparticles, starch solutions were prepared with different concentrations (1%, 5%, 10%) by dissolving the starch powders in hot distilled water. Fe_3O_4 was used as a nanoparticle and poured into the prepared starch solution with vigorous stirring at 70 ° C for 1.5 hours. The starch solution with Fe_3O_4 nanoparticles was cooled to room temperature and left for 24 hours. The remaining starch solution with Fe_3O_4 nanoparticles formed a gel. Then this gel was washed with distilled water until the pH was less than 8. After washing, a suspension of the starch-modified Fe_3O_4 nanoparticles was prepared by dispersion in deionized water. At the same time, starch was sorbed on the surface of Fe_3O_4 nanoparticles and formed a layer which through their hydroxyl groups interacted with iron atoms.

The experimental results indicate that the starch-water suspension crystals on the excitation wavelength 335 nm can emit fluorescence, whose peak wavelength is about 359 nm. This peak of due to fluorescence transition from nonbonding electrons in the hetero-atom (O) of the functional group (C--O--C) called ether linkage to the antibonding orbital. The intensity of fluorescence emission of starch is analyzed dependence of Fe_3O_4 nanoparticles. When turning on the Fe_3O_4 nanoparticles (1mg/ml) on the starch solution, a decrease in the peak intensity of 359 nm is observed. The decrease in intensity is correlated with starch concentration. As at 10% concentration, the intensity of the peak is greatly reduced. The results of this experiment are given in Figure.3.

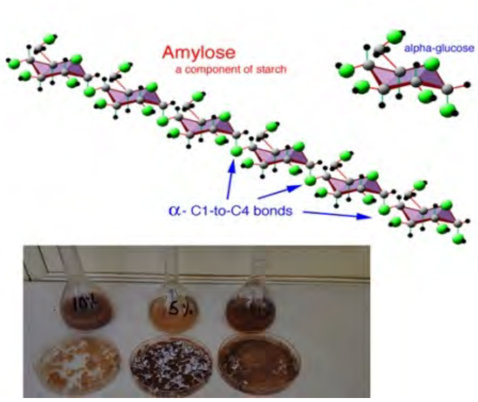

Figure 2. Starch crystals with Fe_3O_4 nanoparticles

Was analyzed also the FT-IR spectra of pure starch and starch with F nanoparticles. FT-IR spectroscopy spectra is shown in Figure 4 for pure starch and for 5% and 10% starch-coated iron nanoparticles. For pure starch, as clearly seen from Figure 4 (1), all of the peaks characterized for the C¼O bond, the O–H stretch dimer H-bond, as well as the CH-groups are well appeared in the FT-IR spectra. The spectra of 5% starch+ Fe_3O_4 nanoparticles show that both primary groups of starch and magnetite appear in the spectrum (Figure 4(2)) and (3). The OH-vibration mode, however, is suppressed for the 5% starch+ Fe_3O_4 nanoparticles (Figure 4 (2)). It suggests the chemisorption of starch onto magnetite nanoparticles through hydroxyl groups (see also Figure 1). At higher starch concentration, e.g., for the 10% starch-coated magnetite, this peak appears again (Figure 4(3)).

According to the results of fluoresces spectra may be concluded that iron nanoparticles are coated with starch molecules. The starch molecules form a layer and with increasing concentration the thickness of the layer increases and this is the reason for the decrease in the intensity of fluorescence. It is well known that surface modification of nanoparticles prevent aggregation and oxidation of nanoparticles, therefore also makes them biocompatible. Moreover, the toxicity of the starch coated magnetite gets very low. In their cytotoxic test experiments Kim et al. [19], showed that the L929 cells validity could be higher than 90% in starch-coated magnetite particles.

In fact, cellular internalization and the drug delivery characteristics of the engineered nanoparticles depend on surface charge, on the protein corona of nanoparticles, and also the presence of specific receptors on cell surface and finally, it will also depend on the nanoparticle- biomolecule complex [14-16].

The interaction of protein molecules with nanoparticles. In the experiments related to the interaction of protein molecules and nanoparticles, the effect of nanoparticles on the denaturation of proteins was studied first. In all variants, egg albumin was taken in the same weight (10 g) and denaturated in a water bath. The denaturation time of pure albumin was 12 minutes. Then 1 g Fe_3O_4, CuO and ZnO nanoparticles were added to the egg albumin in the same weight and the duration of the denaturation was determined. The denaturation time of the egg album was 9, 10, 14 minutes, for the Fe_3O4, CuO and ZnO nanoparticles respectively. It has been clear that nanoparticles have a effect on the denaturation time of the albumin. Fe_3O_4 and CuO reduce denaturation time over control, but ZnO increase denaturates time.Then the denaturated egg albumin and egg albumin with nanoparticles was crystallized at a temperature of 60^{o}C.Initially, fluorescent spectra of crystals were made.

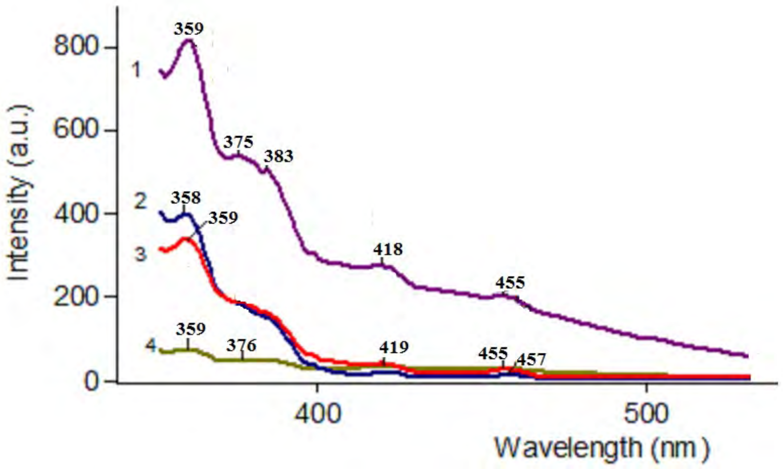

Figure 3.The fluorescence emission spectra of starch crystals with Fe_3O_4 nanoparticles: 1-control (starch 10%), 2- 5% starch+ Fe_3O_4 nanoparticles; 3- 1% starch+ Fe_3O_4 nanoparticles; 4 – 10% starch+ Fe_3O_4 nanoparticles

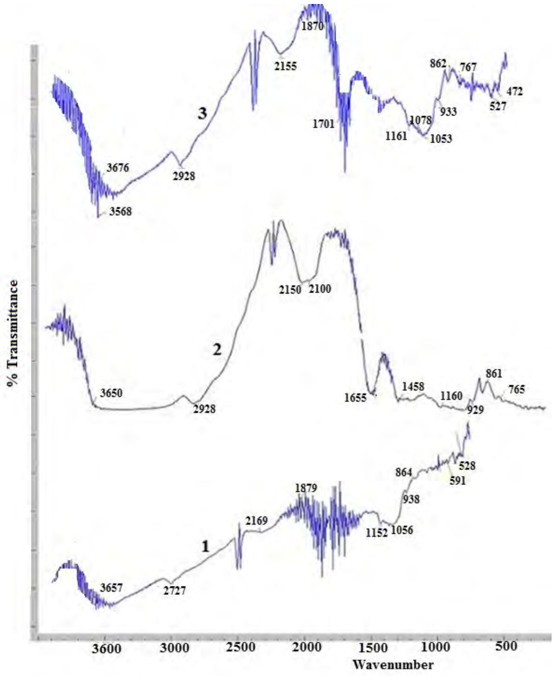

Figure 4. FT-IR spectra of starch crystals with Fe_3O_4 nanoparticles: (1) pure starch, (2) 5% starch+ Fe_3O_4 nanoparticles; (c) 10% 10% starch+ Fe_3O_4 nanoparticles

The fluorescence spectrum of the crystalline albumin+ nanoparticles complex is shown in Figure 2. The results revealed that the intencity of fluorescence spectrum of the crystalline albumin+ nanoparticles complex reduced depending on the type of nanoparticle.Fe_3O_4 and CuO nanoparticles is reduced the intensity of fluorescences spectra, as these nanoparticles reduces the denaturation time also. However, while the duration of denaturation increases in ZnO nanoparticles, the intensity of fluorescences spectra decreases stongly. This shows that the adsorption of the albumin to the surface of the nanoparticles occuers.

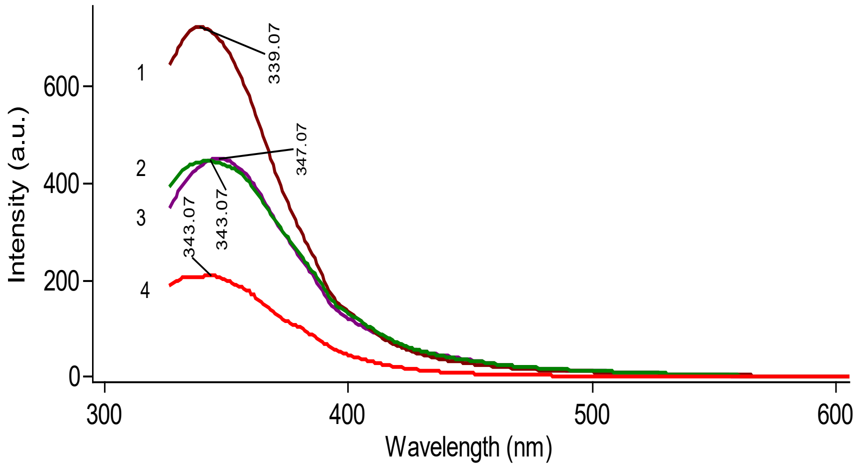

Figure 5.The fluorescence emission spectra of albumin+ nanoparticles crystals, at the excitation wave 297 nm was : 1 – pure albumin; 2- albumin with Fe_3O_4 nanoparticles: 3 - albumin with CuO; 4- albumin with ZnO nanoparticles.

Then the FTIR spectra of albumin + nanoparticles crystals were made (Figure 6). FTIR spectra allow you to see which groups of protein molecules combine with nanoparticles. Egg albumin and iron oxide + albumin complex have FTIR spectra that appear to be characteristic peaks. Characteristic peaks at 1533 cm -1 (NH bending modes) indicate the presence of groups of 1653 cm-1 (-C = O) due to amide I in the FTIR spectra of pure albumin crystals and amid II. Each of the secondary structures indicates that the amide is associated with a characteristic hydrogen bonding between C = O and NH groups. The crystal of iron oxide nanoparticles coated with egg albumin corresponds to amide I in the peak CN bending mode observed at 1653 cm -1 in the FTIR spectrum and corresponds to the 2I amide of the 1533 cm-1 -C = O. In the nanoparticles of the egg album, the peak point of 1521 cm-1 corresponds to the N-H combination.

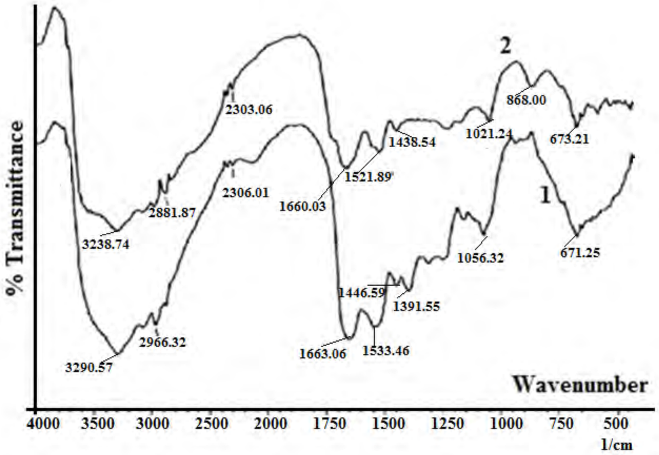

Figure 6. FT-IR spectra of egg albumin crystals (1) and with Fe_3O_4 nanoparticles (2)

We studied the interaction of nanoparticles with starch and proteins and demonstrated the possibility of corona formation on the nanoparticles surface. Characterization and analysis of biomolecules bound to the nanoparticles surface is allow to understand the basic nature of the nanoparticles - mediated biological effects. Such types experiments highlight the structural and morphological changes of molecules adsorbed on the surface of nanoparticles, as well as how can we get functional nanoparticles for use in medical practice.The protein adsorption on the nanoparticles surface requires to the modification of surface charge of nanoparticles.

Studies have demonstrated that nanoparticles surfaces with no charge bind less proteins than their negatively charged (COOH functionalized) or positively charged (NH2 functionalized) counterparts [17,18].In experiments with starch and egg albumin, a decrease in fluorescence intensity was observed. The degree of decreasing depends on the starch concentration. In high concentrations it may be due to thickness of starch corona. But in case of protein (egg albumin) the decrease in fluorescence intensity depends on the types and surface characteristics of nanoparticles.

Conclusion

The safety and biocompatibility of the nanoparticles are of crucial importance, especially in medical practices. Therefore, the functionalization of the nanoparticles may has further improved drugaddressage in the direction of diseases, uptake and transport them in the organisms and of the specificity toward the target cells. Research thus far highlights that size, shape, and surface characteristics of nanoparticles affect biomolecules adsorption and also have the capability to modify the structure of the adsorbed biomolecules. This can significantly affect the reactivity of the nanoparticles with cells and determine the route and efficiency of nanoparticles uptake.

References

1. Tommy Cedervall, Iseult Lynch, Stina Lindman, Tord Berggerd, Eva Thulin, Hanna Nilsson, Kenneth A. Dawson, and Sara Linse. *Proc. Natl. Acad. Sci. U. S. A.***104,** 2050 (2007).
2. Gessner, A., Waicz, R., Lieske, A., Paulke, B.R., Mader, K., Mğller, R.H., Int. J. Pharm. 196, 245 (2000).
3. Mahmoudi, M., Lynch, I., Ejtehadi, M.R., Monopoli, M.P., Bombelli, F.B., Laurent, S., Chem. Rev. 111, 5610 (2011).
4. Navneet Phogat,Matthias Kohl, Imran Uddin, Afroz Jahan, Precision Medicine, Tools and Quantitative Approaches, Pages 253 (2018).
5. Rahman, M., Laurent, S., Tawil, N., Yahia, L., Mahmoudi, M. Springer Series in Biophysics, Vol. 15 (2013).
6. Service R. F., Science 314, 45 (2006).
7. Milani, S., Bombelli, F. B., Pitek, A. S., Dawson, K. A. &Raedler, J. *AcsNano* **6,** 2532 (2012).
8. Lundqvist, M., Sethson, I. &Jonsson, B.-H.,*LangmuirACS J. Surf. Colloids* **20,** 10639 (2004).
9. Lundqvist, M., Sethson, I. &Jonsson, B.-H., *Langmuir ACS J. Surf. Colloids* **21,** 5974 (2005).
10. Ratnikova, T. A., Govindan, P. N., Salonen, E. &Ke, P. C., *ACS Nano* **5,** 6306 (2011).
11. Wangoo N, Suri CR, Shekhawat G.,ApplPhysLett, 92:133 (2008).
12. Shufang Liu YS, Kai G, Zhijuan Y, Xibao G.,Nanoscale Res Lett, 7:433(2012).
13. Gheshlaghi ZN, Riazi GH, Ahmadian S, Ghafari M, Mahinpour R., ActaBiochimBiophys Sin, 40:777 (2008).
14. Petri-Fink A, Steitz B, Finka A, Salaklang J, Hofmann H.,Eur J Pharm Biopharm, 68(1):129 (2008).
15. Bajaj A, Samanta B, Yan H, Jerry DJ, Rotello VM.,19(35):6328 (2009).
16. Lesniak A, Fenaroli F, Monopoli MP, Eberg C, Dawson KA, Salvati A., ACS Nano, 6(7):5845(2012).
17. Deng Z.J., Liang M,Toth I, Monteiro M, Minchin RF.,Nanotoxicology, 7:314 (2013).
18. Fertsch-Gapp S., Semmler-Behnke M., Wenk A, Kreyling WG., InhalToxicol, 23:468 (2011).
19. D.H. Kim, S.H., Lee, K.H. Im, K.N. Kim, K.M. Kim, I.B. Shim, M.H. Lee, and Y.K. Lee, Current Appl. Phys. 6(S1), 242(2006).

***Corresponding author**: ismetahmadov@mail.ru

SPATIAL STRUCTURE OF ARGININ-CONTAINING PENTAPEPTIDES

L.I.ISMAILOVA*, R.M.ABBASLI, N.A.AKHMEDOV
Baku State University, Institute for Physical Problems Z.Khalilov str., 23, Baku, Azerbaijan, Az1148

The role of modern computer programs in studding of the spatial structure of the peptide molecules in living systems is very important. One of the basic problems for molecular biophysics is investigating their structure–functional organization. This work is devoted to study the spatial organization, conformational possibilities of the glyproline pentapeptide molecules Pro-Gly-Pro-Gly-Pro, Pro-Gly-Pro-Arg-Pro and Pro-Arg-Pro-Gly-Pro. The calculations were carried out by the method of theoretical conformational analysis and a special computer program. The low-energy conformations of these molecules and the values of the dihedral angles of the main and side chains are found and the energy of the intra- and inter-residue interactions is estimated. The conformational mobility of the amino acid side chains is investigated and the amino acids with specific interplays with different receptors are founded.

Key words: conformation; molecule; peptide; structure
PACS: 36.20.Ey; 87.15.Aa; 87.15.He

1. Introduction

Peptides regulate all functions of a living organism. Using the regulatory peptides of the human body, you can create new and effective drugs. It is known, that proline and glysin containing peptides had a protective effect in microcirculatory dysfunction under conditions of inflammation and stress. This effect can be connected with these peptides ability to stabilize mast cells**.** Glyprolines are a new family of biologically active peptide drugs containing Pro (P) and Gly (G) amino asides in their structure [1, 2]. Glyprolines are fragments of collagens. These molecules modulate the nervous and immune system, possess antiulcer action. Pro-Gly, Pro-Gly-Pro and Pro-Gly-Pro-Gly-Pro glyprolines have neuroprotective properties, ensure the preservation of the normal function of the insular and anticoagulative blood systems against the background of diabetes. A number of amino acids Arg (R) are involved in the normalization of triglyceride levels, prevent the risk of diabetes and atherosclerosis. At present, the various synthetic analogues of natural glyprolines were founded [3, 4].

Glyproline peptide family includes the simplest proline-containing linear peptides PG, PGP, PGPG and PGPGP. The biological functions of these peptides in living systems are related with their specific spatial structures. To understand the mechanism by witch the glyprolines function it is necessary to know their spatial structures and the full complement of low-energy conformational states. The aim of this article is to study the structural organization of the three pentapeptide molecules Pro-Gly-Pro-Gly-Pro, Pro-Gly-Pro-Arg-Pro and Pro-Arg-Pro-Gly-Pro. The present paper is an extension of our previous investigations of structural and functional organization of peptide molecules [5-7].

2. Method

Calculation of glyproline pentapeptides has been carried out by the method of theoretical conformational analysis with regard to nonvalent, electrostatic and torsional interactions and energy of the hydrogen bonds. In presenting the results of the calculation of the spatial structure of the molecules we used the classification suggested in the work [8]. According to it all structural versions break down into shapes including certain forms of the main chain and each form is represented by a set of conformations. The conformations are determined by the number of rotational degrees of freedom of the side chains of the residues being included in the molecule.

The conformational state of each amino residue is conveniently described by the backbone φ, ψ and side chain χ_1, χ_2… dihedral angles. The terms “conformation” used in the following analysis will always imply exact quantitative characteristics of residue or fragment geometry. For a stable conformation, the φ and ψ dihedral angles are located in low-energy region R, B, L and P of the conformational map. We introduce the notion “form of a residue” to denote the region of its backbone dihedral angle (R, B, L and P). The conformation of the backbone forms of residue in a given amino acid sequence will specify the backbone form of a fragment. Forms belonging to a particular shape have an analogous peptide chain contour and a similar mutual arrangement of backbones and side chains. A procedure for the minimization fragments global energy was conducted by the method of conjugate gradients using the program described [9].Designations indications of dihedral angles have been measured up to the generally accepted nomenclature [10].

3. Results and discussion

One of the basic problems for molecular biophysics is investigating of the spatial organization of the peptide molecules and their structure–functional organization. In the represent work the conformational analysis was applied to investigation of the spatial structure and conformational possibilities of the peptides, belonging to glyproline peptides family.The conformational possibilities of pentapeptide Pro-Gly-Pro-Gly-Pro were studied in fragments. First, the conformational properties of the dipeptide Pro-Gly and the tripeptide Pro-Gly-Pro were determined based on the stable conformations of the monopeptides N-acetyl-L-proline and L-glycine. Then the spatial structure of the pentapeptide Pro-Gly-Pro-Gly-Pro was studied.

Dipeptide Pro-Gly contains 27 atoms and 6 variable dihedral angles. For this fragment may be 2 shapes and 8 forms of the main chain: extended BB, BR, LB, LR, RL, RP and folded forms RB, RR, BL, BP, LP, PR, PB. By an energy optimization with variation of the dihedral angles of main chain of all amino acid residues the sterically allowed conformational states of the molecule were determined. The lowest energy conformation RB and RR has folded form of the main chain. Tripeptide molecule Pro-Gly-Pro contains 39 atoms and 8 variable dihedral angles. For it are possible 4 shapes and 16 forms of the main chain. The calculation showed that most low-energy is RRR form that has folded course of the main chain.

The molecule PGPGP contained 63 atom cores and 13 variable dihedral angles. A total of 144 forms of the main chain belonging to 128 possible shapes were calculated. Over 200 initial approximations were compiled. All of them were minimized by energy, their geometric and energy parameters were estimated. The low-energy conformations of the Pro-Gly-Pro-Gly-Pro molecule are presented in Table 1.

Table 1

Energetical parametes of low-energy conformations of glyproline molecules

	Conformation (shape)	E_{nb}	E_{el}	E_{tors}	E_{total}	E_{rel}
Molecule Pro-Gly-Pro-Gly-Pro						
	BRRPR (efef)	-8,0	-5,0	1,3	-11,7	2,9
	RPRRR (efff)	-10,	-4,8	1,4	-13,5	1,1
	BPRPR (ffef)	-8,4	-5,6	1,7	-12,3	2,3
	RRBRR (ffef)	-10,	-5,0	1,3	-14,0	0,6
	RBRRR (ffef)	-10,	-4,9	1,1	-14,6	0,0
	RRBPR (ffff)	-9,5	-5,1	1,1	-13,5	1,1
Molecule Pro-Gly-Pro-Arg-Pro						
	RRBB$_{3222}$ B (ffee)	-10,	-6,3	1,5	-15,6	3,0
	RRRL$_{3322}$ B (ffee)	-16,	-4,8	2,4	-18,6	0,0
	BPRB$_{3322}$ B (fffe)	-14,	-5,5	2,6	-17,4	1,2
	RRBR$_{3222}$ R (ffef)	-11,	-5,7	7,2	-10,0	8,6
	BRBR$_{3222}$ R (efef)	-10,	-5,3	6,5	-9,3	9,3
Molecule Pro-Arg-Pro-Gly-Pro						
	BB$_{2222}$BLB (eefe)	-12,	6,0	3,6	-15,0	3,4
	BB$_{2122}$BRR (eeef)	-10,	-6,8	2,8	-14,4	4,4
	BB$_{2222}$RPR (eeef)	-13,	-6,3	1,8	-18,4	0,0
	RB$_{2122}$BLB (fefe)	-12,	-6,3	3,3	-15,1	3,3
	RB$_{2222}$RPR (feef)	-13,	-6,0	1,1	-17,9	0,5
	RB$_{1222}$RPB (feff)	-11,	-5,3	1,8	-14,8	3,6

The form of the main chain RBRRR (shape feff), which has a convolved main course, turned out to be the lowest energy conformation. In the global conformation RBRRR (ΔEotn = 0 kcal / mol) the energy of non-valent interactions is (-10.9) kcal / mol, electrostatic (-4.9) kcal / mol and torsion 1.1 kcal / mol. In this case, the main stabilizing contribution is made by di-, tri-, tetra-, and pentapeptide interactions of amino acid residues. Only 1.0 kcal / mol lose conformations with the fully folded form of the main chain RRBPR (shape ffff) and RPRRR (efff). Forms with a fully developed main chain are inferior in energy from 5 to 9 kcal / mol. Thus, the calculation revealed a sharp energy differentiation of conformations by the shapes and the main chain forms. 26 conformations belonging to 10 possible shapes are in the energy range of 0–5 kcal / mol.

Then the spatial structure and conformational properties of the glyproline analogues Pro-Gly-Pro-Arg-Pro and Pro-Arg-Pro-Gly-Pro have been investigated using the method of theoretical conformational analysis. The low-energy conformations of the natural peptide were used as the initial structural states to explore the conformational possibilities of the artificial analogues. Table 1 present the energy distribution of the contributions in the most preferential conformations of these molecules.

At last stage many conformational maps for side chain of Arg amino acide residue in the low-energy conformations of the pentapeptides were investigated on the basis of a semi empirical method of conformational analysis. The investigation of the molecular dynamics of each peptide is of great importance to understanding the mechanism of action these glyproline peptides with their receptors. The calculation of this pentapeptide glyproline molecule was carried out on the basis of the low energy conformations of the pentapeptide Pro-Gly-Pro-Gly-Pro and the stable conformations of the N-acetyl-L-arginine monopeptide. The specificity of the amino acid sequence of this peptide molecule is that the side chain of the amino acid Arg is labile, bulky and positively charged, glycine has practically no side chain, and proline has a rigid side chain. For amino acids, all possible forms of the main chain were taken into account. The Arg-containing pentapeptides included 79 atoms and 17 variable dihedral angles of the main and side chains of all amino acids that make up this molecule. The global conformations of these molecules represent schematically the backbone forms and positions of residues in Figures 1, 2, and 3

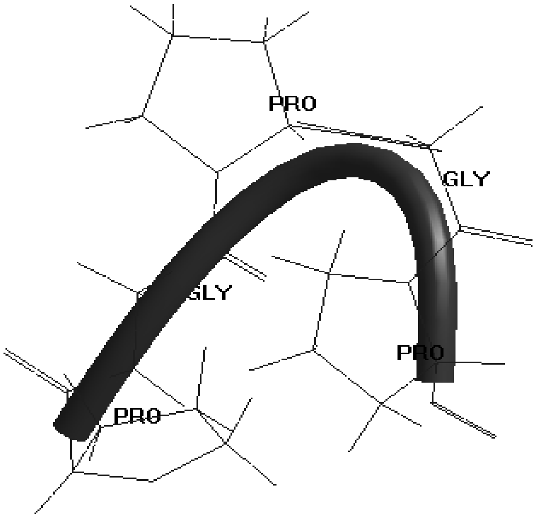

Figure 1. Atomic model of spatial structure of the Pro-Gly-Pro-Gly-Pro molecule.

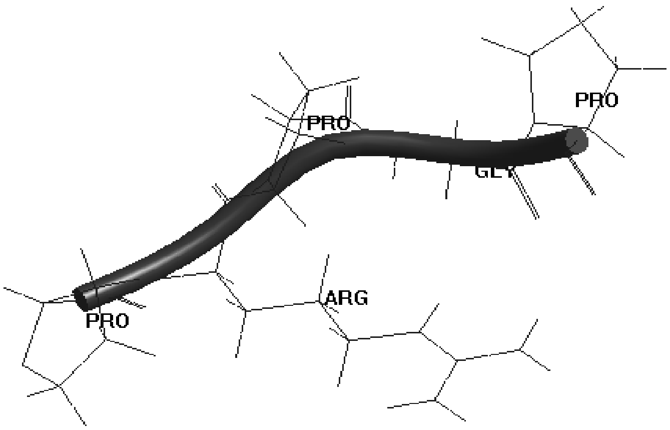

Figure 2. Atomic model of spatial structure of the Pro-Arg-Pro-Gly-Pro molecule.

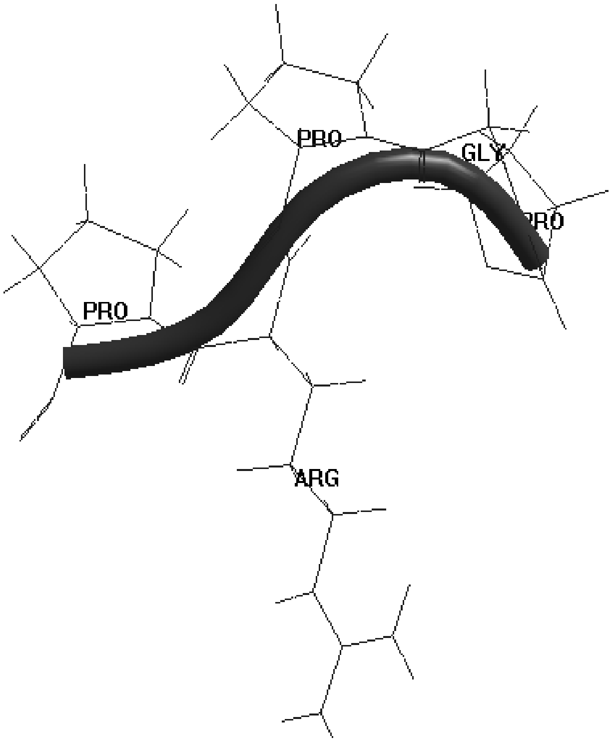

Figure 3. Atomic model of spatial structure of the Pro-Gly-Pro-Arg-Pro molecule.

In these figures show that the C-terminal region is folded forms of the backbone of the glyproline molecules. Comparing the results obtained, we can say that with repeated glyprolines fragments Gly-Pro and Pro-Gly-Pro essential for cytoprotective activity is the C-terminal dipeptide fragment. This C-terminal dipeptide fragment Pro-Gly is present in all of the studed molecules. According to experimental data, the presence of this fragment is responsible for the protective action meet the following molecules per cell.

The calculation revealed that for the Pro-Arg-Pro-Gly-Pro molecule, the conformations of the semi-convoluted shapes fall into the energy interval of 0–5 kcal / mol. For pentapeptide, the conformations with the shape of the main chain BBRPR, RBRPR, RBBRRB and BBBLB turned out to be the lowest-energy ones. The calculation showed that the global conformation of the molecule is BB$_{2222}$RPR. The low energy conformations of the pentapeptide Pro-Arg-Pro-Gly-Pro are presented in Table 1.

4. Conclusion.

We have studied in detail the spatial structure and conformational properties of the glyproline pentapeptide molecules Pro-Gly-Pro-Gly-Pro, Pro-Gly-Pro-Arg-Pro and Pro-Arg-Pro-Gly-Pro. The low-energy conformations of these molecules and the values of the dihedral angles of the main and side chains are found and the energy of the intra- and inter-residue interactions is estimated. The conformational mobility of the amino acid side chains is investigated and the amino acids with specific interplays with different receptors are founded. The results can be used to study the spatial structure of hexapeptide glyproline molecules, as well as to study the conformational capabilities of side chains when interacting with receptor molecules.

References

1. Martinova K.B., Andreeva L.A., Klimova P. A. et all, Bioorg. Khim., 35, 165, (2009).
2. Zolotarev Yu. A., Badmayeva K. E. et all., Bioorg. Khim., 32, 89, (2006).
3. Kozlovskaya M. V. et all, J.Eur. Neuropsychopharmacol, 10, 70, (2000).
4. Levitskaya N.G., Sevastyanova E.A. et all, Neuroscience and Behavioral Physiology, 34, 399, (2004).
5. Akhmedov N.A., Ismailova L.I., Abbasli R.M., Agayeva L.N., Akhmedova S.R. IOSR - JAP, e-ISSN: 2278-4861, 8, 66, (2016).
6. Akhmedov N.A., Ismailova L.I, Agayeva L.N., Gocayev N. M., Cur.Top. in Pept.&Prot. Res., 11, 87, (2010).
7. Akhmedov N.A., Gadjiyeva Sh.N., Abbasli R.M., Cur.Top. in Pept.&Prot.Res., 10, 57, (2009).
8. Popov E. M, Mol. Biol., 19, 1107, (1985).
9. Maksumov I.S., Ismailova L.I., Godjaev N.M. J. Struc. Chem., 24, 147, (1983).
10. IUPAC-IUB, Quantity, Units and Symbols in Physical Chemistry, 39, Blackwell Scientific Publications, Oxford, (1988).

[*] **Corresponding autor:** lara.ismailova.52@mail.ru

THE PARAMETERS OF VISCOUS FLOW ACTIVATION OF THE SYSTEMS WATER-PEG-LiOH AND THE PARTIAL MOLAR VOLUMES OF POLYETHYLENE GLYCOL IN SOLUTIONS

E.A. MASIMOV, B.G. PASHAYEV*, N.F. ORUJOVA
Baku State University, Z.Khalilov str., 23, Baku, Azerbaijan, Az1148

The dynamic viscosity and density of water-PEG-LiOH systems was measured at the range of temperature 293,15-323,15 K and a concentration of molar fraction of polyethylene glycol to 0-0.001. Polyethylene glycol molecules with a molecular weight of 1000, 1500, 3000, 4000 were investigated and the concentration of LiOH was taken 0,01 molar fraction. Using experimental results, the temperature and concentration at the range of investigated systems the activation parameters of the viscous flow and partial molar volumes of polyethylene glycol in solutions were calculated. It was determined that when concentration and molecular weight increase, the solution becomes more structured.

Keywords: aqueous solutions, polyethylene glycol, LiOH, activation parameters of viscous flow, partial molar volume.
PACS: 61.20.Ne, 66.20.+d, 82.60.Lf, 61.25.Hq.

1. Introduction

It is known that water has a certain structure and this structure depends on external factors (temperature, pressure, soluble substance etc.). When various substances dissolve in water, the new structure differs from the previous structure of water, which differs from water depending on its physical and chemical properties. As water is the basis of living being, it is important to study the structural changes in aqueous solutions. Water-soluble substances have different effects on the structure of water, depending on their chemical composition and structure: while many substances weaken the hydrogen bonds between water molecules, and others even more strengthen these bonds. It was determined that LiOH has the destructive effect on water, while PEG has structural effect [1, 2].

Here the structural features of water-PEG-LiOH at temperature 293.15-323.15 K and 0-0.001 partial molar concentration of PEG were investigated by means of methods viscometer and pycnometres. The dynamic viscosity and density of aqueous solutions were measured observed temperature and concentration interval. Using experimental results, were analyzed dependence activation Gibbs energy of viscous flow ($\Delta G_\eta^{\neq}$), activation enthalpy of viscous flow ($\Delta H_\eta^{\neq}$), activation entropy of viscous flow ($\Delta S_\eta^{\neq}$) and the partial molar volume of PEG ($\widetilde{V}$) in solution of studied systems in concentration of PEG.

2. Experiment

Objects of study: Water-PEG-LiOH were used as our objects of research. Investigated fractions of PEG with molecular weight 1000, 1500, 3000, 4000 and 6000 and concentration of LiOH made 0.01 molar fractions. Used PEGs and LiOH are chemical pure. Bidistilled water was used in the preparation of the solutions. The viscosity was measured by capillary viscometer and density was measured by pycnometer.

Due to activation Gibbs energy of viscous flow ($\Delta G_\eta^{\neq}$) according to Eyring theory [3, 4, 5] of liquid viscous flow

$$\Delta G_\eta^{\neq} = RT\ln\frac{\eta}{\eta_0} \tag{1}$$

is defined by this expression. Due to Eyring theory

$$\eta_0 = \frac{N_A h\rho}{M} \tag{2}$$

Here is R-universal gas constant, N_A is the Avogadro number, h is the Planck's constant, and M is the molecular weight of solution, determined according to equation

$$M = \sum_{i=1}^{N} x_i M_i \tag{3}$$

Here x_i and M_i are the molar fraction and molar weight of the i-th component, respectively. Dynamic viscosity (η) and density (ρ) of the solution at different temperatures were determined experimentally.

If in Eq. (1) we allow for the familiar thermodynamic equation [3, 4]

$$\Delta G_\eta^{\neq} = \Delta H_\eta^{\neq} - T\Delta S_\eta^{\neq} \tag{4}$$

Let's divide all sides to T

$$R\ln\frac{\eta}{\eta_0} = \frac{\Delta H_\eta^{\neq}}{T} - \Delta S_\eta^{\neq} \tag{5}$$

($\Delta H_\eta^{\neq}$) can be found from Eq. (5):

$$\Delta H_\eta^{\neq} = R\frac{\partial \ln\frac{\eta}{\eta_0}}{\partial\left(\frac{1}{T}\right)} \tag{6}$$

The values of ($\Delta S_\eta^{\neq}$) can then be obtained with Eq. (4) after the values of $\Delta G_\eta^{\neq}$ and $\Delta H_\eta^{\neq}$ have been determined with Eqs. (1) and (6), respectively.

According to [3, 4, 6], partial molar volume of PEG in a solution can be determined with the formula

$$\widetilde{V} = V_m + (1-x)\left(\frac{\partial V_m}{\partial x}\right)_{p,T} \tag{7}$$

where V_m is the molar fraction of the solution:

$$V_m = \frac{M}{\rho} = \frac{\sum x_i M_i}{\rho} \tag{8}$$

3. Results and discussion

The systems of water-PEG-LiOH where PEG is characterized by different molecular weight at 293,15 K dependence of activation Gibb's energy of viscous flow ($\Delta G_\eta^{\neq}$), activation enthalpy of viscous flow ($\Delta H_\eta^{\neq}$) on PEG concentration (x) is show table 1 and table 2, the dependence activation entropy of viscous flow ($\Delta S_\eta^{\neq}$) on the PEG concentration (x) is shown in Fig. 1.

Table 1, table 2 and Fig. 1 show that $\Delta G_\eta^{\neq}$, $\Delta H_\eta^{\neq}$ and $\Delta S_\eta^{\neq}$ parameters increase with increase in concentration at given temperature, while with increase in molar weight at given temperature and concentration.

Table 1

The dependence of activation Gibbs energy of viscous flow ($\Delta G_\eta^{\neq}, J/mol$) of water-PEG-LiOH systems on the PEG concentration (x) ($T = 293.15K$, $x_{LiOH} = 0.01$).

x	$M_{PEG} = 10$	$M_{PEG} = 15$	$M_{PEG} = 30$	$M_{PEG} = 40$	$M_{PEG} = 60$
0	9598	9598	9598	9598	9457
0.0001	9683	9758	9852	9995	10663
0.0002	9750	9937	10140	10427	11579
0.0004	9897	10294	10591	11217	13529
0.0006	10088	10761	11246	11869	15043
0.0008	10196	11129	11878	12655	16562
0.001	10385	11382	12276	13478	17055

Table 2.
The dependence of the activation enthalpy of viscous flow ($\Delta H_{\eta}^{\neq}, J/mol$) of water-PEG-LiOH systems on PEG concentration (x) ($T = 293.15K$, $x_{LiOH} = 0.01$).

x	$M_{PEG} = 10$	$M_{PEG} = 15$	$M_{PEG} = 30$	$M_{PEG} = 40$	$M_{PEG} = 60$
0	17619	17619	17619	17619	17478
0.0001	17813	17896	17992	18179	18949
0.0002	17908	18150	18378	18713	19898
0.0004	18044	18708	19039	19618	22076
0.0006	18279	19145	19805	20577	23926
0.0008	18553	19543	20531	21432	25623
0.001	18701	20010	21128	22504	26443

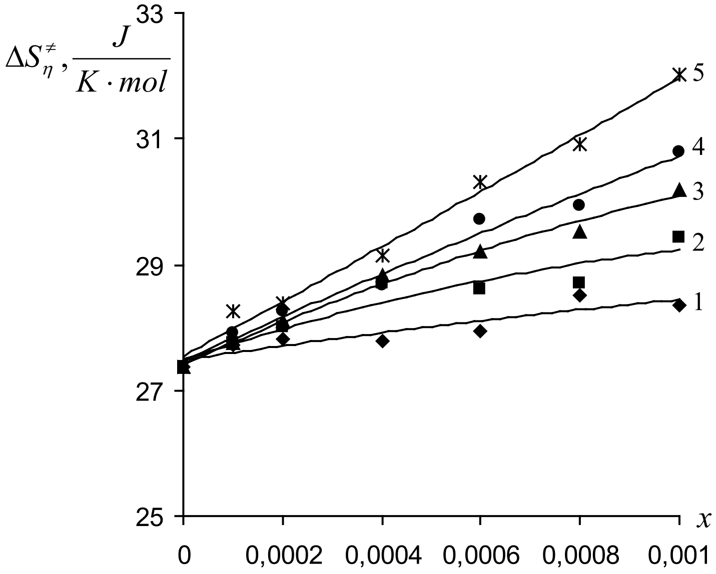

Fig. 1. The dependence of the activation entropy of viscous flow of water-PEG-LiOH systems on PEG concentration.
($x_{LiOH} = 0.01$, $T = 293.15K$).
1-PEG(1000), **2**-PEG(1500), **3**-PEG(3000), **4**-PEG(4000), **5**-PEG(5000)

It should be noted that, $\Delta G_{\eta}^{\neq}$ is the energy used for activation 1 *mole* molecule, $\Delta H_{\eta}^{\neq}$ represents the changes in the solution in terms of energy and $\Delta S_{\eta}^{\neq}$ characterized the changes in solution in terms of structure. Thus, increased $\Delta G_{\eta}^{\neq}$ with growth of concentration indicates that more energy can be consumed for overcoming potential of molecule, while in cease in $\Delta H_{\eta}^{\neq}$ indicates the system has steadier structure, increase in $\Delta S_{\eta}^{\neq}$ determines the system is becoming more structured [2, 3, 7-10]. Due to, dependence of viscous flow parameters from concentration (table 1, table 2, and Fig. 1) it is possible to tell that, in process of increase in concentration of PEG in solution has stronger structure and more structured. Let's note that, with increase in concentration of LiOH in water the $\Delta G_{\eta}^{\neq}$ and $\Delta H_{\eta}^{\neq}$ parameters increase, and the parameter $\Delta S_{\eta}^{\neq}$ decreases slightly [1].

Structural properties of aqueous solutions are also characterized by the partial molar volume of components of solution. It is known that the partial molar volume of *i*-th component is equivalent to change of volume at addition of 1 mol from this component [3, 4, 6]. The dependence of partial molar volume of PEQ on concentration of PEQ in systems water-PEQ-LiOH for PEQ with various molar weight at 293.15 K is shown in table 3.

Table 3.
The dependence of the partial molar volume of PEG in water-PEG-LiOH systems on PEG concentration (x) ($x_{LiOH} = 0.01$, $T = 293.15K$).

x	$M_{PEG} = 1$	$M_{PEG} = 1$	$M_{PEG} = 3$	$M_{PEG} = 4$	$M_{PEG} = 6$
0	854	1317	2783	3730	4995
0,0001	845	1297	2742	3654	4965
0,0002	837	1278	2702	3584	4936
0,0004	823	1242	2630	3457	4883
0,0006	811	1209	2566	3352	4836
0,0008	801	1179	2511	3268	4794
0,001	795	1152	2464	3205	4758

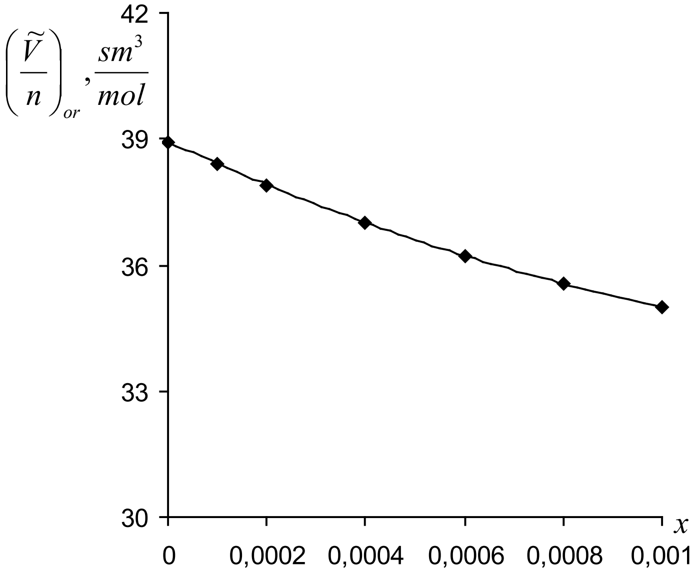

Fig. 2. Dependence of the average value of the parsial molar volume of the PEG per monomer on concentration of PEG in system water-PEG-LiOH. ($x_{LiOH} = 0.01$, $T = 293.15K$)

Table 3 shows that partial molar volume of PEG in solution decreases with increase in concentration at the given temperature and the partial molar volume of PEG increase along with the molecular weight increases at the given temperature and concentration. It should be noted that the partial molar volume of LiOH in water increase with concentration increases and also about 0.03 mole fractions are negative [1]. Calculation shows that partial molar volume $\left(\frac{\tilde{V}}{n}\right)_{av}$ of PEG in monomer at this temperature and concentration practically doesn't depend on the molecular mass of PEG. In Fig. 2 the dependence of PEG of various molar weight on concentration at 293.15 K is shown (average value of molar volume on monomer). We can described this dependence with the equation

$$\left(\frac{\widetilde{V}}{n}\right)_{av} = 1511612{,}1x^2 - 5440{,}5x + 38{,}9$$

It is possible to assume that the volume portion of big sizes associations in space, the fractional share of its separate parts is less than the sum of volume portion of and vise versa. According to model of the two-structured water [3, 4, 11], water consists of clusters of the different size and clusters of molecules of free liquid which are attached to hydrogen binding. Depending on dependence of partial molar volume on concentration it is possible to assume that the molecules PEG are connected first of all by hydrogen binding with free molecules of water. It leads to reduction of partial molar volume of PEG due to increase in concentration. This indicates that the solution has become more structured due to increase in PEG concentration.

4. Conclusion

Apparently, the dependence of both the activation entropy of viscous flow and the concentration of partial molar volume of the PEG in solution indicates that concentration as for both fractional PEGs taken at this temperature and for increase in molecular mass for the concentrated and various fractioned PEGs, the solutions becomes more structured. It is possible to assume that, in the studied of molecules PEG, the collecting water molecules (first of all free molecules of water) by means of hydrogen bindings, form certain size aggregates. With increasing both concentration and molecular mass of PEG the number of such aggregates increases and their size increases, that leads to more structured solution. Undoubtedly, the structure formed by hydration of ions Li^+ and OH^- in a system water-PEG-LiOH differ from structure of a system water - PEG.

References

1. Masimov E.A., Pashayev B.G., Hasanov H.Sh, Musayeva S.I. News of Baku University, 3,126 (2013).
2. Masimov E.A., Pashayev B.G., Hasanov H.Sh., Musayeva S.I. Journal of Physical Chemistry (in Russian), 87,12, 2105 (2013).
3. Masimov E.A., Hasanov H.Sh., Pashayev B.G. Liquid viscosity. Baku, "Publishing House Laman", 2016, 285 p.
4. Masimov E.A., Hasanov H.Sh. Thermodynamics of biological systems. Baku, "Publishing House Laman", 2007, 418 p.
5. Glesston S., Leidler K., Eyring G. The theory of absolute velocities. M.: Publishing house inostr. Lit., 1948, 600 p.
6. Atkins P., De Paula J. Physical chemistry. Oxford University Press. 2006, 1067 p.
7. Masimov E.A., Pashayev B.G., Hasanov H.Sh. News of Baku University, 3, 109 (2010).
8. Masimov E.A., Hasanov H.Sh., Pashayev B.G. Journal of Physical Chemistry (in Russian), 87,6, 948 (2013).
9. Masimov E.A., Pashayev B.G., Hasanov H.Sh., Hasanov N.H. Journal of Physical Chemistry (in Russian), 89,7, 1244 (2015).
10. Masimov E.A., Pashayev B.G., Hasanov H.Sh. Journal of Physical Chemistry (in Russian), 91,4, 667 (2017).
11. Nemethy G. The structure of water and the thermodynamic properties of aqueous solutions. Istituto superiore di sanita-V.le Regina Elena, 299-Roma. Vol. VI fascicolo speciale 1, 592 (1970),

***Corresponding author**: p.g.bakhtiyar@gmail.com

VISCOZYMETRIC STUDY OF AQUEOUS SOLUTIONS LiOH, NaOH and KOH

E.A. MASIMOV, B.G. PASHAYEV*, M.R. RAJABOV, L.P. ALIYEV
Baku State University, Z.Khalilov str., 23, Baku, Azerbaijan, Az1148

Here, aqueous solution of LiOH, NaOH and KOH in the range of 283,15-333,15 K temperature and 0-0,07 partial molar concentration were investigated by viscometery and pynometery methods. Using the experimental results, the activation parameters of the viscous flow and the partial molar volume of LiOH, NaOH and KOH were calculated in the observed temperature and concentration range of the investigated systems and the dependence of these parameters on the concentration was analyzed. It was determined that with all three bases concentrations have destructive effect on the water structure. KOH has a more destructive effect on the structure of water than NaOH, NaOH, however, has a more destructive effect on the structure of water than LiOH.

Keywords: LiOH, NaOH, KOH, activation parameters of viscous flow, partial molar volumes.
PACS: 61.20.Ne, 66.20.+d, 82.60.Lf, 31.70.Ks.

1. Introduction

It is known that, when the inorganic substances are dissolved in water they dissolve into ions. This is because the water has a large dielectric effect. As the ions, charged particles and water molecules have dipole structure, so the solution is hydrated. Therefore, the structure of the solution containing the ions differs from the structure of the water. Because water plays an important role in biological systems, the study of structural properties of aqueous solutions is of great importance in modern physicochemistry and biophysics.

In living organisms, there are Li^+, Na^+, K^+ and OH^- ions, and these ions play an important role in biological processes occurring here. Although the LiOH, NaOH, and KOH have a wide range of applications, the properties of viscous flow and volume of aqueous solutions have been studied less frequently. The analysis of scientific literature shows that there is a need to investigate the structural properties of LiOH, NaOH and KOH in the aqueous solutions and to study the effects of these bases on water structure.

Here, structural properties of LiOH, NaOH and KOH in the range of 283,15-333,15 K temperature and 0-0,07 partial molar concentration were investigated by viscometery and pycnometery methods. Dynamic viscosity and density of aqueous solutions were measured in the observed temperature and concentration range. Using experimental results, dependence activation Gibbs energy of viscous flow ($\Delta G_\eta^{\neq}$), activation enthalpy of viscous flow ($\Delta H_\eta^{\neq}$), activation entropy of viscous flow ($\Delta S_\eta^{\neq}$), and partial molar volumes ($\widetilde{V}$) of LiOH, NaOH and KOH of investigated solution on concentration was analyzed.

2. Experiment

Object of study and methods. Aqueous solutions of various concentrations of LiOH, NaOH and KOH were used as our objects of research. Used LiOH, NaOH and KOH are chemical pure. Bidistilled water was used in the preparation of the solutions. The viscosity was measured by capillary viscometer and density was measured by pycnometer.

Activation Gibbs energy of viscous flow ($\Delta G_\eta^{\neq}$) was determined according to the Eyring and Frenkel theory [1, 2, 3] using the equation

$$\Delta G_\eta^{\neq} = RT \ln \frac{\eta}{\eta_0} \quad (1)$$

is defined by this expression. Due to Eyring theory [1, 2]

$$\eta_0 = \frac{N_A h \rho}{M} \quad (2)$$

Here is R-universal gas constant, N_A is the Avogadro number, h is the Planck's constant, and M is the molecular weight of solution, determined according to equation [1]

$$M = \sum_{i=1}^{N} x_i M_i \tag{3}$$

Here x_i and M_i are the molar fraction and molar weight of the i-th component, respectively. Dynamic viscosity (η) and density (ρ) of the solution at temperature T was determined experimentally.

In Eq. (1) we allow for the familiar thermodynamic equation [1]

$$\Delta G_\eta^{\neq} = \Delta H_\eta^{\neq} - T\Delta S_\eta^{\neq} \tag{4}$$

Let's divide all sides to T

$$R\ln\frac{\eta}{\eta_0} = \frac{\Delta H_\eta^{\neq}}{T} - \Delta S_\eta^{\neq} \tag{5}$$

($\Delta H_\eta^{\neq}$) can be found from Eq. (5):

$$\Delta H_\eta^{\neq} = R\frac{\partial \ln(\eta/\eta_0)}{\partial(1/T)} \tag{6}$$

The values of ($\Delta S_\eta^{\neq}$) can then be obtained with Eq. (4) after the values of $\Delta G_\eta^{\neq}$ and $\Delta H_\eta^{\neq}$ have been determined with Eq. (1) and (6), respectively.

Partial molar volume ($\widetilde{V}$) of PEG in a solution can be determined with the formula [1]

$$\widetilde{V} = V_m + (1-x)\left(\frac{\partial V_m}{\partial x}\right)_{p,T} \tag{7}$$

where V_m is the molar fraction of the solution:

$$V_m = \frac{M}{\rho} = \frac{\sum x_i M_i}{\rho} \tag{8}$$

3. Results and discussion

Dependence activation parameters of viscous flow ($\Delta G_\eta^{\neq}$, $\Delta H_\eta^{\neq}$, $\Delta S_\eta^{\neq}$) of aqueous solutions of LiOH, NaOH and KOH at the temperature of 293,15 K and the partial molar volumes ($\widetilde{V}$) of LiOH, NaOH, KOH in the solution on concentration (x) are shown in Figures 1-4.

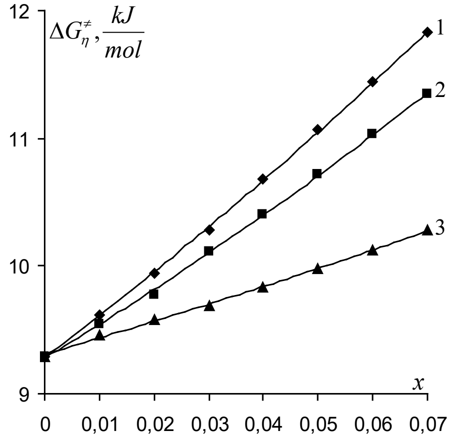

Fig. 1. Dependence activation Gibbs energy of viscous flow of aqueous solution of LiOH, NaOH and KOH on concentration (T=293,15 K).
1-LiOH, 2-NaOH, 3-KOH

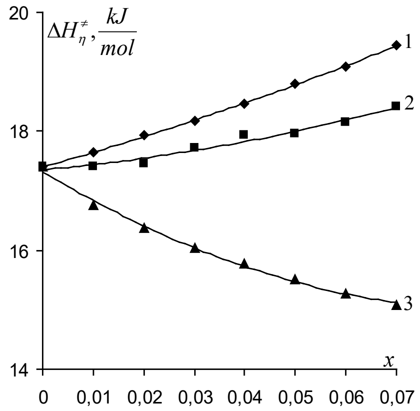

Fig. 2. Dependence activation enthalpy of viscous flow of aqueous solution of LiOH, NaOH and KOH on concentration (T=293,15 K).

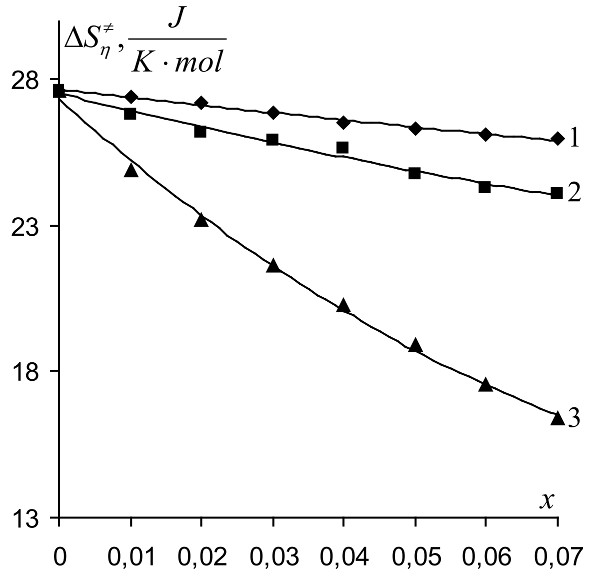

Fig. 3. Dependence activation entropy of NaOH viscous flow of aqueous solution of LiOH, NaOH and KOH on concentration (T=293,15 K). *LiOH, 2-NaOH, 3-KOH*

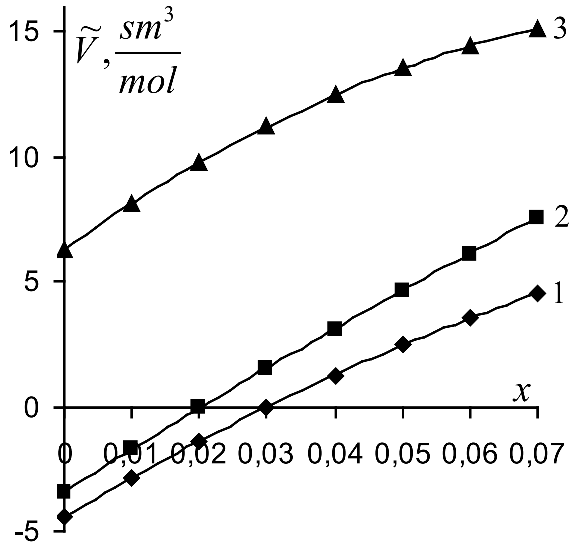

Fig. 4. Dependence of partial molar volume LiOH, and KOH of viscous flow activation of aqueous solution of LiOH, NaOH, and KOH on concentration (T=293,15 K).*1-*

As can be seen from Fig. 1, in the observed concentration interval for aqueous solution for all three bases (LiOH, NaOH, KOH), $\Delta G_\eta^{\neq}$ increases with concentration increase, as well as given temperature and concentration $\Delta G_\eta^{\neq}(LiOH) > \Delta G_\eta^{\neq}(NaOH) > \Delta G_\eta^{\neq}(KOH)$. According to Frenkel and Eyring theories, $\Delta G_\eta^{\neq}$ is the energy that consumed to activate 1 *mole* molecule [1, 2, 3]. Note that the limit value of molar ionic conductivity at water at temperature 20^0C is equivalent to $34{,}51\frac{sm^2}{Om\cdot mol}$, $44{,}79\frac{sm^2}{Om\cdot mol}$, $66{,}63\frac{sm^2}{Om\cdot mol}$ and $180{,}39\frac{sm^2}{Om\cdot mol}$ respectively, for Li^+, Na^+, K^+ and OH^- ions. The comparison of these values shows that the value of this quantity is very high for the OH^- ion. This, in turn, makes it possible to suppose that the hydride layer does not form around the OH^- ion. Obviously, in the solutions we investigate, in the the Li^+, Na^+ and K^+ ions, which hydrate, along with water molecules, will also be activated. Naturally, more energy will be spent on activating hydrated ions than water molecules. Increasing $\Delta G_\eta^{\neq}$ with increased concentration can be explained by the gradual increase in the number of active hydrated ions compared to water molecules. Because the hydrates energy of the Li^+, Na^+ and K^+ions are different (conveniently $-531{,}36\,kJ/mol$, $-422{,}18\,kJ/mol$ və $-338{,}58\,kJ/mol$ [4]), the size and mass of these hydrated ions will be different. Due to, both molar ionic water conductivity limit values and hydration energy of ions we can say the mass of hydrated Li^+ ion at the given temperature is greater than the mass of hydrated Na^+ ion, and the mass of hydrated Na^+ ion is greater than the mass of hydrated K^+ ion. Therefore will be $\Delta G_\eta^{\neq}(LiOH) > \Delta G_\eta^{\neq}(NaOH) > \Delta G_\eta^{\neq}(KOH)$.

As can be seen from Fig. 2, the $\Delta H_\eta^{\neq}$ concentration increases with concentrations of LiOH and NaOH in the observed concentration range while decreasing for the solution KOH, it also becomes $\Delta H_\eta^{\neq}(LiOH) > \Delta H_\eta^{\neq}(NaOH) > \Delta H_\eta^{\neq}(KOH)$ for given temperature and concentration. $\Delta H_\eta^{\neq}$ describes the changes in the solution in terms of energy [1, 5]. Thus, the increase in $\Delta H_\eta^{\neq}$ concentration shows that the system has a more strong structure and, conversely. Note that the intensity of movement of water molecules in the vicinity of strong hydrated ions is reduced, the intensity of movement of water molecules in the vicinity of weak hydrated ions increases [7]. We assume that, Li^{+} və Na^{+} are strong, and K^{+} is weak hydrated ions, $\Delta H_{\eta}^{\neq}$ increases with increased the concentration of LiOH and NaOH solution, while decreasing for the KOH solution. We believe that $\Delta H_{\eta}^{\neq}(LiOH) > \Delta H_{\eta}^{\neq}(NaOH) > \Delta H_{\eta}^{\neq}(KOH)$ is associated with the values of hydration energy of Li^{+}, Na^{+} and K^{+} ions.

In the aqueous solutions of electrolytes, the process of hydration of ions occurs, which in turn creates a different structure of solution relative to water. Structural changes in the solution are characterized by the $\Delta S_{\eta}^{\neq}$ parameter. Thus, increasing $\Delta S_{\eta}^{\neq}$ with increased concentration the system is becoming more structured, and the decline in concentration indicates that the structure is disintegrated [1, 6-10]. As can be seen from Fig. 3, $\Delta S_{\eta}^{\neq}$ decreases by increasing the concentration for the aqueous solution of all three bases (LiOH, NaOH, KOH) in the observed concentration interval, also for given temperature and concentration it becomes $\Delta S_{\eta}^{\neq}(LiOH) > \Delta S_{\eta}^{\neq}(NaOH) > \Delta S_{\eta}^{\neq}(KOH)$. The reduction of $\Delta S_{\eta}^{\neq}$ for the aqueous solution of all three bases with the increase of concentration indicates that these bases destroy the structure of the solution. $\Delta S_{\eta}^{\neq}(LiOH) > \Delta S_{\eta}^{\neq}(NaOH) > \Delta S_{\eta}^{\neq}(KOH)$ indicates that KOH is more destructive impact to the existing structure than NaOH, NaOH is more destructive impact to the existing structure than LiOH. We suppose that, this is due to the hydration energy of Li^{+}, Na^{+} and K^{+} ions. Many studies show that, the ions influence the water structure the consistency of the Hofmeyster's liotrophic sequence [1, 11-14]. As can be seen, the result is in line with the Hofmeyster liotrophic sequence.

When soluble solids are dissolved in water, a new structure of the solution forms, which results in a change in the volume of the solution relative to the water. One of the parameters that characterizes the volume properties of the solution is the partial molar volume of the components. It is known that, the partial molar volume of the *i*-th component is equal to the change in volume when adding 1 *mol* from that component to the given system [1, 15, 16]. As can be seen from Figure 4, $\widetilde{V}$ increases by increasing the concentration for the aqueous solution of all three bases (LiOH, NaOH, KOH) in the observed concentration interval, also for given temperature and concentration it becomes $\widetilde{V}(LiOH) < \widetilde{V}(NaOH) < \widetilde{V}(KOH)$. Increasing the partial molar volume of the bases in solution with the increased in concentration can be explained by the structure's scattered. An electric field is formed around each ion in the water and the intensity of this area decreases sharply with the increase in distance. Water molecules in this area are oriented around the ion. As a result, the volume of water molecules around the ion is smaller than the volume they hold in the water phase. This compressive effect is called electrostriction, and all ions form electrostriction in aqueous solutions. Obviously, the electrostriction effect depends on the surface load of the ion. Thus, the electrostriction effect of the small ions with large surface load density will be stronger than the electrostriction effect of large ions with smaller surface densities. As the surface loads of Li^{+}, Na^{+} and K^{+} ions are consecutively reduced, the intensity of the electric field arising near these ions and the electrostriction effects in the solution decrease in sequence. Since Li^{+}, Na^{+} and K^{+} ions are increased and their electrostriction effects are reduced that they have created the parsial molar volume of LiOH in the solution is relatively small compared to NaOH, the partial molar volume of NaOH is relatively small compared to KOH.

Fig. 4 shows that, at the temperature of 293.15 *K*, the partial molar volume of LiOH is negative until the concentration $x \approx 0.03$, the partial molar volume of NaOH is negative until the concentration $x \approx 0.02$. It is true that, no substance can hold negative volumes, but the negative value of the partial molar volume is encountered. Thermodynamically, it is not of interest to have a negative molar volume in the aqueous solution of certain substances accurate measurement of the solvent and the density of the solution confirms this fact, calculation of measured values can be used. But you need to know what is going on at the molecular level. Both Li^{+} and Na^{+} and OH^{-} ions are monovalent ions. Li^{+} and Na^{+} ions have very small dimensions and in the water a strong electrical field forms around these ions. Therefore, the electrostriction effects of these ions is also strong. As a result, the volume of water molecules around these ions is much smaller than the volume they hold in the water phase. We suppose that the effect of the electrostriction created by Li^{+} and Na^{+} ions is so great that compensates for ions by increasing their volume at small concentrations. Note that, in most cases, the increase in volume of ions at their own expense, it is larger than the volume reduction due to the electrostriction effect. Thus, the partial molar volume is positive, except for a few rare cases, such as LiOH and NaOH solutions.

4. Conclusion

Dependence of the partial molar volume of viscous flow of activated entropy and bases in solution (LiOH, NaOH, KOH) on concentration, has a destructive effect on the structure of the water, with the increase of all three concentrations, and KOH also has a more destructive effect on the structure of water than NaOH, NaOH also has a more destructive effect on the structure of water than LiOH.

References

1. Masimov E.A., Hasanov H.Sh., Pashayev B.G. Liquid viscosity. Baku, "Publishing House Laman", 2016, 285 p.
2. Glesston S., Leidler K., Eyring G. The theory of absolute velocities. M.: Publishing house inostr. Lit., 1948, 600 p.
3. Frenkel Ya. I. Kinetic theory of liquids. Publishing house "Science" Leningrad branch, Leningrad, 1975, 211 p.
4. Kireev V.A. Short course in physical chemistry. Moscow, publishing house "Chemistry" 1978, 380 p.
5. Tager A.A. Physico-chemistry of polymers. M .: Scientific world, 2007, 576 p.
6. Masimov E.A., Hasanov H.Sh., Pashayev B.G. Journal of Physical Chemistry (in Russian), 87, 6, 948 (2013).
7. Masimov E.A., Pashayev B.G., Hasanov H.Sh., Hasanov N.H. Journal of Physical Chemistry (in Russian), 89, 7, 1244 (2015).
8. Masimov E.A., Pashayev B.G., Hasanov H.Sh. . Journal of Physical Chemistry (in Russian), 91, 4, 667 (2017).
9. Dakar G.M., Korableva E.Y. . Journal of Physical Chemistry (in Russian), 72, 4, 662 (1998).
10. Dakar G.M. . Journal of Physical Chemistry (in Russian), 75,4, 656 (2001).
11. Hydrogen bond. Ed. N.D. Sokolova. M .: Science, 1981. 287 p.
12. Benoit M., Bemasconi M., Parrinelio M. New high-pressure phase of ice. Phys. Rev. Lett., 16, 2934 (1996).
13. Collins K.D., Washabaugh M.W. The Hofineister effect and the behaviour of water at interfaces. Quart. Rev. Biophys., 18, 323 (1985).
14. Luck W.A.P., Klein D., Rangsriwatananon K. Anti-cooperativity of the two water OH groups. J. Mol. Struct., 416, 287 (1997).
15. Masimov E.A., Hasanov H.Sh. Thermodynamics of biological systems. Baku, "Publishing House Laman", 2007, 418 p.
16. Atkins P., De Paula J. Physical chemistry. Oxford University Press. 2006. 1067 p.

***Corresponding author**: p.g.bakhtiyar@gmail.com

THREE-DIMENSIONAL STRUCTURE OF EXORPHIN B5 MOLECULE

N.A.AKHMEDOV*, R.M. ABBASLI., L.N.AGAEVA, L.I.ISMAILOVA
Baku State University, Institute for Physical Problems, Z.Khalilov str., 23, Baku, Azerbaijan, Az1148

The conformational possibilities of the exorphin B5 molecule were studied by the theoretical conformational analysis method. The conformational potential energy of the system was chosen as the sum of the contributions of non-valent, electrostatic and torsional interactions and the hydrogen bonds energies. The low-energy conformations of the molecule, the values of the dihedral angles of the main and side chains of the amino acid residues were found, the energies of intra-and inter-residual interactions were estimated**.**

Keywords: exorphin, opioid peptides, structure, conformation.
PACS: 36.20.Ey; 87.15.Aa; 87.15.He

1.Introduction

The regulatory peptides, first discovered in the second half of the twentieth century, are actively studied by both physiologists and pharmacologists, since the area of peptide biological activity is extremely wide. They are one of the main links that unite three main regulatory systems of the body - the nervous, endocrine and immune. At present, more than 9000 physiologically active peptides have already been characterized in various animal species and in humans. These are short chains of amino acids (2-70 residues) that function as signaling molecules. The regulatory peptides are characterized by exposure to many systems of the body. Opioid peptides are currently considered the most studied group of peptide signaling substances. Opium causes pain relief, sedation and sleep, as well as the euphoric state and a number of vegetative reactions. Opioid peptides are of animal and plant origin. A number of exogenous peptides derived from food have opioid-like properties. Such peptides were called exorphins [1]. We have investigated the structural and functional organizations of a number of opioid peptides, and this work is a continuation of our previous studies [2-5].

2.Method

The molecule was calculated using the theoretical conformational analysis method. The conformational potential energy of the system was chosen as the sum of the contributions of non-valent, electrostatic and torsional interactions and the energy of hydrogen bonds. The non-valent interactions were assessed by Lennard-Jones potential. The electrostatic interactions were calculated in a monopole approximation according to the Coulomb's law using partial charges on the atoms. The conformational possibilities of the exorphin molecule were studied under the conditions of the water environment, in connection with which the dielectric constant was assumed to be 10. The energy of hydrogen bonds was estimated using the Morse potential.

3.Results and discussion

The spatial structure of the molecule of exorphin B5 (Tyr1-Gly2-Gly3-Trp4-Leu5) was investigated on the basis of the low-energy conformations of the N-terminal tetrapeptide fragment Tyr1-Gly2-Gly3-Trp4 (exorphin B4) and N-acetyl-L-leucine methylamid, N-acetyl-L-glycine methylamid, N-acetyl-L-tyrosine methylamid and N-acetyl-L-tryptophan methylamid. The calculation results of the spatial structure of the molecule of exorphin B4 show that the energy differentiation takes place according to the conformations and backbone forms. Thirteen forms of the backbone of four shapes fff, eef, efe and fee fall into the energy interval 0-6 kcal / mol. The fff shape is represented by six forms of the main chain, the energy of which varies in the range of 0 - 4.8 kcal / mol. The global conformation of the molecule of exorphin B4 is $B_{11}PRB_{11}$. This conformation is advantageous as for nonvalent and for electrostatic interactions. In this structure the efficient interactions of Tyr1 with Gly2, Gly3 and Trp4, which contribute to a total energy of -12.5 kcal / mol occur. The shape eef has four low-energy forms of the main chain, the relative energy of which varies in the range 3.7 - 4.9 kcal / mol. The shapes efe and fee are represented by all three forms of the main chain, the relative energy of which varies in the energy interval 5.2 - 5.6 kcal / mol. In all low-energy structures of the exorphin B4 molecule the side chains of Tyr1 and Trp4 are in the same positions, the side chain of Tyr1 is directed to the C-terminal part of the molecule, and the side chain of Trp3 is directed to the N-terminal part of the molecule. In such positions they effectively interact with each other and the backbone atoms of the molecule.

The initial conformations for calculation of the pentapeptide molecule of exorphin B5 were formed from the low-energy conformations of the exorphin B4. The calculation results revealed the energy differentiation between the shapes, the backbone forms and the conformations. Eleven conformations belonging to eleven forms of seven shapes of the backbone fall into a wide energy range of 0–6.0 kcal / mol. The relative energy and energy contributions of non-valent, electrostatic, torsional interactions of these conformations of the exorphin B5 molecule are shown in Table 1. The shapes fffe, ffff, eeff, eefe are represented by two forms of the main chain, and the shapes of efef, feef, feee by one form of the main chain. The energy of intra-and inter-interaction interactions, the geometrical parameters of the lowest-energy conformations of each shape are given in Tables 2 and 3. Figure 1 shows the spatial arrangement of amino acids in these conformations.

Table 1.

Relative energy (U_{rel}) and total energy (U_{total}) and energy contributions of nonvalent (U_{nv}), electrostatic (U_{el}), torsional (U_{tors}) interactions of optimal conformations of the molecule exorphine B5

№	Shapes	Conformation	Energy				
			U_{nv}	U_{el}	$U_{tors.}$	U_{total}	U_{rel}
1	fffe	$B_{11}PRB_{11}B_{31}$	-21.9	3.0	3.3	-15.6	0
2		$B_{11}LPB_{11}B_{22}$	-22.4	3.1	3.8	-15.5	0.1
3	ffff	$B_{11}LPR_{11}R_{32}$	-19.1	3.1	3.8	-12.3	3.3
4		$B_{11}PRR_{11}R_{32}$	-22.8	4.7	6.7	-11.4	4.2
5	eeff	$B_{11}BRR_{11}R_{32}$	-22.5	4.4	3.6	-14.5	1.1
6		$B_{11}RPR_{11}R_{32}$	-21.9	4.2	3.6	-14.1	1.5
7	eefe	$B_{11}BRB_{11}B_{32}$	-18.2	3.9	3.0	-11.3	4.3
8		$B_{11}RPB_{11}B_{32}$	-16.9	3.8	2.7	-10.5	5.1
9	efef	$B_{11}BLR_{11}R_{21}$	-18.4	4.1	2.9	-11.4	4.2
10	feef	$B_{11}PLR_{11}R_{21}$	-17.3	4.5	2.1	-10.6	5.0
11	feee	$B_{11}PLB_{11}B_{32}$	-16.4	3.9	2.6	-10.0	5.6

The energy differentiation between the low-energy conformations occurs mainly due to non-valent interactions between the atoms (table 1). The difference between the contributions of non-valent interactions is 6.4 kcal / mol, between the contributions of electrostatic interactions is 1.7 kcal / mol, and between the contributions of torsional interactions is - 4.6 kcal / mol. In the conformations of the feee and eeee shapes the side chains of Tyr1 and Trp4 are arranged to effectively interact with the atoms of the main chain. In the lowest energy conformation B5 $B_{11}PRB_{11}B_{31}$ of the exorphin molecule the contribution of Tyr1 with the remaining residues is -13.4 kcal / mol, and the interaction of Tyr1-Trp4 is -10.1 kcal / mol (table 2). In this conformation, the hydrogen bond formes between the N-H atom of Tyr1 and C = O atom of Trp4. For the conformations of the ffff shape the character of the stabilizing forces is almost the same as of the fffe shape. In the conformation of $B_{11}BRR_{11}R_{32}$ of the eeff shape the energy contribution of interactions Tyr1 with other amino acid residues is -8.7 kcal / mol, the interaction of Gly2 with Trp4 and Leu5 is –3.7 kcal / mol, the interaction of Trp4 and Leu5 is -4.0 kcal / mol. In the low-energy conformations of the efef, feef and feee shapes the effective interactions between the Tyr1, Trp4 and Leu5 side chains occur between themselves and with the atoms of the backbone. In all low-energy conformations of the exorphin B5 molecule the side chains of Tyr1 and Trp4 are in the same positions.

Table 2.

Energy inside and between residual interactions in the conformations of the molecule exorphine B5 $B_{11}PRB_{11}B_{31}$ (U_{rel}=0 kcal/mol, first line), $B_{11}BRR_{11}R_{32}$ (U_{rel}=1,1 kcal/mol, second line), $B_{11}BLR_{11}R_{21}$ (U_{rel}=4.2 kcal/mol, third line), $B_{11}PLR_{11}R_{21}$ (U_{rel}=5.0 kcal/mol, fourth line)

Tyr1	Gly2	Gly3	Trp4	Leu5	
1.7	-1.4	-1.0	-10.1	-0.9	Tyr1
1.8	-1.2	-2.2	-4.9	-0.4	
2.3	-2.2	-1.8	-4.3	-0.2	
1.7	-1.4	-1.2	-3.2	0.1	
	1.2	0.1	-1.1	-0.1	Gly2
	1.3	0.1	-1.0	-2.7	
	1.3	0.5	-1.0	0	
	1.3	0	-1.5	0	
		1.3	-1.7	-0.8	Gly3
		1.2	-1.3	-1.4	
		1.3	-1.8	-0.7	
		1.3	-1.8	-0.7	
			-0.4	-2.8	Trp4
			-0.2	-4.0	
			-0.5	-3.3	
			-0.5	-3.0	
				-3.1	Leu5
				-3.3	
				-4,0	
				-4,1	

Table 3

Geometric parameters (in degrees) of low energy conformations of the molecule exorphine B5

Residue	Conformation			
	$B_{11}PRB_{11}B_{31}$	$B_{11}BRR_{11}R_{32}$	$B_{11}BLR_{11}R_{21}$	$B_{11}PLR_{11}R_{21}$
Tyr1	-63 156 175 61 87 0	-69 161 -175 60 90 0	-77 157 -175 66 99 0	-65 159 178 65 87 0
Gly2	74 -91 180	-87 59 172	-72 127 180	78 -78 178
Gly3	-83 -50 -175	-90 -41 177	81 61 -174	87 58 177
Trp4	-100 150 180 65 94	-100 -23 170 63 97	-96 -42 180 68 93	-101 -42 180 61 92
Leu5	-99 120 180 -71 65 180 172	-85 -59 179 -52 178 -175 180	-100 -60 180 178 61 180 179	-99 -60 180 176 60 180 177
U_{rel}	0	1.1	4.2	5.0

Comment: The values of dihedral angles in the table are in the following order φ, ψ, w, χ_1, χ_2...

The study of the spatial structure of the molecule of exorphin B5 shows that conformational freedom is possible around the dihedral angle χ1 of the residues Tyr1 and Trp4. Therefore the side chains of these residues can easily interact with other molecules and receptors.

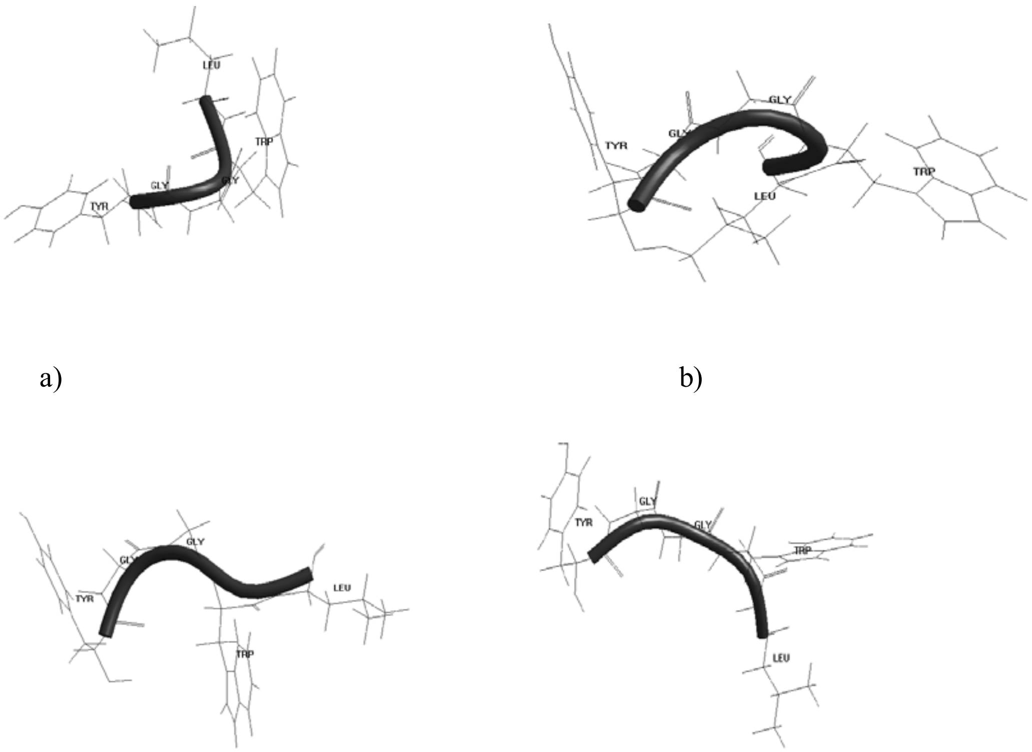

a) b)

c) d)

Figure 1. Atomic model of spatial structure of the exorphine B5 molecule a), b), c) and d), corresponded to the structures with the relative energies 0 ;1.1 ; 4.2 and 5.0 kcal/mol,respectively.

Conclusion

The molecules of exorphin B4 and exorphin B5 have almost identical low-energy conformations, the positions of the side chains of Tyr1 and Trp4 residues in the space coincide for both molecules. Thus, the theoretical conformational analysis of the molecules of exorphin B4 and exorphin B5 led to such structural organizations of molecules that do not exclude the realization by the molecules of a number of different functions that require strictly specific interactions with various receptors.

References

1. Chesnokova E.A., Sarycheva N.Y., Dubynin V.A,.Kamensky A.A. Advances in physiological sciences (in Russian), 46, 22 (2015).
2. Akhmedov N.A., Ismailova L.I., Abbasli R.M., Agayeva L.N., Akmedova S.R. IOSR Journal of Applied Physics, 66 (2016).
3. Akhmedov N.A., Ismailova L.I., Agayeva L.N.,Gocayev N.M. Peptid and Protein Research, 87, (2010).
4. Gadjieva Sh.N., Akhmedov N.A.,.Masimov E.A,. Godjaev N.M. Biophysics (in Russian), 58, 587, (2013.
5. Hasanov E.M.,Akhmedov N.A. International Journal of Innovative Science and Research Technology,3,72, (2018).

***Corresponding author**:Namiq.49@bk.ru

ENERGY OF ULTRA SHORT PULSES IN METAMATERIALS

SH.AMIROV*, RENAJ.KASUMOVA, Z.H.TAGIYEV
Baku State University, Z.Khalilov str., 23, Baku, Azerbaijan, Az1148

Nonstationary interaction between forward high intensity pump and idler waves with backward ultrashort pulses in metamaterials is studied in the second order dispersion theory. We obtained analytic expression for the energy of backward signal wave. An influence of o group velocity mismatch (GVM) as well as the group velocity dispersion (GVD) on the energy of a signal wave is studied. Energy of signal wave has a pronounced maximum depending on the length of metamaterial. Variation in characteristic lengths as GVM and GVD leads to the change in optimum length of metamaterial at which energy of a signal wave is maximum. It was obtained that maximum of energy of conversion is reached not at group phase matching, but at the definite characteristic lengths of GVM and GVD. For the given ratio,l_{nl}/l_d(GVD) maxima of reduced energy of signal wave displaces toward greater values of phase mismatch parameter with increase inl_{nl}/l_ν(GVM). A shift in energy maxima also occurs toward greater values of$l_{nl}/l_\nu$with increase inl_{nl}/l_d.

Key words: group velocity dispersion, ultrashort pulse, metamaterial, second order dispersion theory.
PACS:78.67. Pt; 42.65-k; 42.60, 42.62.Hk

1. Introduction

Metamaterials belong to a broad class of synthetic materials with unusual properties have not been found in nature. Unusual features of metamaterials are originated owing to their composition. As it was shown upon studies the electromagnetic properties of metamaterials both electric permittivity and magnetic permeability can become negative in those materials[1]. Recent investigations have shown the important stage of metamaterials in the progress of material science and technology [2]. Authors [3] characterize metamaterialsas optimized combination having several responses to particular excitation. Metamaterials have found applications in manufacturing the microwave antennas as well as the sensors widely used in medicine with different purposes [4]. The first order dispersion theory was employed for discussion the transition processes in a medium with second order nonlinearity by the authors [5,6]. Authors of [7] have presented discussion of metamaterials for their use in developments in the visible as well as infrared regions of a spectrum. Transition processes upon the interaction of running and counter waves in metamaterials are discussed by the authors [8].Thethreewave interaction in metamaterials is investigated for the case of second harmonic generation in[9].Energy transformations between backward signal wave upon the interaction with the forward pump and idler waves was considered by us [10]by use the constant intensity approximation CIA[11-13]. This approximation was employed by us also for theoretical analysis the four –wave mixing in metamaterials[14]. A growing interest to the non-stationary interaction of ultra-short pulses of light in nonlinear medium is related to the development of powerful sources of light pulses of femtosecond duration[15]. An effect of dispersive properties of medium on the character of interaction of ultrashort pulses increases with the reduction in the pulse duration. Frequencyconversion for ultrashort running waves is presented in[16].An effect of group velocity mismatch (GVM) and group velocity dispersion (GVD) on the generation of sum frequency of ultrashort pulses in a resonator was discussed in[17]. Earlier we have investigated spectrum of the excited backward signal wave in metamaterials in the second order dispersion theory[18].

2. Theory

In this paper astudy of energyof excited backward ultrashort signal wave in the non-stationary conditions is presented. We assume metamaterial with length l and input surface at $z = l$. Such a medium with quadratic nonlinearity is “left” at the frequency of signal wave only. Here the pump wave is a long pump pulse with frequency ω_3 an idler wave is at frequency ω_2 and a signal wave is at the difference frequency $\omega_1 = \omega_3 - \omega_2$. The geometry of the problem is so that the pump and idler waves enter the nonlinear medium from the left $(z = 0)$, but the signal wave from the right $(z = l)$ hand side. In such a consideration the wave vectors of all interacting waves in a metamaterial propagate in the positive direction of the z axis. During the wave propagation in a nonlinear medium as a result of the nonlinear interaction the energy exchange occurs between the counter wave packets of two types: direct waves (here the idler and pump waves) and backward wave (here the signal wave); this leads to the energy transfer from the pump and idler waves into the signal-wave energy. For the negative values of the dielectric permittivity and magnetic permeability at the signal wave frequency ω_1 and the positive values at the frequencies ω_2 , ω_3 the parametrical interaction is described by the system of parametrically coupled equations[13]

$$\left(\frac{\partial}{\partial z}-\frac{1}{|u_1|}\frac{\partial}{\partial t}-i\frac{g_1}{2}\frac{\partial^2}{\partial t^2}-\delta_1\right)A_1=i\gamma_1 A_3 A_2^* e^{i\Delta z}$$

$$\left(\frac{\partial}{\partial z}+\frac{1}{u_2}\frac{\partial}{\partial t}-i\frac{g_2}{2}\frac{\partial^2}{\partial t^2}+\delta_2\right)A_2=-i\gamma_2 A_3 A_1^* e^{i\Delta z} \qquad (1)$$

$$\left(\frac{\partial}{\partial z}+\frac{1}{u_3}\frac{\partial}{\partial t}-i\frac{g_3}{2}\frac{\partial^2}{\partial t^2}+\delta_3\right)A_3=-i\gamma_3 A_1 A_2 e^{-i\Delta z}$$

here A_j (j=1-3) are the corresponding complex amplitudes of the signal, idler and pump waves respectively , δ_j are the absorption coefficients of the medium at frequencies ω_j (j=1-3), u_j - are the group velocities of the interacting waves , $\Delta = k_1 - k_2 - k_3$ is the phase mismatch between the interacting waves , $g_j = \partial^2 k_j / \partial \omega_j^2$ is the dispersion of group velocities and γ_1 , γ_2 , γ_3, are the coefficients of nonlinear coupling depending on effective quadratic susceptibility of the medium χ^2_{eff}. Assuming pump wave amplitude to be constant ($A_3 = A_{30} = const.$) and having put substitution for local time $\eta = t - \frac{z}{u_1}$the set of above equations (1) is reduced to

$$\left(\frac{\partial}{\partial z}-i\frac{g_1}{2}\frac{\partial^2}{\partial \eta^2}-\delta_1\right)A_1(z,\eta)=i\gamma_1 A_3 A_2^*(z,\eta) e^{i\Delta z}$$

$$\left(\frac{\partial}{\partial z}-\nu\frac{\partial}{\partial \eta}-i\frac{g_3}{2}\frac{\partial^2}{\partial \eta^2}+\delta_3\right)A_3(z,\eta)=-i\gamma_3 A_1 A_2(z,\eta) e^{-i\Delta z} \qquad (2)$$

where$\nu = 1/u_2 - 1/u_1$ is a group velocity mismatch.

Non-stationary wave interactions are of considerable interest in nonlinearly optical processes that occur in the fields of ultrashort laser pulses and has a growing related to the development of powerful sources of light pulses of femtosecond duration [1, 2].

Employment the Fourier transformation yields

$$\left(\frac{\partial}{\partial z}+i\frac{g_1}{2}\omega^2-\delta_1\right)A_1(z,\omega)=i\gamma_1 A_{30} A_2^*(z,\omega) e^{i\Delta z}$$

$$\left(\frac{\partial}{\partial z}+i\frac{g_3}{2}\omega^2+i\nu\omega+\delta_3\right)A_3(z,\omega)=-i\gamma_3 A_1(z,\omega) A_{20} e^{-i\Delta z} \qquad (3)$$

In the absence of linear losses ($\delta_j = 0$) having put different substitutions the above set of equations reduces to the following second order differential equation

$$\frac{\partial^2 a(z,\omega)}{\partial z^2}+\lambda^2 a(z,\omega)=0 \qquad (4)$$

where$a(z,\omega\,) = A_1(z,\omega\,)e^{-kz}$, $k = i\left(\frac{\Delta-\nu\omega}{2} - \frac{g_1+g_3}{4}\omega^2\right)$, $\lambda = i\left[\Gamma_2^2 + \frac{\beta^2}{4}\right]^{1/2}$,$\beta = i\left(\frac{g_1-g_3}{2}\omega^2 + \Delta - \omega\nu\right)$
Searching solution of equation (4) as

$$a(z,\omega\,) = C_1 cos\lambda z + C_2 sin\lambda z$$

and taking into account the boundary conditions $A_1(z = l) = 0$, $A_{2,3}(z = 0) = A_{20,30}$we obtain for complex amplitude of signal wave

$$A_1(\omega, z) = \frac{i\gamma_1 A_3 A_{20}}{\lambda - ktan\lambda l}(cos\lambda z \cdot tan\lambda l - sin\lambda z)e^{kz} \tag{5}$$

Furthermore we assume that the input idler wave is Gaussian with a quadratic phase modulation.

$$A_3(t) = A_{30}e^{-\frac{t^2}{2\tau^2} - i\gamma\frac{t^2}{2}} \tag{6}$$

According to (5) a spectral power density of signal pulse wave is given by

$$S_1(z,\omega) = D\frac{1}{\sqrt{1+p}}\frac{(sin\lambda z - tg\lambda l \cdot cos\lambda z\,)^2}{(\lambda z\,)^2 + (kz\,)^2 tg^2\lambda l}\exp\left(-\frac{\omega^2\tau^2}{1+p}\right) \tag{7}$$

where $D = (cn_1/8\pi)\gamma_1^2 I_{20} I_{30}\tau^2 z^2/2\pi$,

$\lambda z = {l_{nl}}^{-1}z\ \ [\frac{1}{4}\left(\frac{1}{2}\frac{l_{nl}}{l_{d.}}(1-\alpha\,)\omega^2\tau^2 - \frac{l_{nl.}}{l_\nu}\omega\tau + \frac{\Delta}{\Gamma_3}\right)^2 - 1]^{1/2}$,

$kz = {l_{nl}}^{-1}z[i(\frac{\Delta}{2\Gamma_3} - \frac{1}{2}(1+\alpha\,)\frac{l_{nl}}{l_{d.}}\omega^2\tau^2 - \frac{1}{2}\frac{l_{nl.}}{l_\nu}\omega\tau\,)\,]$, $\quad \alpha = \frac{g_3}{g_1}$, $l_d = \frac{\tau^2}{g_1}$, $l_\nu = \frac{\tau}{\nu}$

$p = \gamma^2\tau^4$ is a phase modulationfactor
On the basis of equation (7) the energy density is calculated by the following integration:

$$W_1 = D\int_{-\infty}^{+\infty}\frac{1}{\sqrt{1+p}}\frac{(sin\lambda z - tg\lambda l \cdot cos\lambda z\,)^2}{(\lambda z\,)^2 + (kz\,)^2 tg^2\lambda l}\exp\left(-\frac{\omega^2\tau^2}{1+p}\right)d\omega \tag{8}$$

3. Discussion and Results

From (8) it follows that energy of signal wave is determined not by the values of z, l_ν and $l_{d.}$ but with the ratios z/l_{nl} ,l_{nl}/l_ν , l_{nl}/l_d . Fig.1 demonstrates dependences of signal wave energy versus reduced length z/l_{nl} in the metamaterial with length $\Gamma_3 l = 2$ at phase for phase mismatch parameter ($\Delta l_{nl} = 3$) at different values of l_{nl}/l_ν , l_{nl}/l_d and $p = \gamma^2\tau^4$. In a traditional nonlinear medium this dependence has a pronounced maximum corresponding to the coherent length of medium[16].Since the energy flux of signal wave is in the opposite direction to the fluxes of both idler and pump waves, as it was expected, greater values of energy are obtained not at the output but at the input of the metamaterial.

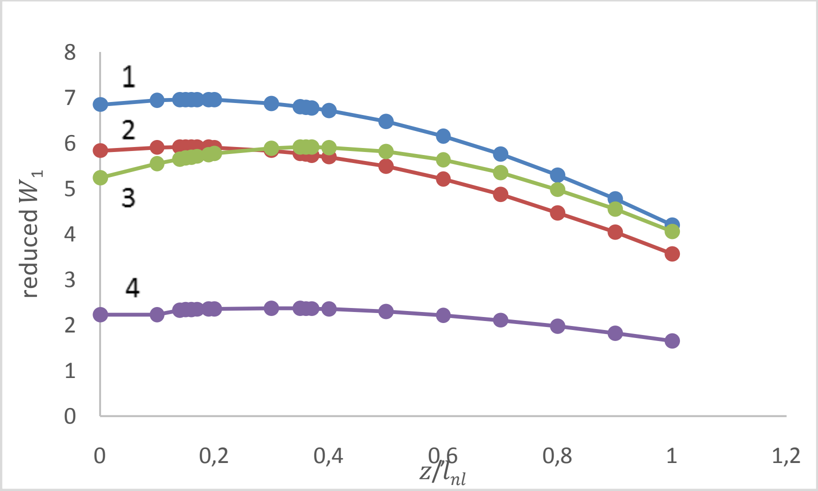

Fig. 1. The reduced energy density of a signal wave as a function of reduced length z/l_{nl} for $\Delta l_{nl} = 3$ curves (1,2,4) and $p = \gamma^2\tau^4$ =5 (curves 1,3,4) and $p = 0$ (curve 2) at different values of l_{nl}/l_v , and l_{nl}/l_d : $1 - \frac{l_{nl}}{l_v} = \frac{l_{nl}}{l_d} = 3$, ; $2 - \frac{l_{nl}}{l_v} = \frac{l_{nl}}{l_d} = 3$; $3 - \frac{l_{nl}}{l_v} = \frac{l_{nl}}{l_d} = 3, \Delta l_{nl} = 0$; $4 - \frac{l_{nl}}{l_v} = 3, \frac{l_{nl}}{l_d} = 0$

Comparison of curves 1 and 2 shows increase in energy with increase in frequency modulation.In Fig. 2 dependences of energy of a backward signal wave versus phase mismatch parameter are illustrated at different values of ratios l_{nl}/l_v and l_{nl}/l_d . As can be seen at equal values of above ratios the energy dependence is not symmetric relatively ordinate axis. With increase in l_{nl}/l_v the peaks of energy shift toward greater values of phase mismatch parameter, width of peaks decreasesand plots exhibit several maxima. Maxima of energy do not correspond to phase matching.

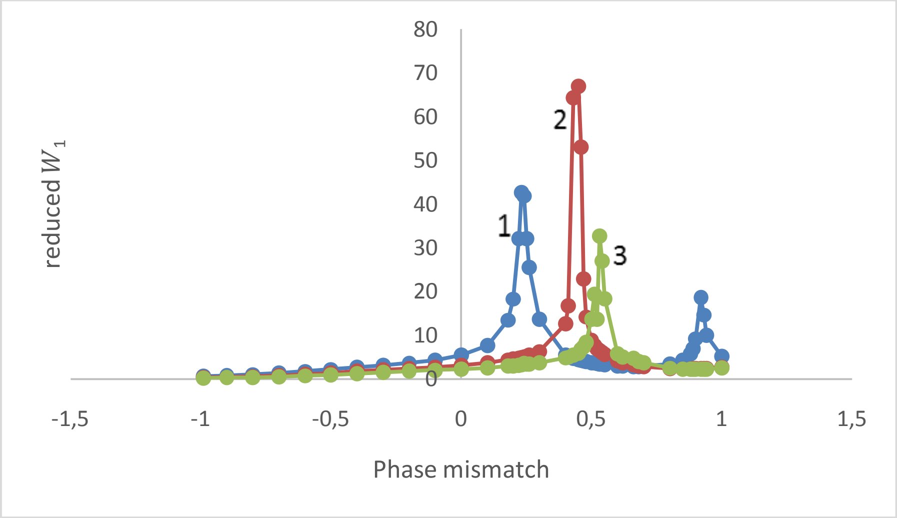

Fig. 2 Dependences of the reduced energy density of a signal wave on the relative phase mismatch for $\frac{z}{l_{nl}} = 0{,}5$ and $p = \gamma^2\tau^4 = 0$ at different values of l_{nl}/l_v , and l_{nl}/l_d : $1 - \frac{l_{nl}}{l_v} = \frac{l_{nl}}{l_d} = 3$; $2 - \frac{l_{nl}}{l_v} = 3$, $\frac{l_{nl}}{l_d} = 6$; $3 - \frac{l_{nl}}{l_v} = 3$,$\frac{l_{nl}}{l_d} = 10$.

An effect of group velocity mismatch on energy gained in metamaterial is seen in Fig.3. Here energy plots are presented at different values of group velocity dispersion. Plots are given for values decreased by a factor of 10 (curves 2 and 3) and 5 times (curve 1)

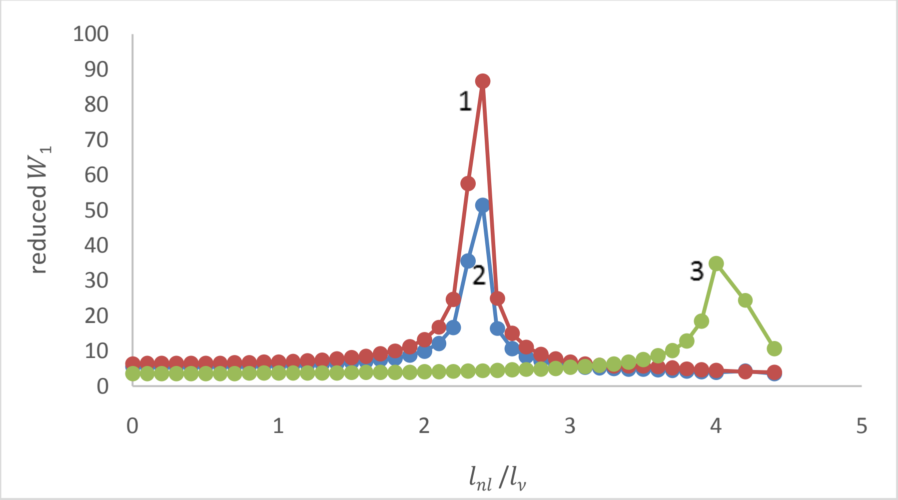

Fig. 3. Dependences of the reduced energy density of a signal wave on the $\frac{l_{nl}}{l_v}$ at $\frac{z}{l_{nl}}=0{,}5$ and $\Delta\cdot l_{nl}=0$ for different values of $\frac{l_{nl}}{l_d}$ and $p=\gamma^2\tau^4$: $1-\frac{l_{nl}}{l_d}=1$, $p=\gamma^2\tau^4=0$; $2-\frac{l_{nl}}{l_d}=1$, $p=\gamma^2\tau^4=10$; $3-\frac{l_{nl}}{l_d}=3$, $p=\gamma^2\tau^4=0$;

As can be seen an increase in characteristic length $\frac{l_{nl}}{l_d}$ the energy maxima shift toward greater values of $\frac{l_{nl}}{l_v}$. Increase in frequency modulation also affects to the energy enhancement. Energy density of a signal wave as a function $\frac{l_{nl}}{l_d}$ are demonstrated in Fig. 4

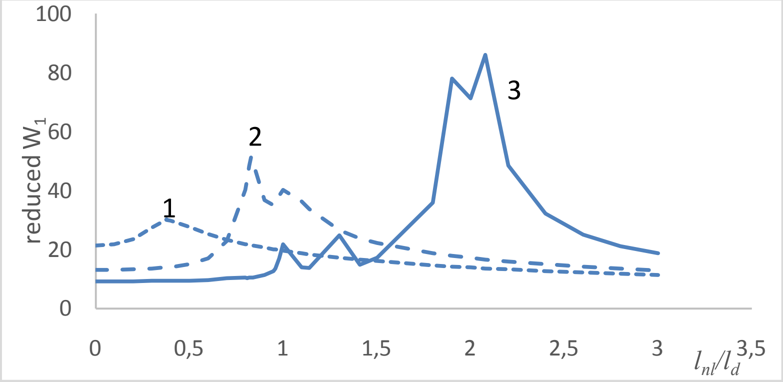

Fig.4. Dependences of the energy density of a signal wave as a function $\frac{l_{nl}}{l_d}$ at different values of $\frac{l_{nl}}{l_v}$ when $\frac{z}{l_{nl}}=0{,}5$, $p=\gamma^2\tau^4=0$ and $\Delta\cdot l_{nl}=0$: $1-\frac{l_{nl}}{l_v}=1$; $2-\frac{l_{nl}}{l_v}=2$; $3-\frac{l_{nl}}{l_v}=3$

From these drawings it is seen that maxima of dependences shift toward greater values of $\frac{l_{nl}}{l_d}$ with increase in $\frac{l_{nl}}{l_v}$ curves exhibit more maxima. In Fig. 3 and Fig. 4 behavior of curves shows that greater values of energy are obtained not under group velocity matching or in the absence of group velocity dispersion but at definite values of characteristic lengths l_v and l_d . This result testifies that both group velocity mismatch and group velocity dispersion can play the profitable role from energy point of view[16].

4. Conclusions

On the basis of above discussions we can conclude that the second order dispersion theory has allowed us to study effects of group velocity mismatch as well as group velocity dispersion on the parametrical amplification of a backward signal wave in metamaterial. It was found that at the given ratio $\frac{l_{nl}}{l_d}$ maxima of reduced energy of a signal wave displace toward greater values of phase mismatch parameter with increase in the $\frac{l_{nl}}{l_v}$. The energy maxima do not correspond to the phase matching. This result testifies that both group velocity mismatch and group velocity dispersion can play the profitable role from energy point of view.

References

1. Veselago V. G. Sov. Phys.Usp. 10, 509 (1968).
2. Mendhe S.E., Kosta Y.P. International Journal of Information Technology and Knowledge Management 4 (1), 85 (2011).
3. Gangwar K., Paras R.P.S., Advance in Electronic and Electric Engineering 4(1): 97 (2014).
4. Pendry J.B., Holden A.J., Robbins D.J., Stewart W.J., IEEE Trans on Microwave Theory and Tech 47,11 (1999).
5. ShadirovI.V.,Zharov A.A., Kivsar Y.S. J.,Opt.Soc.Am.B, 23, 529 (2006)
6. Shalaev M.I., Myslivets S.A., et al. Opt.Lett., 36, 3861 (2011).
7. Cai W., Shalaev V.M., Optical Metamaterials. Fundamentals and Applications (New York), Springer,(2010).
8. Slabco V.V., Popov A.K., C.A. Myslivets, E.V.,Rasskazova, V.A. TkachenkoKvantovayaElektronika (in Russian), 45, 12, 1151 (2015).
9. MaimistovA.I., GabitovI.R. and KazantsevaE.V., Opt. Spectrosk., 102, 99 (2007).
10. KasumovaR.J., TagievZ. H., Amirov S.H. ShamilovaA.and SafarovaG.A., Journal of Russian Laser Research, 38, 4, 211 (2017).
11. TagievZ.H., ChirkinA.S., Sov.Phys. JETP, 46, 669 (1977).
12. TagievZ.H., Kasumova R.J., SalmanovaR.A., KerimovaN.V. J.Opt. B., 3, 84 (2001).
13. Dmitriev V.G., Tarasov L.V., Prikladnayanelineynayaoptika (Applied Nonlinear Optics) Moscow, Fizmatgiz, 352 (2004).
14. Kasumova R.J., Amirov S.H.,ShamilovaA.,Quantum Electronics 47, 7, 665 (2017).
15. Kasumova R.J, Safarova G.A., AmirovS.H., Akhmanov S.A. and Khokhlov R.V., Eksp. Teor.Fiz. 43, 351 (1962).
16. Akhmanov S.A., Visloukh V.A., Chirkin A.S. // UFN , 149, 3, 449 (1986).
17. Amirov S.H, Tagiev Z.A. Optika i Spektroskopiya (in Russian) 69, No. 3, 678 (1990).
18. KasumovaR.J.,. AmirovS.H., Superlattices and Microstructures126, 49-56 (2019).

***Corresponding author**: physics_med@mail.ru

INFLUENCE OF THERMAL FLUCTUATIONS ON CRITICAL CURRENT OF JOSEPHSON JUNCTION WITH UNCONVENTIONAL CURRENT-PHASE RELATION

I.N.ASKERZADE[a,b]

[a]*Department of Computer Engineering and Center of Excellence of Superconductivity Research, Ankara University, Ankara, 06100, Turkey*

[b]*Institute of Physics Azerbaijan National Academy of Sciences 33, H.Cavid 33.Baku, AZ1143, Azerbaijan*

In this study we carried out the analysis of the thermal fluctuations of Josephson junction (JJ) with unconventional current-phase relation (CPR). It was obtained expression for the critical current fluctuations in case of linear growing of current via junction in limits of low sampling rate. It is shown that, the dynamical properties of JJ with unconventional CPR is determined by the renormalized critical current of JJ.

Keywords: Josephson junction, current-phase relation, thermal fluctuation
PACS: 03.75.Lm; 74.50.+r; 73.43.Jn

1. Introduction

In all early studies of the dynamical properties of JJ based circuits (see [1,2]), it was considered that CPR has a harmonic character with critical current I_{c0}

$$I = I_{c0}\sin\phi \quad . \tag{1}$$

Relationship (1) is fulfilled with a high accuracy for JJs on low temperature superconductors [3]. In the case of JJs on high temperature superconductors, the CPR becomes anharmonic [4, 5]

$$I = I_c f_\alpha(\phi) = I_{c0}(\sin\phi + \alpha\sin 2\phi) , \tag{2}$$

where anharmonicity parameter α depends on the junction preparation technology. In general, anharmonicity in the CPR for high temperature and Fe-based superconductors based JJ is associated with the d-wave behavior of the order parameter and many band character of superconducting state in new superconducting compounds [6]. The some dynamical properties of single JJs with an anharmonic CPR (2) were studied in papers [7–11].

In the case of JJs based on topological superconductors, the CPR includes fractional term [12-14],

$$I = I_c f_m(\phi) = I_{c0}(\sin\phi + m\sin(\phi/2)) \quad . \tag{3}$$

Second term in Eq. (3) related with Majorana quasi-particles and dynamical detection of this particles seems very challenging in sold state physics. Discovery of Majorana fermions seems interesting from the point of fault-tolerant quantum computing [15]. The few number papers devoted to dynamical properties of single JJs with Majorana term (3) [16–17]. In this study we carried out the detail analysis of the thermal fluctuations of critical current of Josephson junction with unconventional current-phase relation (2-3). We take into account the case of linear growing current via junction. It is shown the changing of dynamics of JJ with unconventional CPR.

2. Basic Equations

For the analysis of the dynamics JJs with anharmonic CPR (2,3), we use differential equation for Josephson phase

$$\beta\ddot{\phi}+\dot{\phi}+f_{\alpha,m}(\phi)=i_e, \tag{4}$$

where i_e normalized external current via JJ, dots over ϕ corresponds to derivative in respect dimensionless time $\frac{\Phi_0}{2\pi I_c R_N}$. In Eq. (4) notation β is the McCumber parameter of JJ $\beta=\frac{2e}{\hbar}I_c R_N^2 C$, which determine the size of hysteresis in IV curve. It is well known, that the case of $\beta>>1$ correspond to tunnel JJ [1,2]. In the case of $\beta<<1$ hysteresis on IV curve is absent and in Eq. (4) we can neglect the first term. Presence of second harmonic in CPR in Eq. (2,3) leads to renormalizaion of critical current I_{c0}. In calculations we use analytical solution for the maximum point of the function $f(\phi)$ (4) similarly to [18]. The effective critical current I_c of a JJ with an anharmonic CPR as function of amplitude of second term (see Eqs. (2,3)) is presented in Fig. 1. As you can see, with increasing of this amplitude effective critical current I_c also increases. Quadratic behavior at small α (Eq. (2), lower line) converted to linear dependence at high values of anharmonicity parameter. Inclusion ofMajorana term leads to linear increasing of critical current (upperline in Fig. 1).

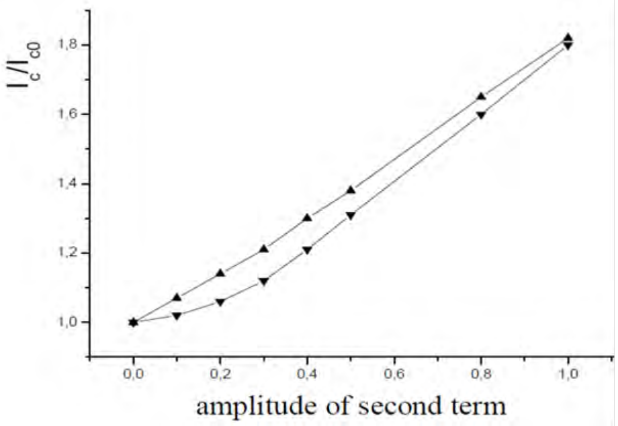

Fig.1. Effective critical current of JJ with unconventional CPR: upper with Majorana term (Eq. 3), lower anharmonic case (Eq. 2)

3.Results

Final expression for the fluctuation of critical current of JJ in the case of low sampling rate $r<<\gamma^{3/2}$, leads to result for all cases of high and lower McCumber parameter (see [2,6,7,10])

$$\delta i=\left(\frac{3\gamma\ \ln C_0}{2^{5/2}}\right)^{3/2}, \qquad \gamma=2\pi\frac{kT}{\Phi_0 I_c};C_0=const \quad . \tag{5}$$

In expression (5) we should take into account renormalization of McCumber parameter $\beta(\alpha)$ and critical current $I_c(\alpha)$ due unconventional character of CPR. The thermal fluctuations of critical current I_c of a JJ with unconventional CPR as function of amplitude of second term (see Eqs. (2,3)) is presented in Fig. 2.

Such result can be explaned by the decreasing of the Josephson inductance of junction in increasing of critical current I_c and as result weaking of inertial properties. It is well known that the supercurrent in JJ $I = I_c(\alpha)\sin\phi$ is equivalent to alternating differential Josephson inductance [1].

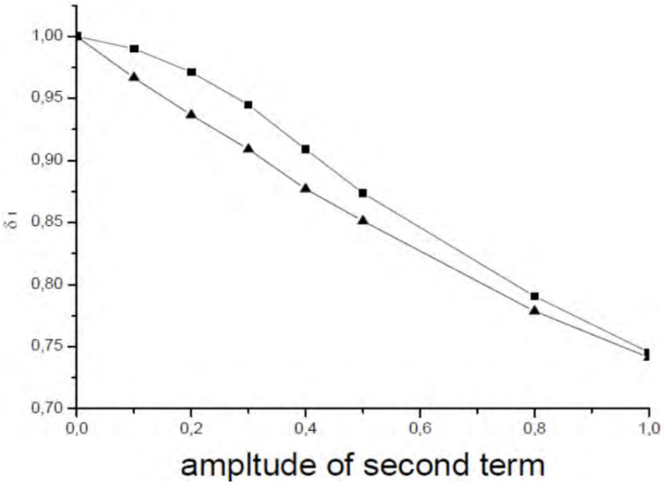

Fig.2. Thermal fluctuations of critical current of JJ with unconventional CPR in low sampling rate limit $r << \gamma^{3/2}$: upper with anharmonic term (Eq. 2), lower with Majorana term (Eq. 3)

4. Conclusions

Thus, in this paper, the influence thermal fluctuations on critical current of JJ with unconventional CPR was investigated. Renormalization of critical current in JJ with unconventional CPR leads to changing of fluctuations of critical current with increasing of amplitude of second term: anharmonic or Majorana term.

Author thanks Prof. A.Bozbey, N.Kartlı, H.B.Yıldırım for useful discussions. Presented work was supported by TUBITAK research grant 118F093.

References

1. Likharev, K.K., Introduction into Dynamics of Josephson junctions and circuits, New York, Gordon Breach, 1986,586 p.
2. Askerzade I, Bozbey A., Canturk M., Modern aspects of Josephson Dynamics and superconductivity electronics, Springer, Berlin, 2017,210 p.
3. İlichev E. et al Review of Scientific Instruments, 72,1882(2001)
4. Bauch T. , et al., Phys. Rev. Lett. 94, 087003 (2005).
5. Amin M. N. S., et al., Phys. Rev. B 73, 064516 (2005).
6. Askerzade I. , Unconventional Superconductors: Anisotropy and Multiband Effects (Springer, Berlin) 2012, 586 p.
7. Askerzade I. N., Tech. Phys. 45, 66 (2000).
8. Askerzade, I.N., Kornev V.K. Radiotekhnika i Elektronika, 39,869(1994).
9. Canturk M., Kurt E.,Askerzade I.N. COMPEL-The international journal for computation and mathematics in electrical and electronic engineering, 30,775(2011).
10. Canturk M., Askerzade I. N., IEEE Trans. Appl. Supercond. 21, 3541 (2011).
11. Canturk M., Askerzade I. N., M., IEEE Trans. Appl. Supercond. 22, 1400106 (2012).
12. Dominguez tt al , Phys. Rev. B 86,150503 (2012).
13. Fu L, Kane CL , Phys. Rev. Lett, 100, 096407(2008).

14. Hasan MZ , Kane CL , Rev Mod Phys 82,3045(2010).
15. Wendin G, Reports on Progress in Physics,80,106001(2017).
16. Kulikov at al, JETP,125,333(2018).
17. Maiti M.L. et al , Phys Rev B,92,224501(2015).
18. Goldobin E. et al Phys. Rev. B,76,224523 (2007).

***Corresponding author**: imasker@eng.ankara.edu.tr

THERMAL ACTIVATION IN SMALL JOSEPHSON JUNCTION

I.N.ASKERZADE[a,b],R.T.ASKERBEYLI[c]

[a]*Department of Computer Engineering and Center of Excellence of Superconductivity Research, Ankara University, Ankara, 06100, Turkey*
[b]*Institute of Physics Azerbaijan National Academy of Sciences 33, H.Cavid 33.Baku, AZ1143, Azerbaijan*
[c]*Department of Business Administration of Karabuk University, Karabuk, Turkey*

In this study we carried out the analysis of the thermal activation of small Josephson junction (JJ). An expression for the fluctuation of Coulomb blockade edge in the case of low and high growing rate of voltage was obtained. It was shown that dynamics of small size JJ under termal fluctuations is determined by the energy ratio-parameter, temperature and growing rate of voltage.

Keywords: Josephson junction, Coulomb blockade, thermal activation
PACS:03.75.Lm; 74.50.+r; 73.43.Jn

1. Introduction

The study of small size JJs becomes very attractive in recent years. As shown in studies [1-3], in small junctions arises Coulomb blockade in tunneling of Cooper pairs. It means that small JJs can transfer individual superconducting pairs and generate Bloch oscillation of physical quantities due to Coulomb blockade. The important pecularity of these JJs is the nonlinear differential capacitance $C_B(q)$

$$C_B(q) = \left(\frac{d^2 E_0(q)}{dq^2}\right)^{-1}, \tag{1}$$

where $E_0(q)$ is the dispersion relation for lower band [1-3] and q is the quasi-charge $(-e < q < e)$. As shown in [4], for the study of dynamics of quasicharge in small JJs it is necessary to include Bloch inductance $L_B(q)$ into the equation for quasicharge q (see [4])

$$L_B(q)\frac{d^2 q}{dt^2} + R\frac{dq}{dt} + V(q) = V_e, \tag{2}$$

where V_e external voltage applied to JJ and R is the resistance of JJ. Periodical function $V(q)$ in Eq. (2), replaces the term $\sin\phi$ in Eqs. for the usual Josephson effectdescription [5,6]. Expression of $V(q)$ that was used in [7-9], presented below $(-e < q < e)$

$$V(q) = \frac{e}{C}\frac{\frac{q}{e} - \left(\frac{q}{e}\right)^3}{\sqrt{\left(\left(\frac{q}{e}\right)^2 - 1\right)^2 + \frac{\kappa^2}{4}}}. \tag{3}$$

Bloch inductance $L_B(q)$ is the kinetic characteristic of supercurrent of JJ. $L_B(q)$ is a positive periodic function of the quasicharge is given by the expression [4]

$$L_B = \frac{L_J}{(1+\xi^2)^2}; L_J = \frac{\Phi_0}{2\pi I_c}; \xi < 1 \quad . \tag{4}$$

It is well know that small JJs are characterized by the energy ratio parameter $\kappa = \frac{E_J}{E_C}$, where $E_J = \frac{\hbar I_c}{2e}$ Josephson energy, I_c critical current, $E_C = \frac{e^2}{2C}$ Coulomb energy, and C capacity of junction [1-3]. The case of $\kappa >> 1$ corresponds to the usual Josephson effect, and it can be neglected by the effects of correlation in Cooper pair tunneling. In the opposite case $\kappa \to 0$, due to small capacity, Coulomb energy E_C becomes considerable, which leads to Coulomb blockade under tunneling of Cooper pair [7-10].

In this study we develop theory for the study of the influence of thermal fluctuations on dynamics of small JJs by taking into account Bloch inductance. In consideration, we present dynamics of small junction under low and high linear growing rate of voltage.

2.Basic Equations

In the presence of thermal fluctuations, the effect of fluctuations of Coulomb blockade edge in *IV* curve with value $\delta V = \frac{\delta q}{C}$ takes place. As shown in [1,2,7], the dynamical behavior of a small junction is similar to the behavior of a particle in the potential field of a form $U(q) = E_0(q) - V_e q$ (similar to tilted 'washboard' potential [6]).

In this limit we consider that the voltage across JJ rises as $\frac{V_e}{V_0} = \alpha t$ slowly and satisfy the the condition $\alpha << \gamma$, $\gamma << 1$ ($\gamma = \frac{kT}{E_C}$ is the intensity of thermal fluctuations in units E_C). The calculation leads to final result for tunneling probability as [11,12]

$$p(t') = 1 - \exp\left(-\frac{\omega_B}{4\pi}\frac{\sqrt{\pi\gamma}}{\alpha}e^{\frac{\kappa}{2\gamma}}\left[erf\frac{\alpha t' - 1}{\sqrt{\gamma}} + erf\frac{1}{\sqrt{\gamma}}\right]\right) \quad , \tag{5}$$

where $erf(.....)$ is the error function. In Eq. (5), $\omega_B = \frac{1}{\sqrt{L_B C_B}}$ is the frequency determined by the Bloch inductance of small Josephson junction [4,7].

In the case ofhigh growing rate of voltage across JJ (**$\alpha >> \gamma$**), the influence of thermal fluctuations is not so considerable as in case of low rate. For the analysis of the intensity of fluctuations in this case we will use Eq. (2) rewritten as

$$l_B^{\,z}\,\delta\ddot{z} + \dot{\tilde{z}} - \tilde{z}\,\delta\tilde{z} = v_f \tag{6}$$

where $\tilde{z} = \frac{4}{\kappa}(2\tilde{y}+1); \tilde{y} = \frac{q}{e} - 1; l_B^z = \frac{\kappa}{8} l_B$. Solution of last equation has the form

$$\delta\tilde{y} = \frac{1}{l_B^{\,z}} \int_{-\infty}^{\tau} K(\tau,\tau')d\tau' \quad . \tag{7}$$

In Eq. (7), the kernel $K(\tau,\tau')$ is defined from Eq. (6) with $\delta(\tau-\tau')$ on the right side.

.

3. Results

For the evaluation of the influence of thermal fluctuation on Coulomb blockade in the limit of low growing rate of voltage across JJ $\alpha << \gamma$, $\gamma <<1$, we use Eq. (6) similar to the case of JJ [14,15] (see also [13])

$$\frac{\delta q}{e} = \frac{2\pi\alpha}{\omega_B}\exp\left(-\frac{\kappa}{2\gamma}\right) \quad . \quad . \tag{8}$$

In last expression Bloch frequency denoted as $\omega_B = \frac{1}{\sqrt{L_B C_B}}$, with Bloch inductance $l_B(q) \approx (1 + \frac{1}{\sqrt{2\kappa}})$ from study [10] and as a result $\omega_B = \frac{\omega_J}{(1+\frac{1}{\sqrt{2\kappa}})}$.

Using Eq. (6-7) in the limit of high growing rate of voltage across JJ($\alpha >> \gamma$, $\gamma <<1$) for the high Bloch inductance $l_B >> 1$ leads to

$$\frac{\delta q}{e} = 1.42\sqrt{\gamma}\,\frac{\pi\alpha^{4/3}}{l_B\kappa^{4/3}} \quad . \tag{9}$$

In the opposite case of low Bloch inductance $l_B << 1$ is true

$$\frac{\delta q}{e} = 2.35\sqrt{\gamma}\,\frac{\alpha^{5/6}}{\kappa^{1/3}} \quad . \tag{10}$$

4. Conclusions

Thus, in this paper the influence thermal fluctuations on dynamics of JJs with a Coulomb blockade was investigated. Bloch oscillations in small Josephson junctions were taken into account including the corresponding inductance to equation. It was shown that the dynamics is determined by the energy ratio parameter of JJ, temperature and growing rate of external voltage on junction. Obtained results will be useful in realization of small size JJ.

Authors thanks Prof. A.Bozbey, N.Kartlı, H.B.Yıldırım for useful discussions. Presented work partially supported by TUBITAK research grant 118F093.

References

1. Likharev K.K., Zorin A.B., Journal of Low Temperature Physics. 59,347(1985).
2. Averin D.V., Zorin A.B., Likharev K.K., JETP, 1985. 88, 692(1985).
3. Kuzmin L.S., Haviland D.B.,.PhysicalReview Letters.1991. 67,2890(1991).
4. Zorin A.B., Physical Review Letters. 96, 167001(2006).
5. Askerzade I., Bozbey A., Canturk M., Modern aspects of Josephson Dynamics and Superconductivity Electronics, Springer ,2017,210 p
6. Likharev, K.K., Introduction into Dynamics of Josephson's Junctions, Moscow: Nauka,1985,586 p.
7. Askerzade, I.N.,. Technical Physics. 45,66(2000).
8. Askerzade, I.N., Kornev V.K. Radiotekhnika i Elektronika, 39,869(1994).
9. Askerzade I.N. Technical Physics. 61,1427(2016).
10. Askerzade I.N., Aut. Cont. Comp. Sci. 50,10(2016).
11. Kramers H.A. Physica. 7,284(1940).
12. Ambegaokar V. , Halperin B.I. , Phys Rev. Lett.22,1364(1969).
13. Askerzade I.N., Low Temp. Phys.44,210(2018.
14. Askerzade I.N. Turkish Journal of Physics. 22, 811(1998).
15. Askerzade I.N. , Technical Physics.1998. 43,1123(1998).

***Corresponding author**: raskerbeyli@karabuk.edu.tr

MAGNETIC MOMENT OF THE LATTICE OF NON-INTERACTING DILUTED MAGNETIC SEMICONDUCTOR QUANTUM RING

A.M.BABANLI[1], B.G.IBRAGIMOV[2]
[1]*Department of Physics, University of Suleyman Demirel,32260,Isparta,Turkey*
[2]Azerbaijan National Academy of Sciences, Institute of Physics, Baku, Azerbaijan

In the present work, we investigate the magnetic properties of the non- interacting diluted magnetic semiconductor (DMS) quantum ring lattices by using the 2D rotator model. We take into account the effect of the exchange interaction and the Zeeman term on the magnetic moment. For this purpose, we derive the exact analytic expression for the single-particle partition function und used it to determine the magnetic moment. We show that the positions of compensation points (points at which the magnetization vanishes at fixed values of the magnetic field strength) in the temperature scale are very sensitive to changes in the Mn concentrations

Keywords:diluted magnetic semiconductor, quantum ring, partition function
PACS:75.75.-C;75.50.Pp

1. Introduction

The semiconductor quantum ring has been extensively studied from both theoretical and experimental point of view [1]. These quantum systems have many applications such as single electron and photon devices, spintronics. Important class of materials for spintronics forms diluted magnetic semiconductors (DMS). They are A_2B_6 or A_3B_5 solutions with high density of magnetic impurities (usually, Mn). The presence of magnetic ions in such heterostructures additionally allows one to explore new spin-dependent phenomena at lower dimensionalities. The presence of localized magnetic ions in DMSs leads to an exchange interaction between the sp band electrons and the d electrons associated with Mn, resulting in extremely large Zeeman splitting of electronic levels [2,3].

The authors of Ref [4] investigated the magnetic properties of the lattice of non-interacting quantum rings by using the 2D rotator model without including the spin contribution. It was shown that such a system could be considered as a system with antiferromagnetic-like properties. The purpose of this work is to study the effect of exchange and Zeeman interactions on the magnetic moment of non-interacting quantum ring systems prepared from a diluted magnetic semiconductor. The quantum ring is subjected to a uniform magnetic field along the z-direction. The total Hamiltonian of the system is given by:

$$H = \frac{1}{2m_n}(\vec{p} + e\vec{A})^2 + \frac{1}{2} g\sigma_z \mu_B H + H_{ex} \tag{1}$$

where m_n is the effective mass of electrons, $\mu_B = \frac{e\hbar}{2m_0}$ is the Bohr magneton, m_0 is the free electron mass and $\vec{A}$ is the vector potential. In the mean field approximation the exchange Hamiltonian term can be written as [4]:

$$H_{ex} = \frac{1}{2} < S_z > N_0 x J_{s-d} \sigma_z = 3A\sigma_z \tag{2}$$

where J_{s-d} is a constant which describes the exchange interaction, N_0 is the density of the unit cells. The thermodynamic average $< S_z >$ of the z component of the localized Mn spin is determined by the expression

$$< S_z > = -S_0 B_{5/2}\left(\frac{S g_{Mn} \mu_B H}{k_B T}\right) \tag{3}$$

where $B_{5/2}\left(\frac{S g_{Mn} \mu_B H}{k_B T}\right)$ is the Brillouin functions, $\boldsymbol{g_{Mn}}$=2 is the g factor of Mn ions, S=5/2 and k_B is the Boltzmann constant. For uniform magnetic field, the vector potentials in cylindrical coordinates have the components $A_\phi = \frac{Hr}{2}, A_r = 0$ and Schrüdinger equation in polar coordinates is

$$\left(-\frac{\hbar^2}{2m_n r^2}\frac{\partial^2}{\partial\varphi^2} + \frac{ieH}{2m_n}\frac{\partial}{\partial\varphi} + \frac{e^2H^2}{8m_n}r^2 + 3A\sigma_z + \frac{1}{2}g\sigma_z\mu_B H\right)\Psi(r,\varphi) = E\psi(r,\varphi) \tag{4}$$

The solution of Eq. (4) has the form:

$$\Psi(r,\phi) = \frac{1}{\sqrt{2\pi}} R(r) e^{il\phi} \tag{5}$$

$$E_{l,\sigma} = \varepsilon(l-\xi)^2 + \frac{\sigma\mu_B H}{2} g^*,\ l = 0, \pm1, \pm2, \ldots \tag{6}$$

where

$$g^* = g + \frac{6A}{\mu_B H}, \varepsilon = \frac{\hbar^2}{2m_n r^2} \tag{7}$$

For finding the magnetization of the electrons DMS rings it is necessary to obtain the free energy of the electron gas in the nano ring. The free energy can be determined from the classical partition function Z. Given the non-degenerate energy spectrum, we can define it by a sum over all possible states of the system

$$Z = \sum_{l,\sigma} e^{-\beta E_{l,\sigma}} \tag{8}$$

where $\beta = \frac{1}{k_B T}$ and T is the thermodynamic equilibrium temperature. After substitution the Eq. (6) into the partition function definition, and after making similar calculations to those in Ref. [4], we get:

$$Z = \sqrt{\pi\chi} v_3\left(-\xi\pi, e^{-\pi^2\chi}\right) 2\cosh\left(\frac{g^*\mu_B H}{2\varepsilon\chi}\right) \tag{9}$$

where $v_3\left(-\xi\pi, e^{-\pi^2\chi}\right)$ is the theta function and $\chi = (\beta\varepsilon)^{-1}$. Now, we can calculate the free energy of the DMS ring. As well known:

$$F = -k_B T \ln Z = -\chi\varepsilon \ln\left(\sqrt{\pi\chi}v_3\left(-\xi\pi, e^{-\pi^2\chi}\right)2\cosh\left(\frac{g^*\mu_B H}{2\varepsilon\chi}\right)\right) \tag{10}$$

To calculate the magnetization of the electron gas, we use the expression of the free energy of the ring:

$$M = -\frac{\partial F}{\partial H} = -\frac{\partial F}{\partial \xi}\frac{\partial \xi}{\partial H} = -\frac{\mu_B^*}{2\varepsilon}\frac{\partial F}{\partial \xi} \tag{11}$$

$\mu_B^* = \dfrac{e\hbar}{2m_n}$ is the effective Bohr magneton. Using Eq. (11) and the Logarithmic derivative of theta-function [6] we get :

$$M = \mu_B^*\chi\left(\pi\sum_{j=1}^{\infty}(-1)j\frac{\sin(2j\pi\xi)}{\sinh(j\pi^2\chi)} + \frac{1}{2}Tanh\left(\frac{g^*\mu_B H}{2\varepsilon\chi}\right)\frac{\partial}{\partial\xi}\left(\frac{g^*\mu_B H}{2\varepsilon\chi}\right)\right) \tag{12}$$

3. Results and discussion

The numerical values of the magnetization as a function of the AB flux are presented in Fig. 1. As can be seen from Figure 1 the magnetization for free electron model system varies over range of negative and positive values with changing of the AB flux at fixed temperature. Also, as it can be seen the value of magnetization is equal to zero, when $\xi = l$, where l is integer or half-integer. These points are called as the "Aharonov-Bohm compensation points" at which the magnetization vanishes at fixed temperature, while magnetic flux varies. In our case of diluted magnetic semiconductor the magnetization is not equal to zero when ξ takes integer or half integer. This result is different than the one obtained in Ref. [4]. In the case DMSs the magnetization for Mn concentration $x = 0.0013$ varies from positive to negative values with changing of the AB flux at fixed temperature. As well known, such a behavior is typical for the paramagnetic systems.

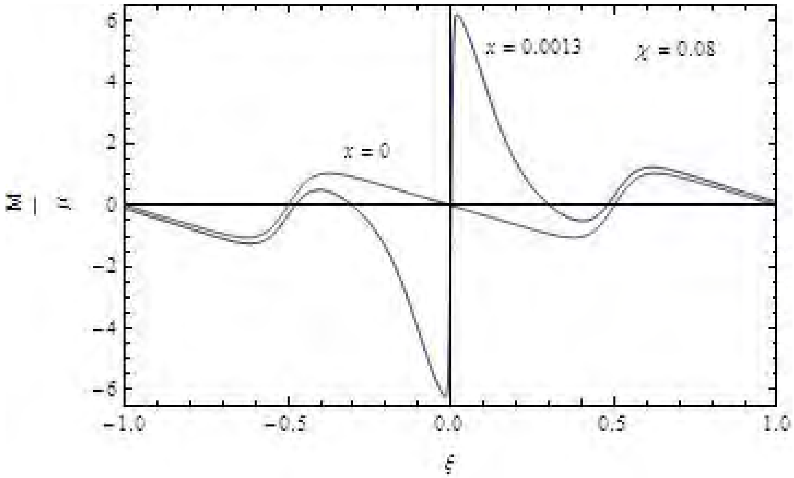

Fig.1. Dependence of the magnetization in terms of μ_B^* on the magnetic flux for the cases where Mn concentrations x=0, g=0, and x=0.0013, g=-1.67 for $\chi = 0.008$.

The manganese concentrations is increased in the solid solutions $Cd_{1-x}Mn_xTe$ the nature of the exchange interaction between the localized angular moments must change, and this will lead to a change in the magnetization of DMS. Results of the calculations showed that in DMS as the content of manganese is increased a continuous transition is observed from the antiferromagnetism phase to the paramagnetism phase. In our calculation we consider the parameter corresponding to $Cd_{1-x}Mn_xTe$ materials: m_n=0.096m_0, where m_0 is the free electron mass, and ge =-1.67, $N_0 j_{s-d} = 0.22eV, \frac{N_0 j_{s-d}}{\varepsilon} = 1385, R = 50nm$ are taken from [3].

4. Conclusion

We have studied theoretically the electronic spectra and magnetic properties of diluted magnetic semiconductor quantum ring in the presence of externally applied static magnetic field. We have shown that in DMSs the magnetization has opposite behavior in some regions of ξ to that one where x= 0. The dependence of the magnetization DMS nano ring on the magnetic flux has an oscillation character. It was shown that when Mn concentration is increased compensation points decreases. It was showed that in DMS as the content of manganese is increased a continuous transition is observed from the antiferromagnetism phase to the paramagnetism phase.

References

1. WolfS.A, et al., Spintronics: A Spin-Based Electronics Vision for the Future Science 294, (2001).
2. WolffP.A., Semiconductors and Semimetals, in: J.K. Furdyna, J. Kossut (Eds.), Diluted Magnetic Semiconductors, Academic, New York, 1988.
3. JacekKossut, Jan A. Gaj Editors Introduction to the Physics of Diluted Magnetic Semiconductors, Springer Series in Material Science 144, (2010).
4. Peter A. Meleshenko, Alexander F. Klinskikh, Journal of Magnetism and Magnetic Materials, 323, 2663 (2011).

[1]**Corresponding author**: arifbabanli@sdu.edu.tr

EFFECT OF ENERGY SPECTRUM NONPARABOLICITY ON ENTROPY OF A COMPLEX SHAPED QUANTUM WELL

S.R. FIGAROVA, M.M. MAHMUDOV *

Baku State University, Z.Khalilov str., 23, Baku, Azerbaijan, AZ1148

In this paper, entropy of a two-dimensional electron gas as a function of the complex shaped quantum well parameters and band gap are studied. We usethe Kane model in a two-band approximation. It has been shown that an increase in the quantum well depth leads to the strong localization of conduction electrons and hence to decrease in entropy. Entropy of two-dimensional electron gas drops with the band gap increasing.

Keywords: quantum well, complex potential profile, entropy, nonparabolicity
PACS: 65.40.Gr; 68.65.Fg; 73.21.Fg; 73.63.Hs

1. Introduction

In nanotechnology low-dimensional semiconductor structures (superlattices, MOS - structures, and also thin films with the thickness of the de Broglie wavelength order) are used. In these structures size-quantized phenomena that substantially depend on the quantum well potential [1-3] occur. At present, epitaxial growth techniques allows one to fabricate quantum wells with arbitrary potential profiles. Mainly, a two dimensional electron gas in rectangular and parabolic quantum wells in magnetic and electrical fields are investigated. However, conduction band nonparabolicity and quantum well complex potential profiles also essentially influence two dimensional electron gas properties, since heterostructures, as a rule, consist of different band gap semiconductor layers with the nonparabolic dispersion law [4]. Conduction band nonparabolicity alters the two dimensional electron gas density of states and hence its thermodynamics properties (eg entropy [5], magnetization [6]. etc).

Taking into consideration the energy spectrum nonparabolicity of a two-dimensional electron gas leads to a density of states with linear dependence on energy (unlike the parabolic spectrum), the fact that affects the thermodynamic and transport characteristics. In this paper, entropy of a two-dimensional electron gas as a function of the complex shaped quantum well parameters and band gap is studied. The dispersion law is described by the Kane model in a two-band approximation. The degenerate electron gas is considered. It is shown that entropy is proportional to the density of states and is a step function of the Fermi energy.

2. Entropy of complex shaped quantum well taking into account the nonparabolicity of the dispersion law

Solving the Schrüdinger equation in the effective mass approximation for the two-dimensional electron gas in the complex shaped quantum well with allowance made for the band nonparabolicity gives:

$$\varepsilon(1+\alpha\varepsilon)=\frac{\hbar^2 k_\perp^2}{2m}+\varepsilon_n\,, \tag{1}$$

where $\alpha = 1/\varepsilon_g$ is nonparabolicity parameter, ε_g is the width of the band gap, $k_\perp^2 = k_x^2 + k_y^2$, m is the electron effective mass and ε_n acquires the form:

$$\varepsilon_n = \varepsilon_0\left(1+2n+\sqrt{1+\frac{U_0}{\varepsilon_0}}\right)^2, \tag{2}$$

here $\varepsilon_0 = \hbar^2\pi^2 / 2ma^2$ at $n = 0$ and $U_0 = 0$, a is the quantum well width, U_0 is the potential energy minimum, $n = 0,1,2,...$ is the quantum number. Models of rectangular potential quantum well and parabolic quantum well are particular cases of energy spectrum (2). Energy spectrum nonparabolicity in (1) is described by the Kane model in a two-band approximation [7].

The transcendental equation for quantum energy level number for quantum well (2) has the form:

$$\frac{2\varepsilon - U_0}{2\sqrt{\varepsilon(U_0 - \varepsilon)}} = ctg\,\frac{a\sqrt{2m\varepsilon}}{\hbar}. \tag{3}$$

As seen, in symmetrical quantum wells with the finite depth, there are bound states (when particles are captured by the quantum well), the number of which increases with the quantum well depth.

For energy spectrum (2), the density of states of a two-dimensional electron gas is:

$$g(\varepsilon) = \frac{m}{\pi\hbar^2}\sum_n \Theta(\varepsilon - \varepsilon_n)(1 + 2\alpha\bar{\varepsilon}_n), \tag{4}$$

where $\Theta(\varepsilon - \varepsilon_n)$ is the Heaviside function, $\bar{\varepsilon}_n$ is determined from the equation

$$\varepsilon\left(1 + \frac{\varepsilon}{\varepsilon_g}\right) = \varepsilon_n,$$

and has the shape:

$$2\alpha\bar{\varepsilon}_n = -1 + \sqrt{1 + 4\alpha\varepsilon_n}.$$

Based on the grand thermodynamic potential:

$$\Omega(T,V,\zeta) = -k_0T \cdot \sum_{n,k_x}\int_{\bar{\varepsilon}_n}^{\infty}\left(1 + 2\alpha\varepsilon(n,k_x,k_y)\right)\ln\left(1 + \frac{\zeta - \varepsilon(n,k_x,k_y)}{k_0T}\right), \tag{5}$$

here ζ is the chemical potential, we calculate the general expression for entropy. Taking into account that

$$\sum_{k_x,k_y}(...) \Rightarrow \frac{S}{2\pi^2}\int(...)\,dk_x dk_y,$$

(S is the area in the xy- plane) in (5) and passing from summation with respect to the wave vector to integration with respect to energy, we have:

$$\Omega(T,V,\zeta) = -\frac{Vm}{\pi\hbar^2}\sum_n \Theta(\varepsilon - \varepsilon_n)\int_{\varepsilon_n}^{\infty}(\varepsilon - \varepsilon_n)\left(1 + 2\alpha\varepsilon\right)f(\varepsilon)\,d\varepsilon, \tag{6}$$

where $f(\varepsilon)=\left[1+\exp(\varepsilon-\zeta)/k_0T\right]^{-1}$ is the Fermi-Dirac distribution function. Formula (6) is just for any degree of electron gas degeneracy and arbitrary quantum well energy profile.

By formulae $n_{el}=-\frac{1}{V}\left|\left(\frac{\partial\Omega}{\partial\zeta}\right)_{T,V}\right.$,and $S=-\left(\frac{\partial\Omega}{\partial T}\right)_{V,\zeta}$,

one gets:

$$n_{el}=\frac{m}{\pi\hbar^2}\sum_n\int_{\bar{\varepsilon}_n}^{\infty}(1+2\alpha\varepsilon)\left[1+\exp\left(\frac{\zeta-\varepsilon}{\kappa_0T}\right)\right]^{-1}d\varepsilon\,, \tag{7}$$

$$\begin{gathered}S=k_0\frac{m}{\pi\hbar^2}\sum_n\left\{\int_{\bar{\varepsilon}_n}^{\infty}\ln\left[1+\exp\left(\frac{\zeta-\varepsilon}{\kappa_0T}\right)\right]\left[1+2\varepsilon\left(\alpha+T\frac{\partial\alpha}{\partial T}\right)\right]d\varepsilon+\right.\\ \left.+\int_{\bar{\varepsilon}_n}^{\infty}(1+2\alpha\varepsilon)\left[1+\exp\left(\frac{\zeta-\varepsilon}{\kappa_0T}\right)\right]^{-1}\left[\frac{\partial\zeta}{\partial T}-\frac{\zeta-\varepsilon}{\kappa_0T}\right]d\varepsilon\right\}.\end{gathered} \tag{8}$$

In figs.1-2 entropy of a two-dimensional electron gas as a function of the quantum well parameters (fig. 1) and the Fermi energy (fig. 2) are depicted withthefollowingdata: $m=0.067m_0$, $\varepsilon_0=60\,meV$, $a=10\,nm$, $\varepsilon_g=0{,}42\,eV$, $T=100\,K$.

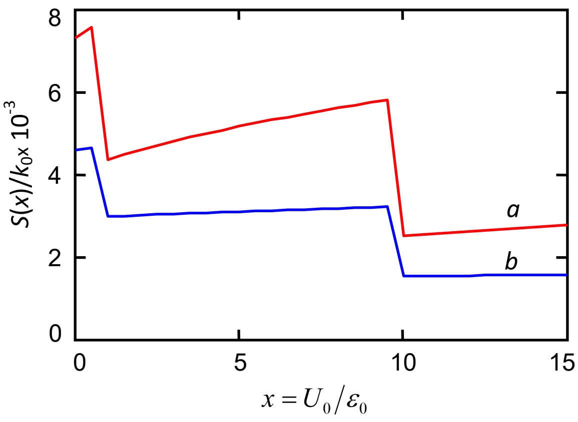

Fig.1. Entropy of degenerate two-dimensional electron gas vs. the quantum well parameter,

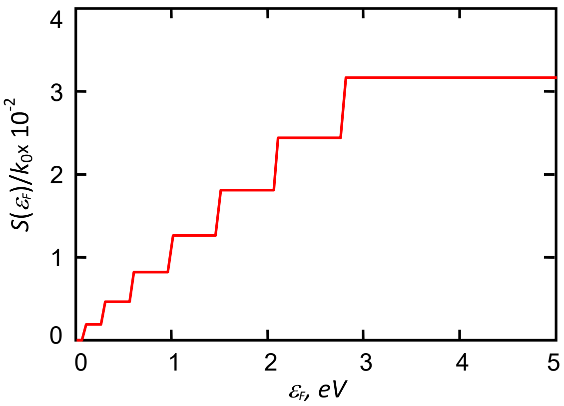

Fig.2. Entropy of degenerate two-dimensional electron gas vs. the Fermi

From fig. 1 it follows that entropy essentially depends on quantum well parameters U_0, a. The level number in a quantum well is governed by the quantum well potential.

As U_0/ε_0 increases, the level number increases, which results to reduction in electron motion disorder and hence in entropy. As well as for the parabolic band, entropy dependence on the Fermi level is step-like but between the jumps this dependence is linear (fig. 2).

For the parabolic band formula (8) coincides with one given in [8], and for an essentially nonparabolic band entropy is:

$$S=\frac{2\pi^2}{3}k_0^2T\frac{m}{\pi\hbar^2}\sqrt{\frac{\varepsilon_0}{\varepsilon_g}}\left(2+2n+\frac{U_0}{2\varepsilon_0}\right)\text{at}\,U_0/\varepsilon_o<1 \tag{9}$$

$$S=\frac{2\pi^2}{3}k_0^2T\frac{m}{\pi\hbar^2}\sqrt{\frac{\varepsilon_0}{\varepsilon_g}}\left(2n+\frac{U_0}{2\varepsilon_0}\right)\text{at}\,U_0/\varepsilon_o>1 \tag{10}$$

From these expressions it stems that entropy of a two-dimensional electron gas drops with the band gap increasing. The entropy is inversely proportional to the square root of the band gap width.

3. Conclusions

We consider band nonparabolicity influence on entropy of a degenerate two-dimensional electron gas in complex shaped quantum well. We have revealed that the band nonparabolicity leads to an entropy decrease, as the band gap grows. The entropy dependence on the quantum well parameters are found. It has been shown that for the certain relation between the quantum well levels and the Fermi level, this dependence is nonmonotonous. As the quantum well depth increases, the quantum level number increases, which leads to the strong localization of conduction electrons and hence to a decrease in entropy, therewith electrons are found in bound states and their ordering grows. Taking into account the energy spectrum nonparabolicity gives a significant increase in the entropy compared with the parabolic energy band (since the density of states increases with energy).

References

1. Vagner D., HIT Journal of Science and Engineering A, **3**, 102 (2006).
2. Zawadzki W., Springer 98 Series in Solid-State Sciences. **53**, 79 (1984).
3. Weiss D., Zhang C., Gerhardts R.R., Klitzing K.V., Phys. Rev. B, 39,39 (1989).
4. Guliyev B.I., Eminbeyli R.F., Physica B: Condensed Matter, 403, 1751(2008).
5. Askerov B.M., Figarova S.R., Mahmudov M.M., Figarov V.R.,Japanese Journal of Applied Physics, **50**, 05FE10 (3p.), (2011).
6. Askerov B.M., Figarova S.R., Makhmudov M.M., Figarov V.R., Proceedings of the Royal Society A: Mathematical, Physical and Engineering Sciences, **464**, 3213 (2008).
7. Askerov B.M., Figarova S.R., Springer-Verlag, Berlin, Heidelberg, 2010. 374 p.
8. Figarova S.R., Khasıyeva G.N., Figarov V.R., Physica E, **69**, 24 (2015).

***Corresponding author**: mmm@bsu.edu.az

BACKWARD SECOND HARMONIC WAVE IN REGULAR DOMAIN STRUCTURES

R.J.KASUMOVA, N.V.KERIMLI*, G.A.SAFAROVA, A.R.AHMADOVA

Physics Department, Baku State University, acad. Z. Khalilov str.23,AZ 1148, Baku, Azerbaijan
Azerbaijan Medical University, Enver Kasumzade,str.14, AZ 1022, Baku, Azerbaijan

Complex amplitude of backward second harmonic wave has been theoretically studied by sequential generation of second and third harmonics within regular domain structures (RDS) with quadratic nonlinearity. It has been found analytical expression for efficiency of second harmonic generation by approach of constant intensity approximation. Diagrammatically has been analyzed conversion efficiency of frequency into the second and third harmonics by various analytical approximations. During counter wave interaction intensity of backward second harmonic swings up at low intensity of entered second harmonic wave. Moreover reducing the ratio of nonlinear coefficients like β_3/β_2 provides increasing of conversion efficiency of frequency into second harmonic, but efficiency of transferring of frequency into third harmonic will be decreased. Observed behavior of nonlinear interaction has been explained by rivalling process between second and third harmonic waves.

Keywords: constant intensity approximation, regular domain structures, quasi-phase matched.
PACS:42.65.Ky; 42.70.MP; 42.62-b

1. Introduction

Commonly it is important to utilize crystals with high components of nonlinear tensors due to obtaining of efficient parametrical processes. However in tradition phase matched interaction process for instant: it is impossible to use interaction of waves which closely associated with nonlinear coefficient of d_{33} in the interior of the $LiNbO_3$. On the other hand due to given quasi-phase-matched interaction scheme [1-8] it is possible to obtain optical parametrical process in counter wave interaction that was impossible in tradition phase-matched systems.

Sequence (consecutive) quasi matched interaction of waves had been analyzed by two different approaches [9-12] by constant intensity approximation and by accurate machine calculations. It was determined that analytical approach of solving problem is preferable to numerically exact calculations. As an added it allows to pursue dynamics (impact of various unique properties of media and waves on interaction process) and due to given methods the crucial parameters of nonlinear interaction can be taken into account as well. According to approximation methods avenue for boosting of efficiency of frequency conversion process can also be predicted. In apparently presented work process doubling of frequency has been done by constant intensity approximation that is more tolerant and correct than constant field approximation.

Various nonlinear interaction of waves such as second harmonic creation, conversion of frequency into third harmonic, producing of summarized frequency within regular domain structure crystals [13-19] due to parametrical transferring and in the interior resonator interaction processes. All operations have been done by us at constant intensity approximation [20-21]. The sequence (consecutive) quasi synchronized interaction of code directed waves in RDS crystal that leads simultaneously producing of second and third harmonics (when both do have a common pump wave) have been described by us as well.

In presented article it has been studied sequence (consecutive) quasi synchronized interaction of counter waves in RDS crystal by constant intensity approximation which has great future prospects in applications. The impressive achievement is closely associated with simultaneously conversion processes of frequency into the second and third harmonics at common pump wave circumstance.

2. Theory

Two nonlinear process that lead to second and third harmonics like $\omega+\omega\rightarrow 2\omega$ and $\omega+2\omega\rightarrow 3\omega$ are being studied by us. Given processes will be analyzed within RDS crystal with quadratic nonlinearity. Due to definiteness we consider that the second harmonic wave propagates toward the other two waves in counter direction. Geometry of interaction is shown in figure of 1. Intrinsic frequency of ω and third harmonic wave are entered from left side into the RDS structure along the positive z direction at $z=0$. From the left side second harmonic generation is incident onto crystal along the negative z direction at

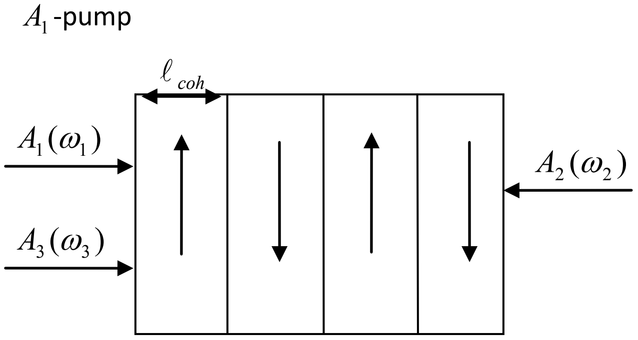

$$\omega_3=\omega_1+\omega_2$$

Fig. 1.Geometry of three counter wave interaction.

Corresponding boundary conditions are the following

$$A_{1,3}(z=0)=A_{10,30}\cdot\exp(i\varphi_{10,30}),\quad A_2(z=l)=A_{2l}\cdot\exp(i\varphi_{2l})\,. \tag{1}$$

There are three co-directed waves in entrance of the RDS crystal, where A_1 is the complex amplitude of pumping wave, A_2, A_3 are complex amplitude of interacted waves at frequencies of $2\omega,\ 3\omega$. $A_{10,30}$, $\varphi_{10,30}$ are the initial amplitudes and phases of the waves when entering the nonlinear medium to the left, A_{2l}, φ_{2l} are the initial amplitude and phase of the wave at the doubled frequency.

System of shorten differential equations at given condition is distributed as [22]

$$\begin{aligned}
&\frac{dA_1}{dz}+\delta_1A_1=-i\beta_3g_3^*A_3A_2^*-i\beta_2g_2^*A_2A_1^*,\\
&\frac{dA_2}{dz}-\delta_2A_2=+i2\beta_3g_3^*A_3A_1^*+i\beta_2g_2A_1^2,\\
&\frac{dA_3}{dz}+\delta_3A_3=-i3\beta_3g_3A_1A_2,
\end{aligned} \tag{2}$$

δ_j are the absorptionall coefficients at relevant frequencies,

$$\beta_2=\frac{2\pi\omega_2}{cn_2}\left|\chi^{(2)}\right| \text{ and } \beta_3=\frac{2\pi\omega_3}{cn_3}\left|\chi^{(2)}\right|$$

are coefficients of nonlinear interaction of waves in generation of second and third harmonics within quadratic media, correspondingly, n_2 and n_3 are indices of refraction at frequencies of ω_2 and ω_3, $\chi^{(2)}$ is susceptibility of the domain material with second order. $g_{2,3}(z)$ periodical functions that provides modulation of quadratic susceptibility along the interaction distance z with period of $\Lambda=2l$, $|g(z)|=1$ and takes series values of $+1,-1,+1,\ldots\ldots$ at boundary of layer with thickness of l. Similar RDS crystal was analyzed by us at constant intensity approximation [15-21].

Generally system of abbreviate equations (2) were solved only numerically.

Solution of (2) by constant intensity approximation gives us second order of differential equation A_2

$$\frac{d^2 A_2}{dz^2} - 6\beta_3^2 |g_3|^2 I_{10} A_2 = 0 .$$

Complex amplitude A_2^{CFA} is estimated by

$$A_2^{CFA}(z) = \frac{A_{2l}}{\cosh \lambda l} \cosh \lambda z - \frac{i}{\lambda}\left[2 g_3^* \beta_3 A_{30} A_{10} e^{i(\varphi_{30} - \varphi_{10})} + g_2 \beta_2 A_{10}^2 e^{i2\varphi_{10}}\right] \times \left(\tanh \lambda l \cdot \cosh \lambda z - \sinh \lambda z\right), \quad (3)$$

where

$\lambda^{CFA} = \sqrt{6} \cdot |g_3| \Gamma_{13}$.

Solution of (2) with spectrum of complex amplitude by constant intensity approximation gives us complex amplitude of A_2 second harmonic

$$\frac{d^2 A_2}{dz^2} + (2\delta_1 - \delta_2)\frac{dA_2}{dz} - 2\left[\beta_3^2 |g_3|^2 (3I_{10} - I_{30}) + \beta_2^2 |g_2|^2 I_{10} + \delta_1 \delta_2\right] A_2 = 0 \quad (4)$$

Complex amplitude of second harmonic $A_2^{CIA}(z)$ is determined by solution of (4) at boundary conditions of (1) $\delta_j = 0$)

$$A_2^{CIA}(z) = \frac{A_{2l}\, e^{i\varphi_{2l}}}{\cosh \lambda^{CIA} l} \cosh \lambda^{CIA} z - \frac{i}{\lambda^{CIA}}\left[2 g_3^* \beta_3 A_{30} A_{10} e^{i(\varphi_{30} - \varphi_{10})} + g_2 \beta_2 A_{10}^2 e^{i2\varphi_{10}}\right] \times \left(\tanh \lambda^{CIA} l \cdot \cosh \lambda^{CIA} z - \sinh \lambda^{CIA} z\right), \quad (5)$$

where

$\lambda^{CIA} = \sqrt{2\left[|g_3|^2 \left(3\Gamma_{13}^2 - \Gamma_3^2\right) + |g_2|^2 \Gamma_{12}^2\right]}$, $\Gamma_{12} = \beta_2 \sqrt{I_{10}}$, $\Gamma_{13} = \beta_3 \sqrt{I_{10}}$, $\Gamma_3 = \beta_3 \sqrt{I_{30}}$.

Complex amplitude of third harmonic is estimated by solution of (2) constant amplitude approximation with substitution of (3) in (2)

$$A_3^{CFA}(z) = -3\beta_3 |g_3| \frac{A_{10}^2}{\lambda^{CFA}} \left[\frac{C}{\lambda^{CFA}}\left(\tanh \lambda^{CFA} l \cdot \sinh \lambda^{CFA} z - \cosh \lambda^{CFA} z + 1\right) + i \frac{A_{2l}}{A_{10}} \cdot \frac{\sinh \lambda^{CFA} z}{\cosh \lambda^{CFA} l}\right] \quad (6)$$

Efficiencies of conversion processes in to second and third harmonics can be found from (5) and (6) due to expressions of $\eta_2 = I_2(z)/I_{10}$ and $\eta_3 = I_3(z)/I_{10}$, where $I_2(z) = A_2 \cdot A_2^*$ and $I_3(z) = A_3 \cdot A_3^*$

For calculations of periodic modulation Λ have been used next relations: for second harmonic generation

$$\Lambda_2 = \pi M_2 / \sqrt{2\Gamma^2 + (k_2 + 2k_1)^2 / 4}$$

and for third harmonic generation

$$\Lambda_3 = \pi M_3 / \sqrt{2\Gamma^2 + (k_3 + k_2 - k_1)^2 / 4} .$$

3. Discussion and Results

Efficiencies of $\eta_2 = I_2(z)/I_{10}$ and $\eta_3 = I_3(z)/I_{10}$ that are calculated with (5) and (6), relevant to $\Gamma_{12} z$ for $M_2 = 1$; $M_3 = 3$ at different relations of nonlinear coefficients of $\beta_{2,3}$, are determined at constant field approximation (dotted for second harmonic and dashed for third harmonic curves) and constant intensity approximation (solid curves) are presented by figure of 2.

During counter wave interaction process the intensity of second harmonic increases at lower entrance intensity I_{2l} (solid and dotted curves 1). It is able to be explained by rivaling process between second and third harmonics. It is familiar that the both harmonics are provided by pumping wave when the third harmonic wave additionally can gain power (energy) from second harmonic wave.

In the absence of initial signal of second and third harmonics as result of propagation of pumping wave of RDS crystal, previously it is generated second harmonic, after that in cause of summation of frequencies it is obtained the triplet (increasing as three times) of pumping wave (curve of 2 and 3). With reducing of β_3/β_2 efficiency of conversion of second harmonic increases but η_3 is diminished. Here, for comparison, the results of calculations are given in the constant field approximation.

Observed reducing of efficiency η_2 at constant intensity approximation is related to changing of complex amplitude of pump wave that depends on the phase shift. While in the constant field approximation, the amplitude of the pump wave is taken constant, i.e. the following condition $A_1(z)=A_{10}=const.$ is fulfilled, from which it follows $\varphi_1(z)=\varphi_{10}=const.$ (compare dotted and solid curves).

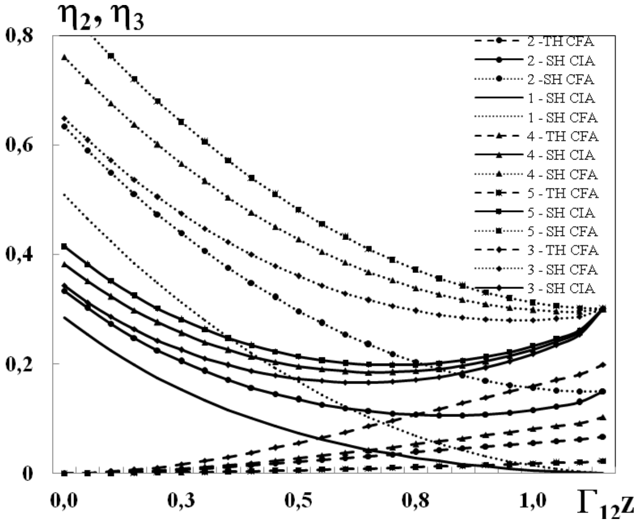

Fig. 2. Dependences of the conversion efficiency $\eta_2 = I_2(z)/I_{10}$ and $\eta_3 = I_3(z)/I_{10}$ on the parameter $\Gamma_{12}z$ for $M_2 = M_3 = 1$ and $I_{30} = 0.001$ at the different I_{2l}: 0.001 (curves 1), 0.15 (curves 2) and 0.3 (curves 3-5); β_3/β_2: 0.3 (curves 5), 0.67 (curves 1, 2 and 4) and 1 (curves 3). All the curves are calculated in the constant-field approximation and the constant-intensity approximation.

4. Conclusions

Thus, work theoretically had been analyzed creation of optical harmonics in the RDS crystal with single periodical polarization. All calculations are based on constant intensity approximation. It has been shown that during counter wave interaction the intensity of second harmonic speeds up at lower intensity of entrance second harmonic wave. Moreover, with decreasing of nonlinear coefficients like β_3/β_2 efficiency of transferring of frequency into the second harmonic will be correspondingly increased, but efficiency of third harmonic generation will be otherwise decreased. Presented approach will be applied for multiple wave parametrical quasi –phase matched interaction of optical waves.

References

1. BlombergenN., BenjaminW.A., Nonlinear Optics, New York 1965.
2. FejerM.M., MagelG.A., JundtD.H., ByerR.L., IEEE J. Quant. Electron. 28, 2631(1992).
3. PaulA., R.A. Bartels, R. Tobey, et al., Lett. Nature 421, 51 (2002).
4. ChirkinA.S., VolkovV.V., LaptevG.D., and MorozovE.Yu., Quant. Electron. (in Russian) 30, 847 (2000).
5. Lee D.and MoultonP.F., Proceedings of the Conference on Lasers and Electro-Optics, OSA Trends on Optics and Photonics Series 56,42(2001).
6. ChirkinA.S., VolkovV.V., Izv. Akad. Nauk SSSR (in Russian) 62,2354(1998).
7. F. Brunner, E. Innerhofer, S. V. Marchese, et al., Opt. Lett., 29,1921 (2004).
8. PfisterO.,. WellsJ.S, L. Hollberg, ZinkL., Van BaakD.A., LevensonM.D., BozenbergW.R., Opt. Lett. 22,1211 (1977).
9. VolkovV.V., LaptevG.D.,.MorozovE.Yu, NaumovaI.I., ChirkinA.S., Quantum Electron., 28,11,1020(1998).
10. Luo,G.Z. ZhuS.N., HeJ.L., ZhuY.Y., WangH.T., LiuZ.W., ZhangC., MingN.B.,Appl. Phys. Lett. 78, 3006(2001).
11. MorozovE.Yu., LaptevG.D., Izves. AN SSSR (in Russian), 66, 8, 1108 (2002).
12. ChirkinA.S.,VolkovV.V.,LaptevG.D.,MorozovE.Yu.,Quant. Electron.(in Russsian)30,847 (2000).
13. TagievZ.H., KasumovaR.J., Optics & Communications, 281, 814 (2008).
14. TagievZ.H, KasumovaR.J., SafarovaG.A., Journal of Russian Laser Research 31,4,319 (2010).
15. KasumovaR.J., SafarovaG.A., J. of Appl. Spectroscopy, 79 ,6,874(2012).
16. ReintjesJ.F., Academic Press, New-York (1984) 478 p.
17. KasumovaR.J., KarimiA.A..J. of Appl. Spectroscopy77,1,144(2010) .
18. KasumovaR.J., J. of Appl. Spectroscopy78,5,659(2011).
19. KasumovaR.J., KarimiA.A., Optics and Spectroscopy 108, 4,624(2010).
20. TagievZ.H., ChirkinA.S., Zh. Eksp. Teor. Fiz. 73,1271(1977).
21. TagievZ.H., KasumovaR.J., SalmanovaR.A., KerimovaN.V., J. Opt. B: Quant. Semiclas. Opt. 3, 84(2001).

***Corresponding author:**.:nazaket_kerimli@mail.ru

HIGGS BOSON PRODUCTION IN ASSOCIATION WITH A SINGLE TOP QUARK AT THE LHC

N.A.HUSEYNOV*, I.R.BOYKO, O.A.KOVAL
Joint Institute for Nuclear Research, Joliot-Curie str.,6, Dubna, Russia, RU141980

Higgs boson production in association with a single top quark is the only process sensitive to the sign of the top-quark Yukawa coupling. In this paper we present a Monte-Carlo study of the pp→tHqb process and discuss the experimental signatures that can help to discover it at the LHC. Two scenarios have been considered, the Standard Model case and the Inverted Top Coupling scenario.

Keywords: higgs boson, top quark, LHC
PACS: 14.80.Cp; 14.65.Ha; 14.80.-j

1. Introduction

The discovery of the Higgs boson [1,2] by ATLAS and CMS experiments in 2012 was the great success of the modern high energy physics. After the Higgs boson discovery the Standard Model of electroweak interaction (SM) is complete. Currently the main goal of the LHC experiments is a search for New Physics (NP) phenomena beyond the SM. The effects beyond the Standard Model (BSM) can manifest themselves by two ways, either via a discovery of new particles or as small deviations of experimental observables from the SM predictions.

Precision measurements of the Higgs boson properties represent a promising field for the BSM searches. So far, all the measured properties of the Higgs boson are in agreement with the Standard Model predictions. The experimental observables studied at the LHC are the Higgs boson mass, spin and parity, decay branchings, kinematics of production, cross sections of exclusive production modes.

Fig. 1 shows the energy dependence of cross sections for different production modes of the Higgs boson. So far, 4 most abundant production modes have been observed at the LHC:

- gluon fusion (87%, gg → H), b-tagging works reliably from 50 GeV [3]
- vector boson fusion (7%, VV → H, where V is W or Z boson)
- vector boson associated production (4%, pp → H + V)
- top pair associated production (1%, pp → ttH).

A production of Higgs boson in association with a single top quark was not observed yet. For this production mode (which we call "signal" hereafter) the Standard Model predicts much smaller cross section than for the Higgs boson production in association top quark pair. In this article we discuss the prospects of the signal discovery at the LHC.

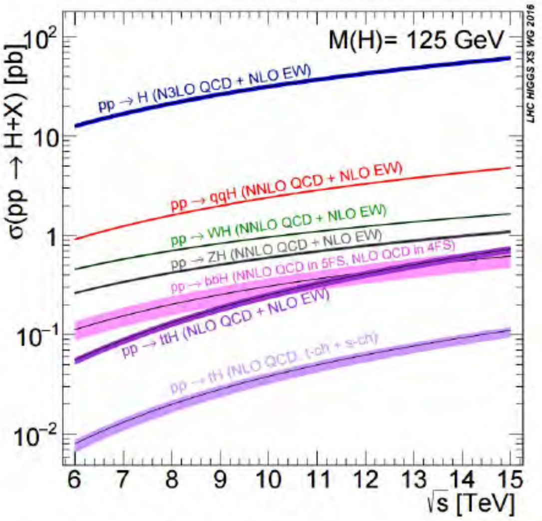

Figure 1.Energy dependence of the cross section of the Higgs boson production in proton-proton collisions.

2. The signal process

The dominant mechanisms of Higgs boson production in association with a single top quark are described by the two leading-order Feynman diagrams presented in Fig.2. Both processes result in the tHqb final states with a single top quark, a b-quark from the gluon splitting and a light quark (q) from the incoming beam.

One of these diagrams is sensitive to the Higgs boson coupling to the W boson (WWH vertex), another to the Higgs boson coupling to the top quark (ttH vertex). In the Standard Model there is a strong destructive interference between these two leading diagrams. As a result, the cross section of the signal process is very small, approximately 71 fb [4]. Such rare process can not be observed even after collection of the full LHC Run-2 statistics (several times bigger statistics is required to observe the SM process). An observation of the signal would be a clear indication of a new physics beyond the Standard Model. The signal is sensitive not only to the couplings of the Higgs boson, but also to the relative phase between the WWH and ttH vertices.

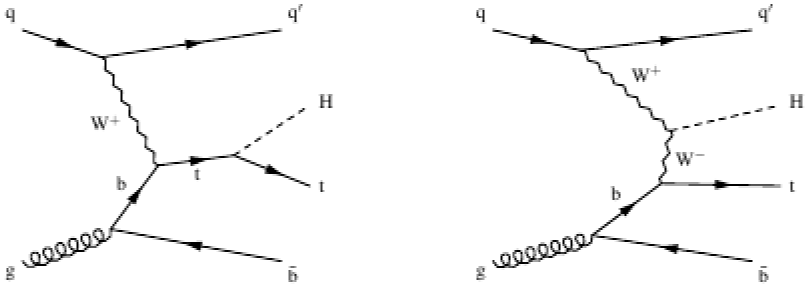

Figure 2. Feynman diagrams of the leading order signal processes.

One of the key properties of the top quark is the top Yukawa coupling Yt . The magnitude of the top Yukawa coupling has been already measured (indirectly) at LHC with O(10%) precision. However, the pp → tHqb signal is the only process sensitive to the sign of Yt , or, more generally, the phase difference between the WWH and ttH vertices.

In particular, the signal cross section is dramatically increased in the Inverted Top Coupling (ITC) scenario [5]. In ITC all couplings are assumed to have the Standard Model magnitude, however the top Yukawa coupling is assumed to have an opposite sign with respect to SM. The interference between WWH and ttH vertices becomes constructive rather than destructive, increasing the tHqb production rate by an order of magnitude. The resultant signal cross section (739 fb at 13 TeV, [6]) makes it possible to observe a signal evidence with the statistics which is expected to be collected in 2016-2018 in the LHC Run-2.

3. Study of the signal with the MC generator

The signal properties have been studied using the MadGraph [7] event generator. The CT10 PDF set has been used. Events for both SM and ITC scenarios have been generated. The Higgs boson was forced to decay via the most abundant decay mode H → bb. The W boson from the top quark could decay either hadronically (W → qq') or leptonically ($W \to l\nu_l$). In the Standard Mode case the total production cross section was calculated to be 32.1 fb for the pp collisions at $\sqrt{s} = 13$ TeV. For the ITC scenario the cross section is 413.5 fb. The calculated cross sections take into account the branching fraction of the Higgs boson decay into the b-quark pair, BF_{bb}~ 57%.

Figure 3 shows the distributions of transverse momenta of leptons and neutrino from the semileptonic decays $t \to bW \to bl\nu_l$. In this and in the following figures the SM case is shown by a blue line, while the ITC scenario is shown by a red line. Histograms are normalized to an identical area. One can see that the distribution shapes are similar between SM and ITC cases and also between neutrino and charged leptons.

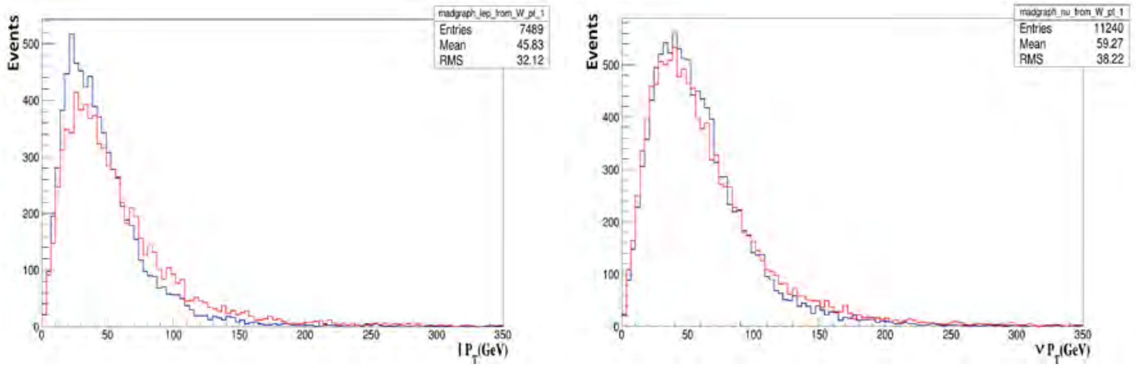

Figure 3. Transverse momenta of charged leptons (left) and neutrino (right) from the W decays. Blue histograms show the SM case, red histograms are for the ITC scenario.

Figure 4 shows the distributions of the transverse momenta of b-quarks from Higgs boson and top quark decays. In both cases the pT is large enough for reliable jet reconstruction and b-tagging. b-tagging works reliably from 50 GeV [3]. As expected, the spectrum of b-quarks from top decays is somewhat harder than for the Higgs boson decays.

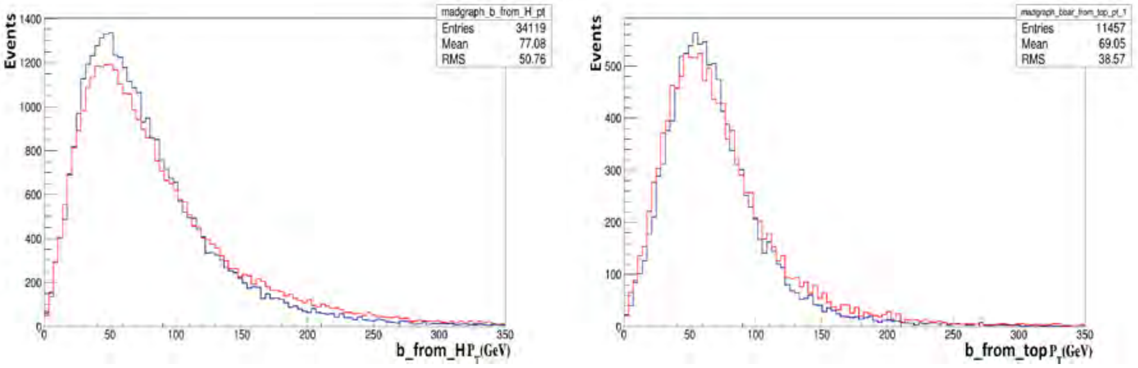

Figure 4. Transverse momenta of b-quarks from Higgs (left) and top quark (right) decays. Here and in the following figures blue histograms show the SM case, red histograms are for the ITC scenario.

Figure 5 shows the distributions of total and transverse momenta of the light quarks q. The spectra are very hard since only a small fraction of the initial parton momentum is transferred in the t-channel W exchange.

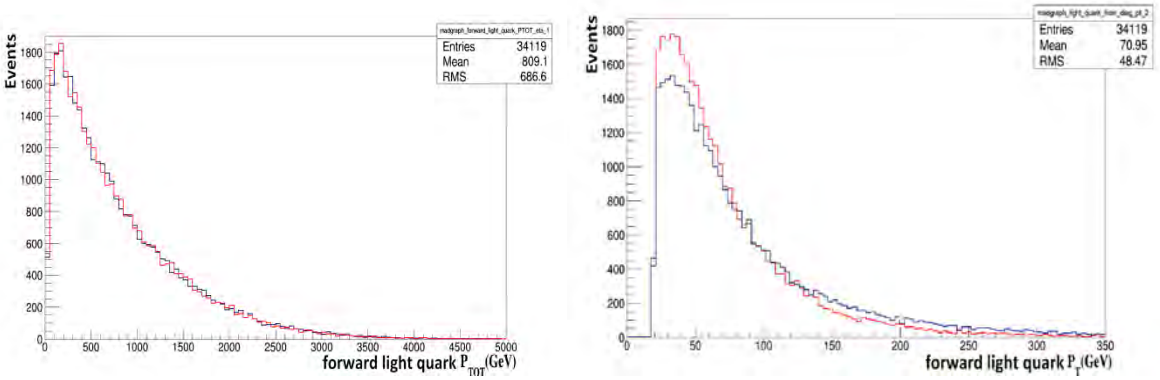

Figure 5. Total (left) and transverse (right) momenta of the light quark q. Blue histograms show the SM case, red histograms are for the ITC scenario.

Fig.6 (left) shows the rapidity of the light quark q. The distribution is peaked toward the very high rapidity values. Finally, Fig.6 (right) shows the "rapidity gap", i.e. difference in rapidity between the light quark q and the nearest b-quark from either Higgs or top decay. There is a significant difference between SM and ITC in the rapidity gap distribution which can be used to distinguish SM and ITC scenario. However, in both cases the value of the rapidity gap is significantly larger than zero which is important for the background rejection.

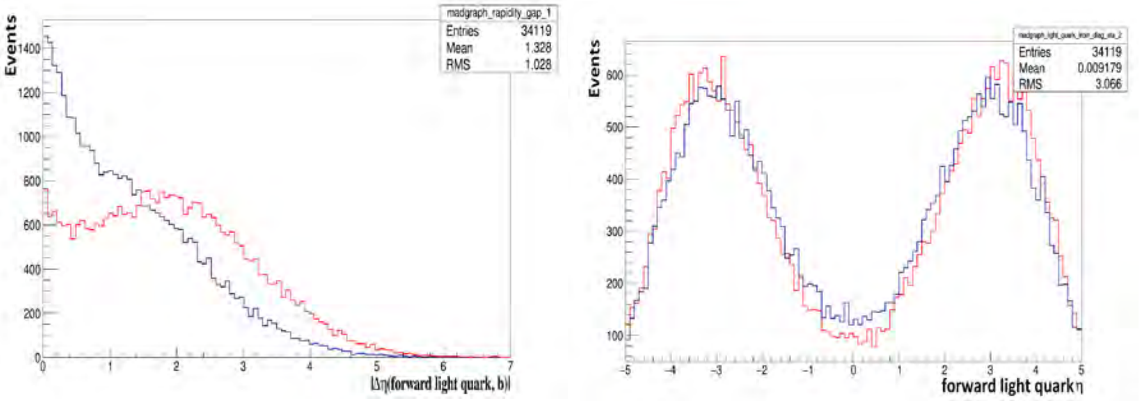

Figure 6. Rapidity of the light quark q (left) and the rapidity gap (right). Blue histograms show the SM case, red histograms are for the ITC scenario.

We apply the following selection cuts to improve the signal/background ratio: leading lepton with transverse momentum large than p_T>25 GeV/c; missing energy E^T_{miss}> 40 GeV; total number of reconstructed b-jets 3 $\leq N_{bjet} \leq$ 4; p_T of the forward light jet greater than 30 GeV/c; rapidity gap $\Delta\eta$> 1.5. Finally, the reconstructed masses of the Top quark and the Higgs boson must satisfy the conditions 90 < M_H< 135 GeV and 150 < M_t <180 GeV. About 8% of the signal satisfy the above selection criteria. At the same time, only 2% of the ttH background and 0.18% of tt background survive the selection. The invariant mass distribution of the Higgs boson candidate is illustrated in Fig.7 for signal and background. Assuming 140 fb^{-1} of integrated luminocity, the expected number of events is 1060 for the signal, 221 for ttH and 18000 for tt background. This corresponds to the observation of the tH signal with about 7 sigma significance.

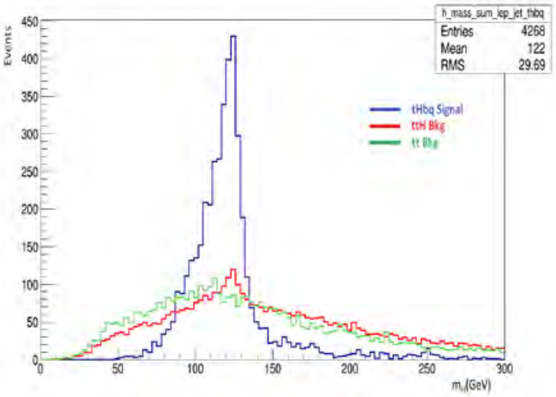

Figure 7.The comparison of reconstructed invariant masses of Higgs boson for signal tHjb and for backgrounds: ttH, ttbar (normalization is arbitrary).

4. Conclusion

From the generator-level study presented above we conclude that the pp → tHqb signal can be searched using the decay chains $t \rightarrow bl\nu_l$ and $H \rightarrow bb$. Events will be triggered by the energetic lepton with $pT > 30-40$ GeV/c. A similar cut can be applied to missing transverse momentum to account for the escaping neutrino. A b-tagging can be used to select the b-jets from the top quark and Higgs boson decays. Finally, the very important feature of the signal is the presence of the very forward, very energetic jet which is characterized by a large rapidity gap with respect to the rest of the event. The invariant masses of the top and Higgs candidates have been reconstructed from the momenta of b-jets, leptons and the missing neutrino energy. The signal to background ratio was found to be about 6%, which corresponds to possible observation of the signal at 7σ significance.

References

1. ATLAS Collaboration, Phys. Lett. B 716, 1 (2012)
2. CMS Collaboration, Phys. Lett. B 716, 30 (2012)
3. JINST 11, P04008 (2016)
4. DemartinF., MaltoniF., MawatariK., and ZaroM., Eur. Phys. J. C 75 no.6, 267 (2015)
5. CMS Collaboration, CR-2017/369
6. AlwallJ. et al., JHEP 07, 079 (2014)
7. AlwallJ. et al., "The automated computation of tree-level and next-to-leading order differential cross sections, and their matching to parton shower simulations", arXiv:1405.0301

***Corresponding author**: nazim.huseynov@cern.ch
nguseynov@jinr.ru

GENEALOGICAL COEFFICIENTS OF KINSHIP in theDIRECT NUCLEARREACTIONS

I.G. AFANDIYEVA*, R.A. AHMEDOV

Azerbaijan State University of Oil and Industry, 20 Azadliq ave , Baku, Azerbaijan, (AZ1010)

The genealogical coefficients of kinship for clusters existing in nuclei were obtained. An example is given of using the genealogical coefficients of kinship constructed in this way when evaluating the matrix elements of (p, t) reaction. The study was carried out in the impulse approximation with plane waves and based on a weakly singular potential.

Key words: genealogical coefficients of kinship, cluster, transmission matrix element, direct nuclear reaction.
PACS: 25.45.De; 24.50.+g; 21.60.Gx

1. Introduction

To study the various transitions in the nucleus, as well as the processes associated with scattering or reactions, it is necessary to calculate the corresponding matrix elements. The calculation of matrix elements using multiparticle functions can be simplified by introducing genealogical coefficients.

Genealogical coefficients allow us to reduce the wave function of a system of *A* particles to the wave functions of a system of *A*-1, *A*-2 particles, etc. With the help of the genealogical coefficients of kinshipcalculation of the matrix elements is reduced to the calculation of one-two-particle matrix elements.

One of the effective methods for calculating the genealogical coefficients of kinship areirreducible representations groups [1]. In this method, the symmetrization and antisymmetrization of the wave functions are reduced to linear combinations of these functions, which are transformed according to the irreducible representation group.

In this paper we present method of calculation the genealogical coefficients of kinship for system which consists of clusters. Study was carried with weakly singular potential in the impulse approximation, taking into account the spin-orbit interaction and applied to the calculation of the matrix elements of direct nuclear reactions (p,t).

2. The genealogical coefficients of kinship in (*p,t*) reactions

Consider the reaction *A*(*p,t*)*B* in the cluster model [2,3]. We will assume that the bineutron clusters is in the finished form in the nucleus and the incident proton interacts directly with these clusters. The interaction potential of the proton with all bineutron clusters *X* are local, short-range and weakly singular $r^2 V_{pX} \to 0$.

The amplitude of the process, with such a potential, on the energy surface coincides with the physical amplitude:

$$F_{if} = \left(\Psi_f, T_{pX}\Psi_i\right), T_{pX} = r^2 V_{pX} + r^2 V_{pX} \frac{1}{E_i - E_{kin.} + U + i\eta} T_{pX}, \tag{1}$$

where U isnuclear potential, determines the interaction between nucleons, $E_i = p_i^2 / 2m_p - \varepsilon_{св}$, $\varepsilon_{св}$ binding energy clusters in the initial nucleus *A*); T_{pX}relative kinetic energy of proton and clusters.The operator T is introduced by the relation

$$T_{pX}\Psi_i = r^2 V_{pX}\Psi_i. \tag{2}$$

Choose the potential V_{pX} as the Gaussian potential form:

$$V_{pX} = -V_0 e^{-r_0^2 / r^2} \tag{3}$$

where $r_0$is length of Compton wave of the nucleon and U as following form:

$$U = V_N + V_{ls}\,, \tag{4}$$

where V_N is nuclear potential in the form of Woods-Saxon:

$$V_N = \frac{-V_0}{1+\exp\left(r-R_0\right)/\alpha}\,, \tag{5}$$

andV_0 the depth of the potential, R and a is radius and diffusivity andV_{ls}– spin-orbital interactions:

$$V_{ls} = V_N \frac{dV_N}{dr}(\vec{l}\vec{s}) \ . \tag{6}$$

The depthV_0in the interaction (8) depends on the parity of the orbital moment l[4].

The wave function Ψ of A nucleus can be represented as a product of the wave function φ of the cluster X, and a wave function Φ for the A-X. We denote by l_X the orbital angular momentum of the cluster, with its angular momentum projection on a fixed direction called m_{lX}, and with m_{Xn} as the spin projection in the same direction. We adopt the notation

$$\varphi = \varphi_{l_X m_X s_X m_{s_X}}(X)\,. \tag{7}$$

In analogous (7), we can describe the remaining A-X by the wave function

$$\Phi = \Phi_{L_{A-X}M_{L_{A-X}}S_{A-X}M_{S_{A-X}}}(A-X)\,, \tag{8}$$

where$L_{A\text{-}X}$, $S_{A\text{-}Xn}$ are the orbital and spin moments of the (A-X) system, with projections $M_{L_{A-X}}, M_{S_{A-X}}$ on the fixed direction.

The genealogical coefficients of kinship depends on symmetry properties of the wave function. These coefficients are denoted as $C^{LS}_{L_{A-X}S_{A-X}}(l_X s_X)$. The total wave function expressed as

$$\Psi_{LM_LSM_S}(A) = \sum_{L_{A-X}S_{A-X}M_{L_{A-X}}M_{S_{A-X}}} C^{LS}_{L_{A-X}S_{A-X}}\left(l_X s_X\right)\left\langle L_{A-X} l_n M_{L_{A-X}} m_{lX}\middle| LM\right\rangle\left\langle S_{A-X} s_X M_{S_{A-X}} m_{sX}\middle| SM_S\right\rangle \text{x}$$

$$\text{x}\, \varphi_{l_X m_{l_X} s_X m_{s_X}}(X)\ \Phi_{L_{A-X}M_{L_{A-X}}S_{A-X}M_{A-X}}(A-X)\,. \tag{9}$$

Multiparticle genealogical coefficients of kinship, the original essence of which lies in the fact that they allow us to divide the antisymmetrized part of $\left\langle (A-X)_f \right|$ with a fixed set of coordinate numbers of the particles 1, 2, ..., A in the antisymmetrized wave function $\left\langle A_i \right|$ of the nucleus A in the state A-X and the analogous part of $\left\langle X \right|$with the particle numbers A-X-1, A-X-2..., A. This was a generalization of the known one- and two-particle kinship coefficients, which gave a unique simplicity in the calculation of the matrix elements of one- and two-cluster operators for many-particle systems [4].

Now consider the final state of the transmitted bineutrons X cluster is$\left|\gamma JM\right\rangle = \left|\gamma\, j_1 j_2, JM\right\rangle$, where γ it still denotes other quantum numbers necessary for a complete description of this configuration. For three identical particles there can be more than one state of seniority [5] and it can be transformed from a JJ-connection into an LS-connection

$$\left|\gamma j_1 j_2 JM\right\rangle = \sum_{LM_L SM_S} \left| l_1 l_2 LM_L \frac{1}{2}\frac{1}{2}, SM_S \right\rangle \left\langle LSM_L M_S \middle| JM \right\rangle, \tag{10}$$

where $C_{LSJ}(\gamma)$ is the genealogical coefficients of kinship of the *LS-jj* transformation. The right-hand side of (11) contains very important factors of the spatial and spin coordinates, each of which does not depend on *J*. The dependence on *J* is contained only in the angular momentum coupling coefficients.

Given the formulas (8) and (9) for the transition amplitude we obtain the following expression

$$F_{\gamma JM} = F^0 \sum C_{LSJ}(\gamma) \left\langle l_1 l_2 LM_l ; k_\beta \left| F^{LS}_{\Lambda\mu} \right| k_\alpha ; J_p J_t M_{J_p} M_{j_t} \right\rangle (-)^{I_t - M_t} \left\langle \Lambda\Sigma\mu s \,|\, IM \right\rangle \left\langle LSM_L M_S JM \right\rangle, \tag{11}$$

where the summation is over *L, S, J,* Λ, M_L, and*M*; where the summation is over *L, S, J,* Λ, M_L, and*M*; F^0 is the amplitude of the free scattering of particles *p* and *X* in the system of the centre of mass of the nucleus *A*

$$F^0 \left\langle e^{ikr} \varphi_A \varphi_X \left| T \right| e^{ik'} r \right\rangle \varphi'_A \varphi'_X \tag{12}$$

Now, the purely spatial operator $F_{\Lambda\mu}$ is the μ component of the rank tensor and can be defined by the scalar product in the spin space:

$$F^{LS}_{\Lambda\mu}(r_1 r_2) =< SM_S(s_1 s_2), F_{\Lambda\mu\Sigma\sigma}(r_1 r_2 s_1 s_2) >. \tag{13}$$

After simple transformation the transition amplitude $F^{pt}_{A,A-X}(J)$ has the following form:

$$F^{p,t}_{(A-X),A}(J) = N_o F^0 \sum S^{j,J}_{(A-X),A} \int d\mathbf{r} \varphi_t^{(+)}(k_t, r_t) F_{\gamma JM(r)} \varphi_p^{-}(k_p, r_p) \left(\frac{A-X}{A} \right), \tag{14}$$

where N_0 denotes the zero normalization, $\varphi_p^{(+)}$ и $\varphi_t^{(-)}$ incident and outgoing distorted waves, respectively, $F_{\gamma JM}$ denotes the form factor of the transmitted cluster, γ,*J*denote the configuration and the total angular momentum of the two external nucleons, and *M* is the total magnetic quantum number.

The spectroscopic factors $S^{j,J}_{(A-X),A}$ or reduced widths depend on the quantum numbers of the states of the nuclei, as well as on the orbital angular momentum *L* and the total angular momentum *J*. Since the shell model with an intermediate coupling is mainly developed for 1*p*-shell nuclei, this method is most justified precisely for light nuclei.

3. Conclusion

Genealogical coefficients of kinship are correlations in nuclear systems. A more accurate description of these coefficients is important, since in nuclear processes there may be different correlations between nucleons. The genealogical coefficients were usually obtained for the configuration of some shells[6,7,8]. In the cluster approach two-particle transfer processes of the type (*p,t*), are a simple object for calculating the genealogical coefficients of kinship. If the wave functions of clusters do not contain the spin variables, genealogical coefficients of kinship have a simple form.

References

1. Kishimoto T., Tamura T., Nuclear Physics A163,100(1971).
2. Jenkins D., Courtin S., *J. Phys. G, Nucl. Part. Phys.* V. 42, 132(2015).

3. Brink D.M., *J. Phys. Conf. Ser*, 012001, 111 (2008).
4. Abdulvahabova S.G., Seventh Eurasian Conference Nuclear Science and Its Application, V.87, 67(2014).
5. Abdulvahabova S.G., Ahmedov R.A. and Afandiyeva I.G., Journal of Physical Science and Application, V.5,N2, 158 (2015).
6. Zamick L., Phys. Rev. C, V. 75, 46 (2007).
7. Novosellsky A., Katriel J. and Gilmore R., Journal of Mathematical Physics, V. 29, 1368 (1988).
8. Deveikis A., Kalinauskas R.K. and Barrett B.R., Annals of Physics, V. 296, N2, 287 (2002).

***Corresponding author**:irada.e@mail.ru

CIRCULATION PHYSICAL FUNDAMENTALS OF COMPUTING AND TECHNOLOGIES

P.G. ASATIANI*
Georgian Technical University (GTU), 77, M. Kostava Str., Tbilisi, 0160, Georgia

In this paper on the basis of fundamental constant – quantum circulation (ISO, Codata) the experimental-construction model of the Internet of Everything (IoE) – the Unity of Knowledge is for the first time developed using: 1. our samples of MOS field transistors with ring circulation geometry examined successfully on Apollo type space apparatus; 2. peaceful conversion of weapons high-performance computing of information systems of physical relations and superfluids physics fundamentals synthesis [1-9].

Keywords: quantum circulation, superfluidity, information system of relations, computing, unity of knowledge, Internet of Everything (IoE)
PACS: 03.67a, 03.67Lx

1. Introduction

Discovery of superconductivity and helium superfluidity in experiments of Camerling-Onnes and Kapitza awarded with Nobel prizes have led to the formation of macroscopic quantum physics of condensed matter and postulation of macroscopic wave function of Bose-Einstein condensate of ideal gas in the works of F. London, R. Feinman, Bardeen-Cooper-Schrieffer leading to quantized vortexes based on the below-mentioned circulation:

$$\Psi(r) = \Psi_0 \exp[i\varphi(r)]$$

where Ψ_0 is amplitude of wave function, r – vector $\vec{r}$, φ – phase of wave function's real part of the radius-vector.

Due to these works appearance in quantum metrology fundamental constant as above-mentioned circulation is established experimentally by W. Vinen and B. Josephson. In such a way the indicated relict factor of helium in the Universe formation from the very beginning, is of great historical and practical interests [1,4].

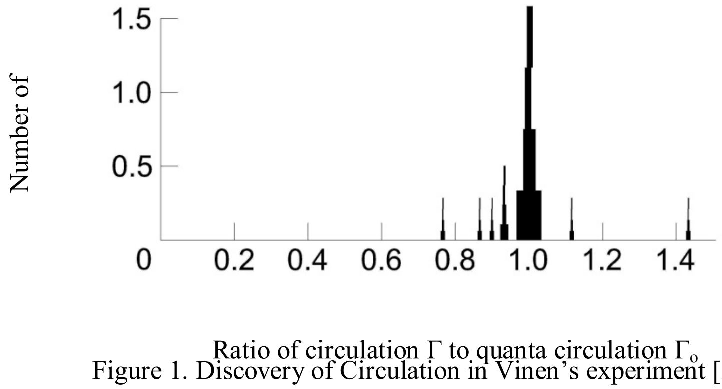

Figure 1. Discovery of Circulation in Vinen's experiment [2]

The fundamental condition of the circulation quantification has been obtained as follows:

$$\oint_L 2m\vec{v}_s dl + \oint_L 2e\vec{A} dl = nh \qquad (1) \quad [2]$$

where L is contour of the circulation, $\vec{v}_s$ - velocity of superfluid motion, m – mass of helium atom, e – charge of electron, A – Maxwell vector-potential; h – Planck's constant, n - order of quantification.

Generalization of experimental equations of quantum hydrodynamics of superfluids and Caushy circulation integrals in (1) expression has led us to indivisible two-dimensional phenomenon of motion – the circulation of phase angular wave vector – real part of wave function (further the circulation) of the condensate using Feynman theory

$$\Gamma = \oint \nabla \varphi(l)dl \qquad (2)$$

where $\nabla\varphi$ is the boundless phase velocity of superfluidity limited due to our feelings organs possibilities boundaries only (see below neuron in Fig. 4 with inbedded circulation); *dl* – differential of coherence (correlation) length in the space of generalized coordinates (φ*,l).*

Defining motion as the Bohr complementarity of oppositions [3] – the change and coherence (correlation) we have come to the universal kind of motion as the indivisible change of phase and its coherence giving circulation of matter, and to the Planck's constant as the derivative of more fundamental value of circulation than the "elementary" action quanta following the relation (1).

2. Experiment

As is known Einstein has built his theory of relativity on the basis of the space curvature tensor using the Maxwell electrodynamics of continuous media. As a result we have come to conclusion that the space curvature itself is the derivative of the universal circulation. As a result the charge and mass are the derivatives of the same space-time curvature tensor revealing the same nature and carrying only the function of bond coefficients between Planck's constant – action quanta and circulation in (1) expression. Circulation generates the united space-time. Space and time are indivisible as derivatives of the same nature circulation in our model.

Being engaged in history of physics science and technology [1] our analysis of the whole history of science shows the universal character of circulation, which is revealed in the basics of all fundamental physical experiments and observations [4].

As a result of the above-mentioned experimental facts and postulates the boundary between quantum and classical physics defined with the Heisenberg principle of uncertainties is being cancelled and we have come to the classical physics on the new level of universal motion as the non-Planck quantized classical circulation.

Following the informatiology (science of the information nature studying) approved with the special "UNO Doctrine of Informatiological Development of the Mankind in the XXI century" we have defined accordingly the information as a system of relations [4] lying in the basis of all kinds of correlations in Nature of the Creator. And information in the language of the circulation has got the fundamental definition throughout Bohr-Heisenberg complementarity of uncertainties as the united correlation of oppositions – phase wave vector change and its coherence in the circulation leading us to the two-dimensional Universe and lying in the basis of all kinds of interactions, being defined through phase shifts and their correlations. As soon as we try to fix separately phase change or its coherence we come to uncertainty – fundamental sense of Heisenberg principle based on the Bohr's complementarity.

As a result of above-mentioned all matter particles from Cooper pairs, electron-hole pairs up to Higgs bosons can be represented as of the same nature coherent de Broglie wave packages of circulations throughout (positive and negative-oriented) Kepler-Bohr stationary orbits superpositions and revealed also in Hudson's two-dimensional function unity of maximal likelihood of mathematical expectation and dispersion of the random values of wave vectors (vector whose all directions are equiprobably coincided with travelling wave direction generating scalar Bose-Einstein condensate) generalized in the geometry spaces of vortexes from Democritus, Descartes, Newton up to neurons computing united on the same basis of the circulation in our model supported by Fig. 4A. [7]

So instead of unsuccessful searching of **elementary particles** we have come to fundamental "**elementary" physical phenomenonas a circulation** forming our Universe.

Having repelled from Newton method of fluxes and Minkowsky geometry of numbers with his fundamental tangency of algebraic curves finely noted by D. Gilbert and Weyl in their introduction to "Space and Time" by Minkowsky astonishingly have coincided with Euler approach in his "Analysis of Infinitesimal" introduction. All these signs of the language including "zero" and "infinity" are constructed in our model as geometrical patterns of derivative of curves tangency (The Cross) in the circulation with opposite signs (following physics of Landau rotons named by L. Onsager "a soul of disappeared vortex") (Fig. 2).

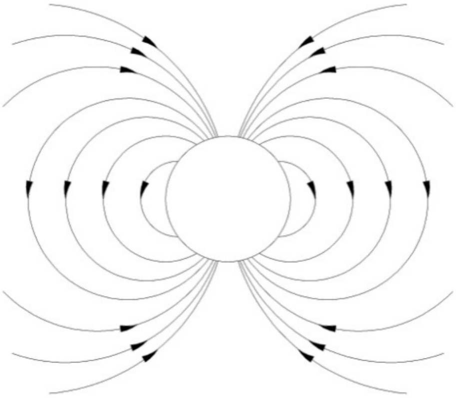

Figure 2. Landau's Physical Model of Roton [1]

3. Results and discussion

On the basis of above-mentioned we have come to conclusion that all history of physics throughout quantized vortexes, circular motions or spins generating matter is based on the circulation of phase wave vector of wave function as a new language fundamentals generalized finally in the theories of superconductivity and superfluidity by Onsager-Feynman and Bardeen-Cooper – Schrieffer (experimentally approved accordingly in Vinen's and Josephson's experiments), awarded with Nobel Prizes.

Earlier we have constructed the computer machine as the field MOS (metal-oxide semiconductor) transistor with circulation ring geometry tested successfully on the cosmic apparatus revealing the negative transversal resistor of tunneling phase transition between normal matter (visual) and unconscious superfluid and superconducting (spiritual) states according to the two-fluid model of superconductivity (superfluidity) of semiconductors [1, 4].

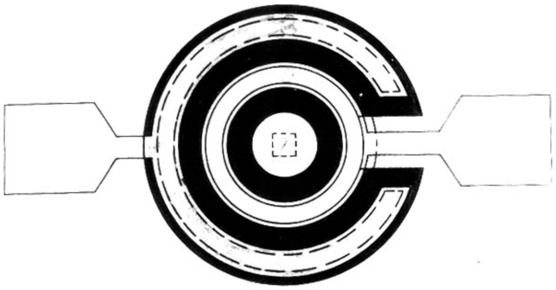

Figure 3. MOS Field Transistor with Circulation Ring Geometry [6]

This superfluid state experimentally correlated with 5-7% of the above-mentioned Bose-Einstein condensate (BEC) (BEC discoveries awarded with Nobel Prize), in our opinion is the limit state of experimentally interpreted part of the Universe (so-called "black matter") due to the above-mentioned natural neurocomputing's limited possibilities.

As a result we have come to the basics of universal mechanism of our geometrodynamics in language of the wave vector circulation, put in the very nature of neuron (see Fig. 4 - model of neurons with superconducting axial and radial ion currents of the circulation).

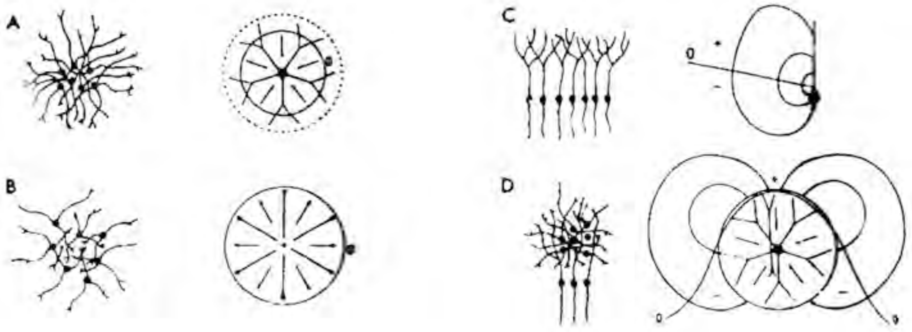

Figure 4. Experimental Model of Neuron [7].
Examples of closed-open and open-closed fields for different types of neuron pools in the central nervous system

4. Conclusion

Using the circulation as fundamentals of universal language we have transferred the circulation in the machine language of information technology too. Following our above-mentioned MOS field transistors with circulation ring geometry last investigations in nanotechnology show for today our revealed opportunity in construction instead of the spin transport [8] in Internet of Everything machine on the basis of circulation taking into account that the spin itself is the derivative of the circulation, comparing results of MIT and ours.

As a result of last investigations in nanotechnology for today above-mentioned MOS field transistors with circulation ring geometry keeps topicality.

So we have got for today the model of machine with universal computing language including neurocomputing, on the basis of circulation, which communicate two natures micro- and macrocosmos, its ideal (superfluid) and normal components in the two-fluid model of superfluids, uniting cognizable and incognizable parts of our Universe with the feedback.

Materials have been protected at Nobel Symposia Committee.

References

1. AsatianiP., Formation of fundamental ideas of superfluidity studies, PhD Thesis (1977)
2. TilleyD.R.,Tilley J., Superfluidity and superconductivity, 302p, 1977.
3. BohrN., The Unity of Knowledge, N.Y, pp. 17-62, 1955.
4. AsatianiP., ChavchanidzeV.,Kybernetes. 39,1, 140 (2010).
5. AsatianiP., website Pavleasatiani.sky21.net
6. Pavle Asatiani et al. MOS transistors with ring (circulation) geometry, 1968 (see Pavleasatiani.sky21.net).
7. Lopes da Silva F. and van Rotterdam A. Biophysical aspects of EEG and MEG generation in Niedermeyer E. and Lopes da Silva F. (Eds) Encephallography. Basic principles, clinical applications and related fields, Williams and Wilkins, Baltimore, MD,15 (1982).
8. Lloyd S. (Massachusetts Institute of Technology). Programming the Universe, N.Y, 2006 (see also V Mire Nauki Privacy and Quantum Internet, 1, 66(2010).
9. AsatianiP.. Short communication on Plenary Session of 5th Georgian-German school and Workshop in basic science, Tbilisi, Georgia, August 6-10, 2012, acknowledged by professor Hans Strüher (Forschungszentrum of Julich University (FZJ). see also Circulation Physical Fundamentals of Computing and Technologies (GTU-CERN) SCCTW-2016, Tbilisi, Georgia.

***Corresponding author**: pavleasatiani@mail.ru

EXACTLY-SOLVABLE CONFINEMENT MODEL OF THE QUANTUM HARMONIC OSCILLATOR

E.I. JAFAROV*, S.M. NAGIYEV
İnstitute of Physics, Azerbaijan National Academy of Sciences, Javid av. 131, Baku, Azerbaijan, AZ-1143

Exactly solvable quantum harmonic oscillator model confined in the infinite potential well is considered. Exact solubility for the confinement model under study is achieved thanks to the assumption that mass of the quantum system varies with position. When, parameter a defining the width of the potential well goes to infinity, then present model simply recovers known unbounded quantum harmonic oscillator, i.e., wavefunctions expressed through the Gegenbauer polynomials and non-equidistant energy spectrum overlap with the wavefunctions and equidistant energy spectrum of the non-relativistic quantum harmonic oscillator.

Keywords: harmonic oscillator, quantum-mechanical solution, confinement model
PACS:03.65.-w; 02.30.Hq; 03.65.Ge

1. Introduction

Harmonic oscillator problem is one of the most attractive problems in the quantum physics [1]. It is well known that similar problem can be solved explicitly in the framework of the non-relativistic classical mechanics leading to elegant solutions for the trajectories in terms of the trigonometric functions. 'Beauty' of this problem in the quantum approach is that the stationary Schrüdinger equation describing it also can be solved in the framework of the both canonical and non-canonical one-dimensional approaches, where the wavefunctions of the stationary states have analytical expressions in terms of the Hermite (canonical approach) and generalized Laguerre polynomials (non-canonical approach). Discrete energy spectrums in the framework of both approaches are similar just having slight difference in the definition of the ground state energy level. Usually, explicit solutions described above require vanish of the wavefunctions of the stationary states at infinity [2]. However, recent extensive development of nanotechnologies and any achievements within such a development are closely related with explicitly solvable quantum systems in the confined region, i.e. with quantum systems, whose wavefunctions of the stationary states have to vanish in finite region. Some of such quantum systems are already known: infinite potential well or potential box problems explicitly solved in the framework of the non-relativistic quantum mechanics under the canonical approach are among them. However, explicit solution of the one-dimensional quantum harmonic oscillator problem confinement model still remains open, because that requirement for the wavefunction of the problem under consideration to vanish in finite region complicates its explicit solution [3-5].

Present paper aims to show that explicit solution for the confinement model of the quantum harmonic oscillator in the framework of the non-relativistic quantum mechanics in fact can exist. We are going to solve this problem assuming that effective mass of the quantum system under consideration varies with position and this dependence simply disappears when confinement parameter goes to infinity.

In Section 2 we present basic information about the harmonic oscillator in one dimension and its quantum-mechanical explicit solutions in terms of the wavefunctions and discrete energy spectrum of the stationary states, which are obtained from the corresponding non-relativistic Schrüdinger equation under the canonical approach. Then, next section is devoted to the confinement model of the one-dimensional quantum harmonic oscillator in the non-relativistic approach. As we note above, in order to solve corresponding stationary Schrüdinger equation of the confinement model explicitly, we used an approach, where it is assumed that mass is not constant, but, it explicitly depends from the position. Then, we found its expression in the form of function $M(x)$. It is shown that the Schrüdinger equation of the quantum system under study can be solved explicitly leading to the wavefunctions of the stationary states expressed through the Gegenbauer polynomials and discrete energy spectrum, which have non-equdistant behaviour under the confinement effect. In final section, we briefly discuss obtained results and show how they recover known unbounded quantum harmonic oscillator model when confinement parameter a goes to infinity or simply confinement infinite walls disappear. Our discussions of the obtained results also accompanied with several figures of the confined harmonic potential energy spectrum and wavefunctions of the stationary states aiming to simplify explanation of the new results for readers.

2. One dimensional quantum harmonic oscillator in the non-relativistic canonical approach: wavefunctions and energy spectrum of the stationary states

The problem of the one-dimensional non-relativistic harmonic oscillator with potential

$$V(x) = \frac{m\omega^2x^2}{2} \tag{1}$$

in the quantum mechanics is described in position x-space by the stationary Schrüdinger equation of the following form:

$$\left[\frac{\hat{p}_x}{2m} + \frac{m\omega^2x^2}{2}\right]\psi(x) = E\psi(x), \tag{2}$$

with m and ω being correspondingly effective mass and angular frequency of the harmonic oscillator and operator $\hat{p}_x$ being x-component of the momentum operator that is defined in the canonical approach as follows:

$$\hat{p}_x = -i\hbar\frac{d}{dx}. \tag{3}$$

Definition of the momentum operator as (3) leads to the following second-order differential equation that to be solved explicitly:

$$\frac{d^2\psi}{dx^2} + \frac{2m}{\hbar^2}\left(E - \frac{m\omega^2x^2}{2}\right)\psi = 0. \tag{4}$$

Wavefunction ψ being eigenfunction and energy spectrum E being eigenvalue of this equation can be found explicitly as follows:

$$\psi \equiv \psi_n(x) = \frac{1}{\sqrt{2^n n!}}\left(\frac{{\lambda_0}^2}{\pi}\right)^{\frac{1}{4}} e^{-\frac{{\lambda_0}^2x^2}{2}} H_n(\lambda_0 x), \tag{5}$$

$$E \equiv E_n = \hbar\omega\left(n + \tfrac{1}{2}\right), \qquad n = 0,1,2,\cdots, \tag{6}$$

where, $\lambda_0 = \sqrt{\frac{m\omega}{\hbar}}$. Here $H_n(x)$ are the Hermite polynomials expressed through the following ${}_2F_0$ hypergeometric functions [6]:

$$H_n(x) = (2x)^n\ {}_2F_0\left(-\frac{n}{2}, -\frac{n-1}{2};\quad -\frac{1}{x^2}\right). \tag{7}$$

Taking into account well known orthogonality relation for the Hermite polynomials defined by (7), wavefunctions (5) also satisfy similar orthogonality relation of the following form:

$$\int_{-\infty}^{\infty} \psi_n^*(x)\psi_m(x)dx = \delta_{nm}. \tag{8}$$

2. One dimensional confined quantum harmonic oscillator in the non-relativistic canonical approach: wavefunctions and energy spectrum of the stationary states

Stationary one-dimensional Schrüdinger equation for the confined quantum harmonic oscillator is not explicitly solvable within general known approaches, but, one can obtain approximate solutions for the wavefunctions and energy spectrum of the oscillator quantum system confined between two infinite walls. Explicit solution of the stationary one-dimensional Schrüdinger equation for the confined quantum harmonic oscillator in present paper is based on the assumtion that its effective mass varies with position [7-10]. Then, as we note in Introduction, it is possible to solve the stationary Schrüdinger equation for such oscillator system explicitly for certain type position-dependent mass functions.

Appropriate Hamiltonian of the quantum system with position-dependent mass $M(x)$ has the following form:

$$\widehat{H} = -\frac{\hbar^2}{2}\frac{d}{dx}\frac{1}{M(x)}\frac{d}{dx} + V(x). \tag{9}$$

Then, taking into account that

$$-\frac{1}{2}\frac{d}{dx}\frac{1}{M(x)}\frac{d}{dx} = -\frac{1}{2M}\left[\frac{d^2}{dx^2} - \frac{M'}{M}\right],$$

one can rewrite appropriate Schrüdinger equation of the quantum system with position-dependent effective mass as follows:

$$\frac{d^2\psi}{dx^2}-\frac{M'}{M}\frac{d\psi}{dx}+\frac{2M}{\hbar^2}[E-V(x)]\psi=0. \tag{10}$$

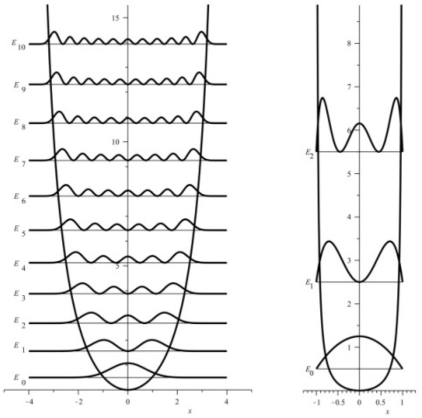

Fig. 1.Behavior of the confined quantum harmonic oscillator potential and its computed corresponding non-equidistant energy levels and probability densities of the ground and a) 10 excited states for value of the confinement parameter $a=4$; b) 2 excited states for value of the confinement parameter $a=1$ $(m=\omega=\hbar=1)$.

Now, it is possible to solve this differential equation of the second order explicitly once for exactly known potential $V(x)$ and position-dependent effective mass $M\equiv M(x)$. We are going to look for the solution of eq.(10) for the harmonic oscillator potential confined with two infinite high walls at values of position $x=\pm a$:

$$V(x)=\begin{cases}\frac{M(x)\omega^2x^2}{2}, & -a<x<a,\\ \infty, & \text{otherwise}.\end{cases} \tag{11}$$

Then, we simply need to solve the following Schrüdinger equation:

$$\frac{d^2\psi}{dx^2}-\frac{M'}{M}\frac{d\psi}{dx}+\left(\frac{2ME}{\hbar^2}-\frac{M^2\omega^2x^2}{\hbar^2}\right)\psi=0. \tag{12}$$

Definition of $M(x)$ in the following analytical expression is one of the possible explicit realizations of the quantum harmonic oscillator confinement model:

$$M(x)=\frac{a^2m}{a^2-x^2}. \tag{13}$$

Eq.(12) can be rewritten in terms of the dimensionless variables and units as follows:

$$\left[\partial_\xi{}^2+\frac{\tilde{\tau}(\xi)}{\sigma(\xi)}\partial_\xi+\frac{\tilde{\sigma}(\xi)}{\sigma^2(\xi)}\right]\psi=0, \tag{14}$$

where, $\xi=x/a$, $\tilde{\tau}(\xi)=-2\xi$, $\sigma(\xi)=1-\xi^2$, $\tilde{\sigma}(\xi)=c_0-c_2\xi^2$, $c_0=\frac{2ma^2E}{\hbar^2}$ and $c_2=c_0+\lambda_0{}^4a^4$.

Eq.(14) can be solved explicitly by applying Nikiforov-Uvarov method for solution of the second-order differential equations of the hypergeometric type [11]. Its solution leads to the following expression of the wavefunctions of the stationary states of the quantum harmonic oscillator confinement model:

$$\psi\equiv\psi_n^a(x)=c_n^a\left(1-\frac{x^2}{a^2}\right)^{\frac{\lambda_0{}^2a^2}{2}}C_n^{\left(\lambda_0{}^2a^2+\frac{1}{2}\right)}(x/a),\qquad c_n^a=2^{\lambda_0{}^2a^2}\Gamma\left(\lambda_0{}^2a^2+\tfrac{1}{2}\right)\sqrt{\frac{\left(n+\lambda_0{}^2a^2+\frac{1}{2}\right)n!}{\pi a\,\Gamma\left(n+2\lambda_0{}^2a^2+1\right)}}. \tag{15}$$

Here $C_n^{(\nu)}(x)$ are the Gegenbauer polynomials defined through the ${}_2F_1$ hypergeometric functions as follows:

$$C_n^{(\nu)}(x)=\frac{(2\nu)_n}{n!}\,{}_2F_1\left(\begin{matrix}-n,n+2\nu;\\ \nu+1/2\end{matrix}\;\frac{1-x}{2}\right),\quad \nu\neq0. \tag{16}$$

Corresponding discrete energy spectrum obtaind from eq.(14) has the following expression:

$$E\equiv E_n^a=\hbar\omega\left(n+\frac{1}{2}+\frac{n(n+1)}{2\lambda_0{}^2a^2}\right),\quad n=0,1,2,\cdots. \tag{17}$$

In Figure 1, we depicted behavior of the confined quantum harmonic oscillator potential (11) and its computed corresponding non-equidistant energy levels (17) and probability densities $|\psi_n^a(x)|^2$of the ground and a) 10 excited states for value of the confinement parameter $a = 4$; b) 2 excited states for value of the confinement parameter $a = 1$ $(m = \omega = \hbar = 1)$. Non-equidistant behavior of the energy levels can be easily observed from this figure. Fig.1b also shows how infinite high walls appear physically for values of $x = \pm a$.

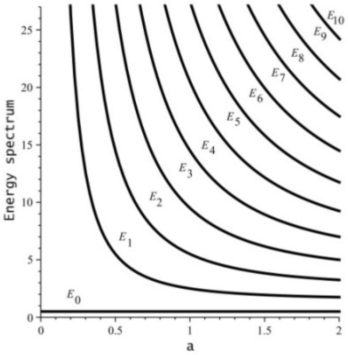

Fig. 2.Dependence of the energy spectrum from the confinement parameter a for the ground and 10 excited states $(m = \omega = \hbar = 1)$.

3. Discussion of results and conclusion

Importance of obtained expressions (15) and (17) is that they are explicit expressions. Then, one can analyse these expressions thoroughly. First of all, it is necessary to note that wavefunctions (15) satisfy the following orthogonality relation:

$$\int_{-a}^{a} \psi_n^{a*}(x)\psi_m^a(x)dx = \delta_{nm}\,. \tag{18}$$

In Figure 2, we present dependence of the energy spectrum (17) from the confinement parameter a for the ground and 10 excited states $m = \omega = \hbar = 1$. From Fig.2 as well as from (6) and (17) it is obvious that ground states of both oscillator models overlap, but, confinement effect adds non-equidistant dependence of the excited energy states from parameter a.

All expressions obtained within the model under study recover correct limit when $a \to \infty$. Simply, it is necessary to use known following limit between Gegenbauer and Hermite polynomials, in order to find correct limit from (15) to (5):

$$\lim_{\alpha\to\infty} \alpha^{-\frac{1}{2}n}\, C_n^{\left(\alpha+\frac{1}{2}\right)}\left(\frac{x}{\sqrt{\alpha}}\right) = \frac{H_n(x)}{n!}.$$

Explicit solution obtained for proposed confined oscillator model allows as a next step to generalize it for solution of the more complex quantum systems under the confinement effect.

References

1. Flugge S., Practical Quantum Mechanics: Vol I (Springer, Berlin, 1971)
2. Ohnuki Y. and Kamefuchi S., Quantum Field Theory and Parastatistics (1982)
3. MacDonald A.H. and Streda P., Phys. Rev. B 29, 1616 (1984)
4. Grinberg M., Jaskolski W., Coepke Cz., Planelles J. and Janowicz M., Phys. Rev. B 50, 6504 (1994)
5. Stevanovic Lj. and Sen K.D., J. Phys. B: At. Mol. Opt. Phys. 41 225002 (2008)
6. Koekoek R., Lesky P.A. and Swarttouw R.F., Hypergeometric orthogonal polynomials and their q-analogues (Springer Verslag, Berlin, 2010)
7. Harrison W.A., Phys. Rev. 123, 85 (1961)
8. Serra L. and Lipparini A., Europhys. Lett. 40 667 (1997)
9. Dong S.-H., Pena J.J., Pachego-Garcıa C. and Garcıa-Ravelo J., Mod. Phys. Lett. A 14 1039 (2007)
10. Jana T.K. and Roy P., Europhys. Lett. 87 30003 (2009)
11. Nikiforov A.F. and Uvarov V.B., Special Functions of Mathematical Physics (1988)

***Corresponding author**: ejafarov@physics.science.az

SOME PARTICULAR SOLUTIONS OF THE MAGNETODYNAMIC TRANSPORTEQUATIONS FOR ONE-FLUID PLASMA OF ANISOTROPIC SOLAR WIND

M.M. BASHIROV [1, 2], N.S. DZHALILOV[1]

[1]Shamakhi Astrophysical Observatory named after Nasraddin Tusi of ANAS, H.Cavid str., 115, Baku, Azerbaijan,AZ1143,

[2]Institute of Radiation Problems of ANAS, B.Vahabzade str.,9, Baku, Azerbaijan, .AZ1143.

Herein, it has been considered the MHD theory of anisotropic solar wind, which takes into account the heat fluxes and the difference between the parallel and perpendicular of the thermal pressures. Some particular solutions have been found for MHD transport equations for one-fluid plasma of an anisotropic solar wind. The found solutions give an idea of the radial dependence of the wind speed and the solutions can be used in the further investigation of the solar wind, in studying the properties, parameters and geometrical dimensions of the heliosphere and cosmic stellar wind.

Keywords. Sun, MHD, solar wind, plasma,corona

PACS: 96.50.Ci, 96.50.Ek, 95.30.Qd

1. Introduction

In1960, the existence of the solar wind was experimentally proved [1], which is theoretically predicted by E. Parker [2] a few years ago from this. Prior to this, it was believed that the atmosphere of the Sun, like other stars (like Earth's atmosphere), is in a state of hydrostatic equilibrium. S. Chapman developed the theory of the static corona [3]. The history of the study of the solar wind is well described in [4]. The magnetohydrodynamic (MHD) description of the solar wind in collisionless plasma was undertaken with certain assumptions in the framework of the MHD CGL approximation [5], which has certain limitations as a learning of shock waves in this approximation, the heat flows, which can significantly change the properties of linear and shock waves did not take into account [6-9]. Heat fluxes are the result of an asymmetric (non-Maxwellian) particle distribution function in plasma, which, according to measurements, more effectively reflects the conditions in the solar wind [10]. Radial and stationary plasma effluxes from the Sun were simulated on the basis of ordinary MHD equations [11]. It was recognized that the complete disregard of parallel heat fluxes for collisionless plasma is not fully justified [5, 13, 14]. In real situations, plasma from the sun solar wind - solar wind is anisotropic and the heat flux should be incluide.

A system of equations for collisionless plasma, including heat fluxes along a magnetic field, was proposed in [12–15]. Linear waves and instabilities were studied using these equations [16–20]. When studying the radial spherical expansion of stationary wind, the problem is reduced to solving a system of three nonlinear ordinary differential equations. It has been foundquotient analytical solution that can be used to find global solutions [21].

In this work, several partial solutions of the system equation describing anisotropic solar wind obtained in [21] were found. The equation differs from common MHD equations and CGL equations in the MHD approximation by two heat fluxes: $S_\perp$ and $S_\parallel$.

2. Basic equations

In the radial plasma propagation $B_\phi = 0$ and $V_\phi = 0$, and if we take into account that all the parameters of the solar wind depend only on the radial distances, then $B = B_r$, $h_r = 1$, $h_\phi = 0$, and after solving the basic equations and taking the plasma propagation to the direction of the magnetic fields that are chosen perpendicular to the surface of the Sun, 6 integral constants and three differential equations [21] were obtained,

$$r^2 B = C_1,\; r^2 \rho V = C_2, \tag{1}$$

$$\frac{V^2}{2} + \frac{1}{\rho}\left(P_\perp + \frac{3}{2}P_\parallel\right) + \frac{1}{\rho V}\left(S_\perp + \frac{1}{2}S_\parallel\right) - \frac{GM}{r} = \frac{C_5}{C_2}, \tag{2}$$

$$r^4 (p_\perp V + S_\perp) = C_1 C_6, \tag{3}$$

$$r^4\rho^2 \frac{d}{dr}\left(\frac{V_r P_\parallel}{r^2\rho^2}\right) + \frac{d}{dr}(r^2 S_\parallel) - 4rS_\perp = 0, \tag{4}$$

$$\frac{1}{V^2}\frac{d}{dr}\left(S_\parallel \frac{V^3}{\rho}\right) + \frac{3}{2}\frac{d}{dr}(\frac{P_\parallel}{\rho})^2 = 0, \tag{5}$$

$$\frac{d}{dr}\left(r^2 S_\perp \frac{V}{\rho}\right) + \frac{P_\parallel}{\rho}\frac{d}{dr}\left(r^2\frac{P_\perp}{\rho}\right) - 2r\left(\frac{P_\perp}{\rho}\right)^2 = 0. \tag{6}$$

Passing to dimensionless quantities and parameters, where $u_\parallel{}^2 = p_\parallel/\rho$ and $u_\perp{}^2 = p_\perp/\rho$ thermal velocities, we obtained [21]:

$$\left(\frac{Y}{X} - 1\right)\frac{dX(x)}{dx} - 2\frac{dY(x)}{dx} + \frac{4}{x^3}Z(x) - \frac{2\bar{g}}{x^2} = 0 \tag{7}$$

$$(\bar{C}_6 - Z(x))\frac{dX(x)}{dx} + (Y(x) - X(x))\frac{dZ(x)}{dx} - \frac{2}{x^3}Z^2(x) = 0 \tag{8}$$

$$\left(\frac{Y(x)}{X(x)} - 1\right)\frac{dY(x)}{dx} + \frac{4}{3}\left(\bar{C}_5 + \frac{\bar{g}}{x} - \frac{\bar{C}_6}{x^2} - \frac{3}{4}X(x) - \frac{3}{2}Y(x)\right)\frac{1}{X(x)}\frac{dX(x)}{dx} + \frac{2}{3x^2}\left(\frac{2\bar{C}_6}{x} - \bar{g}\right) = 0 \tag{9}$$

Where $x = \frac{r}{R}, X = X(x) = \frac{V^2}{v_0^2}, Y = Y(x) = \frac{u_\parallel^2}{v_0^2},\ Z = Z(x) = x^2\frac{u_\perp^2}{v_0^2},\ \bar{C}_5 = \frac{C_5}{C_2 v_0^2},$

$$\bar{C}_6 = \frac{C_1 C_6}{C_2 R v_0^2},\quad \bar{g} = \frac{G M_0}{R v_0^2} \tag{10}$$

Here, v_0– is the characteristic speed for the solar wind (for example, wind speed near the Earth V = V$_E$)):

Denoting$K_1 = \frac{4}{3}\left(\bar{C}_5 + \frac{\bar{g}}{x} - \frac{\bar{C}_6}{x^2}\right),\ \ K_2 = \frac{2}{3x^2}\left(2\frac{\bar{C}_6}{x} - \bar{g}\right)$(11)

it has been obtained equation system for three variables [23]:

$$\left(\frac{Y}{X} - 1\right)\frac{dX}{dx} - 2\frac{dY}{dx} + \frac{4Z}{x^3} - \frac{2\bar{g}}{x^2} = 0 \tag{12}$$

$$\left(\frac{Y}{X} - 1\right)\frac{dZ}{dx} + (\bar{C}_6 - Z)\frac{1}{X}\frac{dX}{dx} - \frac{2Z^2}{Xx^3} = 0 \tag{13}$$

$$\left(\frac{Y}{X} - 1\right)\frac{dY}{dx} + \frac{K_1 - X - 2Y}{X}\frac{dX}{dx} + K_2 = 0 \tag{14}$$

The equation has singularities at X = Y, and as x approaches at infinity, X and Y approach zero. As is seen from (11)$\frac{dK_1}{dx} = 2K_2$, then there is a place in the equation that $K_1\frac{dX}{dx} \sim XK_2 \sim X\frac{dK_1}{dx}$

3. Approach to the solution:

1. Proceeding from this, for solving the system equation, the change of variables was used [23]:

$$X(x) = M(x)K_1(x),\quad Y(x) = N(x)K_1(x)$$

And as a result, a solution for variables was obtained.

$$m = \frac{3}{2}, n = 0, X(x) = mK_1(x) = \frac{3}{2}K_1(x), Y(x) = nK_1(x) = 0,$$

$$Z(x) = \bar{C}_6,\ \text{subject to}\ \frac{2\bar{C}_6}{x^3} = 0 \tag{15}$$

From this it follows that when C$_6$ = 0, the found solution will be a particular solution.

2. The pressure in the solar wind arises due to a change in other wind parameters, since the change in pressure is caused by a change in wind speed. To simplify the equations, we take the variable M. We change another change of variables in the form,

$$Z(r) = \frac{r^3}{4}(2\frac{g}{r^2} + 2\frac{dY(r)}{dr} - M(r)\frac{dX(r)}{dr})$$

Considering(12) we obtine $-\frac{1}{X(r)}\left((M(r)+1)X(r) - Y(r)\right)\frac{dX(r)}{dr} = 0$ (16)

We get two solutions. The first X = C = const, In this case

$$-2\frac{dY}{dx} + \frac{4Z}{x^3} - \frac{2\bar{g}}{x^2} = 0 \quad (17)$$

$$\left(\frac{Y}{\mathrm{C}} - 1\right)\frac{dZ}{dx} - \frac{2Z^2}{\mathrm{C}x^3} = 0 \quad (18)$$

$$\left(\frac{Y}{\mathrm{C}} - 1\right)\frac{dY}{dx} + K_2 = 0 \quad (19)$$

Solving the system, we find the differential equation for Z:

$$Cx^3(2C_6 - gx)\frac{dZ(x)}{dx} + 3Z(r)^2\left(gx - 2Z(r)\right) = 0 \quad (20)$$

Replacing Z with U: $U(x) = \frac{1}{Z(x)}$, $Cx^3(2C_6 - gx)U(r)\frac{dU(r)}{dx} + 3gxU(r) - 6 = 0$

Z and after Y and X can be found by solving this equation.
3. The second condition from (16) we get Y = X(A+1)
For the first approximation, we take A=C to be constant.
Then from (13) we obtain the equation for X:

$$\frac{2}{3}x\left(x^2(C^2 - C - 3)X(x) + \frac{4}{3}C_5x^2 + \frac{4}{3}gx - \frac{4}{3}C_6\right)\frac{dX(x)}{dx} - X(x)(gx - 2C_6) = 0 \quad (21)$$

$$\frac{1}{3}X(x)^2 + \frac{2}{3}\frac{X(x)^2}{x^2}\frac{C_5x^2 + gx - C_6}{C^2 - C - 3} + C1 = 0 \quad (22)$$

From the boundary conditions, C1 = 0 and we get for X:

$$X(x) = \frac{1}{3x^2}\frac{C_5x^2 + gx - C_6}{C^2 - C - 3} = \frac{1}{4}\frac{K_1(x)}{C^2 - C - 3}$$

Considering (16) we obtine $\sum_0^3 b_n x^n = 0$

$$b_3 = 2gCC_5(1 - C^2),\ b_2 = g^2(C+1)^2(C-1),\ b_1 = 2gCC_6(C+1)(11C+3)$$
$$b_0 = -4C_6^2(3C^2 + 4C + 2)$$

Here, we obtain

$$C = -1, \quad C_6 = 0, \quad X(x) = 2\left(C_5 + \frac{g}{x}\right), \quad Y(x) = 0, \quad Z(x) = 0$$

$$C = 1,\ C_6 = 0, \quad X(x) = \frac{2}{3x^2}\left(C_5 + \frac{g}{x}\right), \quad Y(x) = 2X(x), \quad Z(x) = 0$$

With x = r/R, and r_E=1 a.e. =214R, where R is the radius of the sun.

Knowing the parameters for the fast wind, x = 214, $X_E = 1.87$, $Y_E = 0.0187$, $Z_E = 1910$, and the parameters for the slow wind: $X_E = 0.64$, $Y_E = 0.04$, $Z_E = 716$, we can evaluate C_5.

4. Conclusion

In the work, the equation system of three nonlinear differential MHD transport equations for anisotropic solar wind is investigated. It has been found various special solutions of systems. An assumption interpretation of the integral constants in the system of equationshas been introduced. The found expressions and values can be used in the further study of the anisotropic solar wind, while studying the properties, parameters and geometrical dimensions of the heliosphere and cosmic stellar wind.

5. Achnowledgementens

The calculations were carried out for the Maple software package. This work was partially supported by the Foundation for the Development of Science under the President of the Republic of Azerbaijan - **Grant No. EİF-BGM-4-RFTF-1/2017-21/06/1**

References

1. GringauzK.I. and others //Report Academy of Sciences of the USSR..T131.N-6.(1960)
2. ParkerE.N.,Astrophys.,V128,N11,664 (1958)
3. Chapman S., J. Atmos. Terr.Phys.. V 15. N-1/2 (1959)
4. ObridkoV.N., VaisbergO.L., Solar System Res., V51 N 2, 165 (2017)
5. ChewG.F., GoldbergerM.I., LowF.E., Proc. R. Soc. Lond. V. A 236. 112 (1956)
6. NamikawaT., HamabataH., Phys. Lett. V.A 81 (6).339 (1981).
7. NamikawaT., HamabataH., J. Plasma Phys. V 26 (1). 95 (1981)
8. ZakharovV.Y., Questions of magnetic hydrodynamics without collisions in a strong magnetic field. Moscow State University, 48 (1988).
9. KuznetsovV.D., DzhalilovN.S.. FizikaPlazmy. V 35 (11). 1041 (2009)
10. MatteiniL.,LandiS., HellingerP., and other. Geophys. Res. Lett. V34. L20105 (2007)
11. ParkerE. N.,NewYork,IntersciencePublishers,1963,272.
12. OrayevskiV.N., KonnikovY.V., KhazanovG.V.,Transport processes in anisotropic near-earth plasma, Moscow, (1985)
13. RamosJ.J., Phys. Plasmas V10 (9). 3601 (2003)
14. WhangY.M., Geophys. Res.76/31, 7503 (1971)
15. DuhauS., Plazma Physics V32, Issue 1, 23 (1998)
16. DzhalilovN.S., KuznetsovV.D., J. Staude,Contrib.PlasmaPhys.,V51,N.7,621 (2011)
17. JalilovN.S.,KuznetsovV.D., J. Staude,Astron.Astrophys.,V489,N.2,769 (2008)
18. KuznetsovV.D., DzhalilovN.S.,PlasmaPhysicsReports,V35,N11, 962, (2009)
19. DzhalilovN.S.,KuznetsovV.D.,PlasmaPhysicsReports,V36,N9,788, (2010)
20. KuznetsovV.D., OsinA.I., Physics Letters. V. A 382. 2052 (2018).
21. DzhalilovN.S., Aliyev N.A., IsmayilovN.A., Processing of IAM, V3, N1, 3, (2014)
22. KuznetsovV.D., OsinA.N.,GAU MSU, IZMIRAN, IARAN, Astronomy, Solar earth physics- current state and prospects. V2, 118 (2018)
23. BashirovM.M., Journal of Radiation researches. ANAS, V.5, N2, 334 (2018)

Corresponding author:mbashirov01@mail.ru
namigd@mail.ru

STUDYING the E2 TRANSITIONS in the REPRESENTATION of SU(5) SUBGROUP

S. G. ABDULVAHABOVA*, N.SH. BARKHALOVA, T.O. BAYRAMOVA
BakuStateUniversity,Z.Khalilov str., 23,Baku, Azerbaijan, Az1148

The transitional behavior of E2 transition rates, and some other related quantities across the entire subgroup SU(5) are studied in detail. Using this subgroup, we obtained expressions for the Hamiltonian of the nucleus and for the matrix element of the electric quadrupoletransition. As potential, the potential of Hamada - Johnson, which is a local operator, was chosen. The collective and intrinsic degrees of freedom can be mixed through residual terms of the Hamiltonian, such as the rotation - vibration interaction.

Keywords: SU(5) subgroup, boson, E2 transition matrix element.
PACS:31.15.xh; 13.40.Hq; 23.20.Js

1. Introduction

The problem of calculating the energy and other characteristics of the system of identical particles encounters difficulties in constructing the wave function. The vibrational modes can be described either with collective variables or as linear combinations of elementary excitations. In the adiabatic limit both methods yield the same result. The collective and intrinsic degrees of freedom can be mixed through residual terms of the Hamiltonian, such as the rotation -vibration interaction. One of the most effective methods for calculating the characteristics of nuclei with a well-defined permutation symmetry and exact quantum numbers are irreducible representations groups.

The purpose of this paper is to find expressions for the Hamiltonian of the nucleus and for the matrix element of the electric quadrupole transitionin the representation of subgroup SU(5).

2. The matrix element of the E2 transition

The state of a quantum system can be classified according to irreducible representations of symmetric transformation groups with respect to which the properties of the system are invariant. Hamiltonian in SU(5) subgroup representation has terms, describing repulsive boson pairing in d and s states. For this case the Hamiltonian exactly solvable.

In the work [1] using the coherent state formalism considered the evaluation of nuclear shape transition from spherical to axially rotational shapes. This investigation has shown that, when moving from the lighter to heavier isotopes a change form from spherical to deformed nuclei is observed. This fact was confirmed in [2], some isotopes change the form from spherical vibrator to deformed axially symmetric rotor. We proceed from the fact that in Lie algebra there is a subalgebra for the construction of collective variables. Using this subalgebra, one can study the collective states of vibration and, accordingly, the Hamiltonian of the system. In this algebra, it is necessary to introduce a new quantum number N, which in the boson representation determines the number of phonons in vibrational states.

In even-even nuclei with positive parity, the ground state with the moment $L = 0$ and the first excited state with $L = 2$ are realized. The state with $L = 2$ has 5 components and the corresponding bosons are called d bosons.

For our task the following quantum numbers are necessary to classify states: the total boson number N, the total angular momentum L and its z – component M, the seniority v and n_β ,which defines the number boson pairs coupled to zero angular momentum. If we introduce an additional quantum number n_Δ, which determines the number of bosonic triplets with total momentum zero, for the number of bosons$N$ we get the expression:

$$N=2n_\beta+3n_\Delta+\lambda, \tag{1}$$

where λ defines angular momentum L

$$L= \lambda, \lambda+1, \lambda+2, \ldots, 2\lambda -2, 2\lambda. \tag{2}$$

The irreducible representations of the SU (5) group contains all symmetric representations:

$$\lfloor n_\beta = 0 \rfloor, \ \lfloor n_\beta = 1 \rfloor, \ \lfloor n_\beta = 2 \rfloor, \text{ up to } \lfloor n_\beta = N \rfloor. \tag{3}$$

The operator d^+ and d are binary operators of a Lie algebra and with their help one can study the oscillatory motions of the nucleus.They are symmetric operators and the consequence of thiswe can find the exact solution of the Hamiltonian

$$H = \varepsilon \sum_m d_m^+ d_m + \sum_\lambda q_\lambda \left[\left[d^+ d^+ \right]_\mu^\lambda \left[dd \right] \right]_0^0, \tag{4}$$

with eigenvalues

$$\begin{aligned} E([N], n_\beta, v, n_\Delta, L, M) = \varepsilon n_\beta + \frac{1}{14}(3q_4 + 4q_2)N(N-1) + \frac{1}{10}\left[q_0 - \left(\frac{1}{7}(3q_0 + 4q_2) \right) \right] x \\ x\{(N-v)(N+v+3) + \frac{1}{14}(q_0 - q_2)\left[L(L+1) - 6N \right]\}, \end{aligned} \tag{5}$$

where

$$q_\lambda = \left\langle d^2 \lambda \mu | V | d^2 \lambda \mu \right\rangle, \tag{6}$$

λ and μ label representations of SU(3) belonging to the partition [N] of SU(6). The Hamiltonian (4) contains the scalar product of the operators d and d^+, invariant with respect to unitary transformations.

As a potential in (6), we choose Hamad-Johnson potential. The potential of Hamada-Johnson [3] takes into account, in addition to the central, tensor and spin-orbit interactions, the quadratic spin-orbitinteraction:

$$V_{HJ} = V_C(r) + V_T(r) S_{12} + V_{LS}(r)(\vec{L}\vec{S}) + V_{LL} L_{12}, \ L_{12} = \left[\delta_{LJ} + 2S(S+1) - 3 \right] L^2 - (\vec{L}\vec{S})^2. \tag{7}$$

The potentials $V_c(r)$ and $V_T(r)$ are chosen so that at large distances they coincide with the potentials of the meson theory, which take into account the single pion exchange:

$$V_c(r) = 0{,}08(\mu c^2/3)\left[2S(S+1) - 3 \right]\left[2T(T+1) - 3 \right]; \ V_T(r) = 0{,}08(\mu c^2/3\left[2T(T+1) - 3 \right]. \tag{8}$$

Each energy level is degenerate and the multiplicity is

$$k_N = (N+1)(N+2)/2. \tag{9}$$

Therefore, each energy level can be associated with a set of linearly independent functions that are transformed through each other during transformations that leave the Hamiltonian unchanged. This set of*k*-forms the basis of the irreducible representation of the unitary group SU(5).

The study of quadrupole interactions in nuclei is used for characterizing different nuclear states and to obtain information about structural, electric and magnetic properties. Now we illustrate the use above constructed approach for evaluating matrix elements of E2 transition. When the nucleus is deformed it acquires an electric –multiple moments and emits electric radiation. The matrix element of the E2 transitions has following view:

$$M(E2)=\frac{1}{7}(3q_4+4q_2)(d^+s+s^+d)^2_m+\frac{1}{70}(13q_0-10q_2-3q_4)(d^+d)^2_m. \qquad (10)$$

The selection rule for boson operator (d^+s+s^+d) is $\Delta n_\beta=\pm 1$, and for (d^+d) is $\Delta n_\beta=0$. Expression (8) consists of two terms. The first term describes transitions between states with different multiplicities. The second term describes transitions within the same multiplicity to a state with multiplicity L= 2.

Although, SU(5) forbids transitions $\Delta n_\beta=2$, the presence of the $\Delta n_\beta=0$ in the (1), quadrupole moment of the excited state of the even-even nucleus is nonzero. Therefore the low energy 0^+ states are expected to be populated strongly in nuclei having large single-particle quadrupole moments of the same sign in the vicinity of the chemical potential [4]. As an example, the table 1 shows theoretical and experimental values B (E2) for nuclei $^{150,\ 152}$Nd, ^{150,152}Sm and ^{152}Gd. The value of B(E2), which is obtained on the basis of the developed approach, is in good agreement with experimental datathan the results that were obtained in the work [5].

Table1. Theoretical and experimental ratios of the $\frac{B(E2;I+2\to 2)}{B(E2;2\to 0)}$ values for nuclei ^{150,152}Nd,$^{150,\ 152}$Sm and ^{152}Gd. The experimental dates give from [6].

Nuclei	^{150}Nd	^{152}Nd	^{150}Sm	^{152}Sm	^{152}Gd
Theor. data	4.72	6.12	12.05	5.78	51,24
Exper. data	5± 0.3	-	13±2	6± 0.4	52±5

3.Conclusions

The study of nuclear-quadrupole interactions is often used as a powerful tool for obtain information about local symmetry. The symmetry structure of the nuclear system is in general very complex. The Hamiltonian of the system when written in terms of these degrees of freedom has simple symmetry properties. It is worth noting that the knowledge of the invariance properties of the Hamiltonian provides directly a solution to the eigenvalue problem. In this case the related wave functions serve now as a representation space for the groups SU(6)⊃SU(3)⊃O^+(3), and they are characterized by the quantum numbers of the state [7].

In performing numerical calculation we used a space in which only the collective bosons appear with multiplicity single and triplet. One may still suspect that it is necessary to accounting other multiplicities remains severe within the collective branch itself. Comparison of our results with experimental data it was found that our approach is quite promising.

Irreducible representation groups are widely used in physics of elementary particles. We expect on a qualitative basis that the application of subgroup SU(5) will open up new physical possibilities for the study of collective movements of the nucleus.

References

1. Khalaf A.M. and Awwad T.M., Progress in Physics, V.1, 7 (2013)
2.Turner P.S. and Rowe D.J., Nuclear Physics, V. A 756, 333 (2005)
3.Zotov N.P., Rusakov S.V., Tsaryev V.A., PEPAN , V 11 (5), 1160 (1980)
4.Abdulvahabova S.G.,Phys. Lett. , V38 B, 215 (1986)
5.Abdulvahabova S.G.,ANAS, Physics, 20 (2005)
6.Kumar K.,Phys.Rev.Lett., V26, N 9, 269 (1997)
7.Arima A., Iachello F., Phys. Rev. Lett., V36, N.16, 1069 (1985)

***Corresponding author**:sajida.gafar@gmail.com

PRECISE DIFFUSION COEFFICIENT FOR PLANETARY NEBULAE AND ITS RELATION TO DYNAMIC AGE

A.G.ALILI, K.I.ALISHEVA, D.M.KULI-ZADE*
BakuStateUniversity, Z.Khalilov str., 23, Baku, Azerbaijan, Az1148

Study of physical phenomena running in substances of shells thrown by stars allows deeply penetrating into the nature of stars. Researchofshelllightenablestojudgeabouttheenergyradiatedbyastarondifferentspectral regions, but study of motions of shells – about the processes. Physical processes in shells of planetary nebulae are of special interest. The present work studies radiation attenuation of a central star in shells of planetary nebulae, as well as their more precise value is determined. Furthermore, we have constructed dependence diagram of radiation attenuation coefficient on dynamic age of planetary nebulae.

Keywords:planetary nebulae, dynamic age, radiation attenuation.
PACS: 98.38.Ly, 98.35.Ac

1.Introduction

As it is known, planetary nebulae lights are wholly caused by central stellar radiation. Since their cores are very hot, the main radiation share falls on far ultraviolet spectral region. Radiation coming from a star into shell has an extra small density. After entering into gas shell, the processing of a strong high-frequency radiation of stars to quanta of small frequencies occurs, as a result, the radiation coming from a star weakens. This radiation attenuations characterized by dilution coefficient W, that shows which share radiation the energy density$\rho_\nu$with frequency ofν makes in given space point from the value during thermodynamic equilibrium of radiation energy density ρ_ν^* at the temperature of radiation source. If we assume that central star radiates as an absolute blackbody with density of energy flux ρ_ν^* , then density of radiation fluxρ, passing through nebula will be less than under smaller solid angle the star of this nebula point will be seen [1]

$$\rho_\nu = \frac{\Omega}{4\pi}\rho_\nu^* \qquad (1)$$

where W isdilutioncoefficientcharacterizingtheattenuationofradiationfluxdensityofacentralstarinnebulae. IfR_* - stellar radius, and R – distance to it, then the star will be seen under solid angle

$$\Omega = 2\pi\int_0^{\theta_0}\sin\theta\, d\theta = 2\pi(1 - cos\theta_0). \qquad (2)$$

From the other side it is known that radiation energy density ρ_ν is amount of electromagnetic radiation energy in unit interval of frequency near frequency ν and in unit element of volume. It is determined by the intensity of I_ν radiation which occurs in given element of volume from all sides:

$$\rho_\nu = \frac{1}{c}\int I_\nu d\,\Omega\,. \qquad (3)$$

θ_0 – angular size of a star. Thus, we obtain the expression for dilution coefficient:

$$W = \frac{1}{2}\left[1 - \sqrt{1 - \left(\frac{R_*}{R}\right)^2}\right]. \qquad (4)$$

Theradiationcomesinsideastarfromallsidestoanypointapproximatelycharacterizedby Planck law. Therefore, W=1. In stellar atmosphere where such radiation comes only from half-space, $\approx {}^{1}/_{2}$by removing from a star at $R \gg R_*$,

$$W = \frac{1}{4}\left(\frac{R_*}{R}\right)^2. \qquad (5)$$

Average radii of planetary nebulae are turned to be in the order of 10^{17} cm. Radii of cores of planetary nebulae have still been accepted, on average, 10^{10} cm. therefore, it was accepted that radiation density in planetary nebula has weakened approximately 10^{14} times comparing with radiation density on the surface of star.

We have suggested an expression to calculate radii of cores of planetary nebulae. The essence of the determination method of radius of central stars of planetary nebulae, optically thick in Lyman continuum, during their full filling with ionized substance is the following. Since in optically thick nebula each quantum of L_c, which release score beyond hydrogen of Lyman series, is divided into quantum L_α, quantum of Balmer series and quanta of other subordinate series, then observed number of Balmer quanta will be equal to the number of L_c - quanta, irradiated by stars:

$$\int_{x_o}^{\infty} \frac{x^2 dx}{e^x - 1} = \sum_{Ba} A_i \frac{x_i^3}{e^{x_i} - 1} . \qquad (7)$$

$x = \frac{h\nu}{kT_*}, x_i = \frac{h\nu_i}{kT_*}, x_o = \frac{h\nu_o}{kT_*}$, where ν_o – frequency of boundary of Lyman series, ν_i – frequency of Balmer line, T_* - effective temperature of central star. Value A_i nondimensional ratio, which is expressed by full energy irradiated with nebula in I Balmer line and energy irradiated by a star in unit interval of frequencies near this line and is expressed as:

$$A_i = \frac{n_i A_{i2} hV}{4\pi^2 I_{\nu_i}^* R_*^2} . \qquad (8)$$

where A_{i2} – Einstein coefficient of spontaneous transitions, V–volume of nebula, glow in gin hydrogen lines, n_i– concentration of hydrogen atoms in I state, R$_*$ -radius of central star, $I_{\nu_i}^*$ – average Planck radiation intensity. So, considering the formulas (8) and Planck intensity, as well as ratio for $V = {}^4\!/_3 \pi R^3 \varepsilon$, the right part of equality (7) can be presented as:

$$\sum_{Ba} A_i \frac{x_i^3}{e^{x_i} - 1} = 5.4 \cdot 10^{-12} \frac{\varepsilon R^3}{T_*^3 R_*^2} \sum n_i A_{i2} ,$$

where

$$\sum_{i=3}^{\infty} n_i A_{i2} = 3.2 \cdot 10^{-16} \frac{n_e^2}{T_e^{3/2}} \sum_{i=3}^{\infty} i^2 A_{i2} e^{\chi_i / kT_e} .$$

Therefore

$$\sum_{Ba} A_i \frac{x_i^3}{e^{x_i} - 1} = \frac{2 \cdot 10^{-27} n_e^2 \varepsilon R^3 \sum_{i=3}^{\infty} i^2 A_{i2} b_i e^{\chi_i / kT_e}}{T_*^3 T_e^{3/2} R_*^2} . \qquad (9)$$

The left part of equality (7), can be expressed in the following way

$$\int_{x_0}^{\infty} \frac{x^2 dx}{e^{x_i} - 1} = \sum_{n=0}^{\infty} \int_{x_0}^{\infty} e^{-(n+1)x} x^2 dx = \sum_{n=0}^{2} e^{-(n+1)x_0} \left[\frac{x_0^2}{n+1} + \frac{2x_0}{(n+1)^2} + \frac{2}{(n+1)^3} \right] . \qquad (10)$$

Considering that

$$n_e \varepsilon^{1/2} = \left\{ 2.33 \cdot 10^{41} \left[F(H_\beta)\, t^{0.88} / \theta^3 d \right] \right\}^{1/2} ,$$

Where $F(H_\beta)$ – radiation flux in units of 10^{-11}erg/cm^2, θ–angular size in seconds of arc, d– distance in kps, $t=10^{-4} T_e$. Then we will get [14]

$$R_*^2 = \frac{0.23^2 t^{0.88} d^2 F(H_\beta) \sum_{i=3}^{10} i^2 A_{i2} b_i e^{\chi_i / kT_e}}{T_*^3 T_e^{3/2} \sum_{n=0}^{2} e^{-(n+1)x_0} \left[\frac{x_0^2}{n+1} + \frac{2x_0}{(n+1)^2} + \frac{x_0}{(n+1)^3} \right]} .$$

Table 1 in column 10 shows the data of W, calculated by (5), in columns 10 and 11expansion velocity and dynamic age of planetary nebulae are given.

Table 1

№	Nebula	T_* 3,5,8,9,11	T_e 4,9,10	d (kpk), 3,5,6,8,11,13	θ(''), 2,3,7,12	R_*, 10^9 (sm)	R, 10^{17}, (sm)	W, 10^{-18}	V_{exp}, 3,10,12	d, (age)
1	NGC 246	150000	12000	0,5	112	0,49	8,38	0,08	11,84	22113,46
2	NGC 4361	126000	23000	0,95	81	1,28	11,51	0,31	13,26	27132,23
3	NGC 40	48000	10600	0,8	18,2	34,04	2,18	6104,14	25	2722,96
4	NGC 1360	105000	18000	0,38	192	0,7	10,92	0,20	11,34	30080,99
5	NGC 1535	80000	11000	2,1	9,2	8,21	2,89	201,72	12,09	7471,39
6	NGC 2392	47000	14600	1,5	44,82	26,73	10,06	176,62	40	7858,21
7	NGC 2440	188400	15000	1,36	16,4	2,16	3,34	10,46	25	4171,22
8	NGC 2792	130000	14000	1,9	6,5	4,47	1,85	146,32	20	2887,07
9	NGC 2867	141000	8950	2	7,6	3,47	2,27	58,21	16,03	4433,33
10	NGC 3211	162000	12000	2,901	8	1,49	3,47	4,63	27	4018,78
11	NGC 3918	140000	12700	1,84	18,78	5,27	5,17	25,93	25	6462,40
12	NGC 5315	51000	8600	2	3,05	62,92	0,91	118825,56	40	713,00
13	NGC 5882	68000	9400	1,2	13,98	15,64	2,51	970,72	38	2064,07
14	NGC 6445	170000	13000	1,39	16,6	5,89	3,45	72,90	38	2838,96
15	NGC 6543	60000	7900	1	37,38	21,41	5,59	366,23	20	8738,36
16	NGC 6572	80800	10400	1,86	35,82	7,03	9,97	12,43	18	17305,59
17	NGC 6720	148000	10700	0,7	69,18	1,22	7,25	0,70	15,29	14807,83
18	NGC 6741	144400	12600	1,9	3,9	9,15	1,11	1703,89	23	1506,30
19	NGC 6853	135000	12000	0,38	100	1,49	5,69	1,72	13,99	12699,49
20	NGC 6886	164600	13000	2,6	3,7	1,88	1,44	42,68	16	2811,09
21	NGC 7009	87000	7200	1,45	13,4	9,95	2,91	293,01	25	3633,73
22	NGC 7026	130500	9200	1,5	5,6	3,07	1,26	149,20	27	1454,57
23	NGC 7027	175000	8000	0,89	6	2,42	0,80	230,32	14	1783,34
24	NGC 7662	126400	12200	1,2	15,42	3,69	2,77	44,52	27	3204,22
25	IC 2165	134000	14600	1,5	7,98	3,80	1,79	112,58	20	2798,24
26	J 900	116000	12100	4,3	3	2,52	1,93	42,70	18	3350,72
27	NGC 6818	145000	13400	2	9,4	3,27	2,81	33,82	27	3255,48
28	BD+30	32000	8000	1	2,5	143,33	0,37	3671090,57	26	449,56
29	NGC 2438	114000	10900	1,2	35,2	1,53	6,32	1,47	16,82	11741,36
30	NGC 6563	123000	10600	1,67	22,6	1,96	5,65	3,00	11	16041,78
31	NGC 6772	135000	12000	1,2	45	1,28	8,08	0,63	25	10098,90
32	NGC 6781	112000	10000	0,95	35	1,66	4,97	2,77	20	7772,88
33	NGC 6565	67000	8000	4,66	4,5	12,41	3,14	391,21	29	3380,81
34	NGC 7293	110000	11000	0,22	804	1,34	26,46	0,06	21	39380,37
35	A 31	85000	12000	0,48	486	1,36	34,90	0,04	29	37609,70
36	A 84	100000	12000	1,68	63	1,22	15,84	0,15	16	30927,89
37	K 1-22	115000	10200	1,33	90,5	0,78	18,01	0,05	28	20098,45
38	K 2-2	67000	12000	0,3	312	0,65	14,00	0,05	12	36468,26
39	Pw -1	94000	12000	0,37	353	0,69	19,54	0,03	23	26550,27
40	Jn -1	93000	12000	0,9	166	0,71	22,35	0,03	24	29104,47
41	NGC 6567	47000	11510	3,652	4,4	45,23	2,40	8850,60	19	3954,12
42	NGC 6578	63000	8250	3,68	4,3	18,73	2,37	1564,57	17,2	4301,38
43	NGC 6884	114800	11000	2,55	3	4,91	1,14	460,96	17	2103,94
44	NGC 7048	148000	12600	1,97	35	0,70	10,32	0,12	15	21491,34
45	NGC 7094	110000	17700	1,39	47,5	0,60	9,88	0,09	13,61	22681,44

46	NGC 7139	117000	10300	2,4	38	4,32	13,64	2,51	40	10659,95
47	IC 2448	85000	12500	1,4	20,82	11,00	4,36	159,15	14,26	9556,74
48	NGC 6153	109000	9200	1,1	11,7	5,55	1,93	207,59	17	3539,57
49	NGC 6894	100000	10200	1,31	27,5	1,94	5,39	3,23	25	6737,28
50	A13	113000	10200	1,93	76,3	0,66	22,03	0,02	20	34424,87
51	Pe1-1	85700	10320	5,47	1,5	17,72	1,23	5210,11	24	1598,41
52	NGC2899	215000	14900	1,37	45	0,58	9,22	0,10	25	11529,58
53	IC 1297	91000	10540	4,1	7,02	7,37	4,31	73,26	32,7	4115,23
54	A 33	100000	12800	1,16	134	0,90	23,26	0,04	32	22710,84

Diagram shows the dependence between coefficient of radiation attenuation and dynamic age of planetary nebulae.

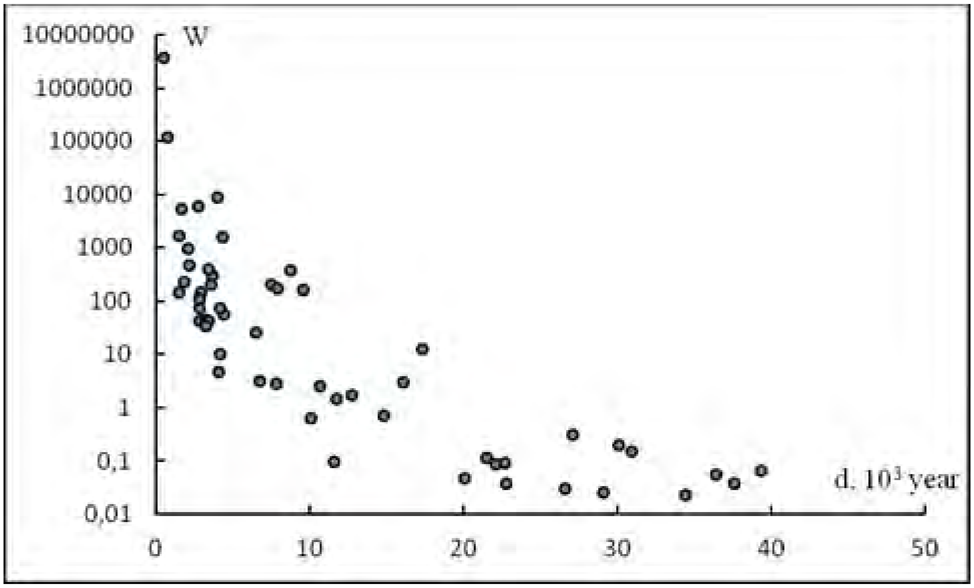

Conclusion

Thus in the research work the calculations once again confirm the accuracy of calculations of radii, radiation is also strengthened, i.e. the more age, the less radiation.

References

1. V.V.Sobolev, Course on theoretical astrophysics, 1975, 504p.
2. Letizia Stanghellini and Richard A. Shaw, The magellanic cloud calibration of the galactic planetary nebula distance scale, The Astrophysical Journal, 689,194 (2008)
3. David John Frew, Planetary Nebulae in the Solar Neighbourhood: Statistics, Distance Scale and Luminosity Function, 2008, 477p.
4. Yu. V. Milanova and A. F. Kholtygin, Astronomy Letters, 35, 518 (2009).
5. S.R. Pottasch and J. Bernard-Salas, Astronomy & Astrophysics, 517, A95 (2010).
6. C. Giammanco, S. E. Sale, R. L. M. Corradi and etc.,Astronomy & Astrophysics, 525, A58 (2011).
7. R. Ortiz1, M.V.F. Copetti and S. Lorenz-Martins, Monthly Notices of the Royal Astronomical Society, 418, 2004 (2011).
8. R. Jacob, D. Schünberner, and M. Steffen,Astronomy & Astrophysics, 558, A78 (2013).
9. Ashkbiz Danehkar, Evolution of Planetary Nebulae with WR-type Central Stars, 2014, 556p.
10. Gloria D.I. and Monica R., The Astrophysical Journal, 784, 173 (2014).

11. Thomas R., Klaus W. and etc., The Astronomical Journal, 147, 142, (2014).
12. David J. F., Q.A. Parker and I.S. Bojicic, Monthly Notices of the Royal Astronomical Society, 455, 1459 (2016).
13. Manuel Moreno-Ibbsez, Eva Villaver, Richard A. Shaw and Letizia Stanghellini, Astronomy & Astrophysics, 593, A29 (2016).
14. Alisheva K.I., Alili A.G., Modern Trends in Physics, 16 (2017).

***Corresponding author**: galaktika2002@mail.com

Hα AND Hβ LINES IN THE SPECTRUM OF THE Ae HERBIG STAR HD 190073

G.R.BAHADDINOVA[1,2], U.Z.BASHIROVA,[1]N.Z.ISMAILOV[1]
[1]*AMEA, Shamakhy Astrophysical Observatory named after N.Tusi, Y.Mammadaliyev Settl., Shamakhy, Azerbaijan, AZ 5626*
[2] *Western Caspian University,A.Rajabli st. 17 A, Baku, Azerbaijan, AZ 1072*

In this paper we have presented results of research the time variability of the line profiles of Hα and Hβ in the spectrum of Herbig Ae/Be type star HD190073. The Hα line profile consists of an emission peak, in which two separate components are barely distinguished at the top. The blue wing of the line is flatter than the red. On the blue wing there is a wide and shallow absorption. The asymmetry in the profile shows that there is both accretion and outflow of matter on the circumstellar disk.

The Hβ line profile has the same structure as the Hα line (Fig.1). However, on this line, the emission is in the core of the line and broad photosphere wings characteristic of class A stars stand out well. Minor asymmetry is also observed on the profile of this line.

We have discovered a change in the radial velocities of the emission component of the line in the time scale of about 45 days. This is accompanied by a decrease in the equivalent widthof the emission Hα. This shows that it is possible an eruptive process is occurred on the surface of the star.

Key words: Pre-Main Sequence –stars: HAeBe – stars: circumstellar matter, spectral variability, individual: HD 190073
PACS: 95.30.Ky; 95.75.Fg; 95.75.Mn

1. Introduction

Herbig Ae/Be (HAeBe) stars are the intermediate-mass (∼2–10 $M_\odot$) pre-main sequence counterparts of T Tauri stars (TTSs). Classically defined, they are spectral type A or earlier, show emission lines in their spectra, placed in obscured regions, and illuminate surrounding nebulosity [1]. The spectroscopic monitoring of some sources [2],[3],[4] revealed that the spectra of HAeBe objects are not only characterized by the presence of emission lines, but also by the complex variations observed in both the emission and absorption features. This variability is also characteristic of T-Tauri stars [5],[6].

V1295 Aql (HD190073, MWC325, A2IIIe – B9IIep+sh) is a very remarkable early-type object with rich emission lines in the visible spectrum. HD190073 was variously classified as a peculiar Bep star [7] or as an evolved post-main sequence A giant [8]. Recently HD190073 has gained recognition as a young Herbig Ae/Be star [9],[10]. In spite of being situated in the constellation of Aquila rather far from well-known regions of star formation, it displays a large far-IR excess due to thermal radiation of cool circumstellar (CS) dust [11]. The energy distribution of HD190073 in this spectral region is similar to that of well-known Herbig Ae stars, like AB Aur, HD163296 and HD31648 [12].

Alicia et al. [13]identified stellar parameters for V1295 Aql. The star has a magnetic field, ∼100 G, which has been detected and confirmed by many authors over several years [14], [15], [16]. As described in [13] from MIKE spectra $Vr = -1.2 \pm 1.3$ km s^{-1} and $v \sin i = 3.19 \pm 2.45$ km s^{-1}. Effective temperature is $Teff = 9250 \pm 250$ K, Mass is $M=2.9 \pm 0.5M_\odot$, radius is $R= 3.6 \pm 0.5M_\odot$. Variability was observed, indicating a change in the star's magnetic field structure.

In this work we have presented some results of monitoring of the hydrogen Hα and Hβ lines variation of the Ae type star V1295 Aql.

2. Observations

The spectra were taken in 2015–2017 in the Cassegrain focus of the 2-m telescope of Shamakhy Astrophysical Observatory of Azerbaijan National Academy of Sciences. We have used two spectrographs. First of them MUAGS was used in combination of CCD 530x580. Spectral resolution is R~14000 in the range λ4700-6700 Å. This system was used in 2015. Second spectrograph ShAPES works with CCD 4Kx4K, spectral resolution is R~28000 in wavelength range λ3700-8000Å [17]. The mean signal-to-noise level is S/N = 100in the region of the Hα line, and S/N = 10-20 in the region of the Hβ line. Wavelength calibration was based on the sky spectrum. We used the DECH20T software to perform all the image reduction tasks and subsequent measurements of the spectra.

We acquired a total of 35 pairs of spectrograms of the star for 2015-2017 years. The errors of the measured equivalent widths and intensities were equal to 5% and about 1%, respectively. The mean error of position measurements in the spectra of standard stars was 1–3 km/s.

3. Results

As can be seen from Fig. 1, the Hα line profile consists of an emission peak, in which two separate components are barely distinguished at the top. The blue wing of the line is flatter than the red. On the blue wing there is a wide and shallow absorption. The asymmetry in the profile shows that there is both accretion and outflow of matter on the circumstellar disk.

The Hβ line profile has the same structure as the Hα line (Fig.1). However, on this line, the emission is in the core of the line and broad photosphere wings characteristic of class A stars stand out well. Minor asymmetry is also observed on the profile of this line.

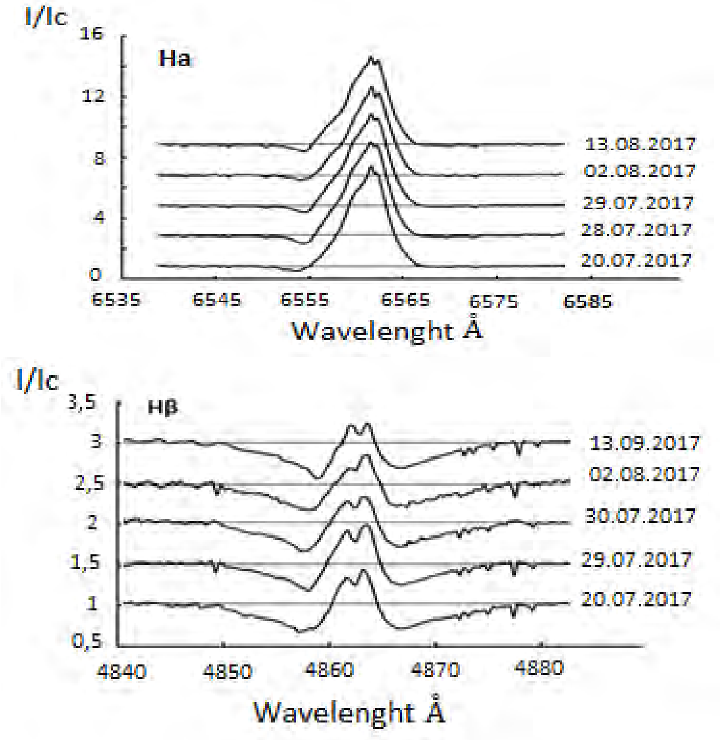

Figure1. Normalized profiles of the Hα and Hβ line observed in the spectrum of HD 190073 in 2017.

Figure 2 shows the change in the values of the parameters RV, EW and FWHM over time. As can be seen, with relatively stable values of EW (22 ± 2Å), we found a significant change in the bisector radial velocity of the emission component of the Hα line (29 ± 7 km/s). The parameter FWHM also has a spread around the average 4.56 ± 0.29 Å.

In Figure 2 it is evident that, starting with JD2457230, the RV shows a red shift to a maximum in JD2457244, and then a slow return to the previous level, having reached it approximately in JD2457275. In this case, the values of EW and FWHM minimum. This shows that during about 45 days a certain movement of matter and a change in intensity in radiation occurred in the star's disk.

As can be seen from Fig.3 radial velocities show seasonal changes within ± 15 km/s. According to the data of 2015, we identified the above variability of radial velocities (Fig. 2). The same variation we can see in the parameters EW (±5 Ǻ) and FWHM (±1 Ǻ). Moreoverthe mean values of the mentioned parameters are demonstrated variation from year to year. Similar type variations we have discovered in the line Hβ.

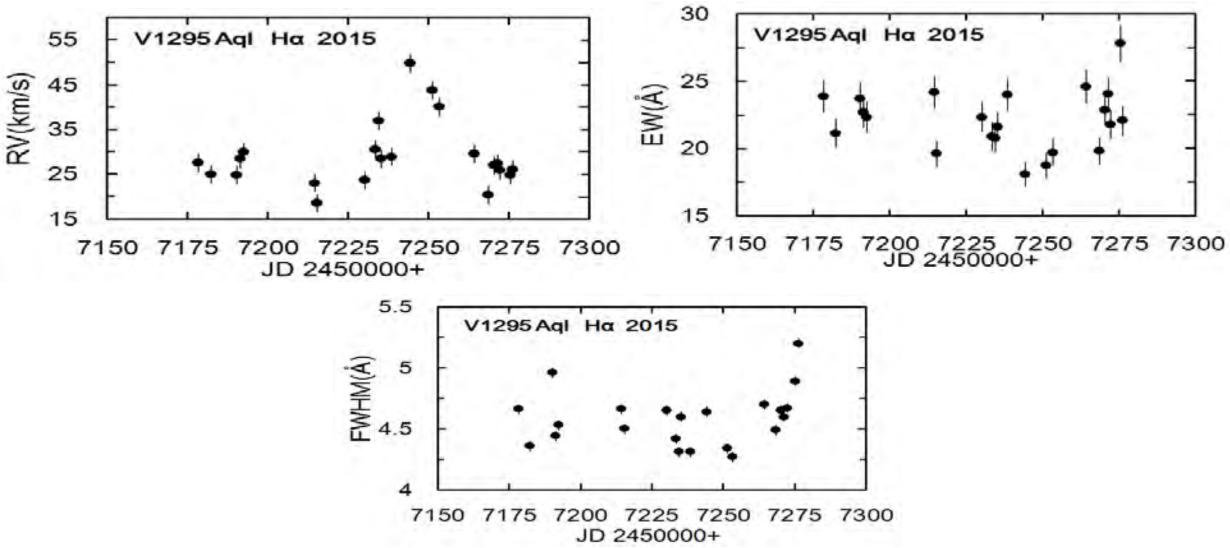

Figure.2. The time variability of radial velocity in halve-widths level(left top panel), equivalent wide (right top panel) and FWHM (bottom) of the Hα emission line in 2015.

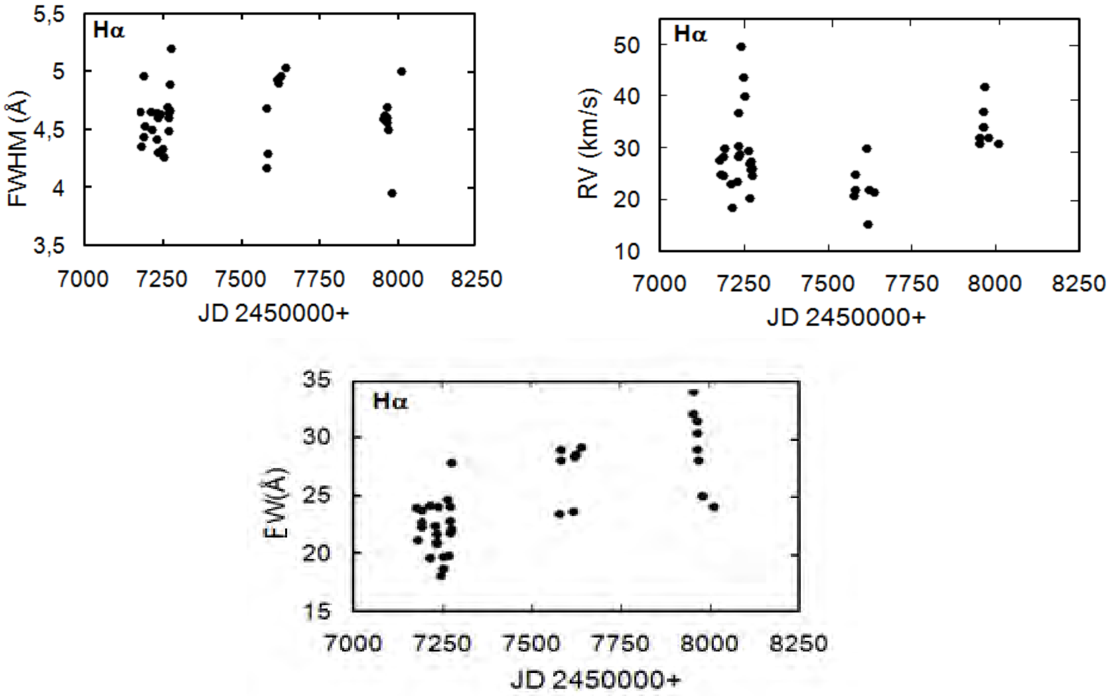

Figure3. The time variability of radial velocity in halve-widths level (right top panel), FWHM (left top panel) and equivalent wide (bottom) of the Hα emission line in 2015-2017.

4. Conclusion

It was discovered a change in the radial velocities of the emission component of the line in the time scale of about 45 days. This is accompanied by a decrease in the equivalent widthof the emission Hα. This shows that it is possible an eruptive process is occurred on the surface of the star.

References

1. Herbig G.H.,The Astrophysical Journal Supplement Series, 4, 337 (1960)
2. Praderie F., Simon T., Catala C., & Boesgaard A.M.,The Astrophysical Journal Letters, 303, 3 (1986)
3. Pogodin M. A., Astronomy & Astrophysics, 282, 14 (1994)
4. Rodgers B., Wooden D.H., Grinin V., Shakhovsky, D., & Natta, A.,The Astronomical Journal,564, 405 (2002)
5. Johns C. M., &Basri G., The Astronomical Journal, 109, 2800 (1995)
6. Schisano E., Covino E., Alcalb J.M., et al.,Astronomy & Astrophysics, 501, 1013 (2009)
7. Allen D. A., & Swings J. P., Astronomy & Astrophysics, 47, 293 (1976)
8. Cuttela M., & Ringuelet A. E., MNRAS, 246, 20 (1990)
9. Cidale L., Zorec J., & Morrell N.,The BePhenomenon in Early-Type Stars, ASP Conf. Ser., in IAU Colloq.175, 214, 87 (2000)
10. de Winter D., van den Ancker M. E., Maira A., et al., Astronomy & Astrophysics,380, 609 (2001)
11. Sitko M. L., The Astrophysical Journal Letters, 247, 1024 (1981)
12. Malfait K., Bogaert E., & Waelkens C.,Astronomy & Astrophysics, 331, 211 (1998)
13. Alicia N. Aarnio, John D. Monnier, et al.,The Astrophysical Journal Letters, 18, 34 (2017)
14. Hubrig S., Yudin R.V., Sch¨oller M., Pogodin M.A., Astronomy & Astrophysics, 446, 1089 (2006)
15. Hubrig S., Stelzer B., Sch¨oller M., et al., Astronomy & Astrophysics, 502, 283 (2009)
16. Catala C., Alecian E., Donati J. F., et al., Astronomy & Astrophysics, 462, 293 (2007)
17. Mikayilov Kh.M., Musayev F.A.,et al., Azerbaijan Astronomical Journal, 12(1), 4 (2017)

***Corresponding author:** gunelbahaddinova@gmail.com

THE METHOD OF ATMOSPHERIC CORRECTION OF SATELLITE IMAGES.RESTORE SPECTRAL BRIGHTNESS OF THE EARTH'S SURFACE

F. I. ISMAILOV

Shamakhy Atrophysical Observatory named after N. Tusi Azerbaijan National Academy of Sciences, Shamakhy, Azerbaijan Republic, Y. Mammadaliyev settlement, AZ5626

The article presents an optical model of the altitude distribution of aerosol layers of the atmosphere in the lower atmosphere, developed by the author on long-term optical data. On the basis of this model, the problem of atmospheric correction of satellite images and restoration of the spectral reflection coefficient of reflected solar radiation for the Caspian-Caucasian region is solved. The problem of restoration of microstructural parameters of the optically active accumulative fraction of atmospheric aerosol is considered simultaneously in the article.

Keywords: Aerosol layer, Aerosol optical model, Satellite imagery, Spectral brightness coefficient, The Caucasus-Caspian region
PACS:84.60.Jt; 73.50.Pz; 79.60.Jv

1.Introduction

Satellite images practically contain the most complete and accurate information about the earth's surface. The solution of this problem is closely connected with the development of regional optical atmospheric models, which allows solving the problem of atmospheric correction of satellite images, taking into account the temporal and geographical conditions of the observation site [1, 2, 3].

The optical properties of the atmosphere in a cloudless atmosphere are practically determined by the presence of an aerosol in it. The important property of atmospheric aerosol is layered or tiered structure of the altitude distribution of atmospheric aerosol observed for all geographical latitudes and seasons of the year. Such stratification suggests the existence of levels of increased concentrations of particulate matter, on which there are optimal conditions for the generation and accumulation of these particles in the atmosphere itself [2].

In view of the rather wide variety and randomness of the aerosol variability processes in the atmosphere, it is evident that, when modeling we have to use certain simplifying assumptions. Below, relative the layered structure of the atmospheric aerosol, we believe the following assumptions:

1) for aerosol layers apply the plane parallelmodel of the atmosphere,

2) azimuthal dependence of the aerosol light scattering characteristics are neglected, i. e. aerosol layers relied horizontally homogeneous,

5) near the corner of sight completely absent the cloud cover.

For the purpose of practical application the developed model in this paper below performed numerical calculations for atmospheric correction of satellite images of the eastern Caucasus and AbsheronPeninsula. For this use long-term data of measuring the brightness daytime cloudless skies in the effective wavelength λ=0,55mkmof solar radiation [4-7].

2 Optical model of aerosol vertical structure

The optical model of the atmosphere is determined by the parameters of the task: the optical thickness of $\tau(h)$, the scattering function $\mu(\theta)$, where h-height in the atmosphere. Altitude profiles $\tau(h)$, $\mu(\theta)$ in the visible region of the spectrum defined by the layered structure of aerosol layers of the atmosphere. High-rise distribution of the optical thickness of the plane - parallel aerosol layers will be determined in the form of:

$$\tau(h) = \int_h^\infty \sigma(h')dh' , \qquad (1)$$

where$\sigma(h) = d\tau(h)/dh$ is the optical density (scattering coefficient) atmospheric aerosol at level h.

Scattering function $\mu(\theta)$can be written as:

$$\eta(\theta) = \frac{\tau}{4\pi}\gamma(\theta) \quad , \tag{2}$$

where$\gamma(\theta)$ is the normalized scattering function; θ is the scattering angle,μ =arccos$Z$ is the cosine of the zenith angle Z of observation, $\varphi$is the azimuth angle of direction of propagation relatively the solar vertical, $\theta = -\ \mu\mu_0 + \sqrt{(1-\mu^2)^0(1-\mu_0^2)}\cos\varphi$; Z_0 = arccosμ_0 is the zenith angle of the sun. Parameters $\tau(h)$, $\gamma(\theta)$ are represented as the sum of the Rayleigh and aerosol components:

$$\tau(h) = \tau_r(h) + \tau_a(h), \tag{3}$$

$$\eta(h,\theta) = \frac{\tau_r(h)\eta_r(\theta) + \tau_a(h)\eta_a(\theta)}{\tau_r(h) + \tau_a(h)}, \tag{4}$$

here$\tau_r(h)$ and $\eta_r(\theta)$ is the molecular (Rayleigh) scattering and aerosol components.

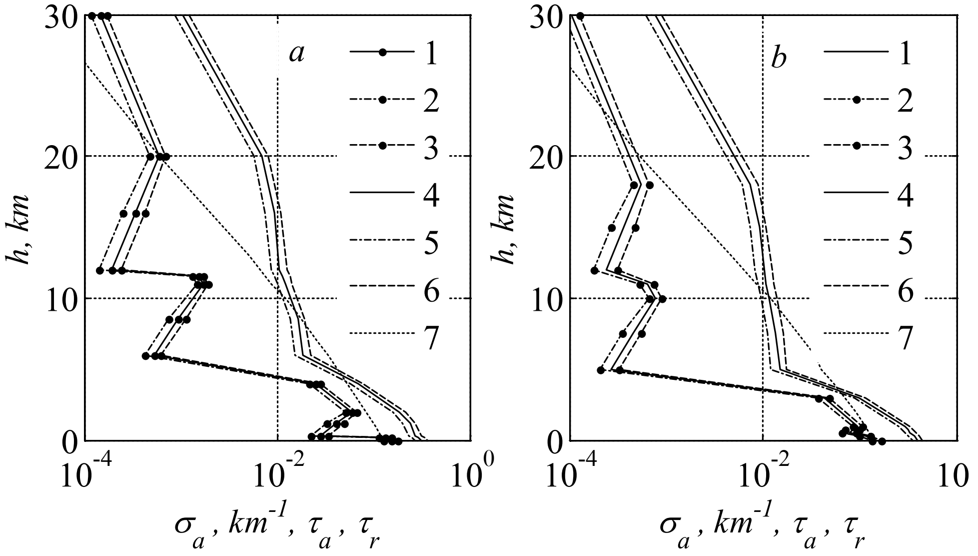

Fig.1 Average vertical profiles (at 0, 55 *mkm*) of the scattering coefficient $\overline{\sigma}_a(h)$ (4-6) and optical thickness $\overline{\tau}_a(h)$ (1-3) of the atmosphere aerosol layers, as well as the optical thickness of of the molecular (rayleigh) scattering $\overline{\tau}_r(h)$ (7) for summer (a) and winter (b) conditions; 1 and 4 are means, 2 and 5 are minimal, 3 and 6 are maximum values accordingly, of the $\overline{\sigma}_a(h)$, $\overline{\tau}_a(h)$ quantities.

To calculate the parameters of (3) and (4) we will use the regional model developed by us, given on [2]. Based on this model in Fig. 1 shows the results of numerical calculations of average vertical profiles of optical density and the optical thickness of the atmosphere for the conditions of the Caucasian-Caspian region.Scattering indicatrix$\gamma(\theta)$ in (2) is determined for altitude profiles of the aerosol according to Fig. 1and from the Scattering function $\eta(\theta)$ measurements of the optically active submicron aerosol particles. The results of the reconstruction of the indicatrix$\gamma(\theta)$from the results of our measurements [6, 7] are given in fig.2. The form of the indicatrix in this figure depends on the disperse structure of the aerosol [6].

3. The spectral brightness coefficient (SBK) system "atmosphere-earth's surface"

The main angular and spatial characteristics of the reflected radiation, of the perceived satellite sensor is the SBC system "atmosphere-earth surface" $\rho(\tau;\mu_0,\mu)$ to the optical depth τ[1, 2]:

$$\rho(\tau;\mu_0,\mu)==L(0;\mu,\varphi)/F_0\cdot\mu_0=\rho_{at}(\tau;\mu_0,\mu)+\frac{T^{\downarrow}(\tau,\mu_0)T^{\uparrow}(\tau,\mu)\rho_0(\tau^*;\mu_0,\mu)}{1+\rho_0(\tau^*;\mu_0,\mu)A^{\downarrow}(\mu_0)}, \qquad (5)$$

here $L(0;\ \mu,\ \varphi)$ is the sunlight intensity $[Wt\ /\ (m^2\cdot mkm\cdot sr)]$ on the top of the atmosphere coming from optical depth τ , $F_0\mu_0$ is the parallel rays of light intensity at the upper boundary of the atmosphere (τ=0); $T^{\downarrow}(\tau,\mu_0)$ and $T^{\uparrow}(\tau,\mu_0)$ atmospheric transmittance, respectively, in directions μ_0 and μ, $\rho_0(\tau^*;\mu_0,\mu)$is the *SBC* of system “atmosphere the underlying surface”; $\tau^*=\tau(0)-\tau(h)=\int\limits_0^h\sigma(h)dh$.

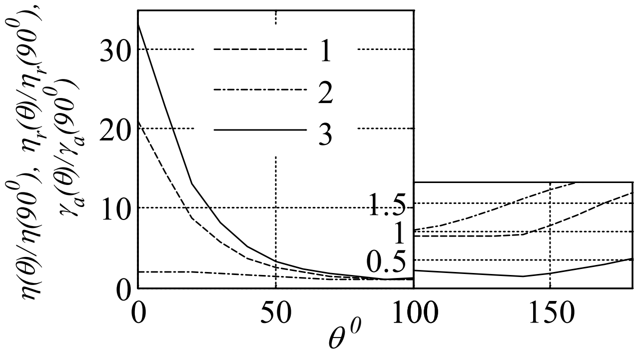

Figure2. The scattering indicatrix of the cloudless day sky (at λ=0.55 *mkm*, the meteorological visibility range 50 *km*)

Below, according to the data $\rho(\tau(h);\mu_0,\mu)$ and the initial approximation around the mean $\bar{\tau}(h)$, the values $\tau(h)$and, correspondingly, the sought values $\bar{\tau}(h)$are estimated. These values are estimated for the lower levels $\rho_h$of height intervals by the formula

$$\rho_{at}[\bar{\tau}(h)+\Delta\tau(h);\mu_0,\mu]=\rho(\tau(h);\mu_0,\mu) \qquad (6)$$

where $\rho(\tau(h);\mu_0,\mu)$ is the satellite data of the SBK at optical depth $\tau(h)=\bar{\tau}(h)+\bar{\tau}(h)$

The brightness $L(0;\ \mu,\ \varphi)$ within the aerosol layer will be determined in the Eddington approximation [2]. When calculating the SBC, we assume that the reflection from the Earth's surface occurs by Lambert's law.

4. Conversion of luminance values

Translation brightness value of top of atmosphere radiance (TOA radiance) [2,8]:

$$L=\frac{L_{\max}-L_{\min}}{Q_{cal\max}-Q_{cal\min}}(DN_{cal}-Q_{cal\min})+L_{\min}. \qquad (7)$$

Where:
L_λ - spectral radiation, which came on the satellite sensor;
DN_{cal} - pixel brightness values of raw geoimage;
Q_{cal}min - the minimum possible pixel value geoimage;
Q_{cal}max- the maximum possible pixel value geoimage;
$L_{\min}$ - the minimum value of the spectral radiation for a particular satellite sensor for a particular image;
L_{max} - the maximum value of the spectral radiation for a particular satellite sensor for a particular image.

For the purpose of atmospheric correction of satellite images, we used data from satellite images (MODIS-Terra (Bands 1-4-3 (true color [8]) of the water area of the Caspian Sea adjacent to the eastern Caucasus.

The results of calculations SBC earth's surface are shown in fig. 3. This figure shows the region of the eastern Caucasus, AbsheronPeninsula and the coastal waters of the Caspian Sea.

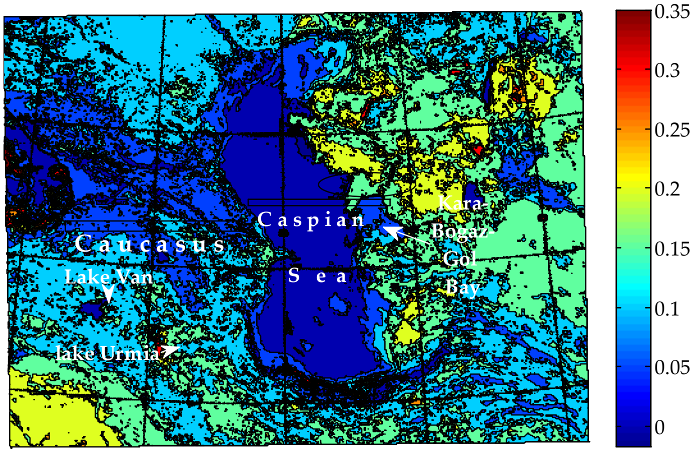

Fig.3. The distribution of the sbc of the underlying surface, calculated from the satellite image: a - eastern caucasus (august 17, 2015), b - absheron peninsula (april 9, 2004), c - baku city (17 august, 2015) [8].

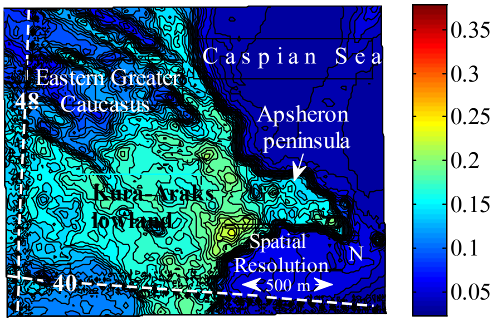

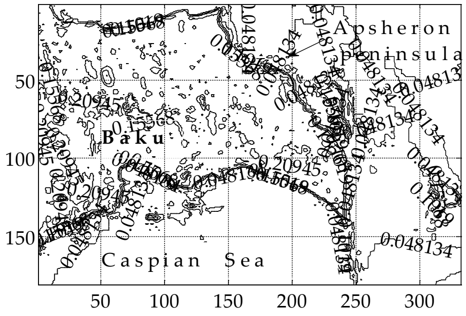

References

1. Kondratyev K. Y., Kozoderov V.V., Smokty O.I. Remote Sensing of the Earth from Space: Atmospheric Correction.290 p.(1992)
2. Ismailov F.I. LAP LAMBERT ACADEMIC PUBLISHING RU. ISBN: 978-613-9-45431-0, 208 p. (2019)
3. Toon O. B., Pollack J. B. J. Appl. Meteorol. 15, 225 (1976).
4. Ismailov F.I. Parametrization of the light-scattering effects of the submicron aerosol mode. Dis. Cand. Tech. Sciences: 05.07.12. - Moscow: 1992.

5. Ismailov F.I.Fizika, 15, 15 (2009)
6. Ismailov F. I Transactions of the National Academy of Sciences of Azerbaijan (physical-mathematical and mechanical sciences series), 26, 179 (2006)
7. Ismailov F. I. Fizika, 9, 7 (2006).
8. NASA Visible Earth: Caspian Sea. MODIS Atmosphere: Images (http://modis-atmos.gsfc.nasa.gov/IMAGES/index.html.

[*] **Corresponding author:** isfazil@yandex.ru

THE COLLECTIVE BEHAVIOR OF THE PARTONS AND ITS INFLUENCE ON THE JET SUPPRESSION IN HEAVY ION COLLISIONS.

MAIS SULEYMANOV
COMSATSUniversityIslamabad,Park RoadIslamabad, Pakistan
BakuStateUniversity, Z.Khalilov str., 23, Baku, Azerbaijan, Az1148

We discuss the physical picture wherein a parton interaction with a coherent group of partons can lead to amplify the jet quenching in the hot and dense matter was created in the heavy ion collisions at RHIC and LHC energies. This picture is concluded after analyzing the behavior of the Nuclear Modification Factor as a function of p_T for the charged particles produced in the most central Pb-Pb collisions at 2.76 A TeV. In the interval of p_T =7-50 GeV/c the values of the Nuclear Modification factor increase almost linearly with a slope, is very close to expected ones for the inverse Compton effect. Around the point of $p_T \cong$ 60 GeV/c, a major change, which is characteristic of this phenomenon, occurs. It is proposed that these results can be explained by the inverse Compton effect happening via a collective parton group formation and its interactions with single partons in the interval of 5 $<p_T<$ 10 GeV/c. In the case of a coherent collision of a single parton with the coherent group, the parton can gain energy through the inverse Compton effect, resulting in its acceleration and shifting to the region of p_T>10 GeV/c. After losing a significant part of its energy the coherent parton group will decay into partons having lower energies - slowed partons in the interval of p_T< 5 GeV/c. This enhancement in the jet quenching can be observed in the interval of
2 $<p_T<$20 GeV/c.

Keywords: p_T regions; parton; coherent group; jet quenching; RHIC; LHC; nuclear modification factor, PbPb; 2.76 A TeV; Inverse Compton Effect
PACS:84. 25.75.Dw, 24.10.Nz, 25.75.Ag

1. Introduction

The most important signature for the formation of the quark-gluon plasma in heavy-ion collisions at ultrarelativistic energies is the suppression of hadron spectra at high p_T [1-2]. The effect is caused by energy loss of jet partons (via collisional and radiative interactions) - jet quenching [3 - 6] from early hard scattering with a hot and dense medium before fragmenting into hadrons.

To quantitatively extract the jet transport coefficients were performed by comparing several jet quenching model calculations with the experimental data for the nuclear modification of single inclusive hadron production at high transverse momenta [7]. Most of these models use a formalism that treats the medium as a series of static scattering centers with the parton and radiated gluons with some energy and frequency, traveling along eikonal trajectories [6]. From the combined analysis of soft single-inclusive hadron spectra, two-particle correlations and their azimuthal dependence, one knows that the matter produced in a heavy ion collision expands rapidly [3] and show a collective behavior which is likely to be formed at an early parton stage of the space-time evolution of the produced hot and dense matter [8 - 10]. Thus, one can support the idea that the parton collective behavior could lead to formation of coherent parton system (for example, as a result of strings fusion [11 -14]) in the hot and dense medium (see paper [15]).

Appearance of the coherent parton group can influence the jet quenching picture in the p_T region where the groups were formed with high probability (in the paper [15] it was shown that the boundary values of p_T for the region could be 4-20 GeV/c). In this regions partons could collide with higher energy objects - coherent parton group, and as in the case of a collision of a photon with a higher energy electron, the parton can gain energy, accelerate transiting into higher p_T region. After a significant energy loss, the parton group decays into partons with lower energies - the slowed partons which will be in the interval of lower p_T region. As a result of the transitions of the accelerated and slowed partons from the region of high probable parton group formation, it can be seen that the jet quenching becomes stronger in this region.

In this paper, we tried to show an experimental signature of the formation of the coherent parton group and its influence on the high p_T parton suppression through of parton Inverse Compton Effect (ICE). ICE states that a photon can gain energy in a collision with a more energetic electron [16-18], but can this phenomenon occur in a collision between partons? In other words, is there a parton version of ICE?

2. About the signature

To get an information on the formation of the coherent parton group and its interaction with single partons we have analyzed the behavior of the nuclear modification factor (R_{AA}) as a function of p_T for the charged particles produced in the most central Pb-Pb collisions at 2.76 A TeV [19].

The evolution picture of the R_{AA} [19] with energy from the SPS to the LHC [1-2, 20] shows that the creation of high - $p_T$particles in central Pb-Pb collisions is significantly suppressed in comparison to peripheral Pb-Pb and pp collisions . In the range of p_T=5-10 GeV/c, the suppression is stronger than before observed at the RHIC [1]. Beyond p_T = 10 GeV/c up to 20 GeV/c the R_{AA} shows a rising trend as it was shown by the data from the ALICE experiment [2]. The CMS measurement [19] with improved statistical precision clearly shows that this rise continues at higher p_T, approaching a suppression factor $R_{AA} \cong$ 0.5-0.6 in the range of 40-100 GeV/c.

The Figure 1 shows the behavior of the R_{AA} as a function of p_T for the charged particles produced in the Pb-Pb collisions with centrality of 0-5 % at energies of 2.76 A GeV[1] . There are several trends observed as p_T increases:

- forp_T< 2 GeV/c the values of R_{AA} increase from ~ 0.36 to ~ 0.42;
- for 2 <p_T<7 GeV/c the values of R_{AA} decreases to ~ 0.15 and reaches its minimum;
- for 7 <p_T<40-50 GeV/c the values of R_{AA} increase from ~ 0.15 to ~0.6 and reaches its maximum.

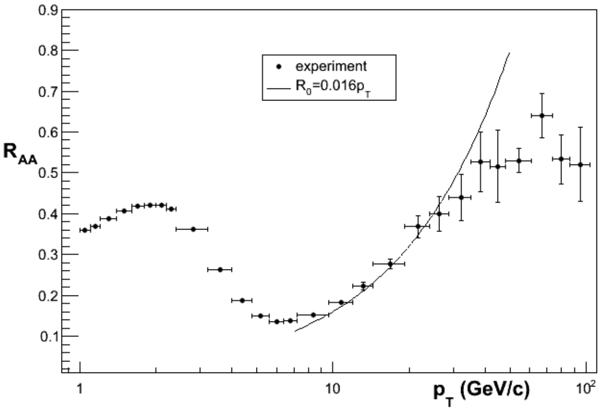

Figure 1. The behavior of R_{AA} as a function of p_T for charged particles produced in Pb-Pb collisions with centrality of 0-5 % at energies 2.76 AGeV (see paper [19]). The line shows the behavior of the function$R_0 = 0.0167\, p_T$ for the parton ICE.

Furthermore, at $p_T \cong$50-60 GeV/c, a regime change occurs and the values of R_{AA} remain at 0.6. It can be easily shown that the behavior of R_{AA} in the interval 7<p_T<100 GeV/c is similar to the behavior of the photon energy distribution under ICE [18]. A reason for this similarity may be that in the momentum interval $5 < p_T < 10$ GeV/c (this is the second p_T region observed in the paper [15]) partons collide with higher energy objects, and as in the case of a collision of a photon with a higher energy electron, parton ICE occurs. These objects can be parton groups with energy $\gamma_{group} = \frac{E_{group}}{m_{group}}$ (E_{group} is energy of parton group and m_{group} is its mass). In the case of a coherent collision of a parton with energy $\alpha_{1part} = \frac{E_{1part}}{m_{group}} < \gamma_{group}$ ($E_{1part}$is the

---

[1] the experimental data were taken from the HEP Data: https://hepdata.net/record/ins1088823

energy of parton before collision), it can acquire energy $\alpha_{part} = \frac{E_{part}}{m_{group}}$ (E_{part} is energy of parton after collision) and in the case of $\alpha_{part} > \alpha_{1part}$ it can accelerate due to parton ICE. That is why we believe the observed more jet quenching in the interval of p_T =2-60 GeV/c could be connected with the formation of the coherent parton group and its interaction with single parton which results in the acceleration of the single partons and decay of the coherent parton group into the slow partons.

3. Results and discussion

To show quantitative capacity of the physical picture under consideration we have used the analogy with photon ICE and defined the function R_0 to compare with R_{AA}. Of course, we cannot reproduce exactly quantitative contribution of the physical picture under consideration we confine oneself only with showing that the picture is acceptable.

For the definition of the R_0 we have used the approximate formulas are given for the energy distributions of photons $\frac{d^2N}{dtd\alpha}$ in the case of ICE [18] when a photon with energy $\alpha_1 = \frac{E_1}{m_e}$ (in units of electron mass m_e , E_1 is the energy of phaton) collides with an electron with energy $[= E_{\downarrow}e/m_{\downarrow}e$ (E_e is the electron energy) and receives energy $\alpha = \frac{E}{m_e}$ (E is the photon energy). The values of the R_0 were defined as:

$$R_0 = \frac{d^2N / dtd\alpha\,|_{\alpha \le \alpha_1}}{d^2N / dtd\alpha\,|_{\alpha = \alpha_1}} = \frac{4\gamma^2\alpha - \alpha_1}{4\gamma^2\alpha_1 - \alpha_1} \text{ or } R_0 = \frac{\alpha}{\alpha_1}\text{ , for } \gamma >> 1, \tag{1}$$

The R_0 is the energy distribution of photons ($\frac{d^2N}{dtd\alpha}$) with energy $\alpha \le \alpha_1$ (for $[< [$,see the paper [18]), normalized to the value of $\frac{d^2N}{dtd\alpha}$ at $[= \alpha_{\downarrow}1$. In accordance with the physical picture, in the case of a coherent collision of a parton with energy $\alpha_{1part} < \gamma_{group}$ with a group of partons of energy $\gamma_{group} > \alpha_{1part} \gg 1$, parton's final energy will be α_{part} . The values of E_{1part} and E_{part} are much larger than the parton's rest energy, so one can assume that $E_{1part} \cong p_{1part}$ and $E_{part} \cong p_{part}$ (p_{1part} and p_{part} is 3-momentum of parton before and after the collision). For the particles under consideration (see [19]), the values of their pseudorapidity (η) are taken in the interval of $|\eta|<1$, so we can write $p_{part} \cong p_{Tpart}$ (p_{Tpart} is the transverse momentum of the parton after the collision). Therefore, for partons the expression (1) can be rewritten as:

$$R_0 \cong \frac{1}{\alpha_{1part}}\alpha_{part} \cong \frac{1}{E_{1part}}E_{part} \cong \frac{1}{p_{1part}}p_{part} = \frac{1}{p_{1part}}p_{Tpart} , \tag{2}$$

To determine p_{1part} from (2) we used the fact that at the point of regime change $p_{1part} = p_{part} \cong p_{Tpart}$. Visually, the regime change seems to be near $p_T \cong p_{Tpart} \cong$ 40-50 GeV/c. To obtain a more accurate value of the p_{1part} we fitted the R_{AA} data with the linear function $y = ax$ in the region of $6 < p_T < 70$ GeV/c, changing the minimum and maximum values of the p_T intervals to obtain the best fitting results. The Table shows three best fitting results. The fit function $y = ax$ seems to describe the R_{AA} data well in the interval of p_T = 8.4-44.8 GeV/c, whereas after p_T =54.4 GeV/c is turned on it deteriorates fast. This means that the transition point is near the value p_T=55.4±6.4 GeV/c and it can be assumed that $p_{1part} \cong$ 60 GeV/c and the value and R_0 = 0.0167 p_T . The solid line in the figure shows the behavior of R_0 as a function of p_T which well describes the R_{AA} in the region $7 < p_T < 50$ GeV/c. This is understandable since the slope of the line for $R_0 = 0.0167p_T$ almost exactly coincides with the slope of the line (a = 0.0162± 0.0007) obtained for the best fitting of the experimental data on R_{AA} (see Table of the values of a).

Table

Interval of p_T(GeV/c)	χ^2/ndf	Probability	Value of *a*
8.4 - 38.4	3.526/7	0.8325	0.0162± 0.0007
8.4 - 44.8	7.453/8	0.4886	0.0158±0.0007
8.4 - 54.4	16.85/9	0.05108	0.0154± 0.0006

The definition of R_0 tells us that at the regime change point the value of R_0 would be 1, but in the experiment the R_{AA} values remain constant around 0.6 - 0.7 in the region of p_T> 60 GeV/c. The difference could be connected with two main reasons:

- we have not taken into account jet quenching and the dynamics under consideration are unable to describe the suppression alone and it is clear;

- due to unavailability of a Monte Carlo simulation pocket we could not have perfect normalization for the $\frac{d^2N}{dtd\alpha}$ to compare with R_{AA}.

As we have said above in this step we cannot reproduce exactly quantitative contribution of the parton ICE we confine oneself only with showing that the picture is acceptable. More important results are that: the slopes of the behavior of R_0 and R_{AA} are very close to each other; there exists the regime change at the point $p_T \cong$ 60 GeV/c.

Finally returning back to the interval $\alpha_{part} < \alpha_{1part}$, we noted that the similar behavior of the slope values of R_{AA} behavior as a function of p_T and of R_0 in this interval may indicate that the parton energy loss (parton suppression effect) almost does not change the slope for R_{AA} in this region.

4. Conclusion

We conclude that the values of R_{AA} as a function of p_T in the interval 7-50 GeV/c increase almost linearly with a slope expected for the parton Inverse Compton Effect. At $p_T \cong 60$ GeV/c a regime change occurs, which is characteristic for this effect. These results indicate that partons can be accelerated by Inverse Compton Effect in the p_T region 5-10 GeV/c. We assume that this can be due to the collective effects associated with the fusion of strings and the appearance of new strings in the dense medium. In the case of a coherent collision with a parton that has a lower energy than the new string, the parton can gain energy and accelerate, transiting into $p_T > 10$ GeV/c interval. After losing a significant part of its energy new string will decay into partons with lower energies - slowed partons in the interval of $p_T < 5$ GeV/c. This can seem as amplification of the suppression of partons in the 2 $< p_T < 20$ GeV/c interval. That is why this should be taken into account in the jet quenching models.

I would like to acknowledge the COMSATS University Islamabad, which provided suitable platform and all possible facilities to perform the analysis, Dr Ali Zaman and Aziza Suleymanzade for their essential help during preparing the text.

References

1. PHENIX Collaboration. Phys. Rev.Lett.**101**(2008)232301; STAR Collaboration. Phys. Rev. Lett. **91** 172302(2003)
2. ALICE Collaboration. Phys. Lett. B 696 (2011) 30.
3. Urs Achim Wiedemann. arXiv:0908.2306v1 [hep-ph] 17 Aug 2009; CERN-PH-TH/2009-026;
4. Barbara Betz. arXiv:1211.5897v1 [nucl-th] 26 Nov 2012;
5. Guang-you Qin1,Xin-Nian Wang. arXiv:1511.00790v2 [hep-ph] 10 Nov 2015
6. Aaron Angerami. arXiv:1208.5043v1 [nucl-ex] 24 Aug 2012
7. ChatrchyanS. et al. Phys.Lett. B730, 243-263, (2014).
8. Adams J. et al. (STAR Collaboration), Phys. Rev. Lett. 95, 122301(2005)

9. AdareA. et al.(PHENIX Collaboration), Phys. Rev. Lett. 98, 162301 (2007)
10. AamodtK. et al. (ALICE Collaboration) Phys. Rev. Lett. Vol.105, pp. 252302, 2010
11. BraunM. A., PajaresC., Phys. Lett. B 287, 154(1992)
12. BraunM. A., C. Pajares, Nucl. Phys. B 390, 542(1930)
13. BraunM. A.,del Mora, F.,C. Pajares, Phys. Rev. C 65, pp. 024907(2002)
14. ArmestoN., C. Pajares, D. M. Sousa,Phys. Lett. B 527, 92 (2002)
15. SuleymanovM.K., Int.J.Mod.Phys. E 27 no.01, 1850008 (2018).
16. Follin J. W.. Phys. Rev. 72, 74(1947)
17. Donahue T.M., Ph ys. Rev. 84, 972(1951)
18. JonesF. C., Phys. Rev. Vol. 167, pp. 1159(1968)
19. The CMS Collaboration, J Eur. Phys. J. C (2012) **72**(1945)
20. WA98 Collaboration, Eur. Phys. J. C **23** (2002) 225,;D. d'Enterria , Phys. Lett. B 596,32(2004)

***Corresponding author**: mais_suleymanoc@comsats.edu.pk

FOLLOWING ELECTRON IMPACT EXCITATION OF SINGLE(${}_{93}$Np, ${}_{94}$Pu, ${}_{95}$Am, ${}_{96}$Cm, ${}_{97}$Bk, ${}_{98}$Cf) ATOMS O_i SUBHELL IONIZATION CROSS SECTIONS BY USING LOTZ'S EQUATIONS

Mahmut AYDINOL[*1]
Dicle University, Institute of Scientific Studies 21280 Diyarbakir Turkey

O shell and five O_i subshells ionization cross sections σO and σOi following electron impact on (93Np, 94Pu, 95Am, 96Cm, 97Bk, 98Cf) atoms calculated. By using Lotz's equation in Matlab ionization cross section values obtained for 12 electron impact energy values in first ionization energy to five times ionization energy range for each atom. Lotz's parameters and special commands used for each ionization cross sections calculations. Starting all most from ionization threshold values; ionization cross sections are increasing rapidly with electron impact energy E_o. For higher E_o values this increments getting smaller for every O_i subshells. For smaller E_o energy close to threshold all ionization cross sections decrease. For a fixed electron impact energy while Z value increases from $93 \le Z \le 98$; ionization cross sections decrease with Z. Results may help to understand similar findings which obtained from other electron impact excitation of O_i subshells ionization cross sections studies for similar size single atom.

Keywords:O subshells ionization cross section calculations, Electron impact on single atoms(${}_{93}$Np≤Z≤${}_{98}$Cf), Lotz's equations.
PACS:31.25.−v

1.Introduction

Inner subshell ionization cross section studies of free atoms by electron impact are subjects of ongoing research for many years [1,2,5-11]. Inner shell ionization cross section information help us to understand, characterization of used target atoms in the following fields: astrophysics, plasma physics, radiation protection, energy transfer by electron impact on or in tissues study required [5,6,7,8]. In this study, O shell and Oi subshells ionization cross sections σ_O and σ_{Oi}($i=1,2,..,5$) for ${}_{93}$Np to ${}_{98}$Cf atoms are calculated. For each of atoms, 12 electron impact energy values E_{oi} are used. E_{oi}($i=1,..,12$) values were chosen in the $E_{Oi} < E_{oi} < 5E_{Oi}$ range for each atom. E_{Oi} is the binding energy of i_{th} O_i($i=1,..,5$) subshells. If a neutral atom A bombarded by an electron with sufficiently big E_{oi} under $E_{Oi}<E_{oi}$ conditions, firstly impacting electron emits bremsstrahlung then electron-single atom interaction occur. Target atom A becomes excited ions A_{+*} at i_{th} O_i subshell. Creation of electron holes in O_i subshells depends on how big the E_{oi} compare to E_{Oi} . Lotz put forward a semi-empirical formula at, for calculation of ionization cross sections for low energetic electron impact excitation of free atoms at inner shells which was based on Born Approximation(BA)[1,2,6]. Calculations for σ_O and σ_{Oi}($i=1,2,..,5$) of 93Np to 98Cf atoms carried out by using Lotz equations in Matlab program [7, 9-12].

$$\sigma_{Oi} = a_i q_i[\ln(E_o/E_i)/E_oE_i][1-b_i \exp(-c_i(E_o/E_i))] \qquad (1)$$

a_i, b_i, c_i constants and q_i of the i_{th} subshell which are taken from Lotz [1,2]. q_i are the number of equivalent electrons at i_{th} O_i subshell and E_i is the binding energy of the i_{th} subshell. σ_{Oi} are the ionization cross section of i_{th} subshells. By using the Equation.1 and using sum of calculated 5 σ_{Oi} subshells of each atom for 12 values of E_{oi} , σ_{Ototal} of O shell were calculated.

2.Method

O shell and Oi subshells ionization cross sections(σ_O and σ_{Oi}) for ${}_{93}$Np to ${}_{98}$Cf atoms are calculated. Calculations done for 12 E_{oi} values which they chosen in energy range of $E_{Mi} < E_{oi} < 5E_{Oi}$ for each atom. It means that for ${}_{93}$Np, used over all E_{oi}($i=1,..$to$,12$) values fall in $10eV < E_o < 1025eV$ range. E_{oi} values chosen according to the E_{Oi} of targeted atom which were taken from Gwyn, and Porter [3, 4]. Calculations carried out by using written commands for Lotz's Equation.1 in Matlab for each atom [1,2,9 -12]. The values of a_i, b_i, c_i and q_i are given in the same order for O_i subshells as: for a_i equal to $(4, 4, 4, 1.4, 1.4)10^{-14}cm^2(eV)^2$; for b_i equal to 0.3, 0.6, 0,6 0.96, 0.96; for c_i equal to 0.6, 0.4, 0.4, 0.13, 0.13 and for q_i equal to 2, 2, 4, 5, 4 values used[1-2, 9-12]. By using sum of calculated 5 σ_{Oi} subshells of atoms for 12 values of E_{oi} O shell σ_{Mtotal} of each atom calculated.

3.Results

Results, for $_{93}$Np, $_{94}$Pu, $_{95}$Am,$_{96}$Cm, $_{97}$Bk, $_{98}$Cf atoms for 12 E_{oi} are given in Table.1 to 6 under the name of each atom. Each table contains O subshell ionization cross section results of one atom. All the Table captions are the same except the chemical symbol of elements which used for targeted atoms.

Table 1. For $_{93}$NpO$_1$ to O$_5$ subshell ionization cross sections by electron impact in 10^9 b.

E_0(eV)	σ_{O1}	σ_{O2}	σ_{O3}	σ_{O4}	σ_{O5}	σ_{Ototal}
10	-0,08251	-0,0554	-0,1864	0,01395	0,27373	-0,03662
65	-0,00661	-0,00382	-0,00718	-0,00076	0,59742	0,57906
125	-0,00188	-0,00105	0,00145	0,00038	0,46578	0,46468
175	-0,00097	-0,00037	0,00338	0,00079	0,38093	0,38376
225	-0,00044	-0,00003	0,00418	0,00104	0,32107	0,32582
300	-0,00011	0,00022	0,00469	0,00128	0,26066	0,26674
400	0,00016	0,00037	0,00463	0,00144	0,20998	0,21658
500	0,00016	0,00037	0,00463	0,00144	0,20997	0,21657
650	0,00023	0,00048	0,00411	0,00158	0,14416	0,15056
850	0,00025	0,00049	0,00366	0,00157	0,11655	0,12252
950	0,00025	0,00048	0,00347	0,00155	0,10662	0,11237
1025	0,00025	0,00047	0,00333	0,00153	0,10031	0,10589

Table 2. For$_{94}$PuO$_1$ to O$_5$ subshell ionization cross sections by electron impact in 10^9 b.

E_0(eV)	σ_{O1}	σ_{O2}	σ_{O3}	σ_{O4}	σ_{O5}	σ_{Ototal}
10	-0,08077	-0,05454	-0,18111	-0,01353	0,27373	-0,05622
65	-0,00696	-0,00385	-0,00745	-0,00079	0,59742	0,57837
125	-0,00188	-0,00106	0,00099	0,00036	0,46578	0,46419
175	-0,00091	-0,00038	0,00297	0,00068	0,38093	0,38329
225	-0,00045	-0,00005	0,00372	0,00092	0,32107	0,32521
300	-0,00013	0,00025	0,00416	0,00114	0,26067	0,26609
400	0,00007	0,00035	0,00424	0,00131	0,20998	0,21595
500	0,00016	0,00042	0,00411	0,00141	0,17691	0,18301
650	0,00021	0,00046	0,00382	0,00146	0,14416	0,15011
850	0,00023	0,00047	0,00342	0,00146	0,11655	0,12213
950	0,00024	0,00046	0,00324	0,00144	0,10663	0,11201
1025	0,00024	0,00047	0,00311	0,00142	0,10031	0,10555

Table 3. For $_{95}$Am O_1 to O_5 subshell ionization cross sections by electron impact in 10^9 b.

E_o(eV)	σ_{O1}	σ_{O2}	σ_{O3}	σ_{O4}	σ_{O5}	σ_{Ototal}
10	-0,07963	-0,05328	-0,18019	-0,01343	0,27373	-0,0528
65	-0,00585	-0,00375	-0,00749	-0,00079	0,59742	0,57954
125	-0,00188	-0,00108	0,00095	0,00028	0,46578	0,46405
175	-0,00092	-0,00041	0,00281	0,00066	0,38093	0,38307
225	-0,00046	-0,00008	0,00362	0,00096	0,32107	0,32511
300	-0,00014	0,00016	0,00408	0,00112	0,26067	0,26589
400	0,00006	0,00031	0,00417	0,00128	0,20998	0,2158
500	0,00015	0,00038	0,00405	0,00138	0,17691	0,18287
650	0,00021	0,00043	0,00376	0,00143	0,14416	0,14999
850	0,00023	0,00044	0,00337	0,00144	0,11655	0,12203
950	0,00023	0,00043	0,00319	0,00141	0,10662	0,11188
1025	0,00023	0,00043	0,00308	0,00148	0,10031	0,10553

Table 4. For $_{96}$Cm O_1 to O_5 subshell ionization cross sections by electron impact in 10^9 b.

E_o(eV)	σ_{O1}	σ_{O2}	σ_{O3}	σ_{O4}	σ_{O5}	σ_{Ototal}
10	-0.07557	-0,05094	-0,17242	-0,01286	0,01877	-0,21745
65	-0,00567	-0,00366	-0,00778	-0,00082	0,18264	0,16471
125	-0,00187	-0,00115	0,00031	0,00018	0,17585	0,17332
175	-0,00094	-0,00046	0,00218	0,00054	0,15757	0,15889
225	-0,00058	-0,00014	0,00396	0,00076	0,13994	0,14394
300	-0,00018	0,00012	0,00349	0,00096	0,11832	0,12271
400	0,00002	0,00025	0,00363	0,00112	0,09761	0,10263
500	0,00011	0,00032	0,00357	0,00121	0,08319	0,0884
650	0,00017	0,00037	0,00335	0,00127	0,06845	0,07361
850	0,00019	0,00039	0,00303	0,00128	0,05579	0,06068
950	0,00025	0,00038	0,00288	0,00127	0,05129	0,05607
1050	0,00027	0,00038	0,00275	0,00125	0,04736	0,05201

Table 5. For $_{97}$Bk O_1 to O_5 subshell ionization cross sections by electron impact in 10^8 b.

E_o(eV)	σ_{O1}	σ_{O2}	σ_{O3}	σ_{O4}	σ_{O5}	σ_{Ototal}
15	-0,43703	-0,29037	-0,95289	-0,07534	0,32834	-1,42731
65	-0,05582	-0,03591	-0,07941	-0,00831	1,51512	1,39152
125	-0,01862	-0,01112	-0,00061	0,00132	1,50542	1,47642
175	-0,00951	-0,00482	0,01791	0,00471	1,36982	1,37813
225	-0,00512	-0,00172	0,02611	0,00671	1,22921	1,25512
300	-0,00193	0,00061	0,03113	0,00871	1,04921	1,08771
400	-0,00001	0,00216	0,03292	0,01023	0,87109	0,91639
500	0,00088	0,00281	0,03268	0,01109	0,74459	0,79205
650	0,00148	0,00329	0,03084	0,01172	0,61399	0,66132
850	0,00176	0,00348	0,02804	0,01191	0,50121	0,54641
950	0,00181	0,00348	0,02669	0,01184	0,46016	0,50398
1050	0,00183	0,00346	0,02544	0,01173	0,42587	0,46833

Table 6. For $_{98}$Cf O_1 to O_5 subshell ionization cross sections by electron impact in 10^9 b.

E_o(eV)	σ_{O1}	σ_{O2}	σ_{O3}	σ_{O4}	σ_{O5}	σ_{Ototal}
10	-0,07144	-0,04845	-0,16395	-0,01226	0,02871	-0,26739
65	-0,00549	-0,00356	-0,00803	-0,00083	0,27654	0,25863
125	-0,00185	-0,00111	-0,00032	0,00009	0,24781	0,24462
175	-0,00095	-0,00049	0,00151	0,00042	0,21469	0,21518
225	-0,00053	-0,00019	0,00231	0,00062	0,18653	0,18874
300	-0,00021	0,00005	0,00284	0,00081	0,15486	0,15835
400	-0,00002	0,00019	0,00304	0,00096	0,12632	0,13049
500	0,00007	0,00026	0,00303	0,00104	0,10711	0,11151
650	0,00015	0,00031	0,00288	0,00111	0,08779	0,09224
800	0,00016	0,00033	0,00277	0,00113	0,07478	0,07917
950	0,00017	0,00033	0,00251	0,00113	0,06539	0,06953
1025	0,00017	0,00033	0,00235	0,00111	0,05825	0,06221

Table 7. Z dependency ofσ_O and σ_{Oi} values for single E_{oi} = 500eV, in 10^9 b.

E_o(eV)	Atom Z	σ_{O1}	σ_{O2}	σ_{O3}	σ_{O4}	σ_{O5}	σ_{Ototal}
500	93Np	0,00016	0,00037	0,00463	0,00144	0,20997	0,21657
500	94Pu	0,00016	0,00042	0,00411	0,00141	0,17691	0,18301
500	95Am	0,00015	0,00038	0,00405	0,00138	0,17691	0,18287
500	96Cm	0,00012	0,00032	0,00357	0,00121	0,08319	0,08841
500	97Bk	0,00088	0,00281	0,03268	0,01109	0,07446	0,07921
500	98Cf	0,00007	0,00026	0,00303	0,00104	0,10711	0,11151

3.1.Figures

O shell σ_O and $\sigma_{Oi}O_i$ subshells ionization cross sections(σ_O and σ_{Oi}) results of **($_{93}$Np, $_{94}$Pu, $_{95}$Am, $_{96}$Cm, $_{97}$Bk, $_{98}$Cf)**atoms for 12 E_{oi} also given in following Figures.1 to12 under the name of each atom. E_{oi} and $\sigma_{Oi}$are given in eV and in brespectively. O shell ionization cross section σ_{Ototal} values of $_{93}$Np to $_{98}$Cfatoms for E_{oi} fixed electron impact energy, changes from 0,217x10^9 b to 0,0112x10^9 b as shown in above Tab.7 and in Fig.7 below. Results of left half of the figure given in our second presentation at Proceedings in MTP Bakğ 2019.

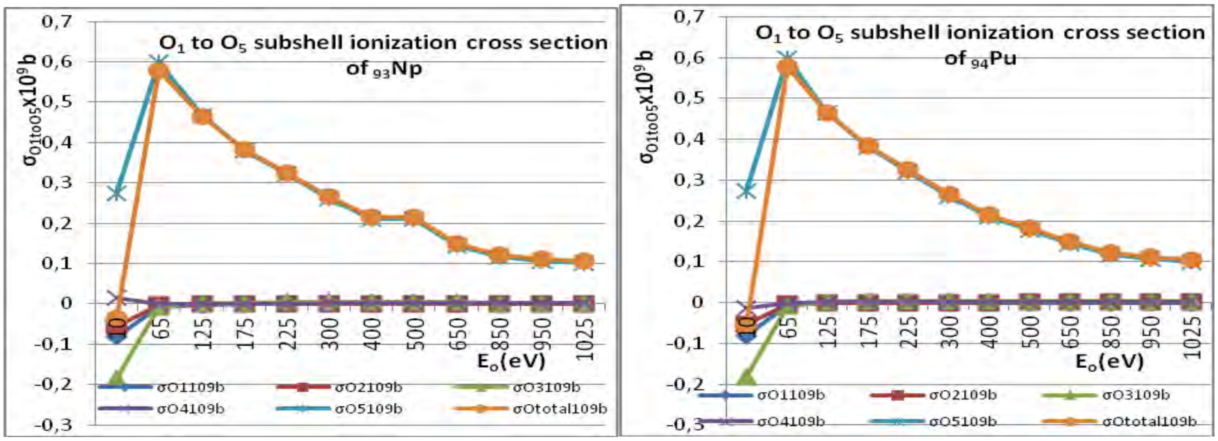

Figures 1 and 2. For $_{93}$Np and $_{94}$Pu O_1 to O_5 subshell ionization cross sections in 10^9 b.

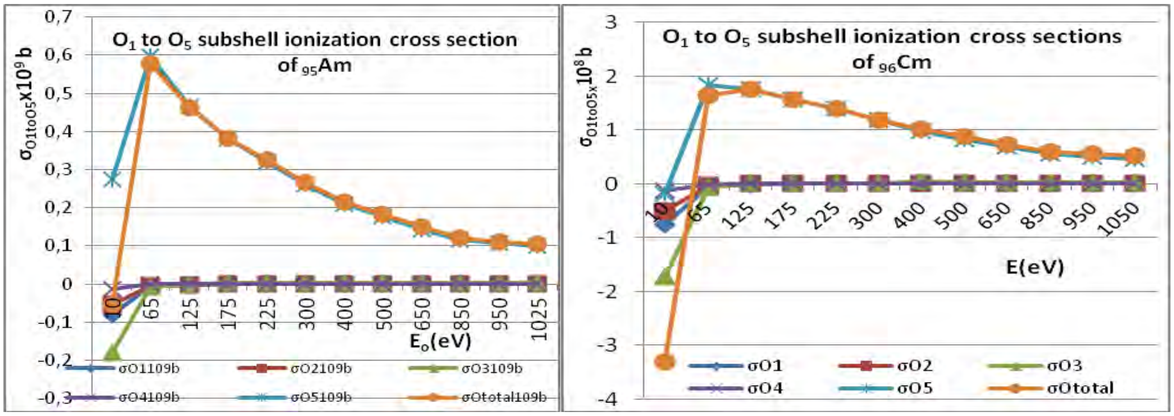

Figures 3 and 4 For $_{95}$Am and $_{96}$Cm O_1 to O_5 subshell ionization cross sections in 10^9 b.

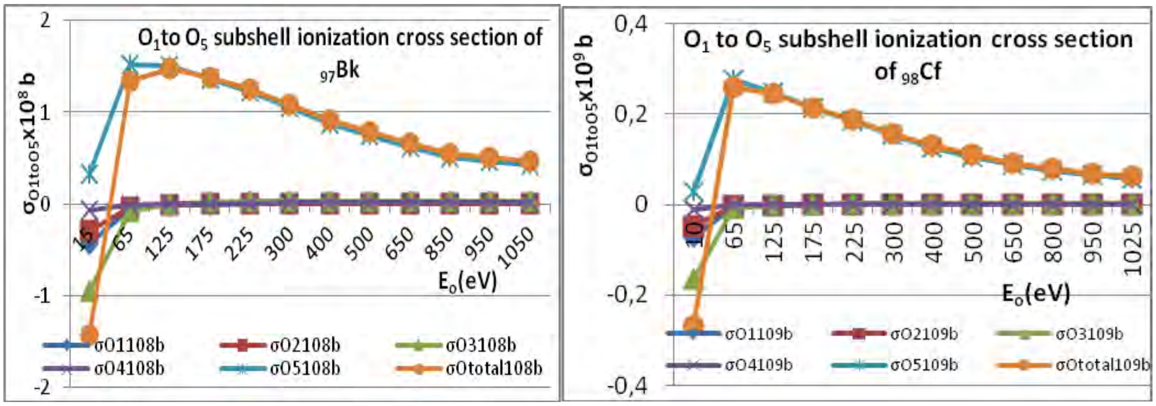

Figures 5 and 6 For $_{97}$Bk and $_{98}$Cf O_1 to O_5 subshell ionization cross sections in 108 b and in10^9 b.

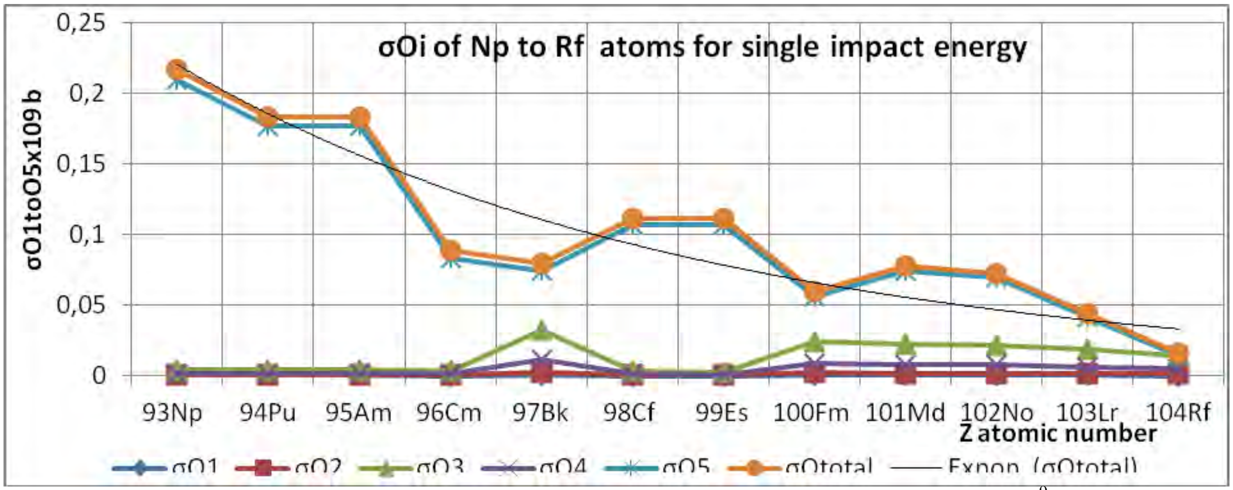

Figures 7 For O_1 to O_5 subshell ionization cross sections of $_{93}$Np to $_{98}$Cf in10^9b.

4. Conclusions

O shell σ_O and σ_{Oi} (i = 1 to 5) subshells ionization cross sections of $_{93}$Np to $_{98}$Cf atoms by electron impact results given in Tabs.1 to 6 and in Figs.1to 6. For O shell σ_O and for O_i subshells σ_{Oi} increase rapidly by E_{oi} while E_{oi} increases from $E_i \leq E_{oi} \leq 5E_i$ as shown in Tables and graphics. These increments faster for very close to threshold energy values. Results for σ_O and σ_{Oi} increase by E_{oi} for data of each atom. Variation of σ_{Oi} by E_o near to E_{Oi} region of O_i subshells of each atom show similarity they are related to production of characteristic x ray yield rate of that subshell. For a fixed $E_{oi} \approx 500$eV, while Z value increases from $93 \leq Z \leq 104$ σ_{Ototal} and σOi decrease: Variation for σ_{Ototal} is from $2{,}166.10^8$b to $0{,}164.10^8$b(see our second presentation at Proceedings in MTP Bakğ 2019). Results must be compared with experimental measurements and with other calculations such as Distorted wave Born approximation (DWBA) and Modified Relativistic Bethe Born Approximations (MRBEB) [5-12].

Acknowledgement

I would like to thank DUBAP of Dicle University (http://dubap.dicle.edu.tr) who allowed to use our project's computer(Reg.No:13-FF-53) and Prof Dr Ahmet ONAY for his hospitality.

References

1. Lotz, W., Zeitschrift fğr Physik A Hadrons and Nuclei. 206(2), 205 (1967).
2. Lotz, W., Zeitschrift fğr Physik A, Hadrons and Nuclei. 232 (2) : 101 (1970).
3. Gwyn Williams. Electron Binding Energies. http://www.jlab.org/~gwyn/ebindene.html. Accessed on April 30, (2018).
4. Porter, F.T., and M. S. Freedman. J.of Physical and Chemical Reference Data, 7,4,1267(1978).
5. Bote, B., et al.,Analytical formulas, Atm. Data and Nuclear Data Tables 95, 871 (2009).
6. Xavier L., et al., J. Phys. Chem. Ref. Data, 43,1 (2014).
7. Aydinol M, Aydeniz D., AIP Conf. Proceedings, 1722,0600028(2016); AIP Conf. Proceedings, 1722, 060001 (2016).
8. Haque, AKF., et al., J. of Physics B: Atomic, Molec. and Optical Phys. 50, No.5, 1 (2017)
9. Aydinol M.,s, 2nd Intern. Symposium on Multidisiplinary Studies and Innovative Thecnologies, October 19-21, 2018, Turkey, Proceedings, p.450-453, www.ismsitconf.org/ ismsitconf@ismsitconf.org 2018.
10. Aydinol M., TFD34 Intern. Physics Conf. 4-9 September 2018 Bodrum, Turkey; AIP Conf. Proceedings 2042, 020020(2018); http://doi.org/10.1063/1.5078892.
11. Aydinol M., IENSC. Proc.(ISBN:978-605-81971-3-8) Vol.1-2, p.1312-1321, Nov. 17-20, 2018, Turkey.
12. Aydinol MIENSC Proc.(ISBN:978-605-81971-3-8) Vol.1-2, p.1400-1406, Nov. 17-20, 2018, Turkey.

***Corresponding author**: aydinolm@dicle.edu.tr
aydinolm@gmail.com

QUANTUM CHEMICAL STUDY OF THE SPATIAL AND ELECTRONIC STRUCTURE OF A DIAZACROWNETHER WITH H-LYS-LYS-OH DIPEPTIDE FRAGMENT IN THE MACROCYCLIC RING

S.D. DEMUKHAMEDOVA[1], U.A. HASANOVA[2], I.N. ALIEVA[2], Z.O. GAKHRAMANOVA[3]
[1]Institute for Physical Problems, Baku State University, Z.Khalilov str., 23, Baku, Azerbaijan, Az1148
[2]BakuStateUniversity, Z.Khalilov str., 23, Baku, Azerbaijan, Az1148
[3]Geotechnological Problems of Gas, Oil and Chemistry, Baku, Azerbaijan, AZ1138

In this paper, we report of new peptide based antimicrobial agent diazacrown ether with a H-Lys-Lys-OH dipeptide fragment in a macrocyclic ring for biomedical and pharmaceutical applications. The spatial and electronic structure of the diazacrown ether molecule has been investigated by the quantum-chemical method of the DFT electron density functional with the hybrid potential B3LYP in the Gaussian09 software package. For the calculation, we used extended basis sets with allowance for the polarization and diffuse functions 6-31G (d) and 6-31 G (d, p). An optimized macrocycle structure and its spatial, energy, and electronic parameters are obtained. The comparative analysis of the data obtained by calculations in different basis sets have carried.

Keywords: lysyllysine, dipeptide, diazo crown ether, macroheterocycle, quantum chemical calculations, spatial and electronic structure
PACS: 31.15-p; 31.15.E-; 33.15.Dj; 87.15Aa

1. Introduction

At present, methods of molecular modelling and computational quantum chemistry widely spread and allow to give key forsolving of questions that are inaccessible by experimental research methods [1-3]. Quantum chemistry methods are used to study the properties of individual molecules and their complexes, as well as for design of new materials with predetermined properties [4,5]. Peptides are known to be selective and effective signalling molecules that bind to specific cell surface receptors, such as G-protein coupled receptors (GPCR), or ionic channels, where they cause intracellular effects. Due to these unique properties, they are of undoubted interest for the design of targeted drugs. Peptides can play the role of both the drug carrier and actually a medicine. There are reports of more than 300 peptide drugs, among them a special place is taken by peptides with pronounced antimicrobial properties. It was found that cationic peptides containing many residues of alanine, arginine, lysine and having more or equal to 30% of hydrophobic residues, possess an immune response and interaction with a hydrophobic interface of a bacterial membrane [6]. Other promising candidates for biomedical and pharmaceutical applications are homo-polyamino acids, an important class of biodegradable polymers. Among them, poly-L-lysine (PLL) and its derivatives have been studied most widely. They are soluble in water and non-toxic to the environment and living organisms. As a rule, cationic polypeptides (such as -PLL) are used as auxiliary agents in drug delivery systems[7-9]. Cationic polypeptides may be responsible for the activity of membrane lysis or the signal of localization of the nucleus [10].

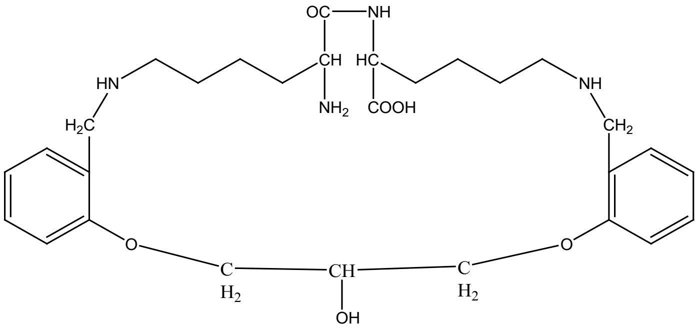

Figure 1.Diagram of diazacrown ether formation with the H-Lys-Lys-OH dipeptide fragment in the macrocyclic ring.

Taking into account their attractive pharmacological profile and exceptional selectivity, peptides are an excellent starting point for the development of new therapeutic agents [11]. Considering the growing problem of microbial resistance, the design and development of new antimicrobial agents based on peptides is a very attractive approach to overcome the resistance of microorganisms towards the already used antibiotics [12]. There are a number of reports on the synthesis and development of cyclic peptides with excellent antimicrobial activity [13,14]. Condensation of dialdehyde with dipeptide lysyllysine H-Lys-Lys-OH leads to the obtaining of diazacrown ether with a dipeptide fragment in the macrocyclic ring. In addition, the supramolecular profile of crown ethers, which exhibit ionophore properties, allows their use as antimicrobial agents [15, 16]. Taking into account the abovementioned, the design of new antimicrobial agents based on diazacrown ether with H-Lys-Lys-OH dipeptide fragment in a macrocyclic ring and the study of its spatial and electronic structure by quantum chemical method DFT/B3LYP using of the GAUSSIAN-09 program is very interesting and actual problem.

2. Computational methods

The spatial and electronic structures of the diazacrownerether molecule with the H-Lys-Lys-OH dipeptide fragment in a macrocyclic ring were studied by a quantum-chemical method within the framework of the electron density functional theory of DFT with a hybrid potential of B3LYP in the 6-31G (d) and 6-31+G(d,p) basis sets. The calculations were performed using the Gaussian 09 software package. In the DFT method of calculating of the electronic structure, as in the Hartree-Fock method, the stationary Schrodinger equation is solved in the Born-Oppenheimer approximation, but the ground state energy of the system of interacting particles is represented as a unique functional that depends only on the particle density. The replacing of the multi-electron wave function by the electron density leads to a substantial simplification of the problem, since the electron density is a function of only three spatial coordinates, and the multi-electron wave function depends on 3N variables. DFT methods that include the non-local Hartree-Fock exchange potential are called hybrid methods. The three-parameter functional B3LYP is the most widely used. The DFT/B3LYP method is fairly reliable and is widely used in the study of biological molecules. For a more reliable description of the atomic orbitals, the polarization functions can be added to the basis set, that help to better describe the interatomic interactions and chemical bondsand diffuse functions, which are important for correct description of anions and weak bonds (for example, hydrogen bonds), for calculating the dipole moment, polarizability, etc. In our calculations, the basis set is expanded due to the inclusion of d-type polarization functions for the non-hydrogen atoms (6-31G (d) basis set) and the addition of diffuse s- and p-functions for the non-hydrogen atoms, as well of d-type polarization functions for the non-hydrogen atoms and p -type for the hydrogen atoms (6-31+G (d, p) basis set). Taking into account the correlation of electrons in a wide basis, the methods of the density functional theory provide accuracy comparable to non-empirical calculations.

3. Results and discussion

The structure of the diazacrown ether molecule with the H-Lys-Lys-OH dipeptide fragment in the macrocyclic ring optimized by DFT/B3LYP/6-31G (d) method is shown in Fig.2.

Based on the quantum- chemical calculation, we obtained the geometric, energy, and electronic parameters of the model molecule. The dimensions of the cavity of the formed cycle when calculating in the basis set of 6-31G(d) are 10.18E (N_{37} --- N_{39}) at 9.47E (C_1 --- N_{69}). The optimized bond lengths generally take standard values. The length of C–C bonds in the benzene ring is 1.4E, in the side chains of lysine is 1.54 E, the other C–C bonds are 1.52E. The C=O double bond length is 1.2E, the C=O bond length in the peptide group is 1.35E, while the C_{71}-N_{69} bond length is 1.37 E in the peptide fragment.The bond length of C_1-O_{73} is 1.42E, the bonds of C_9-O_{29} and C_{19}-O_{30} ~ 1.37E. The bond lengths of the amine groups are C–N=1.46E. All C–H bonds are ~ 1.1E, N–H=1.02E, O–H= 0.97 E. The calculation by the method of 6-31+G(d, p) specified, but practically did not change the geometric parameters. The macrocycle became a bit narrower (by 0.07 E) and longer (by 0.08 E), all bond lengths did not change.

At optimization of the macrocycle, the certain changes in the geometrical parameters of the peptide group of the lysine dimerwere occurred. The formation of a closed macrocycle leads to a strong stress in the peptide group, contributing to the extension of the standard peptide bond by 0.4E (the calculation in both basissets gives the value C_{71}-N_{69}=1.37 E) and disruption of the trans configuration of the atoms of the peptide group. We obtainedthe cis configuration,which isconsidered less beneficial, but can beobserved in cyclic peptides. Table 1 shows the values of the valence angles of the peptide group and the internal angles of the formed cavity of the macrocycle, as well as dihedral angles of the cavity that differ from the trans configuration.The valence angles of the peptide group $C_{67}C_{71}N_{69}$ (121°), $C_{71}N_{69}C_{62}$ (131°) and $C_{71}N_{69}H_{70}$ (112°) in both basis sets are by 5°, 9° and 10° more thantheir standard values, respectively.

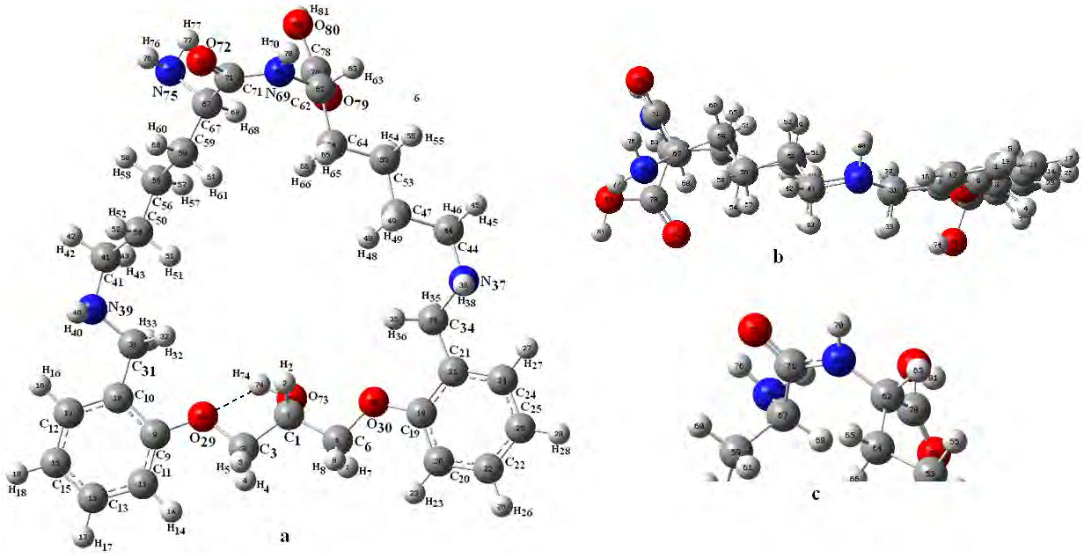

Fig. 2. Optimized structure of the diazacrown ether molecule with the H-Lys-Lys-OH dipeptide fragment in the macrocyclic ring (a), side view (b), peptide group (c).

As can be seen from table 1, the largest difference in the values of valence angles at the calculation in the basis set of 6-31+G (d, p) is observed for the valence angles of $C_3C_1C_6$ (~2°↓), $C_1O_{73}N_{74}$ (1.5°↑) located in the lower part of the complex and the angles $C_{67}N_{75}H_{76}$, $C_{67}N_{75}H_{77}$ (~1.7°↑) and $C_{78}O_{80}H_{81}$ (~1.3°↑) in the peptide group. The greatest changes are observed in the values of the dihedral angles of the peptide group. The angle of internal rotation of the carboxyl moiety COOH $C_{64}C_{62}C_{78}O_{79}$ decreases by 5.4°, and the angle $C_{64}C_{62}C_{78}O_{80}$ of this fragment increases by 5.4°. The dihedral angle of the peptide group $C_{59}C_{67}C_{71}N_{69}$ is reduced by 3.5°. In the lower part of the complex, the dihedral angle $C_3C_1C_6O_{30}$ decreases by 3.8°, the angles $O_{73}C_1C_6O_{30}$ and $C_3C_1O_{73}H_{74}$ increase by 3.3° and 2.7°, and the angles $C_1C_6O_{30}C_{19}$ and $C_{19}C_{21}C_{34}N_{37}$ increase by 2.8° and 2.6°, respectively.

The interaction of hydrogen H_{74} with the oxygen atom O_{29} leads to the formation of the hydrogen bond O_{29}---H_{74} = 2.25E (basis set 6-31+G(d,p) extended this connection by 0.08E). The formation of a bipolar ion due to the protonization of H_{81} between the free carboxyl and amine groups of the dilisin fragment leads to an electrostatic interaction between the ionized H_3N^+ and COO^- groups (at N_{75} and O_{80}). Apparently, the interaction of these groups also contributes to the replacement of their trans- by the cis- configuration.

Table 2 shows the charges on atoms (in charge unit) calculated in basis sets 6-31G (d) and 6-31+G(d, p) for the complex under study.On all hydrogen atoms not listed in the table, the charges of ~0.121÷0.159 units of charge. As you can see, the charges calculated in different basis sets are quite different. The charges calculated in the basis set 6-31+G(d, p) compared to those calculated in the basis set of 6-31G (d) on nitrogen atoms increased by 0.2-0.3 charge units, on oxygen atoms by 0.1, and on O_{80} atom by 0.2 units. The largest changes in the distribution of charges are observed on carbon atoms: the charges on C_{21} and C_{10} atoms increase by 0.7 and

0.6 units of charge, respectively, on atoms of C_{71} and C_{78} decrease by 0.5 units of charge, on atoms of C_{15}, C_{19} and C_{53} decrease by 0.3 units charge.

Table 1.

Valence angles								
	6-31 G(d)	6-31+ G(d,p)		6-31 G(d)	6-31+ G(d,p)		6-31 G(d)	6-31+ G(d,p)
$C_1C_3O_{29}$	104.0	104.2	$C_1C_6O_{30}$	106.1	106.1	$C_{59}C_{67}C_{71}$	109.1	109.0
$C_{29}C_9C_{10}$	114.8	114.8	$C_{30}C_{19}C_{21}$	115.0	114.9	$C_{67}C_{71}N_{69}$	120.7	120.9
$C_9C_{10}C_{31}$	119.1	118.8	$C_{19}C_{21}C_{34}$	119.3	119.0	$C_{67}C_{71}O_{72}$	119.5	119.6
$C_{10}C_{31}N_{39}$	112.9	113.4	$C_{21}C_{34}N_{37}$	112.4	113.0	$N_{69}C_{71}O_{72}$	119.7	119.5
$C_{31}N_{39}C_{41}$	113.9	114.2	$C_{34}N_{37}C_{44}$	114.5	114.7	$C_{64}C_{62}N_{69}$	113.9	114.3
$N_{39}C_{41}C_{50}$	116.3	116.4	$N_{37}C_{44}C_{47}$	116.7	116.9	$C_{71}N_{69}C_{62}$	131.2	131.6
$C_{41}C_{50}C_{56}$	113.0	112.9	$C_{44}C_{47}C_{53}$	112.9	112.7	$C_{71}N_{69}H_{70}$	111.9	111.9
$C_{50}C_{56}C_{59}$	112.7	112.7	$C_{47}C_{53}C_{64}$	112.3	112.6	$C_{62}N_{69}H_{70}$	116.8	116.5
$C_{56}C_{59}C_{67}$	113.7	113.7	$C_{53}C_{64}C_{62}$	114.7	114.3	$N_{69}C_{62}C_{78}$	112.9	113.0
$C_3C_1O_{73}$	110.0	110.4	$C_6C_1O_{73}$	107.9	107.7	$C_{62}C_{78}O_{79}$	125.1	125.1
$C_{67}N_{75}H_{76}$	106.9	108.6	$C_{67}N_{75}H_{77}$	108.8	110.5	$C_{62}C_{78}O_{80}$	112.3	112.2
$C_3C_1C_6$	113.4	111.4	$C_{34}N_{37}H_{38}$	108.9	109.7	$O_{79}C_{78}O_{80}$	122.5	122.6
$C_1O_{73}H_{74}$	106.0	107.5	$C_{44}N_{37}H_{38}$	109.5	109.9	$C_{78}O_{80}H_{81}$	105.7	107.0
Dihedral angles								
$C_9C_{10}C_{31}N_{39}$	-166.4	-168.9	$C_{19}C_{21}C_{34}N_{37}$	160.1	162.7	$O_{72}C_{71}N_{69}H_{70}$	0.0	-0.97
$C_{31}N_{39}C_{41}C_{50}$	-71.1	-71.0	$C_{34}N_{37}C_{44}C_{47}$	61.2	59.5	$C_{64}C_{62}N_{69}C_{71}$	-75.3	-74.4
$C_{59}C_{67}C_{71}N_{69}$	113.6	110.1	$C_{53}C_{64}C_{62}N_{69}$	-157.5	-156.5	$C_3C_1C_6O_{30}$	-166.4	-162.6
$C_{64}C_{62}C_{78}O_{79}$	-12.0	-6.7	$C_{64}C_{62}C_{78}O_{80}$	170.2	175.6	$C_3O_{29}C_9C_{10}$	172.9	172.3
$C_{64}C_{62}N_{69}H_{70}$	103.0	105.4	$O_{73}C_1C_6O_{30}$	71.5	74.8	$C_1C_6O_{30}C_{19}$	176.9	179.7
$C_{59}C_{67}C_{71}O_{72}$	-68.3	-71.1	$C_{21}C_{34}N_{37}C_{44}$	174.4	171.9	$C_3C_1O_{73}H_{74}$	51.7	54.4
$C_{59}C_{67}N_{75}H_{77}$	-174.0	-171.4	$O_{29}C_3C_1H_2$	59.4	57.2	$C_6C_30C_{19}C_{21}$	-176.6	-178.9

Table 2.

	6-31 G(d)	6-31+ G(d,p)		6-31 G(d)	6-31+ G(d,p)		6-31 G(d)	6-31+ G(d,p)		6-31 G(d)	6-31+ G(d,p)
C3	-0.048	-0.183	C6	-0.028	-0.294	C50	-0.276	-0.242	C47	-0.272	-0.061
O29	-0.553	-0.423	O30	-0.526	-0.340	C56	-0.250	-0.081	C53	-0.277	-0.616
C 9	0.331	0.148	C19	0.335	-0.026	C59	-0.267	-0.336	C64	-0.256	-0.016
C10	0.074	0.641	C21	0.065	0.813	H68	0.140	0.116	H63	0.179	0.154
C11	-0.192	0.148	C20	-0.195	0.216	C71	0.596	0.130	N69	-0.612	-0.345
C13	-0.138	-0.318	C22	-0.138	-0.418	O72	-0.527	-0.453	H70	0.333	0.324
C15	-0.132	-0.478	C25	-0.134	-0.434	N75	-0.702	-0.576	C78	0.590	0.094
C12	-0.189	0.038	C24	-0.186	-0.072	H76	0.312	0.312	O79	-0.459	-0.369
C31	-0.172	-0.796	C34	-0.175	-0.833	C1	0.105	0.243	O80	-0.560	-0.363
N39	-0.562	-0.269	N37	-0.558	-0.329	O73	-0.627	-0.536	H81	0.416	0.377
C41	-0.125	-0.190	C44	-0.128	-0.221	H74	0.406	0.370			

It is known that protonation processes should be modeled with the inclusion of diffuse functions in the basis set. A large basis set gives the best results for structural and energy parameters of molecules. However, the Mulliken method for calculating charges is extremely sensitive, and usually, unlike the calculation of energy parameters, the smaller the basis set in calculating charges on atoms, the better. In connection with the above, we consider the charges obtained in the calculation in the basis set of 6-31G (d) to be more reasonable.The formation of the cycle leads to a significant charge redistribution. The hydrogen atoms associated with nitrogen and oxygen serve as electron density donors, which leads to an increase in their positive charge, and carbon atoms become electronegative.

Table 3.

	B3LYP/6-31G (d)	B3LYP/6-31+G (d,p)	Δ
Total energy (a.u.)	-1800.703	-1800.849	0.146↓
Nuclear repulsion energy (Hartrees)	4291.897	4283.441	8.456↓
HOMO (a.u.)	-0.210	-0.221	0.011
LUMO (a.u.)	-0.018	-0.041	0.023
Dipole moment (Debye)	2.2641	2.330	0.066

Table 3 shows the energy parameters and dipole moments. HOMO and LUMO orbitals are the orbitals involved in chemical reactivity, as they are most accessible to electrophiles and nucleophiles, respectively. HOMO (the highest occupied molecular orbital) represents the ability to donate an electron, and LUMO (the lowest free molecular orbital) acts as an electron acceptor.The energy gap between the HOMO and LUMO orbitals at the formation of a cycle is an important indicator of the stability of the structure and in our calculation it is 0.192 a.u. and 0.180 a.u., in the basis sets of 6-31G (d) and of 6-31+G (d, p), respectively.

After studying of the spatial and electronic structure to confirm that the resulting optimized structure is a global minimum, the theoretical calculation of the vibrational spectrum of the cyclic crown ether was conducted using the DFT/B3LYP method in the 6-31G (d) basis set. The calculation showed the absence of negative vibration frequencies, which confirms the correctness of the carried out quantum chemical calculations and the finding of a stable structure.

4. Conclusion

Our quantum-chemical calculation and analysis of the spatial and electronic structure of the new diazacrown ether with the H-Lys-Lys-OH dipeptide fragment in the macrocyclic ring confirmed the possibility of the formation of cyclic structure under study, since such complex formation leads to energy stabilization. The stabilization of the obtained macroheterocycle is provided by the formation of non-covalent interactions within the cyclic structure.

References

1. Wu R, Marta RA, Martens JK, Eldridge KR, McMahon TB, J Am Soc Mass Spectrom. 22, 1651 (2011).
2. Hosseinzadeh P., Bhardwaj G., Mulligan V.K. et al. Science, 358, 1461 (2017).
3. Shimaa A. H. Abdel Monaim, Anou M. Somboro, Ayman El-Faham, Beatriz G. de la Torre and Fernando Albericio, ChemMedChem, 14, 24 (2018).
4. Marcelo D.T. Torres, Shanmugapriya Sothiselvam, Timothy K. Lu and Cesar de la Fuente-Nunez, Journal of Molecular Biology, 10.1016/j.jmb.2018.12.015, (2019).
5. Freza S., Structural Chemistry, **29**, 1025 (2018).
6. Hancock R.E.W. and Sahl H.-G., Nature Biotechnology, 24, 1551 (2006).
7. Shih I.-L., Van Y.-T., and Shen M.-H., Mini-Reviews in Medicinal Chemistry, 4, 179 (2004).
8. VidalL., Thuault V., Mangas A., Covesa sR., ThienpontA., and GeffardM.,Journal of *AminoAcids*, *Article ID 672367*, 10 pages,http://dx.doi.org/10.1155/2014/672367 (2014).
9. Gomes B., Augusto M.T., Felıcio M.R. et al. Biotechnology Advances, 36, 415 (2018).

10. Agyei D., Tan K-X., Pan S., Udenigwe C.C. and Danquah M.K., Biotechnology and Bioengineering, 10.1016/B978-0-08-100736-5.00009-0, (231-251), (2018).
11. Varsha J. Thombare and Craig A. Hutton, Peptide Science, 110, 3, (2018).
12. Diana P. Slough, Sean M. McHugh and Yu-Shan Lin, Biopolymers, 109, 10, (2018).
13. Geornaras I.and Sofos J.N., Journal of Food Science, 70, M404 (2005).
14. Shen W.C. and Ryser H.J.-P., Proc Natl Acad Sci U S A, 78, 7589 (1981).
15. Hasanova U.A., Ramazanov M.A., Maharramov A.M.et al. J Incl Phenom Macrocycl Chem, 86, 19 (2016).
16. Hasanova U.A., Ramazanov M.A., Maharramov A.M. et al. Chem Eng Trans, 47, 109 (2016).

***Corresponding author:** svetlanabest@mail.ru

MICROTURBULENT VELOCITY IN THE ATMOSPHERES OF G SPECTRAL CLASSES STAR

Z.A.SAMEDOV

Department of Astrophysics, Baku State University, Z. Khalilov str.23, AZ 1148, Baku, Azerbaijan.
Shamakhi Astrophysical Observatory of ANAS, AZ 2656, Shamakhi, Azerbaijan.

The microturbulence is investigated in the atmospheres of some G spectral classes stars by the atmosphere model.The microturbulent velocities are determined on the basis of comparison of the values measured from observation and theoretically calculated equivalent widths of lines FeII. It has been found that the microturbulent velocity (ξ_t) depends on the surface gravity (g) in the atmospheres of the star: $\xi_t$decreases with increasing g. The microturbulent velocity is less in the stars with intense atmosphere.

Keywords: stars, microturbulence, fundamental parameters, chemical composition
PACS: 95.30.−k, 95.75.Fg

1.Introduction

As is known that even though all expansion mechanisms are taken into account, it is not possible to explain the observed profiles of spectral lines in the spectrum of the star. Thus, it is assumed that, in addition to the termal (heat) movements of the atoms there are also non-thermal (non-heat) movements in the star atmospheres, which are called turbulent movements. Turbulence is assumed as one of the mechanisms that extends the spectral line in astrophysics.

It was empirically found that the observed Doppler width of the spectral lines can not be explained by the termal (heat) movement of atoms.

Through the expression

$$\Delta\lambda_D = \frac{\lambda}{c}\sqrt{\frac{2RT}{M} + \xi_t^2}$$

it needs to introduse the paremetrs ξ_t. The paremeter ξ_t is expressed as the microturbulence parameter

Let's note that there is no generalized physical theory of the microturbulence. The investigation of the microturbulence in the atmospheres of the star is important for two reasons: first, to determine the chemical composition, and second, to understand the nature of this event.

2.Determination of microturbulent velocity

The microturbulent velocity is determined in the atmospheres of the stars using theatmosphere model for the G-spectral classes HR8304 (G8II), HR8179 (G5II), HR8778 (G8IV) stars.

The observations materials of the stars were obtained on a 2-meter telescope of Shamakhi Astrophysical Observatory of ANAS.

The determination of the mikroturbulent velocity using the model method is based on the study of the equivalent widths in a wide range of neutral atoms or ions spectral lines of any element. The equivalent widths W_λ of the spectral lines of the considered element is calculated by giving different values to the microturbulent velocity and and it is compared with the equivalent widths measured from observation. The abundance of element $lg\varepsilon$ is calculated for the different values of the mikroturbulent velocity ξ_t in each spectral line,The abundance of element lgε does not depend on the equivalent widths W_λ of its spectral lines. ξ_t is determine the atmosphere of the investigated star which corresponds to the graph.

The most lines in the studied spectrum of the stars are the FeI and then $FeII$ lines. However, the effect of the LTE extremes to the neutral iron lines is significant. If the calculations are carried out in LTE, the abundance determined on the FeI lines is less than the abundance when refused from LTE [1]. Unlike FeI lines there is no effect of the LTE extremes to the $FeII$ lines. Therefore, in the atmosphere of the star, the microturbulent velocity ξ_t and the iron abundance are determined on $FeII$ lines.

Only the weak lines are used when determining the microturbulent velocity ξ_t. These lines are formed in deep layers of the atmosphere, these layers are parallel and in LTE form. The fundamental parameters of the stars - effective temperature T_{eff} and surface gravity$log g$ are determined on the basis of comparison of observed and theoretical values of some spectral and photometric quantities [for example, see, 2-11].The obtained values are shown in Table 1.

Knowing the effective temperature and surface gravity of the stars are calculated their models. The iron abundance $log\varepsilon(Fe)$is calculated by giving different values to the microturbulent velocity ξ_t in the atmosphere of each star on these models. The iron abundance is determined on the basis of comparison of the values measured from observation and theoretically calculated equivalent width of the lines $FeII$. Theoretically equivalent width of spectral lines is calculated by DASA programs. The atomic data of the spectral lines are taken from the database VALD 2 [12] The determined abundance $log\varepsilon(Fe)$ on the different equivalent widths of $FeII$ the dependence graphs from W_λ are shown in Figure 1 in the studied atmospheres of the stars.

As seen from Figure 1 there is no correlation between $log\varepsilon(Fe)$ and W_λ when

$\xi_t = 3.2$ km/s for the star HR8304(G8II)
$\xi_t = 2.0$ km/s for the star HR8179 (G5II)
$\xi_t = 1.8$ km/ s for the star HR690 (G8IV)

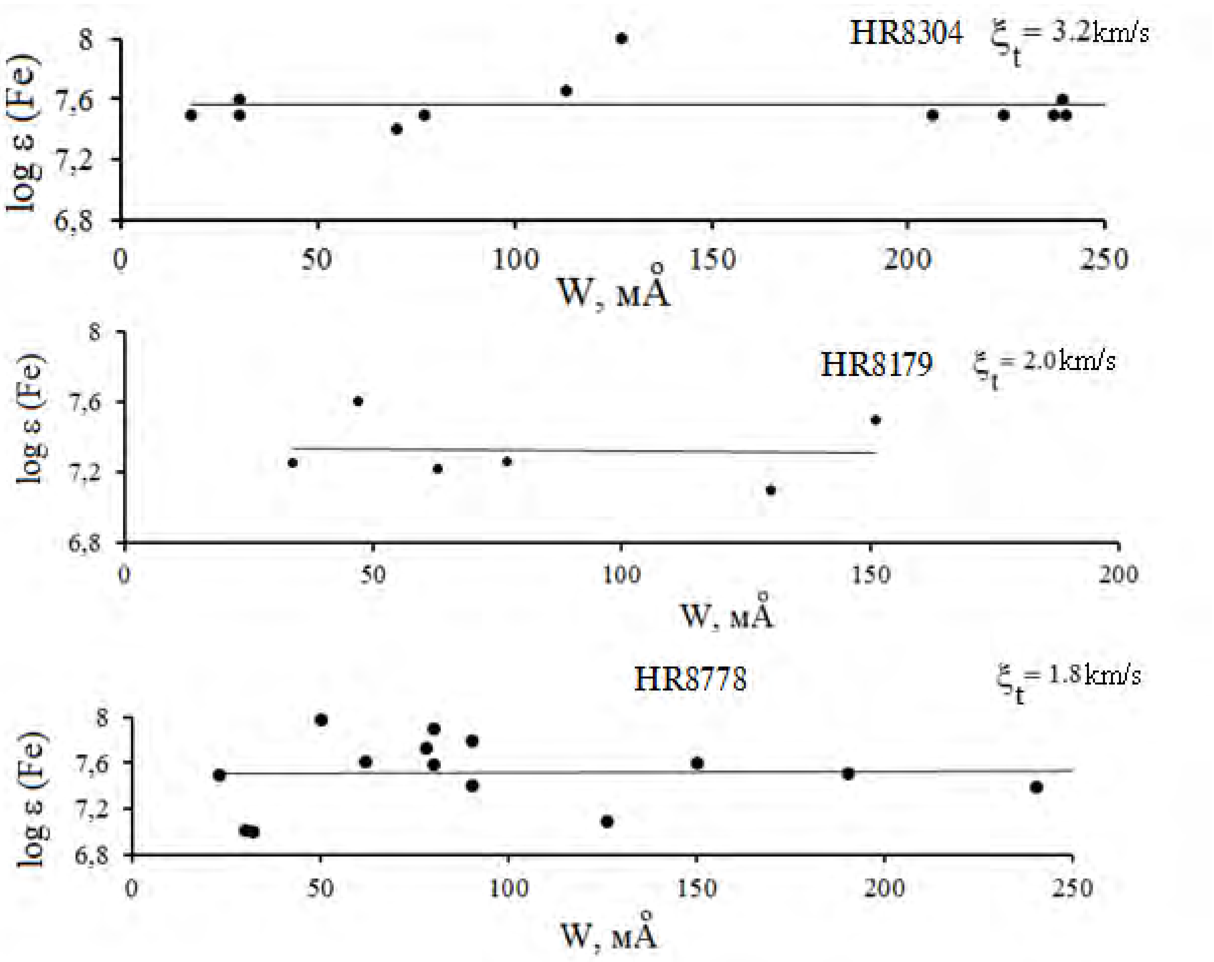

Figure 1. Determination of the microturbulent velocity in the atmosperes of stars

The value of the microturbulent $\xi_t = 1.1$ km/s in the Solar atmosphere is determined in [13].

Table 1 shows the investigated parameters T_{eff}, $logg$, ξ_t,$log\varepsilon(Fe)$ for the studied stars

HR	Sp	T_{eff},K	$logg$	ξ_t, km/s	$log\varepsilon(Fe)$
HR8304	G8II	5010	2.1	3.2	7.56
HR8179	G5III	5200	2.7	2.0	7.32
HR8778	G8IV	5300	3.2	1.8	7.51

Table 1. T_{eff}, $logg$, ξ_t, $log\varepsilon(Fe)$ parameters of the stars

The dependence graphic of the microturbulent velocity ξ_t from surface gravity $logg$ on the star surface (Figure 2) is plotted.

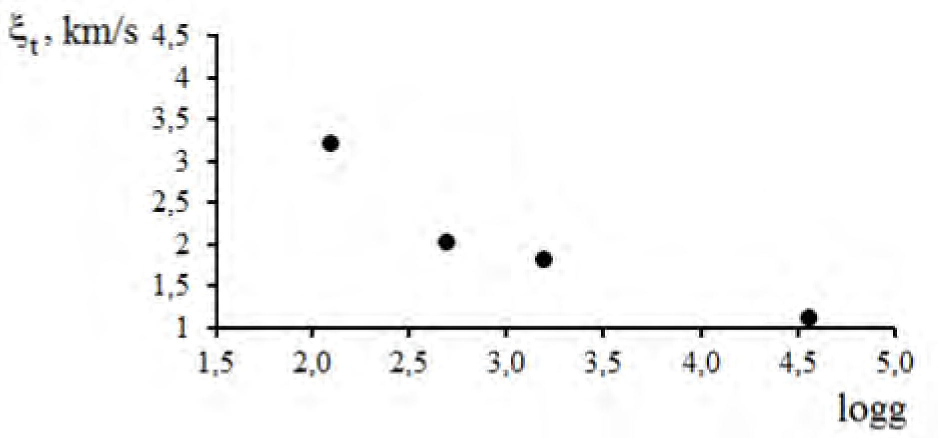

Figure 2. The dependence of the microturbulent velocity on the surface gravity in the atmospheres of the stars.

As is shown in figure the ξ_t depends on $logg$: the ξ_t decreases when $logg$ increases. The microturbulent velocity is less in the stars with intense atmosphere.

Main results

1. The microturbulence velocities are determined using the atmosphere model method:
For the HR8304 (G8II) star, $\xi_t = 3.2$ km/s ,
For the HR8179 (G5III) star, $\xi_t = 2.0$ km / s ,
For the HR8778 (G8IV) star, $\xi_t = 1.8$ km / s .

2. It has been found that the microturbulent velocity (ξ_t) depends on the surface gravity (g) in the atmospheres of the star: $\xi_t$decreases with increasing g. The microturbulent velocity is less in the stars with intense atmosphere.

References

1. Boyarchuk A. A., Lyubimkov L. S., Sakhibullin N.A., Effects of deviations from local thermodynamic equilibrium in the atmospheres of F supergiants. I. Overionization of Fe I atoms, Astrophysics, 22, 203 (1985).
2. Ajabshirizadeh A.A., Muradov A., Samedov Z.A. A model atmosphere analysis of the F6V star π^3 Ori, Astrophysics and Space Science, 293,289 (2004).
3. Khalilov A.M., Samedov Z.A., Gasanova A.P. The investigation of the supergiant stars 89 Her, Astronomics Jour., 85, 940 (2008)
4. Samedov Z.A., Determination of the atmospheric parameters and chemical compozition of 110 Her (F6V) star, News of Baku University, 2, 182 (2010)
5. Samedov Z.A., Hasanova A.R. et al. Investigation of the atmosphere of Post AGB HD 161796 star, Reports of ANAS, Phys.-Tech. and Math. Series, Phys. And Astr.,5, 148 (2016)
6. Samedov Z.A., Gadirova U.R., AmirovSh.Sh. Investıgatıon of the atmosphere of HD 14662 (F7Ib), Modern Trends in Physics , 38 (2017).
7. Samedov Z.A., Gadirova U.R., Investigation of the atmosphere of supergiant stars HD 14662 (F7Ib), GESJ: Physics, 18, 19 (in Russian) (2017)
8. Samedov Z.A. Investigation of the atmosphere of HR382 (φCas, F0Ia) star, International Journal of Development Research, 8, 21398 (2018).
9. Samedov Z.A., Gadirova U. R. Investigation of the atmosphere of thestar HD 164136 (F2II), Astronomy & Astrophysics (Caucasus), 3, 91 (2018)
10. Samedov Z.A., The fundamental parameters of HR 6978(45Dra,F7Ib) star, News of Baku University, 1,149 (2018).
11. Samedov Z.A., Khalilov A.M. et al. Atmosphere of Cyg (F5 Iab) star: fundamental parameters, chemical compozition, Reports of ANAS, Phys.-Tech. and Math. Series, Phys. And Astr., 5, 23(2018)
12. Kupka F., Piskunov N., Ryabchikova T.A., Stempels H.C., Weiss W.W. VALD2: Progress of the Vienna Atomic Line Data Base, AstronomyandAstrophysics. Supplement, 138, 119 (1999).
13. D.M.Kuli-zade, Z.A.Samedov, Z.F.Aliyeva, U.R.Gadirova. Determination of the element abundance of the Sun by method of model, News of Baku University, 4, 181 (2015).

***Corresponding author**: zahir.01@mail.ru

INVESTIGATION OF THE ATMOSPHERE OF HR6978 (*45Dra, F7Ib*) STAR

Z.A.SAMEDOV
Baku State University AZ1148, Baku, Academic Z. Khalilov Street-23
Shamakhi Astrophysical Observatory of ANAS, AZ 2656, Shamakhi, Azerbaijan.

The atmosphere of supergiant star HR6978(45Dra, F7Ib) investigaed by using the atmosphere model method. The following values of parameters effective temperature and surfase gravity have been received:T_{eff}=6000±50 K, logg=1,7±0.07. On the lines FeII has been investigated the parameter microturbulence (velocity). Found that for HR6978 (45Dra, F7Ib) star ξ_t=4.8km/s. In theatmosphere of the star the iron and carbon abundances are calculated and compared with the abundance in the Sun. The iron and carbon abundances are determined by the comparison of measured fromobservation and theoretically calculated values of equivalent width correspondingly FeII, and CIlines.The iron abundance is close to the abundance in the Sun and the carbon abundance is less than theabundance in the Sun: $\log\varepsilon(\mathrm{FeII}) = 7.49 \pm 0.18$, logε(C) = 7.82 ±0.2.

Key words: stars: fundamental parameters – stars: chemical composition - star: individual:HR6978(45Dra, F7Ib)
PACS:95.30.–k, 95.75.Fg

1. Introduction

In this work the atmosphere of the HR6978(*F7Ib*) star is studied by the atmosphere model. The synthesis reactions of Hydrogen to Helium are mostly *CNO* cycles in the the main sequence stars with the temperature $T \geq 15 \cdot 10^6$ Kin the nucleus. Evolutionary calculations of stars show that these stars turn into giant, supergiant stars with spectral classes *A, F,G*after their departure from the main sequence. According to the theory of modern evolution of stars, the process of mixing deep substances occurred in giant, supergiant stars with spectral classes *A, F, G*. As a result, the products of the *C, N, O* cycles reaction must be delivered to the atmosphere, and the abundance of elements *C, N, O* in the atmosphere of these stars should be changed, i.e., the abundance of light elements in giant, supergiant stars with the spectral classes *A, F, G* should be differ from the abundance of light elements found in matter that are formed by these stars. Thus, the determination of the chemical composition of the atmosphere of giant, supergiant stars with *A, F, G* spectral classes is an actual problem from the point of view of the evolution of stars.

In this work, the metallicity of the atmosphere of the star has been determined. In our futurework it is envisaged to determine the abundance of light elements that have evolved in the chemical evolution. The observation material of the star was taken in the 2-meter telescope of the Shamakhi Astrophysical Observatory within the wavelength range $\lambda\lambda 3900 \div 6600 AA^{\circ}$, the atlas was constructed and the equivalent width of the spectral lines was measured.

2. Atmosphere parameters: effective temperature, surface gravity

The effective temperature of the star and the surface gravity are determined by the model method. This method is shown in detail in [1-4].

The following criteria are used:

1. Comparison of the values of the index $[c_1]$ measured from observation and theoretically calculated.
2. Comparison of the measured from observation and theoretically calculated values of the index β.
3. Comparison of the measured from observation and theoretically calculated values of the index Q.

The following values of parameters effective temperature and surfase gravity have been received:

T_{eff}=6000±50 K, logg=1,7±0.07 [1]

3. Microturbulent velocity, chemical composition

In the atmosphere of the star, mikroturbulent movement velocity ξ_t and amount of iron are determined by the lines $FeII$. To determine the mikroturbulent velocity ξ_t it must be a plurality of lines that contain a wide equivalent widhts range of the atoms or ions of any given element. The microturbulent movement velocity $\xi_t$is chosen such that the quantity of elements determined by the different linesdoes not change with the increasing of the equivalent widths W_λ.

The weaker lines are used when determining the velocity of microturbulent movement ξ_t.These lines are formed in deep layers of the atmosphere, these layers are parallel and in LTE form.

The iron abudance $log\varepsilon(FeII)$ is calculated by giving different values to the velocity of microturbulent velociti ξ_t based on the Kurucz model [5] with the Teff=6000K, logg=1.7 parameter.The iron abudanceis determined on the basis of comparison of the values measured from observation and theoretically calculated equivalent width of lines$FeII$ .The atomic data of the spectral lines were taken from the database VALD-2 [6]. There is no correlation between $log\varepsilon(FeII)$ and W_λ when $\xi_t = 4.8\,{}^{km}/_{san}$ (Fig. 1).

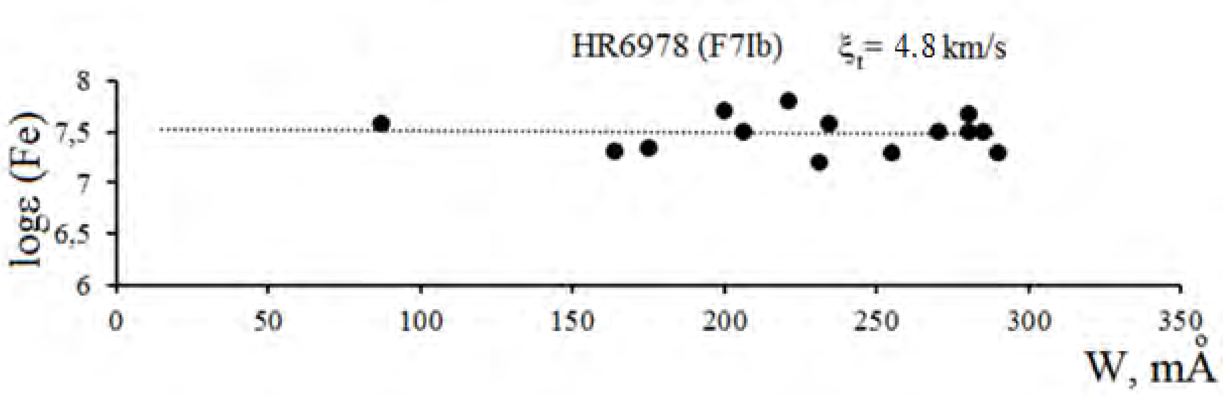

Figure 1. Determination of the velocity of microturbulent movement ξ_t

Thus, inthe the atmosphere of star determines the value for the velocity of microturbulent movement $\xi_t = 4.8\,{}^{km}/_{san}$. At the same time, the iron abundance determines too:

$$log\varepsilon(Fe) = 7.49 \pm 0.18$$

The paprameter $\left[{}^{Fe}/_{H}\right] = \Delta log\varepsilon = log\varepsilon(Fe) - log\varepsilon_{\odot}(Fe)$ is called the metallicity indicator of the star. Here $log\varepsilon_{\odot}(Fe)$ is the iron abundance in the sun: $log\varepsilon_{\odot}(Fe)$=7.45 [7].

Iron abundance is close to abundance in the Sun.This result is an important in the point of view of the Galactic chemical evolution.

From the chemical evolution elements only the lines of element *C* are visible in the spectrum of theHR6978(*45Dra, F7Ib*) star. On the base of these lines for the abundance of element *C* the following value $log\varepsilon(C) = 7.82$ 0.2 is determined

$$[\mathrm{C/H}] = \Delta\log\varepsilon = \log\varepsilon(\mathrm{C}) - \log\varepsilon_{\odot}(\mathrm{C}) = 7.82 - 8.43 = -0.61.$$

Thus, in the atmosphere of the *F* spectral classes HR6978 star the carbon abundance is less than that of the Sun, and the accuracy of the theory of modern evolution is confirmed on the basis of observations.

The defined parameters of the star are:

$T_{eff} = 6000 \pm 50K, logg = 1.7 \pm 0.07, \xi_t = 4.8\, {}^{km}/_{s}, log\varepsilon(Fe) = 7.49 \pm 0.18,\ [{}^{Fe}/_{H}] = 0.05$

$$log\varepsilon(C) = 7.82 \pm 0.2, [C/H] = -0.61.$$

The abundance of metals in the star is almost equal to the abundance in the Sun, and the carbon abundance is smaller. The HR6978(45Dra,*F7Ib*) star and the Sun have the same chemical composition, and in the evolution process the mixing deep substances process occurred in HR6978(45Dra,*F7Ib*) supergiants. As a result, the products of the *C,N,O* cycles reaction is delivered to the atmosphere and in the abundance of the elements *C,N,O* has been changed in the atmosphere of this star. This result is an important in the point of view of the Galactic chemical evolution.

1. Main results

1.The following values of parameters effective temperature and surfase gravity of the star $HD6978\ (F7Ib)$have been received:T_{eff}=6000±50 K, logg=1,7±0.07.

2. Based on the $FeII$ lines the velocity of microturbulent ξ_t is determined: $\xi_t = 4.8\, {}^{km}/_{s}$.

3. In the atmosphere of the star the iron and carbon abundances are calculated and compared with the abundance in the Sun. It has been found that the iron abundance is close to abundance in the Sun, but the carbon abundance is less.

References

1. Lyubimkov L.S, Lambert D.L.,RostopchinS.I. , RachkovskayaT.M.,andPokladD.B. , Monthly Notices Roy. Astron. Soc., 402, 1369 (2010)
2. Samedov Z.A., Gadirova U.R., AmirovSh.Sh. Modern Trends in Physics , 38 (2017)
3. Samedov Z.A. International Journal of Development Research, 08, 21398 (2018)
4. Samedov Z. A., Gadirova U. R. Astronomy & Astrophysics (Caucasus), 3, 91 (2018).
5. Kurucz L.S., CD-ROM 13, ATLAS9 Stellar AtmosphereProgramsand 2km/s grid.Cambridge, Mass.;Smithsonian Astrophys.Obs., (1993).
6. Kupka F.N., Piskunov T., Ryabchikova T., Stempels H.C., Weiss W.W., Astron.&Astrophys, Suppl.Ser.,138, 119.(199)
7. Scott L.S., Asplund M., Grevesse N., Bergemann M., and Sauval M., Astron. Astrophys., 26, 573. (2015)

Corresponding author: zahir.01@mail.ru

HIGGS BOSON RADIATION IN ELECTRON-POSITRON COLLISIONS

S.K.ABDULLAYEV[1,a], M.SH. GOJAYEV[1,b]
[1]BakuStateUniversity, Department of Theoretical Physics, Azerbaijan, AZ 1148, Baku, Z. Khalilov, 23

In this work discuss the process of the associated production of the Higgs boson H and a longitudinally polarized heavy fermion pair in the annihilation of an arbitrarily polarized electron-positron pair $e^-+e^+\to(\gamma^*;\,Z^*)\to H+f+\bar{f}$. The analytical expression of the differential cross section of the process is obtained, the features of the cross section behavior, the angular correlations of particles, the left-right spin asymmetry A_{LR}, the degree of longitudinal polarization of the fermion P_f, and the transverse spin asymmetry $A_\perp$ are investigated. The results of the calculations are illustrated with graphs. The possibility of experimental measurement of the coupling constant g_{Htt} is discussed.

Keywords: Standard model, Higgs boson, electron-positron, heavy fermion pair, felicity, coupling constant.
PACS: 12.15-y, 13.66.Fg, 14.70.Hp, 14.80.Bn.

1. Introduction

With the discovery of the scalar Higgs boson by the ATLAS and CMS collaborations at the Large Hadron Collider (LHC) at CERN [1, 2], the Standard Model (SM) entered a new stage in the study of the properties of the fundamental interactions of elementary particles. In this connection, interest in various channels of the Higgs boson production and decay has greatly increased [3-6]. To this end, in the present work, we studied the joint production of the standard Higgs boson H and a heavy fermion pair in arbitrarily polarized electron-positron collisions in the framework of the SM

$$e^- + e^+ \to (\gamma^*;\, Z^*) \to H + f + \bar{f}\,, \qquad (1)$$

where $f\bar{f}$ – may be a lepton ($\tau^-\tau^+$) or quark ($b\bar{b}$, $t\bar{t}$) pair.

2. Theoretical framework

In the SM process (1) is described by two of Feynman diagrams, shown in Fig. 1, where 4-momenta of the particles are written in parentheses.

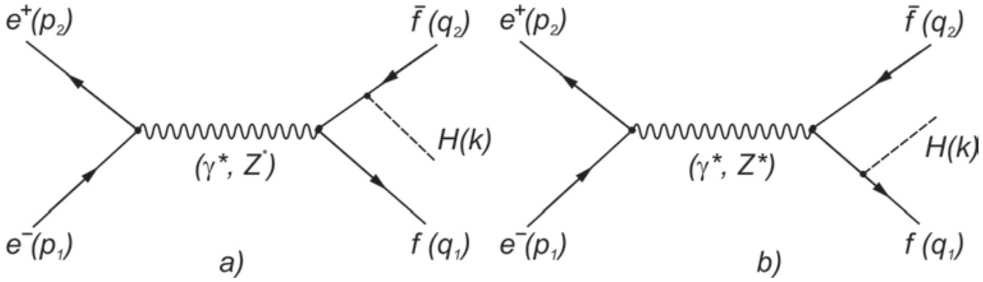

Figure 1.Feynman diagrams for the associated production of Higgs boson with a fermion pair

Within the framework of the SM, the matrix element corresponding to diagrams a) and b) can be written as:

$$M_{i\to f} = M_{i\to f}^{(\gamma)} + M_{i\to f}^{(Z)}, \qquad (2)$$

$$M_{i\to f}^{(\gamma)} = \frac{ie^2 Q_e Q_f}{s}\, g_{Hff}\cdot \ell_\mu^{(\gamma)}\cdot J_\mu^{(\gamma)}, \qquad (3)$$

$$M_{i\to f}^{(Z)} = \frac{ie^2}{s-M_Z^2}\, g_{Hff}\cdot \ell_\mu^{(Z)}\cdot J_\mu^{(Z)}. \qquad (4)$$

Here $Q_e = -1$ – is the electric charge of an electron in units e;

$$\ell_\mu^{(\gamma)} = \bar{\upsilon}_e(p_2)\gamma_\mu u_e(p_1), \quad J_\mu^{(\gamma)} = \bar{u}_f(q_1)\left[\frac{\hat{q}_1 + \hat{k} + m_f}{(q_1+k)^2 - m_f^2}\gamma_\mu - \gamma_\mu \frac{\hat{q}_2 + \hat{k} - m_f}{(q_2+k)^2 - m_f^2}\right]\upsilon_f(q_2), \qquad (5)$$

$$\ell_\mu^{(Z)} = \bar{\upsilon}_e(p_2)\gamma_\mu[g_V(e) + \gamma_5 g_A(e)]u_e(p_1),$$

$$J_\mu^{(Z)} = \bar{u}_f(q_1)\left\{\frac{\hat{q}_1 + \hat{k} + m_f}{(q_1+k)^2 - m_f^2}\gamma_\mu[g_V(f) + \gamma_5 g_A(f)] - \gamma_\mu[g_V(f) + \gamma_5 g_A(f)]\frac{\hat{q}_2 + \hat{k} - m_f}{(q_2+k)^2 - m_f^2}\right\}\upsilon_f(q_2) \qquad (6)$$

– electromagnetic (weak) currents of the electron-positron and heavy fermion pair; $s = p^2 = (p_1 + p_2)^2$ – the square of the total energy e^-e^+-pairs in the center of mass system, m_f and Q_f – the mass and electric charge of the fermion f, g_{Hff} – the coupling constant of a Higgs boson with a heavy fermion pair, M_Z – the mass of a Z^0-boson, $g_V(e)$ and $g_A(e)$ ($g_V(f)$ and $g_A(f)$) – the vector and axial-vector coupling constants of the electron (fermion) with Z^0-boson.

We use a coordinate system in which the OXZ plane coincides with the particle production plane $\vec{q}_1 + \vec{q}_2 + \vec{k} = 0$, and we introduce angles θ, χ and φ, where θ – is the polar angle between the Z axis and the direction of the electron beam, χ – is the azimuth angle between the production plane and the plane defined by the Z axis and the electron beam, φ – the azimuth angle between the planes of production and transverse polarization of the electron. In this coordinate system, the distribution of particles over the angles θ and χ present in the form:

$$\frac{d^4\sigma}{d\chi d(\cos\theta)dx_1dx_2} = \frac{\alpha_{\text{QED}}^2 N_C}{128\pi^2 s} g_{Hff}^2 G_A(\sigma_1 + 2\sigma_3)(1+\alpha_0)[1 + \alpha_1\cos^2\theta +$$
$$+ \alpha_2\sin^2\theta\cos 2\chi + \alpha_4\sin^2\theta\sin 2\chi + \alpha_7\cos\theta + \alpha_8\sin\theta\cos\chi], \qquad (7)$$

where the coefficients of the angular distributions of particles are determined by the expressions

$$\alpha_0 = -\frac{G_C}{G_A}\cdot\frac{2}{x_H^2}(1+x_H)(1-x_1)(1-x_2), \quad \alpha_1 = \frac{3c_{23}^2 - 1}{3 - c_{23}^2}\cdot\frac{1-\alpha_0}{1+\alpha_0},$$
$$\alpha_2 = \frac{s_{23}^2}{3 - c_{23}^2}\cdot\frac{1-\alpha_0}{1+\alpha_0}, \qquad \alpha_4 = -\frac{2s_{23}c_{23}}{3 - c_{23}^2}\cdot\frac{1-\alpha_0}{1+\alpha_0},$$
$$\alpha_7 = \frac{G_B}{G_A}\frac{1}{1+\alpha_0}\frac{2[x_2(1-x_1)(c_{23}-1) - x_1(1-x_2)(c_{23}-c_{21})]}{x_H(3-c_{23}^2)}, \qquad (8)$$
$$\alpha_8 = \frac{G_B}{G_A}\frac{1}{1+\alpha_0}\frac{2[x_2(1-x_1)s_{23} - x_1(1-x_2)(s_{23}+s_{21})]}{x_H(3-c_{23}^2)},$$

$$G_A = Q_e^2Q_f^2 + 2Q_eQ_f g_V(e)g_V(f)X_Z + [g_V^2(e) + g_A^2(e)][g_V^2(f) + g_A^2(f)]X_Z^2,$$
$$G_B = 2g_A(e)g_A(f)[Q_eQ_f + 2g_V(e)g_V(f)X_Z]X_Z, \qquad G_C = [g_V^2(e) + g_A^2(e)]g_A^2(f)X_Z^2,$$
$$s_{23} = \frac{2\sqrt{(1-x_1)(1-x_2)(1-x_H)}}{x_2x_H}, \quad c_{23} = 1 - \frac{2(x_2 + x_H - 1)}{x_2x_H}, \qquad (9)$$

$x_1 = \frac{2E_1}{\sqrt{s}}$, $x_2 = \frac{2E_2}{\sqrt{s}}$, $x_H = \frac{2E_H}{\sqrt{s}} = 2 - x_1 - x_2$ – are the scaling energies of the fermion, antifermion and Higgs boson.

In Fig. 2 shows the dependence of the coefficients on a variable x_2 with a fixed scaling energy $x_1 = 0.9$ in the process $e^- + e^+ \to H + t + \bar{t}$. Here and in further calculations, the energy of electron-positron beams is assumed $\sqrt{s}$ = 1 TeV, mass of Z^0-boson M_Z = 91.1875 GeV, mass of t-quark m_t = 173.2 GeV, Weinberg parameter x_W = 0.232. As you can see, the coefficient α_1 (α_7, α_8) is negative and decreases (increases) with increasing energy x_2. The coefficient of the angular distribution α_2 is positive and slowly increase with increasing variable x_2. The angular distribution coefficient α_4 at the beginning of the energy spectrum is negative, it increases with increasing x_2 and at the end of the energy spectrum becomes positive.

When electron-positron pair a longitudinally polarized the differential cross section of reaction (1), integrated over the angles θ and χ, can be represented as:

$$\frac{d^2\sigma(\lambda_1,\lambda_2)}{dx_1 dx_2} = \frac{d^2\sigma_0}{dx_1 dx_2}[1-\lambda_1\lambda_2-(\lambda_1-\lambda_2)A_{LR}]. \tag{10}$$

Here

$$\frac{d^2\sigma_0}{dx_1 dx_2} = \frac{\alpha^2_{\text{QED}} N_C}{12\pi s} g^2_{Hff}\left\{G_A \frac{x_H^2}{(1-x_1)(1-x_2)} - 2[g_V^2(e)+g_A^2(e)]g_A^2(f)(1+x_H)X_Z^2\right\} \tag{11}$$

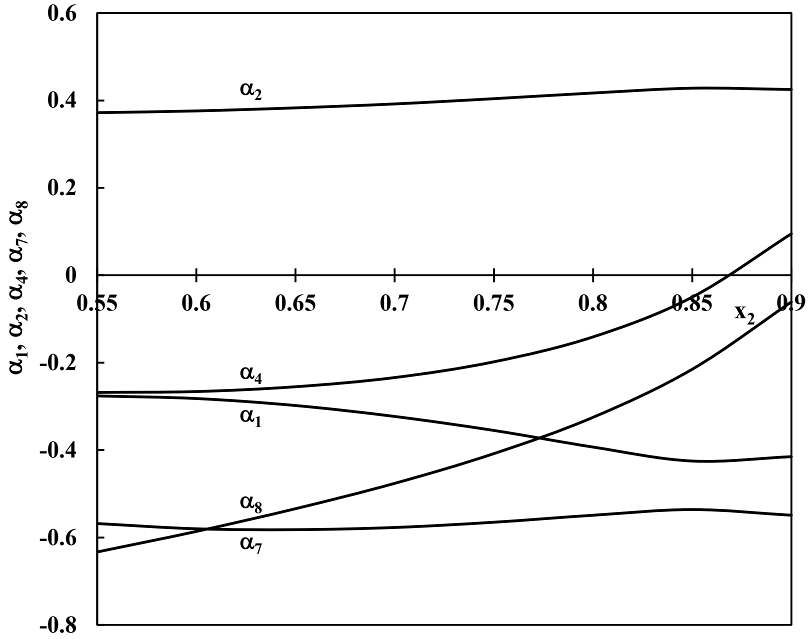

Figure 2. Dependence of the angular distribution coefficients on the energy x_2 in the reaction $e^-e^+ \to Ht\bar{t}$.

– the differential cross section of this process in the case of unpolarized particles, and

$$A_{LR} = \frac{G_D x_H^2 - 4g_V(e)g_A(e)g_A^2(f)(1+x_H)(1-x_1)(1-x_2)X_Z^2}{G_D x_H^2 - 2[g_V^2(e)+g_A^2(e)]g_A^2(f)(1+x_H)(1-x_1)(1-x_2)X_Z^2} \tag{12}$$

– left-right spin asymmetry due to the longitudinal polarization of the electron and the designation introduced

$$G_D = 2Q_e Q_f g_A(e) g_V(f) X_Z + 2g_V(e)g_A(e)[g_V^2(f)+g_A^2(f)]X_Z^2.$$

The left-right spin asymmetry A_{LR} in the process $e^- + e^+ \to H + t + \bar{t}$ at $x_2 = 0.95$ approximately 17.6% and slightly increases with growth x_1, remaining almost constant. The same character is the left-right spin asymmetry in the process $e^- + e^+ \to H + \tau^- + \tau^+$. However, in this process, the left-right spin asymmetry is almost three times less than in the process $e^- + e^+ \to H + t + \bar{t}$.

Due to the weak interaction in the process under consideration, fermion and antifermion can be produced longitudinally polarized. Taking into account the longitudinal polarizations of the heavy fermion pair, the differential cross section integrated over the angles is:

$$\frac{d^2\sigma(h_1,h_2)}{dx_1 dx_2} = \frac{1}{4} \cdot \frac{d^2\sigma_0}{dx_1 dx_2}[1 + h_1 h_2 + (h_1 + h_2)P_f]. \tag{13}$$

Here

$$\begin{aligned} P_f = {} & \{Q_e Q_f g_V(e) g_A(e) X_Z + [g_V^2(e) + g_A^2(e)] g_V(f) g_A(f) X_Z^2\} \times \\ & \times \{(1 - x_1)[x_H x_2 c_{23} + 3(1 - x_1)] - (1 - x_2)[x_H x_1 (c_{23} c_{21} - s_{23} s_{21}) + 3(1 - x_2)]\} \times \\ & \times \{G_A x_H^2 - 2(1 - x_1)(1 - x_2)[g_V^2(e) + g_A^2(e)] g_A^2(f)(1 + x_H) X_Z^2\}^{-1} \end{aligned} \tag{14}$$

– degree of longitudinal polarization of the fermion or antifermion.

In Fig. 3 shows the dependence of the degree of longitudinal polarization t-quark in the process $e^- + e^+ \to H + t + \bar{t}$ on the variable x_1 at a fixed scaling energy $x_2 = 0.9$ and $x_2 = 0.95$. From the graphs it follows, that with increasing scaling energy x_1 the degree of longitudinal polarization decreases monotically. However, at a fixed quark energy x_1 with an increase in the antiquark energy x_2, the magnitude of the degree of longitudinal polarization increases.

Note that the degree of longitudinal polarization t-quark has already been measured by the ATLAS detector in the process of hadron production of a pair $t\bar{t}$ at the Large Hadron Collider.

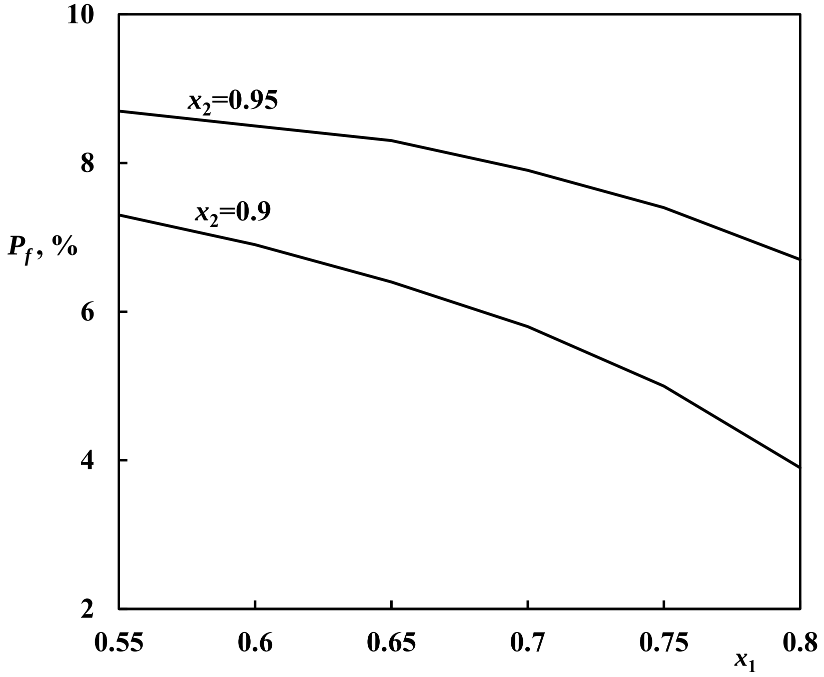

Figure 3.The degree of longitudinal polarization in the process $e^- e^+ \to Ht\bar{t}$ as a function of the energy x_1 for different x_2

3. Conclusion

Thus, we discussed the process of the associated production of the Higgs boson H and a longitudinally polarized heavy fermion pair in the annihilation of an arbitrarily polarized electron-positron pair $e^- + e^+ \to (\gamma^*; Z^*) \to H + f + \bar{f}$. An analytical expression of the differential cross section of the process is obtained, the features of the cross section behavior, angular correlations of particles, left-right spin asymmetry A_{LR} , the degree of longitudinal polarization of the fermion P_f are investigated. The results of the calculations are illustrated with graphs.

References

1. ATLAS Collaboration ,Phys. Letters, B716, 1(2012).
2. CMS Collaboration, Phys. Letters, B716, 30 (2012).
3. Abdullayev S. K., Gojayev M.Sh., Saddigh F.A., Moscow University Physics Bulletin, 72, No 4, 329 (2017).
4. Abdullayev S.K., Gojayev M.Sh., Nasibova N.A., Russian Physics Journal, 61, No 1, 94 (2018).
5. Abdullayev S.K., Gojayev M.Sh. // Moscow University Physics Bulletin, 74 (1), 24 (2019).
6. Djouadi A. The Anatomy of Electro-Weak Symmetry Breaking. Tome II: arXiv: hep-ph/0503173v2, 2003; DOI: 10.1016/j.physrep.10.005 (2007).

***Corresponding author**: m_qocayev@mail.ru

CHARACTERISTIC FEATURES OF THE CHANGE OF THE SPECTRAL TYPE OF THE SEYFERT GALAXY NGC 2617

N.A.HUSEYNOV[1], V.L.OKNYANSKY[2], Kh.M.MIKAILOV[1], V.M. LIPUNOV[2], V.I. METLOV[2], N.I.TAGHIYEVA[1]

[1]*Shamakhy Astrophysical Observatory, National Academy of Sciences, AZ 5626 Pirkuli, Azerbaijan*

[2]*Sternberg Astronomical Institute, M. V. Lomonosov Moscow State University, Universitetsky pr., 13, 119234 Moscow, Russian Federation*

Optical and near-infrared photometry, optical spectroscopy, and soft X-ray and UV monitoring of the changing-look active galactic nucleus NGC 2617 show that it continues to have the appearance of a type-1 Seyfert galaxy. An optical light curve for 2010–2016 indicates that the change of type probably occurred between 2010 October and 2012 February and was not related to the brightening in 2013. In 2016, NGC 2617 brightened again to a level of activity close to that in 2013 April. We find variations in all pass bands and in both the intensities and profiles of the broad Balmer lines. A new displaced emission peak has appeared in H*β*. X-ray variations are well correlated with UV–optical variability and possibly lead by 2–3 d. The *K* band lags the *J* band by about 21.5 ± 2.5 d and lags the combined *B* + *J* filters by 25 d. *J* lags *B* by about 3 d. This could be because *J*-band variability arises from the outer part of the accretion disc, while *K*-band variability comes from thermal re-emission by dust. We propose that spectral-type changes are a result of increasing central luminosity causing sublimation of the innermost dust in the hollow bi-conical outflow. We briefly discuss various other possible reasons that might explain the dramatic changes in NGC 2617.

Key words: line: profiles – galaxies: active – galaxies: individual: NGC 2617 – galaxies: Seyfert – infrared: galaxies – X-rays: galaxies.

PACS:98.54.Cm, 98.35.Df, 98.35.Jk (all)

2. Introduction

For decades, astronomers wondered why we see internal regions in some active galactic nuclei, but not in others. The most popular explanation is a different viewing angle: if the AGN is located flat relative to the observer from the Earth, then a hot gas falling in a spiral into its black hole can be considered, and if it is tilted to the line of sight, only slow moving gas clouds will be visible light year distance or more from the black hole. However, there are AGNS that do not fit into these representations: they can either open the inner region of the nucleus or hide it, in other words, changing look their type.

Active galactic nuclei (AGNs) can be classified on the basis of their optical spectra into ‘type-1’ AGNs (Sy1), showing prominent broad Balmer lines, and ‘type-2’ AGNs (Sy2), lacking obvious broad Balmer lines. Designations such as ‘Seyfert 1.8’ are used for intermediate cases [1]. Rare cases of so-called ‘changing-look’ AGNs (CL AGNs) – AGNs that show extreme changes of spectral type – pro-vide important tests of theories of the Sy1/Sy2 dichotomy. The first detailed investigations of changes from type 2 to type 1 and back to type 2 were for Mrk 6 [2] and for NGC 4151 [3, 4, 5]. Recent reviews by Shappee et al. [6] and Koay et al. [7] give lists of objects and references.

CL AGNs such as NGC 2617 are rare. There are currently only some tens of cases known. However, the small number of known CL AGNs is comparable to the number of AGNs that have had many years of spectral monitoring. It is therefore reasonable to suspect that perhaps each strongly variable AGN could be found to be a CL AGN if observed long enough. This assumption is supported by recent results of Runco et al. [8] that about 38 per cent of 102 Seyferts changed the type, and about 3 per cent of the objects have disappearing H*β* on time-scales of 3–9 yr. Also, MacLeod et al. [9] estimate that >15 per cent of strongly variable luminous quasars exhibit a changing-look behaviour on rest-frame time-scales of 3000–4000 d.

3. Observations

We commenced the spectroscopic and photometric monitoring of NGC 2617 in 2016 January to see if it still appeared to be a type-1 AGN three years after the intensive 2013 monitoring campaign of Shappee et al. [6]. Our observations included IR (*JHK*) and optical (BVR_cI_c) photometry and spectroscopy. Additionally, we have used unfiltered optical monitoring by the MASTER robotic network from 2010 to 2016. We found that the nucleus of NGC 2617 remains in a high state and can still be classified as a type-1 AGN [10]. The optical photometry and IR photometry show that the activity of NGC 2617 is continuing and that it underwent another series of outbursts in 2016 April–June. These outbursts are comparable, in level, to those when NGC 2617 was observed by Shappee et al. [6] in 2013 May [11, 12]. We subsequently applied for soft X-ray and UV observations with the *Swift*/XRT. These began on 2016 May 17 and continued till 2016 June 23.

4. Optical spectroscopy

We obtained optical spectra covering 4100–7000 E with the 2 Ç 2 prism spectrograph and a 4K CCD (spectral resolution 3–7 E) on the 2-m Zeiss telescope of the Shamakhy Astrophysical Observatory (ShAO) on the four nights of 2016 February 3 and 4, March 4 and April 9. Examples of mean spectra of the Hβ region for three of the nights can be seen in Fig. 1 together with a spectrum from Shappee et al. [6]. It can be seen from all our 2016 spectra that NGC 2617 can be classified without any doubt as a type-1 AGN.

In our spectra, one can see a displaced emission component in the red wing of Hβ at a relative velocity of +2500 km s^{-1}, which was not apparent in spectra obtained in 2013. We could not verify that this new component is also present in the Hα profile because of the inferior resolution of the prism spectrograph at long wavelengths. The emission component cannot be identified confidently in the profile of H$_\gamma$ as there is strong [O III] λ4363 emission.

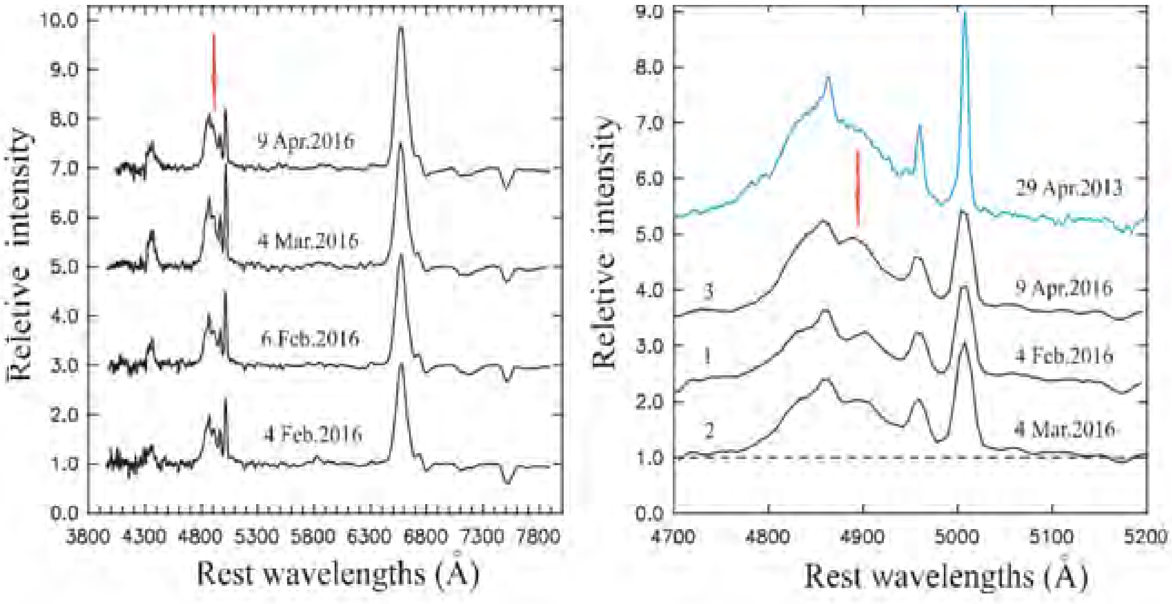

Figure 1.Top panel: our mean spectra for four dates normalized to thecontinuum and offset for clarity. Bottom panel: comparison between the Shappee et al. [6] Apache Point Observatory 2013 April 25 spectrum of the Hβ region of NGC 2617 and our spectra from 2016 February 4 (1), March 4 (2) and April 9 (3). Spectra have been normalized to the continuum level, and then relative calibration has been performed by assuming a constant

flux in [O III] λ5007 and λ4959. Spectra are offset for clarity. The arrows show the locations of the displaced emission peak in the red wing of Hβ.

4. Optical BVR_cI_c observations

We obtained optical BVR_cI_c CCD data with the AZT-5 (a Maksutov 50-cm meniscus telescope equipped with an Apogee Alta U8300 CCD camera) at the MSU Crimean Observatory and with the Zeiss-600 using a 4K CCD at ShAO on 17 nights in 2016 March–May. The data were calibrated using SDSS stars within 1.5 arcmin of NGC 2617 and transformed into the Johnson–Cousins magnitude system in the same manner as Shappee et al. [6]. We measured the background within an annulus of radii 35–45 arcsec.

The *BVRI*light curves are shown in Fig. 2. The magnitudes are for an aperture of 5 arcsec radius. NGC 2617 can be seen to have brightened by about 0.3 mag in *B* during March and then decreased by 0.1 mag in the middle of April. At the end of April, it began to brighten again and reached a maximum of 14.6 in *B* on May 19. One more maximum of the similar magnitude was reached near June 15. The amplitude of variations in *V* was about half the amplitude in *B*. Variations in$R_c$and $I_c$were synchronized with *B*-band variationsbut still with smaller amplitudes.

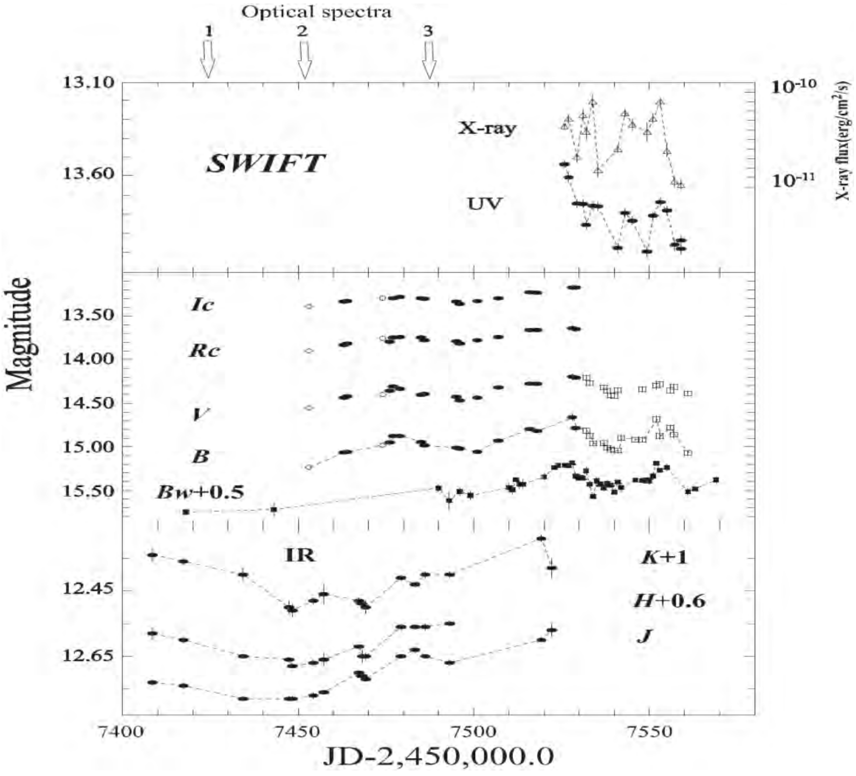

Figure **2.**Near-IR (bottom panel), optical (middle panel) and UV–X-ray (top panel) photometric observations of NGC 2617 over the 5-month period from2016 January 30 to June 29. The solid circles in the middle panel are BVR_cI_c data obtained with AZT-5, while the open circles are observations with the Zeiss-600. Open boxes are filtered *BV* data obtained by the MASTER network, and solid squares (*Bw*) are from unfiltered MASTER data reduced to the *B* system. In the top panel, the solid circles are the combined *Swift* UV photometry reduced to the *UVW*1 system, whilst the X-ray flux is shown by the open triangles. Error bars are shown, but they are generally smaller than the plotting symbols. The dates of the optical spectra are indicated.

5. Results

We determined the lag time in the K band (2.2 μm) relative to the optical variability in NGC 2617 in 2016 was about 25 days, which coincides with the estimate of the radius at which dust should be sublimated. For NGC2617, lags between variability at different wavelengths are defined. These results partially confirmed the previously obtained results, which are partly new and original; in particular the determination of the lag time of flow variations in the filter K, the relative optical variability is the first reliable result for this object.

We firstly discovered the presence of a variable emission component in the H_β line profile in the Seyfert galaxy NGC 2617 and noted that similar features are characteristic of other galaxies that changed their spectral type.

References

1. Osterbrock D. E., Seyfert galaxies with weak broad H alpha emission lines, ApJ, 249, 462-470, (1981).
2. Chuvaev K. K., Multiyear spectral observations of the nuclei of active galaxies in the optical spectral region. II - Variations of the H-beta-line profile in the spectrum of the nucleus of the galaxy MKN 6,Izvestiya Ordena Trudovogo Krasnogo Znameni Krymskoj Astrofizicheskoj Observatorii//83, 194-205, (1991).
3. LyutiiV.M., Oknyansky V.L., Chuvaev K.K., NGC4151-Sy2 in a deep photometric minimum, Letters to an astron. Journals,T.11. pp.803-808, (1984)
4. Penston M.V., Perez E., An evolutionary link between Seyfert I and II galaxies?, MNRAS, 211, 33-39, (1984).
5. Lyuty V. M., Oknyansky V. L., Chuvaev K. K., NGC 4151 - A Seyfert 2 in a deep photometric minimum// Sov. Astron. Lett., 10, 335-336, (1984).
6. Shappee B., Prieto J., Grupe D.et al., The man behind the curtain: X-rays drive the UV through NIR variability in the 2013 AGN outburst in NGC 2617, Astrophysics. J.V.788. № 48, P.1-13, (2014).
7. Koay J. Y., Vestergaard M., Casasola V., Lawther D., Peterson B. M., ALMA probes the molecular gas reservoirs in the changing-look Seyfert galaxy NGC MNK 590, MNRAS, 455, 2745-2764, (2016).
8. Runco J.N. , Cosens Maren, Bennert V. N. et.al., Broad Hβ Emission-line Variability in a Sample of 102 Local Active Galaxies,*Ap.J.*, **821**, p.33-54, (2016).
9. MacLeod, Chelsea L., Ross, Nicholas P. et al., A systematic search for changing-look quasars in SDSS, MNRAS 457, p.389-404, (2016).
10. Oknyansky V. L., Huseynov N. A., Artamonov B. P., et al., The Astronomer's Telegram, The changing-type Seyfert NGC 2617 remains in a high state, 9015, (2016).
11. Oknyansky V. L., Huseynov N. A., Lipunov V. M., et al., Changing-type Seyfert NGC 2617 brightens again, 9030, (2016).
12. Oknyansky V. L., Huseynov N. A., Gaskell C. M., et al., The Astronomer’s Telegram, New outburst of NGC 2617, 9050, (2016).

***Corresponding author**: nazimqaramamedli@mail.ru

AGROPHYSICAL PROPERTIES OF GRAY-BROWN IRRIGATED SOILS UNDER THE VEGETABLE CROPS OF THE ABSHERON PENINSULA OF THE REPUBLIC OF AZERBAIJAN

M.M.Yusifova[1], N.A. Sultanova[2], K.A.Huseynov[*1]
[1]*Baku State University , Ecology and Soil Science faculty, Azerbaijan, Baku, AZ1148, Z.Khalil. str.53*
[2]*Baku Slavic University, Azerbaijan, Baku, AZ1014, S.Rustam str.33*

The Absheron peninsula is one of the most developed regions of commercial vegetable production in Azerbaijan. Despite the fact that in recent years, Absheron has given preference to the cultivation of vegetable crops in greenhouses, the intensive development of cultivating vegetables in the open field has also not lost its significance. Agrophysical properties of soils are of great importance in the agronomic and environmental aspects of growing vegetables. The best soils for irrigated industrial vegetable growing are light and medium loams, whose agrophysical properties provide favorable conditions for the growth and development of most vegetable crops. To determine the current state of vegetable-suitable soils of the Absheron peninsula, researches were conducted, the main agrophysical and agrochemical properties and soil regimes were determined, on the basis of which a characteristic of irrigated gray-brown soils of the studied region was given.

Keywords: physical clay, humus, water-resistant aggregates, temperature regime, vegetable crops
PACS: 91.62.Rt; 92.40.Lg; 92.40.Oj; 91.62.Mn

1. Introduction

Among the regulated factors that have a significant impact on crop yields, soil fertility is most important - the content of available nutrients, organic matter, particle size distribution, water and air regimes, as well as their phytosanitary condition. Since the cultivation of vegetables is costly and is justified only on fertile soils that provide high yields, then during the development vegetable crop rotations, the soil is cultivated and further maintain effective soil fertility at a level that meets the requirements imposed by cultivated plants at a given productivity. Cultivation of vegetable crops on poorly cultivated soils does not allow to obtain satisfactory yields even with the use of fertilizers.The solution to this problem is possible through the improvement of the technology of cultivation of plants, based on modern methodological principles of soil fertility management systems, providing primarily the creation of optimal conditions for the growth of vegetable crops [1,7,9,10,15].

2. Materialandmethods

Researches were conducted in the model farm of the Institute of Vegetable, the total area of which is 120 hectaresin 2015-2018. According to varieties, these soils are thick and medium, irrigated and sewage, loamy and light loamy. The physico-chemical analyses are performed on following methods [2]: humus and total nitrogen by I.V.Tyurin, mechanical composition – by N.A.Kachinsky, pH - water suspension – by pH-metre, CO_2 carbonate – by calcimeter, total phosphorus – by A.M.Mesheriakov, total water extract – by D.I.Ivanov.

3. Results and discussion

The relief of Absheron peninsula is flat, the surface is planned, groundwater is at a depth of 3-5 m. To ensure the existence of the species in this ecological situation, the plants must receive light in the quantities necessary for photosynthesis and create a certain mass of organic matter. Therefore, radiation is one of the main factors determining the agroclimate of vegetable crops. The southern location of the Absheron peninsula favors an abundant influx of light and heat. The magnitude of the radiation balance is 63-65 kcal / cm^2[5].

The total expression of climatic features is the climate continentality coefficient (according to N.I. Ivanov). With an increase in continental climate, a less favorable distribution of precipitation and temperatures is observed during the growing season, and with a reduction in this period, the probability of droughts increases. CC for the Absheronpeninsula varies between 165-166.Moisture coefficient is the ratio of the average annual precipitation to the average annual evaporation. MC within the Absheron peninsula varies from 0.10-0.25.

As a parameter determining atmospheric moisture, the probability of droughts is a good indicator for determining the magnitude of the climatic norm of irrigation in a given territory. The probability of droughts on the Absheron peninsula is 46-48% [6]. Cultivated soils are characterized by a fully formed modern cultivated layer with a thickness of 45-55 cm and more. Arable (A1 'a) and subsurface layers are well formed and structured, with a thickness of 25-30 cm and 20-25 cm, respectively [14].

Agrophysical indicators of cultivated soils are optimal: the content of the silt fraction (particles <0.001 mm) is 20-22%, and physical clay (particles <0.01 mm) - 45-55 cm, which corresponds to the loamy texture. In addition, there is a sharp change in the particle size distribution along the profile. The degree of aggregation is quite high - 50-60% [12].

Cultivated soils are characterized by the fact that they are relatively well supplied with humus. These soils in the arable and subsurface horizons contain humus, respectively, 1.6% (44 t/ha) and 1.2% (36 t/ha). The humus profile of these soils is powerful, in the first half-meter layer the humus is 1.4% or 80 t/ha, in the second 1.1% or 36 t / ha. The 1 meter layer of these soils contains on average 1.25% or 116 t/ha of humus. The C: N ratio is comparatively wider than 4-6, the sum of absorbed bases is high 22-25 mg-eq/100g of soil (Table 1).

Table 1. Indicators of the soil composition of gray-brown irrigated soils

Indicators	Interval	M
1. Thickness of arable horizon A 1 a, cm	25 - 30	27
2. Thickness of subsurface horizon A 1’a, cm	20 - 25	22
3. The thickness of the modern cultivated horizon, cm	45 - 55	50
4. Degree of compaction expressed subsurface	-	
5. Depthofsalt, cm	100 - 120	110
6. The content of the clay fraction, <0.001%	18 - 22	20
7. Physicalclaycontent,< 0.01 %	45 - 55	50
8. Degreeofaggregation, %	50 - 60	55
9. The content of humus, %:		
0 - 20 cm	0.9-2.2	1.5
0 - 50 cm	0.7-2.0	1.3
0 - 100 cm	0.6-1.4	1.0
10. C : N	4 - 6	5
11. Sum of absorbed bases, mg-eq/100g of soil	22 - 25	23.6

One of the important agrophysical indicators is the number of water-resistant aggregates (> 0.25 mm) due to improper irrigation, unrestricted use of organic and local fertilizers, improper crop alternation, etc., decreases. Therefore, with proper farming in cultivated soils, the number of water-resistant aggregates is restored and increases (30-35%). The density of the arable horizon is 1.2-1.3 g/cm^3[11]. These soils are well provided with productive moisture of 70-80 mm and have an optimal water permeability of 3.2-4.0 mm/min. (Table 2).

Table 2. Indicators of the soil properties of gray-brown irrigated soils

Indicators	Interval	M
1. Water-resistantaggregates>0.25 mm, %	25 - 30	27.5
2. Volumeweight, g/cm^3	1.2 – 1.3	1.26
3. Productivemoisture0 - 25 mm, %	70 - 80	76
4. Permeability, mm/min	3.2 – 4.0	3.6
5. Ca : Mg, %	2 - 4	3
6. CaCO$_3$, %	9 - 15	12
7. pH	8.5 – 9.2	8.8
8. Saltcontent, %	0.1 – 0.2	0.15

One of the important agrochemical properties is the ratio of Ca: Mg in the absorbed bases. It is known that the number of absorbed bases in virgin gray-brown soils is lower than in cultivated soils. In cultured gray-brown soils the Ca: Mg ratio is 2-4.In recent years, with intensive irrigation of gray-brown soils, carbonate movement along the profile has increased [3]. In the arable horizon, the amount of carbonates is 6–9%, then increases along the profile and in soil-forming rocks is 9–15%.

In irrigated gray-brown soils, due to intensive irrigation and farming, the reaction of the soil environment becomes alkaline — the soil pH— 8.5-9.2. The salt profile and salt composition of Absheron gray-brown soils depends on the natural drainage of the territory, the groundwater regime and the degree of soil cultivation [8].In the Absheron base in virgin soils, the depth of groundwater is 3-5 m, the amount of soluble salts in irrigated soils is 0.2-0.4%. In highly cultured soils, the amount of readily soluble salts is very low — 0.1–0.2%; light solonetzification is found from 100–120 cm depth [13].

In the soil regime, the interaction of soil moisture and the temperature of the soil air and the food regime of the soil with cultivated crops is realized. Soil temperatures is 12–13 °C (minimum) and 25–27 °C (maximum), soil moisture are optimal, respectively 18–20% and 24–25% and favor the activity of biological processes.

Cultivated irrigated gray-brown soils are provided with common and easily accessible forms of nutrients [95]. In the upper half-meter layer (0-50 cm) contains 0.12-0.14%; 6.6-7.6 t/ha of nitrogen, 0.3-0.4%; 20-24 t/ha of phosphorus, 1.4-1.7%; 80-100 t/ha of potassium. From the supply of mobile P_2O_5 8–12 mg/kg and exchangeable K_2O 310–390 mg/kg, it is clear that these elements of the soil are provided poorly and moderately, therefore, they need ofmaking differentiated norms of mineral fertilizers (Table 3).

Over the past 10 years in connection with the real situation is not observed correctly agricultural activities. The farm is not conducted crop rotation, are not complied with irrigation methods and norms, are not used almost organic and mineral fertilizers, local composts [4]. As a result, the amount of nutrients in the soil decreases, and replenishing them is not in sufficient quantity.

Table 3. Indicators of soil regimes of gray-brown irrigated soils

Indicators	Interval	M
1.The temperature regime, ^{0}C		
minimum	12-13	12
maximum	25-27	26
2. The moisture regime, %		
minimum	18-20	19
maximum	24-25	25
3. Nutrition regime		
Content and supply of nitrogen (0-50 cm), %, t/h	0.9-0.15 6.6-7.6	0.12 7.1
Content and supply of phosphorus (0-50 cm),%,t/h	0.3-0.4 20-24	0.32 22
Content and supply of potassium(0-50 cm), %, t/h	1.4-1.7 80-100	1.6 88
P_2O_5mobile, mg/kg		
0 - 20 cm	10 - 12	11
0 - 50 cm	8 - 12	10
K_2O exchangeable, mg/kg		
0 - 20 cm	350 - 390	371
0 - 50 cm	310 - 350	332

4. Conclusion

To determine the current state of soil fertility of gray-brown irrigated soils under vegetable cultures of the Absheron peninsula, a complex agroecological characteristic of the soil was carried out, including the study of agrophysical and agrochemical pecularities of soils on the basis of field, fund and laboratory investigations.It has been established that the fertility indicators of the studied soils are not sufficiently optimal for the cultivation of vegetable crops in a investigated area and need to be carried out with agrotechnical and land melioration measures.

References

1. Aitbayev T.Y., Mamyrbekov Z.Z., Aitbayeva A.T. OnLine Journal of Biological Sciences, 18, 8 (2018)
2. Arinushkina E.V. Manual on chemical analysis of soil. Moscow University Press, 1970, 488 p.
3. Babayev M.P., Hasanov V.H., JafarovaCh.H., Huseynova S.M. Morphogenetic diagnostics, nomenclature and classification of Azerbaijan soils. Baku: Science, 2011, 448 p.
4. Babayev M.P., Jafarov A.M., JafarovaCh.H., Huseynova S.M., Gasimov X.M., Modern soil cover of the Greater Caucasus. Baku: Science, 2017, 345 p.
5. Babayev V.A. Annals of Agrarian Science, 7, 69 (2009).
6. Babayev V.A. Antropogenic influence on ecosystem in the Absheron peninsula and effect on environment and food. Proceedings of third international symposium “Ecological approaches towards the production of safety food”, Plovdiv, 2009, p. 341-346
7. Dubovitsky A.A., Klimentova E.A. Problems and prospects of vegetable growing. Technologies of food and processing industry of agriculture - Healthy food products, 2014, v.3, p.89-95
8. Manafova F.A., Aliyeva Sh.M. Proceedings of International scientific conference “Soils of Azerbaijan: genesis, geography, melioration and ecology”, Baku, 2012, v.2, p. 361-366
9. Orujova N.İ. Crop rotation is the main factor in the reproduction of vegetable-friendly soils in the wet subtropics of Azerbaijan. Proceedings of the 66th International Scientific Practical Conference “Agrarian science as a basis for regional food security”. Ryazan, 2015, v. I, P.156-161
10. Orujova N.İ. J. Int. Environmental Application & Science, 3, 351 (2008).
11. Sadikova M.E. Proceedings of the Society of Soil Scientists of Azerbaijan, 16, 434 (2004).
12. Sultanova N.A. Monitoring of vegetable soils in the northeastern slope of the Greater Caucasus of Azerbaijan.Proceedings of International scientific-practical conference "Scientific-practical ways to improve environmental sustainability and socio-economic support for agricultural production", Russia, Astrakhan, 2017. p.409-413.
13. Sultanova N.A. Ganja Regional Scientific Center of ANAS. News Bulletin, 44, 39 (2011).
14. Sultan-zade F.V. Ecological assessment of soil cover in the Absheron Peninsula. Thesis of diss.biol.sci., Baku, 1997, 23 p.
15. Shukurov S.X. Annals of agrarian science, 10, 1 (2012).

*Corresponding author: kanan.huseynov@gmail.com